Journal of Experimental and Theoretical Physics, Vol. 94, No. 6, 2002, pp. 1043–1056.
Translated from Zhurnal Éksperimental'noĭ i Teoreticheskoĭ Fiziki, Vol. 121, No. 6, 2002, pp. 1219–1234.

GRAVITATION, ASTROPHYSICS

Neutrino Interaction with Nucleons in the Envelope of a Collapsing Star with a Strong Magnetic Field

A. A. Gvozdev* and I. S. Ognev**

Yaroslavl State University, ul. Sovetskaya 14, Yaroslavl, 150000 Russia
**e-mail: gvozdev@univ.uniyar.ac.ru*
***e-mail: ognev@univ.uniyar.ac.ru*

Received January 29, 2002

Abstract—The interaction of neutrinos with nucleons in the envelope of a remnant of collapsing system with a strong magnetic field during the passage of the main neutrino flux is investigated. General expressions are derived for the reaction rates and for the energy–momentum transferred to the medium through the neutrino scattering by nucleons and in the direct URCA processes. Parameters of the medium in a strong magnetic field are calculated under the condition of quasi-equilibrium with neutrinos. Numerical estimates are given for the neutrino mean free paths and for the density of the force acting on the envelope along the magnetic field. It is shown that, in a strong toroidal magnetic field, the envelope region partially transparent to neutrinos can acquire a large angular acceleration on the passage time scales of the main neutrino flux. © *2002 MAIK "Nauka/Interperiodica".*

1. INTRODUCTION

Collapsing systems with rapidly rotating remnants are of great interest in astrophysics. Such remnants can be formed during the explosions of type II supernovae [1, 2], during the mergers of close neutron-star binaries [3], and during accretion-driven collapse [4]. About 10% of the released gravitational energy is known to transform into the thermal energy of the remnant and to be emitted in the form of neutrinos, irrespective of the origin of the collapse [1–5]. A core rotating like a solid and a disk (envelope) rotating with an angular velocity gradient are formed in the remnant of collapse on time scales of the order of a second. The compact core of typical sizes $R_c \sim 10$ km, subnuclear densities, and high temperatures ($T \gtrsim 10$ MeV) is opaque to neutrinos. Being less dense and hot ($T \sim 3$–6 MeV), the envelope with typical sizes of several tens of kilometers is partially transparent to neutrinos [2–5]. Within several seconds after its formation, the remnant of collapse effectively cools down via neutrino radiation. The neutrino luminosities during this period are typically $L_\nu \sim 10^{52}$ erg s^{-1} [5] (the passage stage of the main neutrino flux). This neutrino flux could have a strong effect on the dynamics of the envelope; in particular, it could trigger its ejection [6]. Detailed calculations show that, for a spherically symmetric collapse, the neutrino absorption by the envelope is not intense enough for its ejection [7]. However, such envelope ejection is possible for a millisecond remnant of collapse with a strong toroidal magnetic field (the magnetorotational model of a supernova explosion [1]).

Because of its rapid rotation and large viscosity, convection, a turbulent dynamo, and large angular-velocity gradients arise in the remnant of collapse. These processes can lead to the rapid (of the order of several seconds) generation of a strong poloidal magnetic field with a strength up to $B \sim 3 \times 10^{15}$ G on a coherence length $L \sim 1$ km in the core of the remnant of collapse [8]. Having arisen in this way, the strong poloidal field can persist in a young neutron star for about 10^3–10^4 years. Duncan and Thompson [8] called such young pulsars magnetars. There are strong grounds for suggesting that magnetars are observed in nature as soft gamma-ray repeaters (SGRR) [9] or as anomalous X-ray pulsars (AXP) [10]. An angular-velocity gradient in the envelope leads to the generation of a secondary toroidal magnetic field through the winding of field lines of the primary poloidal magnetic field frozen in the rotating envelope plasma. In this case, strong poloidal magnetic fields of strength $B \sim 10^{15}$–10^{17} G can emerge in the envelope of a millisecond remnant of collapse in typical times of ~1 s [11]. Such strong fields can significantly affect the envelope dynamics even if they persist for several seconds. For example, a magnetic field of strength $B \sim 10^{17}$ G can produce an anisotropic gamma-ray burst [12] and, as we already pointed out above, can trigger the ejection of the supernova envelope [1].

Significantly, such strong magnetic fields can arise in the envelope during the passage of the main neutrino flux through it (within several seconds after collapse). Therefore, it is of interest to investigate the possible dynamical effects that emerge when the neutrino flux passes through a strongly magnetized envelope. Effects of this kind are discussed in the literature. For example, Bisnovatyĭ-Kogan [13] estimated the magnetar velocity

gained through a neutrino dynamical kick in the case where the magnetic-field strengths on its hemispheres differed significantly. In this case, the kick arises because the energy transferred from the neutrinos to the medium in β processes depends on the magnetic-field strength. However, we will discuss the dynamical effects of a different nature. Because of the parity violation in weak processes, neutrinos are known to be emitted and absorbed in a magnetic field asymmetrically, which can lead to macroscopic momentum transfer from the neutrinos to the medium [14, 15]. Thus, the envelope region filled with a strong toroidal magnetic field can acquire a large macroscopic angular momentum when an intense neutrino flux passes through it [16].

Here, we estimate the asymmetry in momentum transfer from the neutrinos to the medium during the neutrino interaction with nucleons in the envelope of a remnant of collapse at the stage of the main neutrino radiation. This paper has the following structure. In Section 2, we stipulate basic physical assumptions about the parameters of the medium, magnetic-field strengths, and the neutrino distribution function. In Section 3, we derive general expressions for the reaction rates and for the components of the energy–momentum transferred from the neutrinos to a volume element of the medium per unit time in the direct URCA processes for a strong magnetic field. In Section 4, the same quantities are calculated for the scattering of (anti)neutrinos of all types by nucleons of a magnetized medium. Numerical estimates for the parameters of the medium, neutrino mean free paths, and the force density along the magnetic field are presented in Section 5. In Section 6, we compare our results with the results of similar calculations and briefly discuss the possible dynamical effects of the parity violation in the envelope of a collapsing star. The calculations of our basic results are detailed in Appendices A, B, and C. Throughout the paper, we use a system of units with $c = \hbar = k_B = 1$.

2. PHYSICAL ASSUMPTIONS

Here, we investigate basic neutrino–nucleon processes in the envelope of a remnant of collapse with a strong magnetic field at the stage of the main neutrino radiation. We consider the direct URCA processes

$$n + \nu_e \longrightarrow p + e^-, \tag{1}$$

$$p + e^- \longrightarrow n + \nu_e, \tag{2}$$

$$p + \tilde{\nu}_e \longrightarrow n + e^+, \tag{3}$$

$$n + e^+ \longrightarrow p + \tilde{\nu}_e \tag{4}$$

and the scattering of neutrinos of all types by nucleons:

$$N + \nu_i \longrightarrow N + \nu_i, \tag{5}$$

$$N + \tilde{\nu}_i \longrightarrow N + \tilde{\nu}_i, \tag{6}$$

$$\nu_i = \nu_e, \nu_\mu, \nu_\tau, \quad N = n, p.$$

Note that β decay is suppressed under the conditions considered. A quantitative estimate of the asymmetry in momentum transfer follows from the expression for the energy–momentum transferred in these processes from the neutrinos to a unit of volume of the medium per unit time:

$$\frac{dP_\alpha}{dt} = \left(\frac{dQ}{dt}, \mathcal{J}\right) = \frac{1}{V} \times \int \prod_i dn_i f_i \prod_f dn_f (1 - f_f) \frac{|S_{if}|^2}{\mathcal{T}} q_\alpha. \tag{7}$$

Here, dn_i and dn_f are the numbers of initial and final states in the element of phase volume; f_i and f_f are the distribution functions of the initial and final particles; $|S_{if}|^2/\mathcal{T}$ is the square of the S-matrix element for the process per unit time; and q_α is the 4-momentum transferred to the medium in a single reaction. An important quantity that characterizes the process is also its rate Γ defined as

$$\Gamma = \frac{1}{V} \int \prod_i dn_i f_i \prod_f dn_f (1 - f_f) \frac{|S_{if}|^2}{\mathcal{T}}. \tag{8}$$

In particular, the neutrino mean free paths can be easily determined from this quantity:

$$\bar{l}_\nu = \frac{N_\nu}{\Gamma_\nu^{\text{tot}}}, \tag{9}$$

where N_ν is the local neutrino number density and Γ_ν^{tot} is the sum of the absorption and scattering rates for the neutrinos of a given type.

In the reactions of neutrino interaction with matter, we separate the medium and the neutrino flux passing through it. By the medium, we mean free electrons, positrons, and nucleons with an equilibrium Dirac distribution function:

$$f_i = \frac{1}{\exp(E_i/T - \eta_i) + 1},$$

where $\eta_i = \mu_i/T$ and E_i, and μ_i are the energy and chemical potential for the particles of a given type. We disregard the effect of envelope rotation on the distribution functions, because the rotation velocity is nonrelativistic even for a millisecond remnant of collapse. At typical (for the envelope) densities ($\rho \sim 10^{11}$–10^{12} g cm^{-3}) and temperatures ($T \sim$ several MeV), the e^+e^- plasma is ultrarelativistic and the nucleon gas is a Boltzmann nonrelativistic one.

We consider the case of a strong magnetic field, i.e., assume that the parameters of the medium and the magnetic-field strength are related by

$$m_p T \gg 2eB \gtrsim \mu_e^2, \quad T^2 \gg m_e^2, \tag{10}$$

where m_p and m_e are the proton and electron masses and $e > 0$ is an elementary charge. Condition (10) implies that the electrons and positrons occupy mainly the lower Landau level, while the protons occupy many levels.

The quantity (7) is known to be zero [17] for a thermal equilibrium of the neutrinos with the medium. However, we consider the envelope region where the neutrino distribution function deviates from the equilibrium one. In the model of spherically symmetric collapse, the local (anti)neutrino distribution without a magnetic field can be fitted as follows [5, 18]:

$$f_\nu = \frac{\Phi_\nu(r, \chi)}{\exp(\omega/T_\nu - \eta_\nu) + 1}. \tag{11}$$

Here, χ is the cosine of the angle between the neutrino momentum and the radial direction, ω is the neutrino energy, T_ν is the neutrino spectral temperature, and η_ν is the fitting parameter. In this paper, we ignore the effect of a magnetic field on the neutrino distribution function. This approximation is good enough when the neutrino mean free path is larger than or of the order of the region occupied by a strong magnetic field. In the model considered in [11], this region does not exceed a few kilometers in size, whereas the mean free paths for the neutrinos of different types are estimated to be 2–5 km. Thus, in our subsequent calculations, we use the neutrino distribution function (11). We will return to a discussion of this issue in Section 5.

3. DIRECT URCA PROCESSES

We used the standard low-energy Lagrangian for the weak interaction of neutrinos with nucleons to calculate the *S*-matrix element of the direct URCA processes. Our calculations of the square of the *S*-matrix element are detailed in Appendix A. In the limit of a strong magnetic field, where the electrons and positrons occupy only the ground Landau level, we derived the expression

$$\frac{|S_{if}|^2}{\mathcal{T}} = \frac{G_F^2 \cos^2\theta_c \pi^3}{2L_y L_z V^2 \omega\varepsilon} \exp\left(-\frac{Q_\perp^2}{2eB}\right) \times \left[\sum_{n=0}^{\infty} \frac{|M_+|^2}{n!}\left(\frac{Q_\perp^2}{2eB}\right)^n \delta^{(3)} + \sum_{n=1}^{\infty} \frac{|M_-|^2}{(n-1)!}\left(\frac{Q_\perp^2}{2eB}\right)^{n-1} \delta^{(3)}\right], \tag{12}$$

where

$$|M_+|^2 = 4(\varepsilon + p_\parallel) \times [(1 + g_a)^2(\omega + k_\parallel) + 4g_a^2(\omega - k_\parallel)], \tag{13}$$

$$|M_-|^2 = 4(1 - g_a)^2(\varepsilon + p_\parallel)(\omega + k_\parallel). \tag{14}$$

Here, $\delta^{(3)}$ is the delta function of the energy, the momentum along the magnetic field, and one of its transverse components that are conserved in the reactions; $Q_\perp^2$ is the square of the transferred momentum across the magnetic field in the corresponding reaction; n is the index of summation over the proton Landau levels; ε, $p_\parallel$, ω, and $k_\parallel$ are the energy and the momentum component along the magnetic field for the electron and neutrino, respectively; $\mathcal{T} L_x L_y L_z$ is the normalization 4-volume; g_a is the axial constant of a charged nucleon current ($g_a \approx 1.26$ in the low-energy limit); G_F is the Fermi constant; and θ_c is the Cabibbo angle.

Note that we derived the above expression for $|S_{if}|^2$ in [16]. It is identical to that from [19] and [20] when the erroneous sign of the axial constant g_a is corrected (for the formal change $g_a \longrightarrow -g_a$). However, the paper [21], where only the term $n = 0$ in the square of the *S*-matrix element was calculated, contains a difference in expression (13). To obtain the expression for S^2 from [21], the factor $(1 + g_a^2)$ must be substituted for $(1 + g_a)^2$ in the first term of the amplitude (13).

For convenience, we calculate the 4-momentum, dP_α/dt, transferred to the medium in the direct URCA processes involving neutrinos (1), (2) and antineutrinos (3), (4) separately. Using the *T* invariance of the square of the *S*-matrix element for these processes and explicit particle distribution functions for the medium, we can represent the quantity (7) as

$$\frac{dP_\alpha^{(\nu, \tilde\nu)}}{dt} = \int \frac{d^3k}{(2\pi)^3} k_\alpha \mathcal{H}^{(\nu, \tilde\nu)} \times \left[\left(1 + \exp\left(-\frac{\omega}{T} \pm \delta\eta\right)\right) f_{\nu, \tilde\nu} - \exp\left(-\frac{\omega}{T} \pm \delta\eta\right)\right]. \tag{15}$$

Here, $\delta\eta = (\mu_e + \mu_p - \mu_n)/T$, k_α is the 4-momentum of the (anti)neutrino, and $\mathcal{H}^{(\nu, \tilde\nu)}$ is the absorption coefficient in the (anti)neutrino absorption reaction defined as

$$\mathcal{H}^{(\nu, \tilde\nu)} = \int dn_p dn_n dn_e \frac{|S_{if}|^2}{\mathcal{T}} \times \left\{\begin{array}{l} f_n(1 - f_p)(1 - f_{e^-}) \\ f_p(1 - f_n)(1 - f_{e^+}) \end{array}\right\}. \tag{16}$$

Note that under β-equilibrium conditions, when

$$\eta_\nu = \delta\eta = \frac{\mu_e + \mu_p - \mu_n}{T},$$

expression (15) for the transferred momentum is

$$\frac{dP_\alpha^{(\nu, \tilde\nu)}}{dt} = \int \frac{d^3k}{(2\pi)^3} \times k_\alpha \left(1 + \exp\left(-\frac{\omega}{T} \pm \eta_\nu\right)\right) \mathcal{H}^{(\nu, \tilde\nu)} \delta f^{\nu, \tilde\nu}, \tag{17}$$

where $\delta f^{\nu,\tilde{\nu}}$ is the deviation of the neutrino distribution function from the equilibrium one. Thus, the 4-momentum transferred from the neutrinos to the medium is nonzero only in a partially transparent (to neutrinos) envelope and vanishes in a dense β-equilibrium remnant core.

We calculated the absorption coefficient (16) in the strong-field limit (10) by assuming the nucleon gas to be nondegenerate. In this case, the calculation technique is simplified sharply compared to the more general case. For this reason, we discuss the details of our calculation of the absorption coefficient in Appendix B. Here, we present only the final result that was previously published [16] without explaining the details of our calculations:

$$\mathcal{K}^{(\nu,\tilde{\nu})} = \frac{G_F^2\cos^2\theta_c}{2\pi}eBN_{(n,p)} \times\left((1+3g_a^2)-\frac{k_\parallel}{\omega}(g_a^2-1)\right)\left(1+\exp\left(\pm a-\frac{\omega}{T}\right)\right)^{-1}, \tag{18}$$

where the terms of order eB/m_pT were discarded. Here, N_n, N_p, m_n, and m_p are the neutron and proton number densities and masses,

$$a = \frac{\mu_e-\Delta}{T}, \quad \Delta = m_n - m_p.$$

Note that the derived expression is identical to that in [19].

For completeness, we give the expressions for the energy density dQ/dt and for the rates Γ of the direct URCA processes (1)–(4):

$$\left\{\begin{matrix}\Gamma\\ dQ/dt\end{matrix}\right\}_{n+\nu_e\to p+e^-} = \mathcal{A}J_\nu\frac{N_n}{N_B}\left\{\begin{matrix}T^3C_2(a,T_\nu,\eta_\nu)\\ T^4C_3(a,T_\nu,\eta_\nu)\end{matrix}\right\}, \tag{19}$$

$$\left\{\begin{matrix}\Gamma\\ dQ/dt\end{matrix}\right\}_{p+e^-\to n+\nu_e} = \mathcal{A}\frac{N_p}{N_B}e^{\Delta/T} \times\left\{\begin{matrix}T^3B_2(a)-T^3J_\nu D_2(a,T_\nu,\eta_\nu)\\ -T^4B_3(a)+T^4J_\nu D_3(a,T_\nu,\eta_\nu)\end{matrix}\right\}, \tag{20}$$

$$\left\{\begin{matrix}\Gamma\\ dQ/dt\end{matrix}\right\}_{p+\tilde{\nu}_e\to n+e^+} = \mathcal{A}J_{\tilde{\nu}}\frac{N_p}{N_B}\left\{\begin{matrix}T^3C_2(-a,T_{\tilde{\nu}},\eta_{\tilde{\nu}})\\ T^4C_3(-a,T_{\tilde{\nu}},\eta_{\tilde{\nu}})\end{matrix}\right\}, \tag{21}$$

$$\left\{\begin{matrix}\Gamma\\ dQ/dt\end{matrix}\right\}_{n+e^+\to p+\tilde{\nu}_e} = \mathcal{A}\frac{N_n}{N_B}e^{-\Delta/T} \times\left\{\begin{matrix}T^3B_2(-a)-T^3J_{\tilde{\nu}}D_2(-a,T_{\tilde{\nu}},\eta_{\tilde{\nu}})\\ -T^4B_3(-a)+T^4J_{\tilde{\nu}}D_3(-a,T_{\tilde{\nu}},\eta_{\tilde{\nu}})\end{matrix}\right\}, \tag{22}$$

where the dimensional coefficient $\mathcal{A}$ is defined as

$$\mathcal{A} = \frac{2G_F^2\cos^2\theta_c}{(2\pi)^3}(1+3g_a^2)eBN_B,$$

$$N_B = N_n + N_p.$$

Our introduced functions B_n, C_n, and D_n can be expressed in terms of the integrals as follows:

$$B_n(a) = \int_0^\infty\frac{Z^n dZ}{\exp(Z-a)+1},$$

$$C_n(a,T_\nu,\eta_\nu) = \int_0^\infty\frac{Z^n dZ}{(\exp(a-Z)+1)\left(\exp\left(\frac{ZT}{T_\nu}-\eta_\nu\right)+1\right)},$$

$$D_n(a,T_\nu,\eta_\nu) = \int_0^\infty\frac{Z^n dZ}{(\exp(Z-a)+1)\left(\exp\left(\frac{ZT}{T_\nu}-\eta_\nu\right)+1\right)}.$$

The parameter

$$J_\nu = \left(\int f_\nu d^3k\right) \times\left(\int\left(1+\exp\left(\frac{\omega}{T_\nu}-\eta_\nu\right)\right)^{-1}d^3k\right)^{-1} \tag{23}$$

has the meaning of the ratio of the actual local neutrino number density to the value for the Fermi–Dirac distribution at the same spectral temperature T_ν.

Our calculations of the components of momentum (15) transferred to the medium during neutrino reradiation show that the emerging radial force is much weaker than the gravitational force and cannot significantly affect the envelope dynamics. Thus, of interest is the force component acting along the magnetic field. For a toroidal field, the density of this force can be represented as

$$\mathcal{J}_{\parallel}^{urca} = \frac{1}{6}\frac{g_a^2-1}{3g_a^2+1}\mathcal{A}T^4\left[\frac{N_p}{N_B}(3\langle\chi_\nu^2\rangle-1)e^{\Delta/T}B_3(a) + \frac{N_n}{N_B}(3\langle\chi_{\tilde\nu}^2\rangle-1)e^{-\Delta/T}B_3(-a)\right] \quad (24)$$
$$-\frac{1}{2}\frac{g_a^2-1}{3g_a^2+1}\left[(1-\langle\chi_\nu^2\rangle)\frac{dQ_\nu}{dt}+(1-\langle\chi_{\tilde\nu}^2\rangle)\frac{dQ_{\tilde\nu}}{dt}\right].$$

Here,

$$\langle\chi_\nu^2\rangle = \left(\int\chi^2\omega f_\nu d^3k\right)\left(\int\omega f_\nu d^3k\right)^{-1}, \quad (25)$$

where $\langle\chi_\nu^2\rangle$ is the mean square of the cosine of the angle between the neutrino momentum and the radial direction. As follows from this expression, the asymmetry in momentum transfer is nonzero for two reasons: either the neutrino distribution is anisotropic ($\langle\chi^2\rangle \neq 1/3$), or energy is transferred to the medium in the URCA processes (1)–(4) ($dQ_{\nu,\tilde\nu}/dt \neq 0$). Interestingly, for an isotropic neutrino distribution, the force density is directed along the field when the medium cools down and opposite to the field when it heats up through the URCA processes.

4. THE NEUTRINO SCATTERING BY NUCLEONS

We used the nonrelativistic vacuum wave functions of nucleons with a certain spin component along the magnetic-field direction to calculate the *S*-matrix element in the reactions of (anti)neutrino scattering by nucleons (5) and (6). Our calculations are detailed in Appendix C. Below, we give only the final expression for the square of the *S*-matrix element for the neutrino scattering by nucleons:

$$\frac{|S_{if}|_\nu^2}{\mathcal{T}} = \frac{(2\pi)^4G_F^2}{2V^3\omega\omega'}\delta^{(4)}[(c_v^2+3c_a^2)\omega\omega' + (c_v^2-c_a^2)\mathbf{k}\cdot\mathbf{k}' + 2c_vc_a(\omega k_\parallel' + \omega' k_\parallel)(S+S') - 2c_a^2(\omega k_\parallel' - \omega' k_\parallel)(S-S') + (c_v^2-c_a^2)(\omega\omega'+\mathbf{k}\cdot\mathbf{k}')SS' + 4c_a^2k_\parallel k_\parallel' SS'] \quad (26)$$

The expression for $|S_{if}|^2/\mathcal{T}$ for the antineutrino scattering by nucleons can be derived from (26) by the change $k \longleftrightarrow k'$:

$$|S_{if}|_{\tilde\nu}^2(k,k') = |S_{if}|_\nu^2(k',k). \quad (27)$$

Here, c_v and c_a are the vector and axial constants for a neutral nucleon current. In the low-energy limit [22],

$$c_v = -\frac{1}{2},\quad c_a \approx -\frac{0.91}{2} \quad \text{for neutrons,}$$
$$c_v = \frac{0.07}{2},\quad c_a \approx \frac{1.09}{2} \quad \text{for protons.} \quad (28)$$

The conservation of energy–momentum is defined as

$$\delta^{(4)} = \delta^{(4)}(\mathcal{P}+k-\mathcal{P}'-k'),$$

where $k = (\omega, \mathbf{k})$; $k' = (\omega', \mathbf{k}')$; $\mathcal{P}$ and $\mathcal{P}'$ are the 4-momenta of the initial and final neutrinos and nucleons, respectively; $k_\parallel$ and $k_\parallel'$ are the momentum components of the initial and final neutrinos along the magnetic field; and S and S' are the components of the polarization vectors for the initial and final nucleons along the magnetic field ($S = \pm 1$).

Analysis of the kinematics of the neutrino scattering by nucleons shows that the energy transferred in these reactions to an element of the medium is negligible compared to the energy transferred in the URCA processes. This can also be verified by a direct calculation using the technique detailed in Appendix C. Therefore, below, we are concerned only with the momentum transferred along the magnetic field. This component arises from a partial polarization of the nucleon gas in the field, because nucleons with different polarizations have different energies:

$$E_N = m_N + \frac{\mathcal{P}^2}{2m_N} - g_NS\frac{eB}{2m_N},$$

where g_N is the nucleon magnetic factor ($g_n \approx -1.91$ for the neutron and $g_p \approx 2.79$ for the proton). Taking into account the energy of interaction between the nucleon magnetic moment and the magnetic field, we obtained the following expression for the force density along the magnetic field during the scattering of neutrinos of one type by neutrons or protons (see Appendix C for the details of our calculations):

$$\mathcal{J}_\parallel^{(\nu_i)} = -\frac{G_F^2g_N}{2\pi}\frac{eB}{m_NT}N_NN_\nu \times\left\{(c_vc_a\langle\omega_\nu^3\rangle + c_a^2T\langle\omega_\nu^2\rangle)\left(\langle\chi_\nu^2\rangle-\frac{1}{3}\right) - c_a^2(\langle\omega_\nu^3\rangle - 5T\langle\omega_\nu^2\rangle)\left(\frac{5}{3}-\langle\chi_\nu^2\rangle\right) + 2c_a^2J_\nu(\langle\omega_\nu^3\rangle - 5T_\nu\langle\omega_\nu^2\rangle)(1-\langle\chi_\nu^2\rangle)\right\}, \quad (29)$$

where

$$\langle \omega_\nu^n \rangle = \left(\int \omega^n f_\nu d^3k\right)\left(\int f_\nu d^3k\right)^{-1}, \quad (30)$$

J_ν and $\langle \chi_\nu^2 \rangle$ are the quantities defined in the same way as in the URCA processes, and N_ν is the local neutrino number density. During the antineutrino scattering (6), the momentum transferred to the medium per unit time is given by expression (29) with the formal change $c_a^2 \longrightarrow -c_a^2$:

$$\mathcal{P}_\parallel^{(\tilde{\nu}_i)}(c_a^2) = \mathcal{P}_\parallel^{(\nu_i)}(-c_a^2). \quad (31)$$

For the Boltzmann neutrino distribution

$$f_\nu = \Phi_\nu(r, \chi)\exp\left(-\frac{\omega}{T_\nu}\right),$$

expression (29) can be simplified:

$$\mathcal{P}_\parallel^{(\nu_i)} = -\frac{6G_F^2 g_N}{\pi}\frac{eB}{m_N}N_N N_\nu T_\nu^2\left\{4c_a^2(2-\langle\chi_\nu^2\rangle) + \frac{5T_\nu}{T}\left[c_v c_a\left(\langle\chi_\nu^2\rangle - \frac{1}{3}\right) - c_a^2\left(\frac{5}{3} - \langle\chi_\nu^2\rangle\right)\right]\right\}. \quad (32)$$

Note also that, in the envelope of the remnant of collapse, the parameters of the distribution functions for the neutrinos and antineutrinos of type μ and τ are virtually identical [23]. This allows a simple expression to be written for the total (neutrinos plus antineutrinos of a given type) force density along the magnetic field:

$$\mathcal{P}_\parallel^{(\nu_i)} = -\frac{G_F^2 c_v c_a g_N}{\pi} \times \frac{eB}{m_N T}N_N N_\nu \langle\omega_\nu^3\rangle\left(\langle\chi_\nu^2\rangle - \frac{1}{3}\right). \quad (33)$$

As can be seen from formulas (29) and (31)–(33), there is an asymmetry in momentum transfer along the magnetic field, as in the URCA processes, either for an anisotropic neutrino distribution ($\langle\chi^2\rangle \neq 1/3$) or when the neutrino spectral temperature differs from the temperature of the medium ($T_\nu \neq T$). Interestingly, the force densities along the field, $\mathcal{P}_\parallel^{(\nu_i)}$, during the scattering by neutrons and protons are directed oppositely. This follows from the fact that the expression for the force density is proportional to the nucleon magnetic factor g (recall that $g_n \approx -1.91$ for the neutron and $g_p \approx 2.79$ for the proton). Under actual conditions in the envelope of the remnant of collapse, it is commonly assumed that $N_p/N_B \ll 1$. We see from expressions (29) and (31) that the force density is proportional to the nucleon number density. Thus, the scattering by neutrons mainly contributes to the quantity $\mathcal{P}_\parallel$.

For completeness, below, we give expressions for the dominant contribution (with terms on the order of $eB/m_N T$ and $\sqrt{T/m_N}$ disregarded) to the rate (8) of scattering of (anti)neutrinos of any type by nucleons:

$$\Gamma^{sc} = \frac{G_F^2}{\pi}(c_v^2 + 3c_a^2)N_N N_\nu \langle\omega_\nu^2\rangle \times\left[1 - J_\nu\left(1 - \frac{4T_\nu\langle\omega_\nu\rangle}{\langle\omega_\nu^2\rangle}\right)\right]. \quad (34)$$

Recall that c_v and c_a are the vector and axial constants of a neutral nucleon current, which change only when the type of nucleon changes [see (28)] in the scattering reactions. Note that the scattering reaction rates and, hence, the neutrino mean free paths in these processes are virtually independent of the magnetic field.

5. NUMERICAL ESTIMATES

For the force density along the magnetic field generated in the processes of neutrino interaction with nucleons (1)–(6) to be numerically estimated, the parameters of the medium and the neutrino radiation must be specified. Recall that we consider a sufficiently dense ($\rho \sim 10^{11}$–10^{12} g cm^{-3}) and hot ($T \sim$ several MeV) envelope region that is partially transparent to neutrinos. Part of this envelope with a characteristic size of 1–3 km is assumed to be filled with a strong toroidal magnetic field of typical strength $B \gtrsim 10^{16}$ G. For such envelope parameters and magnetic-field strengths, condition (10) is satisfied and, hence, all our expressions are valid. Recall that we used the local nonequilibrium neutrino distribution function (11) while disregarding the effect of the magnetic field on it. Below, we verify the validity of this approximation by estimating the mean free paths for the neutrinos of various types and by comparing them with the size of the region filled with a strong magnetic field. The results from [23] were used to fit the neutrino-radiation parameters. In the above paper, a numerical solution was obtained for the neutrino distribution function at the stage of the main neutrino radiation after spherically symmetric collapse.

Analysis of the numerical values for $\langle\omega_\nu\rangle$ and $\langle\omega_\nu^2\rangle$ from [23] shows that the distribution functions for the neutrinos of various types are well fitted by the parameters

$$T_{\nu_e} \approx 3.3 \text{ MeV}, \quad T_{\tilde{\nu}_e} \approx 4.5 \text{ MeV}, \quad T_{\nu_{\mu,\tau}} \approx T_{\tilde{\nu}_{\mu,\tau}} \approx 6.6 \text{ MeV}, \quad \eta_{\nu_e} \approx 2.8, \quad \eta_{\tilde{\nu}_e} \approx 2.0, \quad \eta_{\nu_\mu,\nu_\tau} \approx \eta_{\tilde{\nu}_\mu,\tilde{\nu}_\tau} \approx 2.2. \quad (35)$$

For numerical estimates, we chose an envelope region with a typical density of the medium $\rho \approx 5 \times 10^{11}$ g cm^{-3}

and assumed the magnetic-field strength in it to be $B \approx 4 \times 10^{16}$ G. The local neutrino number densities in this region are

$$N_{\nu_e} \approx 9 \times 10^{32}\ \text{cm}^{-3}, \quad N_{\tilde{\nu}_e} \approx 3 \times 10^{32}\ \text{cm}^{-3},$$
$$N_{\nu_{\mu,\tau}} \approx N_{\tilde{\nu}_{\mu,\tau}} \approx 2.7 \times 10^{32}\ \text{cm}^{-3}. \tag{36}$$

The following values of our introduced parameters J_ν correspond to these number densities:

$$J_{\nu_e} \approx 0.23, \quad J_{\tilde{\nu}_e} \approx 0.05, \quad J_{\nu_{\mu,\tau}} \approx J_{\tilde{\nu}_{\mu,\tau}} \approx 0.01. \tag{37}$$

Accordingly, the mean square of the cosine of the angle between the neutrino momentum and the radial direction is

$$\langle \chi^2_{\nu_i} \rangle \approx \langle \chi^2_{\tilde{\nu}_i} \rangle \approx 0.385. \tag{38}$$

At the stage of the main neutrino radiation (within about 1–3 s after collapse), the parameters of the medium vary slowly through hydrodynamic processes compared to the time scales of 10^{-2}–10^{-3} s on which a quasi-equilibrium is established through the dominant URCA processes. For this reason, the medium is assumed to be in quasi-equilibrium:

$$\Gamma_{n \to p} = \Gamma_{p \to n}, \tag{39}$$

$$\frac{dQ}{dt} = 0, \tag{40}$$

where $\Gamma_{n \to p}$ and $\Gamma_{p \to n}$ are the sums of the rates of the processes with the conversion of a neutron into a proton and a proton into a neutron, respectively, and dQ/dt is the total amount of energy transferred in the neutrino processes to a unit volume of the medium per unit time. Recall that, under the envelope conditions considered, the URCA processes give a dominant contribution to the establishment of equilibrium. Together with the electroneutrality condition,

$$\frac{N_p}{N_B} = \frac{eB\mu_e}{2\pi^2 N_B}, \tag{41}$$

the quasi-equilibrium equations for the medium (39) and (40) allow only the density of the medium and the magnetic-field strength to be considered as free parameters. Numerically solving this system of equations yields

$$T \approx 3.8\ \text{MeV}, \quad a \approx 2.8, \quad \frac{N_p}{N_B} \approx 0.07. \tag{42}$$

For these parameters, the neutrino mean free paths (9) are estimated to be

$$\bar{l}_{\nu_e} \approx 3\ \text{km}, \quad \bar{l}_{\tilde{\nu}_e} \approx 5\ \text{km},$$
$$\bar{l}_{\nu_\mu, \nu_\tau} \approx \bar{l}_{\tilde{\nu}_\mu, \tilde{\nu}_\tau} \approx 2.5\ \text{km}. \tag{43}$$

Comparison of the neutrino mean free paths with the size of a region, ~1–3 km, filled with a strong magnetic field shows that the magnetic field cannot significantly affect the neutrino distribution functions.

Note that the neutrino scattering by nucleons gives a contribution to the ν_e mean free path comparable to the URCA processes and a dominant contribution to the $\tilde{\nu}_e$ mean free path. Thus, the $\tilde{\nu}_e$, ν_μ, and ν_τ mean free paths are virtually independent of the magnetic-field strength.

It is of interest to compare the contributions to the momentum transfer along the magnetic field from the URCA processes and from the neutrino scattering by nucleons. The scattering of μ and τ (anti)neutrinos by neutrons [see (33)] gives a dominant contribution to the force density in reactions (5) and (6), whereas the reactions with electron neutrinos [see formula (24) under the quasi-equilibrium conditions] give a dominant contribution in processes (1)–(4). Therefore, the ratio of the force densities can be represented as

$$\frac{\mathcal{J}_\parallel^{(scat)}}{\mathcal{J}_\parallel^{(urca)}} \approx \frac{4 c_V c_a g_n}{g_a^2 - 1} \frac{B_5(\eta_{\nu_x})}{B_3(a)} \frac{J_{\nu_x}}{Y} \frac{T_{\nu_x}}{m_n} \left(\frac{T_{\nu_x}}{T} \right)^5, \tag{44}$$

where $\nu_x = \nu_\mu$, ν_τ and $Y = N_p/(N_p + N_n)$ is the chemical composition parameter of the medium. By substituting numerical parameters of the medium and the neutrinos in this expression, we can easily verify that it is of the order of unity, although the T_{ν_x}/m_n ratio is small.

Under the quasi-equilibrium conditions for the medium (39) and (40), the expression for the force density along the magnetic field in the URCA processes (24) is greatly simplified. Its numerical estimate for the above parameters is

$$\mathcal{J}_\parallel^{(urca)} \approx 1.4 \times 10^{20}\ \frac{\text{dyne}}{\text{cm}^3} \left(\frac{B}{4.4 \times 10^{16}\ \text{G}} \right). \tag{45}$$

As expected, the scattering of neutrinos of all types by neutrons gives a numerically larger estimate for the total [over all types of (anti)neutrinos] force density than do the URCA processes:

$$\mathcal{J}_\parallel^{(scat)} \approx 3.0 \times 10^{20}\ \frac{\text{dyne}}{\text{cm}^3}$$
$$\times \left(\frac{B}{4.4 \times 10^{16}\ \text{G}} \right) \left(\frac{\rho}{5 \times 10^{11}\ \text{g/cm}^3} \right). \tag{46}$$

We numerically analyzed the quasi-equilibrium conditions in the envelope region specified by the range of densities $2 \times 10^{11} \le \rho \le 10^{12}$ g cm^{-3} with the neutrino parameters at a given density from [23]. Our analysis shows that the force density changes smoothly with increasing density of the medium. In the scattering processes, the force density increases almost linearly; in the URCA processes, the monotonic rise gives way to a decrease at $\rho \approx 8 \times 10^{11}$ g cm^{-3}. The value of $\rho = 5 \times 10^{11}$ g cm^{-3} that we chose for our estimates is actually a point with a mean force density in the above range of

densities. Note that the force generated in the two processes is directed along the field (i.e., the effect in all processes of neutrino interaction with nucleons is accumulated) and is large. Interestingly, under the quasi-equilibrium conditions, the force density is completely and mainly determined by anisotropy of the angular neutrino distribution function in the URCA processes and in the scattering process, respectively.

To discuss the possible macroscopic effects of neutrino radiation on the magnetized medium of the envelope, below, we give an estimate of the angular acceleration that arises in an envelope element under the total force density of neutrino spinup:

$$\dot{\Omega} \sim 10^3 \text{ s}^{-2}\left(\frac{B}{4.4\times 10^{16}\text{ G}}\right)\left(\frac{R}{10\text{ km}}\right), \qquad (47)$$

where R is the distance from the envelope volume to the center of the remnant of collapse. To obtain this estimate, we assumed that the macroscopic momentum is transferred to the entire envelope element. Note that this angular acceleration is large enough to spin up the envelope region filled with a strong magnetic field to millisecond rotation periods in a time of ~1 s.

6. DISCUSSION

Here, we investigate the possible dynamical effects of parity violation during the neutrino interaction with nucleons in the envelope of a collapsing star with a strong magnetic field. These effects are known to disappear in an optically thick (for neutrinos) medium [19], where the neutrino mean free path is much smaller than the characteristic size of the envelope of the remnant of collapse (see Section 5). This determines the range of envelope densities and temperatures under consideration.

Another important question is: At what strengths of the magnetic fields might their significant effect on the processes under consideration be expected? Currently, the field effect on individual neutrino–nucleon processes is being intensively studied. In particular, Leinson and Perez [21] calculated the neutrino luminosity in the direct URCA processes in the core of a neutron star (a strongly degenerate nucleon medium with a typical density $\rho > \rho_{\text{nucl}} = 2.8\times 10^{14}$ g cm^{-3} and temperature $T \sim$ 0.1 MeV). It is argued that the magnetic field significantly affects the luminosity only upon reaching an enormous strength $B \gtrsim 7\times 10^{17}$ G. Baiko and Yakovlev [20] showed that the direct URCA processes could have neutrino luminosities higher than the modified URCA processes at field strength $B \gtrsim 10^{16}$ G. Calculations of the Rosseland mean absorption coefficients for neutrinos in the envelope of a collapsing star indicate that fields $B \gtrsim 4\times 10^{15}$ G are required to change these coefficients at least by 5% [24]. As a continuation of these studies, Lai and Arras [19] calculated the collision integral for basic neutrino–nucleon processes in the Boltzmann equation for the neutrino distribution function and its first moments. Estimates of the P-odd terms in the moments of the collision integral show that the effects of asymmetry in momentum transfer along the magnetic field in the envelope of a collapsing star can be significant only when strengths $B \gtrsim 10^{16}$ G are reached. The emergence of such (in order of magnitude) magnetic fields when estimating the P-odd effects is natural. Indeed, only the electrons and positrons at the ground Landau level contribute to the P-odd part of the absorption coefficients for the direct URCA processes. The significant dynamical effects related to the parity violation take place at a high e^+e^- plasma density at the ground Landau level, which is ensured by conditions (10).

Assuming that the plasma electrons and positrons are only at the ground Landau level, we derived simple analytic expressions for the force density along the magnetic field (24), rate, and energy transferred to a unit volume of the medium per unit time (19)–(22) in the URCA processes, as well as general expressions for the force density (29) and the rate (34) of scattering of neutrinos of any type by nucleons. The asymmetry in momentum transfer along the field in these processes is nonzero only in the envelope region partially transparent to neutrinos ($\langle\chi^2\rangle \neq 1/3$, $T_\nu \neq T$). Assuming that the medium is in quasi-equilibrium via the dominant URCA processes specified by Eqs. (39) and (40), we find the equilibrium parameters of the medium. Numerical estimates of the force density along the field (45) and (46) for the equilibrium parameters of the medium show that, in the sum of the processes of neutrino interaction with nucleons, the asymmetry in momentum transfer is accumulated and this asymmetry is quantitatively large (47).

It makes sense to compare our estimates with calculations of the same quantities in the processes of neutrino interaction with a strongly magnetized e^+e^- plasma [25]. It is important to note that the force density along the field in these process is directed along the field and may be of the same order of magnitude as that in the neutrino–nucleon processes. Thus, the asymmetry in momentum transfer along the field is accumulated through the parity violation in all significant processes of neutrino interaction with the medium. Note, however, that a Fermi–Dirac distribution with a spectral temperature T_ν used in [25] gives the number of neutrino states significantly overestimated under actual conditions in an envelope partially transparent to neutrinos. Indeed, our introduced parameter J_ν is much less than unity in the envelope region with the densities and temperatures under consideration [see estimate (37)]. Thus, in this envelope region, the force density in the processes of neutrino interaction with a magnetized e^+e^- plasma is low compared to its value in the processes of neutrino interaction with nucleons.

An asymmetry in momentum transfer along a toroidal magnetic field gives rise to the angular acceleration (47) of the envelope region filled with such a strong

field. This acceleration is large enough to spin up this envelope region to millisecond rotation periods in a time of ~1 s. This large (in magnitude) and local (coordinate-dependent) angular acceleration can cause a rapid change in the gradient of angular velocities in the envelope, which, in turn, can change the mechanism of subsequent generation of a toroidal magnetic field. Indeed, in the presence of an additional angular acceleration in the envelope, the toroidal magnetic field can grow with time much faster than a linear law [11]. This toroidal-field rearrangement can affect the mechanisms of supernova envelope ejection [1] and the formation of an anisotropic gamma-ray burst in a failed supernova [26]; it can also trigger the growth of MHD instabilities [27]. However, to investigate the effect of neutrino spinup on the envelope dynamics and the generation mechanism of a toroidal field requires analyzing a complete system of MHD equations. This is a complex problem far outside the scope of this paper. We hope that it will find its researchers.

ACKNOWLEDGMENTS

We wish to thank N.V. Mikheev for a discussion of virtually all fundamental questions of this paper and S.I. Blinnikov for interest and advice on important points of our study. We are also grateful to G.S. Bisnovatyĭ-Kogan, V.M. Lipunov, V.B. Semikoz, M.E. Prokhorov, M.V. Chistyakov, and participants of the Moscow Workshop of Astrophysicists (Sternberg Astronomical Institute, Moscow State University) for valuable remarks. This work was supported by the Russian Foundation for Basic Research (project no. 01-02-17334) and the Education Ministry of Russia (project no. E0011-11.0-5).

APPENDIX A

Calculating $|S|^2$ for the Direct URCA Processes

In the low-energy limit, the effective S-matrix element of the URCA processes (1)–(4) can be represented as [5]

$$S_{if} = \frac{G_F\cos\theta_c}{\sqrt{2}}\int d^4x[\bar{\Psi}^{(n)}_{p\sigma}\gamma_\alpha(1+g_a\gamma_5)\Psi_{n\sigma'}] \times[\bar{\Psi}_e\gamma_a(1+\gamma_5)\Psi_\nu] \quad \text{(A.1)}$$

(we use the γ matrices in spinor representation with a different sign of γ_5 [28]). Here, Ψ_e, Ψ_ν, $\Psi_{n\sigma'}$, and $\Psi^{(n)}_{p\sigma}$ are the wave functions of the electron, neutrino, neutron, and proton (at the nth Landau level), respectively; θ_c is the Cabibbo angle; g_a is the axial constant of a charged nucleon current ($g_a \approx 1.26$ in the low-energy limit); and σ and σ' are the components of the double proton and neutron spin along the magnetic field, respectively. We performed our calculations in a coordinate system where $\mathbf{B} = (0, 0, B)$ in the gauge $A_\mu = (0, 0, Bx, 0)$. When the e^+e^- plasma occupies only the ground Landau level, the wave functions of relativistic electrons can be chosen in the form

$$\Psi_e = \frac{\exp[-i(\varepsilon t - p_2 y - p_3 z)]\xi_0(\eta')}{\sqrt{2\varepsilon L_y L_z}}U_e,$$
$$\eta' = \sqrt{eB}\left(x + \frac{p_2}{eB}\right),$$
$$U_e = \sqrt{\varepsilon + m_e}\begin{pmatrix} U \\ -p_3/(\varepsilon + m_e)U \end{pmatrix}, \quad \text{(A.2)}$$
$$U = \begin{pmatrix} 0 \\ 1 \end{pmatrix},$$

where $p = (\varepsilon, p_1, p_2, p_3)$ is the electron 4-momentum and $\varepsilon = \sqrt{p_3^2 + m_e^2}$ is its energy. In what follows,

$$\chi_n(x) = \frac{(eB)^{1/4}e^{-\eta^2/2}}{\sqrt{2^n n!\sqrt{\pi}}}H_n(x), \quad \text{(A.3)}$$

$H_n(x)$ are the Hermitean polynomials, and

$$V = L_x L_y L_z \quad \text{(A.4)}$$

is the normalization volume.

The wave function of the nonrelativistic protons at the nth Landau level was chosen in the form

$$\Psi^{(n)}_{p\sigma} = \frac{\exp[-i(E_p t - P_2 y - P_3 z)]}{\sqrt{2E_p L_y L_z}}\Phi^{(n)}_\sigma,$$
$$\eta = \sqrt{eB}\left(x - \frac{P_2}{eB}\right),$$
$$\Phi^{(n)}_\sigma = \sqrt{E_p + m_p}\begin{pmatrix} V_\sigma \\ 0 \end{pmatrix}, \quad \text{(A.5)}$$
$$V_{\sigma=+1} = \begin{pmatrix} \chi_n(\eta) \\ 0 \end{pmatrix},$$
$$V_{\sigma=-1} = \begin{pmatrix} 0 \\ \chi_{n-1}(\eta) \end{pmatrix},$$

where $P = (E_p, P_1, P_2, P_3)$ is the proton 4-momentum, and

$$E_p = m_p + \frac{P_3^2}{2m_p} + \frac{eBn}{m_p}$$

is the nonrelativistic energy of a charged particle at the nth Landau level. The standard wave function for neutrons is

$$\Psi_{n\sigma'} = \frac{\exp[-i(E_n t - q_1 x - Q_2 y - Q_3 z)]}{\sqrt{2E_n V}} \times \sqrt{E_n + m_n}\begin{pmatrix} W_{\sigma'} \\ 0 \end{pmatrix}, \quad W^+_{\sigma'} W_{\sigma'} = 1, \tag{A.6}$$

where $q = (E_n, q_1, q_2, q_3)$ is the neutron 4-momentum, and

$$E_n = m_n + \frac{\mathbf{q}^2}{2m_n}.$$

We assume the neutrino to be a standard massless Dirac particle of left-handed helicity with the wave function [28]

$$\Psi_\nu = \frac{\exp[-i(\omega t - k_1 x - k_2 y - k_3 z)]}{\sqrt{2\omega V}}\sqrt{\omega}\begin{pmatrix} W \\ -W \end{pmatrix}, \quad W^+ W = 1, \tag{A.7}$$

where $k = (\omega, k_1, k_2, k_3)$ is the neutrino 4-momentum. Squaring S_{if}, integrating over d^4x, and summing over the particle Landau levels and polarizations yields

$$\frac{|S_{if}|^2}{\mathcal{T}} = \frac{G_F^2 \cos^2\theta_c \pi^3}{2L_y L_z V^2 \omega\varepsilon}\exp\left(-\frac{Q_\perp^2}{2eB}\right) \times \left[\sum_{n=0}^{\infty}\frac{|M_+|^2}{n!}\left(\frac{Q_\perp^2}{2eB}\right)^n \delta^{(3)} + \sum_{n=1}^{\infty}\frac{|M_-|^2}{(n-1)!}\left(\frac{Q_\perp^2}{2eB}\right)^{n-1}\delta^{(3)}\right]. \tag{A.8}$$

Here, $\delta^{(3)}$ is the delta function of the energy, momentum along the magnetic field, and one of its transverse components conserved in the reactions; $Q_\perp^2$ is the square of the transferred momentum across the magnetic field in the corresponding reaction; and n is the index of summation over the proton Landau levels. The quantities $|M_+|^2$ and $|M_-|^2$ are defined as

$$|M_\sigma|^2 = \frac{1}{4m_p m_n}\sum_{\sigma'=-1}^{1} L_{\alpha\beta} N^{\sigma\sigma'}_{\alpha\beta}, \tag{A.9}$$

$$L_{\alpha\beta} = \mathrm{tr}[\rho_\nu \gamma_\alpha (1+\gamma_5)\rho_e \gamma_\beta (1+\gamma_5)], \tag{A.10}$$

$$N^{\sigma\sigma'}_{\alpha\beta} = \mathrm{tr}[\rho_{n\sigma'}\gamma_\alpha(1+g_a\gamma_5)\rho_{p\sigma}\gamma_\beta(1+g_a\gamma_5)]. \tag{A.11}$$

Below, we give the neutrino, electron, neutron, and proton density matrices that correspond to the wave functions:

$$\rho_\nu = \frac{\hat{k}(1-\gamma_5)}{2}, \quad \rho_e = (\hat{p}_\parallel + m_e)\Pi_-, \quad \rho_{n\sigma'} = m_n(1+\hat{u})\Pi_{\sigma'}, \quad \rho_{p\sigma} = m_p(1+\hat{u})\Pi_\sigma, \quad \hat{k} = k_\alpha\gamma_\alpha, \quad \hat{u} = u_\alpha\gamma_\alpha, \quad \hat{p}_\parallel = p_0\gamma_0 - p_3\gamma_3, \quad \Pi_\sigma = \frac{1+\sigma i\gamma_1\gamma_2}{2}. \tag{A.12}$$

Here, Π_σ is the projection operator of the density matrix for a charged fermion in a magnetic field (recall that σ, $\sigma' = \pm 1$ are the components of the double proton and neutron spin along the magnetic field). To ensure the covariance of our calculations, we inserted $u_\mu = (1, 0, 0, v)$, the 4-velocity of the medium along the field, in the nucleon density matrix (at the end of our calculations, we assume that $v = 0$).

In the subsequent calculations, we used the following properties of the projection operator:

$$\Pi_\sigma^2 = \Pi_\sigma, \quad \Pi_\sigma\Pi_{-\sigma} = 0, \quad \Pi_\sigma\gamma_{\alpha\parallel} = \gamma_{\alpha\parallel}\Pi_\sigma, \quad \Pi_\sigma\gamma_{\alpha\perp} = \gamma_{\alpha\perp}\Pi_{-\sigma}, \quad \Pi_\sigma\gamma_5 = \gamma_5\Pi_\sigma, \tag{A.13}$$

where $\gamma_{\alpha\parallel} = \gamma_{1,2}$ and $\gamma_{\alpha\perp} = \gamma_{0,3}$. Since the velocity vector v of the medium has only longitudinal components, the nucleon trace (A.11) can be reduced to

$$N^{\sigma\sigma'}_{\alpha\beta} = m_p m_n \mathrm{Sp}[\Pi_{\sigma'}\gamma_\alpha\gamma_\beta(1-g_a^2)] + m_p m_n \mathrm{Sp}[\Pi_{\sigma'}\gamma_\alpha\Pi_\sigma\hat{u}_\parallel\gamma_\beta\hat{u}_\parallel(1+g_a^2-2g_a\gamma_5)]. \tag{A.14}$$

In the subsequent calculation of this expression, it is convenient to separate out the contributions from identical and different nucleon polarizations. The matrices γ_α and γ_β have only longitudinal components ($\gamma_\alpha = \gamma_{\alpha\parallel}$, $\gamma_\beta = \gamma_{\beta\parallel}$) when $\sigma = \sigma'$ and only transverse components ($\gamma_\alpha = \gamma_{\alpha\perp}$, $\gamma_\beta = \gamma_{\beta\perp}$) when $\sigma = -\sigma'$. This is easy to obtain from the properties of the polarization operator (A.13). To calculate the nucleon trace requires the expressions

$$\mathrm{tr}[\gamma_{\alpha\parallel}\gamma_{\beta\parallel}\Pi_\sigma] = 2\bar{\Lambda}_{\alpha\beta}, \tag{A.15}$$

$$\mathrm{tr}[\gamma_{\alpha\parallel}\gamma_{\beta\parallel}\gamma_5\Pi_\sigma] = 2\sigma\tilde{\varphi}_{\alpha\beta}, \tag{A.16}$$

$$\mathrm{tr}[\gamma_{\mu\parallel}\gamma_{\nu\parallel}\gamma_{\rho\parallel}\gamma_{\delta\parallel}\Pi_\sigma] = 2(\tilde{\Lambda}_{\mu\nu}\tilde{\Lambda}_{\rho\delta} + \tilde{\Lambda}_{\mu\delta}\tilde{\Lambda}_{\nu\rho} - \tilde{\Lambda}_{\mu\rho}\tilde{\Lambda}_{\nu\delta}), \tag{A.17}$$

$$\mathrm{tr}[\gamma_{\mu\parallel}\gamma_{\nu\parallel}\gamma_{\rho\parallel}\gamma_{\delta\parallel}\gamma_5\Pi_\sigma] = 2\sigma(\tilde{\Lambda}_{\mu\nu}\tilde{\varphi}_{\rho\delta} + \tilde{\Lambda}_{\rho\delta}\tilde{\varphi}_{\mu\nu}), \tag{A.18}$$

$$\Pi_\sigma\gamma_{\alpha\perp}\gamma_{\beta\perp}\Pi_\sigma = -(\Lambda_{\alpha\beta} - i\sigma\varphi_{\alpha\beta})\Pi_\sigma. \tag{A.19}$$

In what follows, $\Lambda_{\mu\nu} = (\varphi\varphi)_{\mu\nu}$ and $\tilde{\Lambda}_{\mu\nu} = (\tilde{\varphi}\tilde{\varphi})_{\mu\nu}$, where $\varphi_{\mu\nu} = F_{\mu\nu}/B$ and $\tilde{\varphi}_{\mu\nu} = \tilde{F}_{\mu\nu}/B$ are the tensor and

dual tensor of the external electromagnetic field reduced to dimensionless form. The calculated nucleon trace can be reduced to

$$N^{\sigma\sigma'}_{\alpha\beta}\big|_{\sigma=\sigma'} = 2m_p m_p[(1-g_a^2)\tilde{\Lambda}_{\alpha\beta} + (1+g_a^2)(2(u\tilde{\Lambda})_\alpha(u\tilde{\Lambda})_\beta - u^2\tilde{\Lambda}_{\alpha\beta}) - 2g_\alpha\sigma((u\tilde{\Lambda})_\alpha(\tilde{\varphi}u)_\beta + (\tilde{\varphi}u)_\alpha(u\tilde{\Lambda})_\beta)], \quad (A.20)$$

$$N^{\sigma\sigma'}_{\alpha\beta}\big|_{\sigma=-\sigma'} = 2m_p m_p(\Lambda_{\alpha\beta} + i\sigma\varphi_{\alpha\beta}) \times[-(1-g_a^2) + (1+g_a^2)(u\tilde{\Lambda}u) + 2g_a\sigma(u\tilde{\varphi}u)]. \quad (A.21)$$

Since tensors (A.20) and (A.21) have only longitudinal and transverse components, respectively, it is convenient to break up the lepton trace into the same structures. When it is convolved with the nucleon trace, only the completely longitudinal and completely transverse parts of the lepton trace will give a nonzero answer:

$$L_{\alpha\beta}N^{\sigma\sigma'}_{\alpha\beta} = N^{\sigma\sigma'}_{\alpha\beta}\big|_{\sigma=\sigma'}L^{\parallel}_{\alpha\beta} + N^{\sigma\sigma'}_{\alpha\beta}\big|_{\sigma=-\sigma'}L^{\perp}_{\alpha\beta}. \quad (A.22)$$

After simple transformations using the properties of the polarization operator (A.13), the corresponding constructions can be reduced to

$$L^{\parallel}_{\alpha\beta} = 2\mathrm{tr}[\gamma_{\beta\parallel}\hat{k}_\parallel\gamma_{\alpha\parallel}\hat{p}_\parallel(1-\gamma_5)\Pi_-], \quad (A.23)$$

$$L^{\perp}_{\alpha\beta} = 2\mathrm{tr}[\gamma_{\beta\perp}\hat{k}_\parallel\gamma_{\alpha\perp}\hat{p}_\parallel(1-\gamma_5)\Pi_-]. \quad (A.24)$$

Using the above properties (A.15)–(A.19), these expressions can be easily calculated and represented as

$$L^{\parallel}_{\alpha\beta} = 4((p\tilde{\Lambda})_\alpha(k\tilde{\Lambda})_\beta + (k\tilde{\Lambda})_a(p\tilde{\Lambda})_\beta - \tilde{\Lambda}_{\alpha\beta}(p\tilde{\Lambda}k)) + 4((\tilde{\varphi}p)_\alpha(k\tilde{\Lambda})_\beta + (p\tilde{\Lambda})_\alpha(\tilde{\varphi}k)_\beta), \quad (A.25)$$

$$L^{\perp}_{\alpha\beta} = 4(\Lambda_{\alpha\beta} - i\varphi_{\alpha\beta})((k\tilde{\Lambda}p) + (k\tilde{\varphi}p)). \quad (A.26)$$

For completeness, we present the convolution of the nucleon and lepton traces in covariant form:

$$N^{\sigma\sigma'}_{\alpha\beta}\big|_{\sigma=\sigma'}L^{\parallel}_{\alpha\beta} = 8m_p m_n[2(1+g_a^2)((up)_\parallel(uk)_\parallel) + 4g_a\sigma(u\tilde{\varphi}p)(u\tilde{\varphi}k) + 2(1+\sigma g_a)^2 \times((up)_\parallel(uk)_\parallel + (up)_\parallel(u\tilde{\varphi}k) + (uk)_\parallel(u\tilde{\varphi}p))], \quad (A.27)$$

$$N^{\sigma\sigma'}_{\alpha\beta}\big|_{\sigma=-\sigma'}L^{\perp}_{\alpha\beta} = 16m_p m_n(1+\sigma) \times[(1+g_a^2)(u\tilde{\Lambda}u) - (1-g_a^2)][(k\tilde{\Lambda}p) + (k\tilde{\varphi}p)]. \quad (A.28)$$

In the selected frame of reference, where the nucleon medium is at rest [$u = (1, 0, 0, 0)$, $(kp)_\parallel = (k\tilde{\Lambda}p) = k_0p_0 - k_3p_3$), these expressions are

$$N^{\sigma\sigma'}_{\alpha\beta}\big|_{\sigma=\sigma'}L^{\parallel}_{\alpha\beta} = 16m_p m_n(1+\sigma g_a)^2 \times(p_0+p_3)(k_0+k_3), \quad (A.29)$$

$$N^{\sigma\sigma'}_{\alpha\beta}\big|_{\sigma=-\sigma'}L^{\perp}_{\alpha\beta} = 32m_p m_n(1+\sigma) \times g_a^2(p_0+p_3)(k_0-k_3). \quad (A.30)$$

Hence, it is easy to obtain the final expression for the square of the amplitude (A.9) of the process being calculated:

$$|M_\sigma|^2 = 4(p_0+p_3) \times[(1+\sigma g_a)^2(k_0+k_3) + 2(1+\sigma)g_a^2(k_0-k_3)]. \quad (A.31)$$

Note that in the case of nonrelativistic nucleons under consideration, the square of the amplitude depends only on the longitudinal electron and neutrino momentum components.

APPENDIX B

The Neutrino Absorption Coefficient

Below, we give the details of our calculation of the absorption coefficient $\mathcal{H}^{(\nu)}$ (16) for process (1) involving neutrinos. We used standard expressions for an elements of phase volume:

$$dn^{(e)} = \frac{dp_2^{(e)}dp_3^{(e)}L_yL_z}{(2\pi)^2}$$

for charged particles and

$$dn = \frac{d^2pV}{(2\pi)^3}$$

for uncharged particles. The proton distribution function was assumed to be the Boltzmann one. Eliminating the integration over the proton momentum due to the $\delta^{(3)}$ function, we note that the absorption coefficient does not depend on the p_2 component of the electron momentum. Since $p^2 = eBx_c$ in a magnetic field (x_c is the centroid coordinate of the distribution of the electron wave function across the magnetic field), we can eliminate the integral over the p^2 component of the electron momentum:

$$\int dp_2 = eBL_x.$$

The remaining δ function in energy can be simplified. Since the electrons and neutrinos are ultrarelativistic particles and the nucleons are nonrelativistic particles, their momenta are of the order of $P^2 \sim Tm$ (for nucleons) and $p^2 \sim T^2$ (for ultrarelativistic particles). Assuming the nucleon masses to be identical (where this does not cause any misunderstanding), we obtain

$$\delta(E_n - E_p^{(n)} + \omega - \varepsilon) = \delta\left(\frac{\mathbf{q}^2}{2m_n} - \frac{(q_\parallel + k_\parallel - p_\parallel)^2}{2m_p} - \frac{eBn}{m_p} + \omega - \varepsilon + (m_n - m_p)\right) \quad (B.1)$$

$$\approx \delta\left(\frac{q_\perp^2}{2m_n} - \frac{eBn}{m_p} + \omega - \varepsilon + (m_n - m_p)\right),$$

where $q_\perp$ and $q_\parallel$ are the particle momentum components across and along the magnetic field, respectively. Since the dimensionless parameter

$$b = \frac{eB}{2m_pT} \ll 1,$$

we may neglect this term in one of the δ functions in the expression for the square of the *S*-matrix element (12) by combining the two sums. In this case, the expression for the absorption coefficient is simplified and can be represented as

$$\mathcal{K}^{(\nu)} = \frac{2G_F^2\cos^2\theta_c}{(2\pi)^4}eB \times\left((1+3g_a^2)+\frac{(1-g_a^2)k_\parallel}{\omega}\right)\int f_nF(q_\perp^2,b)d^3q, \tag{B.2}$$

$$F(q_\perp^2,b) = \int_0^\infty \frac{dy}{1+\exp(\eta_e-y)}\sum_{n=0}^\infty\frac{1}{n!}\left(\frac{x}{b}\right)^n \times\exp\left(-\frac{x}{b}\right)\delta\left(x-bn-y+\frac{\omega+m_n-m_p}{T}\right).$$

Here, $x = q_\perp^2/2m_nT$ and $y = \varepsilon/T$. Note that the function $F(q_\perp^2, b)$ has a simple asymptotic behavior for $b \longrightarrow 0$, and bn is a finite number. The latter condition follows from the fact that, as the magnetic field weakens, the number of Landau levels that contribute to the sum under consideration increases in inverse proportion to field strength. In this case, the sum over the proton Landau levels may be replaced by an integral. It can also be shown that, in this limit,

$$\lim_{\substack{b\to 0\\ bn\not\to 0}}\left[\frac{1}{n!b}\left(\frac{x}{b}\right)^n\exp\left(-\frac{x}{b}\right)\right] = \delta(x-bn), \tag{B.3}$$

where δ is the Dirac delta function. Hence, it is easy to find that

$$\lim_{\substack{b\to 0\\ bn\not\to 0}}[F(q_\perp^2,b)] = \frac{1}{1+\exp(\eta_e-(\omega+m_n-m_p)/T)}. \tag{B.4}$$

Since the function $F(q_\perp^2, b)$ does not depend on $q_\perp^2$ in the limit under consideration, the integration in (B.2) can be brought to the end. Given the definition of the neutron number density,

$$N_n = \frac{2}{(2\pi)^3}\left(\int f_nd^3q\right),$$

we obtain the final expression for the neutrino absorption coefficient in the limit considered:

$$\mathcal{K}^{(\nu)} = \frac{G_F^2\cos^2\theta_c}{2\pi}eBN_n \times\frac{(1+3g_a^2)+(1-g_a^2)k_\parallel/\omega}{1+\exp(-\eta_e-(\omega+m_n-m_p)/T)}. \tag{B.5}$$

The absorption coefficient for process (3) involving antineutrinos can be calculated in a similar fashion to give

$$\mathcal{K}^{(\tilde\nu)} = \frac{G_F^2\cos^2\theta_c}{2\pi}eBN_p \times\frac{(1+3g_a^2)+(1-g_a^2)k_\parallel/\omega}{1+\exp(-\eta_e-(\omega-m_n+m_p)/T)}. \tag{B.6}$$

APPENDIX C

The Force Density along the Magnetic Field for the Neutrino Scattering by Nucleons

In the low-energy limit, the effective Lagrangian for the neutrino scattering by nucleons is [5]

$$\mathcal{L} = \frac{G_F}{\sqrt{2}}(\bar U_N(\mathcal{P}')\gamma_\alpha(c_v+c_a\gamma_5)U_N(\mathcal{P})) \times(\bar U_\nu(k')\gamma_a(1+\gamma_5)U_\nu(k)). \tag{C.1}$$

Here, U_N and U_ν are the Dirac nucleon and neutrino bispinors, and c_v and c_a are the vector and axial constants of a neutral nucleon current. At low energies [22], $c_v = -1/2$ and $c_a \approx -0.91/2$ for neutrons and $c_v = 0.07/2$ and $c_a \approx 1.09/2$ for protons. Using the nonrelativistic density matrix for the polarized nucleons, $\rho = m_N(1 + \boldsymbol{\xi}\cdot\boldsymbol{\sigma})$, where $\boldsymbol{\xi} = \pm\mathbf{B}/B$ is the nucleon polarization vector along the magnetic field and $\boldsymbol{\sigma}$ are the Pauli matrices, it is easy to obtain the following expression for the square of the *S*-matrix element for the neutrino scattering by nucleons per unit time:

$$\frac{|S_{if}|_\nu^2}{\mathcal{T}} = \frac{(2\pi)^4G_F^2}{2V^3\omega\omega'}\delta^{(4)}(\mathcal{P}+k-\mathcal{P}'-k') \times[(c_v^2+3c_a^2)\omega\omega'+(c_v^2-c_a^2)\mathbf{k}\cdot\mathbf{k}' + 2c_vc_a(S+S')(\omega k_\parallel'+\omega' k_\parallel) - 2c_a^2(S-S')(\omega k_\parallel'-\omega' k_\parallel) + (c_v^2-c_a^2)SS'(\omega\omega'+\mathbf{k}\cdot\mathbf{k}')+4c_a^2SS'k_\parallel k_\parallel'], \tag{C.2}$$

Here, $k = (\omega, \mathbf{k})$ and $k' = (\omega', \mathbf{k}')$ are the 4-momenta of the initial and final neutrinos; $k_\parallel$ and $k_\parallel'$ are the components of these momenta along the magnetic field; and *S*, $S' = \pm1$ ($S = \boldsymbol{\xi}\cdot\mathbf{B}/B$ are the components of the polariza-

tion vectors for the initial and final nucleons along the magnetic field). The square of the S-matrix element for the antineutrino scattering by nucleons can be derived from (C.2) by the change $k \longleftrightarrow k'$:

$$|S_{if}|^2_{\tilde{\nu}} = |S_{if}|^2_{\nu}(k \longleftrightarrow k'). \quad \text{(C.3)}$$

Since we consider the neutrino scattering by nucleons in a strong magnetic field, for the subsequent calculations, it is necessary to take into account the contribution to the nucleon energy from the interaction of their magnetic moment with the magnetic field:

$$E_N = m_N + \frac{\mathcal{P}^2}{2m_N} - \frac{g_N SeB}{2m_N},$$

where g_N is the nucleon magnetic factor ($g_n \approx -1.91$ for the neutron and $g_p \approx 2.79$ for the proton).

Next, we can simplify the δ function in energy. Using the fact that $\mathcal{P}, \mathcal{P}' \sim \sqrt{m_N T}$ and $k, k' \sim T$ and disregarding all terms on the order of $\sqrt{T/m_N}$, we obtain

$$\begin{aligned}\delta(\omega - \omega' + E_N - E'_N) &= \delta\Big(\omega - \omega' + \frac{\mathcal{P}^2}{2m_N} \\ &- g_N(S - S')\frac{eB}{2m_N} - \frac{(\boldsymbol{\mathcal{P}} + \mathbf{k} + \mathbf{k}')^2}{2m_N}\Big) \quad \text{(C.4)} \\ &\approx \delta\Big(\omega - \omega' - g_N(S - S')\frac{eB}{2m_N}\Big).\end{aligned}$$

It is convenient to perform the subsequent calculations by separating the contributions from $S = S'$ and $S = -S'$. Eliminating in momentum of the final nucleon with an allowance for the δ function and taking into account that all terms linear in $k_\parallel$ and $k'_\parallel$ give no contribution, we obtain the following expression for the density of the force acting along the magnetic field:

$$\mathcal{J}^{(\nu)}_\parallel = \sum_S (\mathcal{J}^{(\nu)}_\parallel\big|_{S=S'} + \mathcal{J}^{(\nu)}_\parallel\big|_{s=-S'}),$$

$$\begin{aligned}\mathcal{J}^{(\nu)}_\parallel\big|_{S=S'} &= \frac{2G_F^2 c_\nu c_a}{(2\pi)^8}\int d^3\mathcal{P}\, f_N(\mathcal{P})\int d^3k\, f_\nu(k) \\ &\times \int d^3k'(1 - f_\nu(k'))\frac{S}{\omega\omega'}(\omega' k_\parallel^2 - \omega k_\parallel'^2)\delta(\omega - \omega'),\end{aligned} \quad \text{(C.5)}$$

$$\begin{aligned}\mathcal{J}^{(\nu)}_\parallel\big|_{S=-S'} &= \frac{2G_F^2 c_a^2}{(2\pi)^8}\int d^3\mathcal{P}\, f_N(\mathcal{P}) \\ &\times \int d^3k\, f_\nu(k)\int d^3k'(1 - f_\nu(k')) \\ &\times \frac{S}{\omega\omega'}(\omega' k_\parallel^2 + \omega k_\parallel'^2)\delta\Big(\omega - \omega' - \frac{g_N SeB}{m_N}\Big).\end{aligned} \quad \text{(C.6)}$$

Here, we use the fact that the nucleon gas is a Boltzmann one and, hence, $1 - f_N \approx 1$.

Since $eB/m_N T \ll 1$, the distribution function for the initial nucleons can be written as

$$f_N(\mathcal{P}) \approx \Big(1 + \frac{g_N SeB}{2m_N T}\Big)\exp\Big(-\frac{\mathcal{P}^2}{2m_N T} + \eta_N\Big), \quad \text{(C.7)}$$

where η_N is the nonrelativistic nucleon degeneracy parameter. Interacting over the initial-nucleon momentum and using the fact that the nucleon number density is

$$N_N \approx \frac{2}{(2\pi)^3}\int \exp\Big(-\frac{\mathcal{P}^2}{2m_N T} + \eta_N\Big)d^3\mathcal{P}, \quad \text{(C.8)}$$

we obtain the following expression for (C.5) and (C.6):

$$\mathcal{J}^{(\nu)}_\parallel\big|_{S=S'} = \frac{G_F^2 c_\nu c_a}{(2\pi)^5} N_N T^6 S\Big(1 + g_N S\frac{eB}{2m_N T}\Big)I_1, \quad \text{(C.9)}$$

$$\begin{aligned}I_1 &= \int_0^\infty y^2 dy \int_0^\infty y'^2 dy' \int_{-1}^1 d\chi \int_0^{2\pi} d\varphi \int_{-1}^1 d\chi' \\ &\times \int_0^{2\pi} d\varphi'\, f_\nu(y, \chi)(1 - f_\nu(y', \chi')) \\ &\times (y(1 - \chi^2)\cos^2\varphi - y'(1 - \chi'^2)\cos^2\varphi')\delta(y - y'),\end{aligned} \quad \text{(C.10)}$$

$$\mathcal{J}^{(\nu)}_\parallel\big|_{S=-S'} = \frac{G_F^2 c_a^2}{(2\pi)^5} N_N T^6 S\Big(1 + g_N S\frac{eB}{2m_N T}\Big)I_2, \quad \text{(C.11)}$$

$$\begin{aligned}I_2 &= \int_0^\infty y^2 dy \int_0^\infty y'^2 dy' \int_{-1}^1 d\chi \int_0^{2\pi} d\varphi \int_{-1}^1 d\chi' \int_0^{2\pi} d\varphi'\, f_\nu(y, \chi) \\ &\times (1 - f_\nu(y', \chi'))(y(1 - \chi^2)\cos^2\varphi + y'(1 - \chi'^2)\cos^2\varphi') \\ &\times \delta\Big(y - y' - g_N S\frac{eB}{m_N T}\Big).\end{aligned} \quad \text{(C.12)}$$

Here, $y = \omega/T$, $y' = \omega'/T$, $\chi = \cos\theta$, and $\chi' = \cos\theta'$, where θ and θ' are, respectively, the angles between the momenta of the initial and final neutrinos and the radial direction; and φ and φ' are the azimuthal angles. Since the square of the S-matrix element for the process involving antineutrinos can be derived by the change $k \longleftrightarrow k'$, it is easy to note that the expression for the momentum transferred along the magnetic field in the process of antineutrino scattering by nucleons is given by the formal change $c_a^2 \longrightarrow -c_a^2$:

$$\mathcal{J}^{(\tilde{\nu})}_\parallel(c_a^2) = \mathcal{J}^{(\nu)}_\parallel(-c_a^2). \quad \text{(C.13)}$$

For the integrals (C.10) and (C.12) to be calculated, we must use an explicit neutrino distribution function. We choose it in the form (11):

$$f_\nu(k) = \Phi_\nu(r, \chi)F_\nu(\omega),$$

where

$$F_\nu(\omega) = \left[1 + \exp\left(\frac{\omega}{T_\nu} - \eta_\nu\right)\right]^{-1},$$

η_ν being the fitting parameter.

It is convenient to express the final result in terms of the mean neutrino-flux parameters (23), (25), and (30). For the distribution function used, these parameters can be represented as

$$J_\nu = (4\pi)^{-1}\int \Phi_\nu(r, \chi)d\Omega, \tag{C.14}$$

$$\langle \chi_\nu^2 \rangle = \left(\int \chi^2 \Phi_\nu(r, \chi)d\Omega\right)\left(\int \Phi_\nu(r, \chi)d\Omega\right)^{-1}, \tag{C.15}$$

$$\langle \omega_\nu^n \rangle = \left(\int \omega^{n+2} F_\nu(\omega)d^3\omega\right)\left(\int \omega^2 F_\nu(\omega)d^3\omega\right)^{-1}. \tag{C.16}$$

For completeness, we present the result of our calculation of the contributions to the force density from different nucleon polarizations separately:

$$\sum_S \mathcal{J}_\parallel^{(\nu)}\Big|_{S=S'} = -\frac{G_F^2 g_N c_\nu c_a}{2\pi} \times \frac{eB}{m_N T} N_N N_\nu \langle \omega_\nu^3 \rangle \left(\langle \chi_\nu^3 \rangle - \frac{1}{3}\right), \tag{C.17}$$

$$\sum_S \mathcal{J}_\parallel^{(\nu)}\Big|_{S=-S'} = -\frac{G_F^2 g_N c_a^2}{2\pi}\frac{eB}{m_N T} N_N N_\nu \times \left[T\langle \omega_\nu^2 \rangle \left(\langle \chi_\nu^2 \rangle - \frac{1}{3}\right) - (\langle \omega_\nu^2 \rangle - 5T\langle \omega_\nu^2 \rangle) \times \left(\frac{5}{3} - \langle \chi_\nu^2 \rangle\right) + 2J_\nu(\langle \omega_\nu^2 \rangle - 5T_\nu \langle \omega_\nu^2 \rangle)(1 - \langle \chi_\nu^2 \rangle)\right]. \tag{C.18}$$

It is easy to verify that each of these expressions is zero for a thermal equilibrium of the neutrinos with the medium ($T_\nu = T$, $J_\nu = 1$, $\langle \chi_\nu^2 \rangle = 1/3$), as follows from fundamental physical principles.

REFERENCES

1. G. S. Bisnovatyĭ-Kogan, Astron. Zh. **47**, 813 (1970) [Sov. Astron. **14**, 652 (1971)]; G. S. Bisnovatyĭ-Kogan, *Physical Problems of the Theory of Star Evolution* (Nauka, Moscow, 1989).
2. S. E. Woosley, Astrophys. J. **405**, 273 (1993); A. MacFadyen and S. E. Woosley, Astrophys. J. **524**, 262 (1999).
3. M. Ruffert and H.-T. Janka, Astron. Astrophys. **338**, 535 (1998).
4. H. C. Spruit, Astron. Astrophys. **341**, L1 (1998).
5. G. G. Raffelt, *Stars as Laboratories for Fundamental Physics* (Univ. of Chicago Press, Chicago, 1996).
6. S. A. Colgate and R. H. White, Astrophys. J. **143**, 626 (1966).
7. D. K. Nadyozhin, Astrophys. Space Sci. **49**, 399 (1977); **51**, 283 (1977); **53**, 131 (1978).
8. R. C. Duncan and C. Thompson, Astrophys. J. Lett. **392**, L9 (1992).
9. C. Kouveliotou, T. Strohmayer, K. Hurley, *et al.*, Nature **393**, 235 (1998).
10. X.-D. Li and E. P. J. van den Heuvel, Astrophys. J. Lett. **513**, L45 (1999).
11. G. S. Bisnovatyĭ-Kogan and S. G. Moiseenko, Astron. Zh. **69**, 563 (1992) [Sov. Astron. **36**, 285 (1992)].
12. W. Kluzniak and M. Ruderman, Astrophys. J. Lett. **508**, L113 (1998).
13. G. S. Bisnovatyĭ-Kogan, Astron. Astrophys. Trans. **3**, 287 (1993).
14. N. N. Chugaĭ, Pis'ma Astron. Zh. **10**, 210 (1984) [Sov. Astron. Lett. **10**, 87 (1984)].
15. O. F. Dorofeev, V. N. Rodionov, and I. M. Ternov, Pis'ma Zh. Éksp. Teor. Fiz. **40**, 159 (1984) [JETP Lett. **40**, 917 (1984)].
16. A. A. Gvozdev and I. S. Ognev, Pis'ma Zh. Éksp. Teor. Fiz. **69**, 337 (1999) [JETP Lett. **69**, 365 (1999)].
17. A. Kusenko, G. Segre, and A. Vilenkin, Phys. Lett. B **437**, 359 (1998).
18. S. J. Hardy and D. B. Melrose, Astrophys. J. **480**, 705 (1997).
19. F. Arras and D. Lai, Phys. Rev. D **60**, 043001 (1999).
20. D. A. Baiko and D. G. Yakovlev, Astron. Astrophys. **342**, 192 (1999).
21. L. B. Leinson and A. Perez, JHEP 9809:20 (1998).
22. G. Raffelt and D. Seckel, Phys. Rev. D **52**, 1780 (1995).
23. S. Yamada, H.-T. Janka, and H. Suzuki, Astron. Astrophys. **344**, 533 (1999).
24. D. Lai and Y.-Z. Qian, Astrophys. J. **505**, 844 (1998).
25. A. V. Kuznetsov and N. V. Mikheev, Zh. Éksp. Teor. Fiz. **118**, 863 (2000) [JETP **91**, 748 (2000)].
26. R. Popham, S. E. Woosley, and C. Fryer, Astrophys. J. **518**, 356 (1999).
27. H. C. Spruit, Astron. Astrophys. **349**, 189 (1999).
28. V. B. Berestetskii, E. M. Lifshitz, and L. P. Pitaevskii, *Quantum Electrodynamics* (Nauka, Moscow, 1989; Pergamon, Oxford, 1982).

Translated by V. Astakhov

Journal of Experimental and Theoretical Physics, Vol. 94, No. 6, 2002, pp. 1057–1069.
Translated from Zhurnal Éksperimental'noĭ i Teoreticheskoĭ Fiziki, Vol. 121, No. 6, 2002, pp. 1235–1248.

NUCLEI, PARTICLES, AND THEIR INTERACTION

The Schwinger Effect and Possibilities for Its Observation Using Optical and X-ray Lasers

V. S. Popov

Institute for Theoretical and Experimental Physics,
ul. Bol'shaya Cheremushkinskaya 25, Moscow, 117218 Russia

Received December 25, 2001

Abstract—The probability W of e^+e^- pair production from a vacuum in an intense variable electric field generated with powerful optical or X-ray lasers is calculated. Two characteristic ranges are considered: $\gamma \ll 1$ and $\gamma \gg 1$, where γ is the adiabaticity parameter. The probability W is shown to increase sharply with γ (at a fixed field strength F). The dependence of W and the momentum spectrum of electrons and positrons on the laser pulse shape is discussed in detail. Numerical calculations were performed for a laser pulse with a Gaussian envelope and for some pulsed fields. © *2002 MAIK "Nauka/Interperiodica".*

1. INTRODUCTION

Quantum electrodynamics (QED) predicts the possibility of electron–positron (e^+e^-) pair production from a vacuum in a strong electric field [1]. This nonlinear effect, which is outside the scope of perturbation theory and was first considered for a static field, was also theoretically studied for time-varying electric-type fields, i.e., when the following conditions are satisfied:

$$J_1 = \frac{1}{4}F_{\mu\nu}F^{\mu\nu} = \frac{1}{2}(\mathbf{B}^2 - \mathbf{E}^2) < 0,$$

$$J_2 = \frac{1}{4}F_{\mu\nu}\tilde{F}^{\mu\nu} = 0,$$

where J_1 and J_2 are the electromagnetic field invariants. In particular, a spatially uniform field

$$\mathscr{E}(t') = \{F\varphi(t), 0, 0\}, \quad \mathbf{B}(t') = 0 \qquad (1)$$

was considered for $\varphi(t) = \cos t$ [2–10]. Such a field can be realized at antinodes of the standing light wave that emerges when adding two coherent laser beams.[1] In (1), t' is the time, $t = \omega t'$ is a dimensionless time, F is the amplitude of the electric field, ω is its characteristic frequency, and the function $\varphi(t)$ specifies the laser pulse shape. Below, we assume that φ is an analytic function of t^2, $\varphi(-t) = \varphi(t)$, with $|\varphi(t)| \le \varphi(0) = 1$ everywhere on the real axis (i.e., $t = 0$ is the time of field maximum when e^+ and e^- emerge from beneath the barrier [3]). Examples of such fields are $\varphi(t) = \cos t$, $1/\cosh^2 t$, $\exp(-t^2)$, etc.

This process (called the Schwinger pair production mechanism) is of fundamental importance in QED and in quantum field theory in general.[2] However, previous estimates [4, 25, 26] show that it could not be observed with the then available optical lasers. Therefore, the results of [1–8] were generally believed to be of purely theoretical interest in QED.

Recently, however, the situation has changed. First, the power of optical and infrared lasers rose by many orders of magnitude (fields that exceed the characteristic atomic field $F_a \approx 5.14 \times 10^9$ V/cm by one or two orders of magnitude have been achieved [27, 28]). Second, projects to create free-electron X-ray lasers on the TESLA electron–positron collider in DESY and the corresponding facilities in SLAC, in which coherent photon beams with energies of the order of several keV are supposed to be produced, are being designed (see, e.g., [10, 29]). Hence, the theory of the Schwinger effect must be considered in more detail in view of the new experimental possibilities. This is the subject of the recently published paper by Ringwald [10] and Alkofer *et al.* [30].

Here, we continue to discuss this range of questions. Let us briefly describe the content of our paper. The probabilities W of e^+e^- pair production from a vacuum for infrared, optical, and X-ray lasers are calculated in

[1] A plane wave of arbitrary intensity and spectral composition has the invariants $J_1 = J_2 = 0$ and produces no pairs in a vacuum [1].

[2] Processes similar to the Schwinger pair production are encountered in various fields of modern physics, for example, in the theory for quantum evaporation of black holes [11, 12], when considering the early evolutionary stages of the Universe [13, 14], in the theory for multiphoton ionization of semiconductors [15], etc. A physically similar process is the spontaneous production of positrons in the electric field of a superheavy nucleus with change $Z > Z_{cr}$ [16–19] ($Z_{cr} \approx 170$ for a spherical nucleus) or during the adiabatic approach of two heavy nuclei with $Z_1 + Z_2 > Z_{cr}$ [17–22]. See, e.g., [23, 24] for the current status of this problem.

Sections 2 and 3. We discuss two limiting regimes: $\gamma \ll 1$ and $\gamma \gg 1$, where γ is the adiabaticity parameter:[3]

$$\gamma = \frac{\omega}{\omega_t} = \frac{mc\omega}{eF} = \frac{\hbar\omega}{eF\lambda\!\!\!^{-}_e} \tag{2}$$

(here, ω_t is the frequency of electron tunneling through the gap $2mc^2$ between the lower and upper continua in an electric field F [3, 8]). We calculated the dependence of W on the field amplitude F and frequency ω for various types of lasers (both available and currently designed ones). The dependence of W and momentum spectrum of the e^+ and e^- being produced on the function $\varphi(t)$ in (1), i.e., on the laser pulse shape, is analyzed in Section 4. The probability W is shown to increase sharply with decreasing pulse duration, particularly for $\gamma \gg 1$ (i.e., for $\omega \gg \omega_t$). We present the results of our numerical calculations for a laser pulse with a Gaussian envelope and consider the $e^\pm$ momentum spectrum in the adiabatic range $\gamma \ll 1$ and for $\gamma \gg 1$. Our results are discussed in Section 5. Details of our calculations and auxiliary formulas are given in the Appendices.

Here, we use the following notation: $\epsilon = F/F_{cr}$ is the reduced electric field; $F_{cr} = m^2c^3/e\hbar \approx 1.32 \times 10^{16}$ V/cm is the critical (Schwinger [1]) field in QED ($eF_{cr}\lambda\!\!\!^{-}_e = mc^2$); $F_a = m^2e^5/\hbar^4 = \alpha^3 F_{cr}$ is the atomic field; $\alpha = e^2/\hbar c = 1/137$; $K_0 = 2mc^2/\hbar\omega = \lambda/\pi\lambda\!\!\!^{-}_e$ is the multiquantum parameter for the process; $\lambda = 2\pi c/\omega$ is the laser wavelength; $\lambda\!\!\!^{-}_e = \hbar/mc = 386$ fm; m is the electron mass; and, as a rule, $\hbar = c = 1$ (in this case, $\gamma = 2/K_0\epsilon$). Below, we assume that the conditions $\epsilon \ll 1$ and $K_0 \gg 1$ are satisfied. These conditions ensure that the quasi-classical approximation is applicable to the problem under consideration.

Our results were announced in part in [31].

2. BASIC EQUATIONS

Let us first consider a monochromatic laser field: $\varphi(t) = \cos t$. Using the imaginary-time method [3] to describe the subbarier electron motion in the relativistic case (between the boundaries of the lower and upper continua), we can show that the probability of pair production from a vacuum in the state with momenta $\pm\mathbf{p}$ for $e^\pm$, to within a preexponetial factor [2–4], is

$$w(\mathbf{p}) = \frac{d^3W}{d^3p} \propto \exp\left\{-\frac{\pi}{\epsilon}\left[\tilde{g}(\gamma) + \tilde{b}_1(\gamma)\frac{p_\parallel^2}{m^2} + \tilde{b}_2(\gamma)\frac{p_\perp^2}{m^2}\right]\right\}, \tag{3}$$

where the function $\tilde{g}(\gamma)$ and the coefficients $\tilde{b}_{1,2}(\gamma)$ of the momentum spectrum for $\gamma \gtrsim 1$ significantly depend on the pulse shape (1) (see Section 4), and $\tilde{g}(0) = \tilde{b}_2(0) = 1$ and $\tilde{b}_1(\gamma) \propto \gamma^2$ for $\gamma \longrightarrow 0$ (here, the tilde means that these functions refer to pair production, in contrast to similar functions $g(\gamma)$ and $b_{1,2}(\gamma)$ in the theory for multiphoton ionization of atoms [32]). The difference between $g(\gamma)$ and $\tilde{g}(\gamma)$, etc., is due to different forms of the dispersion law $E(\mathbf{p})$ for an electron in subbarrier motion (in addition, γ for these two processes has different orders of magnitude). The total probability W per invariant Compton 4-volume $\lambda\!\!\!^{-4}_e/c = m^{-4} \approx 7.25 \times 10^{-53}$ cm^3 s can be determined by integrating (3) over d^3p with allowance for energy conservation during n-photon absorption. The corresponding (cumbersome) formulas are given in [4] and can be used for numerical calculations.

However, these formulas are significantly simplified[4] for $\gamma \ll 1$ and $\gamma \gg 1$. In the former case (a low frequency ω and a strong electric field), the $n\omega$ spectrum is virtually continuous and

$$W = \frac{m^4}{2^{3/2}\pi^4}\epsilon^{5/2}\exp\left\{-\frac{\pi}{\epsilon}\tilde{g}(\gamma)\right\}, \tag{4}$$

$$\tilde{g}(\gamma) = 1 - \frac{1}{8}\gamma^2 + \frac{3}{64}\gamma^4 + \ldots,$$
$$\tilde{b}_1 = \frac{1}{2}\gamma^2\left(1 - \frac{9}{8}\gamma^2 + \ldots\right), \quad \tilde{b}_2 = 1 - \frac{1}{4}\gamma^2 \tag{4'}$$

(compared to a constant field, the preexponential factor in (4) contains a small factor proportional to $\sqrt{\epsilon}$; its origin is discussed in Appendix A). The next coefficients of these expansions can also be calculated (see Appendix C).

Assuming that the maximum electric field F is reached when laser radiation is focused in the volume $\Delta V = \lambda^3$ (diffraction limit) and that the pulse duration is T, we find the total number of e^+e^- pairs produced from a vacuum:

$$N(T) = 0.354K_0^4\epsilon^{5/2} \times \exp\left\{-\frac{\pi}{\epsilon}\left[1 - \frac{1}{2(K_0\epsilon)^2}\right]\right\}N', \tag{5}$$

[3] It was introduced in [2, 3]. Note that it characterizes the dynamics of particle tunneling through a time-varying barrier and is similar to the well-known Keldysh parameter in the theory for multiphoton ionization of atoms and ions by laser radiation [15].

[4] See Eqs. (20), (21) and (A.12) in [4] for $\gamma \ll 1$ and $\gamma \gg 1$, respectively. The formulas used by Ringwald (see (18) in [10]) for $\gamma \ll 1$ closely match (4), while, for $\gamma \gg 1$, they differ from (8) only in the numerical factor $2/\sqrt{\pi} \approx 1.13$, which is unimportant for the subsequent estimates.

if the laser pulse spans $N' = \omega T/2\pi$ field periods. For the pair production rate (in the volume λ^3), we obtain

$$\frac{dN}{dt'}[\mathrm{s}^{-1}] = 4.34\times 10^{19}(K_0\sqrt{\epsilon})^3\exp\left(-\frac{\pi}{\epsilon}\right), \quad \gamma \ll 1. \tag{6}$$

In the other limit, $\gamma \gg 1$, we have

$$\tilde{g}(\gamma) = \frac{4}{\pi\gamma}\left[\ln\gamma + c_0 + \frac{\ln\gamma}{4\gamma^2} + \ldots\right],$$
$$\tilde{b}_1(\gamma) = \frac{2}{\pi\gamma}\left[\left(1-\frac{3}{4\gamma^2}\right)\ln\gamma + c_1\right], \tag{7}$$
$$\tilde{b}_2 = \frac{2}{\pi\gamma}\left[\left(1-\frac{1}{4\gamma^2}\right)\ln\gamma + c_2\right],$$

$c_0 = c_1 = 2\ln 2 - 1 \approx 0.386$, $c_2 = 2\ln 2$, and the pair production probability is represented as the sum of the probabilities of n-photon processes:

$$W = \sum_n w_n,$$
$$w_n = \frac{2}{\pi^3}m^4K_0^{-5/2}\left(\frac{e}{4\gamma}\right)^{2n} q(n-K_0), \tag{8}$$

where $n > K_0 = 2m/\omega$, $e = 2.718\ldots$, and

$$q(x) = \frac{1}{2}e^{-2x}\int_0^{2x}\frac{e^t dt}{\sqrt{t}}$$
$$\approx \begin{cases} \sqrt{2x}\left(1-\frac{4}{3}x+\ldots\right), & x \longrightarrow 0, \\ \frac{1}{\sqrt{8x}}\left(1+\frac{1}{4x}+\ldots\right), & x \longrightarrow \infty. \end{cases}$$

Since the probability w_n in this case rapidly decreases with increasing n and since $q(x)$ is a weak function of order unity (its maximum value of 0.541 is reached at $x = x_m \approx 0.427$; see [33, p. 121]), the estimates

$$W \approx \frac{m^4}{2^{3/2}\pi^3}\left(\frac{\omega}{m}\right)^{5/2}\left(\frac{4\gamma}{e}\right)^{-2K_0}, \quad \gamma \gg 1, \tag{9}$$

$$N(T) \approx 2\pi K_0^{3/2}\exp\left(-2K_0\ln\frac{4\gamma}{e}\right)N', \tag{10}$$

where N' has the same meaning as that in (5), follow from (8). Comparison of formulas (5) and (10) shows that (at a fixed electric field F), the pair production probability for $\gamma \gg 1$ is many orders of magnitude higher than that in the adiabatic range $\gamma \ll 1$ (this is also the case for multiphoton ionization of atoms [15, 32] and, generally, for particles tunneling through an oscillating barrier if the frequency of its oscillations $\omega \gg \omega_t$). At $\gamma \sim 1$, expressions (5) and (10) are joined in order of magnitude.

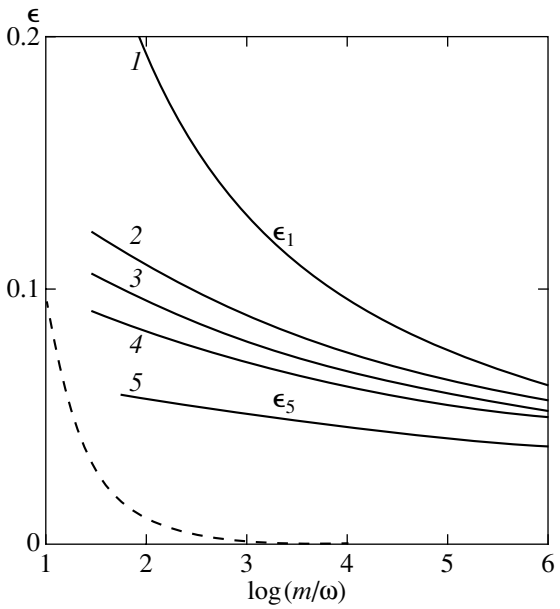

Fig. 1. The reduced electric field $\epsilon = F/F_{cr}$ required to produce one electron–positron pair in the volume $\Delta V = \lambda^3$ in time T. The solid curves correspond to the following pulse durations: one field period $T = 2\pi/\omega$ (ϵ_1, curve *1*), $T = 10^{-12}$, 10^{-10}, 10^{-8}, and 1 s (curves *2*–*5*, respectively). The domain of adiabaticity lies above the dashed curve for which $\gamma = 1$.

3. NUMERICAL CALCULATIONS

Let us turn to numerical estimates. Figure 1 shows the reduced electric field ϵ that corresponds to the production of one e^+e^- pair in the volume $\Delta V = \lambda^3$ for several laser pulse durations: from $T = 2\pi/\omega$ (curve *1*, one field period) to $T = 1$ s (curve *5*). For optical lasers, these values are similar but the difference between them increases sharply with ω if $\hbar\omega \gtrsim 1$ keV. This is in agreement with the estimates ($K_0 \gg 1$) that follow from (5) and (10):

$$\epsilon_1 \sim \frac{\pi}{4\ln K_0}, \quad \epsilon_5 \sim \frac{\pi}{3(\ln K_0 + 15)},$$

where ϵ_1 and ϵ_5 correspond to curves *1* and *5*, respectively. The dashed curve in this figure corresponds to $\gamma = 1$, with the adiabaticity parameter for all points above this curve being $\gamma < 1$.

In Figs. 2–4, the total number of pairs (in the volume λ^3) is plotted against electric-field strength; the curve numbers in Fig. 2 correspond to the photon energies in Table 1. As we see from these figures, the number of pairs increases with field strength F so rapidly (particularly for $\lambda \gtrsim 1$ μm) that there may be said to be a laser breakdown of vacuum [4]. At a fixed F, the number of pairs increases with wavelength λ. This is because all curves refer to the adiabatic range $\gamma \ll 1$ (see Fig. 1 and column $F^{(1)}$ in Table 1), in which N is proportional to the volume ΔV of the focusing region. Since N expo-

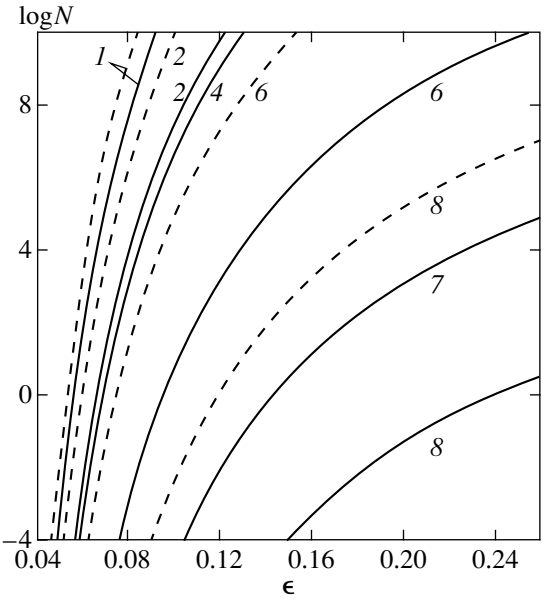

Fig. 2. The number N of e^+e^- pairs produced in the volume λ^3 in time T: in one period (solid curves) and in $T = 1$ ps (dashed curves). The curve numbers correspond to the lasers listed in Table 1.

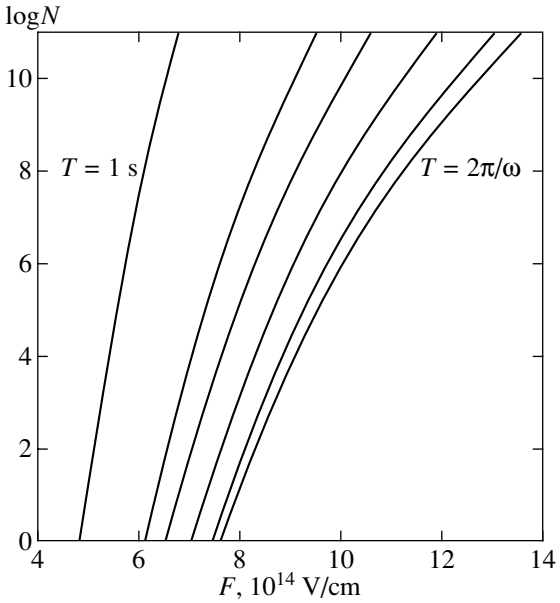

Fig. 3. The number N of e^+e^- pairs versus field amplitude F for a Ti–sapphire laser. The curves (from right to left) correspond to the pulse durations $T = 2.6$ fs (one field period), 0.01 ps, 1 ps, 100 ps, 10 ns, and 1 s; $\Delta V = \lambda^3$.

nentially depends on the field [see (5)], an increase in pulse duration by many orders of magnitude, from one period to 1 s, causes a relatively small displacement of the $N = N(\epsilon, \omega)$ curves toward weaker fields (for optical lasers, Fig. 3). For X-ray lasers (Fig. 4), the minimum required field decreases more appreciably.

Table 2 gives the field strengths F_N required for the production of N electron–positron pairs in one period $T = 2\pi/\omega$ and in the time $T = 1$ s. For optical lasers, the observation threshold of the Swinger effect (i.e., $N = 1$) is reached at $F = (0.5\text{–}1.0) \times 10^{15}$ V/cm. This value is one and a half orders of magnitude smaller than the critical field F_{cr} (a dash in Table 2 means that the calculated $F_N \gtrsim F_{cr}$ and the inverse effect of the particles produced from a vacuum on the external field must be taken into account in such fields). Since $\gamma < 1$ for all the cases considered in Table 2, formula (5) is applicable here. Thus, $\gamma = 1$ is reached at $F \approx 4.6 \times 10^{10}$ V/cm for a ruby laser, at $F \approx 2.9 \times 10^{11}$ V/cm for $\lambda = 109$ nm [34], etc., which is significantly lower than the corresponding F_N.

If $\gamma \gg 1$, then the dependence of N on the field amplitude is no longer exponential but a power law:

$$N \propto \gamma^{-2K_0} \propto F^{2K_0},$$

which corresponds to a multiphoton regime (the perturbation theory of high order K_0 in external field F). In this case, (10) gives values that are many orders of magnitude larger than those extrapolated with the adiabatic formula (5). The ratio of the corresponding numbers is

$$\rho \sim (K_0\epsilon)^{2K_0}\exp(\pi/\epsilon),$$

so that, for example, $\rho \sim 4 \times 10^{10}$ at $K_0 = 5$ and $\epsilon = 0.1$; $\rho \sim 10^{21}$ at $K_0 = 10$ and $\epsilon = 0.05$; $\rho \sim 10^{35}$ at $K_0 = 10$ and $\epsilon = 0.03$; etc. Therefore, it would be easier to observe the Schwinger effect for $\gamma \gtrsim 1$ (at a given field F), which is also clear from physical considerations: in this case, the external field changes its direction many times in

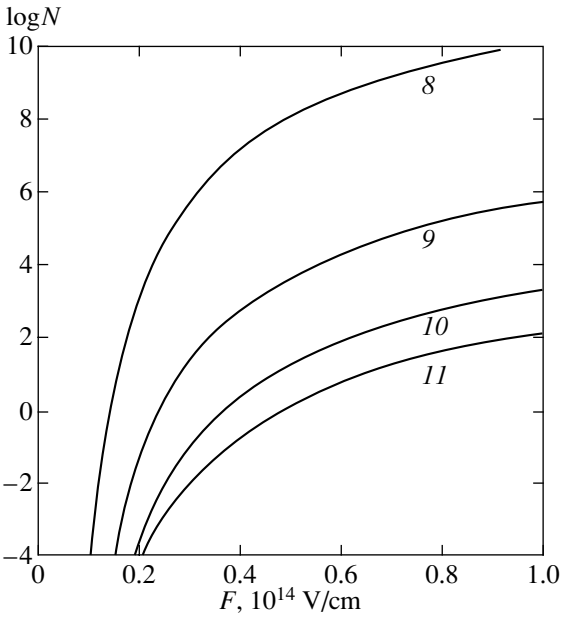

Fig. 4. Same as Fig. 2 for X-ray lasers (at $T = 2\pi/\omega$). Curves *8* and *9* correspond to the numbers in Table 1; the photon energies for curves *10* and *11* are $\hbar\omega = 50$ and 100 keV, respectively.

Table 1. Laser parameters

No.	λ, nm	ħω, eV	K_0	$F^{(1)}$	Type of laser
1	1.24(4)	0.1	1.02(7)	2.59(9)	–
2	1.06(4)	0.117	8.74(6)	3.02(9)	CO_2 [34]
3	1064	1.165	8.77(5)	3.01(10)	Nd–YAG [34]
4	785	1.58	6.47(5)	4.08(10)	Ti–sapphire
5	694	1.786	5.72(5)	4.64(10)	Ruby
6	109	11.4	8.97(4)	2.94(11)	Free-electron laser [35]
7	25	50	2.06(4)	1.29(12)	–
8	1.24	1.0(3)	1.02(3)	2.59(13)	X-ray laser [10]
9	0.1	1.24(3)	82.4	3.20(14)	[10]

Note: λ is the wavelength, K_0 is the multiquantum parameter, and $F^{(1)}$ is the electric field with γ = 1; the notation $a(b) \equiv a \times 10^b$.

the tunneling time; as a result the barrier width decreases and its penetrability increases sharply (which is clearly seen from the imaginary-time method [3, 8]).

Unfortunately, $\gamma \gg 1$ only in weak fields ($\epsilon \ll 1/K_0$), where the probability W itself is extremely low. As with multiphoton ionization of atoms, $K_0 \lesssim 10$–20 are actually required here, implying that $\hbar\omega \gtrsim 100$ keV. In this case, for example, at $K_0 = 10$, $\gamma \sim 3$, and $T = 1$ s, we would have $\epsilon \approx 0.03$ and $N \sim 10^{10}$, while, according to the adiabatic approximation, virtually no pairs are produced in such fields. However, such γ-ray lasers are likely to be produced only in the rather distant future.

4. THE DYNAMIC SCHWINGER EFFECT

In the optical range, extremely intense fields can be achieved by shortening the laser pulse; its duration becomes comparable to the optical period, and its shape is far from an ideal sine wave [27, 28]. To all appearances, the same is also true for X-ray lasers. Therefore, let us consider the effect of pulse shortening on the probability of the Schwinger effect.

The momentum spectrum of the electrons and positrons produced from a vacuum by the electric field (1) is given by formula (3), in which[5]

$$\tilde{g}(\gamma) = \frac{4}{\pi}\int_0^1 \chi(\gamma u)(1-u^2)^{1/2}du,$$

$$\tilde{b}_1(\gamma) = -\gamma\tilde{b}_2'(\gamma) = \frac{2}{\pi}\int_0^1 \frac{\chi(\gamma u)-\chi(\gamma)}{(1-u^2)^{3/2}}du, \qquad (11)$$

$$\tilde{b}_2(\gamma) = \frac{2}{\pi}\int_0^1 \chi(\gamma u)(1-u^2)^{-1/2}du = \frac{1}{2\gamma}\frac{d}{d\gamma}[\gamma^2\tilde{g}(\gamma)],$$

and the function $\chi(u)$ is completely determined by the shape of the field pulse $\varphi(t)$ and has the same form as in the theory for multiphoton ionization of atoms. Thus, $\chi(u) = (1 + u^2)^{-1/2}$ for monochromatic radiation $\varphi(t) = \cos t$, $\chi(u) = 1/(1 + u^2)$ for a soliton-like pulse $\varphi(t) = 1/\cosh^2 t$, etc. (see [32] for more detail).

For a Gaussian pulse, $\varphi(t) = \exp(-t^2/2\sigma^2)$, the inverse function $u = u(\chi)$ is defined explicitly:

$$u = \sigma\sqrt{-2\ln\chi_1}F_1(1/2;\ 3/2;\ -\ln\chi),$$
$$0 < \chi \le 1,$$

Table 2. Typical parameters for observing the Schwinger effect

λ, nm	F_N, 10^{15} V/cm			
	$N = 1$	$N = 10^3$	$N = 10^6$	$N = 10^9$
1.06(4)	0.739	0.838	0.967	1.14
	0.481	0.521	0.570	0.627
1064	0.873	1.02	1.21	1.49
	0.521	0.570	0.628	0.698
785	0.899	1.05	1.25	1.56
	0.527	0.577	0.636	0.707
694	0.902	1.06	1.27	1.59
	0.530	0.580	0.640	0.712
109	1.07	1.29	1.61	2.13
	0.569	0.627	0.697	0.785
25	1.26	1.56	2.04	2.91
	0.605	0.671	0.752	0.855
0.1	3.15	5.74	–	–
	0.774	0.890	1.04	1.25

Note: F_N is the electric-field strength at which N electron–positron pairs are produced in the volume $\Delta V = \lambda^3$: in one field period (first row) and in 1 s (second row, at given N and λ). The notation $a(b) \equiv a \times 10^b$.

[5] The derivation of these formulas by the imaginary-time method [43] is omitted here.

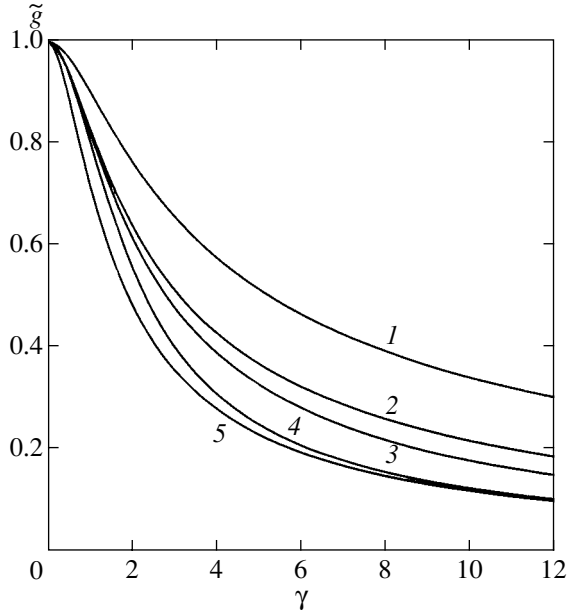

Fig. 5. The function $\tilde{g}(\gamma)$ for the Schwinger effect versus adiabaticity parameter γ. Curves *1–5* refer to the following fields: (*1*) $\varphi(t) = \cos t$; (*2*) $\varphi(t) = \exp(-t^2)$; (*3*) $\varphi(t) = 1/\cosh^2 t$; (*4*) $\varphi(t) = 1/(1 + t^2)$; and (*5*) $\varphi(t) = (1 + t^2)^{-2}$.

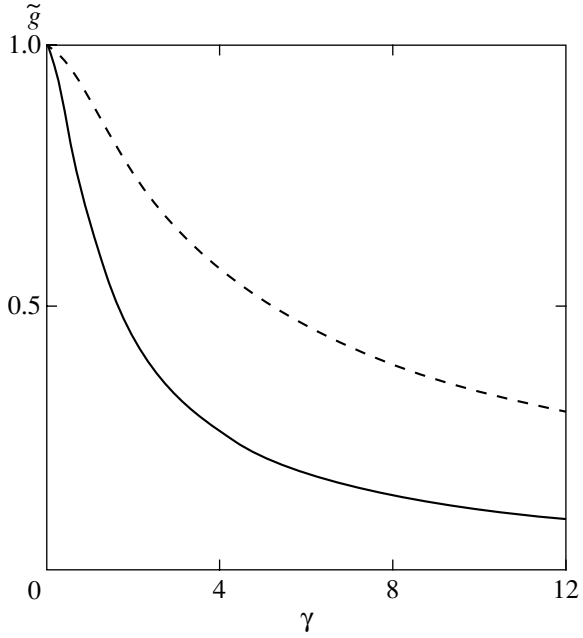

Fig. 6. Same as the preceding figure for a pulse $\varphi(t) = (1 - t^2)/(1 + t^2)^2$ (solid curve). For comparison, the plot of $\tilde{g}$ versus γ is shown for monochromatic light (dashed curve).

where ${}_1F_1$ is a degenerate hypergeometric function. Similarly, for

$$\varphi(t) = (1 + t^2)^{-\alpha}, \quad \alpha \geq 1, \tag{12}$$

we have

$$\chi = (1 - \tau^2)^{\alpha},$$
$$u = \int_0^{\tau} (1 - t^2)^{-\alpha} dt = \tau F(\alpha, 1/2; 3/2; \tau^2), \tag{12'}$$

where $F(\ldots) \equiv {}_2F_1(\ldots)$ is the Gaussian hypergeometric function. Eliminating the parameter τ, we obtain a simple equation,

$$u = \frac{1}{2} \int_{\chi^{1/\alpha}}^{1} \frac{dy}{y^{\alpha}\sqrt{1 - y}}, \tag{12''}$$

which defines the inverse function $u(\chi)$ for any $\alpha \geq 1$. Hence,

$$\chi(u) = 1 - \alpha u^2 + \frac{1}{6}(7\alpha^2 - 3\alpha)u^4 + \ldots, \quad u \longrightarrow 0, \tag{13}$$

and for $u \longrightarrow \infty$,

$$\chi(u) \approx \begin{cases} [2(\alpha - 1)u]^{-\alpha/(\alpha - 1)}, & \alpha > 1, \\ 4\exp(-2u), & \alpha = 1. \end{cases} \tag{13'}$$

The larger the exponent α, the more rapid the decay of the field pulse (12) when $t \longrightarrow \infty$, and the slower the decrease in $\chi(u)$ at infinity. In [32], we present a general recipe for calculating the function $\chi(u)$ from the specified pulse shape $\varphi(t)$. As we see from (11), the problem then reduces to quadratures.

Note also that for numerical calculations, it is convenient to rewrite (11) as

$$\tilde{g}(\gamma) = \frac{4}{\pi} \int_0^{\pi/2} \chi(\gamma \sin\theta) \cos^2\theta d\theta,$$
$$\tilde{b}_2(\gamma) = \frac{2}{\pi} \int_0^{\pi/2} \chi(\gamma \sin\theta) d\theta. \tag{14}$$

Using these equations, we calculated the function $\tilde{g}(\gamma)$ and the coefficients $\tilde{b}_{1,2}(\gamma)$ of the momentum spectrum for several pulse fields. The results of our calculations for $\tilde{g}(\gamma)$ are shown in Figs. 5 and 6. In all cases, the function $\tilde{g}(\gamma)$ monotonically decreases with increasing adiabaticity parameter; the probability *W* at a given field *F* increases sharply (because $\epsilon \ll 1$) and begins to depend significantly on the pulse shape $\varphi(t)$. This phenomenon arising at high frequencies $\omega \gtrsim \omega_t$ may be called the dynamic Schwinger effect.

Below, we also present the results of our calculations for a modulated electromagnetic pulse with a Gaussian envelope:[6]

$$\varphi(t) = \exp(-t^2/2\sigma^2)\cos t, \quad (15)$$

which (for an appropriate choice of σ) can serve as a model of an ultrashort laser pulse or the electric field in a standing light wave. In this case, the function $\chi(u)$ can be numerically determined from the equations

$$\chi = \frac{\exp(-\tau^2/2\sigma^2)}{\cosh\tau}, \quad u = \int_0^\tau \exp\left(\frac{t^2}{2\sigma^2}\right)\cosh t\,dt \quad (16)$$

(here, τ is a parameter, $0 < \tau < \infty$). The pulse (15) shortens with decreasing σ: its amplitude decreases in one laser-field period by the factor $\delta \approx \exp(-2\pi^2/\sigma^2)$. As we see from Fig. 7, the decrease of $\tilde{g}(\gamma)$ in the exponent shows up at $\sigma \sim 5$ and is significant at $\sigma = 1$. As for the coefficients $b_{1,2}(\gamma)$, their dependence on σ may be ignored for $\sigma \geq 3$, but for $\sigma \lesssim 1$, the momentum spectrum broadens appreciably (see [31] for more detail).

However, these effects show up in full measure for $\gamma \gtrsim 1$, while, for $\gamma \ll 1$, the dependence on γ is contained only in the terms of order γ^2. Assuming that near the maximum of the electric field

$$\varphi(t) = 1 - \frac{a_2}{2!}t^2 + \frac{a_4}{4!}t^4 - \ldots, \quad a_2 > 0, \quad (17)$$

we obtain the adiabatic expansions

$$\tilde{g}(\gamma) = 1 - \frac{1}{8}a_2\gamma^2 + \frac{1}{192}(10a_2^2 - a_4)\gamma^4 + O(\gamma^6),$$
$$\tilde{b}_1(\gamma) = \frac{1}{2}a_2\gamma^2 + \ldots, \quad \tilde{b}_2(\gamma) = 1 - \frac{a_2}{4}\gamma^2 + \ldots. \quad (18)$$

To a first approximation in γ^2, the dependence on the laser-pulse shape is universal:

$$w(\mathbf{p}) \approx \exp\left\{-\left[\frac{\pi}{\epsilon}\left(1 - \frac{1}{8}\tilde{\gamma}^2\right) + \frac{1}{eF}(\tilde{\gamma}^2 p_\parallel^2 + p_\perp^2)\right]\right\}, \quad (19)$$

where $\tilde{\gamma} = \sqrt{a_2}\,\gamma$ and $a_2 = -\varphi''(0)$ is the curvature of the pulse near its top. In this case, $p_\perp \sim \Delta p_\perp \sim \sqrt{eF} = m\sqrt{\epsilon} \ll m$ and $p_\parallel \sim \gamma^{-1}p_\perp \sim mK_0\epsilon^{3/2}$. Thus, the transverse $e^\pm$ pulse is nonrelativistic (because $\epsilon \ll 1$). In the longitudinal direction, however, $p_\parallel \gtrsim m$ if the field strength satisfies the conditions $K_0^{-3/2} \ll \epsilon \ll 1$ or $\gamma \lesssim \sqrt{\epsilon}$. Since $K_0 \sim 10^6$ for optical lasers, these conditions are satisfied with a margin. The next corrections to (18) and (19) can also be determined (see Appendix B, where the antiadiabatic case $\gamma \gg 1$ is also discussed).

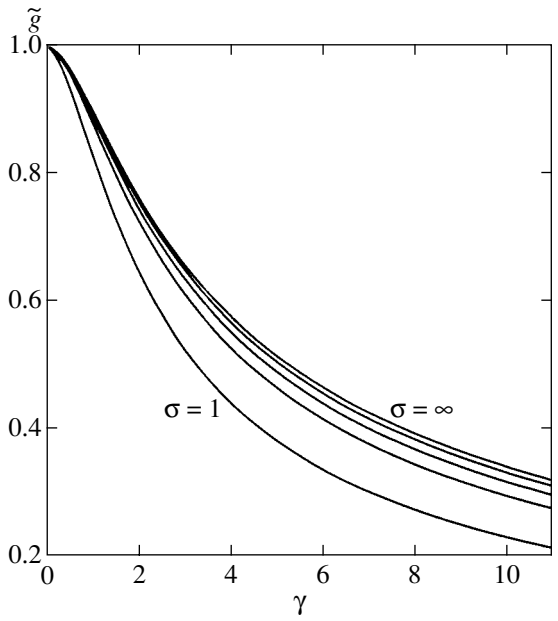

Fig. 7. The function $\tilde{g}(\gamma)$ versus adiabaticity parameter for a modulated light pulse (15). For the curves (from the bottom upward), $\sigma = 1, 2, 3, 5$, and ∞ (the last case corresponds to a monochromatic laser field).

As we see from (19), the angular distribution of the $e^\pm$ being produced for $\gamma \ll 1$ is sharply anisotropic and elongated along the electric field. On the other hand, we have $p_\parallel \approx p_\perp$ for $\gamma \gg 1$ and the $e^\pm$ momentum spectrum approaches an isotropic one. [see (B.12) in Appendix B].

Note now that the curves in Figs. 1–3 were calculated using formulas (5) and (10), which are valid for a monochromatic field ($\sigma = \infty$). However, they refer to the adiabatic range. Therefore, it follows from Fig. 6 that their change with decreasing laser-pulse duration may be disregarded up to $\sigma \sim 1$. For example, for the pulse, we have $a_2 = 1 + \sigma^{-2}$ and

$$\tilde{g}(\gamma) = 1 - \frac{1 + \sigma^2}{8\sigma^2}\gamma^2 + \frac{7 + 14\sigma^2 + 9\sigma^4}{192\sigma^4}\gamma^4 + \ldots. \quad (20)$$

On the other hand, in the limit $\gamma \longrightarrow \infty$,

$$\tilde{g}(\gamma) \approx \frac{4}{\pi\gamma}\begin{cases}\sigma\sqrt{2\ln(2\gamma/\sigma^2)}, & \sigma < \infty,\\ \ln\gamma, & \sigma = \infty\end{cases} \quad (21)$$

(see Appendix C). Inserting the truncating factor $\exp(-t^2/2\sigma^2)$ in (15), i.e., reducing the laser-pulse duration, causes the asymptotic behavior of the function $\tilde{g}(\gamma)$ to change: for monochromatic radiation, $\ln\gamma$ changes to $\sigma\sqrt{\ln\gamma}$, but the asymptotic behavior changes only at $\gamma \gg \max(1, \sigma^2)$. Thus, pulse shortening

[6] This model is commonly used in laser physics. The full width of the envelope at half maximum is $\sigma\sqrt{8\ln 2} \approx 2.4\sigma$.

decreases the function $\tilde{g}(\gamma)$ and, thereby, increases the probability W and facilitates an experimental observation of the Schwinger effect.

5. CONCLUDING REMARKS

(1) Above, we assumed that (1) represents a classical coherent field with $\hbar\omega \ll mc^2$. Therefore, our results do not refer to a collision of two γ-ray beams from accelerators [where e^+e^- pairs can also be produced if $\hbar(\omega^1 + \omega^2) > 2mc^2$ but incoherently].

(2) Since the Schwinger mechanism for currently available lasers can be realized only in the adiabatic regime, it operates almost in the same way as in a constant field (see Appendix A). For $\gamma \gg 1$, the pair production probability (at a fixed field amplitude F) increases sharply, but this regime is possible only after the creation of γ-ray lasers with photon energies of several tens of keV.

(3) As we see from formula (C.4), the coefficients of γ^{2n} ($n \geq 2$) in the adiabatic expansions (4') are numerically small and decrease with increasing n. As a result, the range of applicability of these expansions extends up to $\gamma \gtrsim 1$, while, for $\gamma < 1$, the Schwinger pair production is closer to the tunneling regime than to the multiphoton one. When calculating the probability W for currently available lasers, we may restrict ourselves to several terms in expansions (4') for the functions $\tilde{g}(\gamma)$ and $\tilde{b}_{1,2}(\gamma)$.

(4) Our calculations refer to the case where the total time of periodic-field action T spans many periods and satisfies the conditions

$$2\pi/\omega \ll T \ll 1/w. \tag{22}$$

In this case, the switching-on and switching-off of the field may be ignored and, on the other hand, the total transition probability is still low: $wT \ll 1$. Under these conditions (which are generally satisfied in experiments, except for very strong fields), the number of pairs $N_{\mathbf{p}}(t)$ with momenta $\pm\mathbf{p}$ is a linear function of time and has the meaning of pair production probability w per unit time. For $\epsilon \ll 1$, the probability w is exponentially small and conditions (22) are satisfied.

If, alternatively, $wT \gtrsim 1$, then $N_{\mathbf{p}}(t)$ is no longer a linear function and a more accurate analysis is needed. As was first shown by Narozhnyĭ and Nikishov [6], $N_{\mathbf{p}}(t)$ is nontrivial in this case: for scalar bosons, the function $N_{\mathbf{p}}(t)$ can either periodically oscillate with increasing t or increase exponentially (depending on which region, stability or instability, the solution to the Mathieu equation is in). At the same time, for fermions, $N_{\mathbf{p}}(t)$ is always a periodic function of time t. Subsequently, these results were confirmed by independent calculations [4, 7].

The following theoretical-group fact underlies the appearance of various functions $N_{\mathbf{p}}(t)$ for bosons and fermions: the problem of pair production from a vacuum in a uniform electric field $\mathscr{E}(t)$ has the dynamic symmetry group SU(1, 1) for scalar particles and the group SU(2) for spinor particles [36]. The group SU(1, 1) contains three one-parameters subgroups such that any other one-parameter subgroup is conjugate ($g' = S^{-1}gS$) with one of them:

$$g_1 = \begin{pmatrix} \cosh(\theta/2) & \sinh(\theta/2) \\ \sinh(\theta/2) & \cosh(\theta/2) \end{pmatrix},$$

$$g_2 = \begin{pmatrix} e^{-i\theta/2} & 0 \\ 0 & e^{-i\theta/2} \end{pmatrix}, \tag{23}$$

$$g_3 = \begin{pmatrix} 1 + i\theta/2 & \theta/2 \\ \theta/2 & 1 - i\theta/2 \end{pmatrix}$$

(θ is the real transformation parameter). The group SU(1, 1) is known [37] to be isomorphic to the second-order group SL(2, R) of real matrices $\tilde{g}$ with the determinant equal to unity:

$$\tilde{g}(\theta) = S^+ g(\theta) S, \quad S = \exp\left(-i\frac{\pi}{4}\sigma_x\right), \tag{24}$$

with

$$\tilde{g}_1(\theta) \equiv g_1(\theta),$$

$$\tilde{g}_2 = \begin{pmatrix} \cos(\theta/2) & \sin(\theta/2) \\ -\sin(\theta/2) & \cos(\theta/2) \end{pmatrix}, \tag{25}$$

$$\tilde{g}_3 = \begin{pmatrix} 1 & \theta \\ 0 & 1 \end{pmatrix}.$$

Hence, we immediately see that $g_i(\theta_1)g_i(\theta_2) = g_i(\theta_1 + \theta_2)$ and, therefore, $[g_i(\theta)]^N = g_i(N\theta)$. Accordingly, we obtain for these three classes of matrices

$$N_{\mathbf{p}}(t) \propto \begin{cases} \sinh^2(N\rho) \sim \exp(2N\rho) & \text{for } g_1, \\ [\sin(N\rho)/\sin\rho]^2 & \text{for } g_2, \\ N^2 & \text{for } g_3 \end{cases} \tag{26}$$

(the last case lies at the boundary between the stability and instability regions and can hardly be realized in practice). Here, N is the number of field periods, and $\rho = \ln\mu$ and μ are the multipliers. Calculating the latter for a specific periodic field $\mathscr{E}(t)$ is a separate problem [according to the Floquet theorem, $\psi(t + 2\pi/\omega) = \mu\psi(t)$]. Formulas (24) describe three possible types of $N_{\mathbf{p}}(t)$ for bosons.

On the other hand, any element of the (compact) group SU(2) can be reduced by rotation to the canonical

form $g_2(\theta)$. Therefore, only the oscillatory regime is possible in the problem of Dirac particle pair production.[7] Note that this case is analogous to the transitions in a two-level atom under the effect of a periodic perturbation close to resonance (see [39], Para. 40).

We emphasize that solutions (24) refer to the case of $wT \gtrsim 1$, which can actually be realized only for very strong fields with $F \gtrsim F_{cr}$. The possibility of achieving this regime in experiments is presently not obvious.

(5) In the theory of solids and, in particular, for semiconductors, the following dispersion law is used [15, 40]:

$$\varepsilon(p) = \Delta\sqrt{1 + p^2/m_*\Delta}, \quad (27)$$

where m_* is the effective mass and Δ is the width of the band gap that separates the valence band from the conduction band. Formally, (27) is the same as that for a free particle in relativistic mechanics:

$$\varepsilon(\mathbf{p}) = \sqrt{m^2 + p^2}.$$

Therefore, our results can be used after obvious transformations in the theory for multiphoton ionization of semiconductors by a laser pulse (for a monochromatic light field, this was already done in [15]). Here, fields of $\sim 10^5$ V/cm act as F_{cr}; as a result, the corresponding effects are much easier to investigate experimentally.

(6) Presently, QED is in excellent agreement with experiment. In the record case of anomalous magnetic moments of e^- and μ^-, the accuracy reaches 10^{-12}, which is confirmed by calculations of the higher orders of perturbation theory in QED up to $(\alpha/\pi)^4$ (see, e.g., [41]). Therefore, the following question can arise: Is it necessary to carry out experiments to test the Schwinger e^+e^- pair production mechanism in the first place? It may be noted that observation of this process would imply testing the Dirac equation and QED for very strong external fields outside the scope of perturbation theory. Indeed, the fact that the probability (4) exponentially tends to zero as $\epsilon \longrightarrow 0$ is directly related to a factorial increase in the higher orders of perturbation theory and to the divergence of the series of perturbation theory in QED (the so-called Dyson phenomenon [42]). Since this nonperturbative effect cannot be obtained by the summation of a finite number of terms in the series of perturbation theory, its observation is of fundamental interest in QED and in the quantum field theory in general.

It is unlikely that the Schwinger effect for other (apart from $e^\pm$) charged particles will ever be observed experimentally: the critical field $F_{cr} \propto m^2$ and has a fantastic value $F_{cr} \sim 10^{21}$ V/cm even for $\pi^\pm$.

(7) In recent years, rapid progress has been made in laser technology both toward decreasing the wavelength λ[8] and toward increasing the intensity J: $J \gtrsim 10^{21}$ W cm^{-2} for petawatt laser radiation [28], which corresponds to electric fields $F \sim 10^{12}$ V/cm that are two orders of magnitude higher than the atomic ones, has already been reached.

As was noted by Ringwald [10], if X-ray lasers ($\hbar\omega \gtrsim 1$ keV) are created and if it is possible to focus their radiation in a volume of λ^3, then the minimum laser powers P_{min} required for the Schwinger effect to be observed will significantly decrease, because $F \propto \sqrt{P}/\lambda$. Thus, for $\lambda = 0.1$ nm and the pulse duration $T = 0.1$ ps, $P_{min} \approx 4 \times 10^{16}$ W is required to produce one e^+e^- pair. Such powers have long been reached in the optical range, but the possibilities for creating such facilities and for beam focusing in X-ray optics are not yet clear and are for future development (see [10]). The calculations presented above show that it will be possible to observe the Schwinger effect experimentally most likely by further increasing the power of infrared and optical lasers.[9]

ACKNOWLEDGMENTS

I would like to thank L.B. Okun', who drew my attention to the paper [10], for a discussion of the results obtained above and for helpful remarks; M.I. Vysotskii, V.D. Mur, V.A. Novikov, and S.V. Popruzhenko for fruitful discussions at the initial stage of this study; S.V. Bulanov, I.M. Dremin, O.V. Kancheli, N.B. Narozhnyĭ, V.I. Ritus, and E.L. Feinberg for a discussion of the results; S.G. Pozdnyakov for help with numerical calculations; and V.A. Gani and M.N. Markina for help in preparing the manuscript. This work was supported by the Russian Foundation for Basic Research (project no. 01-02-16850).

APPENDIX A

Below, we derive a general relationship between the static (w_{st}) and adiabatic (w_a) tunneling probabilities. Let, in a constant electric field F,[10]

$$w_{st}(F) = A\epsilon^\lambda \exp(-B\epsilon^{-\mu}), \quad \epsilon = F/F_0 \longrightarrow 0 \quad (A.1)$$

[7] The theoretical-group aspect of the problem of pair production from a vacuum for particles of arbitrary spin s was considered in [38].

[8] The creation of a free-electron laser with $\lambda = 109$ nm in the vacuum ultraviolet [35] is a record. The recording of laser radiation with $\lambda = 80$ nm ($\hbar\omega \approx 15$ eV) is also reported [29]. Of course, the powers of these lasers are still too low.

[9] It has to be recognized that use of the terms "Schwinger effect" and "Schwinger pair production" in this paper (and in [31]) may be not fully justified. Indeed, it was assumed above that (according to the experimental situation considered) the electric field strength F is small compared to F_{cr} and, hence, $\exp(-2\pi F_{cr}/F) \ll 1$. In this case, the Schwinger formula [1] reduces (to within exponentially small terms) to the first term of a series obtained previously by Heisenberg and Euler [43]. The author is grateful to V.I. Ritus for this remark.

[10] Here, A, B, λ, and μ are constants; see, e.g., [32, 39].

[this formula, just as (A.3)–(A.5), is asymptotically exact in the weak-field limit]. For a periodic field, for which $F(t + T) = -F(t + T/2) = F(t)$, $\omega \ll \omega_t$, and expansion (15) holds near the field maximum, the transition probability per unit time can be determined by averaging (A.1) over the period:

$$w_a(F) = \frac{2}{T}\int_{-T/4}^{T/4} w_{st}(F(t'))dt' \approx \frac{2A}{\omega T}\epsilon^{\lambda}\exp(-B\epsilon^{-\mu})\int_{-\infty}^{\infty}\exp\left(-B\frac{\mu a_2}{2\epsilon^{\mu}}t^2\right)dt \quad (A.2)$$

($t = \omega t'$); hence

$$w_a(F) = \sqrt{\frac{2}{\pi\mu a_2 B}}\epsilon^{\mu/2}w_{st}(F), \quad \epsilon \ll 1. \quad (A.3)$$

Consider two examples.

(1) For the ionization of atoms and ions by an electric field ($B = 2/3$, $\mu = 1$, $F_0 \equiv F_a = m^2e^5/\hbar^4$; see [39]) and according to [44], we have

$$w_a(F) = \sqrt{3F/\pi F_0}w_{st}(F) \quad (A.4)$$

[the parameters A and λ in (A.1) depend on the quantum numbers of the state; for instance, $\lambda = -1$ and $A = 4$ for the ground level of the hydrogen atom, $\lambda = -(2n_2 + |m| + 1)$ for the state with parabolic quantum numbers $|n_1, n_2, m\rangle$, $\lambda = 1$ for a three-dimensional δ potential, etc.].

(2) For the Schwinger effect, $B = \pi$, $\lambda = 2$, $\mu = 1$, and $F_0 = F_{cr}$. Therefore,

$$w_a(F) = \frac{1}{\pi}\sqrt{\frac{2F}{F_{cr}}}w_{st}(F). \quad (A.5)$$

Since the coefficient $A = m^4/4\pi^3$ [1], we immediately obtain the correct preexponential factor in (4). In all cases where $\mu = 1$ and $w_{st} \propto \exp(-\text{const}/F)$ for $F \longrightarrow 0$, the adiabatic tunneling probability contains, compared to w_{st}, an additional small factor proportional to $\sqrt{\epsilon}$, which does not become unity at an arbitrarily low frequency ω.

So far, we assumed the wave polarization to be linear; i.e., the field $\mathbf{F}(t)$ preserves its direction in space. For elliptical polarization, the relation between the probabilities w_a and w_{st} is more complex and was given in [44]; its derivation has recently been published in [45].

Note that, for a low-frequency field, the probability $w_a(F, \xi)$ can be obtained [45] by averaging expression (A.2) also for strong fields (for any light ellipticity ξ), when the asymptotic expression (A.1) no longer holds but $w_{st}(F)$ can be taken from numerical calculations [46]. In this case, it turns out that, in the suprabarrier range $0.25 \lesssim F \lesssim 1.5$, the dependence of the ionization probabilities w_a and w_{st} on field F is remarkably close to a linear one (which holds neither for weak fields with [39] $w(F) \propto \exp(-2/3F)$ nor in the limit $F \longrightarrow \infty$, where [47, 48] $\mathrm{Im}E(F) \propto (F\ln F)^{2/3}$ for Stark resonances). Following [49], this regime can be called the intermediate asymptotics: $w(F) \approx k(F - F_0)$; the parameters k and F_0 depend on the quantum numbers of the state and can be determined by numerical fitting.

Previously [50], we qualitatively explained the existence of such asymptotics for the problem of the Stark effect in a strong field by using a $1/n$ expansion. Recent numerical calculations (for the ground state of the helium atom in a constant electric field [51] and for H^- in the field of a circularly polarized wave [52]) confirm the presence of a portion of the linear dependence of w on F in the suprabarrier range of fields up to $F \sim F_a$.

APPENDIX B

According to [2, 3, 15], for a monochromatic field $\varphi(t) = \cos t$,

$$\tilde{g}(\gamma) = \frac{4}{\pi}\int_0^1\sqrt{\frac{1-u^2}{1+\gamma^2u^2}}du = \frac{4\nu}{\pi\gamma}\mathbf{D}(\nu), \quad (B.1)$$

$$\tilde{b}_1(\gamma) = \frac{1}{2}\nu^1\tilde{g}(\gamma),$$

$$\tilde{b}_2(\gamma) = \frac{2}{\pi}\int_0^1\frac{du}{\sqrt{(1-u^2)(1+\gamma^2u^2)}} = \frac{2\nu}{\pi\gamma}\mathbf{K}(\nu), \quad (B.2)$$

where γ is the adiabaticity parameter, and $\mathbf{K}$ and $\mathbf{D}$ are the complete elliptic integrals of the first and third kinds, respectively, [33, 53] with modulus ν,

$$\nu = \frac{\gamma}{\sqrt{1+\gamma^2}} = \begin{cases}\gamma - \frac{1}{2}\gamma^3 + \ldots, & \gamma \ll 1,\\ 1 - \frac{1}{2\gamma^2} + \ldots, & \gamma \gg 1.\end{cases}$$

Below, we give expansions for small and large γ. In the former case, expanding $(1 + \gamma^2u^2)^{-1/2}$ in a Taylor series, we derive from (B.1)

$$\tilde{g}(\gamma) = \sum_{n=0}^{\infty}(-1)^n g_n\gamma^{2n}, \quad |\gamma| \le 1, \quad (B.3)$$

$$g_n = \frac{\Gamma^2(n+1/2)}{n!(n+1)!\pi} = \frac{1}{(n+1)}\left[\frac{(2n-1)!!}{n!2^n}\right]^2, \quad (B.4)$$

i.e., $g_1 = 1/8$, $g_2 = 3/64$, $g_3 = 25/1024$, and $g_n \approx 1/\pi n^2$ for $n \longrightarrow \infty$. It can be shown that

$$\tilde{b}_1(\gamma) = -\gamma\tilde{b}_2'(\gamma), \quad \tilde{b}_2(\gamma) = \frac{1}{2\gamma}\frac{d}{d\gamma}[\gamma^2\tilde{g}(\gamma)], \quad (B.5)$$

whence

$$\tilde{b}_1(\gamma) = 4(g_1\gamma^2 - 3g_2\gamma^4 + \ldots),$$
$$\tilde{b}_2(\gamma) = 1 - 2g_1\gamma^2 + 3g_2\gamma^4 + \ldots. \quad (B.6)$$

Thus, the series for the coefficients $\tilde{b}_{1,2}$ of the momentum spectrum are expressed in terms of the same coefficients g_n as in (B.3).

The angular $e^{\pm}$ distribution for $\gamma \ll 1$ is sharply anisotropic: the transverse momentum is nonrelativistic, $p_\perp \sim m\sqrt{\epsilon} \ll m$, while the characteristic longitudinal momentum is much larger: $p_\parallel \sim \gamma^{-1}p_\perp$; this is because the electron and positron can be accelerated along a slowly varying electric field $F\varphi(t)$. In this case, $p_\parallel \gtrsim m$ if $\epsilon \gg K_0^{-2/3}$. Since $K_0 \gtrsim 10^6$ for optical lasers (see Table 1), this condition is always satisfied. Integrating (2) over $d^3p/(2\pi)^3$ and adding up the n-photon absorption probabilities w_n (given that the $n\omega$ spectrum in this case is virtually continuous), we obtain formula (4) for the total probability W. Note that it can also be derived by averaging the static probability w_{st} [1] over the external-field period; see (A.5).

In the opposite case $\gamma \gg 1$ (or $\omega \gg \omega_t$, a rapidly varying field), using formulas (8.112.5), (8.113.3), and (8.114.3) from [53] for the elliptic functions, we have

$$\tilde{g}(\gamma) = \frac{4}{\pi\gamma}\left[A(q)\ln\left(\frac{4}{q}\right) - B(q)\right], \tag{B.7}$$

$$\tilde{b}_i(\gamma) = \frac{2}{\pi\gamma}\left[A_i\ln\left(\frac{4}{q}\right) - B_i\right], \quad i = 1, 2, \tag{B.8}$$

where $q = \sqrt{1-v^2} = 1/\sqrt{1+v^2} \longrightarrow 0$,

$$\begin{aligned} A(q) &= 1 + \frac{1}{4}q^2 + \frac{13}{64}q^4 + \ldots, \\ B(q) &= 1 + \frac{1}{2}q^2 + \ldots, \\ A_1 &= 1 - \frac{3}{4}q^2 - \frac{3}{64}q^4 + \ldots, \\ B_1 &= 1 - \frac{1}{2}q^2 + \ldots, \\ A_2 &= 1 - \frac{1}{4}q^2 - \frac{7}{64}q^4 + \ldots, \\ B_2 &= \frac{1}{4}q^2 + \ldots. \end{aligned} \tag{B.9}$$

Finally, we obtain[11]

$$\begin{aligned} \tilde{g}(\gamma) &= \frac{4}{\pi\gamma} \\ &\times\left\{\left(1 + \frac{1}{4\gamma^2} - \frac{3}{64\gamma^4}\right)\ln(4\gamma) - 1 + O(\gamma^{-4})\right\} \end{aligned} \tag{B.10}$$

and

$$\begin{aligned} \tilde{b}_1 &= \frac{2}{\pi\gamma}\left[\left(1 - \frac{3}{4\gamma^2}\right)\ln(4\gamma) - 1 + \ldots\right], \\ \tilde{b}_2 &= \frac{2}{\pi\gamma}\left[\left(1 - \frac{1}{4\gamma^2}\right)\ln(4\gamma) + \ldots\right], \end{aligned} \tag{B.11}$$

where the terms of order $1/\gamma^2$ or lower were discarded. In the limit $g \longrightarrow \infty$, the $e^{\pm}$ momentum distribution approaches (with a logarithmic accuracy) an isotropic one:

$$w(\mathbf{p}) \propto \exp\{-K_0\ln(4\gamma)p^2/m^2\}, \tag{B.12}$$

and the escaping electrons and positrons are nonrelativistic:

$$p_\parallel \sim p_\perp \sim \sqrt{\frac{m\omega}{\ln(4\gamma)}} \sim \frac{m}{\sqrt{K_0\ln(4\gamma)}} \ll m.$$

APPENDIX C

Here, we describe the derivation of asymptotic expression (21). For $\tau \longrightarrow \infty$, the equations for the function $\chi(u)$ are

$$\begin{aligned} \chi &= 2\exp\left\{-\left(\frac{\tau^2}{2\sigma^2} + \tau\right)\right\}, \\ u &= \frac{\sigma^2}{2\tau}\exp\left(\frac{\tau^2}{2\sigma^2} + \tau\right). \end{aligned} \tag{C.1}$$

Solving the second equation by the iteration method yields

$$\tau = \sigma\sqrt{2\ln\left(\frac{2u}{\sigma^2}\right)}\left[1 + O\left(\frac{\sigma}{\sqrt{\ln u}}\right)\right], \tag{C.2}$$

which allows the following expression to be derived by eliminating τ from (C.1):

$$\chi(u) \approx \frac{\sigma}{u\sqrt{2\ln(2u/\sigma^2)}}, \quad u \longrightarrow \infty. \tag{C.3}$$

Writing (11) as

$$\tilde{g}(\gamma) = \frac{4}{\pi\gamma}\int_0^\gamma \chi(u)\sqrt{1 - \frac{u^2}{\gamma^2}}du = \frac{4}{\pi\gamma}\int_0^\gamma \chi(u)du + \ldots, \tag{C.4}$$
$$\gamma \longrightarrow \infty,$$

we arrive at expression (21) for $\tilde{g}(\gamma)$.

On the other hand, in the limit $\sigma = \infty$ (strictly monochromatic radiation),

$$\chi(u) = \frac{1}{\sqrt{1+u^2}} \approx \frac{1}{u},$$

[11] These expansions are accurate even at small γ: thus, the error δ in the approximation (B.10) is 1, 0.2, and 0.03%, respectively, for $\gamma = 1.5$, 2, and 3.

and, accordingly, the asymptotic behavior of $\tilde{g}(\gamma)$ changes. Indeed, as follows from (C.4),

$$\chi(u) \sim \frac{c}{u(\ln u)^{\beta}} \longrightarrow \tilde{g}(\gamma) \sim \sin\frac{4c}{\pi\gamma}\begin{cases}(\ln\gamma)^{1-\beta}/(1-\beta), & \beta < 1,\\ \ln\ln\gamma, & \beta = 1.\end{cases} \quad \text{(C.5)}$$

Thus, the function $\tilde{g}(\gamma)$ decreases when $\gamma \longrightarrow \infty$ more slowly than $1/\gamma$ if the exponent $\beta \le 1$. The cases considered above correspond to $\beta = 0$ and $\beta = 1/2$.

REFERENCES

1. J. Schwinger, Phys. Rev. **82**, 664 (1951).
2. E. Brezin and C. Itzykson, Phys. Rev. D **2**, 1191 (1970).
3. V. S. Popov, Pis'ma Zh. Éksp. Teor. Fiz. **13**, 261 (1971) [JETP Lett. **13**, 185 (1971)]; Zh. Éksp. Teor. Fiz. **61**, 1334 (1971) [Sov. Phys. JETP **34**, 709 (1972)].
4. V. S. Popov, Pis'ma Zh. Éksp. Teor. Fiz. **18**, 435 (1973) [JETP Lett. **18**, 255 (1973)]; Yad. Fiz. **19**, 1140 (1974) [Sov. J. Nucl. Phys. **19**, 584 (1974)].
5. V. S. Popov and M. S. Marinov, Yad. Fiz. **16**, 809 (1972) [Sov. J. Nucl. Phys. **16**, 449 (1973)].
6. N. B. Narozhnyĭ and A. I. Nikishov, Zh. Éksp. Teor. Fiz. **65**, 862 (1973) [Sov. Phys. JETP **38**, 427 (1974)].
7. V. M. Mostepanenko and V. M. Frolov, Yad. Fiz. **19**, 885 (1974) [Sov. J. Nucl. Phys. **19**, 451 (1974)].
8. V. S. Marinov and V. S. Popov, Fortschr. Phys. **25**, 373 (1977).
9. A. A. Grib, S. G. Mamaev, and V. M. Mostepanenko, *Vacuum Quantum Effects in Strong Fields* (Énergoatomizdat, Moscow, 1988).
10. A. Ringwald, Preprint DESY 01-024 (2001); Phys. Lett. B **510**, 107 (2001).
11. S. W. Hawking, Commun. Math. Phys. **43**, 199 (1975).
12. K. M. Parikh and F. Wilczek, Phys. Rev. Lett. **85**, 5042 (2000).
13. L. Parker, Phys. Rev. **183**, 1057 (1969); Phys. Rev. D **3**, 346 (1971).
14. Ya. B. Zel'dovich and A. A. Starobinskiĭ, Zh. Éksp. Teor. Fiz. **61**, 2161 (1971) [Sov. Phys. JETP **34**, 1159 (1972)].
15. L. V. Keldysh, Zh. Éksp. Teor. Fiz. **47**, 1945 (1964) [Sov. Phys. JETP **20**, 1307 (1964)].
16. I. Pomeranchuk and Ya. Smorodinsky, J. Phys. (Moscow) **9**, 97 (1945).
17. Ya. B. Zel'dovich and V. S. Popov, Usp. Fiz. Nauk **105**, 403 (1971) [Sov. Phys. Usp. **14**, 673 (1972)].
18. V. S. Popov, Zh. Éksp. Teor. Fiz. **59**, 965 (1970) [Sov. Phys. JETP **32**, 526 (1971)]; Zh. Éksp. Teor. Fiz. **65**, 35 (1973) [Sov. Phys. JETP **38**, 18 (1974)].
19. B. Müller, J. Rafelski, and W. Greiner, Z. Phys. **257**, 62 (1972).
20. J. Rafelski and B. Müller, Phys. Lett. B **65**, 205 (1976).
21. V. I. Lisin, M. S. Marinov, and V. S. Popov, Phys. Lett. B **69**, 141 (1977); **91**, 20 (1980).
22. W. Greiner, B. Müller, and J. Rafelski, *Quantum Electrodynamics of Strong Fields* (Springer-Verlag, Berlin, 1985).
23. W. Greiner and J. Reinhardt, *Quantum Aspects of Beam Physics*, Ed. by P. Chen (World Sci., Singapore, 1998), p. 438.
24. V. S. Popov, Yad. Fiz. **64**, 421 (2001) [Phys. At. Nucl. **64**, 367 (2001)].
25. F. V. Bunkin and I. I. Tugov, Dokl. Akad. Nauk SSSR **187**, 541 (1969) [Sov. Phys. Dokl. **14**, 678 (1970)].
26. G. J. Troup and H. S. Perlman, Phys. Rev. D **6**, 2299 (1972).
27. G. A. Mourou, C. P. J. Barty, and M. D. Perry, Phys. Today **51** (1), 22 (1998).
28. S. V. Bulanov, F. Califano, G. I. Dudnikova, *et al.*, Rev. Plasma Phys. **22**, 227 (2001).
29. CERN Courier **40** (6), 26 (2000); **41** (5), 20 (2001).
30. R. Alkofer, M. B. Hecht, C. D. Roberts, *et al.*, Phys. Rev. Lett. **87**, 193902 (2001).
31. V. S. Popov, Pis'ma Zh. Éksp. Teor. Fiz. **74**, 151 (2001) [JETP Lett. **74**, 133 (2001)]; Preprint No. 35-01, ITÉF (Institute of Theoretical and Experimental Physics, Moscow, 2001).
32. V. S. Popov, Laser Phys. **10**, 1033 (2000); Preprint No. 39-00, ITÉF (Institute of Theoretical and Experimental Physics, Moscow, 2000).
33. *Handbook of Mathematical Functions*, Ed. by M. Abramowitz and I. A. Stegun (National Bureau of Standards, Washington, 1964; Nauka, Moscow, 1979).
34. O. Svelto, *Principles of Lasers* (Plenum, New York, 1982; Mir, Moscow, 1984).
35. J. Andruszkow, B. Aune, V. Ayvazyan, *et al.*, Phys. Rev. Lett. **85**, 3825 (2000).
36. V. S. Popov, Zh. Éksp. Teor. Fiz. **62**, 1248 (1972) [Sov. Phys. JETP **35**, 659 (1972)].
37. S. Lang, *SL(2,R)* (Addison-Wesley, Reading, 1975; Mir, Moscow, 1977).
38. A. M. Perelomov, Phys. Lett. A **39**, 165 (1972).
39. L. D. Landau and E. M. Lifshitz, *Course of Theoretical Physics*, Vol. 3: *Quantum Mechanics: Non-Relativistic Theory* (Nauka, Moscow, 1974; Pergamon, New York, 1977).
40. L. V. Keldysh, Zh. Éksp. Teor. Fiz. **33**, 994 (1957) [Sov. Phys. JETP **6**, 763 (1958)].
41. V. W. Hughes and T. Kinoshita, Rev. Mod. Phys. **71**, S133 (1999).
42. F. J. Dyson, Phys. Rev. **85**, 631 (1952).
43. W. Heisenberg and H. Euler, Z. Phys. **98**, 714 (1936).

44. A. M. Perelomov, V. S. Popov, and M. V. Terent'ev, Zh. Éksp. Teor. Fiz. **50**, 1393 (1966) [Sov. Phys. JETP **23**, 924 (1966)].

45. V. S. Popov, Zh. Éksp. Teor. Fiz. **118**, 56 (2000) [JETP **91**, 48 (2000)].

46. V. S. Popov, V. D. Mur, A. V. Sergeev, *et al.*, Phys. Lett. A **124**, 77 (1987); **149**, 418 (1990).

47. L. Benassi, V. Grecchi, E. Harrell, and B. Simon, Phys. Rev. Lett. **42**, 704 (1979); **42**, 1430 (1979).

48. L. Benassi and V. Grecchi, J. Phys. B **13**, 911 (1980).

49. Ya. B. Zel'dovich and V. V. Sokolov, Usp. Fiz. Nauk **146**, 493 (1985) [Sov. Phys. Usp. **28**, 608 (1985)].

50. V. S. Popov, Preprint No. 58-92, ITÉF (Institute of Theoretical and Experimental Physics, Moscow, 1992); Phys. Lett. A **173**, 63 (1993).

51. A. Scrinzi, M. Geissler, and T. Brabec, Phys. Rev. Lett. **83**, 706 (1999).

52. M. V. Frolov, N. L. Manakov, B. Borca, and A. F. Starace, J. Phys. B **34**, L579 (2001).

53. I. S. Gradshteyn and I. M. Ryzhik, *Table of Integrals, Series, and Products* (Fizmatgiz, Moscow, 1962; Academic, New York, 1980).

Translated by V. Astakhov

Journal of Experimental and Theoretical Physics, Vol. 94, No. 6, 2002, pp. 1070–1079.
Translated from Zhurnal Éksperimental'noĭ i Teoreticheskoĭ Fiziki, Vol. 121, No. 6, 2002, pp. 1249–1260.

ATOMS, SPECTRA, RADIATION

Decoherence and Entanglement in Radiative Decay of a Diatomic System

A. M. Basharov*
Moscow State Engineering-Physics Institute, Kashirskoe sh. 31, Moscow, 115409 Russia
**e-mail: bash@online.ru*
Received January 11, 2002

Abstract—It is shown that, in the Markov approximation, relaxation of two noninteracting atoms in the field of a common thermostat leads not only to decoherence but also to the opposite process of the entanglement of atomic states, which can take on a stationary value depending on the initial conditions. This region of initial conditions narrows as the mean number of photons in the thermostat increases. The main radiative mechanism destroying an arbitrary initial entanglement of atoms is interaction of each atom with its own thermostat independent of the other. All Markov relaxation models under consideration are based on the Lindblad equations.

1. INTRODUCTION

Currently, several related but slightly different processes are called decoherence. Traditionally, atomic decoherence is damping of the off-diagonal elements of the atomic density matrix; these elements determine atomic polarization and various phase relations and coherence [1, 2]. A consideration of such a process is accompanied by passage from describing an atom with the use of a wave function to describing it with the use of the density matrix (transition from a pure to a mixed state), which also corresponds to decoherence. Relaxation caused by interactions between an atom and a thermostat is accompanied by the entanglement of atomic states with the states of thermostat particles [3–5]. However, decoherence also implies the removal of entanglement in a separate system of particles [6]. This work is concerned with the arising (and removal) of entanglement of atomic states in a system of two atoms caused by radiative decay.

Recall that entangled states are such states of quantum systems in which the wave function (density matrix) of the system of particles cannot be represented in the form of the product of wave functions (density matrices) of separate particles even if the particles do not interact with each other. Entangled states are a special case of quantum correlations, because simple quantum correlations, for instance, differences between two-particle density matrices and the products of one-particle density matrices, do not always cause entanglement. Such entangled states of a selected system of quantum particles (atoms or photons), rather than of an atom and thermostat particles, have recently been given much attention, in part because entangled states are one of the main resources of quantum information, quantum calculations, quantum teleportation, etc. Well-known Bell states are an example of maximally entangled states of systems of two two-level particles. An example of the entanglement of photon states is the so-called squeezed light [7] used in experiments on teleportation of photon states [8, 9]. Entangled states of noninteracting atoms determine several optical effects [10–12], of which the best known one is superradiation [13, 14]. Dicke states are then entangled states in a system of N particles.

Obtaining entangled atomic states is considered in recent works [15–19]. It is, as a rule, assumed that atoms interact with each other [15–17]. Entanglement then appears to be quite natural. In this work, noninteracting atoms that decay in a common thermostat field are considered. This consideration leads to the conclusion, paradoxical at first sight, that a relaxation process, which usually causes loss of quantum correlations, etc., results in the arising of entanglement in an ensemble of noninteracting atoms. For simplicity, our consideration will be limited to two atoms.

The well-known Dicke model and other models [13, 14] are used to describe collective atomic decay. In this work, new models based on the Lindblad equations are introduced. These models allow the dynamics of atomic states both symmetrical and antisymmetric with respect to particles to be discussed. A general solution to the simplest model equations was obtained; the other equations were studied numerically. The Peres–Horodecki criterion [20, 21], which is stronger than Bell's inequalities, was used as a criterion of the entanglement of atomic states. The eigenvalues of the two-particle atomic density matrix transposed according to Peres and Horodeckis were calculated to find that there existed a region of problem parameters in which atomic states resulting from the decay of nonentangled initial atomic wave functions become entangled. It was found that one of the principal conditions of the entanglement

1063-7761/02/9406-1070$22.00

of atomic states during radiative decay was the presence of a common thermostat. The degree of entanglement of atomic states is very sensitive to the mean number of photons in the thermostat. The region of parameter values at which entanglement arises narrows as the mean number of photons increases. A common thermostat is, however, incapable of completely destroying initial entanglement related to atomic states antisymmetric with respect to particles. The main factor that destroys entanglement is interaction of each atom with "its own" thermostat independent from the others. Note that we do not take into account interaction between atoms to most clearly reveal the effect of entanglement caused by interaction with a common thermostat. As far as the thermostat is concerned, it is understood to be an arbitrary broadband electromagnetic radiation whose initial state satisfies the δ-correlation condition and whose mean photon creation and annihilation operator values are zero. Such a radiation can be created by parametric generators, and its state may be squeezed [1, 2]. In the latter case, electromagnetic radiation is often called squeezed vacuum.

The paper is organized as follows. In Section 2, Ito quantum stochastic equations are derived, and collective relaxation approximations and models used in what follows are discussed. One-particle equations for the atomic density matrix are used in Section 3 to determine the most favorable conditions for the entanglement of atomic states. In Section 4, a general solution for the model of the decay of atoms in a common thermostat field at zero temperature in the unidirectional approximation is obtained, and the Peres–Horodecki criterion of the entanglement of atomic states is considered. Effects of the temperature, thermostat squeezing, phase parameter, and model type on the minimum eigenvalue of the Peres–Horodecki matrix characterizing the degree of entanglement of atoms are considered in Section 5. In Conclusion, we discuss the mechanisms responsible for either atomic entanglement or complete atomic decoherence and point to an analogy between the results of this work and some quantum information theory results.

2. MAIN COLLECTIVE RELAXATION MODELS

The interaction of two identical two-level quiescent atoms with a quantized electromagnetic field in the electric dipole approximation is described by the Hamiltonian

$$\mathcal{H} = \mathcal{H}^A + \mathcal{H}^F + \mathcal{V},$$

$$\mathcal{H}^A = \frac{\hbar\omega_0}{2}(C_3 \otimes \hat{1} + \hat{1} \otimes C_3),$$

$$\mathcal{H}^F = \sum_{\mathbf{q}\lambda} \hbar qc\left(b^+_{\mathbf{q}\lambda} b_{\mathbf{q}\lambda} + \frac{1}{2}\right), \tag{1}$$

$$\mathcal{V} = -\frac{i}{\sqrt{V_s}} \sum_{\mathbf{q}\lambda} \sqrt{2\pi\hbar qc}(\mathbf{e}_{\mathbf{q}\lambda} \cdot \mathbf{d}_{10})$$
$$\times b_{\mathbf{q}\lambda}(e^{i\mathbf{q}\cdot\mathbf{r}_1} C_+ \otimes \hat{1} + e^{i\mathbf{q}\cdot\mathbf{r}_2} \hat{1} \otimes C_+) + \text{H.c.}$$

Here, $\mathcal{H}$ is the Hamiltonian of the system of two two-level atoms situated at points $\mathbf{r}_1$ and $\mathbf{r}_2$, and $C_- = |0\rangle\langle 1|$ and $C_+ = |1\rangle\langle 0|$ are the operators of annihilation and creation, respectively, of two-level atom excitations. Together with the C_3 operator, they provide a realization of the SU(2) algebra, $[C_+, C_-] = C_3$, $[C_3, C_\pm] = \pm 2C_\pm$. Symbols $|0\rangle$ and $|1\rangle$ denote the vectors of atomic states corresponding to the lower and upper energy levels, respectively, and $\hbar\omega_0$ is the energy difference between these levels. The $\mathbf{d}_{10}$ value is the matrix element of the dipole moment of the atom. $\mathcal{H}^F$ is the Hamiltonian of the electromagnetic field whose operators of creation and annihilation of photons with wave vector $\mathbf{q}$ and polarization $\mathbf{e}_\mathbf{q}\lambda$ are given by $b_{\mathbf{q}\lambda}$ and $b^+_{\mathbf{q}\lambda}$, respectively, $[b_{\mathbf{q}\lambda}, b^+_{\mathbf{q}'\lambda'}] = \delta_{\mathbf{q}\mathbf{q}'}\delta_{\lambda\lambda'}$. Next, $\mathcal{V}$ is the operator of resonance interaction between the atoms and the transverse component of the electromagnetic field, and V_s is the volume within which the electromagnetic field is confined. For simplicity, $\mathcal{V}$ is written without taking into account recoil effects of photon absorption and emission. In what follows, we also ignore polarization effects (omit vector signs). In addition, (1) implies that the interaction of atoms with the longitudinal electromagnetic field component, which determines the operator of dipole–dipole interaction of atoms, is not taken into account to more definitely separate the entanglement effects due to relaxation processes in a common thermostat field.

First, consider the simplest situation when the electromagnetic field propagates in one direction. Note that all known exactly integrable models of resonance interaction between quantized fields and two-level atoms correspond to precisely this situation [22, 23]. For instance, let $\mathbf{q} = q\mathbf{e}_z = \omega\mathbf{e}_z/c$. The interaction operator takes the form

$$\mathcal{V} = -i\sum_\omega g(w) d_{10} b_\omega$$
$$\times\left(C_+ \otimes \hat{1} + \exp\left(\frac{i\omega\mathbf{r}_2 \cdot \mathbf{e}_z}{c}\right)\hat{1} \otimes C_+\right) + \text{H.c.}, \tag{2}$$

where $b_\omega \equiv b_{\omega\mathbf{e}_z/c}$ and, for simplicity, $\mathbf{r}_1$ is set equal to 0. We assume the initial electromagnetic field state $|\Phi_0\rangle$ to be δ-correlated,

$$\begin{aligned}
\langle\Phi_0|b^+_\omega b_{\omega'}|\Phi_0\rangle &= N(\omega)\delta(\omega-\omega'),\\
\langle\Phi_0|b_\omega b^+_{\omega'}|\Phi_0\rangle &= (1+N(\omega))\delta(\omega-\omega'),\\
\langle\Phi_0|b_\omega b_{\omega'}|\Phi_0\rangle &= M(\omega)\delta(2\Omega_\Gamma-\omega-\omega'),\\
\langle\Phi_0|b^+_\omega b^-_{\omega'}|\Phi_0\rangle &= M^*(\omega)\delta(2\Omega_\Gamma-\omega-\omega').
\end{aligned} \tag{3}$$

This means that the electromagnetic field is treated as a thermostat with central frequency Ω_Γ, photon density $N(\omega)$ at frequency ω, and squeezing parameter $M(\omega)$,

$$M(\omega) \le \sqrt{N(\omega)(N(\omega)+1)}.$$

The interaction with this thermostat will be described in the Markov approximation. It is assumed that the $g(\omega)$ coupling constant, the $N(\omega)$ and $M(\omega)$ electromagnetic field parameters, and the $\exp(i\omega\mathbf{r}_2 \cdot \mathbf{e}_z/c)$ exponential function are independent of frequency, and the photon annihilation operator in the Heizenberg approximation is described by free evolution and, therefore, the Heizenberg equation for an arbitrary atomic operator is as follows:

$$\begin{aligned}\dot{\mathcal{A}} &= -\frac{i}{\hbar}[\mathcal{A}, \mathcal{H}^A] \\ &+ \sqrt{\chi}[\mathcal{A}, \mathcal{C}_+]b(t) - \sqrt{\chi}[\mathcal{A}, \mathcal{C}_-]b^+(t).\end{aligned} \tag{4}$$

Here,

$$\begin{aligned}\mathcal{C}_\pm &= C_\pm \otimes \hat{1} + e^{\mp i\theta}\hat{1} \otimes C_\pm, \qquad (5)\\ \theta &= \frac{\omega \mathbf{r}_2 \cdot \mathbf{e}_z}{c}, \quad \chi = 2\pi g^2(\omega_0),\\ N &= N(\omega_0), \quad M = M(\omega_0),\\ b_\omega &= b_\omega(t_0)e^{-i\omega(t-t_0)},\\ b(t) &= \frac{1}{\sqrt{2\pi}}\int d\omega e^{-i\omega(t-t_0)}b_\omega(t_0).\end{aligned}$$

As photons with frequencies close to the ω_0 resonance frequency are only effective in resonance interactions, the frequency integration is performed from $-\infty$ to $+\infty$. Note also that photons emitted by atoms do not influence the evolution of the thermostat, and the interaction of atoms in absorption of a photon emitted by one of them is therefore not taken into account in (4).

Equation (4) is the Langevin quantum equation and, like all Langevin equations with multiplicative noise, is not defined mathematically. To supplement the definition of (4), let us introduce quantum Wiener processes $B(t, t_0)$ as follows:

$$\begin{aligned}B(t, t_0) &= \int_{t_0}^{t} dt' b(t'),\\ [B(t, t_0), B^+(t, t_0)] &= t - t_0.\end{aligned}$$

Using the standard definitions of the Ito integral and differential [1, 24], we obtain the Ito quantum stochastic equation for the atomic operator A in the form

$$\begin{aligned}d\mathcal{A} &= -\frac{i}{\hbar}[\mathcal{A}, \mathcal{H}^A]dt\\ &+ \sqrt{\chi}d_{10}[\mathcal{A}, \mathcal{C}_+]dB(t) - \sqrt{\chi}d_{10}^*[\mathcal{A}, \mathcal{C}_-]dB^+(t)\\ &+ \frac{\chi|d_{10}|^2}{2}(N+1)(\mathcal{C}_+[\mathcal{A}, \mathcal{C}_-] + [\mathcal{C}_+, \mathcal{A}]\mathcal{C}_-)dt\\ &+ \frac{\chi|d_{10}|^2}{2}N(\mathcal{C}_-[\mathcal{A}, \mathcal{C}_+] + [\mathcal{C}_-, \mathcal{A}]\mathcal{C}_+)dt\\ &- \frac{\chi d_{10}^2}{2}M(\mathcal{C}_+[\mathcal{A}, \mathcal{C}_+] + [\mathcal{C}_+, \mathcal{A}]\mathcal{C}_+)dt\\ &- \frac{\chi(d_{10}^*)^2}{2}M^*(\mathcal{C}_-[\mathcal{A}, \mathcal{C}_-] + [\mathcal{C}_-, \mathcal{A}]\mathcal{C}_-)dt,\end{aligned} \tag{6}$$

where

$$\begin{aligned}dB^+(t)dB(t) &= Ndt,\\ dB(t)dB^+(t) &= (1+N)dt,\\ dB(t)dB(t) &= Mdt, \quad dB^+(t)dB^+(t) = M^*dt,\\ dtdt &= dtdB(t) = dtdB^+(t) = dB(t)dt = dB^+(t)dt = 0.\end{aligned} \tag{7}$$

Such a "refinement" provides the fulfillment of the Ito differentiation rule; namely, for arbitrary atomic operators $\mathcal{A}_1$ and $\mathcal{A}_2$, we have

$$d(\mathcal{A}_1\mathcal{A}_2) = (d\mathcal{A}_1)\mathcal{A}_2 + \mathcal{A}_1 d\mathcal{A}_2 + (d\mathcal{A}_1)(d\mathcal{A}_2).$$

Ito quantum stochastic equation (6) with algebra (7) completely describes the evolution of atoms that interact with a "unidirectional" thermostat in the Markov approximation. Applying standard methods to this equation, we easily obtain the equation for the diatomic density matrix $\mathcal{R}$,

$$\frac{d\mathcal{R}}{dt} = \frac{i}{\hbar}[\mathcal{R}, \mathcal{H}^A] + \hat{\Gamma}\mathcal{R}, \tag{8}$$

which contains the relaxation operator

$$\begin{aligned}\hat{\Gamma}\mathcal{R} &= \frac{\chi|d_{10}|^2}{2}(N+1)\\ &\times(\mathcal{R}\mathcal{C}_+\mathcal{C}_- + \mathcal{C}_+\mathcal{C}_-\mathcal{R} - 2\mathcal{C}_-\mathcal{R}\mathcal{C}_+)\\ &+ \frac{\chi|d_{10}|^2}{2}N(\mathcal{R}\mathcal{C}_-\mathcal{C}_+ + \mathcal{C}_-\mathcal{C}_+\mathcal{R} - 2\mathcal{C}_+\mathcal{R}\mathcal{C}_-)\\ &+ \frac{\chi d_{10}^2}{2}(2\mathcal{C}_+\mathcal{R}\mathcal{C}_+ - \mathcal{R}\mathcal{C}_+\mathcal{C}_+ - \mathcal{C}_+\mathcal{C}_+\mathcal{R})M\\ &+ \frac{\chi(d_{10}^*)^2}{2}(2\mathcal{C}_-\mathcal{R}\mathcal{C}_- - \mathcal{R}\mathcal{C}_-\mathcal{C}_- - \mathcal{C}_-\mathcal{C}_-\mathcal{R})M^*.\end{aligned} \tag{9}$$

Equations (8) and (9) describe collective relaxation of two atoms in unidirectional electromagnetic field (3). They are easy to generalize to one-dimensional and three-dimensional fields.

In the one-dimensional model, in addition to operators (5), we introduce the operators

$$\mathscr{C}'_{\pm} = C_{\pm} \otimes \hat{1} + e^{\pm i\theta}\hat{1} \otimes C_{\pm}, \quad (10)$$

which differ from (5) by the replacement of θ with –θ. The equation for the diatomic density matrix then takes the form

$$\frac{d\mathscr{R}}{dt} = \frac{i}{\hbar}[\mathscr{R}, \mathscr{H}^A] - \hat{\Gamma}\mathscr{R} - \hat{\Gamma}'\mathscr{R}, \quad (11)$$

where $\hat{\Gamma}'$ differs from $\hat{\Gamma}$ by the replacement of $\mathscr{C}_{\pm}$ with $\mathscr{C}'_{\pm}$. We assume that the χ, N, and M parameters in $\hat{\Gamma}'$ also differ from similar parameters in $\hat{\Gamma}$; these parameters will be primed. The primed and unprimed parameters may differ because the system of two atoms is irradiated from two sides by two different broadband fields, for instance, created by degenerate parametric generators [2]. Note that the derivation of (11) is fully analogous to the case of unidirectional electromagnetic field propagation with the exception that, in addition to one pair of Wiener quantum processes $B(t, t_0)$ and $B^+(t, t_0)$, we must consider the second pair $B'(t, t_0)$ and $B'^+(t, t_0)$ corresponding to the field that propagates in the opposite direction $\mathbf{e}_z$. These pairs of processes are independent of each other,

$$dB(t)dB'(t) = dB(t)dB'^+(t)$$
$$+ dB^+(t)dB'(t) = dB^+(t)dB'^+(t) = 0.$$

Note that, if $\chi = \chi'$, $N = N'$, $M = M'$, and $\theta = 0$, (11) coincides with (8) and (9) for $\theta = 0$ and the χ constant renormalized as $\chi \longrightarrow 2\chi$.

For the three-dimensional electromagnetic field model, the kinetic equation for the diatomic density matrix can most simply be obtained if the atoms are situated in a volume whose linear dimensions are much smaller than the wavelengths of resonance modes, that is, on the assumption $\mathbf{r}_1 = \mathbf{r}_2$. We can then conveniently introduce photon annihilation and creation operators averaged over various wave vector orientations, for instance,

$$b_\omega = \frac{1}{4\pi}\int d\Omega_{\mathbf{k}} b_{\mathbf{k}}.$$

Using the additional assumption that the initial state of the electromagnetic field is δ-correlated with respect to averaged operators and applying standard reasoning, we obtain the Ito quantum equations in form (6); these equations correspond to Wiener processes constructed on averaged operators. They yield the same expressions (8) and (9) for the diatomic density matrix with $\theta = 0$.

The form of (8), (9), and (11) is common to kinetic equations that describe relaxation in the Markov approximation, which has for the first time been proved by Lindblad [25] for the case of the absence of squeezing on very general assumptions about the properties of the thermostat and the character of evolution of the dynamic system. For this reason, a brief derivation of the kinetic equations through constructing Ito quantum stochastic equation (6) is only necessary from the point of view of atomic dynamics for determining the form of the $\mathscr{C}_{\pm}$ and $\mathscr{C}'_{\pm}$ operators and similar operators responsible for coupling of the quantum system with independent thermostats. Note that stochastic equations (6) and (7) are much more informative than the corresponding kinetic equations because they can also be used to draw conclusions about photon dynamics through handling *in*- and *out*-fields and the stochastic equation for the evolution operator [1]. The approach based on the use of Ito quantum stochastic equations also makes it possible to consider repeat actions of the same quantum Wiener process realization on an atomic system. Such implications are, however, not discussed in this work.

For generality, models (8), (9), and (10) should be augmented by two relaxation operators Γ_1 and Γ_2 describing interactions of each atom with independent thermostat fields. The most general model of Markov relaxation of a diatomic system interacting with broadband quantized electromagnetic fields is therefore given by the equations

$$\frac{d\mathscr{R}}{dt} = \frac{i}{\hbar}[\mathscr{R}, \mathscr{H}^A] - \hat{\Gamma}\mathscr{R} - \hat{\Gamma}'\mathscr{R} - \hat{\Gamma}_1\mathscr{R} - \hat{\Gamma}_2\mathscr{R}. \quad (12)$$

Here, $\hat{\Gamma}$ and $\hat{\Gamma}'$ are defined by (9) (with $\mathscr{C}'_{\pm}$, χ', N', and M' for $\hat{\Gamma}'$), and Γ_1 and Γ_2 are defined by an expression similar to (9) but with other main values,

$$\hat{\Gamma}_j\mathscr{R} = \frac{\chi^{(j)}|d_{10}|^2}{2}(N^{(j)} + 1)$$
$$\times (\mathscr{R}\mathscr{C}_+^{(j)}\mathscr{C}_-^{(j)} + \mathscr{C}_+^{(j)}\mathscr{C}_-^{(j)}\mathscr{R} - 2\mathscr{C}_-^{(j)}\mathscr{R}\mathscr{C}_+^{(j)})$$
$$+ \frac{\chi^{(j)}|d_{10}|^2}{2}$$
$$\times N^{(j)}(\mathscr{R}\mathscr{C}_-^{(j)}\mathscr{C}_+^{(j)} + \mathscr{C}_-^{(j)}\mathscr{C}_+^{(j)}\mathscr{R} - 2\mathscr{C}_+^{(j)}\mathscr{R}\mathscr{C}_-^{(j)}) \quad (13)$$
$$+ \frac{\chi^{(j)}d_{10}^2}{2}M^{(j)}(2\mathscr{C}_+^{(j)}\mathscr{R}\mathscr{C}_+^{(j)} - \mathscr{R}\mathscr{C}_+^{(j)}\mathscr{C}_+^{(j)} - \mathscr{C}_+^{(j)}\mathscr{C}_+^{(j)}\mathscr{R})$$
$$+ \frac{\chi^{(j)}d_{10}^{*2}}{2}M^{(j)*}(2\mathscr{C}_-^{(j)}\mathscr{R}\mathscr{C}_-^{(j)} - \mathscr{R}\mathscr{C}_-^{(j)}\mathscr{C}_-^{(j)} - \mathscr{C}_-^{(j)}\mathscr{C}_-^{(j)}\mathscr{R}),$$

where

$$\mathscr{C}_{\pm}^{(1)} = \mathscr{C}_{\pm} \otimes \hat{1}, \quad \mathscr{C}_{\pm}^{(2)} = \hat{1} \otimes C_{\pm}. \quad (14)$$

Equations (12) and (9), (10), (13), and (14) make it possible to consider collective effects in a system of two atoms that arise when the atoms interact with the field of a common thermostat. A wider range of problems can be covered if $\mathcal{H}^A$ is understood not only as a Hamiltonian of a system of two isolated quiescent two-level atoms but also as interaction operators between atoms and external classical electromagnetic fields.

3. KINETIC EQUATIONS FOR ONE ATOM

As we assume that atoms do not interact with each other, it would be interesting to consider the kinetic equations for each of them. This would allow us to draw conclusions about the range of parameter values within which the entanglement of atomic states caused by collective radiative decay can be expected.

The one-particle density matrix and the one-particle relaxation parameter are as usual determined by taking the trace over the states of the second atom, $\rho = \mathrm{tr}_2\mathcal{R}$, $\hat{\Gamma}\rho = \mathrm{tr}_2\hat{\Gamma}\mathcal{R}$. Let us denote the one-particle density matrix to which the first space in the tensor product $\otimes$ corresponds by $\rho^f = \mathrm{tr}_l\mathcal{R}$ (indices *f*, from "first," and *l*, from "last," are used to describe the first and second atoms, respectively). Its matrix elements will be written in the form

$$\rho^f_{11} = \mathcal{R}_{ee} + \mathcal{R}_{ff}, \quad \rho^f_{00} = \mathcal{R}_{ll} + \mathcal{R}_{gg},$$

$$\rho^f_{10} = \mathcal{R}_{el} + \mathcal{R}_{fg},$$

where the following notation is used:

$$\rho^f_{10} = \langle 1|\rho^f|0\rangle, \text{ etc.}, \quad \mathcal{R}_{el} = \langle e|\mathcal{R}|l\rangle, \text{ etc.},$$

$$|g\rangle = |0\rangle\otimes|0\rangle, \quad |e\rangle = |1\rangle\otimes|1\rangle,$$

$$|f\rangle = |1\rangle\otimes|0\rangle, \quad |l\rangle = |0\rangle\otimes|1\rangle.$$

Here, $|f\rangle$ is the state of the two-particle system in which the first atom is excited and the second is in the ground state, etc. The following equation for the monatomic density matrix can easily be obtained:

$$\frac{d\rho^f}{dt} = \frac{i}{\hbar}[\rho^f, H^f] - \hat{\Gamma}^f\rho^f, \tag{15}$$

where, for definiteness, the one-particle density matrix is assumed to describe the first atom. The notation used in (15) is as follows. The value

$$H^f = \frac{1}{2}\hbar\omega_0 C_3 + V$$

is the sum of the Hamiltonian of the isolated quiescent two-level atom with transition frequency ω_0 and the interaction operator between the atom and external particles and fields not considered or mentioned above (for instance, with a classical electromagnetic field). The relaxation operator

$$\hat{\Gamma}^f = \hat{\Gamma}^f_1 + \hat{\Gamma}^f_0 + \hat{\Gamma}'^f_0$$

is the sum of the $\hat{\Gamma}^f_1$ operator of the relaxation of the first atom caused by its interaction with "its own" thermostat (with which the second atom does not interact), and the $\hat{\Gamma}^f_0$ relaxation operator determined by collective relaxation of the system of two atoms in the field of the common thermostat. The matrix elements of the relaxation operators mentioned above are as follows:

$$\begin{aligned}
\hat{\Gamma}^f_1\rho^f_{11} &= \chi^{(1)}(N^{(1)}+1)|d_{10}|^2\rho^f_{11} - \chi^{(1)}N^{(1)}|d_{10}|^2\rho^f_{00},\\
\hat{\Gamma}^f_1\rho^f_{00} &= -\chi^{(1)}(N^{(1)}+1)|d_{10}|^2\rho^f_{11}\\
&\quad + \chi^{(1)}N^{(1)}|d_{10}|^2\rho^f_{00},\\
\hat{\Gamma}^f_1\rho^f_{10} &= \chi^{(1)}\left(N^{(1)}+\frac{1}{2}\right)|d_{10}|^2\rho^f_{10} + \chi^{(1)}(d_{10})^2M^{(1)}\rho^{f*}_{00};
\end{aligned} \tag{16}$$

$$\begin{aligned}
\hat{\Gamma}^f_0\rho^f_{11} &= \chi(N+1)|d_{10}|^2\rho^f_{11} - \chi N|d_{10}|^2\rho^f_{00}\\
&\quad + \frac{1}{2}\chi|d_{01}|^2(\mathcal{R}_{fl}e^{-i\theta} + \mathcal{R}_{lf}e^{i\theta}),\\
\hat{\Gamma}^f_0\rho^f_{00} &= -\chi(N+1)|d_{01}|^2\rho^f_{11} + \chi N|d_{10}|^2\rho^f_{00}\\
&\quad - \frac{1}{2}\chi|d_{01}|^2(e^{-i\theta}\mathcal{R}_{fl} + e^{i\theta}\mathcal{R}_{lf}),\\
\hat{\Gamma}^f_0\rho^f_{10} &= \chi\left(N+\frac{1}{2}\right)|d_{01}|^2\rho^f_{10} + \chi d^2_{10}M\rho^{f*}_{10}\\
&\quad - \frac{1}{2}\chi|d_{10}|^2e^{i\theta}(\mathcal{R}_{ef} - \mathcal{R}_{lg}).
\end{aligned} \tag{17}$$

The $\hat{\Gamma}'^f_0$ relaxation operator differs from $\hat{\Gamma}^f_0$ in the replacement of θ with $-\theta$ and χ, *N*, and *M* with χ', *N*', and *M*'.

The dynamics of a single atom without taking into account any other atoms is described by (15) with the relaxation operator $\hat{\Gamma}^f = \hat{\Gamma}^f_1 + \hat{\Gamma}^f_0$, where $\hat{\Gamma}^f_1$ is given by (16) and $\hat{\Gamma}^f_0$, by (17) without terms containing the matrix elements of two-particle density matrix $\mathcal{R}$. It follows that, in spite of the absence of interaction between atoms, the presence of a common thermostat substantially changes monatomic dynamics. For the specified effects to be most pronounced, the following conditions should be met:

(1) Neither of the atoms should have "its own" thermostat independent of the others (that is, $\hat{\Gamma}^f_1 = 0$).

(2) The common thermostat should have zero temperature (that is, should not contain photons, $N = M = 0$).

The differences in monatomic dynamics become smoothed as the temperature of the common thermostat increases, which is clearly seen at $N \gg 1$. The terms in (17) that contain the matrix elements of the two-particle density matrix $\mathcal{R}$ can then be ignored. Importantly, the squeezing of the common thermostat at $N \gg 1$ generally does not have a significant influence on the differences in monatomic dynamics. However, at small N values, we can, as usual, expect a substantial effect of thermostat squeezing at nonzero phases θ.

If each atom has a thermostat of its own, the influence of the common thermostat will also become negligible at some instant.

It follows from the aforesaid that very favorable conditions for the arising of entanglement in a system of two noninteracting atoms is the presence of only one common thermostat with zero temperature. At nonzero temperatures, favorable conditions may also appear in the presence of thermostat squeezing.

4. THE PERES–HORODECKI CRITERION

Consider the simplest model of collective decay (8), (9), (5) in the absence of photons in the thermostat, $N = M = 0$. In addition to the matrix notation introduced above, we will use $\mathcal{R}_{ij}$, where index i runs over the values 1, 2, 3, and 4, or g, f, l, and e.

Clearly, the nonzero matrix elements of the $\mathcal{C}_\pm$ operators are

$$\langle f|\mathcal{C}_+|g\rangle = \langle g|\mathcal{C}_-|f\rangle = 1,$$

$$\langle l|\mathcal{C}_+|g\rangle = \langle g|\mathcal{C}_-|l\rangle^* = e^{i\theta},$$

$$\langle e|\mathcal{C}_+|f\rangle = \langle f|\mathcal{C}_-|e\rangle^* = e^{-i\theta},$$

$$\langle e|\mathcal{C}_+|l\rangle = \langle l|\mathcal{C}_-|e\rangle = 1.$$

In the matrix form, we have

$$\mathcal{C}_+ = \begin{pmatrix} 0 & 0 & 0 & 0 \\ 1 & 0 & 0 & 0 \\ e^{-i\theta} & 0 & 0 & 0 \\ 0 & e^{-i\theta} & 1 & 0 \end{pmatrix},$$

$$\mathcal{C}_- = \begin{pmatrix} 0 & 2 & e^{i\theta} & 0 \\ 0 & 0 & 0 & e^{i\theta} \\ 0 & 0 & 0 & 1 \\ 0 & 0 & 0 & 0 \end{pmatrix}.$$

Let us find a general solution to (8) and (9). Note that the $\mathcal{C}_\pm$ operator matrix elements between the two-particle entangled state

$$|a\rangle = 2^{-1/2}(|f\rangle - \exp(-i\theta)|l\rangle)$$

and $|g\rangle$ or $|e\rangle$ are zero,

$$\langle e|\mathcal{C}_+|a\rangle = \langle g|\mathcal{C}_-|a\rangle = 0.$$

The $|a\rangle$ and

$$|s\rangle = 2^{-1/2}(|f\rangle + \exp(-i\theta)|l\rangle)$$

vectors together with $|g\rangle$ and $|e\rangle$ form a new orthonormalized basis in the space of diatomic system states. In this basis, (8) and (9) take the simplest form, namely,

$$\frac{d\mathcal{R}_{gg}}{d\tau} = 2\mathcal{R}_{ss}, \quad \frac{d\mathcal{R}_{ee}}{d\tau} = -2\mathcal{R}_{ee},$$

$$\frac{d\mathcal{R}_{ss}}{d\tau} = 2\mathcal{R}_{ee} - 2\mathcal{R}_{ss}, \quad \frac{d\mathcal{R}_{aa}}{d\tau} = \frac{d\tilde{\mathcal{R}}_{ag}}{d\tau} = 0,$$

$$\frac{d\tilde{\mathcal{R}}_{ae}}{d\tau} = -\tilde{\mathcal{R}}_{ae}, \quad \frac{d\mathcal{R}_{sa}}{d\tau} = -\mathcal{R}_{sa}, \tag{18}$$

$$\frac{d\tilde{\mathcal{R}}_{sg}}{d\tau} = 2e^{i\theta}\tilde{\mathcal{R}}_{es} - \tilde{\mathcal{R}}_{sg}, \quad \frac{d\tilde{\mathcal{R}}_{se}}{d\tau} = -2\tilde{\mathcal{R}}_{se},$$

$$\frac{d\tilde{\mathcal{R}}_{eg}}{d\tau} = -\tilde{\mathcal{R}}_{eg}.$$

Here, $\tau = \chi|d_{10}|^2 t$ is the dimensionless time, and a tilde denotes the slow [compared with $\exp(\pm i\omega_0 t)$] part of the density matrix, for instance,

$$\mathcal{R}_{sg} = \tilde{\mathcal{R}}_{sg}\exp(-i\omega_0 t),$$

$$\mathcal{R}_{eg} = \tilde{\mathcal{R}}_{eg}\exp(-2i\omega_0 t), \text{ etc.}$$

A general solution to (4) is given by

$$\mathcal{R}_{ss} = (2\mathcal{R}_{ee}^{(0)}\tau + \mathcal{R}_{ss}^{(0)})e^{-2\tau}, \quad \mathcal{R}_{ee} = \mathcal{R}_{ee}^{(0)}e^{-2\tau},$$

$$\mathcal{R}_{aa} = \mathcal{R}_{aa}^{(0)},$$

$$\mathcal{R}_{gg} = 1 - \mathcal{R}_{aa}^{(0)} - \{\mathcal{R}_{ss}^{(0)} + \mathcal{R}_{ee}^{(0)}(1 + 2\tau)\}e^{-2\tau},$$

$$\tilde{\mathcal{R}}_{ag} = \tilde{\mathcal{R}}_{ag}^{(0)}, \quad \tilde{\mathcal{R}}_{ae} = \tilde{\mathcal{R}}_{ae}^{(0)}e^{-\tau}, \tag{19}$$

$$\mathcal{R}_{sa} = \mathcal{R}_{sa}^{(0)}e^{-\tau}, \quad \tilde{\mathcal{R}}_{se} = \tilde{\mathcal{R}}_{se}^{(0)}e^{-2\tau},$$

$$\tilde{\mathcal{R}}_{eg} = \tilde{\mathcal{R}}_{eg}^{(0)}e^{-\tau},$$

$$\mathcal{R}_{sg} = \mathcal{R}_{sg}^{(0)}e^{-\tau} + 2e^{i\theta}\tilde{\mathcal{R}}_{es}^{(0)}(e^{-\tau} - e^{-2\tau}),$$

where superscript (0) labels the initial density matrix value. We have the obvious relations

$$\mathcal{R}_{ff} = \frac{1}{2}(\mathcal{R}_{ss} + \mathcal{R}_{aa} + \mathcal{R}_{as} + \mathcal{R}_{sa}),$$

$$\mathcal{R}_{ll} = \frac{1}{2}(\mathcal{R}_{ss} + \mathcal{R}_{aa} - \mathcal{R}_{as} - \mathcal{R}_{sa}),$$

$$\tilde{\mathcal{R}}_{el} = \frac{1}{\sqrt{2}}e^{i\theta}(\tilde{\mathcal{R}}_{es} - \tilde{\mathcal{R}}_{ea}),$$

$$\tilde{\mathcal{R}}_{ef} = \frac{1}{\sqrt{2}}(\tilde{\mathcal{R}}_{ea} + \tilde{\mathcal{R}}_{es}),$$

$$\tilde{\mathcal{R}}_{gl} = \frac{1}{\sqrt{2}}e^{i\theta}(\tilde{\mathcal{R}}_{gs} - \tilde{\mathcal{R}}_{ga}), \quad (20)$$

$$\tilde{\mathcal{R}}_{gf} = \frac{1}{\sqrt{2}}(\tilde{\mathcal{R}}_{ga} + \tilde{\mathcal{R}}_{gs}),$$

$$\tilde{\mathcal{R}}_{fl} = \frac{1}{2}e^{i\theta}(\tilde{\mathcal{R}}_{as} + \tilde{\mathcal{R}}_{ss} - \tilde{\mathcal{R}}_{aa} - \tilde{\mathcal{R}}_{sa}).$$

Equations (19) and (20) are the general solution to the problem of radiative decay of two quiescent and noninteracting identical atoms placed into one thermostat, whose action on the atoms is described in the Markov approximation.

Consider a stationary solution to (8), (9). The nonzero two-particle density matrix elements have the form

$$\mathcal{R}^{st}_{gg} = 1 - \mathcal{R}^{(0)}_{aa}, \quad \mathcal{R}^{st}_{ff} = \mathcal{R}^{st}_{ll} = \frac{1}{2}\mathcal{R}^{(0)}_{aa},$$

$$\tilde{\mathcal{R}}^{st}_{gl} = -\frac{1}{\sqrt{2}}e^{i\theta}\tilde{\mathcal{R}}^{(0)}_{ga}, \quad \tilde{\mathcal{R}}^{st}_{gf} = \frac{1}{\sqrt{2}}\tilde{\mathcal{R}}^{(0)}_{ga}, \quad (21)$$

$$\tilde{\mathcal{R}}^{st}_{fl} = -\frac{1}{2}e^{i\theta}\tilde{\mathcal{R}}^{(0)}_{aa}.$$

To determine whether or not stationary solution (21) is entangled, let us use the Peres–Horodecki criterion [20, 21], which is as follows. Consider the two-particle density matrix transposed with respect to the indices of one of the atoms, for instance, the second atom. We will call this matrix the Peres–Horodecki matrix. The necessary condition of the factorizability of the density matrix is positiveness of all its eigenvalues. For entangled states, at least one eigenvalue of such a density matrix is negative. For instance, for entangled states $|s\rangle$ and $|a\rangle$, the negative eigenvalue in question is –1/2. The negative Peres–Horodecki matrix eigenvalue can be used as an entangled state characteristic. The stationary Peres–Horodecki matrix has the form

$$\mathcal{R}^{P-Hst} = \begin{pmatrix} 1-\mathcal{R}^{(0)}_{aa} & \frac{1}{\sqrt{2}}\tilde{\mathcal{R}}^{(0)}_{ga} & -\frac{1}{\sqrt{2}}e^{-i\theta}\tilde{\mathcal{R}}^{(0)*}_{ga} & -\frac{1}{2}e^{-i\theta}\mathcal{R}^{(0)}_{aa} \\ \frac{1}{\sqrt{2}}\tilde{\mathcal{R}}^{(0)*}_{ga} & \frac{1}{2}\mathcal{R}^{(0)}_{aa} & 0 & 0 \\ -\frac{1}{\sqrt{2}}e^{i\theta}\tilde{\mathcal{R}}^{(0)}_{ga} & 0 & \frac{1}{2}\mathcal{R}^{(0)}_{aa} & 0 \\ -\frac{1}{2}e^{i\theta}\tilde{\mathcal{R}}^{(0)}_{aa} & 0 & 0 & 0 \end{pmatrix}.$$

Its eigenvalues are determined by the equations

$$\lambda_1 = \frac{1}{2}\mathcal{R}^{(0)}_{aa},$$

$$4\lambda\left\{\left(\lambda - \frac{1}{2}\mathcal{R}^{(0)}_{aa}\right)(1 - \mathcal{R}^{(0)}_{aa} - \lambda) + \left|\tilde{\mathcal{R}}^{(0)}_{ga}\right|^2\right\} \quad (22)$$

$$+\left(\lambda - \frac{1}{2}\mathcal{R}^{(0)}_{aa}\right)\mathcal{R}^{(0)2}_{aa}.$$

An analysis of (22) shows that there are parameter regions in which one of the eigenvalues of the Peres–Horodecki matrix is negative. It only makes sense to discuss the possibility of the entanglement of atomic states for the initial conditions that correspond to the factorized diatomic density matrix $\mathcal{R}^{(0)} = \rho^{f(0)} \otimes \rho^{l(0)}$.

First consider pure atomic states, for which monatomic density matrices can be represented in the form

$$\rho^{f(0)} = \frac{|0\rangle\langle 0| + \alpha_f^*|0\rangle\langle 1| + \alpha_f|1\rangle\langle 0| + |\alpha_f|^2|1\rangle\langle 1|}{1 + |\alpha_f|^2},$$

$$\rho^{l(0)} = \frac{|0\rangle\langle 0| + \alpha_l^*|0\rangle\langle 1| + \alpha_l|1\rangle\langle 0| + |\alpha_l|^2|1\rangle\langle 1|}{1 + |\alpha_l|^2}. \quad (23)$$

We then have

$$\mathcal{R}^{(0)}_{aa} = \frac{1}{2}(\mathcal{R}^{(0)}_{ff} + \mathcal{R}^{(0)}_{ll} - e^{i\theta}\mathcal{R}^{(0)}_{lf} - e^{-i\theta}\mathcal{R}^{(0)}_{fl})$$

$$= \frac{|\alpha_f - \alpha_l e^{i\theta}|^2}{2(1 + |\alpha_f|^2)(1 + |\alpha_l|^2)} \equiv 2a,$$

$$\left|\mathcal{R}_{ag}^{(0)}\right|^2 = \frac{1}{2}\left|\mathcal{R}_{fg}^{(0)} - e^{i\theta}\mathcal{R}_{lg}^{(0)}\right|^2$$

$$= \frac{\left|\alpha_f - \alpha_l e^{i\theta}\right|^2}{2(1+|\alpha_f|^2)^2(1+|\alpha_l|^2)^2} \equiv 2a\beta,$$

$$\beta^{-1} = (1+|\alpha_f|^2)(1+|\alpha_l|^2),$$

and the second equation in (22) can be written as

$$\lambda^3 + \lambda^2(a-1) - \lambda a(3a-1+2\beta) + a^3 = 0,$$

where $0 < \beta < 1$ and the a parameter changes from zero [for identical initial atomic states and $\theta = 0$) to 1/4 [for $\alpha_f = -\alpha_l^{-1}\exp(i\theta)$ and also for all $|\alpha_f| \gg 1 \gg |\alpha_l|$ and vice versa, $|\alpha_f| \ll 1 \ll |\alpha_l|$].

One of the eigenvalues denoted by λ_- becomes negative for different initial purely quantum atomic states. The larger the a and β parameter values, the smaller λ_-. If $a = 1/4$ and $\alpha_f = -\alpha_l^{-1}\exp(i\theta)$, the β parameter takes on a maximum value of 1/4 at $|\alpha_f| = 1$. We then have a minimum λ_- value, $\lambda_- \approx -0.17$. It follows that stationary entanglement arises in the atomic system, and the λ_- parameter monotonically decreases during collective decay. An interesting situation arises when one of the atoms populates the lower level. The decay of the second atom excites the first one and causes entanglement in this system of two atoms.

Depending on the initial conditions and phase θ incursion, stationary entanglement may well be absent, for instance, at identical states and $\theta = 0$. Nevertheless, atomic states become somewhat entangled during collective decay. For the case considered above, the minimum λ_- value is $\lambda_- \approx -0.026$.

Next, consider mixed initial atomic states. Let

$$\rho^{f(0)} = \begin{pmatrix} n_0 & p^* \\ p & 1-n_0 \end{pmatrix}, \quad \rho^{l(0)} = \begin{pmatrix} m_0 & q^* \\ q & 1-m_0 \end{pmatrix}.$$

Let the atoms be unpolarized, $p = q = 0$. Then, $\mathcal{R}_{ag}^{(0)} = 0$, and one of the Peres–Horodecki matrix eigenvalues is always

$$\lambda_- = \frac{1}{2}(1 - 2a - \sqrt{1-4a+8a^2}),$$

$$a = \frac{1}{4}\{(1-n_0)m_0 + n_0(1-m_0)\}.$$

This eigenvalue is always negative except when both atoms populate either the upper or the lower level. The $\lambda_- \approx -0.1$ minimum value is determined by the largest possible a value, $a = 1/4$. One of the atoms is then not excited, the other populates the upper level, and the atoms are in the pure state.

Radiative decay of two atoms in a common thermostat also causes the arising of atomic correlations in the absence of entanglement. An example is the decay of the excited atomic state $|1\rangle$. For a monatomic system, we have usual radiative decay

$$\rho_{10}^f = 0, \quad \rho_{11}^f = e^{-\tau}, \quad \rho_{00}^f = 1 - e^{-\tau}. \tag{24}$$

Collective decay of two excited atoms is described by the equations

$$\begin{aligned} &\mathcal{R}_{ss} = 2\tau e^{-2\tau}, \quad \mathcal{R}_{ee} = e^{-2\tau}, \\ &\mathcal{R}_{gg} = 1 - (1+2\tau)e^{-2\tau}, \\ &\mathcal{R}_{ag} = \mathcal{R}_{aa} = \mathcal{R}_{ae} = \mathcal{R}_{sa} \\ &= \mathcal{R}_{se} = \mathcal{R}_{eg} = \mathcal{R}_{sg} = 0, \end{aligned} \tag{25}$$

or, in the g, f, l, and e variables,

$$\mathcal{R}_{ff} = \mathcal{R}_{ll} = \tau e^{-2\tau}, \quad \mathcal{R}_{fl} = e^{i\theta}\tau e^{-2\tau},$$

$$\mathcal{R}_{ef} = \mathcal{R}_{el} = \mathcal{R}_{gl} = \mathcal{R}_{gf} = 0.$$

Here, the initial condition is the occurrence of both atoms in the excited state (only the $\mathcal{R}_{ee}^{(0)} = 1$ matrix element is nonzero). The one-particle density matrix of each atom evolves as follows:

$$\begin{aligned} &\rho_{11}^f = e^{-2\tau}(1+\tau), \quad \rho_{00}^f = 1 - (1+\tau)e^{-2\tau}, \\ &\rho_{10}^f = 0. \end{aligned} \tag{26}$$

According to the Peres–Horodecki criterion, state (25) is not entangled, although the equation for the one-particle density matrix is not closed and is governed by the dynamics of the two-particle density matrix,

$$\hat{\Gamma}\rho_{11}^f = \rho_{11}^f + \frac{1}{2}(\mathcal{R}_{fl}e^{-i\theta} + \mathcal{R}_{lf}e^{i\theta}),$$

$$\hat{\Gamma}\rho_{00}^f = -\rho_{11}^f - (e^{-i\theta}\mathcal{R}_{fl} + e^{i\theta}\mathcal{R}_{lf}),$$

$$\hat{\Gamma}\rho_{10}^f = \rho_{10}^f - \frac{1}{2}e^{i\theta}(\mathcal{R}_{ef} - \mathcal{R}_{lg}).$$

5. THE INFLUENCE OF MODEL PARAMETERS ON ENTANGLEMENT

Our analysis shows that effective entanglement of atomic states almost always occurs in the model of collective radiative decay in a thermostat field at zero temperature. We consider the factors that interfere with such an entanglement.

According to (17), stationary entanglement should disappear as the density of photons in the thermostat increases no matter what the degree of thermostat squeezing. The dependence of the minimum Peres–Horodecki matrix eigenvalue λ_- on the density of photons in the common thermostat at zero and maximum squeezing degrees and phase shifts $\theta = 0$ and $\pi/2$ is shown in Fig. 1. According to this figure, maximum

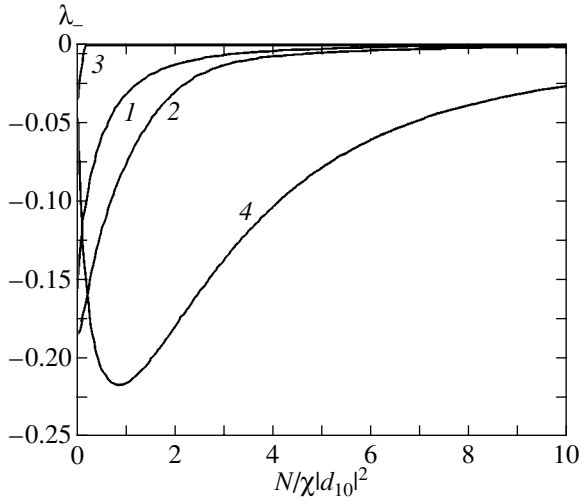

Fig. 1. Minimum Peres–Horodecki matrix eigenvalue as a function of photon density. Curves *1* and *2* correspond to phase shift $\theta = 0$ and squeezing factors $|M| = 0$ and $|M| = \sqrt{N(N+1)}$, respectively. Curves *3* and *4* correspond to phase shift $\theta = \pi/2$ and squeezing factors $|M| = 0$ and $|M| = \sqrt{N(N+1)}$, respectively. Initial atomic states are taken in form (23) with $\alpha_f = -\alpha_l$.

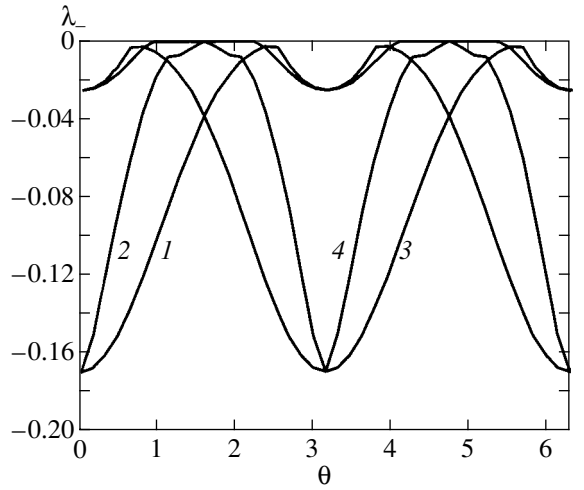

Fig. 2. Minimum Peres–Horodecki matrix eigenvalue as a function of phase shift for (*1*, *3*) unidirectional and (*2*, *4*) one-dimensional models at zero temperature. The curves correspond to initial states in form (23) with (*1*, *2*) $\alpha_f = -\alpha_l = 1$ and (*3*, *4*) $\alpha_f = \alpha_l = 1$.

thermostat squeezing at a low photon density increases the degree of entanglement at a $\theta = \pi/2$ phase shift.

The phase shift dependence of λ_- is shown in Fig. 2. The unidirectional and one-dimensional models give equal λ_- extrema, also when the atoms have different coupling constants for waves propagating in different directions. Numerical simulation results therefore show that λ_- extrema weakly depend on whether the thermostat model is unidirectional or one-dimensional and allow us to suggest that the unidirectional model (which coincides with the three-dimensional model at $\theta = 0$) is a good abstraction for studying atomic entanglement under different conditions including simultaneous action of several independent thermostats and different coherent field resonance actions on atoms.

Note that a nonzero phase value destroys stationary entanglement in the one-dimensional model, but the rate of this process is substantially lower than that of attaining a stationary value at a zero phase.

So far as the role played by independent thermostats, each acting on one of the atoms, is concerned, it is clear from (16) that they destroy any stationary entanglement in the system of atoms, even if the initial state of the atoms is entangled. In time dynamics, entanglement can also arise in the atomic system when independent thermostats act on the atoms. Numerical calculations show that, when each atom is under the action of a single "its own" thermostat, we obtain an interesting dependence of minimum Peres–Horodecki matrix eigenvalues on the coupling constants between atoms and "their own" thermostats. For initial conditions (23) at $\alpha_f = -\alpha_l = 1$ and in the absence of squeezing of either common or "own" thermostat, the dependence of λ_- on $\chi^{(1)}$ is very close to that shown by curve *4* in Fig. 1.

6. CONCLUSION

Recall that we ignored longitudinal electric-field-induced dipole–dipole interatomic interaction effective at small interatomic distances and all other interatomic interaction types to elucidate the role played by the common thermostat in the entanglement of atomic states. The thermostat itself is described by a Wiener quantum process independent of the state of the atoms. For this reason, the inverse effect of emission and absorption of quanta by atoms is also excluded. The interaction of atoms with their common thermostat is determined by an operator of type (5) with certain symmetry properties with respect to permutations of atoms. At the same time, diatomic states include at least two types of states ($|s\rangle$ and $|a\rangle$) different with respect to permutations of atoms. These states participate differently in relaxation dynamics. In the simplest case, one type of states ($|a\rangle$) evolves in a unitary way, whereas the dynamics of the second type ($|s\rangle$) is nonunitary. As a result, balance of representing the nonentangled initial state through the $|s\rangle$ and $|a\rangle$ basis vectors of the entangled basis is violated. In some time, atomic states therefore become entangled. It follows that the role played by a common thermostat in entanglement reduces to providing substantially different dynamics of atomic states that differ in symmetry properties with respect to permutations. The $|a\rangle$ states and the situation under consideration provide for a simple physical realization of the so-called "decoherfence free subspaces" [26]

extensively discussed in recent years in the quantum information theory.

This can be not only the difference between unitary and nonunitary evolutions of the atomic states of the entangled basis but also the difference in the rates of atomic state damping during common nonunitary evolution. As to the decay of two atoms initially populating the upper excited level, it does not cause entanglement of atomic states because the initial states are characterized by only one symmetry type with respect to permutation of the atoms. Also, the interaction of atoms with one quantized electromagnetic field mode in the absence of any relaxation channels should not result in the entanglement of atomic states because the dynamics of atomic states of different symmetries will be unitary. This problem, however, requires additional inquiries.

The results of this work can also be looked at from a different point of view. The arising of stationary entanglement means that, in the model under consideration, collective radiative decay of an arbitrary initial state does not lead to the establishment of thermodynamic equilibrium, if the thermodynamically equilibrium state is understood to be the stationary state of the model of one atom. This is most clearly seen for zero temperature and the unidirectional model. On the other hand, the presence of independent thermostats and arbitrarily small coupling constants with these thermostats destroys stationary entanglement and establishes thermodynamic equilibrium in the system solely as a result of radiative processes. In my opinion, this is evidence in favor of such a Markov model of radiative decay that includes independent thermostats in addition to the common thermostat [see (12) and (13)]. The opposite assertion also appears to be true. Namely, in studies of the entanglement of atoms caused by some other reasons, for instance, by dipole–dipole interatomic interaction, it is necessary to take into account not only relaxation of a separate atom caused by interaction with its own thermostat, as, e.g., in [15–17], but also collective relaxation, which, according to the conclusions drawn in this work, is responsible for its own mechanism of the entanglement of atomic states.

Note that the conclusion of the entanglement of atomic states drawn in this work is in agreement with the recent data on an increase in the information capacity of quantum communication channels under the conditions of the action of correlated noise on them [27], if quantum channel is understood as monatomic dynamics.

ACKNOWLEDGMENTS

The author thanks V.N. Gorbachev and A.I. Maimistov for useful discussions. This work was financially supported by the Russian Foundation for Basic Research (project no. 00-02-17803).

REFERENCES

1. C. W. Gardiner, *Quantum Noise* (Springer-Verlag, Berlin, 1991).
2. L. Mandel and E. Wolf, *Optical Coherence and Quantum Optics* (Cambridge Univ. Press, Cambridge, 1995; Fizmatlit, Moscow, 2000).
3. M. B. Menskiĭ, *Quantum Measurings and Decoherence. Models and Phenomenology* (Fizmatlit, Moscow, 2001).
4. D. Giulini, E. Joos, C. Kiefer, *et al.*, *Decoherence and the Appearance of a Classical World in Quantum Theory* (Springer-Verlag, Berlin, 1996).
5. S. Bose, I. Fuentes-Guridi, P. L. Knight, and V. Vedral, quant-ph/0103063.
6. C. Simon and J. Kempe, quant-ph/0109102.
7. D. F. Walls and G. J. Milburn, *Quantum Optics* (Springer-Verlag, Berlin, 1995).
8. S. Ya. Kilin, Usp. Fiz. Nauk **169**, 507 (1999).
9. I. V. Bargatin, B. A. Grishanin, and V. N. Zadkov, Usp. Fiz. Nauk **171**, 625 (2001).
10. C. P. Yang and G. C. Guo, Physica A (Amsterdam) **273**, 352 (1999).
11. G. C. Guo and C. P. Yang, Physica A (Amsterdam) **260**, 173 (1998).
12. V. N. Gorbachev, A. I. Zhiliba, and A. I. Trubilko, Izv. Akad. Nauk, Ser. Fiz. **66**, 345 (2002).
13. A. V. Andreev, V. I. Emel'yanov, and Yu. A. Il'inskiĭ, *Cooperative Phenomena in Optics* (Nauka, Moscow, 1988).
14. M. G. Benedict, A. M. Ermolaev, V. A. Malyshev, I. V. Sokolov, and E. D. Trifonov, *Super-Radiance: Multiatomic Coherent Emission* (Inst. of Physics Publ., Bristol, 1996).
15. G. K. Brennen, C. M. Caves, P. S. Jessen, and I. H. Deutsch, Phys. Rev. Lett. **82**, 1060 (1999).
16. A. Beige, S. F. Huelga, P. L. Knight, *et al.*, J. Mod. Opt. **47**, 401 (2000).
17. I. V. Bargatin, B. A. Grishanin, and V. N. Zadkov, Fortschr. Phys. **48**, 637 (2000).
18. L. M. Duan, J. I. Cirac, P. Zoller, and E. S. Polzik, Phys. Rev. Lett. **85**, 5643 (2000).
19. B. Julsgaard, A. Kozhekin, and E. S. Polzik, quant-ph/0106057.
20. A. Peres, Phys. Rev. Lett. **77**, 1413 (1996).
21. M. Horodecki, P. Horodecki, and R. Horodecki, Phys. Lett. A **223**, 1 (1996).
22. V. I. Rupasov, Zh. Éksp. Teor. Fiz. **83**, 1711 (1982) [Sov. Phys. JETP **56**, 989 (1982)].
23. V. I. Yudson, Zh. Éksp. Teor. Fiz. **88**, 1757 (1985) [Sov. Phys. JETP **61**, 1043 (1985)].
24. A. I. Maimistov and A. M. Basharov, *Nonlinear Optical Waves* (Kluwer, Dordrecht, 1999), Appendix 1.
25. G. Lindblad, Commun. Math. Phys. **48**, 119 (1976).
26. D. A. Lidar, I. L. Chuang, and K. B. Whaley, Phys. Rev. Lett. **81**, 2594 (1998).
27. C. Macchiavello and G. M. Palma, quant-ph/0107052.

Translated by V. Sipachev

Journal of Experimental and Theoretical Physics, Vol. 94, No. 6, 2002, pp. 1080–1087.
Translated from Zhurnal Éksperimental'noĭ i Teoreticheskoĭ Fiziki, Vol. 121, No. 6, 2002, pp. 1261–1269.

ATOMS, SPECTRA, RADIATION

Relativistic Constraints on the Distinguishability of Orthogonal Quantum States

S. N. Molotkov* and S. S. Nazin

Institute of Solid-State Physics, Russian Academy of Sciences, Chernogolovka, Moscow oblast, 142432 Russia
**e-mail: molotkov@issp.ac.ru*

Received February 7, 2001

Abstract—The constraints imposed by special relativity on the distinguishability of quantum states are discussed. An explicit expression relating the probability of an error in distinguishing two orthogonal single-photon states to their structure, the time t at which a measurement starts, and the interval of time T elapsed from the start of the measurement until the time at which the outcome is obtained by an observer is given as an example. © *2002 MAIK "Nauka/Interperiodica".*

Many issues of nonrelativistic quantum information theory, for example, information transmission over quantum communication channels, lead to the problem of quantum-state distinguishability.

The major postulates of classical, nonrelativistic physics assume that any measurement of the state of a physical system by an observer can be made as accurately as one likes and without perturbing the initial state. Moreover, since the limiting velocity is unrestricted, there are no prohibitions on carrying out measurements, including nonlocal ones in space, in an arbitrary short (formally, zero) time. Therefore, any two states of a physical system can be distinguished reliably, instantly, and without their perturbation.

In nonrelativistic quantum mechanics, any measurement in a quantum system generally leads to a perturbation of its initial state. There is a fundamental difference in distinguishing the states of a quantum system in one of the two orthogonal or nonorthogonal states. For orthogonal states, the question of which state a quantum system is in can be answered with confidence (with a zero probability of error) and without perturbing its initial state [1, 2]. The possibility of obtaining the outcome by an observer (for nonlocal measurements) in a zero time contains in hidden form no restrictions on the limiting velocity.

Nonorthogonal states are fundamentally indistinguishable with confidence; i.e., the question of which of the two nonorthogonal states a quantum system is in can never be answered with a zero probability of error. An exact lower limit for the probability of such error can be established [3–5]. Therefore, all nonrelativistic quantum cryptographic exchange protocols use nonorthogonal states. There are no fundamental prohibitions on distinguishing (although with some probability of error) nonorthogonal states in a zero time.

In relativistic quantum mechanics, additional (compared to nonrelativistic quantum mechanics) constraints on the time it takes to distinguish quantum states must also arise. The fundamental constraints imposed by special relativity on the measurability of dynamical variables for quantum systems were first considered in 1931 by Landau and Pierls [6]. Qualitative considerations based on analysis of uncertainty relations together with a restriction on the limiting velocity led the authors of [6] to conclude that, for example, the momentum cannot be accurately determined in the relativistic range (in contrast to the nonrelativistic case) in any finite time. In fact, these authors concluded that no nonlocal dynamical variables of a quantum system are measurable in the relativistic range.

In nonrelativistic quantum mechanics, an arbitrarily accurate measurement of the momentum of a quantum system is not forbidden, although the eigenvector of the momentum operator is an infinitely extended (in space) plane wave. To be more precise, a plane wave is not a physically realizable state, because it does not belong to the Hilbert space of quadratically integrable functions but is a generalized eigenvector of the momentum operator [7] (a linear continuous functional in framed Hilbert space [8]). The generalized eigenvector (plane wave) can be approximated as closely as one likes by the normalized state localized in a finite but arbitrarily large spatial region, by such a state that the mean value of the momentum operator measured in this state will be arbitrarily close to the plane-wave momentum. Such a momentum measurement implies that the state present in an arbitrarily large spatial region is entirely measurable. Since access to any region in nonrelativistic quantum mechanics is possible in a zero time, there are basically no restrictions on an arbitrarily accurate measurement, for example, of the momentum. Given the restrictions imposed by special relativity, access to an infinite region requires an infinite time and, in this sense, the dynamical variables are indeterminable. To

be more precise, these are indeterminable if we require their absolutely accurate measurement in a finite time.

The problem of measuring quantum systems in the relativistic case was further investigated in 1933 by Bohr and Rozenfeld [9]. The critical remarks made in [9] regarding the results from [6] do not cancel the restrictions imposed in [6], because the latter follow from the restrictions dictated by special relativity. The contrary would imply abandoning special relativity. The arguments of [6] were later reproduced in unchanged form in [10].

The orthogonality of two quantum states is generally a nonlocal property both in Hilbert space and in Minkowski space–time. However, this does not imply that, for example, two orthogonal states cannot be distinguished by local measurements (local in the sense that the outcome of the measurement can be assigned to a certain point of space).

In connection with problems of quantum information theory, we will be concerned with the restrictions imposed by relativistic quantum theory on the time of obtaining the outcome of a measurement when distinguishing two orthogonal states of a quantum system. Although the considerations that it takes a finite time for the observer to obtain the outcome are general, this time itself depends on the state structure.

Here, we give an example of the problem of distinguishing two orthogonal single-photon states. For these states, the error in distinguishing them can be related in general form to the time interval T from the start of a measurement until the time when the observer obtains the outcome.

For our purposes, it will suffice to restrict the analysis to pure states, because any state can be represented as a statistical mixture of pure states (although this representation is generally ambiguous).

Let there be a pair of orthogonal states in Hilbert space $\mathcal{H}$, $|\psi_{0,1}\rangle \in \mathcal{H}$ and $\langle\psi_0|\psi_1\rangle = 0$. Several levels can be naturally separated by the detail of the measuring procedure in quantum mechanics [4, 11–14]. The simplest description of the measurement process allows only the following questions to be answered: What outcomes are possible in a given measurement (i.e., what is the space of possible outcomes of the measurement Θ)? What is the relative frequency (probability) of a particular outcome (i.e., the outcome of the measurement belongs to the measurable set $\Delta \subset \Theta$) for a given initial state ρ of the quantum-mechanical system being measured? In this sense, the measurements are in one-to-one correspondence with positive decompositions of unity on Θ in the Hilbert space $\mathcal{H}$ of system states [3, 4, 11–14], i.e., the families of Hermitean operators $M_t(\Delta)$, $\Delta \subset \Theta$ in the Hilbert space $\mathcal{H}$ that satisfy the following conditions:

(i) $M_t(\varnothing) = 0$, $M_t(\Theta) = I$ (normalization);

(ii) $M_t(\Delta) \geq 0$ (positivity);

(iii) $M_t(\Delta) = \sum_j M_t(\Delta_j)$ if $\Delta = \cup_j \Delta_j$, $\Delta_j \cap \Delta_i = \varnothing$ at $i \neq j$ (additivity).

In this case, the measure $\mu_{t,\rho}$ of the set Δ is given by

$$\mu_{t,\rho}(\Delta) = \Pr_t(\theta \in \Delta) = \mathrm{Tr}\{\rho M_t(\Delta)\}. \quad (1)$$

In other words, $M_t(\Delta)$ defines a positive operator-valued measure. Different values of t describe physically different measurements. Here, we introduce the parameter t, the time at which the measurement starts. We emphasize that, below, the time t is a parameter and does not belong to the space of outcomes. The time at which the outcome is obtained by the observer (the acquisition and delivery of classical information from a nonlocal instrument to the observer) is denoted by T.

Specifying a positive operator-valued measure is the formal description of a physical instrument—a black box. There is a quantum state at its input, and a classical quantity (function) defining the probability distribution (1) arises at its output. In general, this is not the most detailed description of the instrument, because the same decomposition of unity can be implemented with different instruments.

A special case of this measure is the spectral orthogonal decompositions of unity that correspond to the families of spectral projectors of self-adjoint operators in $\mathcal{H}$ for which the following equality holds:

$$M_t(\Delta_1)M_t(\Delta_2) = 0, \quad \text{if} \quad \Delta_1 \cap \Delta_2 = 0.$$

However, this approach ignores the question of which state the system is in after the measurement that yielded a particular outcome. Since we are not yet concerned with the system state after the measurement, we will not use the notion of an instrument (superoperator) [4, 11–14].

The states are clearly distinguishable through a measurement described by the orthogonal decomposition of unity in $\mathcal{H}$

$$\mathcal{P}_0 + \mathcal{P}_1 + \mathcal{P}_\perp = I, \quad \mathcal{P}_{0,1} = |\psi_{0,1}\rangle\langle\psi_{0,1}|, \quad \mathcal{P}_\perp = I - \mathcal{P}_0 - \mathcal{P}_1, \quad (2)$$

where $\mathcal{P}_{0,1}$ are the projectors onto the subspaces $\mathcal{H}_{0,1}$ stretched over $|\psi_{0,1}\rangle$ and $\mathcal{P}_\perp$ is the projector onto the subspace $\mathcal{H}_{0,1}^\perp = (\mathcal{H}_0 \oplus \mathcal{H}_1)^\perp$. The probability of an outcome in channel 0 on the set of outcomes $\Theta = \{0, 1, \perp\}$ if the input state is, for example, $|\psi_0\rangle$, is

$$\Pr\{|\psi_0\rangle\} = \mathrm{Tr}\{|\psi_0\rangle\langle\psi_0|\mathcal{P}_0\} = 1, \quad (3)$$

while, in channels $\mathcal{P}_{1,\perp}$, it is identically equal to zero:

$$\Pr\{|\psi_0\rangle\} = \mathrm{Tr}\{|\psi_0\rangle\langle\psi_0|\mathcal{P}_{1,\perp}\} = 0; \quad (4)$$

the same is true for the input state $|\psi_1\rangle$. Relations (2)–(4) imply that the orthogonal states are clearly distinguishable. Significantly, the duration of the measuring procedure under consideration has not yet been mentioned anywhere.

Our conclusions about the time at which the outcome is obtained refer to the time at which the outcome is brought to the observer; to be more precise, the estimates obtained below give a lower limit for this time. Obtaining such estimates does not require knowing the specific measuring procedure [explicitly specifying the instrument (superoperator)]; the decomposition of unity [specifying the positive Hermitean operators $M_t(\Delta)$] will suffice. The set of outcomes Θ can be arbitrarily complex, but it necessarily contains explicitly or implicitly spatial regions. This is enough to deduce the restrictions imposed by a finite speed of light.

In the relativistic case, as yet there is no clear-cut and internally consistent answer to the question of which state the system is in after a measurement, i.e., what should be meant by the reduction of the state vector for a quantum system. Various aspects of this problem were discussed in [15–18]. A complete, not yet constructed, theory of quantum-mechanical measurements in the relativistic case must be able to answer the question of how the state changes after a measurement. Some questions can also be answered without a full description of the measurement process.

Up until now, only the properties of the abstract Hilbert space of states for a quantum system have been used to prove the statements mentioned above. Since the states of relativistic quantum fields are described by rays in the Hilbert space of states, the measurements are also formally described by the decompositions of unity. In this case, it does not matter which particular realization of the abstract Hilbert space is used; its choice is dictated only by convenience in each particular problem. However, all quantum states must be associated with some physical system. All manipulations and measurements on quantum systems take place in coordinate space (or space–time in the relativistic case). There are no physical systems that would have the degrees of freedom described by the states in some Hilbert space in isolation from the spatial degrees of freedom. The latter is actually dictated by the fact that the various kinds of particles are classified by irreducible representations of the Poincaré group containing a subgroup of translations in Minkowski space–time [7].

In nonrelativistic quantum mechanics, the absence of restrictions on the limiting velocity does not lead to any prohibitions on instantly obtaining the outcomes of nonlocal measurements [even for infinitely extended (in space) states] at an arbitrarily chosen time. A fundamentally different situation arises in relativistic quantum field theory. In quantum field theory, the field states are produced by field operators (or, more precisely, by operator generalized functions) [7]. The smoothing functions (amplitudes) in momentum representation are specified on a mass surface. As a result, the field states are fundamentally nonlocalizable in coordinate space; i.e., the amplitude carriers are nonzero in the entire space [7, 19–22]. At the same time, free field states (for mass and massless fields) localized in space as strongly as one likes—with a degree of localization arbitrarily close to an exponential one, of the order of $\exp(-\alpha|\mathbf{x}|/\ln(\ln(\ldots|\mathbf{x}|)))$, where α may be arbitrary—are admissible. This would not lead to any restrictions, as in the nonrelativistic case, if there were no restrictions on the limiting velocity of propagation. When there is a limiting velocity of propagation for quantum and classical objects, nonlocalizability (which arises from the requirements of special relativity when quantizing the field [7]) leads to a new situation different from the nonrelativistic case. Since access to the entire space is required to reliably distinguish a pair of orthogonal states of the quantized field (such a measurement must be nonlocal in coordinate space), the time it takes for the observer to obtain the outcome is infinite. However, the assertion that an infinite time is required to distinguish the orthogonal states of the quantized field with an absolute accuracy (reliably) is unlikely to be physically satisfactory.

The statement of the problem that requires access to the entire space to reliably (with a unit probability) distinguish the states is meaningless. The observer can never control the entire space. Therefore, it is necessary to relax the requirement of reliable state distinguishability and reformulate the problem as follows. The observer controls some finite (but arbitrary large) spatial region where measurements can be carried out. The question is how the probability of an error in distinguishing the states is related to the size of the region (actually the time T in which the observer can obtain the outcome) and to the structure of the states themselves. To be more precise, an optimal measurement minimizing the error in distinguishing the states must be carried out when specifying the input states and the region size (and, accordingly, the time at which the outcome is obtained).

Let us now consider the most interesting (in applications) case of a gauge field—photons. The electromagnetic field operators are [23]

$$A^{\pm}_{\mu}(\hat{x}) = \frac{1}{(2\pi)^{3/2}}\int \frac{d\mathbf{k}}{\sqrt{2k_0}} e^{\pm i\hat{k}\hat{x}} e^{m}_{\mu}(\mathbf{k}) a^{\pm}_{m}(\mathbf{k}) \qquad (5)$$

and satisfy the commutation relations

$$[A^{-}_{\mu}(\hat{x}), A^{-}_{\nu}(\hat{x}')]_{-} = ig_{\mu\nu}D^{-}_{0}(\hat{x}-\hat{x}'), \qquad (6)$$

where $D_0^-(\hat{x} - \hat{x}')$ is the commutator function for a zero-mass field:

$$D_0^{\pm}(\hat{x}) = \pm\frac{1}{i(2\pi)^3}\int\frac{d\mathbf{p}}{2p_0}e^{\pm i\hat{p}\hat{x}}$$
$$= \frac{1}{4\pi}\varepsilon(x_0)\delta(\hat{x}^2) \pm \frac{i}{4\pi\hat{x}^2}, \quad (7)$$
$$\varepsilon(x_0)\delta(\hat{x}^2) \equiv \frac{\delta(x_0 - |\mathbf{x}|) - \delta(x_0 + |\mathbf{x}|)}{2|\mathbf{x}|}.$$

Here, the quantities with hats denote the four-dimensional vectors: $\hat{k} = (k_0, \mathbf{k})$ and $\hat{x} = (x_0, \mathbf{x})$. Four kinds of photons can be distinguished: two transverse, longitudinal, and temporal photons. The latter two kinds are fictitious and may be excluded from the analysis by introducing an indefinite metric [23]. The shortest way to the answer is related to using a specific gauge. Below, we work in the subspace of physical states in the Coulomb gauge $A_\mu = (\mathbf{A}, \varphi = 0)$, dealing with two physical transverse states of the electromagnetic field. The operator generalized function is the vector in three-dimensional space

$$\vec{\psi}(\hat{x}) = \frac{1}{(2\pi)^{3/2}}\int\frac{d\mathbf{k}}{\sqrt{2k_0}} \times \sum_{s=\pm1}\mathbf{w}(\mathbf{k}, s)\{a(\mathbf{k}, s)e^{-i\hat{k}\hat{x}} + a^+(\mathbf{k}, -s)e^{i\hat{k}\hat{x}}\}. \quad (8)$$

Here, $\mathbf{w}(\mathbf{k}, s)$ is the three-dimensional vector that describes the state of helicity $s = \pm1$,

$$\mathbf{w}(\mathbf{k}, \pm) = \frac{1}{\sqrt{2}}[\mathbf{e}_1(\mathbf{k}) \pm i\mathbf{e}_2(\mathbf{k})],$$
$$\mathbf{e}_1(\mathbf{k})\perp\mathbf{e}_2(\mathbf{k}), \quad |\mathbf{w}(\mathbf{k}, s)|^2 = 1, \quad (9)$$

where $\mathbf{e}_{1,2}(\mathbf{k})$ are the vectors perpendicular to $\mathbf{k}$. The field operators satisfy the Maxwell equations

$$\nabla\times\vec{\psi}(\hat{x}) = -i\frac{\partial}{\partial t}\vec{\psi}(\hat{x}), \quad \nabla\cdot\vec{\psi}(\hat{x}) = 0. \quad (10)$$

The smoothed field operators can be written as

$$\vec{\psi}(f) = \sum_{s=\pm1}\int\vec{\psi}(\hat{x}, s)f(\hat{x}, s)d\hat{x} = \frac{1}{(2\pi)^{3/2}}\int\frac{d\mathbf{k}}{\sqrt{2k_0}} \times \sum_{s=\pm1}\mathbf{w}(\mathbf{k}, s)\{f(\mathbf{k}, s)a^+(\mathbf{k}, s) + f^*(\mathbf{k}, s)a(\mathbf{k}, s)\}, \quad (11)$$

where $f(\mathbf{k}, s)$ are the values of $f(\hat{k}, s)$ on the mass surface and $f(\hat{k}, s)$ is the four-dimensional Fourier transform of an arbitrary function $f(\hat{x}, s)$ from the space of principal functions $\mathcal{J}(\hat{x})$.

We will consider the problem of distinguishing one of the two single-photon states that differ only by the states of helicity. The two single-photon states of a photon field with orthogonal states of helicity and the same spatial amplitude f can be written as

$$|\vec{\psi}_{0,1}\rangle = (\vec{\psi}^+(f_{0,1}))|0\rangle$$
$$= \int d\mathbf{x}\, f(\mathbf{x}, t)\vec{\psi}^+(\mathbf{x}, t, \pm)|0\rangle \quad (12)$$
$$= \frac{1}{(2\pi)^{3/2}}\int\frac{d\mathbf{k}}{\sqrt{2k_0}}f(\mathbf{k})\mathbf{w}(\mathbf{k}, \pm)a^+(\mathbf{k}, \pm)|0\rangle,$$

where

$$\vec{\psi}^+(\mathbf{x}, t, \pm) = \frac{1}{(2\pi)^{3/2}} \times \int\frac{d\mathbf{k}}{\sqrt{2k_0}}\mathbf{w}(\mathbf{k}, \pm)a^+(\mathbf{k}, \pm)e^{-i\hat{k}\hat{x}}, \quad (13)$$
$$f(\mathbf{x}, t) = \int d\mathbf{k}\, f(\mathbf{k})e^{i\hat{k}\hat{x}}.$$

The state with subscript 0 contains components with different $\mathbf{k}$ but only with positive (+) helicity, while the state with subscript 1 contains components with negative (–) helicity. A measurement that allows one of the pair of orthogonal states to be reliably distinguished is described by the orthogonal decomposition of unity in single-particle subspace and can be written as

$$I = \mathcal{P}_0 + \mathcal{P}_1 + \mathcal{P}_\perp, \quad \mathcal{P}_{0,1} = |\vec{\psi}_{0,1}\rangle\langle\vec{\psi}_{0,1}|, \quad \mathcal{P}_\perp = I - \mathcal{P}_0 - \mathcal{P}_1. \quad (14)$$

The operator unity is

$$I = \sum_{s=\pm}\int\mathcal{M}_t(d\mathbf{x}, \pm)$$
$$= \sum_{s=\pm1}\int d\mathbf{k}(\mathbf{w}(\mathbf{k}, s)|\mathbf{k}, s\rangle)(\langle\mathbf{k}, s|\mathbf{w}(\mathbf{k}, s)), \quad (15)$$
$$|\mathbf{k}, s\rangle = a^+(\mathbf{k}, s)|0\rangle,$$

$$\mathcal{M}_t(d\mathbf{x}, \pm) = (\int d\mathbf{k}e^{-i\hat{k}\hat{x}}\mathbf{w}(\mathbf{k}, \pm)|\mathbf{k}, \pm\rangle) \times (\int d\mathbf{k}'\langle\mathbf{k}', \pm|\mathbf{w}(\mathbf{k}', \pm)e^{i\hat{k}'\hat{x}})\frac{d\mathbf{x}}{(2\pi)^3}, \quad (16)$$
$$\langle\mathbf{k}s|\mathbf{k}'s'\rangle = \delta_{ss'}\delta(\mathbf{k} - \mathbf{k}').$$

Let us consider the parameter of time t in the decomposition of unity (16). The integral over the entire space in (15) does not depend on this parameter and is identically equal to the unit operator. Note that t is the same for all points $\mathbf{x}$ [it cannot depend on $\mathbf{x}$; otherwise, (15) will not be the decomposition of unity]. As will be seen below, the time t should be interpreted as the time at

which a measurement is carried out with a classical instrument.

The probability of obtaining different outcomes of the measurements in channels $\mathcal{P}_j$ is

$$\begin{aligned}\Pr_i\{|\vec{\psi}_j\rangle\} &= \mathrm{Tr}\{|\vec{\psi}_i\rangle\langle\vec{\psi}_i|\mathcal{P}_j\} = \left|\langle\vec{\psi}_j|\vec{\psi}_i\rangle\right|^2 \\ &= \delta_{s,s'}\left|\int\int d\mathbf{x}d\mathbf{x}'\, f^*(\mathbf{x},t)D_0^+(\mathbf{x}-\mathbf{x}',t-t')\,f(\mathbf{x}',t')\right|^2 \\ &= \frac{\delta_{s,s'}}{(2\pi)^3}\left|\int f^*(\mathbf{k})\,f(\mathbf{k})\frac{d\mathbf{k}}{2|\mathbf{k}|}\right|^2 = \delta_{i,j}.\end{aligned} \tag{17}$$

The values of $s, s' = +$ and $-$ correspond to $i, j = 0$ and 1, respectively. The field amplitudes $f(\mathbf{x}, t)$ and $f(\mathbf{x}', t')$ are related by the cause-and-effect relation through the propagation effects described by the commutator function. The amplitudes $f(\mathbf{x}, t)$ are the coefficients in the decomposition of the state vector $|\vec{\psi}_{0,1}\rangle$ in different bases, $\vec{\psi}^+(\mathbf{x}, t, \pm)|0\rangle$ and $\vec{\psi}^+(\mathbf{x}', t', \pm)|0\rangle$.

The positive-frequency part of the commutator function is the scalar product of generalized base vectors:

$$\begin{aligned}&D_0^-(\mathbf{x}-\mathbf{x}', t-t') \\ &= -i\langle 0|\vec{\psi}^-(\mathbf{x}, t, \pm)\cdot\vec{\psi}^+(\mathbf{x}', t', \pm)|0\rangle, \quad t > t'.\end{aligned} \tag{18}$$

It can be interpreted [23] as the amplitude of the production of a particle at point $\mathbf{x}'$, t', its subsequent propagation, and the destruction at point $\mathbf{x}$, t.

One may get the impression that the interpretation (18) contradicts (7) and the causality considerations, because the commutator function is also nonzero outside the light cone (where $c^2|t-t'|^2 - |\mathbf{x}-\mathbf{x}'|^2 \neq 0$) and, thus, admits signal propagation faster than the speed of light. This contradiction stems from the fact that the generalized function in this reasoning is represented as an ordinary one. However, the generalized function, or, more precisely, the linear continuous functional on the space of principal functions, is actually not defined on a point-by-point basis (one cannot speak of the values of the generalized function at a point). Such a behavior of the commutator functions is consistent with causality; this question is discussed in detail in [24, 25].

Because the field amplitude $f(\mathbf{x}, t)$ is nonlocalizable (nonzero in the entire space), measurement (14)–(16) and obtaining the outcome with confidence imply access to the entire space at time t [or, more precisely, to the entire region of space where $f(\mathbf{x}, t)$ is nonzero]. Since this region represents the entire space, it takes an infinite time for the observer to reliably distinguish the orthogonal states.

Let us now consider the problem of distinguishing the states where only a finite region of space Ω is accessible to measurements (the complement to complete space $\bar{\Omega}$). The space of outcomes is a Cartesian product of two sets, $\Theta = \{(+,-)\times\Omega \cup ?\}$. The outcomes of the measurements in Ω are accessible to the observer, while the outcome ?, which formally corresponds to detector triggering in $\bar{\Omega}$, is inaccessible. The measurement is described by the decomposition of unity on this set of outcomes that refers to time t:

$$\begin{aligned}I &= I_{\bar{\Omega}} + I_\Omega, \\ I_\Omega &= \int_\Omega (\mathcal{M}_t(d\mathbf{x}, +) + \mathcal{M}_t(d\mathbf{x}, -)).\end{aligned} \tag{19}$$

This decomposition of unity corresponds to a classical instrument continuously distributed in Ω that can yield an outcome in each of the two channels, + or –, at each point $\mathbf{x}$ at time t.

Although the formal decomposition of unity (19) appears nonlocal (contains integration over spatial regions), the outcomes of the measurements themselves are local (the triggering of the classical instrument, the outcome of the measurement, takes place at some spatial point). In the case under consideration, the space of outcomes is the coordinate space itself where measurements takes place, in contrast to the situation where the measurement is described by the orthogonal projectors (2)–(4) in $\mathcal{H}$ (which are also nonlocal in coordinate space but only implicitly, because the state amplitudes are nonlocal). In this case, the set of outcomes is (0, 1, $\perp$) (the outcomes in channels $\mathcal{P}_{0,1,\perp}$) and we cannot say at which spatial point the instrument triggering occurred.

Let it be required that one of the states randomly presented for measurements with known *a priori* probabilities π_0 and π_1 ($\pi_0 + \pi_1 = 1$) be distinguished. When measuring the states, the outcomes can take place in the accessible region or can be absent in it (i.e., the formal outcome ? takes place in the inaccessible region). The probability of an outcome in the inaccessible region $\bar{\Omega}$ is

$$\begin{aligned}&\Pr\{\rho, \bar{\Omega}\} = \mathrm{Tr}\{\rho I_{\bar{\Omega}}\} \\ &= \pi_0\mathrm{Tr}\{\rho_0 I_{\bar{\Omega}}\} + \pi_1\mathrm{Tr}\{\rho_1 I_{\bar{\Omega}}\} = \pi_0 p_t + \pi_1 p_t = p_t,\end{aligned} \tag{20}$$

where

$$p_t = \int_{\bar{\Omega}} d\mathbf{x}|p(\mathbf{x}, t)|^2, \tag{21}$$

$$p(\mathbf{x}, t) = \frac{1}{(2\pi)^{3/2}}\int\frac{d\mathbf{k}}{\sqrt{2|\mathbf{k}|}}f(\mathbf{k})e^{i(\mathbf{k}\cdot\mathbf{x}-|\mathbf{k}|t)}. \tag{22}$$

Note that the function $p(\mathbf{x}, t)$ is essentially identical to the Landau–Pierls wave function for a photon in coordinate representation [26].

Equation (20) describes the probability of recording a photon that has only components with helicity "+" ($\pi_0 p_t$) and "–" ($\pi_1 p_t$) in $\bar{\Omega}$ at time t.

Therefore, if there were no outcome in the accessible region, then the observer should assume with the probabilities

$$p_0 = \frac{\pi_0 p_t}{\pi_0 p_t + \pi_1 p_t} = \pi_0, \quad p_1 = \frac{\pi_1 p_t}{\pi_0 p_t + \pi_1 p_t} = \pi_1 \quad (23)$$

that an outcome took place in the inaccessible region from the states $|\vec{\psi}_0\rangle$ and $|\vec{\psi}_1\rangle$, respectively.

Thus, if an outcome took place in the region inaccessible to the observer, then the probability of an error in distinguishing the states is equal to the product of the probability of an error and the fraction of the outcomes in $\bar{\Omega}$:

$$P_e(\bar{\Omega}) = (\pi_0 p_1 + \pi_1 p_0) p_t. \quad (24)$$

If the states are presented with equal probabilities ($\pi_0 = \pi_1 = 1/2$), then the probability of an error is equal to the fraction of the outcomes in $\bar{\Omega}$. The total probability of all possible outcomes in the entire space of outcomes $\Omega \cup \bar{\Omega}$ is equal to 1 because of the normalization

$$\int d\mathbf{x} |p(\mathbf{x}, t)|^2 = 1.$$

Let us now find the measurement for which the probability of an error is at a minimum and the outcome takes place in the accessible region Ω. In this case,

$$P_e(\Omega) = \pi_0 \mathrm{Tr}\{\rho_0 I_\Omega\} + \min_{E_0} \mathrm{Tr}\{\Gamma E_0\}. \quad (25)$$

In the basis of two orthogonal states of helicity "+" and "–," the operator Γ is

$$\Gamma = \pi_1 \rho_1 - \pi_0 \rho_0 = \begin{pmatrix} \pi_1 |\vec{\psi}_1\rangle\langle|\vec{\psi}_1| & 0 \\ 0 & -\pi_0 |\vec{\psi}_0\rangle\langle|\vec{\psi}_0| \end{pmatrix}. \quad (26)$$

The minimizing measurement can be easily found:

$$E_0 = \begin{pmatrix} 0 & 0 \\ 0 & I_\Omega \end{pmatrix}, \quad E_1 = \begin{pmatrix} I_\Omega & 0 \\ 0 & 0 \end{pmatrix}. \quad (27)$$

In this case, given (26) and (27), the probability of an error in distinguishing the states if the outcome took place in the accessible region is

$$P_e(\Omega) = 0. \quad (28)$$

Given (25) and (28), the total probability of an error is

$$P_e(\Omega, \bar{\Omega}) = P_e(\Omega) + P_e(\bar{\Omega}) = 2\pi_0 \pi_1 p_t = 2\pi_0 \pi_1 \int_{\bar{\Omega}} d\mathbf{x} |p(\mathbf{x}, t)|^2, \quad (29)$$

it is determined by the fraction of the outcomes in the inaccessible region. Since the region Ω and, accordingly, its complement $\bar{\Omega}$ to the complete space were specified at the outset, to minimize the error requires taking such a parameter of time t (the time at which a measurement takes place) that the fraction of the outcomes in the inaccessible region was at a minimum. This condition is intuitively obvious: because the amplitude of $f(\mathbf{x}, t)$ evolves in space–time, we must choose a time for the measurement when the integral of the magnitude of $p(\mathbf{x}, t)$ squared is at a maximum (minimum) in the accessible (inaccessible) region.

In order to find out whether the outcome took place in the accessible region, the observer must examine it after the time t and ascertain whether the instrument was triggered at one of the points in Ω in one of the channels for helicities, + or –. The region Ω is examined in the time T determined by the condition that it is covered by the part of the light cone referring to the past. This is dictated by the requirements of special relativity.

Note that some authors (e.g., [27]) use a different quantity for the probability of recording a photon in a spatial region that describes the degree of localization of the photon energy and a different measurement than (19). Indeed, the Hermitian energy operator $\hat{E}$ can be represented via the spectral decomposition as

$$\hat{E} = \sum_{s=\pm} |\mathbf{k}||\mathbf{k}s\rangle\langle s\mathbf{k}| d\mathbf{k} = \int \frac{d\mathbf{x}}{(2\pi)^3} \times \sum_{s=\pm} \{ (\int \sqrt{|\mathbf{k}|} |\mathbf{k}s\rangle \exp[-i(\mathbf{k}\cdot\mathbf{x} - |\mathbf{k}|t)] d\mathbf{k}) \times (\int \sqrt{|\mathbf{k}'|} \langle \mathbf{k}'s| \exp[i(\mathbf{k}'\cdot\mathbf{x} - |\mathbf{k}'|t)] d\mathbf{k}') \} = \int \sum_{s=\pm} \mathcal{M}_E(t, d\mathbf{x}). \quad (30)$$

Here, $\mathcal{M}_E(t, d\mathbf{x})$ is the measuring operator for the energy density $E(\mathbf{x}, t)$ [see the difference from (19)]. The mean value of the energy operator $\langle \hat{E} \rangle$ in an arbitrary single-photon state [here, in contrast to (8), it is more convenient for brevity not to introduce the vector notation for the state $|\psi\rangle$]

$$|\psi\rangle = \frac{1}{(2\pi)^{3/2}} \sum_{s=\pm} \int \frac{d\mathbf{k}}{\sqrt{2|\mathbf{k}|}} f(\mathbf{k}s) |\mathbf{k}s\rangle \quad (31)$$

by definition is

$$\langle \hat{E} \rangle = \mathrm{Tr}\{\hat{E}|\psi\rangle\langle\psi|\} = \frac{1}{2(2\pi)^3} \sum_{s=\pm} \int |f(\mathbf{k}s)|^2 d\mathbf{k}. \quad (32)$$

The energy near the point dx at time t is, by definition,

$$E(\mathbf{x}, t)d\mathbf{x} = \sum_{s=\pm} \mathrm{Tr}\{\mathcal{M}_E(t, d\mathbf{x})|\psi\rangle\langle\psi|\} = \left(\sum_{s=\pm} |f(\mathbf{x}, t)|^2\right)\frac{d\mathbf{x}}{(2\pi)^3}, \quad (33)$$

where

$$f(\mathbf{x}, t) = \frac{1}{(2\pi)^{3/2}}\int f(\mathbf{k}, s)\exp[i(\mathbf{k}\cdot\mathbf{x} - |\mathbf{k}|t)], \quad (34)$$

which is identical to the expression derived in [27].

In the formulated problem, we are concerned not with the energy density distribution in space but with the probability of distinguishing two orthogonal single-photon states (as integral quantum objects) when access to them is restricted. Therefore, the answer can be expressed using the Landau–Pierls function [26] rather than function (34).

We emphasize once again that the measurement for distinguishing the states described by the decomposition of unity (19) and the measurement to determine the energy density are physically different (different physical devices implementing these measurements correspond to them).

The physical interpretation of the Landau–Pierls function is not so clear as the interpretation of function (34) used in [27] to describe the energy density distribution. In [28], a massless particle is used as an example to show that the covariant measurement of the event time can be expressed in terms of the Landau–Pierls function. Interestingly, the energy measurement given by (34) and the measurement of the event time lead to the Lorenz-invariant energy–time uncertainty relation for a massless particle [28].

Thus, we explicitly found the measurement that minimizes the probability of an error in distinguishing the orthogonal states at a given size of the region accessible to measurement (or, equivalently, the time T at which the outcome is obtained). This minimum possible probability of an error also depends on the structure of the states themselves.

The time T should not be understood as the duration of the measurement process itself. In each specific experiment, the outcome of the measurement emerges at some random point $\mathbf{x}$ of the region Ω (at time t). It may turn out that the outcome in a particular experiment will take place exactly at the observer's location at time t; the time of distinguishing two states is then $T_{\min} = 0$. In a different experiment, the outcome will emerge at a different point. In this case, it takes a finite time for the observer to make sure that the outcome occurred in Ω in one of the channels for helicity. T is the minimum time it takes to reliably distinguish the states when the outcome of the measurement emerges at any point of Ω.

ACKNOWLEDGMENTS

This work was supported by the Russian Foundation for Basic Research (project no. 02-02-16289) and the Kvant Project.

REFERENCES

1. J. von Neumann, *Mathematical Foundations of Quantum Mechanics* (Princeton Univ. Press, Princeton, 1955; Nauka, Moscow, 1964).
2. C. H. Bennett, Phys. Rev. Lett. **68**, 3121 (1992); C. H. Bennett, G. Brassard, and N. D. Mermin, Phys. Rev. Lett. **68**, 557 (1992).
3. C. W. Helstrom, Inf. Control. **10**, 254 (1967); *Quantum Detection and Estimation Theory* (Academic, New York, 1976), Mathematics in Science and Engineering, Vol. 123.
4. A. S. Holevo, *Probabilistic and Statistical Aspects of Quantum Theory* (North-Holland, Amsterdam, 1982); A. S. Holevo, *Statistical Structure of Quantum Theory* (Springer-Verlag, Berlin, 2001), p. 1.
5. C. A. Fuchs, quant-ph/9601020.
6. L. D. Landau and R. Pierls, Z. Phys. **69**, 56 (1931); L. D. Landau, *Collection of Works* (Nauka, Moscow, 1969), Vol. 1, p. 56.
7. N. N. Bogolyubov, A. A. Logunov, A. I. Oksak, and I. T. Todorov, *General Principles of Quantum Field Theory* (Nauka, Moscow, 1987).
8. I. M. Gel'fand and N. Ya. Vilenkin, *Generalized Functions*, Vol. 4: *Applications of Harmonic Analysis* (Fizmatgiz, Moscow, 1961; Academic, New York, 1964).
9. N. Bohr and L. Rozenfeld, Math.-Fys. Medd. **12**, 3 (1933); N. Bohr, *Collection of Scientific Works* (Nauka, Moscow, 1971).
10. V. B. Berestetskii, E. M. Lifshitz, and L. P Pitaevskii, *Course of Theoretical Physics*, Vol. 4: *Quantum Electrodynamics* (Nauka, Moscow, 1982; Pergamon, New York, 1982).
11. K. Kraus, *States, Effects, and Operations* (Springer-Verlag, Berlin, 1983).
12. P. Busch, M. Grabowski, and P. J. Lahti, *Operational Quantum Physics* (Springer-Verlag, Berlin, 1995), Springer Lecture Notes in Physics, Vol. 31.
13. G. Lüders, Ann. Phys. (Leipzig) **8** (6), 322 (1951).
14. M. Ozawa, J. Math. Phys. **25**, 79 (1984); **34**, 5596 (1993).
15. K.-E. Hellwig and K. Krauss, Phys. Rev. D **1**, 566 (1970).
16. Y. Aharonov and D. Z. Albert, Phys. Rev. D **21**, 3316 (1980); **24**, 359 (1981); **29**, 228 (1984).
17. G. C. Ghirardi, *Open Systems and Measurement in Relativistic Theory*, Ed. by H. P. Breuer and F. Petruccione (Springer-Verlag, Berlin, 1999).
18. J. Finkelstein, Phys. Lett. A **278**, 19 (2000).

19. D. A. Kirzhnits, Usp. Fiz. Nauk **90**, 129 (1966) [Sov. Phys. Usp. **9**, 692 (1966)].
20. N. N. Meĭman, Zh. Éksp. Teor. Fiz. **47**, 1966 (1964) [Sov. Phys. JETP **20**, 1320 (1964)].
21. A. M. Jaffe, Phys. Rev. **158**, 1454 (1967).
22. I. Bialynicki-Birula, Phys. Rev. Lett. **80**, 5247 (1998).
23. N. N. Bogoliubov and D. V. Shirkov, *Introduction to the Theory of Quantized Fields* (Nauka, Moscow, 1973; Wiley, New York, 1980).
24. E. Stuekelberg and D. Rivier, Helv. Phys. Acta **22**, 215 (1949).
25. M. Fierz, Helv. Phys. Acta **23**, 731 (1950).
26. L. D. Landau and R. Pierls, Z. Phys. **62**, 188 (1930); L. D. Landau, *Collection of Works* (Nauka, Moscow, 1969), Vol. 1, p. 33.
27. I. Bialynicki-Birula, *Progress in Optics*, Vol. 36: *Photon Wave Function*, Ed. by E. Wolf (North-Holland, Amsterdam, 1996), p. 245.
28. S. N. Molotkov, Pis'ma Zh. Éksp. Teor. Fiz. **74**, 477 (2001) [JETP Lett. **74**, 436 (2001)].

Translated by V. Astakhov

Journal of Experimental and Theoretical Physics, Vol. 94, No. 6, 2002, pp. 1088–1090.
Translated from Zhurnal Éksperimental'noĭ i Teoreticheskoĭ Fiziki, Vol. 121, No. 6, 2002, pp. 1270–1272.

PLASMA, GASES

Nonexponential Decay of Spin Polarization in Rubidium Vapor

T. L. Andreeva, P. L. Rubin*, and V. N. Sorokin

Lebedev Institute of Physics, Russian Academy of Sciences, Moscow, 119991 Russia

**e-mail: rubin@sci.lebedev.ru*

Received October 15, 2001

Abstract—Experimental data on the decay of spin polarization in rubidium vapor are compared with inferences of the theory developed by the authors for spin-polarized Boltzmann gases. It is demonstrated that the nonexponential pattern of polarization decay points to the anisotropy of the indicatrix of inelastic scattering of rubidium atoms at high temperatures. Estimates are obtained of the degree of anisotropy of such inelastic scattering, i.e., scattering with variation of total spin. Under the experimental conditions, the indicatrix of inelastic scattering turns out to be highly extended forward, with the degree of anisotropy of the order of 1000. *© 2002 MAIK "Nauka/Interperiodica".*

The investigation of spin-polarized atoms in vapors of alkali metals has been attracting the attention of numerous researchers recently. This interest is largely associated with the possibility of cooling such vapors down to the onset of Bose condensation [1]. However, spin-polarized gases are of interest as a subject of investigation at high temperatures as well (room temperature or higher).

For example, they may be used to attain fairly high concentrations of polarized 3He atoms employed for fundamental investigations both in nuclear physics and in medicine [2]. Wagshul and Chupp [3] observed an unexpected effect in vapor of polarized rubidium, namely, a substantially nonexponential decay of spin polarization. Note that the nonexponential decay of spin polarization is consistent with the previously obtained [4, 5] results of theoretical analysis of the kinetics of spin-polarized Boltzmann gas. Also in [4, 5], the existence of weakly decaying spin waves in polarized Boltzmann gases (i.e., at high temperatures) was predicted. Both these effects are associated with the anisotropy of the indicatrix of elastic and inelastic scattering of atoms of alkali metals at high temperatures.

Wagshul and Chupp [3] attribute the nonexponential decay of spin polarization of rubidium to the special features of the geometry of experiment, namely, the effect of diffusion of polarized atoms in the region of observation. As was already mentioned above, the nonexponential pattern of decay of spin polarization is a characteristic feature of a polarized gas [4]. The thing is that, in a polarized gas, the microscopic function of particle distribution is a spin index matrix, and it is precisely the elements of the density matrix which are nondiagonal with respect to spin indices that are required in order to calculate the magnetic moment. In this case, one must use the generalized kinetic equation [6] with a collision integral of a special form. For particles with a spin of 1/2, the concrete form of collision integral with due regard for both elastic and inelastic collisions was obtained by us in [5] (referred to as inelastic collisions are collisions in which the spin is not conserved, although the energy may be conserved).

As a result, the decay coefficient of macroscopic magnetic moment in a polarized gas is not a constant and depends on the magnitude of the magnetic moment. This is associated with the fact that the initial equilibrium velocity distribution of particles is disturbed in the process of relaxation, and this leads to the violation of the exponential law of decay of the polarization vector. Therefore, the relaxation rate of polarization depends both on the cross section of the most inelastic process (as is usually the case) and on an additional quantity, namely, the amplitude of inelastic scattering through zero angle. As a result, the equation of polarization decay does not reduce to a simple balance equation, but has the form

$$\dot{M} = \gamma(M)M, \tag{1}$$

where

$$\gamma(M) = \gamma_0 + \gamma_1(M). \tag{2}$$

Here, M is the dimensionless degree of polarization ($0 < M < 1$) proportional to the magnetic moment; the coefficient γ_0 [s^{-1}] defines the decay of magnetic moment in a nonpolarized gas and is proportional to the cross section of the respective dissipative process; and the coefficient γ_1 depends on the magnitude of polarization and is proportional to the real part of the amplitude of dissipative scattering through zero angle, Re[$f(0)$]. By measuring $\gamma(M)$, one can estimate both the spin decay cross section and the value of Re[$f(0)$].

1063-7761/02/9406-1088$22.00 © 2002 MAIK "Nauka/Interperiodica"

At room and higher temperatures, an appreciable anisotropy of the elastic scattering indicatrix is observed (the scattering mainly through small angles) [7]. The estimation of both quantities identified above enables one to determine to what extent this anisotropy is characteristic of inelastic (with respect to spin variables) collisions.

The dependence of γ_1 on M has the form

$$\gamma_1(M) = f(M)M^2. \quad (3)$$

The value of $f(M)$ is found from the solution of a fairly complex integral equation [8]. However, as is usually the case for kinetic coefficients, the order of magnitude of $f(M)$ may be estimated rather simply.

The curve of decay of the spin polarization of rubidium as a function of time, given in [3], enables one to determine $\gamma(M)$ (see Eq. (1)) using the least squares method. In a first approximation, it was assumed that

$$\gamma(M) = a + bM^2. \quad (4)$$

The solution to Eq. (1) may be written as

$$M(t) = \frac{c\sqrt{a}}{\sqrt{\exp(2at) - bc^2}}, \quad (5)$$

where c is the integration constant. It turned out that even the approximation according to Eq. (3) produced a good description of experimental data. The least squares method was used to determine the constants a and b,

$$a = 0.0338 \text{ ms}^{-1}, \quad b = 1.2 \text{ ms}^{-1}.$$

As regards these quantities, the following remarks must be made. The constant a is determined directly from calculation in inverse time units (ms^{-1}). The value of the constant b depends on the units of measurement of M used in calculation. Wagshul and Chupp [3] used some arbitrary units for polarization M. It was assumed that, at the moment of switching off the pumping, the degree of polarization of rubidium vapor reached a close-to-limiting ($M = 1$) value, because it is this situation that usually arises in such experiments (cf., [2]). This assumption made it possible to perform the normalization of the quantity M and to obtain the above-identified value of the parameter b.

The approximation results are given in the figure. The experimental data are indicated in the figure by points; the solid curve indicates the approximation results. The dashed curve indicates an analogous approximation by exponential dependence with a single decay constant. One can see in the figure that a simple exponential approximation is clearly insufficient, as is pointed out by Wagshul and Chupp [3]. The approximation of the decay constant by formula (4) produces a better agreement with the experimental data. Note that the law of polarization decay given by formula (5) (see Eq. (4)) describes the experimental data very accurately, starting from the moment of time $t = 5$ ms. For shorter times (higher values of M), the law of decay exhibits, generally speaking, a more complex pattern as given by Eq. (2).

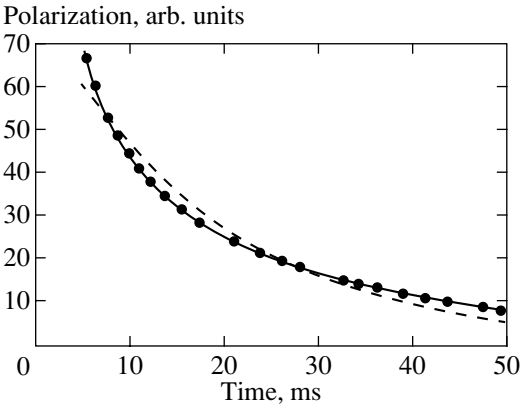

Figure.

The constant a determined above and defining the rate of exponential decay of polarization in a weakly polarized gas ($M \ll 1$) is approximately three times less than its values that are usually given in the literature (see [3] and the references cited there). This corresponds to the similar difference in the values of the cross section σ_d of spin deactivation in collisions of rubidium atoms with one another,

$$\sigma_d = 5 \times 10^{-18} \text{ cm}^2 \text{ and } 1.6 \times 10^{-18} \text{ cm}^2.$$

It was assumed in these estimates that, under the experimental conditions, the density of rubidium atoms was $N = 1.3 \times 10^{14}$ cm^{-3} (160°C), and the mean thermal velocity was 5×10^4 cm/s. We will emphasize that the difference of approximately an order of magnitude between the experimentally obtained value of the cross section of spin deactivation in vapor of polarized rubidium and the respective predicted values has been observed in the literature for quite some time. The calculation gives a value of $\sigma_d \le 10^{-18}$ cm^2 [9]. The value of σ_d obtained by us is less inconsistent with the results of respective calculations [9].

In our opinion, the nonexponential pattern of decay of spin polarization observed clearly in rubidium vapor is associated with the fact that the polarization decay is defined by at least two parameters rather than one. It is known that the exact calculation of kinetic coefficients requires the solution of corresponding integral equations; however, the order of magnitude of the parameter b may be estimated rather easily. The resultant formula contains two parameters, namely, the frequency of elastic atomic collisions and the real part of the amplitude of inelastic scattering (with variation of total spin) through zero angle $f(0)$ (see [8]).

In order to estimate the anisotropy of inelastic scattering of rubidium atoms, one must estimate (in addi-

tion to the quantities a and b) the frequency of elastic collisions of rubidium atoms. Because the vapor of rubidium atoms at high temperatures have not yet been sufficiently studied, the elastic cross section was estimated at πr^2, where the radius r was taken to be 2.53 Å [10]. Now we can estimate the ratio between the real and imaginary parts of the amplitude of inelastic scattering through zero angle $f(0)$. The scattering with variation of total spin is implied, which is responsible for the polarization decay ($\uparrow\uparrow \longrightarrow \uparrow\downarrow$),

$$\frac{\mathrm{Re}[f(0)]}{\mathrm{Im}[f(0)]} \sim 10^3. \quad (6)$$

Note that, in accordance with the optical theorem, the quantity Im[$f(0)$] is proportional to the total cross section of the process being treated (in this case, to the quantity a). As was to be expected, the indicatrix of inelastic scattering of rubidium atoms is highly anisotropic (although the given estimate of the degree of anisotropy of the scattering indicatrix is adequate only as regards the order of magnitude). Note that, at high temperatures, the propagation of weakly decaying spin waves (i.e., of a new collective mode arising under conditions of pronounced anisotropy of elastic atomic scattering [8]) is possible in polarized rubidium vapor.

ACKNOWLEDGMENTS

This study was supported by the Russian Foundation for Basic Research (project no. 99-02-16304).

REFERENCES

1. R. Fitzgerald, Phys. Today **54**, 13 (2001).
2. N. N. Kolachevskiĭ, A. A. Papchenko, Yu. V. Prokof'ichev, *et al.*, Kvantovaya Élektron. (Moscow) **30**, 81 (2000).
3. M. E. Wagshul and T. E. Chupp, Phys. Rev. A **49**, 3854 (1994).
4. T. L. Andreeva and P. L. Rubin, Zh. Éksp. Teor. Fiz. **115**, 865 (1999) [JETP **88**, 476 (1999)].
5. T. L. Andreeva and P. L. Rubin, Zh. Éksp. Teor. Fiz. **118**, 877 (2000) [JETP **91**, 761 (2000)].
6. R. F. Snider, J. Chem. Phys. **32**, 1051 (1960).
7. L. D. Landau and E. M. Lifshitz, *Course of Theoretical Physics*, Vol. 3: *Quantum Mechanics: Non-Relativistic Theory* (Nauka, Moscow, 1989, 4th ed.; Pergamon, New York, 1977, 3rd ed.).
8. T. L. Andreeva and P. L. Rubin, Pis'ma Zh. Éksp. Teor. Fiz. **67**, 777 (1998) [JETP Lett. **67**, 820 (1998)].
9. E. I. Dashevskaya, Opt. Spektrosk. **51**, 71 (1981) [Opt. Spectrosc. **51**, 37 (1981)].
10. N. M. Baron, É. I. Kvyat, E. A. Podgornaya, *et al.*, *Concise Reference Book of Physicochemical Quantities* (Goskhimizdat, Leningrad, 1957).

Translated by H. Bronstein

Journal of Experimental and Theoretical Physics, Vol. 94, No. 6, 2002, pp. 1091–1102.
Translated from Zhurnal Éksperimental'noĭ i Teoreticheskoĭ Fiziki, Vol. 121, No. 6, 2002, pp. 1273–1284.

PLASMA, GASES

The Bose–Einstein Condensation in a Finite One-Dimensional Homogeneous System of Noninteracting Bosons

V. A. Alekseev

Lebedev Institute of Physics, Russian Academy of Sciences, Moscow, 119991 Russia
e-mail: valeks@sci.lebedev.ru

Received October 1, 2001

Abstract—Condensation of the ideal Bose gas in a closed volume having the shape of a rectangular parallelepiped of length L with a square base of side length l ($L \gg l$) is theoretically studied within the framework of the Bose–Einstein statistics (grand canonical ensemble) and within the statistics of a canonical ensemble of bosons. Under the condition $N(l/L)^4 \ll 1$, where N is the total number of gas particles, dependence of the average number of particles in the condensate on the temperature T in both statistics is expressed as a function of the ratio $t = T/T_1$, where T_1 is a certain characteristic temperature depending only on the longitudinal size L. Therefore, the condensation process exhibits a one-dimensional (1D) character. In the 1D regime, the average numbers of particles in condensates of the grand canonical and canonical ensembles coincide only in the limiting cases of $t \longrightarrow 0$ and $t \longrightarrow \infty$. The distribution function of the number of particles in the condensate of a canonical ensemble of bosons at $t \leq 1$ has a resonance shape and qualitatively differs from the Bose–Einstein distribution. The former distribution begins to change in the region of $t \sim 1$ and acquires the shape of the Bose–Einstein distribution for $t \gg 1$. This transformation proceeds gradually that is, the 1D condensation process exhibits no features characteristic of the phase transition in a 3D system. For $N(l/L)^4 \gg 1$, the process acquires a 3D character with respect to the average number of particles in the condensate, but the 1D character of the distribution function of the number of particles in the condensate of a canonical ensemble of bosons is retained at all N values. *© 2002 MAIK "Nauka/Interperiodica".*

1. INTRODUCTION

Rapid development of the methods of confinement and cooling of atomic gases offers new possibilities for the investigation of Bose condensates in various spatial configurations. Shortly after the first theoretical prediction of the possibility of obtaining a one-dimensional (1D) condensate in a parabolic trap [1], this state was realized in a gas confined by an optical grating potential [2]. Almost simultaneously, analogous results were achieved with magnetic and optical traps [3] where a change in parameters of the trap potentials was accompanied by the transition from 3D to 1D behavior.

In this paper, it is demonstrated that 1D condensation can also take place in the homogeneous ideal Bose gas, that is, in the system with a volume bounded by walls (hard boundaries). We will assume that the gas fills a rectangular parallelepiped with the dimensions $L_x = L_y = l$ and $L_z = L$, where $L/l \gg 1$. It turns out that the temperature dependence of the average number of particles in the ground state (condensate) exhibits qualitatively different shapes for various relations between the total number of gas particles N and the parameter l/L. For $N(l/L)^4 \ll 1$, the scale of decrease in population of the ground state of the gas with increasing temperature in the entire domain of existence of the condensate is determined by a characteristic temperature T_1 depending only on the longitudinal size L. Therefore, the condensation process in this case proceeds in a 1D regime, and the T_1 value can be referred to as the 1D condensation temperature. For very large N values, when the reverse condition is valid, $N(l/L)^4 \gg 1$, the 1D character of condensation with respect to the population (i.e., the average number of particles in the condensate) is realized only at very low temperatures $T \ll T_* = (T_1/N)(L/l)^4$ (see Eq. (25) below), while at $T_* \ll T \leq T_3$ the phenomenon exhibits a 3D character (T_3 is the 3D condensation temperature) [4, 5].

We will consider two cases: (i) the grand canonical ensemble (i.e., the Bose–Einstein statistics), whereby only the average number of gas particles in the ensemble is conserved, and (ii) the canonical ensemble of bosons with strictly fixed total number N of particles, which more adequately reflects the situation with a gas confined in a vessel. The statistics of a canonical ensemble for a 3D gas was recently developed in [6–8]. It was found that, despite a radical difference between the distribution functions of the numbers of particles in condensates obeying these statistics, the average number of particles in the ground state for the 3D case in the ensembles of both types is the same. As demonstrated below, the 1D condensation process reveals differences between the two ensembles both in the particle number distribution function and in the average numbers of particles in the ground state (condensate).

It is necessary to note two important features of the phenomenon of 1D condensation in a homogeneous ideal gas, distinguishing this process from that in the 3D case. As is known [4, 5], the 3D condensation temperature is proportional to the gas density ($T_3 \propto N/V$) and remains constant on the passage to the thermodynamic limit as $N \longrightarrow \infty$, $V \longrightarrow \infty$, $N/V \longrightarrow$ const. In contrast to this behavior, the 1D condensation temperature is $T_1 \propto N/L^2$ (see Eq. (5) below) and tends to zero in the limiting transition $N \longrightarrow \infty$, $L \longrightarrow \infty$, $N/L \longrightarrow$ const retaining the gas density. In the other limit, whereby $N \longrightarrow \infty$ and $L \longrightarrow \infty$, so that $N/L^2 \longrightarrow$ const, the condensation temperature remains constant but the system density grows and, beginning with certain N values, the gas can no longer be considered as ideal. This situation is quite analogous to that observed for a 3D condensation in a parabolic trap with (see, e.g., [1]),

$$T_3 \sim \hbar\omega N^{1/3} \propto (N/V^2)^{1/3},$$

where $V = R^3$ is the "oscillator volume," $R = \sqrt{\hbar/m\omega}$, ω is the trap frequency, and m is the particle mass. Therefore, as was repeatedly pointed out [9–12], the 1D condensation effect in a homogeneous ideal Bose gas vanishes in the thermodynamic limit and, hence, can be realized only in a system with limited total number of particles. However, it is easy to obtain estimates showing that this number can be very large. For example, a system with dimensions $l = 10^{-3}$ cm, $L = 1$ cm (the volume can be bounded, for example, by laser fields repulsing particles by striction forces), and $N = 10^{11}$, in which $N(l/L)^4 = 0.1$ and the condensation has a 1D character, is still characterized by a very small gas parameter a^3N/l^2L (e.g., for a scattering length of $a \approx 5 \times 10^{-7}$ cm typical of alkali metals), and, hence, the gas state is close to ideal.

Another important distinction of the 1D condensation from the 3D processes is a smooth decrease in the ratio $\langle n_0\rangle/N$ with increasing temperature ($\langle n_0\rangle$ is the average number of particles in the condensate) in the former case. It was pointed out [7, 8] that finiteness of the particle number N in the 3D case also leads to smearing of the temperature interval in which the ratio $\langle n_0\rangle/N$ turns zero, and it is only for $N \longrightarrow \infty$ that this ratio goes to zero at $T = T_3$ at a nonzero derivative. In the 1D case, a decrease in the ratio $\langle n_0\rangle/N$ is smooth even in the limit as $N \longrightarrow \infty$, so that the concept of the 1D condensation temperature (as the point at which the ratio $\langle n_0\rangle/N$ goes to zero) loses sense and only serves as a characteristic parameter of the problem.

2. ONE-DIMENSIONAL CONDENSATION IN THE BOSE–EINSTEIN STATISTICS (GRAND CANONICAL ENSEMBLE)

In this case, the distribution function $W(n_0, n_1, \ldots)$ of the numbers n_k of particles occurring in the states with the energies E_k, as determined in 1924 by Einstein [13], represents a product of independent distributions

$$W(n_0, n_1, \ldots) = \prod_k w_k(n_k),$$
$$w_k(n_k) = [1 - \exp(\mu - \varepsilon_k)]\exp[(\mu - \varepsilon_k)n_k], \quad (1)$$

where $\varepsilon_k = E_k/T$, T is the temperature (expressed in the energy units), and μ is the chemical potential (in the units of temperature). The average values corresponding to distribution (1) are determined as

$$\langle n_k\rangle = \sum_{n_k=0}^{\infty} n_k w_k(n_k) = \tilde{n}_k$$

and are equal to

$$\tilde{n}_k = [\exp(\varepsilon_k - \mu) - 1]^{-1}. \quad (2)$$

The chemical potential μ is determined from the requirement that the sum of average numbers $\tilde{n}_k$ be equal to the total number of gas particles,

$$\sum_k \tilde{n}_k = N. \quad (3)$$

In a system of free bosons, the energy spectrum of particles is determined by the condition of periodicity of the wave function:

$$\varepsilon_{\mathbf{k}} = \alpha_x k_x^2 + \alpha_y k_y^2 + \alpha_z k_z^2,$$
$$\alpha_{x,y} = \alpha_0 = \frac{(2\pi\hbar)^2}{2mTl^2}, \quad \alpha_z = \alpha = \frac{(2\pi\hbar)^2}{2mTL^2}, \quad (4)$$
$$k_i = 0, \pm 1, \ldots, \quad \alpha \ll \alpha_0,$$

where m is the particle mass. The parameter α is conveniently expressed in terms of the characteristic temperature of the 1D condensation

$$T_1 = \frac{(2\pi\hbar)^2}{4\zeta(2)mL^2}N = \frac{6\hbar^2}{mL^2}N,$$
$$\alpha = \frac{2\zeta(2)}{Nt} = \frac{\pi^2}{3Nt}, \quad t = \frac{T}{T_1}, \quad (5)$$

where $\zeta(x)$ is the Riemann zeta function.

Using formulas (2) and (4), condition (3) can be written as

$$\sum_{\mathbf{k}} \tilde{n}_{\mathbf{k}}$$
$$= \sum_{\mathbf{k}} \{\exp[\alpha_0(k_x^2 + k_y^2) + \alpha k_z^2 - \mu] - 1\}^{-1} = N. \quad (6)$$

At very low temperatures such that $\alpha \gg 1$ (which is equivalent to $t \ll 1/N$), the only nonzero term in (6) is $\tilde{n}_0 = (e^{-\mu} - 1)^{-1}$. This yields

$$\tilde{n}_0 = N, \quad \mu = -\ln\left(1 + \frac{1}{\tilde{n}_0}\right) \approx -\frac{1}{N},$$

and the distribution function (1) describing the numbers of particles $n_{\mathbf{k}}$ in the states $\mathbf{k}$ acquires the form

$$w_0(n_0) = \frac{1}{N} e^{-n_0/N},$$
$$w_{\mathbf{k}\neq 0}(n_{\mathbf{k}}) = \delta_{n_{\mathbf{k},0}}, \quad t \ll \frac{1}{N}. \tag{7}$$

According to (7), there is a finite probability of finding an arbitrary number of particles in the ground state in the complete absence of particles in the excited states. Being obviously deprived of physical meaning, this situation emphasized inconsistency of the distribution (1) at least for $T \longrightarrow 0$. This discrepancy is not only characteristic of the case with a homogeneous Bose gas under consideration, but is generally inherent in the Bose–Einstein statistics as such. The discrepancy is eliminated in the statistics of a canonical ensemble of particles [6–8]. It turns out that, despite a radical difference between the distribution functions of the number of particles in the condensate obeying these statistics, the average numbers of particles in the ground state in the 3D case are the same, while those in the 1D case differ rather slightly. Taking into account that almost all conclusions concerning the properties of condensate were derived so far using the Bose–Einstein statistics, and aiming at a comparison of the results provided by the two approaches, the 1D condensation will also be studied within the framework of the Bose–Einstein statistics despite the obviously contradictory character of the distribution (7).

When the temperature increases, the condition $\alpha \ll 1$ (or $t \gg 1/N$) becomes valid, although the transverse (x and y) degrees of freedom are still "frozen," so that $\alpha_0 \gg 1$. In this temperature interval ($1/N \ll t \ll N^{-1}L^2/l^2$), the system is still essentially one-dimensional. As the temperature grows further, the latter condition changes to $\alpha_0 \ll 1$ and the transverse degrees of freedom (x and y) are operative, so that the system becomes three-dimensional. In order to trace this transition and more exactly indicate the "1D condensation" domain boundaries, let us retain all the degrees of freedom in sum (6) and rewrite this expression as

$$N = \sum_{k_z=-\infty}^{\infty} [\exp(\alpha k_z^2 - \mu) - 1]^{-1}$$
$$+ \sum_{k_z=-\infty}^{\infty} \sum_{\mathbf{k}_\perp \neq 0} [\exp(\alpha k_z^2 + \alpha_0 \mathbf{k}_\perp^2 - \mu) - 1]^{-1}, \tag{8}$$
$$\mathbf{k}_\perp = (k_x, k_y).$$

Taking into account that $\alpha \ll 1$ and $|\mu| \approx 1/\tilde{n}_0 \ll 1$, we may expand the exponential in the first sum and employ the Poisson formula (see, e.g., [14])

$$\sum_{n=-\infty}^{\infty} \Phi(n) = \sum_{s=-\infty}^{\infty} \int_{-\infty}^{\infty} \Phi(x) e^{2i\pi s x} dx \tag{9}$$

to calculate this sum exactly as

$$\sum_{k_z=-\infty}^{\infty} (\alpha k_z^2 + |\mu|)^{-1}$$
$$= \frac{\pi}{\sqrt{\alpha|\mu|}} \frac{1 + \exp(-2\pi\sqrt{|\mu|/\alpha})}{1 - \exp(-2\pi\sqrt{|\mu|/\alpha})}. \tag{10}$$

Transforming the second sum in Eq. (8), using the formula

$$[\exp(z^2 - \mu) - 1]^{-1} = \sum_{p=1}^{\infty} \exp[(-z^2 + \mu)p]$$

and introducing the notation

$$\psi(z) = \sum_{n=-\infty}^{\infty} \exp(-zn^2), \tag{11}$$

we obtain

$$\sum_{k_z=-\infty}^{\infty} \sum_{\mathbf{k}_\perp \neq 0} [\exp(\alpha k_z^2 + \alpha_0 \mathbf{k}_\perp^2 - \mu) - 1]^{-1}$$
$$= \sum_{p=1}^{\infty} \psi\left(\frac{\pi^2}{3Nt} p\right) \left[\psi^2\left(\frac{\pi^2}{3Nt} \frac{L^2}{l^2} p\right) - 1\right] \exp(-|\mu| p). \tag{12}$$

Taking into account Eqs. (11) and (12), setting $|\mu| = 1/\tilde{n}_0$, denoting $\tilde{n}_0/N = x$, and using expression (8), we arrive at the equation

$$1 = \sqrt{3tx} \coth(\sqrt{3t/x}) + \Sigma,$$
$$\Sigma = \frac{1}{N} \sum_{p=1}^{\infty} \psi\left(\frac{\pi^2}{3Nt} p\right) \left[\psi^2\left(\frac{\pi^2}{3Nt} \frac{L^2}{l^2} p\right) - 1\right] \exp\left(-\frac{p}{Nx}\right), \tag{13}$$

describing the relative population x of the ground state.

As can be seen from expression (11), the function $\psi(z)$ tends to the following limits for large and small values of the argument:

$$\psi(z) = \begin{cases} \sqrt{\pi/z}, & z \ll 1, \\ 1 + 2e^{-z}, & z \gg 1. \end{cases} \tag{14}$$

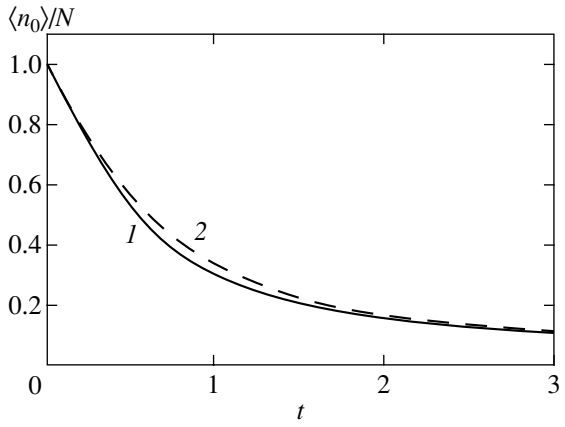

Fig. 1. The temperature dependence of the average number of particles in the 1D condensate of (*1*) a canonical ensemble of bosons (calculated using the distribution function (51)) and (*2*) a grand canonical ensemble (numerical solution of Eq. (17)).

Accordingly, the sum entering into (13) exhibits qualitatively different behavior depending on the ratio of two large parameters N and L^2/l^2. In the interval

$$\frac{1}{N} \ll t \ll \frac{1}{N}\frac{L^2}{l^2}, \tag{15}$$

which includes the values $t \gg 1$ provided that the number of particles N is relatively small,

$$1 \ll N \ll L^2/l^2, \tag{16}$$

the sum entering into (13) is exponentially small and can be neglected. As a result, the ground state population $x = \tilde{n}_0/N$ is determined by the equation

$$\sqrt{3tx} = \tanh(\sqrt{3t/x}). \tag{17}$$

In the case of low temperatures, this equation yields (to within terms on the order of t^2)

$$\frac{\tilde{n}_0}{N} = 1 - t + \frac{1}{5}t^2, \quad \frac{1}{N} \ll t \ll 1. \tag{18}$$

For large t, Eq. (17) yields (to within an exponentially small correction)

$$\frac{\tilde{n}_0}{N} = \frac{1}{3t} - 12te^{-6t}, \quad 1 \ll t \ll \frac{1}{N}\frac{L^2}{l^2}. \tag{19}$$

In the temperature interval indicated in (19), the relative population of the ground state is already very small and, under condition (16) (which is shown below to be sufficient and much stronger than the necessary condition (28)), Eq. (17) describes virtually the entire domain of existence of the condensate (which is one-dimensional for all t). A numerical solution of Eq. (17) is depicted in Fig. 1.

As the temperature increases, condition (15) fails to be valid. For large N ($N \gg L^2/l^2$) this condition is violated even at small t ($t \ll 1$). For $t \sim N^{-1}L^2/l^2$, the sum Σ in the right-hand part of Eq. (13) cannot be studied analytically. However, for $t \gg N^{-1}L^2/l^2$, we may use the asymptotic expression (14) for the function $\psi(z)$ at $z \ll 1$ and represent the sum Σ as

$$\Sigma = \sqrt{At^3}\left(1 - \frac{2\sqrt{\pi}}{\zeta(3/2)}\frac{1}{\sqrt{Nx}}\right), \tag{20}$$

where

$$A = \left(\frac{3}{\pi}\right)^3 \zeta^2\left(\frac{3}{2}\right) N\frac{l^4}{L^4}.$$

The second term in parentheses in the right-hand part of (20) reflects the influence of the exponent present in the sum Σ of Eq. (13). Vanishing as $N \longrightarrow \infty$, this term provides for the ground state population x smoothly (without a discontinuity in the derivative) tending to zero in a narrow vicinity ($|T/T_3 - 1| \leq 1/N^{1/3}$) of the 3D condensation temperature T_3, which is similar to behavior of the gas in a parabolic trap [15]. In order to simplify the analysis, we will no longer consider this effect below and will neglect the second term in parentheses in the right-hand part of (20).

Equation (13) now acquires the form

$$1 - \sqrt{At^3} = \sqrt{3tx}\coth(\sqrt{3t/x}). \tag{21}$$

Note that the left-hand side of this equation represents the relative population of the ground state in the case of a 3D condensation. The second term on the left-hand side of Eq. (21) significantly influences the solution of this equation for $t \sim A^{-1/3} \sim (N^{-1}L^4/l^4)^{1/3}$. One can readily check that, for

$$N \gg L/l \tag{22}$$

these values satisfy the condition $t \gg N^{-1}L^2/l^2$ for which the sum in (20) was calculated. This implies that, under the condition (22), Eq. (21) is applicable for any t. In this stage of analysis, let us assume the condition (22) to be valid.

As follows from Eq. (21), the ground state population goes to zero for $t = t_3 = A^{-1/3}$. In the dimensional notation, this corresponds to the temperature T_3 of the usual 3D condensation of the Bose gas [4, 5]):

$$T_3 = A^{-1/3}T_1 = 2\pi\zeta^{-2/3}\left(\frac{3}{2}\right)\frac{\hbar^2}{m}\left(\frac{N}{l^2L}\right)^{2/3}. \tag{23}$$

However, the $x(t)$ function behaves qualitatively differently for large and small A values (this is admitted by condition (22)).

For large A values ($A \gg 1$), up to temperatures close to t_3 what accounts for virtually the entire domain

of existence of the condensate (in this case $t_3 \ll 1$), Eq. (21) yields

$$\frac{\tilde{n}_0}{N} = 1 - t - \sqrt{At^3}, \quad t_3 - t \gg A^{-2/3}. \tag{24}$$

In a narrow vicinity of the 3D condensation temperature, $t_3 - t \leq A^{-2/3}$, the ground state population smoothly decays to zero. However, Eq. (21) cannot claim to be a correct description of this region, where the second (omitted) term in the parentheses of (20) becomes significant.

The second term in (24) is significant only in the region of small t,

$$\frac{1}{N} \ll t \leq \frac{1}{A} = \left(\frac{\pi}{3}\right)^3 \zeta^{-2}\left(\frac{3}{2}\right)\frac{1}{N}\frac{L^4}{l^4}, \tag{25}$$

and it is this region where the condensate becomes one-dimensional (it should be recalled that the left part of this inequality provides for the general applicability of the whole approach employed in this study). As the N value increases, the interval (25) narrows to vanish as $N \longrightarrow \infty$ (note the small ratio l/L is just what provides for the existence of this interval). For $t > A^{-1}$ ($A^{-1} \ll t_3$), the third term in (24) is greater than the second term in this equation and the condensation becomes three-dimensional. Rewriting (24) in terms of T_3,

$$\frac{\tilde{n}_0}{N} = 1 - \frac{\pi}{3}\zeta^{-2/3}\left(\frac{3}{2}\right)\left(\frac{1}{N}\frac{L^4}{l^4}\right)^{1/3}\frac{T}{T_3} - \left(\frac{T}{T_3}\right)^{3/2},$$

we can see that a nonzero slope (characteristic of the 1D behavior) of this dependence in the region of small temperatures T decreases with increasing N. As $Nl^4/L^4 \longrightarrow \infty$, this slope is close to zero and the condensation becomes three-dimensional for all t.

For $A \ll 1$, dependence of the $\tilde{n}_0/N$ ratio on the temperature qualitatively changes. In this case, $t_3 \gg 1$ and the second term on the left-hand side of Eq. (21) is significant only in the vicinity of t_3. In the limiting cases of small and large t values, Eq. (21) yields

$$\frac{\tilde{n}_0}{N} = \begin{cases} 1 - t + t^2/5, & t \ll 1, \\ \dfrac{1}{3t}\left(1 - \sqrt{At^3}\right)^2, & 1 \ll t \leq t_3. \end{cases} \tag{26}$$

Up to very large t values, whereby the condensate almost completely vanishes, relations (26) coincide with (18) and (19). This implies that, under the condition

$$L/l \ll N \ll L^4/l^4, \tag{27}$$

the left-hand side of which coincides with (22) and the right-hand side corresponds to $A \ll 1$, the average number of particles in the condensate is determined by Eq. (17) and the condensation process is one-dimensional.

Let us return to the condition (22) being violated at $N \leq L/l$. Such N values satisfy the condition (16) under which the condensation is certainly described by Eq. (17). Therefore, the condition

$$N \ll L^4/l^4 \tag{28}$$

is a necessary and sufficient criterion for the condensation process to be one-dimensional and the average number of particles in the condensate to be described by Eq. (17). In this case, the number of particles in the condensate is large ($\tilde{n}_0 \gg 1$) up to temperatures very close to the 3D condensation temperature and, hence, $\mu = -1/\tilde{n}_0$ and the distribution function of the number of particles in the condensate has the form

$$w_0(n_0) = \frac{1}{\tilde{n}_0}\exp\left(-\frac{n_0}{\tilde{n}_0}\right), \quad t < t_3. \tag{29}$$

3. ONE-DIMENSIONAL CONDENSATION IN A CANONICAL ENSEMBLE OF BOSONS

3.1. Summing the Gibbs Distribution

During condensation of a gas within a volume bounded by walls, the total number of particles is conserved,

$$\sum_k n_k = N, \tag{30}$$

rather than the sum of average values (3). In this case, the distribution function of the number of particles in the condensate is determined by summing the Gibbs distribution over all the possible populations of excited states (n_1, n_2, …) with the condition (30) exactly satisfied:

$$w_0(n_0) = \frac{1}{S}\sum_{n_1 + n_2 + \ldots = N - n_0} \exp(-\varepsilon_0 n_0 - \varepsilon_1 n_1 - \ldots), \tag{31}$$

where S is the normalization factor. It was demonstrated [6–8] that the validity of condition (30) in the 3D case leads to a distribution function qualitatively different from expressions (7) and (29) obtained within the framework of the Bose–Einstein statistics, which eliminates the aforementioned discrepancy related to the grand canonical ensemble. As will be demonstrated below, an analogous qualitative difference is observed in for the one-dimensional condensation.

Using the exact mathematical procedure developed in [6–8], the sum in (31) can be rewritten as follows:

$$w_0(n_0) = \frac{1}{S}\frac{1}{2\pi i}\oint z^{-N+n_0-1}\exp[G(z)]dz,$$

$$\exp[G(z)] = \prod_{k\neq 0}[1 - z\exp(-\varepsilon_k)]^{-1},$$

$$G(z) = -\sum_{k\neq 0}\ln[1 - z\exp(-\varepsilon_k)] \quad (32)$$

$$= \sum_{k\neq 0}\sum_{p=1}^{\infty}\frac{1}{p}z^p\exp(-p\varepsilon_k).$$

The integration loop in (32) represents a circle with the center at $z = 0$ and a radius $|z| = e^{\mu} < 1$, which is equivalent to the condition $\mu < 0$. It should be emphasized that Eqs. (32) automatically contain the condition (30) characteristic of the canonical ensemble and are free of any additional limitations.

In the region of very low temperatures, where the condition $\alpha \gg 1$ (or $t \ll 1/N$) is satisfied, the consideration is fully analogous to that presented in [6–8] for the 3D case. In this case, only two values are significant,

$$w_0(n_0 = N) = 1 - 2e^{-\alpha}, \quad w_0(n_0 = N-1) = 2e^{-\alpha},$$

from which it can be seen that, as $T \longrightarrow 0$, the distribution acquires the form of $w_0(n_0) = \delta_{n_0, N}$. This distribution, reflecting the obvious fact that all particles at $T = 0$ occur in the ground state (condensate), radically differs from the Bose–Einstein distribution (7) or (29).

As the temperature increases above a very narrow transition region where $t \sim 1/N$, the system obeys the condition $\alpha \ll 1$ (equivalent to $t \gg 1/N$) and the distribution function (32) can again be studied analytically. Substituting $z = \exp(\mu + ix)$ into (32), we obtain

$$w_0(n_0) = \frac{\exp(\mu n_0)}{S}$$

$$\times\int_{-\pi}^{\pi}\exp[-i(N-n_0)x + F(x,\mu)]dx,$$

$$F(x,\mu) = \sum_{p=1}^{\infty}\frac{\exp[(\mu + ix)p]}{p} \quad (33)$$

$$\times\sum_{\mathbf{k}\neq 0}\exp[-(\alpha k_z^2 + \alpha_0\mathbf{k}_\perp^2)p].$$

In the above considerations, the parameter μ, limited only by the condition $\mu < 0$, was otherwise arbitrary. Note that the sum over $\mathbf{k} \neq 0$ entering into definition of the function $F(x, \mu)$ exponentially decays at large values of the parameter p. This ensures convergence of the series with respect to p and, accordingly, continuity of the function $F(x, \mu)$ at $\mu = 0$. This circumstance allows the distribution $w_0(n_0)$ to be calculated setting $\mu = 0$ in (33).

Denoting $F(x) = F(x, \mu = 0)$, we can conveniently represent this function as a sum of two terms

$$F(x) = F_1(x) + F_3(x),$$

$$F_1(x) = \sum_{p=1}^{\infty}\frac{\exp(ipx)}{p}\sum_{k\neq 0}\exp(-\alpha pk^2),$$

$$F_3(x) = \sum_{p=1}^{\infty}\frac{\exp(ipx)}{p} \quad (34)$$

$$\times\sum_{k=-\infty}^{\infty}\exp(-\alpha pk^2)\sum_{\mathbf{k}_\perp\neq 0}\exp(-\alpha_0 p\mathbf{k}_\perp^2).$$

Now let us study the behavior of the component functions for small values of the parameters: $|x| \ll 1$, $\alpha \ll 1$, and $\alpha_0 \ll 1$. First, consider the function $F_1(x)$. Differentiating with respect to x, we obtain

$$\frac{dF_1}{dx} = i\sum_{p=1}^{\infty}\exp(ipx)\sum_{k\neq 0}\exp(-\alpha pk^2)$$

$$= i\sum_{p=1}^{\infty}\exp(ipx)[\psi(\alpha p) - 1].$$

For small x and α, the summation with respect to p can be replaced by integration in the region $(0, +\infty)$. According to (14), the integral converges to yield

$$\frac{dF_1}{dx} = i\sum_{k\neq 0}\int_0^{\infty}\exp(ixp - \alpha k^2 p)dp = \frac{i}{\alpha}\sum_{k\neq 0}\frac{1}{k^2 - ix/\alpha}.$$

Integrating this expression with respect to x in the interval $(0, x)$ and taking into account that (for small α)

$$F_1(0) = \sum_{p=1}^{\infty}\frac{\psi(\alpha p) - 1}{p} \approx \sqrt{\frac{\pi}{\alpha}}\zeta\left(\frac{3}{2}\right),$$

we eventually obtain

$$F_1(x) = F_1(0) + g\left(\frac{x}{\alpha}\right),$$

$$g(u) = -\sum_{k\neq 0}\ln\left(1 - i\frac{u}{k^2}\right). \quad (35)$$

The function $F_3(x)$, which is exponentially small in the temperature interval (15), cannot be analytically studied in the region of $t \sim N^{-1}L^2/l^2$. However, as demonstrated below, this region is insignificant because (similarly to the case of the Bose–Einstein statistics) the function $F_3(x)$ influences the condensation process only at temperatures on the order of $t \sim N^{-1}L^4/l^4$. At these temperatures, the condition $\alpha_0 \ll 1$ is valid and

the function $F_3(x)$ can be studied analytically. By doubly differentiating $F_3(x)$ with respect to x, we obtain

$$\frac{d^2F_3}{dx^2} = -\sum_{p=1}^{\infty} p\exp(ixp) \times \sum_{k=-\infty}^{\infty} \exp(-\alpha p k^2) \sum_{\mathbf{k}_\perp \neq 0} \exp(-\alpha_0 p \mathbf{k}_\perp^2).$$

Replacing the summation with respect to p (for small x, α, and α_0) by integration and accomplishing this procedure, we obtain

$$\frac{d^2F_3}{dx^2} = -\sum_{k=-\infty}^{\infty} \sum_{\mathbf{k}_\perp \neq 0} \frac{1}{(\alpha k^2 + \alpha_0 \mathbf{k}_\perp^2 - ix)^2}.$$

Doubly integrating this equality with respect to x and using the relations

$$F_3(0) = \pi^{3/2}\zeta\left(\frac{5}{2}\right)\frac{1}{\sqrt{\alpha}\alpha_0},$$

$$\left(\frac{dF_3}{dx}\right)_{x=0} = i\pi^{3/2}\zeta\left(\frac{3}{2}\right)\frac{1}{\sqrt{\alpha}\alpha_0} = i\sqrt{At^3}N,$$

we eventually obtain

$$F_3(x) = F_3(0) + i\sqrt{At^3}Nx + g_3(x/\alpha),$$

$$g_3(u) = -\sum_{k=-\infty}^{\infty} \sum_{\mathbf{k}_\perp \neq 0} \left[\ln\left(1 - \frac{iu}{k^2 + \frac{L^2}{l^2}\mathbf{k}_\perp^2}\right) + \frac{iu}{k^2 + \frac{L^2}{l^2}\mathbf{k}_\perp^2} \right]. \quad (36)$$

The function $g_3(u)$ can be calculated (up to large values of $u < L^2/l^2$) using an expansion into series in powers of u. The first term of this expansion yields (the sum over k is replaced by an integral)

$$g_3(u) \approx -\frac{\pi}{4}\left(\frac{l}{L}\right)^3 u^2 \sum_{\mathbf{k}_\perp \neq 0} \frac{1}{|\mathbf{k}_\perp|^3}, \quad |u| \ll \frac{L^2}{l^2},$$

where the subsequent terms are proportional to increasing powers of the small parameter l/L. For very large u, the sum in $g_3(u)$ can be replaced by an integral to obtain

$$g_3(u) = -\frac{4}{3}\pi^2 \exp\left(\frac{\pi i}{4}\right)\left(\frac{l}{L}\right)^2 u^{3/2}, \quad |u| \gg \frac{L^2}{l^2}.$$

These expressions show that, up to very large u values $1 \ll u < L^2/l^2$, we have $|g(u)| \gg |g_3(u)|$ and the influence of $g_3(u)$ can be ignored. From this, it immediately follows that the shape of the distribution function of the number of particles in the condensate for a 1D system ($l/L \ll 1$) is always (for any N) determined by the "one-dimensional" function $g(u)$ and, hence, is qualitatively different from the shape of a distribution function of the 3D system ($l/L \sim 1$) [8].

Retaining only the significant terms in (35) and (36) and rejecting g_3, we eventually obtain

$$F(x) = F(0) + i\sqrt{At^3}Nx + g\left(\frac{x}{\alpha}\right).$$

Upon substituting this function into the integral in (33) (recall that $\mu = 0$), the value of $F(0)$ can be neglected because this term only influences the normalization factor determined by the relation (33) proper. Substituting $x/\alpha = u$ and taking into account that the condition $\pi/\alpha \gg 1$ allows the integral to be taken between infinite limits, we eventually obtain

$$w_0(n_0) = S^{-1}\varphi\left(\frac{\pi^2}{3t}\left(\frac{n_0}{N} - 1 + \sqrt{At^3}\right)\right),$$
$$\varphi(y) = \frac{1}{2}\int_{-\infty}^{\infty} \exp[iyu + g(u)]du. \quad (37)$$

As can be seen from this expression, the distribution of the number of particles in the condensate is determined by properties of the function $\varphi(y)$. This function can be exactly calculated as demonstrated below.

3.2. Calculating the $\varphi(y)$ Function

Let us begin with calculation of the function $g(u)$ determined by series (35). Differentiating this function with respect to u,

$$\frac{dg}{du} = i\sum_{k\neq 0}\frac{1}{k^2 - iu} = i\left[-\frac{1}{-iu} + \sum_{k=-\infty}^{\infty}\frac{1}{k^2 - iu}\right], \quad (38)$$

and using the Poisson formula (9) leads to

$$\sum_{k=-\infty}^{\infty}\frac{1}{k^2 - iu} = \frac{2\pi i}{2\sqrt{iu}} + 2\left(2\pi i\sum_{s=1}^{\infty}\frac{\exp(2\pi i\sqrt{iu}s)}{2\sqrt{iu}}\right)$$
$$= \frac{\pi e^{\pi i/4}}{\sqrt{u}} + \frac{2\pi e^{\pi i/4}}{\sqrt{u}}\frac{e^{-\gamma\sqrt{u}}}{1 - e^{-\gamma\sqrt{u}}},$$
$$\gamma = 2\pi e^{-\pi i/4}, \quad -\frac{\pi}{2} < \arg u < \frac{3\pi}{2}.$$

Substituting this sum into (38), taking into account that $g(0) = 0$, and integrating (38) in the interval $(0, u)$, we obtain

$$g(u) = -\gamma\sqrt{u} + \int_0^u\left(\frac{1}{x} - \frac{1}{\sqrt{x}}\frac{\gamma e^{-\gamma\sqrt{x}}}{1 - e^{-\gamma\sqrt{x}}}\right)dx.$$

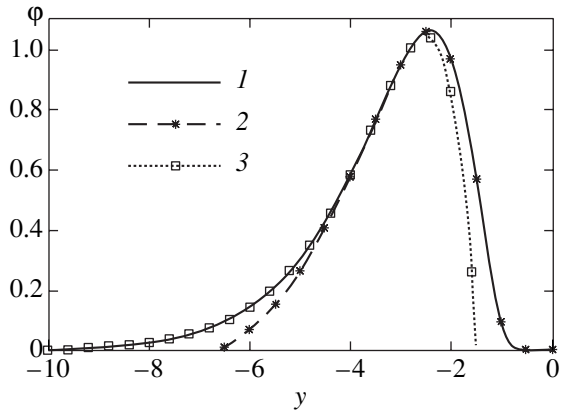

Fig. 2. The function $\varphi(y)$ calculated by (*1*) exact formulas (39) or (40), (*2*) asymptotic formula (43), and (*3*) asymptotic formula (41).

The integral with respect to x can be calculated exactly using the substitution $x = z^2$, which yields

$$g(u) = -\gamma\sqrt{u} - 2\ln\left(\frac{1-e^{-\gamma\sqrt{u}}}{\gamma\sqrt{u}}\right).$$

By definition (37) of the function $\varphi(y)$, we eventually obtain

$$\varphi(y) = \frac{1}{2}\int_{-\infty}^{\infty} e^{iyu}[K(u)]^2 du,$$
$$K(u) = \frac{\gamma\sqrt{u}}{e^{\gamma\sqrt{u}/2} - e^{-\gamma\sqrt{u}/2}}. \quad (39)$$

The function $K(u)$ exhibits no singularities in the upper half-plane. Therefore, the integration path for $y > 0$ in (39) can be replaced by a semicircle situated in the upper half-plane, with the radius R tending to infinity. Since the function $K(u)$ on this semicircle is exponentially small, with a negative exponent proportional to $\sqrt{R}$, we conclude that $\varphi(y) = 0$ for $y > 0$.

On approaching the negative imaginary semiaxis from left and right, the function $K(u)$ acquires equal values. From this, it follows that the points $u = -in^2$ (with n running through all integers from unity to infinity) are the poles of this function. Thus, the integration path for $y < 0$ in (39) has to be closed by a semicircle occurring in the lower half-plane with $R \longrightarrow \infty$ but $R \neq n^2$. As can be readily checked, the integral over a semicircle tends to zero for $R \longrightarrow \infty$ because the integrand is exponentially small. Therefore, the function $\varphi(y)$ is equal to the sum of residues in the second-order poles ($u = -in^2$, $n = 1, 2, \ldots$) of the $K^2(u)$ function. Upon calculating these residues, we obtain

$$\varphi(y) = 4\pi\sum_{n=1}^{\infty}\exp(-|y|n^2)\left(|y|n^2 - \frac{3}{2}\right)n^2, \quad y < 0,$$
$$\varphi(y) = 0, \quad y > 0. \quad (40)$$

For large y ($|y| \gg 1$), the sum in (40) can be restricted to the first term:

$$\varphi(y) = 4\pi(|y| - 3/2)e^{-|y|}, \quad y < 0, \quad |y| \gg 1. \quad (41)$$

In order to study the behavior of $\varphi(y)$ for $|y| \ll 1$, note that this function is related to $\psi(y)$ defined as the series (11) by an obvious formula

$$\varphi(y) = 2\pi\left[|y|\frac{d^2\psi}{d|y|^2} + \frac{3}{2}\frac{d\psi}{d|y|}\right]. \quad (42)$$

Using the Poisson formula (9) leads to the following expression for $\psi(|y|)$ [14]:

$$\psi(|y|) = \sqrt{\frac{\pi}{|y|}}\psi\left(\frac{\pi^2}{|y|}\right).$$

For $|y| \longrightarrow 0$, this expression yields to within exponentially small terms

$$\psi(|y|) = \sqrt{\frac{\pi}{|y|}}\left[1 + 2\exp\left(-\frac{\pi^2}{|y|}\right)\right], \quad |y| \ll 1.$$

Differentiating this expression and substituting the result into (42), we obtain

$$\varphi(y) = 4\pi^5\sqrt{\pi}\left(1 - \frac{3}{2}\frac{|y|}{\pi^2}\right)\frac{\exp(-\pi^2/|y|)}{|y|^{7/2}},$$
$$y < 0, \quad |y| \ll 1. \quad (43)$$

The function $\varphi(y)$ calculated using exact formulas (39) or (40) and the asymptotic expressions (41) and (43) are depicted in Fig. 2. As can be seen from this figure, the $\varphi(y)$ values calculated for $-4 < y < -3$ by formulas (41) and (43) coincide with a high precision. Therefore, it is possible in practice to employ formula (41) for $y < -3.5$ and formula (43) for $-3.5 < y \leq 0$. From this, it follows, in particular, that a maximum of the $\varphi(y)$ function is determined by the asymptotic behavior of (43) and is attained for $y_{\max} \approx -2.41$.

All moments of the function $\varphi(y)$ exist and are readily calculated in the analytical form. These moments, determined by the coefficients of expansion of the $g(u)$ function,

$$g(u) = \sum_{n=1}^{\infty} c_n(iu)^n, \quad c_n = \frac{2}{n}\zeta(2n), \quad |u| < 1,$$

are equal to

$$\langle y^m\rangle = \int_{-\infty}^{\infty} y^m \varphi(y)dy = \pi\left(\frac{d^m}{du^m}e^{g(iu)}\right)_{u=0},$$
$$g(iu) = \sum_{n=1}^{\infty}(-1)^n c_n u^n. \quad (44)$$

In particular, formulas (44) yield

$$\langle y^0\rangle = \int_{-\infty}^{\infty}\varphi(y)dy = \pi,$$
$$\langle y\rangle = -\pi c_1 = -\pi\times 2\zeta(2) = -\pi^3/3, \quad (45)$$
$$\langle y^2\rangle = \pi[2\zeta(4) + 4\zeta^2(2)] = 2\pi^5/15.$$

3.3. Distribution Function of the Number of Particles in the Bose Condensate

Since $\varphi(y) = 0$ for $y > 0$, expression (37) shows that, for $1 - \sqrt{At^3} < 0$ (i.e., for the temperature exceeding the critical temperature of the 3D condensation $t > A^{-1/3} = t_3$), the probability of finding any number of particles in the condensate is zero. Below the critical temperature ($t < t_3$), the number of particles that can be found in the condensate at a nonzero probability is limited by the condition

$$n_0 < (n_0)_{\lim} = N(1 - \sqrt{At^3}) = N[1 - \sqrt{(T/T_3)^3}],$$

and the distribution function $\omega_0(n_0)$ acquires qualitatively different forms, depending on the temperature t and the parameter A.

At the upper boundary of the distribution (i.e., when $n_0 \longrightarrow (n_0)_{\lim}$, the distribution function $w_0(n_0)$ is exponentially small (see Eqs. (37) and 43)). For large A values ($A \gg 1$) in a broad interval of temperatures such that

$$t_3 - t \gg \frac{2}{3}t_3^2 = \frac{2}{3}A^{-2/3}, \quad A \gg 1 \quad (46)$$

(i.e., for $(1 - \sqrt{At^3})/t \gg 1$), the function $w_0(n_0)$ is also exponentially small (see Eq. (41)) at the lower boundary $n_0 = 0$. Therefore, the distribution function $w_0(n_0)$ of the number of particles in the condensate in the temperature interval (46) has the form of a resonance with the maximum at

$$\frac{(n_0)_{\max}}{N} = \frac{3t}{\pi^2}y_{\max} + 1 - \sqrt{At^3}, \quad y_{\max} \approx -2.41, \quad (47)$$

and the peak width on the order of

$$\Delta n_0/N \approx 0.9t. \quad (48)$$

From this it follows that, as $t \longrightarrow 0$, the distribution acquires the shape of a δ function: $w_0(n_0) \longrightarrow \delta(n_0 - N)$. This function qualitatively differs from the analogous distribution function (29) determined within the framework of the Bose–Einstein statistics.

Despite such a sharp difference between the distribution functions, the average number of particles in the condensate under conditions (46) in the statistics of a canonical ensemble coincides with that obtained within the Bose–Einstein statistics. In calculating the average number of particles in the ground state of a canonical ensemble,

$$\langle n_0\rangle = \sum_{n_0=0}^{N} n_0 w(n_0),$$

summation over the distribution function (37) can be replaced by integration. Upon substituting

$$\frac{\pi^2}{3t}\left(\frac{n_0}{N} - 1 + \sqrt{At^3}\right) = y,$$

we obtain

$$\frac{\langle n_0\rangle}{N} = \frac{3t}{\pi^2}\int_{\eta(t)}^{0} y\varphi(y)dy\left(\int_{\eta(t)}^{0}\varphi(y)dy\right)^{-1} + 1 - \sqrt{At^3},$$
$$\eta(t) = -\frac{\pi^2}{3}\frac{1 - \sqrt{At^3}}{t}.$$

In the temperature interval (46), the lower limit of integration in the last expression can be set equal to $\eta = -\infty$. Then, taking into account formulas (45), we arrive at the conclusion that the average $\langle n_0\rangle$ corresponding to the distribution (37) in the temperature interval (46) coincides with the average value $\langle n_0\rangle = \tilde{n}_0$ calculated using (24) within the framework of the Bose–Einstein statistics.

We can also readily calculate a mean square fluctuation corresponding to the distribution function (37) of the canonical ensemble. In the temperature interval (46), this quantity is expressed as

$$\langle (n_0 - \langle n_0\rangle)^2\rangle_{ca} = \frac{1}{5}N^2t^2. \quad (49)$$

This value decreases with the temperature (tending to zero as $t \longrightarrow 0$), thus radically differing from the analogous value corresponding to the Bose–Einstein distribution function (29), for which the mean square fluctuation [5]

$$\langle (n_0 - \tilde{n}_0)^2\rangle_{BE} = \tilde{n}_0^2 + \tilde{n}_0$$

increases with decreasing temperature (tending to $N^2 + N$ as $t \longrightarrow 0$).

When the temperature increases, the first condition in (46) fails to be valid and the shape of the distribution

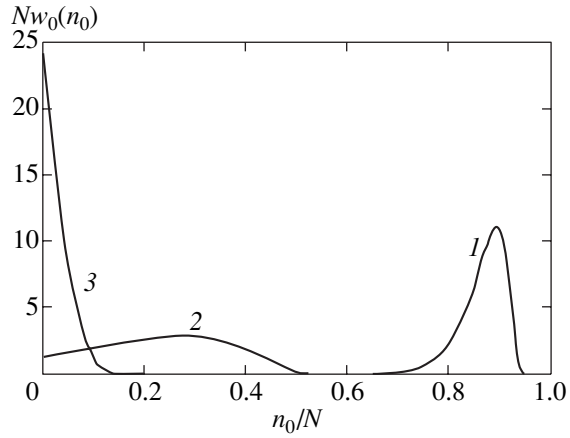

Fig. 3. The distribution function of the number of particles in the condensate of a canonical ensemble calculated for $A = 1$ at various temperatures $t = T/T_1 = 0.1$ (*1*), 0.5 (*2*), and 0.8 (*3*).

function qualitatively changes. In the temperature interval

$$t_3 - t \leq \frac{2}{3}t_3^2 = \frac{2}{3}A^{-2/3}, \quad A \gg 1, \tag{50}$$

the distribution (37) can be rewritten as

$$w_0(n_0) = S^{-1}\varphi\left[\frac{\pi^2}{3t_3}\left(\frac{n_0}{N} - \frac{3}{2}\frac{t_3 - t}{t_3}\right)\right].$$

This function acquires a finite value at $n_0 = 0$ and, at temperatures up to

$$t \leq t_3 + (2/\pi^2)y_{\max}t_3^2 \approx t_3 - 0.5t_3^2,$$

exhibits a maximum reached for

$$\frac{n_0}{N} = \frac{3}{2}\frac{t_3 - t}{t_3} + \frac{3}{\pi^2}y_{\max}t_3.$$

As the temperature grows further, the maximum disappears and the distribution represents a monotonically decreasing function of the number of particles n_0 (Fig. 3).

For small A values ($A \ll 1$), the 3D condensation temperature is such that $t_3 \gg 1$ and we can neglect the term $\sqrt{At^3}$ in the distribution function (37) up to high temperatures ($t \gg 1$):

$$w_0(n_0) = S^{-1}\varphi\left(\frac{\pi^2}{3t}\left(\frac{n_0}{N} - 1\right)\right), \quad A \ll 1. \tag{51}$$

As can be readily checked, in the limiting cases of small and large t, this distribution yields

$$\frac{\langle n_0\rangle}{N} = \begin{cases} 1 - t + \dfrac{4\pi^2}{3t}\exp\left(-\dfrac{\pi^2}{3t}\right), & t \ll 1, \\ \dfrac{1}{3t} - \dfrac{1}{18t^2}, & t \gg 1. \end{cases} \tag{52}$$

A comparison of expressions (52) to (18) and (19) shows that, for $A \ll 1$, the average numbers of particles in the ground state for the Bose–Einstein statistics coincides with that for the canonical ensemble only in the limits of $t \longrightarrow 0$ and $t \longrightarrow \infty$. However, for $t \longrightarrow 0$ ($t \longrightarrow \infty$), the average number of particles in the condensate obeying the Bose–Einstein statistics tends to the limiting value slower (faster) than that in the canonical ensemble. From this, it follows that the average numbers of particles in the ground state for the two statistics do not completely coincide. This conclusion is confirmed by the results of numerical calculations (Fig. 1), although the difference is rather small even in the intermediate region.

For small t ($t \ll 1$), the distribution function (51) has a resonance shape with the peak position determined by expression (47), the width by (48), and the mean-square fluctuation by (49). When the temperature grows, the maximum vanishes. For $t \gg 1$, we may substitute the asymptotic expression (43) into distribution (51) to obtain

$$w_0(n_0) = S^{-1}\left(1 - \frac{n_0}{N}\right)^{-7/2}\exp\left(-\frac{3t}{1 - n_0/N}\right), \quad t \gg 1.$$

The corresponding normalization factor and the average can be calculated by restricting the expansion to the first-order terms with respect to parameter $1/3t$. The resulting distribution function is

$$w_0(n_0) = \frac{3t}{N}\exp\left(-\frac{3t}{N}n_0\right), \quad \langle n_0\rangle = \frac{N}{3t}, \quad t \gg 1.$$

As can be seen from (19), this distribution coincides with (29).

Thus, under the condition (28) equivalent to $A \ll 1$, the phenomenon of condensation exhibits, both in a canonical ensemble of bosons and in the Bose–Einstein statistics, a one-dimensional character with respect to the average number of particles in the condensate. The average numbers of particles in the ground state determined for these ensembles differ rather slightly and coincide in the two limiting cases, $t \longrightarrow 0$ and $t \longrightarrow \infty$. In contrast, at relatively low temperatures $t \leq 1$ (when the number of particles in the condensate is comparable with the total number of gas particles), the distribution functions of the number of particles in the ground state for the two ensembles are qualitatively different. This is manifested by a radical difference in the mean square fluctuations and in all the higher moments.

The condition (28) implies that $T_1 \ll T_3$; as a result, there exists a temperature interval $1 \ll t \ll t_3$ in which the distribution function of the number of particles in the 1D condensate of a canonical ensemble acquires the shape of the Bose–Einstein distribution. In contrast to the 3D case [6–8], this change from a resonance curve (narrowing as $t \longrightarrow 0$) to distribution (29) for $t \gg 1$ proceeds smoothly at a rate independent of the number of gas particles N. Therefore, the 1D condensation does not exhibit features characteristic of the 3D process, for which the transformation of the distribution function with $N \longrightarrow \infty$ has a jumplike character.

3.4. The Distribution Function of the Number of Particles in the Excited States

First, let us find the joint distribution $w_{0,\,i\neq 0}(n_0, n_i)$. Using a procedure analogous to that described in [6–8], we eventually obtain

$$w_{0,\,i\neq 0}(n_0, n_i) = S^{-1}\exp(-\varepsilon_i n_i)$$
$$\times\left\{\varphi\left[\frac{\pi^2}{3t}\left(\frac{n_0 + n_i}{N} - 1 + \sqrt{At^3}\right)\right]\right.$$
$$\left. - \exp(-\varepsilon_i)\varphi\left[\frac{\pi^2}{3t}\left(\frac{n_0 + n_i + 1}{N} - 1 + \sqrt{At^3}\right)\right]\right\}.$$

The distribution of the number of particles in the excited states is determined by summing (integrating) this distribution over the possible $n_0$values:

$$w_{i\neq 0}(n_i) = \sum_{n_0 = 0}^{N} w_{0,\,i\neq 0}(n_0, n_i).$$

In the temperature interval (46), we can neglect unity in comparison with n_0 in the second term and the integration yields an expression

$$w_{i\neq 0}(n_i) = [1 - \exp(-\varepsilon_i)]\exp(-\varepsilon_i n_i),$$

coinciding with the Bose–Einstein distribution (1) for $\mu = 0$.

An analogous result is obtained for $A \ll 1$ in the region of small temperatures ($t \ll 1$). For $1 \ll t < t_3$ and $A \ll 1$, we can use the asymptotic formula (43); as a result, we again obtain distribution (1) with $\mu = -3t/N$, which corresponds to (19).

4. CONCLUSIONS

1. The results of summation of the Gibbs distribution over the discrete energy levels of an ideal Bose gas confined in a closed volume with the transverse dimensions much smaller than the longitudinal size ($l/L \ll 1$) show that, under the condition $N(l/L)^4 \ll 1$ (where N is the total number of gas particles), the average number of particles in the ground state (condensate) determined within the framework of the statistics of a canonical ensemble of bosons, as well as within the Bose–Einstein statistics, is a function of the ratio $t = T/T_1$, where T_1 is a characteristic temperature of the system (see Eq. (5)) depending only on the longitudinal size L. Therefore, the condensation process exhibits a one-dimensional character. In the opposite limiting case ($N(l/L)^4 \gg 1$, the situation changes and the process becomes three-dimensional with respect to the average number of particles in the condensate.

2. Similar to the 3D case [8], the distribution function of the number of particles in the 1D condensate of a canonical ensemble qualitatively differs from an analogous distribution in the Bose–Einstein statistics (grand canonical ensemble), in which the distribution at all temperatures has the form (see Eq. (29)) corresponding to a gradual decrease in the probability $w_0(n_0)$ of finding n_0 particles in the condensate (from a maximum value at $n_0 = 0$ to zero at $n_0 \longrightarrow \infty$). As the temperature decreases, the width of this distribution increases, which is accompanied by the buildup of fluctuations (fluctuational catastrophe). In the statistics of a canonical ensemble at low temperature ($t \ll 1$), the distribution has the form of a resonance. The resonance width (see Eq. (48)) tends to zero with decreasing temperature, which corresponds to suppression of the fluctuations. As the temperature increases, this distribution changes and, for $t \gg 1$, acquires the shape of the Bose–Einstein distribution. Unlike the 3D case, the transformation proceeds smoothly, and the rate of this variation with increasing temperature is independent of the number of gas particles. This is evidence that the 1D condensation does not exhibit features characteristic of the 3D process in the canonical ensemble of bosons, where the transformation of the distribution function with $N \longrightarrow \infty$ has a jumplike character.

3. Despite the radical difference between the distribution functions of the numbers of particles in condensates of the grand canonical and canonical ensembles, the average numbers of particles in the 1D condensates of these ensembles differ rather slightly (but do not coincide as in the 3D case [8]) and tend to be the same in the limiting cases of $t \longrightarrow 0$ and $t \longrightarrow \infty$.

4. Under the condition $l/L \ll 1$, the distribution function of the number of particles in the condensate of a canonical ensemble for any N retains the shape characteristic of the 1D system.

5. The distribution functions of the number of particles in the excited states of the grand canonical and canonical ensembles coincide and are described by the Bose–Einstein distribution.

ACKNOWLEDGMENTS

This study was partly supported by the State Program “Metrology” and the Russian Foundation for Basic Research (project nos. 01-02-17354 and 00-15-96789).

REFERENCES

1. W. Ketterle and N. J. van Druten, Phys. Rev. A **54**, 656 (1996).
2. C. Orzel, A. K. Tuchman, M. L. Fenselan, *et al.*, Science **291**, 2386 (2001).
3. A. Gorlitz, J. M. Vogels, A. E. Leanhardt, *et al.*, Phys. Rev. Lett. **87**, 130402 (2001).
4. A. Einstein, Sitzungsber. K. Preuss. Akad. Wiss., Phys. Math. Kl. **23**, 3 (1925).
5. L. D. Landau and E. M. Lifshitz, *Course of Theoretical Physics*, Vol. 5: *Statistical Physics* (Nauka, Moscow, 1995; Pergamon, Oxford, 1980).
6. V. A. Alekseev, Kvantovaya Élektron. (Moscow) **31**, 16 (2001).
7. V. A. Alekseev, Zh. Éksp. Teor. Fiz. **119**, 700 (2001) [JETP **92**, 608 (2001)].
8. V. A. Alekseev, Kvantovaya Élektron. (Moscow) **31**, 427 (2001).
9. E. M. Lifshitz and L. P. Pitaevskiĭ, *Course of Theoretical Physics*, Vol. 5: *Statistical Physics* (Nauka, Moscow, 1978; Pergamon, Oxford, 1980), Part 2.
10. R. S. Hohenberg, Phys. Rev. **158**, 383 (1967).
11. V. L. Berezinskiĭ, Zh. Éksp. Teor. Fiz. **59**, 907 (1970) [Sov. Phys. JETP **32**, 493 (1971)]; Zh. Éksp. Teor. Fiz. **61**, 1144 (1971) [Sov. Phys. JETP **34**, 610 (1972)].
12. V. Bagnato and D. Kleppner, Phys. Rev. A **44**, 7439 (1991).
13. A. Einstein, Sitzungsber. K. Preuss. Akad. Wiss., Phys. Math. Kl. **22**, 261 (1924).
14. M. A. Evgrafov, *Asymptotic Estimates and Entire Functions* (Nauka, Moscow, 1979; Gordon and Breach, New York, 1961).
15. V. A. Alekseev and D. D. Krylova, Kvantovaya Élektron. (Moscow) **30**, 441 (2000).

Translated by P. Pozdeev

Journal of Experimental and Theoretical Physics, Vol. 94, No. 6, 2002, pp. 1103–1105.
Translated from Zhurnal Éksperimental'noĭ i Teoreticheskoĭ Fiziki, Vol. 121, No. 6, 2002, pp. 1285–1287.

PLASMA, GASES

The Alfvén Dissipation Waveguide

S. M. Churilov

Institute of Solar–Terrestrial Physics, Siberian Division, Russian Academy of Sciences, Irkutsk, 664033 Russia
e-mail: churilov@iszf.irk.ru

Received November 9, 2001

Abstract—The possibility of waveguide propagation of Alfvén waves in an inhomogeneous plasma only through dissipation without dispersion is demonstrated. © *2002 MAIK "Nauka/Interperiodica".*

1. INTRODUCTION

In the first approximation (ideal MHD approximation), Alfvén waves are treated as incompressible movements of a plasma, propagating along a magnetic field **B** with the Alfvén velocity $\mathbf{c}_A = \mathbf{B}/(4\pi\rho)^{1/2}$ (ρ is the density) and accompanied by vibrations of field lines similar to vibrations of a string [1]. The dispersion relation $\omega = \mathbf{c}_A \cdot \mathbf{k}$ implies that such waves cannot be natural oscillations in a transverse-inhomogeneous plasma: initial perturbations of the Alfvén type "scatter" due to mismatching of oscillations of adjacent field lines [2–4]. The inclusion of additional (relative to the ideal MHD) factors such as the inertia of electrons (ions) or the finiteness of the Larmor radius of ions leads to transverse dispersion that "returns" Alfvén waves to the class of natural oscillations of an inhomogeneous plasma and, in particular, permits their channeling (waveguide propagation) along the field lines on which the Alfvén velocity attains it extremum [5–7].

It will be demonstrated below that ordinary (e.g., ohmic) dissipation leads to a similar effect, i.e., waveguide propagation and, hence, the emergence of natural Alfvén oscillations of transverse-inhomogeneous plasma.

2. BASIC EQUATIONS AND THEIR SOLUTIONS

We consider a plasma with an equilibrium density $\rho_0(x)$ in a magnetic field $\mathbf{B}_0(x)$ directed along the z axis. Disregarding the aspects associated with the so-called Alfvén resonance (see, for example, [4]), we consider Alfvén-type oscillations of a given frequency ω, which are independent of y and propagate along the z axis. These oscillations are free of density perturbation, while perturbations of velocity and magnetic field have only the y component in the linear approximation and are described by the equations [8]

$$\begin{aligned}\frac{\partial v_y}{\partial t} &= \frac{B_0}{4\pi\rho_0}\frac{\partial B_y}{\partial z},\\ \frac{\partial B_y}{\partial t} &= B_0\frac{\partial v_y}{\partial z} + \eta\left(\frac{\partial^2 B_y}{\partial x^2} + \frac{\partial^2 B_y}{\partial z^2}\right),\end{aligned} \tag{1}$$

taking into account the magnetic field diffusion η due to finite conductivity. Eliminating v_y and putting

$$B_y = b(x)\exp(-i\omega t + ikz),$$

we arrive at the equation

$$\frac{d^2 b}{dx^2} + \left[\frac{i\omega}{\eta} - \left(1 + \frac{ic_A^2}{\eta\omega}\right)k^2\right]b = 0, \tag{2}$$

whose solutions, which are bounded for $x \longrightarrow \pm\infty$, describe the structure of natural Alfvén oscillations.

We choose the Alfvén velocity profile with a minimum at the center and with a monotonic increase towards the periphery,

$$c_A^2(x) = A^2\left(1 + \frac{x^2}{a^2}\right),$$

and pass to the dimensionless variables

$$\tilde{x} = \frac{x}{a}, \quad \tilde{k} = ka, \quad \tilde{\omega} = \frac{\omega a}{A}, \quad \tilde{\eta} = \frac{\eta}{aA}.$$

Equation (2) leads to the Weber equation (we omit the tildes)

$$\frac{d^2 b}{dx^2} + \left[\frac{i\omega}{\eta} - \left(1 + \frac{i}{\eta\omega}\right)k^2 - \frac{ik^2}{\eta\omega}x^2\right]b = 0, \tag{3}$$

whose general solution is a superposition of the parabolic cylinder functions [9] $D_p(\pm\lambda x)$, where

$$\begin{aligned}p + \frac{1}{2} &= \frac{1}{2}\left(\frac{\omega}{\eta}\right)^{1/2}\left(\frac{\omega}{k} - \frac{k}{\omega} + i\eta k\right)\exp\left(\frac{i\pi}{4}\right),\\ \lambda^2 &= \frac{2k}{(\eta\omega)^{1/2}}\exp\left(\frac{i\pi}{4}\right), \quad |\arg\lambda| < \frac{\pi}{4}.\end{aligned} \tag{4}$$

It can be seen that the given problem is similar to that of energy levels of a quantum oscillator [10]: the solution to Eq. (3) can be bounded only for integral nonne-

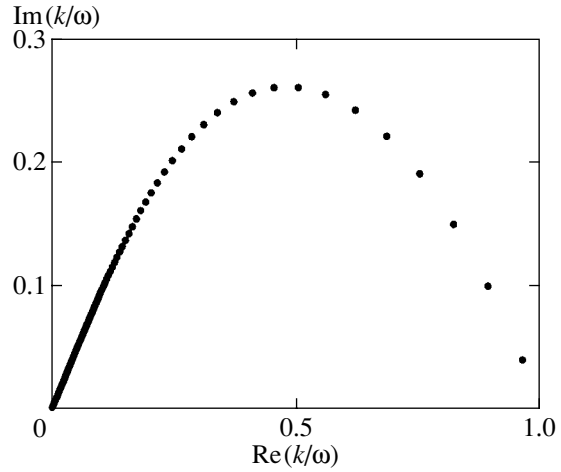

Eigenvalues k_n of Alfvén modes: $\omega = 1$, $\eta = 0.01$.

gative values of $p = n$ and can be expressed in this case in terms of Hermite polynomials [9] $H_n(z)$:

$$b_n(x) = B_n \exp\left(-\frac{\lambda_n^2 x^2}{4}\right) H_n\left(\frac{\lambda_n x}{\sqrt{2}}\right), \quad B_n = \text{const},$$

$$\lambda_n = \lambda(k_n), \quad n = 0, 1, 2, \ldots .$$

Thus, each frequency ω corresponds to a discrete spectrum of (waveguide) modes localized in x:

$$k_n = \frac{\omega}{1 - i\eta\omega}\left[\sqrt{1 - i\eta\omega - i\left(n + \frac{1}{2}\right)^2\frac{\eta}{\omega}}\right. \\ \left. - \left(n + \frac{1}{2}\right)\left(\frac{\eta}{\omega}\right)^{1/2}\exp\left(-\frac{i\pi}{4}\right)\right]. \tag{5}$$

In addition, solutions (3) obviously contain modes with $k = -k_n$ propagating in the opposite direction.

3. DISCUSSION

Formula (5) defines the longitudinal wavelength ($|k_n|^{-1}$) of the corresponding mode as well as its damping length. It can easily be proved that

$$\frac{\varphi}{2} < \arg k_n < \frac{\pi}{4}, \quad \varphi = \arctan(\eta\omega), \quad n = 0, 1, 2, \ldots,$$

i.e., modes attenuate, as should be expected for a dissipative medium, but their Q factor $Q_n = \mathrm{Re}\,k_n/\mathrm{Im}\,k_n$ is always greater than unity. In addition, each mode is characterized by two transverse scales: the localization scale L_n and the scale of variation l_n. For the main ($n = 0$) mode, we have

$$l_0^2 = L_0^2 = \frac{(\eta\omega)^{1/2}}{|k|}$$

(see Eqs. (4)). In accordance with the theorem on zeros of Hermite polynomials [11], we can write

$$L_n^2 \approx (2n + 1)L_0^2,$$

while the scale of variation (the distance between adjacent zeros) is

$$l_n^2 \sim L_0^2/n.$$

For the most interesting case of weak dissipation ($\eta \ll 1$), we will analyze the dispersion equation (5), singling out the following three frequency ranges:[1]

(1) low frequencies (or high mode numbers)

$$\frac{\omega}{n + 1/2} \ll \min\left[1, \left(n + \frac{1}{2}\right)\eta\right], \\ k_n \approx \frac{\omega^{3/2}}{(2n + 1)\eta^{1/2}}\exp\left(\frac{i\pi}{4}\right); \tag{6}$$

(2) moderate frequencies (and mode numbers)

$$\left(n + \frac{1}{2}\right)^2\eta \ll \omega \ll \eta^{-1}, \\ k_n \approx \omega\left[1 - \left(n + \frac{1}{2}\right)\left(\frac{\eta}{\omega}\right)^{1/2}\exp\left(-\frac{i\pi}{4}\right) + \frac{i}{2}\eta\omega\right]; \tag{7}$$

(3) high frequencies

$$\omega \gg \max\left(\eta^{-1}, n + \frac{1}{2}\right), \\ k_n \approx \left(\frac{\omega}{\eta}\right)^{1/2}\exp\left(\frac{i\pi}{4}\right). \tag{8}$$

Strong damping ($\mathrm{Im}\,k_n \approx \mathrm{Re}\,k_n$) of high and low frequencies can be explained by the fact that the longitudinal ($|k_n|^{-1}$) scale of mode variation in the former case and the transverse (l_n) scale in the latter case are comparable with the dissipative scale $l_d = (\eta/\omega)^{1/2}$. For moderate frequencies, both scales of mode variation are quite large,

$$|k_n| l_d \approx (\eta\omega)^{1/2} \ll 1, \quad \frac{l_d^2}{l_n^2} \sim n\left(\frac{\eta}{\omega}\right)^{1/2} \ll 1,$$

which ensures the high Q factor ($Q_n \gg 1$) of these oscillations.

It should be noted that the inequality $\omega \gg \eta^{-1}$ holds either for very frequent collisions or for frequencies beyond the spectrum of Alfvén waves; consequently, the high-frequency range (8) is mentioned only for completeness of the patterns. On the contrary, formulas (7) and (6) describe a typical spectrum of Alfvén modes (see the figure). If the frequency is such that $\eta \ll \omega \ll \eta^{-1}$, the

[1] The names of these ranges are arbitrary; in the generally accepted terminology, the oscillations under investigation are low-frequency oscillations.

modes with not very large numbers lie in the plane of complex k almost equidistantly starting from $k \approx \omega$ for $n = 0$ in accordance with relations (7), and their localization scale is smaller than the inhomogeneity scale,

$$L_n^2 = (2n+1)\left(\frac{\eta}{\omega}\right)^{1/2} \ll 1.$$

As the mode number increases, the quantities $|k_n|$, l_n, and Q_n decrease, and the scale of localization L_n increases. For $n > (\omega/\eta)^{1/2}$, i.e., in the limit (6), this scale becomes larger than the inhomogeneity scale,

$$L_n = (2n+1)\left(\frac{\eta}{\omega}\right)^{1/2} > 1.$$

It is interesting to note that the velocity of mode propagation is equal to the maximum value of the Alfvén velocity in the domain of mode localization. Indeed, the Alfvén velocity for $x^2 = L_n^2$ is given by

$$(1+L_n^2)^{1/2} \approx \begin{cases} 1+\frac{1}{2}L_n^2 = 1+\left(n+\frac{1}{2}\right)\left(\frac{\eta}{\omega}\right)^{1/2}, & L_n \ll 1, \\ L_n = (2n+1)\left(\frac{\eta}{\omega}\right)^{1/2}, & L_n \gg 1 \end{cases}$$

and coincides with the velocities determined from relations (7) and (6), respectively.

REFERENCES

1. B. B. Kadomtsev, *Collective Phenomena in a Plasma* (Nauka, Moscow, 1988), p. 44.
2. A. V. Timofeev, in *Reviews of Plasma Physics*, Ed. by M. A. Leontovich (Atomizdat, Moscow, 1979; Consultants Bureau, New York, 1986), Vol. 9, p. 205.
3. V. A. Mazur, A. B. Mikhaĭlovskiĭ, A. L. Frenkel', *et al.*, in *Reviews of Plasma Physics*, Ed. by M. A. Leontovich (Atomizdat, Moscow, 1979; Consultants Bureau, New York, 1986), Vol. 9, p. 233.
4. A. V. Timofeev, *Resonance Effects in Oscillations of Plasma* (Fizmatlit, Moscow, 2000).
5. A. S. Leonovich, V. A. Mazur, and V. N. Senatorov, Zh. Éksp. Teor. Fiz. **85**, 141 (1983) [Sov. Phys. JETP **58**, 83 (1983)].
6. A. V. Gul'el'mi and A. R. Polyakov, Geomagn. Aeron. **23**, 341 (1983).
7. A. S. Leonovich, V. A. Mazur, and V. N. Senatorov, Fiz. Plazmy **11**, 1106 (1985) [Sov. J. Plasma Phys. **11**, 632 (1985)].
8. L. D. Landau and E. M. Lifshitz, *Course of Theoretical Physics*, Vol. 8: *Electrodynamics of Continuous Media* (Nauka, Moscow, 1982; Pergamon, New York, 1984).
9. *Heigher Transcendental Functions (Bateman Manuscript Project)*, Ed. by A. Erdelyi (McGraw-Hill, New York, 1953; Nauka, Moscow, 1966), Vol. 2.
10. L. D. Landau and E. M. Lifshitz, *Course of Theoretical Physics*, Vol. 3: *Quantum Mechanics: Non-Relativistic Theory* (Nauka, Moscow, 1974; Pergamon, New York, 1977).
11. G. Szego, *Orthogonal Polynomials* (American Mathematical Society, New York, 1959; Fizmatgiz, Moscow, 1962).

Translated by N. Wadhwa

Journal of Experimental and Theoretical Physics, Vol. 94, No. 6, 2002, pp. 1106–1113.
Translated from Zhurnal Éksperimental'noĭ i Teoreticheskoĭ Fiziki, Vol. 121, No. 6, 2002, pp. 1288–1297.

PLASMA, GASES

Polarization Mechanism of Dust Particle Interaction in Plasma

Yu. A. Mankelevich, M. A. Olevanov*, and T. V. Rakhimova

Nuclear Physics Research Institute, Moscow State University, Moscow, 119899 Russia

**e-mail: olevanov_m@mtu-net.ru*

Received November 22, 2001

Abstract—The paper deals with the mechanism of interaction of dust particles in plasma, associated with their polarization in an electric field which may be produced both by an external source and by accumulated charges of neighboring particles. A theoretical calculation is made of forces acting on a macroparticle in an external field, as well as a number of estimations of interaction for different ranges of parameters. It is demonstrated that, under certain conditions, the interaction mechanism being treated may play a significant part in the description of processes occurring in a dust plasma. © *2002 MAIK "Nauka/Interperiodica".*

1. INTRODUCTION

Under experimental conditions, the electron mobility in a dust plasma is usually much higher than the ion mobility. As a result, dust particles in the plasma (given the equality of the electron and ion fluxes to their surface) acquire a significant negative charge, which, under certain conditions, may reach a value of $Z \sim 10^3$–10^4 electron charges. Therefore, a strong interparticle interaction is present in a dust plasma system.

It is obvious that the presence of large charges of dust particles must bring about a noticeable electrostatic repulsion of dust particles. In many instances, however, the observed behavior of the system is just the reverse. A typical example are the processes of agglomeration of dust particles and formation of plasma–dust droplets observed in experiments involving plasma etching. The main characteristic feature of this phenomenon is the rapid growth of particles, beginning with the size of the order of 0.01 μm and up to the size of 10^3 μm, visible to the naked eye [1]. The mechanisms of this process largely remain unclear; it is only clear that, in constructing the pattern of this phenomenon, one must use additional models of dust particle interaction.

Of considerable interest, along with the processes of dust particle growth and cluster formation, are the processes of self-organization occurring in plasma–dust systems. The existence of dust crystals, which were first revealed in 1994 [2–6], is an established fact, although the possibility of their existence was theoretically discussed for quite some time [7, 8]. The building material for such crystals is provided by dust particles whose size may vary up to tens of microns depending on the conditions of an actual experiment. The lattice constant in such crystals usually exceeds considerably the Debye screening length and may reach hundreds of microns.

The necessary condition for the existence of the above-mentioned ordered structures is the presence of forces compensating for the electrostatic repulsion of dust particles. Several models describing such processes are suggested in the literature. Of these, the basic model is the model of particles attraction, which is due to the shielding of plasma flows by a neighboring particle. Khodataev *et al.* [9] have demonstrated that, at long distances between dust particles, the interaction potential varies proportionally to $1/R$, where R is the distance between particles, and the force of attraction may exceed the force of electrostatic repulsion. If the dust particles are close to one another, the charge accumulated by them becomes almost unshielded, and the overlapping of plasma flows by a neighboring particle is no longer capable of compensating for Coulomb repulsion. Khodataev *et al.* [9] have concluded that the potential of interaction between dust particles must be of the molecular type, whose special feature is the existence of some equilibrium distance between dust particles, over which the forces of attraction and repulsion balance each other.

We treat another mechanism of dust particle interaction. As in the case described above, the main reason for its emergence is the asymmetry of plasma particle flows to the dust particle surface; however, the nature of this asymmetry is somewhat different. After being placed into an external electric field, a macroparticle is polarized. The excess of negative charge on one side produces an additional ion flow to this side, while an excess electron flow of exactly the same magnitude is produced on the other side of the particle (see Fig. 1). Because the sum of charges brought by excess flows of charged particles to the surface of a dust particle is zero, the dynamic equilibrium by and large is not disturbed,

and the dust particle charge remains constant in time. The momentum transferred to the dust particle by ions incident on its surface exceeds considerably the momentum brought by electrons. For estimation, we can write

$$\frac{p_i}{p_e} \sim \sqrt{\frac{m_i T_i}{m_e T_e}}.$$

Here, p_i and p_e are the ion and electron momenta; and m_i, m_e and T_i, T_e denote the particle masses and temperatures, respectively. Because the ion mass is three–four orders of magnitude larger than the electron mass, and the ion temperature under conditions of experiments involving low-temperature plasma is usually of the order of 0.01 of the electron temperature, the foregoing ratio is, as a rule, always greater than unity.

Therefore, we arrive at a conclusion that a dust particle in an external electric field is acted upon, in addition to the electrostatic force, by an additional force exerted by plasma flows, the direction of which coincides with the electric field vector (see Fig. 1). In the subsequent section, we will deal with a theoretical calculation of this force.

2. FORCES ACTING ON A MACROPARTICLE IN AN EXTERNAL ELECTRIC FIELD

We will treat a dust particle placed in the external electric field $\mathbf{E}_0$. This may be either the field produced by the charge of the neighboring dust particle, or the field of an external source. In subsequent reasoning, we will assume that the electric field is uniform. As regards the interparticle interaction, this approximation will be valid only at long distances between macroparticles, that is, when the mean distance between macroparticles considerably exceeds their size. The dust particle is assumed to be a micron-sized sphere charged to a floating potential.

In calculating the force exerted on a particle by the surrounding plasma, we will ignore the effect of electrons and take into account only the momentum transferred to the dust particle during collision with ions. This can be done by virtue of the foregoing estimates reinforced by the fact that the ions are accelerated by the dust particle field, while the electrons, on the contrary, are decelerated by this field.

We will direct the z axis along the vector of the external electric field. Because the problem is characterized by axial geometry, it makes sense to search only for the force component acting in the same direction with the field vector. Two other components, after summation of the effects produced on the particle from different directions, will turn out to be zero. Then, the expression for the force will be written as

$$F = \oint_{\Sigma}\int_{\mathbf{v}} m_i \tilde{v}_z f(\mathbf{r}, \mathbf{v})(\tilde{\mathbf{v}} d\mathbf{S}) d\mathbf{v}. \quad (1)$$

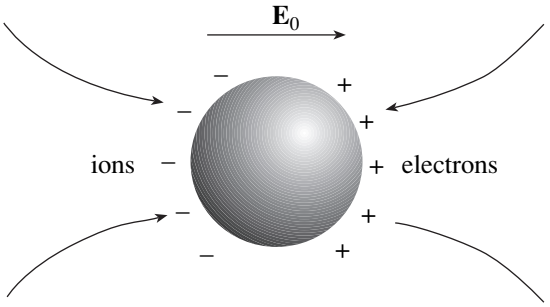

Fig. 1. The redistribution of plasma flows to the surface of a macroparticle placed in an external electric field.

In this expression, the integration is performed over the entire surface of the dust particle, as well as over the velocities of incident ions. The function $f(\mathbf{r}, \mathbf{v})$ is the ion distribution function in the phase space. This function may be derived as the solution of the corresponding kinetic equation. We have also taken into account the fact that the velocity of incident ions at the macroparticle surface, which we designated as $\tilde{\mathbf{v}}$, differs from their thermal velocity $\mathbf{v}$, because, before colliding with the surface, they are accelerated in the field of the negative charge of the dust particle. The relation between the thermal velocity of ions and their velocity at the surface is defined by the energy conservation law,

$$\tilde{v}^2 = v^2 + \frac{2Z_i e\Delta U}{m_i}. \quad (2)$$

The second term in this expression represents the velocity which an ion gathers in the field of the dust particle charge when acted upon by the potential difference between the surface and a point removed from the surface to a distance equal to the free path length.

Two limiting cases are usually treated in this context. The first case describes a situation in which the free path of the ion exceeds the Debye screening length in plasma, $\lambda_i \gg \lambda_d$. In this case, the additional energy acquired by the ion is defined by the potential on the particle surface, $Z_i e\Delta U = Z_i e|\varphi_0|$, where φ_0 is the surface potential. This approximation is referred to as the orbital motion limit [1]. In the second limiting case, $\lambda_i \ll \lambda_d$. Then, the velocity of the ion on the dust particle surface is close to its thermal velocity, $\tilde{v} \approx v$.

In the system being investigated, the ions interact with plasma, dust particles, and neutral gas. The interaction with charged plasma particles is long-range and nonlocal; therefore, in the equations, we will take it into account in the self-consistent field approximation. In the interaction of ions with neutral gas and dust component, on the contrary, pair collisions are of prime importance. We will include this interaction in our model by evaluating the collision integral in the form of relax-

ation term on the right-hand side of the kinetic equation. The relaxation time τ_{eff} may be represented as

$$\tau_{\text{eff}} = \frac{1}{n_d \sigma_d v_i + n_0 \sigma_0 v_i}, \tag{3}$$

where n_d and n_0 denote the concentration of dust and neutral gas, respectively, and σ_d and σ_0 denote the interaction cross section of ions with dust particles and with neutral gas, respectively.

We will assume that the cross section of interaction with neutral gas is constant, $\sigma_0 \sim 10^{-16}$ cm^2, and estimate σ_d in the two limiting cases mentioned above. The orbital motion limit gives

$$\sigma_d = \pi a^2 \left(1 + \frac{2Z_i e|\varphi_0|}{m_i v^2}\right). \tag{4}$$

Here, a is the dust particle size; Z_i and m_i denote the ion charge and mass, respectively; v is the ion velocity; and φ_0 is the value of potential on the dust particle surface. In the second case, which corresponds to the hydrodynamic approximation, we derive

$$\sigma_d \approx \pi a^2. \tag{5}$$

We will now write the kinetic equation for the ion distribution function in the steady-state case,

$$\begin{aligned} &\mathbf{v} \cdot \frac{\partial f(\mathbf{r}, \mathbf{v})}{\partial \mathbf{r}} - \frac{Z_i e}{m_i} \frac{\partial \tilde{U}}{\partial \mathbf{r}} \cdot \frac{\partial f(\mathbf{r}, \mathbf{v})}{\partial \mathbf{v}} \\ &\quad = -\frac{f(\mathbf{r}, \mathbf{v}) - f_0(\mathbf{r}, \mathbf{v})}{\tau_{\text{eff}}}. \end{aligned} \tag{6}$$

In this equation, $\tilde{U}(\mathbf{r})$ is the combined potential produced by the dust particle charge and by the self-consistent field of the plasma, and $f_0(\mathbf{r}, \mathbf{v})$ is the equilibrium distribution function. For further estimation, we will use the Maxwell distribution as the equilibrium function,

$$f_0(\mathbf{r}, \mathbf{v}) = n_i(\mathbf{r}) \left(\frac{m_i}{2\pi T_i}\right)^{3/2} \exp\left(-\frac{m_i v^2}{2T_i}\right). \tag{7}$$

The kinetic equation (6) describes the states of the system in the case of small deviation from equilibrium. We will write its approximate solution,

$$\begin{aligned} f(\mathbf{r}, \mathbf{v}) &= f_0(\mathbf{r}, \mathbf{v}) \\ &- \tau_{\text{eff}} \left(\mathbf{v} \cdot \frac{\partial f_0(\mathbf{r}, \mathbf{v})}{\partial \mathbf{r}} - \frac{Z_i e}{m_i} \frac{\partial \tilde{U}}{\partial \mathbf{r}} \cdot \frac{\partial f_0(\mathbf{r}, \mathbf{v})}{\partial \mathbf{v}}\right). \end{aligned} \tag{8}$$

The resultant expression for the distribution function must be substituted into the integral given by Eq. (1). In so doing, it is sufficient to treat only the last term in expression (8), because all other terms of the ion distribution function are spherically symmetric and, on being integrated over the dust particle surface, will produce zero as the result.

Because the expression for force includes the value of electric field directly on the macroparticle surface, the shielding potential of the plasma can be fully eliminated from treatment when determining this field in the region of interest to us. Then, the potential can be written as

$$\tilde{U}(\mathbf{r}) = -\mathbf{E}_0 \cdot \mathbf{r} + \frac{\mathbf{P} \cdot \mathbf{r}}{r^3} + \varphi_0 \frac{a}{r}. \tag{9}$$

Here, $\mathbf{P}$ is the dipole moment acquired by the dust particle in the external electric field. If the particle is assumed to be conducting, the boundary condition of the constancy of the potential on its surface will produce $\mathbf{P} = \mathbf{E}_0 a^3$. Then, for the electric field in the vicinity of the dust particle, we will have

$$\mathbf{E}(\mathbf{r}) = \mathbf{E}_0 - \frac{\mathbf{P}}{r^3} + 3(\mathbf{P} \cdot \mathbf{r})\frac{\mathbf{r}}{r^5} + \varphi_0 a \frac{\mathbf{r}}{r^3}. \tag{10}$$

We will write the value of the last term in expression (8) for the distribution function directly on the dust particle surface,

$$\begin{aligned} &-\frac{Z_i e}{m_i} \frac{\partial \tilde{U}}{\partial \mathbf{r}} \cdot \frac{\partial f_0(\mathbf{r}, \mathbf{v})}{\partial \mathbf{v}}\bigg|_\Sigma \\ &\quad = -\frac{Z_i e}{T_i} \mathbf{n} \cdot \mathbf{v} \left(3\mathbf{E}_0 \cdot \mathbf{n} + \frac{\varphi_0}{a}\right) f_0(\mathbf{r}, \mathbf{v}). \end{aligned} \tag{11}$$

Here, $\mathbf{n}$ is the normal vector to the dust particle surface. We will substitute the resultant expression into the expression for force in view of Eq. (2). Then, Eq. (1) will take the form

$$\begin{aligned} F &= 3\tilde{n}_i \frac{m_i}{T_i} \left(\frac{m_i}{2\pi T_i}\right)^{3/2} Z_i e E_0 \\ &= \oint\limits_{\Sigma} \int\limits_{\mathbf{v}} (\mathbf{v} \cdot \mathbf{e}_z)(\mathbf{n} \cdot \mathbf{v})^2 (\mathbf{n} \cdot \mathbf{e}_z) \\ &\times \tau_{\text{eff}}(v) \left(1 + \frac{2Z_i e|\varphi_0|}{m_i v^2}\right) \exp\left(-\frac{m_i v^2}{2T_i}\right) dS d^3 v. \end{aligned} \tag{12}$$

Here, $\tilde{n}_i$ is the concentration of ions at the dust particle surface, and $\mathbf{e}_z$ is the unit vector in the direction of the external electric field. We further allowed for the fact that the term containing φ_0/a vanished upon integration.

In order to perform integration, we will introduce two spherical coordinate systems. The integration over the macroparticle surface will be performed in the *xyz* system with the *z* axis directed along the electric field vector. For integration over the velocities, we will use the *x'y'z'* system with the *z'* axis directed along the normal vector at a given point of the surface so that the vector $\mathbf{E}_0$ would lie in the *z'y'* plane (see Fig. 2). In the

primed coordinate system, the vectors have the coordinates

$$\mathbf{v}(\sin\theta\cos\phi, \sin\theta\sin\phi, \cos\theta),$$

$$\mathbf{n}(0, 0, 1),$$

$$\mathbf{e}_z(0, -\sin\vartheta, \cos\vartheta).$$

Here, θ and ϕ represent the polar angles in the $x'y'z'$ system, and ϑ, in the xyz system. Then,

$$\mathbf{n}\cdot\mathbf{v} = v\cos\theta,$$

$$\mathbf{n}\cdot\mathbf{e}_z = \cos\vartheta,$$

$$\mathbf{v}\cdot\mathbf{e}_z = v(\cos\theta\cos\vartheta - \sin\theta\sin\vartheta\sin\phi).$$

We will substitute the resultant relations for scalar products into expression (12),

$$F = 3\tilde{n}_i\frac{m_i}{T_i}\left(\frac{m_i}{2\pi T_i}\right)^{3/2} Z_i e E_0 2\pi a^2$$

$$\times \iiint\limits_{\substack{0<\vartheta<\pi\\ \pi/2<\theta<\pi\\ 0<\phi<2\pi}} \cos^2\theta\cos\vartheta(\cos\theta\cos\vartheta - \sin\theta\sin\vartheta\sin\phi) \tag{13}$$

$$\times \sin\theta\sin\vartheta d\vartheta d\theta d\phi$$

$$\times \int_0^\infty v^5\tau_{\text{eff}}(v)\left(1 + \frac{2Z_i e|\varphi_0|}{m_i v^2}\right)\exp\left(-\frac{m_i v^2}{2T_i}\right)dv$$

and perform integration over the angles. The intermediate result for force will be written as

$$F = Z_i e E_0 \tilde{n}_i \pi a^2 \frac{2m_i}{\sqrt{\pi}T_i}\left(\frac{m_i}{2\pi T_i}\right)^{3/2}$$

$$\times \int_0^\infty v^5\tau_{\text{eff}}(v)\left(1 + \frac{2Z_i e|\varphi_0|}{m_i v^2}\right)\exp\left(-\frac{m_i v_i^2}{2T_i}\right)dv. \tag{14}$$

We substitute the expression for τ_{eff} into Eq. (14), with due regard for (3) and (4), and pass on to the dimensionless integration variable $t = v\sqrt{m_i/2T_i}$. We will further introduce the dimensionless parameter ξ,

$$\xi^2 = \frac{Z_i e|\varphi_0|}{T_i}\frac{1}{1 + n_0\sigma_0/n_d\pi a^2}. \tag{15}$$

After all transformations, we derive

$$F = Z_i e E_0 \frac{\tilde{n}_i}{n_d}\frac{3/2 + (n_0\sigma_0/n_d\pi a^2)\Phi(\xi)}{1 + n_0\sigma_0/n_d\pi a^2}, \tag{16}$$

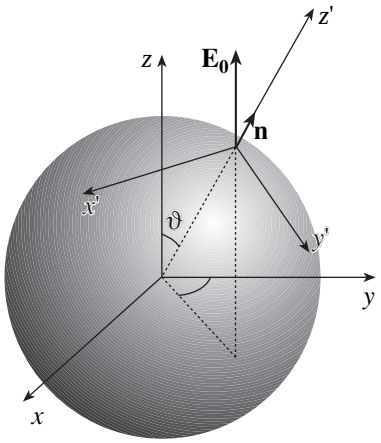

Fig. 2.

where

$$\Phi(\xi) = \frac{4\xi^2}{\sqrt{\pi}}\int_0^\infty \frac{t^4\exp(-t^2)}{t^2 + \xi^2}dt \tag{17}$$

$$= \xi^2(1 - 2\xi^2 + 2\sqrt{\pi}\xi^3\exp(\xi^2)\operatorname{erfc}(\xi)).$$

So, we have derived the expression for the force exerted on a dust particle by plasma flows. Then, in view of the interaction between the macroparticle charge and the external field, the resultant force acting on the dust particle can be represented as

$$F_d = Z_d e E_0\left(\frac{Z_i\tilde{n}_i}{Z_d n_d}\frac{3/2 + (n_0\sigma_0/n_d\pi a^2)\Phi(\xi)}{1 + n_0\sigma_0/n_d\pi a^2} - 1\right). \tag{18}$$

Here, Z_d denotes the dust particle charge.

We will analyze the obtained relations. One can see in Eq. (18) that a dust particle placed in an external electric field behaves as if it possesses some effective charge that differs from the real electric charge accumulated on that particle. The magnitude and sign of this charge are of importance, because these parameters may determine the nature of dust particle interaction in a plasma.

We will investigate this problem in more detail. The measure of effective charge will be provided by the electric charge Z_d accumulated by a dust particle. Then, the relative value of effective charge will be defined in Eq. (18) by the coefficient in brackets. This coefficient depends on the ratio $Z_i\tilde{n}_i/Z_d n_d$, as well as on $Z_i e|\varphi_0|/T_i$ and $n_0\sigma_0/n_d\pi a^2$. The latter two ratios define the dimensionless parameter ξ as well.

If the condition of quasineutrality is valid for the plasma, the charges and particle concentration in the plasma are related as

$$Z_i n_i = n_e + Z_d n_d. \tag{19}$$

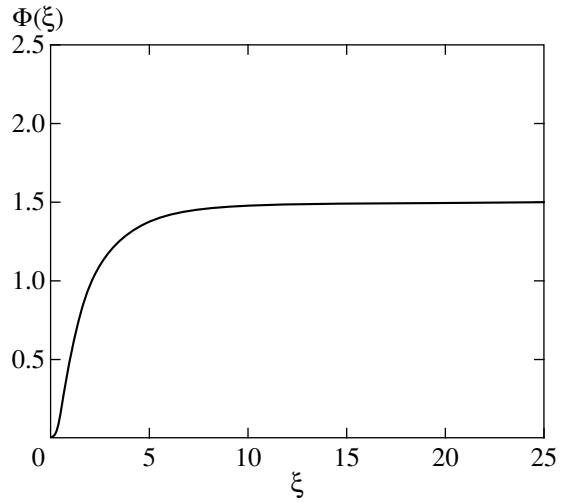

Fig. 3.

We will introduce a dimensionless parameter $P = n_d Z_d / n_e$. This quantity is usually used to characterize the collective effect of the macroparticle field on the processes occurring in the plasma. Under conditions of most experiments in a dust plasma, the relation $P \gtrsim 1$ is valid as a rule; then, the parameter $Z_i \tilde{n}_i / Z_d n_d$ can be transformed to

$$\frac{Z_i \tilde{n}_i}{Z_d n_d} = \beta\left(1 + \frac{1}{P}\right). \tag{20}$$

Here, the coefficient $\beta > 1$ reflects the difference between the ion concentration $\tilde{n}_i$ in the vicinity of the dust particle surface and the concentration n_i in the region of plasma undisturbed by the macroparticle field. This parameter can be estimated using the Boltzmann distribution; however, the resulting estimate will be highly overstated, because the processes of the ions loss on the dust particle surface bring about the reduction of ion concentration in the surface layer. For further estimation, note that $Z_i \tilde{n}_i / Z_d n_d$ always exceeds unity.

We will now investigate the dependence of the resultant force on the dimensionless parameter ξ. We will treat the asymptotic behavior according to Eq. (18) for high and low values of ξ. For this purpose, at $\xi \gg 1$, we will use the expansion

$$\sqrt{\pi}\xi e^{\xi^2}\operatorname{erfc}(\xi) \approx 1 + \sum_{m=1}^{\infty} (-1)^m \frac{1 \times 3 \times \ldots \times (2m-1)}{(2\xi^2)^m}.$$

Then, we retain only the first two nonzero terms in Eq. (17) to derive

$$\Phi(\xi) \approx \frac{3}{2} - \frac{15}{4}\frac{1}{\xi^2}. \tag{21}$$

For low values of ξ, series expansion (17) gives

$$\Phi(\xi) \approx \xi^2. \tag{22}$$

A graph of $\Phi(\xi)$ is given in Fig. 3. One can see in this graph that $\Phi(\xi)$ is a monotonic and bounded function, $0 < \Phi(\xi) < 3/2$.

We will write the expression for force in two asymptotic expressions given above, with due regard for Eq. (20). In the case of validity of Eq. (21), the resultant force has the form

$$F_d \approx Z_d e E_0 \left\{\frac{3}{2}\beta\left(1 + \frac{1}{P}\right) - 1\right\}. \tag{23}$$

Because, under conditions of the majority of experiments, the quantity $Z_i e|\varphi_0|/T_i \sim T_e/T_i$ is much greater than unity, one can see in Eq. (15) that the situation for which the latter formula is valid is realized if the interaction of ions with neutral gas atoms does not prevail too strongly over their interaction with the dust component. We also find that, in this case, a dust particle behaves in the external field as if it possesses a positive charge.

If, as previously, we assume that $Z_i e|\varphi_0|/T_i \sim T_e/T_i \gg 1$, the other limiting case will take place, when the relation $n_0\sigma_0/n_d\pi a^2 \gg 1$ is valid, i.e., the basic relaxation mechanism for ions is their interaction with neutral gas. Then, we substitute Eq. (22) into (18) and take into account the previous inequality to derive

$$F_d \approx Z_d e E_0 \left\{\beta \frac{Z_i e|\varphi_0|}{T_i}\frac{n_d \pi a^2}{n_0 \sigma_0}\left(1 + \frac{1}{P}\right) - 1\right\}. \tag{24}$$

In this limit, a particle will behave in the external field as negatively charged; however, a reverse situation is also possible in the case of a certain combination of parameters. In the general case, the dependence of the effective charge of a dust particle on the parameters of the system $n_0\sigma_0/n_d\pi a^2$ and on $Z_i e|\varphi_0|/T_i$ is given in Fig. 4. The charge is expressed in Z_d units, and the parameter P is taken to be 10^2.

In conclusion, we will dwell on the ratio $Z_i e|\varphi_0|/T_i$, which is always encountered in formulas of the orbital motion limit. As was already mentioned above, this parameter is the ratio of energy acquired by an ion in the field of a macroparticle after traveling a distance equal to the free path to the thermal energy of the ion. The formulas derived by us are valid when the ion free path exceeds the Debye radius in plasma, but they are readily generalized to the opposite case. For this purpose, it is sufficient to replace $Z_i e|\varphi_0|/T_i$ in the formulas by $Z_i e\Delta U/T_i$ (see Eq. (6)) and assume that $Z_i e\Delta U \ll T_i$. Then, after transformations, formula (18) will take the form

$$F_d \approx Z_d e E_0 \left\{\frac{(3/2)\beta(1 + 1/P)}{1 + n_0\sigma_0/n_d\pi a^2} - 1\right\}. \tag{25}$$

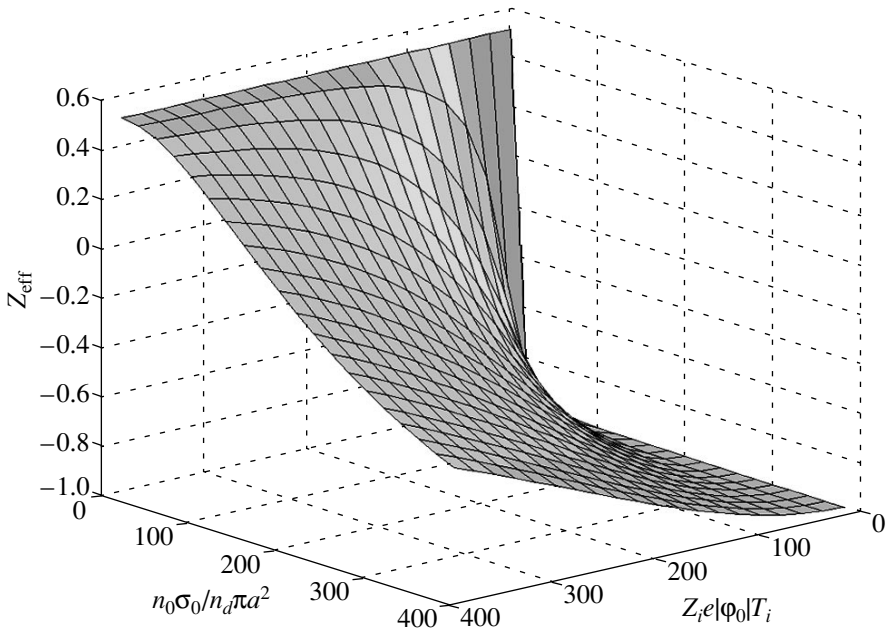

Fig. 4. The effective charge of a macroparticle as a function of the parameters $n_0\sigma_0/n_d\pi a^2$ and $Z_i e|\varphi_0|/T_i$. The charge is expressed in Z_d units, and the parameter P is taken to be 10^2.

This formula corresponds to the hydrodynamic approximation. Its characteristic feature is that no dependence on the ion temperature appears in the final expression for force. As previously, the sign of force may differ and is defined by the plasma parameters.

3. DISCUSSION

The basic result obtained by us in the preceding section is that the presence of plasma may strongly affect the behavior of a dust particle in an external electric field. This brings about the emergence of an additional mechanism of interaction in a plasma–dust system; under certain conditions, this mechanism may play a more important part than even the electrostatic repulsion of particles.

The behavior of the system as a whole is determined by the wide set of parameters, which includes the degree of ionization, the electron and ion temperature, and the pressure and composition of neutral gas, as well as the concentration of dust and the size of its particles. It is also necessary to take into consideration the properties of the material from which the dust is formed. In our model, we assumed that a particle consists of a conducting material; it is for this case that the formulas derived above are valid. Therefore, the dipole moment acquired by dust particles in the electric field of the neighbors and leading, in the final analysis, to the attraction of the dust particles via redistribution of plasma flows may actually be much smaller than in our model. This must be borne in mind when performing estimations for the conditions of a real experiment. Here, we consider qualitatively the dependence of dust particle interaction on a set of external parameters.

In simulating the behavior of dust particles, the shielded Coulomb potential is usually used as the interaction potential. Because the dust particles carry significant like charges, this potential brings about their strong repulsion from one another. Such an effect is indeed observed in most of the experiments involving plasma–dust crystals [2–6, 10–14]. Ordered structures usually arise in specially constructed traps, whose operating principle depends on the experimental conditions and on the special features of the experimental facility. In the vertical direction, the dust cloud is usually maintained owing to the balance of the gravitational and electrostatic forces; in the horizontal plane, the trap is provided either by the gas-discharge chamber walls charged to the floating potential in the plasma or by the specially created configuration of the electric field. In all of the cases described, the ordered structure being formed is not a crystal with a free boundary.

The typical parameters for such experiments [10] are as follows: the gas pressure in the gas-discharge chamber is of the order of 0.1–1 Torr; the electron and ion concentration is approximately 10^8 to 10^{10} cm^{-3}; the electron temperature corresponds to 2–4 eV; and the gas and ion temperature is usually equal to room temperature, i.e., about 0.025 eV. We assume the cross section of ion interaction with neutral gas, which we will need for estimation, to be 10^{-15} cm^2. We will be interested primarily in the general dependence of the behavior of crystal structures in plasma on the neutral gas pressure. Figure 5 gives the dependence of the effective

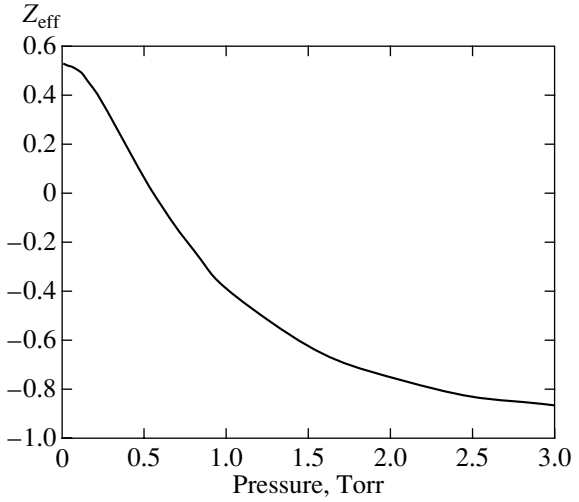

Fig. 5. The effective charge of a macroparticle as a function of the neutral gas pressure. The charge is expressed in Z_d units, $T_i = 0.025$ eV, $T_e = 3.0$ eV, $a = 10$ μm, $n_d = 10^5$ cm^{-3}, $\sigma_0 = 10^{-15}$ cm^2, $P = 10^2$.

charge of a dust particle on the pressure of neutral component. One can see in the figure that some critical pressure exists above which the particles in the external field behave as negatively charged, and, consequently, the entire structure is stably confined in the trap. If the gas pressure drops below the critical value, the particle behavior is reversed. As a result, the dust structure can no longer be held by the field in the state of levitation and must collapse. Such a behavior of crystal was actually observed in the experiment described by Pieper *et al.* [11]. The values of critical pressure given in [11] vary slightly for different gases but are of the same order of 0.5–1 Torr. The only exception from the general pattern is helium, for which the dependence of crystal stability on the pressure of neutral component is inverse. Note that the pressure decrease may also bring about the melting of a crystal, with the system parameters being in the vicinity of the critical point for which the effective particle charge is close to zero. The melting of a crystal with decreasing pressure of neutral gas was observed in a number of studies [12–14].

We have found that, under conditions of experiments involving plasma–dust crystals, Coulomb attraction is of prevailing importance in the particle interaction. For such systems, the dust concentration is relatively low. Meanwhile, another wide scope of phenomena is likewise of great interest. This scope includes processes of dust particle growth and cluster formation. The main characteristic feature of such systems is the high level of dust content in the volume taken up by the plasma. The process of particle growth is very intense in spite of the fact that the particles carry significant like charges. And the fact that the behavior of particles in an external field may vary depending on the conditions being realized can play an important part in analyzing the given phenomenon. We will only outline some steps. So far, we treated the dust concentration n_d and the particle size a as independent parameters. Meanwhile, in a system in which particle growth is possible, these quantities are related to each other. The main characteristic quantity in this case is the amount of dust matter in the volume. Then, the relation between the particle concentration and size may be given by

$$\frac{4}{3}\pi a^3 n_d = \frac{m}{\rho V}. \tag{26}$$

Here, m is the mass of dust matter in the volume, V is the volume filled with dust particles, and ρ is the density of dust matter. For simplicity, we will assume that all macroparticles are of the same size. We express the concentration of particles in terms of their size and the amount of dust matter in the volume to represent the parameter $n_0\sigma_0/n_d\pi a^2$ in the form

$$\frac{n_0\sigma_0}{n_d\pi a^2} = \Omega a. \tag{27}$$

We see that the quantity $n_0\sigma_0/n_d\pi a^2$ increases linearly with the dust particle size, and the proportionality coefficient is defined by the external factors, namely, by the pressure of neutral gas and its composition, as well as by the mass and density of dust matter in the plasma volume,

$$\Omega \sim n_0\sigma_0\frac{\rho V}{m}. \tag{28}$$

As follows from Fig. 4, the increase in the quantity $n_0\sigma_0/n_d\pi a^2$ brings about a reduction of the effective charge; this means that, as the dust particle size increases, the effective charge of dust particles must decrease. Consider the effect of the particle size on the rate of particle growth. For a certain combination of the system parameters, the asymmetry of plasma flows leads to the positive effective charge of the dust particles; this charge determines the system behavior in the external field. This means that particles in such a system must be attracted to one another, even though their like static charges are very high. Therefore, our model enables one to explain the extremely high rate of dust particle growth in a plasma, which was observed in numerous experiments [15–19].

The effect of the particle size on the particle growth rate is usually manifested in the fact that, beginning with some particle size, the rate of dust particle growth decreases abruptly. This becomes clear if we recall that, as the size of particles increases, their effective charge decreases and with time must become negative. The collision cross section of dust particles with one another must be reduced appreciably, which will have an immediate effect on the rate of their growth.

The agglomeration of dust particles and growth of clusters may occur not in any system. Certain condi-

tions are required for this to take place. In our model, the main prerequisite for a fast growth of particles is the presence of a positive effective particle charge; this means that the quantity Ωa must be less than some critical value. One can see from expression (28) that this may be accomplished by increasing the mass of dust matter in the plasma volume. This inference agrees well with the observation results, because the high dust content in the volume is a typical condition for most experiments in studying the processes of dust formation growth.

The model treated in this paper describes only one of the possible mechanisms of macroparticle growth in plasma. Detailed treatment of such processes is the subject for separate investigation.

Along with the phenomena treated above, processes associated with phase transitions in plasma–dust systems have been studied extensively in recent years. In this paper, we have already touched upon this subject when discussing the melting of crystal structures. The existence of no less interesting a phenomenon is reported in [20, 21]. This phenomenon consists in that regions almost completely free of particles may form in dust clouds with a high dust content. A clearly defined boundary is observed between these regions and the dust cloud, and a direct correlation is observed between the system parameters and the very possibility of formation of such regions. This phenomenon may be interpreted as the gas–liquid transition in a plasma–dust system.

Goree *et al.* [22] treated one of the possible theoretical interpretations of this phenomenon. They link the formation of voids in a dust cloud to the formation of regions in which the process of ionization is more intense compared with the remaining volume of the plasma. The increase in the rate of ionization is provided for by the excess of electrons in the resultant void compared with the volume of the dust cloud, because the electrons in the cloud are rapidly absorbed by dust particles, and the electron concentration decreases. The increased rate of ionization results in the emergence of an additional ion flow directed into the external (with respect to the void) space. It is this flow that maintains the equilibrium of the interface between the dust cloud and the void. This approach implies the presence of some collective effect of ion flows on the already existing interface between two media. However, the very stage of phase transition and the conditions under which it arises remain outside of the scope of the suggested theory. Obviously, the nature of the phenomenon being treated will be hard to understand without invoking the mechanisms of interaction between individual particles. From this standpoint, the model of attraction between negatively charged dust particles suggested by us may prove quite useful in trying to explain the presence of surface tension at the boundary of a dust cloud or the conditions for the emergence of instabilities leading to a phase transition.

In conclusion, note that the model suggested in this paper is not only one among other existing possibilities and should be treated as just one of the starting points for further research.

ACKNOWLEDGMENTS

This study was supported in part by the Russian Foundation for Basic Research (project nos. 01-02-17726 and 00-15-96554).

REFERENCES

1. V. N. Tsytovich, Usp. Fiz. Nauk **167**, 57 (1997) [Phys. Usp. **40**, 53 (1997)].
2. J. H. Chu, J. B. Du, and Lin I, J. Phys. D **27**, 296 (1994).
3. J. H. Chu and Lin I, Physica A (Amsterdam) **205**, 183 (1994).
4. J. H. Chu and Lin I, Phys. Rev. Lett. **72**, 4009 (1994).
5. H. Thomas, G. Morfill, V. Demmel, *et al.*, Phys. Rev. Lett. **73**, 652 (1994).
6. A. Melzer, T. Trottenberg, and A. Piel, Phys. Lett. A **191**, 301 (1994).
7. E. Wigner, Trans. Faraday Soc. **34**, 678 (1939).
8. H. Ikezi, Phys. Fluids **29**, 1764 (1986).
9. Ya. K. Khodataev, R. Bingham, V. P. Tarakanov, *et al.*, Fiz. Plazmy **22**, 1028 (1996) [Plasma Phys. Rep. **22**, 932 (1996)].
10. A. P. Nefedov, O. F. Petrov, and V. E. Fortov, Usp. Fiz. Nauk **167**, 1215 (1997) [Phys. Usp. **40**, 1163 (1997)].
11. J. Pieper, J. Goree, and R. A. Quinn, J. Vac. Sci. Technol. **14**, 519 (1996).
12. H. Thomas and G. Morfill, Nature **379**, 806 (1996).
13. A. Melzer, A. Homann, and A. Piel, Phys. Rev. E **53**, 2757 (1996).
14. J. Pieper and J. Goree, Phys. Rev. Lett. **77**, 3137 (1996).
15. G. Selwyn, J. McKillop, K. Haller, and J. Wu, J. Vac. Sci. Technol. A **8**, 1726 (1990).
16. G. Jellum, J. Daugherty, and D. Graves, J. Appl. Phys. **69**, 6923 (1991).
17. G. Praburam and J. Goree, Astrophys. J. **441**, 830 (1995).
18. D. Samsonov and J. Goree, J. Vac. Sci. Technol. A **17**, 2835 (1999).
19. K. Koga, Y. Matsuoka, K. Tanaka, *et al.*, Appl. Phys. Lett. **77**, 196 (2000).
20. D. Samsonov and J. Goree, Phys. Rev. E **59**, 1047 (1999).
21. G. E. Morfill, H. M. Thomas, U. Konopka, *et al.*, Phys. Rev. Lett. **83**, 1598 (1999).
22. J. Goree, G. E. Morfill, V. N. Tsytovich, and S. V. Vladimirov, Phys. Rev. E **59**, 7055 (1999).

Translated by H. Bronstein

Journal of Experimental and Theoretical Physics, Vol. 94, No. 6, 2002, pp. 1114–1120.
Translated from Zhurnal Éksperimental'noĭ i Teoreticheskoĭ Fiziki, Vol. 121, No. 6, 2002, pp. 1298–1305.

FLUIDS

Forced Oscillations of a Magnetic Liquid Drop

Yu. K. Bratukhin[a] and A. V. Lebedev[b, *]

[a]*Perm State University, ul. Bukireva 15, Perm, 614000 Russia*
[b]*Institute of Mechanics of Continua, Ural Division, Russian Academy of Sciences, ul. Akademika Koroleva 1, Perm, 614013 Russia*
**e-mail: lav@icmm.ru*

Received October 16, 2001

Abstract—Oscillations of a magnetic liquid drop suspended in a nonmagnetic viscous medium were studied analytically and experimentally. Oscillations occurred under the action of a linearly polarized alternating magnetic field. The frequency dependence of the amplitude and phase of oscillations was determined in the weak field and laminar flow approximation. The influence of the viscosity of the liquid on the natural drop oscillation frequency was studied. The obtained solution was used in experiments on determining interphase surface tension. *© 2002 MAIK "Nauka/Interperiodica".*

1. INTRODUCTION

Recently, several works concerned with motion and deformation of a magnetic liquid drop in various variable and constant fields have been published [1–7]. The problem of the equilibrium shape of a drop in a constant magnetic field and the methods for theoretical description are considered in detail in [8], where a bibliography on the problem is also given. The shape of a drop is determined by balance of magnetic and surface tension forces. In a variable field, inertia and viscosity of the drop and the surrounding liquid should be taken into account in addition to surface and magnetic forces. It seems at first sight that the problem of drop oscillations turns into a direct analogue of the problem of a harmonic oscillator with viscous friction. Precisely from this standpoint, the problem is considered in [9]. In reality, this analogy is not complete because the equations of motion of a viscous liquid are equations of a higher order. In particular, taking into account viscous friction introduces corrections into the natural frequency of oscillations, which ceases to coincide with the well-known Rayleigh frequency [10, 11]. The natural oscillation frequency means the frequency at which the phase lag between drop and magnetic force oscillations equals $\pi/2$. For a harmonic oscillator, this frequency is independent of friction. For an oscillating drop, the presence of viscous friction changes the type of liquid flow and, accordingly, its effective mass, which is the reason why the eigenfrequency of drop oscillations depends on the viscosity of the liquid.

2. PROBLEM STATEMENT

Let a magnetic liquid drop (the first medium) be placed into a nonmagnetic liquid filling the whole space (the second medium). As an external force that causes system oscillations, we use a linearly polarized alternating magnetic field. The field defined at infinity,

$$\mathbf{H}_\infty = H_\infty \exp(-i\gamma t)\mathbf{e}_z,$$

changes in magnitude at frequency γ [we use the right Cartesian (x, y, z) and spherical (r, θ, φ) coordinate systems with the origin at the center of mass of the drop and the polar axis along $\mathbf{H}_\infty$, $\mathbf{e}_z$ is the unit vector of axis z]; the liquid is quiescent at infinity, there is no gravity, and pressure is constant.

We assume that all parameters of the liquids [densities ρ_i, kinematic and dynamic viscosity coefficients ν_i and η_i (i = 1 and 2 for the first and second media, respectively), surface tension coefficient at the interliquid boundary σ_0, and drop magnetic susceptibility χ] are constant, and the liquids are insoluble in each other (mutually saturated), incompressible, and nonconducting.

Drop oscillations at which its shape slightly deviates from spherical are considered,

$$r = R(\theta, t) = a(1 + \varepsilon(\theta, t)), \quad |\varepsilon(\theta, t)| \ll 1$$

(a is the radius of the unperturbed drop).

The characteristic relaxation time of magnetization (τ) is of the order of 10^{-4}–10^{-6} s for magnetic liquids [13] and is small compared with the period of drop oscillations ($\geq$0.1 s). This means that the magnetization of liquids can to high accuracy be considered equilibrium. Under these conditions, thermal energy released in periodic remagnetization of the magnetic liquid does not cause noticeable drop heating. Indeed, the radial temperature difference within the drop is

$$\Delta T = \frac{\chi_2 \gamma H_\infty^2 a^2}{12(1 + 4\pi\chi_1/3)^2 \lambda},$$

where λ is the heat conductivity of the liquid, and χ_1 and χ_2 are the real and imaginary dynamic susceptibility parts. For the concentrated liquid used in experiments ($a < 0.5$ cm, $\chi_1 \approx 0.5$, $\chi_2 \approx 0.002$, $H_\infty \approx 10$ Oe, $\gamma \approx 1$ Hz, and $\lambda \approx 2 \times 10^4$ erg/(cm s K)), the temperature drop was of the order of 10^{-7} K.

We will introduce dimensionless variables. For this purpose, we select the following values as measurement units: length $[L] = a$, velocity $[v] = \nu_1/a$, pressure $[p] = \eta_1\nu_1/a_2$, time $[t] = a^2/\nu_1$, magnetic field strength $[H] = \sqrt{\nu_1\eta_1/a^2}$, magnetic field induction $[B] = [H]$, and magnetization $[M] = [H]$. The problem includes the following dimensionless parameters: density $\rho = \rho_2/\rho_1$; kinematic and dynamic drop viscosity coefficients $\nu = \nu_2/\nu_1$ and $\eta = \eta_2/\eta_1$, respectively; surface tension coefficient $\sigma = \sigma_0 a/\eta_1\nu_1$; external field amplitude far from the drop $H_0 = H_\infty/[H]$; and equilibrium susceptibility χ. (Note that $\rho = \eta/\nu$.)

Under these conditions, the distribution of velocities $\mathbf{v}_i$, pressures p_i, and magnetic fields $\mathbf{B}_i$ and $\mathbf{H}_i$ in both media ($i = 1$ and 2) and magnetization $\mathbf{M}$ in the drop are determined by the following system of equations of the hydrodynamics and electrodynamics of continua [10, 12]:

$$\frac{\partial \mathbf{v}_1}{\partial t} = -\nabla p_1 + \Delta \mathbf{v}_1, \quad \rho\frac{\partial \mathbf{v}_2}{\partial t} = -\nabla p_2 + \eta\Delta \mathbf{v}_2 + \mathbf{f},$$

$$\mathrm{div}\mathbf{v}_1 = \mathrm{div}\mathbf{v}_2 = 0, \quad \mathrm{curl}\,\mathbf{H}_1 = \mathrm{curl}\,\mathbf{H}_2 = 0,$$

$$\mathrm{div}\mathbf{B}_1 = \mathrm{div}\mathbf{B}_2 = 0, \quad \mathbf{B}_1 = \mathbf{H}_1, \quad \mathbf{B}_2 = \mathbf{H}_2 + \mathbf{M}.$$

The density of magnetic volume forces $\mathbf{f}$ in the drop can be transformed to the gradient form and included in pressure taking into account that the magnetic permeability is constant ($\nabla\mu = 0$) and susceptibility χ linearly depends on substance density ($\mathbf{f} = 0$ in a nonmagnetic liquid) [13].

These equations should be augmented by the obvious conditions at infinity and in the center of the drop,

$$r \longrightarrow \infty\text{: } p_1 \text{ and } H_0 \text{ are constant, } \mathbf{v}_1 = 0;$$

$$r = 0\text{: } p_2 \text{ and } \mathbf{v}_2 \text{ are limited.}$$

At the drop surface $r = R(\theta, t) = 1 + \varepsilon(\theta, t)$, the requirements of vanishing of normal velocity components and continuity of tangent velocity components and normal and tangent stress components should be satisfied, that is,

$$v_{r1} = v_{r2} = \frac{\partial\varepsilon}{\partial t}, \quad \mathbf{v}_1 = \mathbf{v}_2 \ (v_{r1} = v_{r2}, v_{\theta 1} = v_{\theta 2}),$$

$$B_{n1} = B_{n2}, \quad H_{\tau 1} = H_{\tau 2},$$

$$(p_1 - p_2 + 2D\sigma)R = (\sigma_{rr}^{(1)} - \sigma_{rr}^{(2)})R \qquad (1)$$

$$-(\sigma_{r\theta}^{(1)} - \sigma_{r\theta}^{(2)})\frac{\partial\varepsilon}{\partial\theta},$$

$$-(p_1 - p_2 + 2D\sigma)\frac{\partial\varepsilon}{\partial\theta}$$

$$= (\sigma_{\theta r}^{(1)} - \sigma_{\theta r}^{(2)})R - (\sigma_{\theta\theta}^{(1)} - \sigma_{\theta\theta}^{(2)})\frac{\partial\varepsilon}{\partial\theta}.$$

Here, the components of the symmetrical stress tensor σ_{ik} include the hydrodynamic and magnetic components. In particular, for the second phase [13],

$$\sigma_{ik}^{(2)} = \eta\left(\frac{\partial v_i}{\partial x_k} + \frac{\partial v_k}{\partial x_i}\right) + H_iH_k$$

$$+ \frac{1}{2}\delta_{ik}H_j^2 + \frac{1}{2}(M_iH_k + M_kH_i).$$

Equations (1) are written on the assumption of smallness of ε. Note that the requirements of continuity of velocity components tangent to the drop surface are equivalent to the requirement of continuity of velocity vectors on both sides of the interface.

The mean deformed drop curvature $2D$ is calculated by the differential geometry formulas

$$2D = 2 - (\Delta + 2)\varepsilon + 2\varepsilon(\Delta + 1)\varepsilon + O(\varepsilon^3),$$

where Δ is the angular Laplace operator.

A solution to the problem will be sought in the form of the series

$$\mathbf{B}_1 = \mathbf{H}_1 = H_{r1}\mathbf{e}_r + H_{\theta 1}\mathbf{e}_\theta = \mathbf{H}^{(1)} + \mathbf{H}^{(2)} + \ldots,$$

$$\mathbf{H}_2 = H_{r2}\mathbf{e}_r + H_{\theta 2}\mathbf{e}_\theta = \mathbf{h}^{(1)} + \mathbf{h}^2 + \ldots,$$

$$\mathbf{B}_2 = \mathbf{h}^{(1)} + \mathbf{m}^{(1)} + \mathbf{h}^{(2)} + \mathbf{m}^{(2)} + \ldots,$$

$$\mathbf{v}_1 = \mathbf{U}^{(1)} + \mathbf{U}^{(2)} + \ldots, \quad \mathbf{v}_2 = \mathbf{u}^{(1)} + \mathbf{u}^{(2)} + \ldots,$$

$$p_1 = p_0 + Q^{(1)} + Q^{(2)} + \ldots,$$

$$p_2 = 2\sigma + q^{(1)} + q^{(2)} + \ldots\varepsilon = s^{(1)} + s^{(2)} + \ldots,$$

in which each succeeding term is an order of magnitude smaller than the preceding one (p_0 is pressure at infinity). Field amplitude H_0 far from the drop is assumed to be a small parameter, and liquid flow is assumed to be laminar. Its intensity is low because of smallness of amplitude H_0.

Functions of the first approximation. In the linear approximation, the system of hydrodynamic equations admits the trivial solution

$$\mathbf{U}^{(1)} = \mathbf{u}^{(1)} = Q^{(1)} = q^{(1)} = s^{(1)} = 0.$$

The known solution to the magnetic part of the problem can conveniently be written in the form

$$\mathbf{H}^{(1)} = \nabla U\exp(-i\gamma t), \quad \mathbf{h}^{(1)} = \nabla u\exp(-i\gamma t),$$

$$U = (H_0 r + Cr^{-2})\cos\theta, \quad u = \mathscr{H}r\cos\theta = \mathscr{H}z.$$

The $\mathcal{H}$ and C integration constants are determined from the boundary conditions

$$C = -\frac{\chi\mathcal{H}}{3}, \quad \mathcal{H} = \frac{3H_0}{3+\chi}.$$

It follows that, in the first approximation with respect to field amplitude at infinity H_0, the drop remains spherical, and field $\mathbf{h}^{(1)}$ is uniform within the drop.

Functions of the second approximation. Combining second-order terms yields

$$\frac{\partial \mathbf{U}^{(2)}}{\partial t} = -\nabla Q^{(2)} + \Delta \mathbf{U}^{(2)},$$

$$\rho\frac{\partial \mathbf{u}^{(2)}}{\partial t} = -\nabla q^{(2)} + \eta\Delta \mathbf{u}^{(2)},$$

$$\mathrm{div}\mathbf{U}^{(2)} = 0, \quad \mathrm{div}\mathbf{u}^{(2)} = 0,$$

$$\mathrm{curl}\,\mathbf{H}^{(2)} = 0, \quad \mathrm{div}\mathbf{H}^{(2)} = 0, \quad \mathrm{curl}\,\mathbf{h}^{(2)} = 0,$$

$$\mathrm{div}\mathbf{b}^{(2)} = 0,$$

$$\mathbf{b}^{(2)} = \mathbf{h}^{(2)} + \mathbf{m}^{(2)}, \quad \mathbf{m}^{(2)} = \chi\mathbf{h}^{(2)},$$

$$r = 1 + s^{(2)}: U_r^{(2)} = u_r^{(2)} = \frac{\partial s^{(2)}}{\partial t}, \quad U_\theta^{(2)} = u_\theta^{(2)},$$

$$H_r^{(2)} = h_r^{(2)} + m_r^{(2)}, \quad H_\theta^{(2)} = h_\theta^{(2)},$$

$$Q^{(2)} - q^{(2)} - \sigma(\Delta+2)s^{(2)} = 2\frac{\partial}{\partial r}(U_r^{(2)} - \eta u_r^{(2)}) + \Delta p_M,$$

$$0 = \left(\frac{\partial}{\partial r} - 1\right)(U_\theta^{(2)} - \eta u_\theta^{(2)}) + \frac{\partial}{\partial\theta}(U_r^{(2)} - \eta u_r^{(2)}).$$

All second approximation functions are zero at infinity.

After necessary transformations, we obtain the following equations for magnetic pressure jump Δp_M ($\omega \equiv 2\gamma$):

$$\Delta p_M = \frac{1}{2}(H_{r1}^2 - H_{\theta 1}^2 - 2\mu H_{r2}^2 + H_{r2}^2 + H_{\theta 2}^2)$$

$$= \frac{1}{2}\chi^2\mathcal{H}^2\cos^2\theta\exp(-i\omega t).$$

This Δp_M pressure drop deforms the drop along the field at twice the field frequency and turns it into an ellipsoid of revolution with

$$r = 1 + sP_2\exp(-i\omega t)$$

[$P_2 = (3\cos^2\theta - 1)/2$ is the standard second-order Legendre polynomial]. Note that the magnetic component of tangential (along the meridian) stresses on the surface of the undeformed drop identically equals zero,

$$H_{r1}H_{\theta 1} - \mu H_{r2}H_{\theta 2} = 0.$$

Also zero are second-order terms for magnetic fields,

$$\mathbf{H}^{(2)} = 0, \quad \mathbf{h}^{(2)} = 0.$$

The exact solution of the hydrodynamic part of the second approximation can be written in the form

$$\mathbf{U}^{(2)} = \left[\frac{A}{r^4} + \frac{B}{r}h_2^{(1)}(\mu_1 r)\right]P_2\mathbf{e}_r$$

$$+\left\{-\frac{A}{3r^4} + \frac{B}{2r}\left[h_2^{(1)}(\mu_1 r) - \frac{\mu_1 r}{3}h_3^{(1)}(\mu_1 r)\right]\right\}$$

$$\times r\nabla P_2\exp(-i\omega t),$$

$$\mathbf{u}^{(2)} = \left[ar + \frac{b}{r}j_2(\mu_2 r)\right]P_2\mathbf{e}_r$$

$$+\left\{\frac{ar}{2} + \frac{b}{3r}\left[-j_2(\mu_2 r) + \frac{\mu_2 r}{2}j_1(\mu_2 r)\right]\right\}r\nabla P_2\exp(-i\omega t),$$

$$Q^{(2)} = -\mu_1^2\frac{AP_2}{3r^3}\exp(-i\omega t),$$

$$q^{(2)} = \left(\rho\mu_1^2 a\frac{r^2P_2}{2} + \mathrm{const}\right)\exp(-i\omega t),$$

$$\mu_1^2 = i\omega, \quad \mu_2^2 = \frac{i\omega}{\nu}, \quad \mathrm{const} = \frac{1}{2}\chi\mathcal{H}^2 - \frac{1}{6}\chi^2\mathcal{H}^2.$$

Here, $j_n(z)$ and $h_n^{(1)}(z)$ are the Bessel and Hankel nth-order spherical functions of the first kind, respectively [14]. The constant includes the constant contributions of magnetic pressures.

Five integration constants A, B, a, b, and s are determined from the boundary conditions

$$A + Bh_2^{(1)}(\mu_1) = -\mu_1^2 s, \quad a + bj_2(\mu_2) = -\mu_1^2 s,$$

$$-2A + B[3h_2^{(1)}(\mu_1) - \mu_1 h_3^{(1)}(\mu_1)]$$

$$= 3a + b[-2j_2(\mu_2) + \mu_2 j_1(\mu_2)],$$

$$16A + B$$

$$\times[3\mu_1 h_1^{(1)}(\mu_1) - (9+\mu_1^2)h_2^{(1)}(\mu_1) + 5\mu_1 h_3^{(1)}(\mu_1)]$$

$$= 6a + b[\mu_2^2 j_0(\mu_2) - 5\mu_2 j_1(\mu_2) + 16j_2(\mu_2)],$$

$$-\mu_1^2\frac{A}{3} - \rho\mu_1^2\frac{a}{2} + 4\sigma s = 2\left\{-4A - Bh_2^{(1)}(\mu_1)\right.$$

$$\left.+\mu_1 B\left[h_1^{(1)}(\mu_1) - \frac{3h_2^{(1)}(\mu_1)}{\mu_1}\right]\right\}$$

$$-2\eta\left\{a - bj_2(\mu_2) + \mu_2 b\left[j_1(\mu_2) - \frac{3j_2(\mu_2)}{\mu_2}\right]\right\} + \frac{1}{3}\chi^2\mathcal{H}^2.$$

Of greatest interest is the amplitude s of drop oscillations. Therefore, here is the formula for determining it [note that $(1 + s)$ is the semimajor axis of the ellipsoid of revolution

$$1 = \frac{x^2 + y^2}{(1 - s/2)^2} + \frac{z^2}{(1 + s)^2},$$

into which the drop transforms at a maximum deviation from the spherical shape $r = 1$]:

$$s = \frac{2\chi^2\mathcal{H}^2}{\mu_1^2}\frac{\begin{vmatrix} a_2 & a_3 \\ b_2 & b_3 \end{vmatrix}}{\begin{vmatrix} a_1 & a_2 & a_3 \\ b_1 & b_2 & b_3 \\ c_1 & c_2 & c_3 \end{vmatrix}},$$

$$a_1 = 16(\eta - 1), \quad a_2 = \eta\mu_2^2,$$
$$a_3 = 2\eta - 2 - K, \quad b_1 = 5,$$
$$b_2 = 5 - J, \quad b_3 = 1, \qquad (2)$$
$$c_1 = 2\mu_1^2 + 3\rho\mu_1^2 - 12\eta - 48 + 24\sigma/\mu_1^2,$$
$$c_2 = 12\eta J - 60\eta + 3\rho\mu_1^2, \quad c_3 = 2K - 12,$$
$$J = \mu_2\frac{j_1(\mu_2)}{j_2(\mu_2)}, \quad K = \frac{3i + 3\mu_1 - i\mu_1^2}{\mu_1 + i}.$$

Forced drop oscillations. Let us write the complex amplitude s of drop oscillations satisfying (2) in the exponential form

$$s = |s|\exp(i\alpha),$$

where $|s|$ is the amplitude of oscillations and α is the phase shift between drop oscillations and the driving force. [Note that positive α values correspond to "time lag" of oscillations with respect to external actions. This time lag is proportional to $\exp(-i\omega t)$.] According to the general theory of forced oscillations, the amplitude of drop oscillations in the presence of friction is maximum at resonance frequency ω_*, and phase shift α equals $\pi/2$ at eigenfrequency ω_0.

First consider a nondissipative system on the assumption that both liquids are ideal. For this purpose, we will pass to the dimensional form of (2) and let the viscosities of both liquids tend to zero. This gives resonance frequency ω_* in the well-known form [11]

$$\omega_*^2 = \frac{24}{3\rho_2 + 2\rho_1}\frac{\sigma_0}{a^3}. \qquad (3)$$

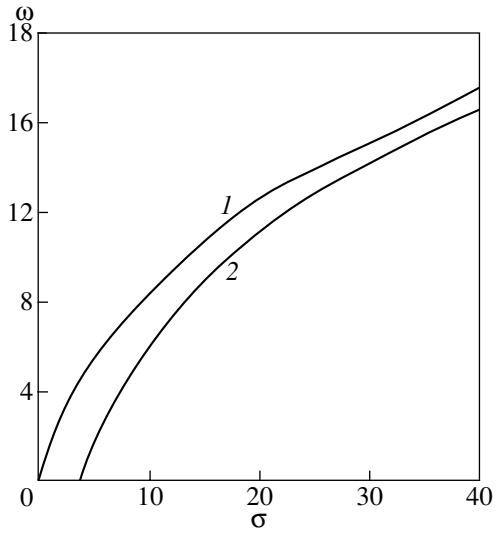

Fig. 1. Resonance frequency ω_* (curve *2*) and normal oscillation frequency ω_0 (curve *1*) as functions of dimensionless surface tension σ for a drop of a liquid in a nonviscous gas.

Equation (3) shows that the Rayleigh frequency of drop oscillations $\omega_*^2 = 8\sigma_0/\rho a^3$ in a weightless gas is smaller than the natural oscillation frequency of a weightless gas bubble in the same liquid ($\omega_*^2 = 12\sigma_0/\rho a^3$) by a factor of one and a half. This can be explained by the involvement of only a small amount of the liquid in bubble oscillations (the velocities in the first phase decrease as the distance increases as $1/r^4$, whereas the distance dependence of velocity in the drop is linear). The effective linear dimension of the system is therefore smaller that the radius a of the inclusion.

Consider another particular case of forced oscillations of a viscous liquid drop in a gas. Let us pass to dimensional values, and let viscosity η_1 tend to zero. This gives

$$s = -2\chi^2\mathcal{H}^2\frac{a_2}{a_1b_2 - a_2b_1}, \quad a_1 = 6,$$
$$a_2 = i\omega - 10 + 2J,$$
$$b_1 = 3i\omega - 12 - \frac{24i\sigma}{\omega}, \quad b_2 = 3i\omega - 60 + 12J,$$

where J is determined by (2). The dependences of the resonance frequency ω_* (curve *2*) and natural frequency ω_0 (curve *1*) on the dimensionless surface tension $\sigma = \sigma_0 a/\eta_2\nu_2$ calculated by this equation for a liquid drop in a nonviscous gas are shown in Fig. 1. According to this figure, $\omega_* = 0$ at $\sigma_* = 3.427$. This means that free drop motion caused by initial perturbation will be aperiodic and nonoscillatory at lower σ values (that is, at higher drop viscosities and fixed σ_0).

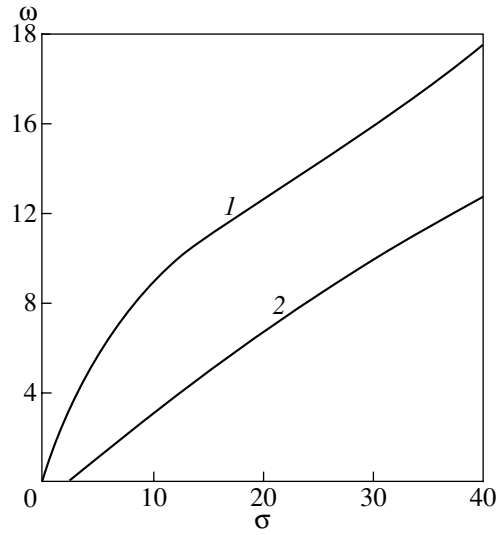

Fig. 2. Resonance frequency ω_* (curve *2*) and normal oscillation frequency ω_0 (curve *1*) as functions of dimensionless surface tension σ for a nonviscous bubble in a liquid.

Using (2) to determine the amplitude and phase of gas bubble oscillations in a liquid requires setting η equal to zero. After necessary transformations, we obtain

$$s = -2\chi^2\mathcal{H}^2\frac{a_2}{a_1b_2 - a_2b_1}, \quad a_1 = 16, \quad a_2 = 2 + K,$$

$$b_1 = 2i\omega - 48 - \frac{24\sigma}{\omega}, \quad b_2 = -12 + 2K.$$

Here, $\sigma = \sigma_0 a/\eta_1\nu_1$ [K is defined in (2)]. The dependences of the resonance frequency ω_* (curve *2*) and the ω_0 frequency (curve *1*) on the dimensionless surface tension for a gas bubble in a viscous liquid are shown in Fig. 2. Bubble free motion will be aperiodic at $\sigma_* < 1.525$. The dependences of the ω_* resonance frequency (curve *2*) and the ω_0 frequency (curve *1*) on the dimensionless viscosity $\eta = \eta_2/\eta_1$ are shown in Fig. 3 for the heterogeneous system "drop in infinite liquid" and the selected dimensionless surface tension value, $\sigma = \sigma_0 a/\eta_1\nu_1 = 10$. The curve separating the regions of aperiodic (region II) and oscillatory (region I) free motion modes on the $\sigma\eta$ plane is shown in Fig. 4 for the same heterogeneous system. Solid circles correspond to various parameters of the liquids used in experiments.

The obtained equations can be applied to solve one of the most complex problems of interphase hydrodynamics, that of determining the interphase surface tension at the boundary between two liquids. The use of computational methods for this purpose is ineffective. The well-known Antonov rule [15] is approximate even for pure liquids. This rule is generally inapplicable to liquids containing colloidal particles coated with a layer of a surface-active substance [3]. The coagulation of particles at the interface endows it with the properties of a rigid film. This substantially distorts the results of tensometric σ_0 measurements, for instance, from the shape of a lying drop or by surface stretching with the use of various bodies.

Applying (2) to determine σ_0 allows the accuracy of measurements to be increased for two reasons. First, the frequency itself can be measured very accurately (many measurements are for this reason reduced to measuring frequencies). Secondly, using (2) eliminates mechanical contact between the surface and sensors of

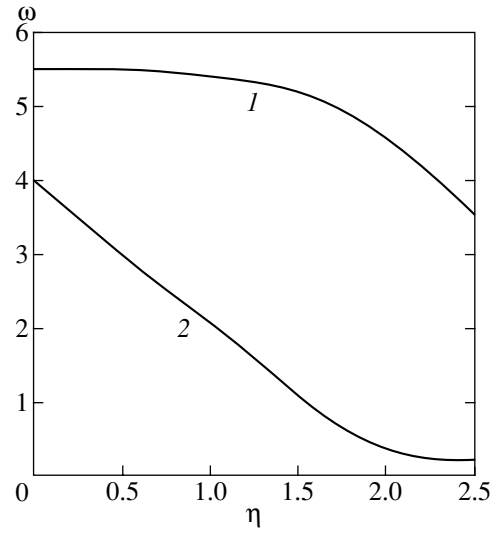

Fig. 3. Resonance frequency ω_* (curve *2*) and normal oscillation frequency ω_0 (curve *1*) as functions of dimensionless viscosity of a heterogeneous system "drop in infinite liquid" for surface tension $\sigma = 10$.

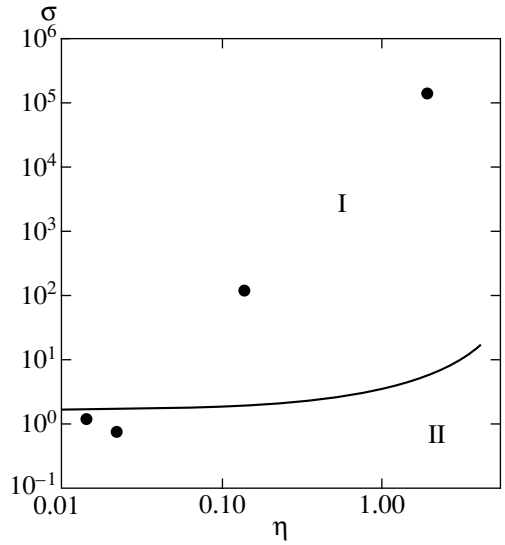

Fig. 4. Curve separating the regions of (I) oscillatory and (II) aperiodic system responses to an external initial perturbation. Solid circles on the $\sigma\eta$ plane correspond to different parameters of the liquids studied in this work.

any kind. In addition, the suggested method can be used to continuously monitor changes in σ_0.

3. EXPERIMENTAL RESULTS

We used a magnetic liquid based on magnetite and decane stabilized by oleic acid. The external media were water, ethylene glycol, glycerol chlorohydrin, and glycerol. These liquids were used because of their low solubilities in hydrocarbons and because they allow a wide range of viscosity values to be covered. The density of the magnetic liquid was varied to equal that of the carrier liquid by changing the concentration of magnetite. The carrier liquid was loaded into a cell with plane transparent walls. To prevent the drop from drifting, it was fixed in the center of the cell with the use of a wire ring of a small diameter (smaller than the diameter of the drop).

A linearly polarized alternating magnetic field of a low frequency (1–10 Hz) was generated with the use of Helmholtz rings fed from a direct current amplifier. A low ohmic resistance was connected in series with the rings, and voltage from this resistance was fed to both inputs of an analog voltage multiplier. The output multiplier voltage was therefore proportional to the square of current intensity in the rings and coincided in phase with the magnetic force that deformed the drop. The phase of drop oscillations was determined with the use of a laser beam. A beam for a helium–neon laser about 0.5 mm in diameter was directed normally to the magnetic field and tangentially to the side surface of the drop in such a way that the intensity of transmitted radiation decreased twofold. The intensity was measured by a photodiode. When the field was switched on, the drop modulated the intensity of light, and a harmonic signal was formed at the output of the photodiode. This signal coincided in phase with drop oscillations. The amplitude of the field was selected from the condition that the illuminated side surface of the drop should be within the diameter of the beam (the signal then remained harmonic). The phase difference between the photodiode current and the signal at the output of the voltage multiplier (that is, the phase of drop oscillations) was measured by an F2-34 digital phase difference meter. The error of phase measurements was 0.02–0.03 deg.

The results obtained in measuring normal drop oscillation frequencies in the four liquids specified above are listed in the table. The parameters of external

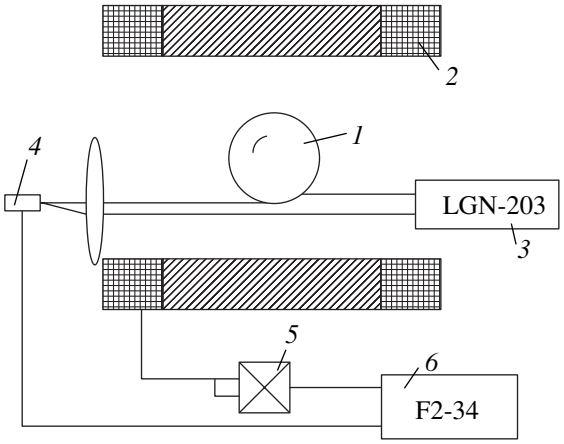

Fig. 5. Scheme of experimental unit: *1*, magnetic liquid drop; *2*, Helmholtz rings; *3*, helium–neon laser; *4*, photodiode; *5*, analog voltage multiplier; and *6*, phase difference meter.

liquids were determined in independent experiments. Their difference from the reference data is explained by the presence of certain amounts of water. Along with liquid parameters, drop diameters *d*, and normal drop oscillation frequencies *f*, the table contains surface tension values calculated taking into account viscosity (σ_0) and in the nonviscous approximation (σ_1). The results of direct interphase surface tension measurements are also given (σ_2). The interphase surface tension was directly determined by analytic balance measurements of the force with which a magnetic liquid film contracted a rectangular wire frame under a layer of a carrier liquid. For a drop suspended in glycerol chlorohydrin, σ_2 was calculated from drop deformation in a constant magnetic field.

The measured σ_2 values exceeded σ_0. In our view, this was caused by coagulation of a thin layer of particles near the drop surface under the action of carrier liquids. This caused the formation of a thin layer of coagulated particles on the drop surface, which hindered drop deformation. In direct σ_2 measurements by stretching the film, the surface was constantly renewed, and the coagulation of particles did not influence the results. For water, which was least soluble in hydrocarbons, the influence of coagulation was virtually unnoticeable (σ_2 was close to σ). For the other liquids, coagulation distorted measurement results. In particular,

Table

Carrier liquid	ρ, g/cm^3	η_1, P	η_2, P	*d*, cm	*f*, Hz	σ_0, dyn/cm	σ_1, dyn/cm	σ_2, dyn/cm
Water	1	0.01	0.0196	0.86	6.56	31.5	28.1	30.3
Ethylene glycol	1.113	0.18	0.025	0.81	3.33	8.41	6.76	10.8
Glycerol chlorohydrin	1.317	1.59	0.035	0.827	1.61	3.73	1.98	4.2
Glycerol	1.251	2.245	0.032	0.734	3.80	13.35	7.35	18.5

coagulation effects manifested themselves by slow changes in the normal drop oscillation frequency.

The σ_0 values calculated taking viscosity into account differed from those obtained in the ideal liquid approximation, σ_1. The difference increased as the viscosity grew. It follows that viscosity influences the normal drop oscillation frequency, and this influence should be taken into account. From the point of view of practical applications, the suggested refined solution to the problem of viscous drop oscillations can serve as a basis for developing a new approach to determining the interphase surface tension [15].

ACKNOWLEDGMENTS

The authors thank A.F. Pshenichnikov, who called their attention to the problem considered in this work and actively participated in discussing its results.

This study was partly supported by the U.S. Civilian Research and Development Foundation for the Independent States of the Former Soviet Union, CRDF award No. PE-009-0.

REFERENCES

1. A. V. Lebedev and K. I. Morozov, Pis'ma Zh. Éksp. Teor. Fiz. **65**, 150 (1997) [JETP Lett. **65**, 160 (1997)].
2. K. I. Morozov, Zh. Éksp. Teor. Fiz. **112**, 1340 (1997) [JETP **85**, 728 (1997)].
3. Yu. K. Bratukhin, A. V. Lebedev, and A. F. Pshenichnikov, Izv. Akad. Nauk, Mekh. Zhidk. Gaza, No. 1, 22 (2000).
4. K. I. Morozov and A. V. Lebedev, Zh. Éksp. Teor. Fiz. **118**, 1188 (2000) [JETP **91**, 1029 (2000)].
5. Yu. I. Dikanskiĭ, M. A. Bedzhanyan, I. Yu. Chuenkova, and V. N. Suzdalev, Magn. Gidrodin., No. 1, 61 (2000).
6. V. V. Chekanov and N. V. Kandaurova, Magn. Gidrodin., No. 1, 69 (2000).
7. E. Janiaud, F. Elias, J.-C. Bacri, *et al.*, Magnetohydrodynamics **4**, 365 (2000).
8. É. Ya. Blum, M. M. Maĭorov, and A. O. Tsebers, *Magnetic Fluids* (Zinatne, Riga, 1989).
9. V. I. Drozdova, Yu. N. Skibin, and V. V. Chekanov, Magn. Gidrodin., No. 4, 17 (1981).
10. L. D. Landau and E. M. Lifshitz, *Course of Theoretical Physics*, Vol. 6: *Fluid Mechanics* (Nauka, Moscow, 1986; Pergamon, New York, 1987).
11. H. Lamb, *Hydrodynamics* (Cambridge Univ. Press, Cambridge, 1932; Gostekhizdat, Moscow, 1947).
12. L. D. Landau and E. M. Lifshitz, *Course of Theoretical Physics*, Vol. 8: *Electrodynamics of Continuous Media* (Nauka, Moscow, 1982; Pergamon, New York, 1984).
13. M. I. Shliomis, Usp. Fiz. Nauk **112**, 427 (1974) [Sov. Phys. Usp. **17**, 153 (1974)].
14. *Handbook of Mathematical Functions*, Ed. by M. Abramowitz and I. A. Stegun (National Bureau of Standards, Washington, 1964; Nauka, Moscow, 1979).
15. A. I. Rusanov and V. A. Prokhorov, *Interphase Tensiometry* (Khimiya, St. Petersburg, 1994).

Translated by V. Sipachev

Journal of Experimental and Theoretical Physics, Vol. 94, No. 6, 2002, pp. 1121–1133.
Translated from Zhurnal Éksperimental'noĭ i Teoreticheskoĭ Fiziki, Vol. 121, No. 6, 2002, pp. 1306–1320.

SOLIDS
Structure

Channeling of Fast Particles in Fullerites

N. K. Zhevago* and V. I. Glebov

Russian Research Centre Kurchatov Institute, pl. Kurchatova 1, Moscow, 123182 Russia
**e-mail: ab2211@technologist.com*

Received November 12, 2001

Abstract—A theory of channeling of relativistic electrons and positrons as well as positively and negatively charged ions in molecular crystals of fullerenes (fullerites) is developed. The crystal potentials are calculated, and the spatial and angular distributions of beams of particles propagating along principal crystallographic directions are determined. A method is developed for taking into account the effect of incoherent scattering on the channeling process. © *2002 MAIK "Nauka/Interperiodica".*

1. INTRODUCTION

Channeling of charged particles in ordinary crystals is studied in detail both theoretically and experimentally (see, for example, [1, 2]). On the other hand, recently discovered fullerenes [3] can be obtained, under certain conditions, in the form of stable molecular crystals with face-centered cubic symmetry [4, 5]. The lattice constant of such crystals (known as fullerites) amounts to $d \approx 1.42$ nm, which is an order of magnitude higher than the corresponding value for ordinary crystals. Channeling in fullerites, as well as channeling in nanotubes considered earlier [6, 7], may be of interest for high-energy physics in view of the possibility of deflection of charged particle beams in bent crystals and the generation of electromagnetic radiation by electrons and positrons. As regards channeling of ions, this effect may be used, due to anomalously large ion mean free paths, for implanting various atoms into fullerites in order to change their electron properties and other physical parameters. In our previous publication [8], we developed a quantum theory of channeling in fullerites on the basis of multiwave diffraction of relativistic electrons and positrons with moderate energies ($\lesssim$10 MeV) as well as a theory of diffraction for soft X rays.

The present work aims at the development of a classical theory of channeling of electrons, positrons, and other charged elementary particles and ions possessing a high energy, so that we can assume that particles move in trajectories. It is well known that the standard theory of channeling is based on the possibility of using crystal potentials averaged along the crystallographic directions and over the thermal vibrations of lattice atoms. In the case of fullerites in which polymerization does not take place and molecules are bound by relatively weak Van der Waals forces, averaging over molecular rotations is also carried out [8]. Potential fluctuations associated with the difference between the real and average potentials are responsible for dechanneling, i.e., gradual departure of particles from the channeling mode during the propagation of the beam through the crystal. Dechanneling ultimately determines the efficiency of channeling for turning the particle beam and for generation of electromagnetic radiation by electrons and positrons. We will develop an approach for taking into account the effect of incoherent scattering on potential fluctuations and will carry out appropriate calculations for dechanneling lengths in the cases of straight and bent fullerites.

2. AVERAGED POTENTIALS OF FULLERITES

According to the channeling theory [1], when a fast charged particle enters a crystal at a grazing angle θ_0 (comparable with the Lindhard angle in order of magnitude) relative to the principal crystallographic directions, the true potential of the crystal can be replaced in the first approximation by a potential averaged along the corresponding directions. Since lattice sites contain fullerenes in the case under investigation, we must first calculate the potential of an individual fullerene. In particular, in fullerene C_{60}, carbon atoms are at the vertices of the frustrum of an icosahedreon. According to Doyle and Turner [9], the Fourier component of the atomic potential can be presented, to a sufficiently high degree of accuracy, in the form of the sum of N Gaussians:

$$f(\mathbf{k}) = 4\pi Ze\sum_{i=1}^{N} a_i \exp\left(-\frac{k^2}{4b_i^2}\right), \qquad (1)$$

where Ze is the charge of the nucleus. It is well known that, in the Born approximation, the quantity defined by Eq. (1) is the amplitude of scattering of an electron by the atom, the quantity $\mathbf{k}$ coinciding with the momentum transferred by the atom upon the scattering of the electron. The fitting parameters a_i and b_i in the given model of the atom are chosen, like their total number N, from the condition of the best approximation of formula (1) to the corresponding values measured in experiments

1063-7761/02/9406-1121$22.00

on the angular distribution of scattered electrons in a wide range of transferred momenta k or to the results of more accurate calculations (e.g., using the Hartree–Fock method). Usually, it is sufficient to take $N = 4$ or 5; the values of the parameters a_i and b_i for various atoms (including carbon) are given in [10]. The inverse Fourier transform of quantity (1) gives the following expression for the atomic potential:

$$\varphi(\rho_a) = \frac{4Ze}{\sqrt{\pi}} \sum_{j=1}^{N} a_j b_j^3 \exp(-b_j^2 \rho_a^2), \qquad (2)$$

where ρ_a is the distance from the nucleus. The region of applicability of the model form factor (1) and the corresponding atomic potential (2) is bounded by large momenta or small distances to the nucleus. In particular, for the set of fitting parameters that will be used in subsequent calculations of averaged potentials, the region of value of k for which a satisfactory (to within ≈0.6%) agreement between formula (1) and tabulated data [10] is observed is bounded from above by the value $k_{\max} \approx 126$ nm^{-1}, which corresponds to distances smaller than the amplitude of thermal vibrations of atoms in fullerite. It should be noted that, using the screening of the nucleus in form (4) as the starting point, we can derive another, more accurate, analytic expression for the potential of carbon atom, which has a regular (Coulomb) form at small distances and coinciding with the tabulated values to within 1% down to distances of 0.002 nm. However, this expression cannot be used for obtaining a sufficiently large number of simple analytic expressions for averaged potentials of a molecular chain (see Eq. (8)). On the other hand, our subsequent calculations will show that the difference between the depths of the potential well for transverse motion in our model of the averaged potential (1) and a more exact model does not exceed 5%.

The potential energy of point particles (elementary particles or nuclei) in the field of an atom is just the product of potential (2) and the charge of a particle. In the case of ions, we must take into account the effect of screening of the nucleus of an ion by the remaining electrons. This can be done as follows. According to Doyle and Turner [9], the Fourier component of the electron distribution in an atom or an ion with the nuclear charge $Z_1 e$ can be presented, to a sufficiently high degree of accuracy, in the form

$$f^{(x)}(\mathbf{k}) = Z_1 \sum_{m=1}^{N_1} a_m^{(x)} \exp\left(-\frac{k^2}{4b_m^{(x)2}}\right), \qquad (3)$$

which is similar to expression (1), but parameters a_m, b_m, and N_1 are now determined by fitting Eq. (3) to more exact values of the scattering amplitude of X-ray photons [10]. Thus, the Fourier component of the charge distribution in an atom (ion), including, in addition to expression (3), the nuclear charge $Z_1 e$, has the form

$$q(\mathbf{k}) = e(Z_1 - f^{(x)}(\mathbf{k})). \qquad (4)$$

We assume, as is usually done in the theory of ion channeling [1], that the velocity of the ion is small as compared to the velocities of electrons on its outer orbits; in addition, the electron energy levels of an ion and fullerenes do not intersect for any impact parameters. In this case, we can disregard inelastic processes of the type of charge exchange between the channeled ion and fullerene atoms and obtain the potential of interaction of a carbon atom with the ion in a simple form. Indeed, in the coordinate representation, the potential energy of interaction between an ion and an atom is the convolution of the atomic potential (2) and the spatial charge distribution in the ion. Consequently, in the momentum representation, the effective atomic form factor $f_{\text{ion}}(\mathbf{k})$ for ion scattering is the product of the right-hand sides of expressions (1) and (4):

$$f_{\text{ion}}(\mathbf{k}) = 4\pi Z Z_1 e \sum_{j=1}^{N(1+N_1)} A_j \exp\left(-\frac{k^2}{4B_j^2}\right). \qquad (5)$$

Parameters A_j and B_j are connected with the known parameters for the scattering form factors of electrons and X-ray photons through the following relations: $A_j = a_j$, $B_j = b_j$ for $j \le N$, $A_j = -a_i a_m^{(x)}$, $B_j^2 = b_i^2 b_m^{(x)2}/(b_i^2 + b_m^{(x)2})$ for $N < j \le N(1 + N_1)$, where i and m run through a sequence of values from one to N and N_1, respectively. It should be noted that, for such an approach, the ion scattering form factor (5) preserves the functional form of the sum of a certain number of Gaussians as in the case of a point particle. This allows us to derive quite simple expressions for the effective potential of interaction between channeled particles and fullerites (see below).

The case of a completely ionized atom corresponds to $a_j^{(x)} = 0$ for all indices j. On the other hand, if the ion is heavy and the degree of ionization is low, we can disregard the difference between the electron distributions in the ion and in the corresponding neutral atom and use for ions the values of parameters $a_m^{(x)}$ and $b_m^{(x)}$ obtained for a neutral atom. In a more general case, the electron distribution in a specific ion should be calculated using the Hartree–Fock method for determining these parameters.

Let us now calculate the molecular potential. In the case of a point charge, we will not distinguish below between the terms "potential" and "potential energy." In the first approximation, we can disregard the effect of valence bonds between individual carbon atoms in a C_{60} fullerene molecule on the distribution of electrons in the molecule; i.e., we can assume that the molecular potential is just the sum of atomic potentials (2) cen-

tered at the vertices of the frustrum of an icosahedron. We will also take into account the fact that under standard conditions, fullerites are nonpolymerized; i.e., individual fullerenes in fullerites are connected only through weak Van der Waals forces and may freely rotate. As a result of the rotations, fullerenes have a random angular orientation and, hence, the molecular potential can be averaged preliminarily over angular coordinates of atoms to obtain the following expression for the molecular potential averaged in this way:

$$U_1(r) = 60\frac{Ze^2}{\sqrt{\pi}rR}\sum_{i=1}^{N} a_i b_i \times [\exp(-b_i^2(r-R)^2) - \exp(-b_i^2(r+R)^2)]. \quad (6)$$

Here, r denotes the distance from the center of fullerene, and $R = 0.353$ nm is the radius of fullerene C_{60}. The charge e of a channeled point particle in formula (6) is assumed to be positive (positron).

Let us suppose that a charged particle is incident at a small angle to one of the principal crystallographic axes. We denote by d_R the distance between two adjacent molecules in a molecular chain of fullerite. We now average the potential of the chain along its direction. This gives the following expression for the averaged potential of the chain:

$$U^{(R)}(\rho) = 60\frac{2Ze^2}{Rd_R}\sum_{i=1}^{N} a_i \times \int_0^\infty \exp(-k_\perp^2 b_i^{-2}/4) J_0(k_\perp \rho)\sin k_\perp R dk_\perp, \quad (7)$$

where J_0 is a Bessel function and $k_\perp$ is the projection of momentum $\mathbf{k}$ on the transverse plane. The effective potential U acting on a positively charged channeled particle in fullerite is the sum of potentials of the form (7) of all n chains parallel to the given crystallographic direction:

$$U(\mathbf{r}) = \sum_n U^{(R)}(|\mathbf{r} - \boldsymbol{\rho}_n|). \quad (8)$$

Here, $\mathbf{r}$ is the vector coordinate of the plane normal to the molecular chains (transverse plane), and $\boldsymbol{\rho}_n$ is the vector coordinate of the nth chain.

Potential (7) corresponds to a static chain of fullerenes and to the static arrangement of carbon atoms at the vertices of the frustrum of an icosahedron in fullerenes, i.e., disregards thermal vibrations of molecules relative to the lattice sites in the fullerite crystal as well as thermal vibrations of carbon atoms in the molecules. Thermal vibrations of atoms tangential to the surface of a molecule obviously do not affect the averaged potential (7) since it was derived using the averaging over molecular rotations. Thermal vibrations of atoms, which are transverse relative to the surface of a molecule, can be taken into account by introducing the Debye–Waller factor e^{-W} into expressions (1) and (7), where $W = k_\perp^2 u_\perp^2/2$, $u_\perp^2$ is the mean square amplitude of thermal vibrations, whose temperature dependence is determined by the well-known Debye formula. Molecular vibrations along a chain obviously do not affect the obtained result either in view of the averaging of the potential along this direction. Transverse thermal vibrations can be taken into account through the Debye–Waller factor e^{-W_f}, which must be introduced in the integrand of formula (7). Assuming that transverse thermal vibrations of molecules are isotropic, we obtain $W_f = k_\perp^2 u_1^2/2$, where u_1^2 denotes the mean square amplitude of thermal vibrations of molecules in the fullerite lattice. The value of the Debye temperature T_D for fullerite obtained from the sound velocity measurements [11] is 55.4 K, which gives the value $u_1 = 1.39 \times 10^{-2}$ nm at room temperature. We are not aware of results on the amplitude of radial vibrations of atoms in fullerenes; it can be assumed, however, that it is close to the analogous amplitude $u_\perp = 8.5 \times 10^{-3}$ nm of vibrations (transverse to planes) in graphite. The amplitudes of thermal (especially, atomic) vibrations are smaller than the distances over which the electron density and potential in a carbon atom change significantly; consequently, their inclusion leads to a noticeable change in the averaged potential (7) only in a relatively narrow region of $|\rho - R| \lesssim u_1 + u_\perp$.

The results obtained above can be used for calculating the fullerite potentials in the case of ion channeling through the obvious substitutions $a_i \longrightarrow A_j$, $b_i \longrightarrow B_j$, $N \longrightarrow N(1 + N_1)$, and $e \longrightarrow Z_1 e$. It should be noted that other representations for the ion–atom potential, which were based, for example, on the Mollier approximation to the Thomas–Fermi model, were also used earlier [1] in the theory of ion channeling in ordinary crystals. It was demonstrated by us earlier [7], however, that such an approach in the case of fullerenes gives exaggerated values for averaged potentials almost in the entire channel region in view of the obvious inapplicability of the Thomas–Fermi model to light atoms.

The results of numerical calculations of averaged fullerite potentials (8) taking into account thermal vibrations of molecules at room temperature are given in Figs. 1 and 2 for various particles and crystallographic directions. Figure 1 corresponds to electrons and the direction along the [110] axes, while Fig. 2 corresponds to positrons and the [100] direction. The form of these potentials differs considerably from that of averaged potentials in ordinary crystals (see, for example, [1]). This difference is due to the fact that the lattice sites of fullerite contain not atoms but giant C_{60} molecules. As a result, a deep potential well appears, say, for positively charged particles (see Fig. 2) not only between chains, but also on the axis of the chains. The existence of a deep axisymmetric well becomes possi-

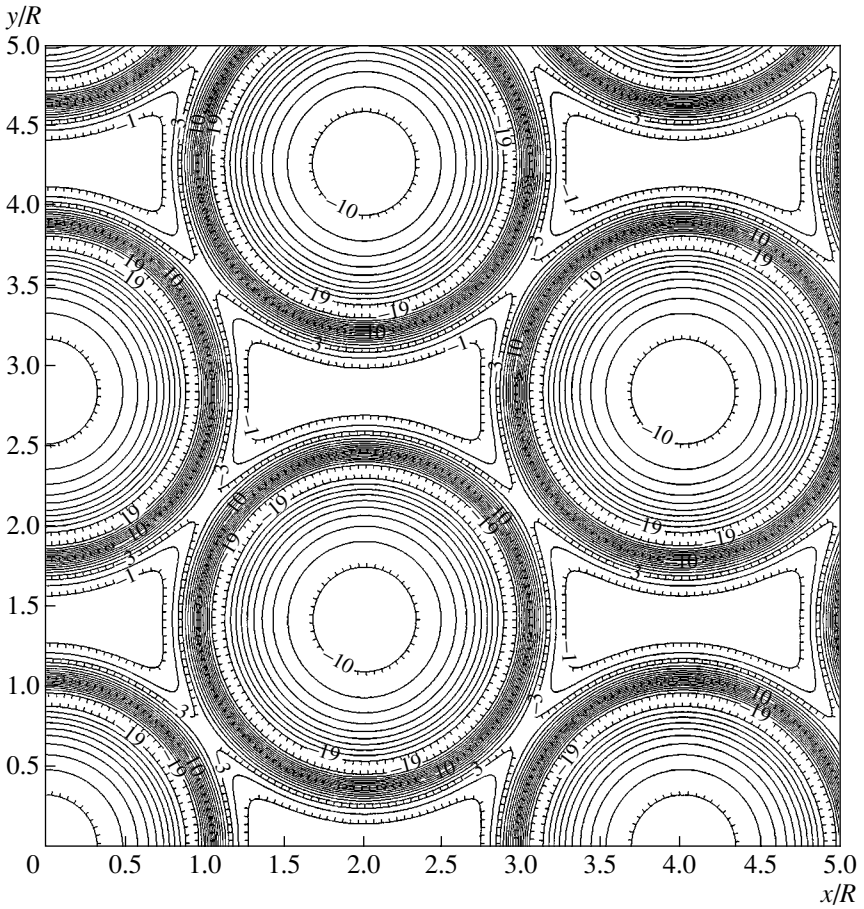

Fig. 1. Contour diagram of the averaged potential corresponding to the [110] axes for negative point particles (electrons). The figures on equipotential curves correspond to values of potential in electronvolts, and dashes indicate the directions of its decrease.

ble for negatively charged particles also. The relative sizes of all wells considerably exceed the corresponding sizes in ordinary crystals, facilitating a more efficient channeling of charged particles in fullerites. In the case of ion channeling, the potentials also have a similar form.

3. CHANNELING OF ULTRARELATIVISTIC PARTICLES IN NORMAL AND BENT FULLERITES

It was shown in our previous publication [8] devoted to the quantum theory of channeling in fullerites that the classical description of light particles (electrons and positrons) becomes justified for much lower energies ($E \sim 10$ MeV) than in ordinary crystals. This result could be expected proceeding from the following considerations. In channeling, like in Bragg diffraction in crystals, the characteristic quantum parameter is the de Broglie wavelength of a particle $\lambda\!\!\!^{-} \approx \hbar/E$ divided by the angle of incidence θ_0, which can be estimated as the Lindhard angle $\theta_L = (2U_0/E)^{1/2}$, where U_0 is the potential well depth for transverse motion. Since the transverse de Broglie wavelength $\lambda\!\!\!^{-}_\perp = \lambda\!\!\!^{-}/\theta_L$ is much larger than $\lambda\!\!\!^{-}$, quantum effects in channeling occur even for relatively high energies of electrons and positrons, amounting to tens of megaelectronvolts (see, for example, [2]). For a correct classical description of motion of channeled particles, it is necessary that the value of $\lambda\!\!\!^{-}_\perp$ be much smaller than the channel size. Although the channels in fullerites are slightly shallower yet broader than in ordinary crystals, the classical approach is possible for them for considerably lower energies of particles. As regards heavy particles (π mesons and protons), the classical theory of channeling both in ordinary crystals and in fullerites is applicable to them virtually for all (even nonrelativistic) velocities [1].

Let us first consider classical channeling of high-energy electrons and positrons in normal (straight) fullerites. The integrals of motion of a particle in potential (8) are the total energy E and the longitudinal (relative to the crystallographic axis) momentum component $p_\parallel$:

$$E = U(\mathbf{r}) + (1 - v_\parallel^2 - v_\perp^2)^{-1/2},$$
$$p_\parallel = v_\parallel(1 - v_\parallel^2 - v_\perp^2)^{-1/2}. \quad (9)$$

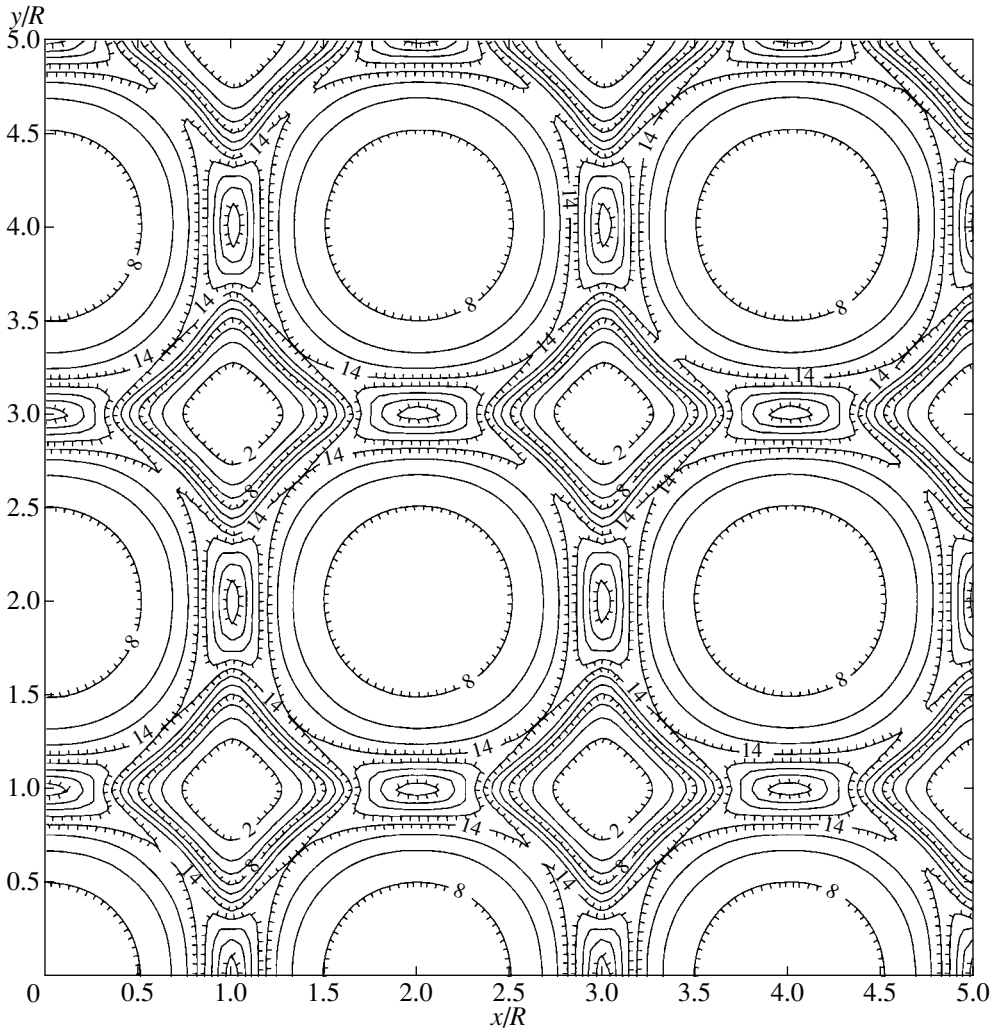

Fig. 2. Contour diagram of the averaged potential corresponding to the [100] axes for positive point particles (positrons).

Here, $v_\parallel$ is the longitudinal velocity component, $\mathbf{v}_\perp = d\mathbf{r}/dt$ is the transverse velocity component, and the relativistic system of units with $m = c = 1$ is used. The transverse energy ε is defined as the difference $\varepsilon = E - (1 + p_\parallel^2)^{1/2}$ and, hence, is also an integral of motion in the averaged potential $U(\mathbf{r})$. In the case of channeling, we always have $\varepsilon \ll E$; taking into account this condition, we obtain from Eqs. (9) the following equation for the transverse velocity component:

$$\mathbf{v}_\perp^2 = \frac{2}{E}[\varepsilon - U(\mathbf{r})]. \tag{10}$$

The form of this equation corresponds to a nonrelativistic transverse motion of a particle with mass E in potential $U(\mathbf{r})$ and expresses the law of conservation of transverse energy for such a particle. In the small-angle approximation, when the inequality $\varepsilon \ll E$ holds, we obtain the following expression for the longitudinal component of the particle velocity in the ultrarelativistic limit $E \gg 1$:

$$v_\parallel = 1 - \frac{1}{2}(E^{-2} + v_\perp^2). \tag{11}$$

The fluctuations of the longitudinal velocity component associated with the presence of the square of the transverse velocity component $v_\perp^2$ in Eq. (11) may be significant (see, for example, [2]) only in analyses of the electromagnetic radiation spectrum of ultrarelativistic particles having a high energy, since the Doppler shift of radiation frequency is determined by the relatively small difference, $1 - v_\parallel$, between the velocity of light and the longitudinal velocity component of an ultrarelativistic particle. However, such fluctuations can be disregarded in the analysis of the scattering of particles, which will be carried out below.

Let us now assume that the crystallographic axis of fullerite is bent in a certain plane with a constant radius

of curvature R_b. We choose the cylindrical system of coordinates ρ, φ, Z with the Z axis perpendicular to the plane of the bend and passing through the center of curvature O. The potential of bent fullerite is obviously independent of the azimuth angle φ since the radius of curvature is assumed to be constant. Thus, in addition to the total energy E, the component M of the relativistic angular momentum of the particle on the Z axis is also an integral of motion:

$$\begin{aligned} E &= U(\mathbf{r}) + (1 - \mathbf{v}_\perp^2 - v_\tau^2)^{-1/2}, \\ M &= \rho v_\tau (1 - \mathbf{v}_\perp^2 - v_\tau^2)^{-1/2}. \end{aligned} \tag{12}$$

Here, $v_\tau = \rho(d\varphi/dt)$ is the modulus of the tangential velocity component, and $\mathbf{v}_\perp$ is the velocity component perpendicular to $\mathbf{v}_\tau$. The system of equations (12) leads to the following equation for the transverse component of the velocity of a particle in the bent crystal:

$$\mathbf{v}_\perp^2 = 1 - \frac{1 + M^2/\rho^2}{[E - U(\mathbf{r})]^2}. \tag{13}$$

Let us now define the transverse energy of a relativistic particle as the difference

$$\varepsilon \equiv E - (1 + M^2/R_b^2)^{1/2}, \tag{14}$$

which is also an integral of motion in a bent crystal. The Cartesian coordinate x of the particle relative to the crystallographic axis (one of the components of vector $\mathbf{r}$) is connected with the cylindrical coordinate ρ introduced above through the relation $x = \rho - R_b$. Since the radius of curvature in the cases of practical importance is larger than the size of the channel ($x \ll R_b$), we obtain from Eq. (13) taking into account definition (14) and condition $\varepsilon \ll E$ (which always holds for channeled particles) the following approximate equation for the transverse velocity component:

$$\mathbf{v}_\perp^2 = \frac{2}{E}[\varepsilon - U(\mathbf{r})] + \frac{2x}{R_b}. \tag{15}$$

Thus, the bending of the crystallographic axis with a constant radius of curvature R_b is taken into account in an analysis of transverse motion by replacing the electrostatic potential $U(\mathbf{r})$ in Eq. (10) by the effective potential

$$U_{\text{eff}}(\mathbf{r}) = U(\mathbf{r}) - \frac{Ex}{R_b}. \tag{16}$$

We assume that all crystallographic axes in fullerite are bent with the same radius of curvature; in this case, the equation of motion (15) is valid in the region of each unit cell of the crystal. The above analysis is completely in accord with intuitive considerations presented in pioneering works by Tsyganov [12], devoted to the effect of rotation of a high-energy particle beam by bent crystal planes.

Like ordinary crystals, fullerites can be bent either mechanically or by passing a high-intensity ultrasonic wave through the crystal. The bending strength of fullerite and its resistance to the action of ultrasound are apparently comparable to the values observed in ordinary crystals of the graphite and even diamond type (this statement is valid for polymerized fullerites). In both methods of bending, the radius of curvature is not constant. It will be shown in the subsequent analysis that, when the radius of curvature changes quite slowly (both in magnitude and direction) along a crystallographic axis, i.e., considerable changes in R_b occur over lengths exceeding considerably the characteristic period of radial vibrations of channeled particles in a potential well, the effective inclusion of bending boils down to the introduction of a centrifugal force of the form $\mathbf{F} = E\mathbf{n}/R_b$ into the equations for transverse motion. Here, $\mathbf{n}$ is the unit vector directed along the radius of curvature. The case when the above condition is violated is more complicated to analyze and will be considered in a separate publication. It should only be noted that, along with centrifugal forces, the forces determined by derivatives of R_b with respect to the longitudinal coordinate (or time) may appear in this case.

In contrast to planar potentials observed in ordinary crystals, the axial potentials in fullerites exhibit a more complex dependence on transverse coordinates and, hence, the equations of motion (10) and (15) can be solved only by using numerical methods. The initial coordinates of a particle are random quantities. Since the transverse dimensions of real beams of particles considerably exceed the size of a unit cell in the transverse plane, we can assume that particles are distributed uniformly over the area of a unit cell.

Let us consider, by way of an example, a beam of relativistic particles with a negligibly small angular divergence $\theta_0 \ll \theta_L$ that penetrates a fullerite crystal parallel to one of the principal crystallographic axes. The channeling effect rapidly leads to a considerable rearrangement of the initial beam distribution in the phase space of transverse coordinates and momenta. We introduce the length $L_0 = R/\theta_L$ coinciding in order of magnitude with $\lambda/4$, where λ is the characteristic wavelength of radial vibrations of particles in the axial channel. Numerical calculations show that almost complete rearrangement occurs only at relatively large (of the order of $10L_0$) penetration depths in fullerite. Figures 3 and 4 show the equilibrium spatial distribution of a beam of negatively or positively charged particles within a unit cell for different directions [110] and [100]. The circle in the figures has the radius of fullerene. Channeled negative particles are concentrated at the periphery and at the center of the channel, where their potential energy has a local maximum (see Fig. 1) and, hence, the hanging effect takes place. In the case of positive particles, two different potential wells exist (Fig. 2), one of which corresponds to channeling in the space between the chains, while the other, shal-

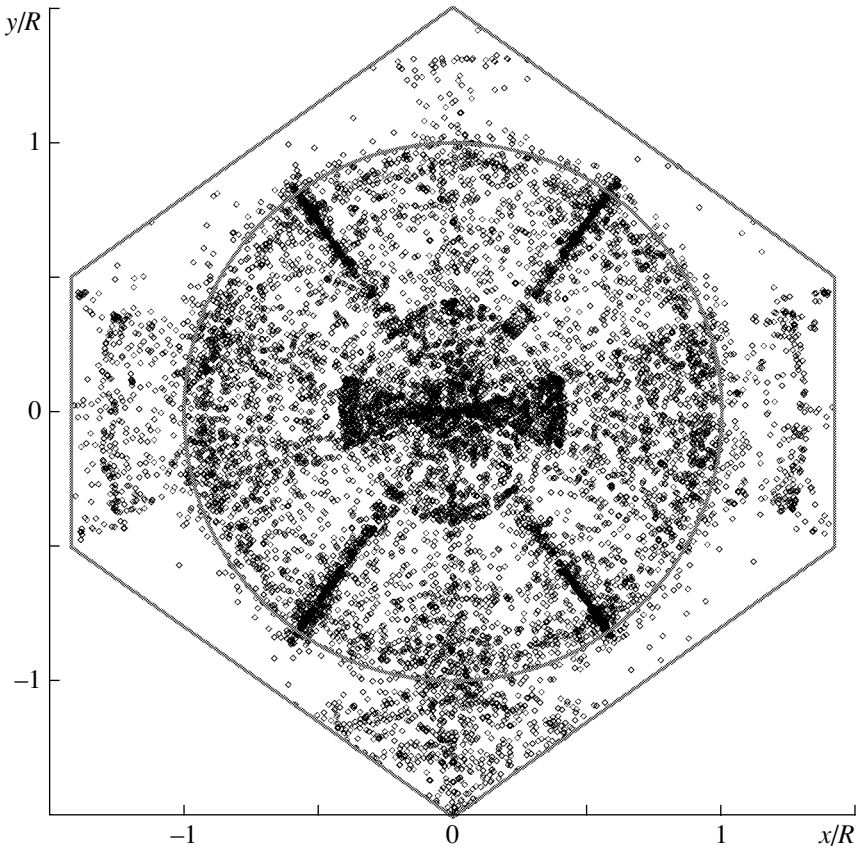

Fig. 3. Equilibrium spatial distribution of a negative particle beam within a unit cell in the case of axial channeling along the [110] direction.

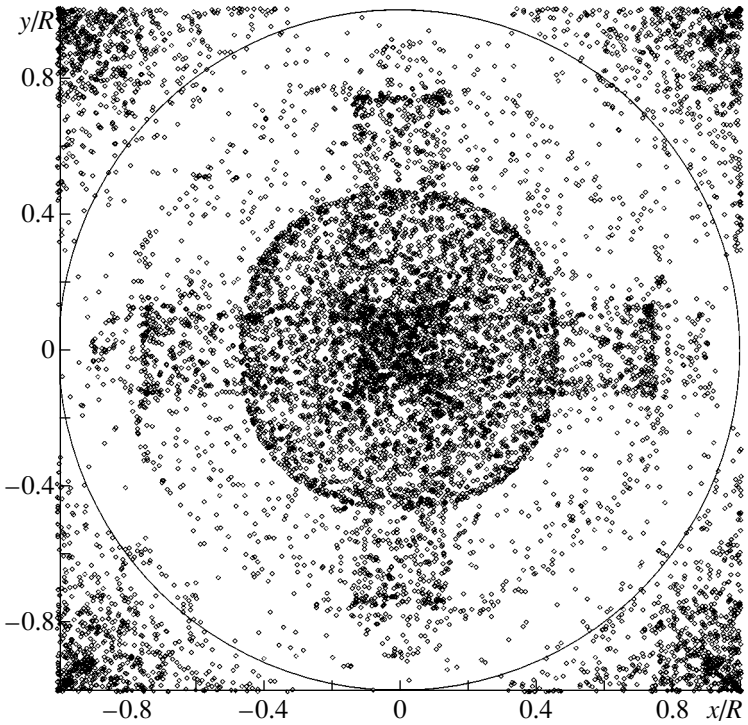

Fig. 4. Equilibrium spatial distribution of a positive particle beam within a unit cell in the case of axial channeling along the [100] direction.

lower, well, possessing a higher axial symmetry, corresponds to channeling in the chains. Since potential wells are concave, a positive particle beam is concentrated in the vicinity of the centers of these two different channels. The spatial redistribution of the beam of channeled particles has important consequences; in particular, it must noticeably change the cross sections of all secondary processes for which close collisions of particles with atoms (nuclei) of the medium are important (e.g., for Rutherford scattering). We will consider once again the effects of spatial redistribution of particle beams in fullerites in the following analysis of dechanneling.

It should be noted that, in accordance with the Liouville theorem on conservation of the phase space volume in the absence of dissipative processes, the spatial focusing of particle beams must be accompanied by the corresponding broadening of their initial angular distribution, which is confirmed by appropriate calculations which will not be presented here.

4. INCOHERENT SCATTERING AND DECHANNELING

The averaged potential (8) completely corresponds to coherent scattering of particles by molecular chains. In this case, we assume that incoherent scattering effects at individual atoms and electrons of the medium are relatively weak and can be disregarded in the first approximation. We will now analyze the effect of potential fluctuations due to rotations and thermal vibrations of fullerenes at a crystal lattice and calculate the dechanneling length, i.e., the mean free path of particles in fullerite, over which a considerable fraction of initially channeled particles escape from the channel as a result of incoherent scattering.

Let us consider in greater detail the scattering of a fast particle at a chain of vibrating fullerenes. We denote by $\boldsymbol{\rho}_0$ and z the transverse radius vector and the longitudinal coordinate of the particle, respectively. Further, we assume that $\boldsymbol{\rho}_i^{(m)}$ denotes the vector deviation of the ith molecule from the chain axis as a result of thermal vibrations, $w(\boldsymbol{\rho}_i)$ is the probability density of such a deviation, and $N = \Delta z/d_R$ is the number of molecules on the path Δz of the particle. The particle experiences the action of the potential $U_1(r_i, \phi_i, \vartheta_i)$ of the ith molecule, where $r_i = \sqrt{|\boldsymbol{\rho}_i^{(m)} - \boldsymbol{\rho}_0|^2 + (z - id_R)^2}$ is the distance from the particle to the center of fullerene, and ϕ_i, ϑ_i are the angles defining the random orientation of fullerene. The increment of the transverse momentum $\mathbf{q}$ of the particle under the assumption that the acts of scattering at different fullerenes occur independently can be presented as the sum of corresponding increments $\mathbf{q}_i$ upon scattering at each molecule:

$$\mathbf{q} = \sum_{i=1}^{N} \mathbf{q}_i.$$

We also assume that the changes in the transverse coordinate $|\Delta\boldsymbol{\rho}_0|$ of the particle over a path of length Δz are smaller than the distance over which the potential of the scatterer changes significantly. According to [13], for high energies of particles, this condition may hold even for initial angles of incidence (relative to the chain axis) considerably exceeding the Lindhard angle. This leads to the following expression for the momentum transferred as a result of scattering at an individual molecule:

$$\mathbf{q}_i = \nabla \int_{-\infty}^{\infty} U_1(\sqrt{|\boldsymbol{\rho}_i - \boldsymbol{\rho}_0|^2 + z^2}, \phi_i, \vartheta_i)\, dz,$$

where ∇ is the gradient in the transverse plane.

Disregarding further the correlation of thermal vibrations and rotations of neighboring molecules, we arrive at the conclusion that the average (over thermal vibrations and angular orientations of molecules) increment of the transverse momentum $\langle \mathbf{q}(\boldsymbol{\rho}_0)\rangle$ in this case is also the sum of the corresponding mean values for scattering at each molecule; i.e.,

$$\langle \mathbf{q}\rangle = \sum_{i=1}^{N} \langle \mathbf{q}_i\rangle,$$

where

$$\langle \mathbf{q}_i(\boldsymbol{\rho}_0)\rangle = (4\pi)^{-1}\nabla \int_0^{2\pi}\int_0^{\pi}\int_{-\infty}^{\infty} U_1(\sqrt{|\boldsymbol{\rho}_i - \boldsymbol{\rho}_0|^2 + z^2}, \phi_i, \vartheta_i)$$
$$\times\, w(\boldsymbol{\rho}_i)\sin\vartheta_i\, dz\, d\vartheta_i\, d\phi_i\, d^2\rho_i.$$

Thus, the average increment of the transverse momentum is determined by the fullerene potential averaged over the longitudinal coordinate, thermal vibrations, and orientations of fullerenes, which is in line with the basic concept in the theory of channeling in fullerites developed above.

In the next approximation, we must take into account the probability of possible deviations $\mathbf{q}$ from its mean value $\langle \mathbf{q}\rangle$. Let the number of molecules N on the above-indicated path remain quite large; according to the central limit theorem in probability theory, the deviation probability distribution has a Gaussian form. Mean square fluctuations of the increment of transverse momentum can be presented in the form

$$\langle (\mathbf{q} - \langle \mathbf{q}\rangle)^2\rangle = \sum_{i=1}^{N} (\langle \mathbf{q}_i^2\rangle - \langle \mathbf{q}_i\rangle^2),$$

where $\langle \mathbf{q}_i^2\rangle$ is the mean square momentum transferred to the particle during scattering by an individual fullerene. We assume further that the scattering by all

fullerene atoms occurs independently and take into account the fact that the particle can also be scattered by electrons of the medium. In this case, the mean square transferred momentum can be determined in the same way as in the analysis of multiple scattering in an amorphous medium. However, since the mean square momentum $\langle \mathbf{q}^2 \rangle$ is a function of $\boldsymbol{\rho}_0$, we must take into account the nonuniform distribution of scatterer density in the transverse plane of the crystal. Thus, the motion of a fast particle in fullerite can be presented as a relatively smooth motion in the averaged potential of molecular chains superimposed by stochastic perturbations associated with incoherent scattering from individual atoms and electrons of the medium. The self-consistency of this approach will be discussed below.

It is well known that the mean square angle of multiple scattering by atoms (screened nuclei) per unit length in an amorphous medium can be presented in the form

$$\langle \theta_a^2 \rangle = 4\pi n_a (Ze^2)^2 E^{-2} L_a,$$

where n_a is the number density of nuclei averaged over the volume and $L_a = \ln(191Z^{-1/3})$ is the Coulomb logarithm. For scattering by electrons of the medium which can be regarded as free, a similar expression has the form $\langle \theta_a^2 \rangle = 4\pi n_e e^4 E^{-2} L_e$, where n_e is the electron number density averaged over volume and $L_e = \ln(1194Z^{-2/3})$ (see, for example, [13]). The logarithmic factors L_a and L_e used here take into account the screening of the Coulomb field over relatively long as well as short distances significant for scattering.

Multiple scattering by electrons in an amorphous medium is found to be $1/Z$ times the scattering by nuclei; however, the situation may change in the case of channeling. It was noted above that, in the case of channeling, we must take into account, first, the nonuniform distribution of the number density of nuclei, $n_a(\mathbf{r})$, and electrons, $n_e(\mathbf{r})$, over the coordinates $\mathbf{r}$ in the transverse plane of the channel and, second, the redistribution of the flux density of channeled particles, which was considered above. An analytic expression for the radial distribution of the electron number density in an individual fullerene chain can be derived by using relation (3) in the same way as we derived formulas (7) and (8) for potentials and has the form

$$n_e^{(R)}(\rho) = 60 \sum_{j=1}^{4} \frac{Z a_j^{(e)}}{4\pi R d_R} \times \int_0^\infty \exp\left(-\frac{k_\perp^2}{4 b_j^{(e)2}}\right) J_0(k_\perp \rho) \sin kR dk_\perp. \quad (17)$$

For the distribution of the number density of atoms in an individual fullerene chain taking into account their displacement from their equilibrium positions due to thermal vibrations of fullerenes, we obtain

$$n_a^{(R)}(\rho) = \frac{60}{(2\pi)^{3/2} u_1 R d_R} \times \int_0^\infty \left\{ \exp\left[-\frac{(\sqrt{\rho^2 + z^2} - R)^2}{2u_1^2}\right] - \exp\left[-\frac{(\sqrt{\rho^2 + z^2} + R)^2}{2u_1^2}\right] \right\} \frac{dz}{\sqrt{\rho^2 + z^2}}. \quad (18)$$

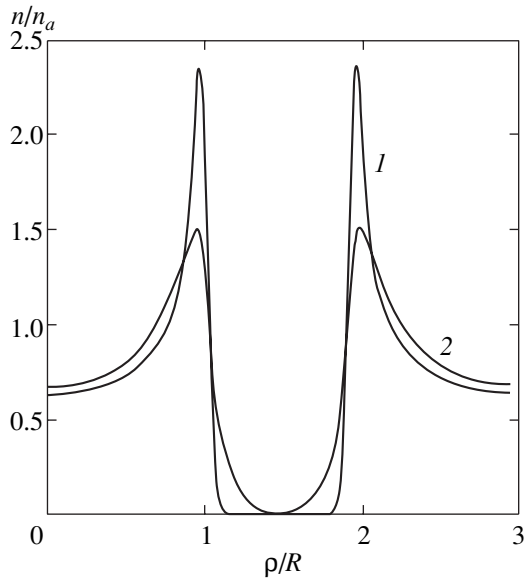

Fig. 5. Number density distribution for nuclei (curve *1*) and electrons (curve *2*) as a function of the distance from the [100] axis along the straight line connecting two adjacent [100] axes spaced by the maximum distance. The distribution density is normalized to values averaged over volume; the distance is measured in units of fullerene radius.

In order to derive the corresponding distributions in the transverse plane, we must carry out additional summation in formulas (17) and (18) over all fullerene chains parallel to the crystallographic direction along which the channeling takes place. Figure 5 shows the variation of the nuclear, $n_a(\mathbf{r})$ (curve *1*), and electron, $n_e(\mathbf{r})$ (curve *2*), number densities along the straight line connecting two adjacent fullerene chains in the [100] channel, which are separated by the largest distance. The amplitude u_1 of thermal vibrations of fullerenes was calculated in the framework of the Debye model with temperature $T_D = 55.4$ K measured in experiments [11], while the temperature of fullerite was assumed to be equal to room temperature. Thermal vibrations weakly affect the electron distribution since their amplitude is smaller than the size of electron shells in an atom. The distribution of nuclei in the region $\rho \geq R$ is determined exclusively by thermal vibrations, but the

effect of thermal vibrations in the region $\rho < R$ is insignificant in view of the stronger effect of molecular rotations. The above calculations show that the particles channeled in the chains must experience much stronger incoherent scattering from atoms than the particles channeled between the chains since, in addition to potential fluctuations due to thermal vibrations of molecules, there exist much stronger fluctuations associated with their rotation; for this reason, the number density of nuclei in this case is of the order of the number density averaged over the volume.

The algorithm of our calculations of the trajectories of particles incident on fullerite at a grazing angle θ_0 relative to fullerene chains can be described as follows. First, a random initial transverse coordinate $\mathbf{r}_0$ of a particle, which was distributed uniformly over the area of a unit cell in the transverse plane of fullerite, was played by using the Monte Carlo method. Then, the equation of transverse motion in the averaged potential (8), i.e.,

$$\frac{d}{dt}\mathbf{p}_\perp = -\nabla U(\mathbf{r}) \tag{19}$$

(where $\mathbf{p}_\perp = Ed\mathbf{r}/dt$ is the transverse momentum component of the particle), was integrated numerically over the segment Δt to find the values of the transverse coordinate r_1 and the transverse momentum $\mathbf{p}_{\perp 1}$ at instant $t_1 = \Delta t_1$. The time interval Δt_1 was chosen so that the relative changes in the number density $n_a(\mathbf{r})$ and $n_e(\mathbf{r})$ of nuclei and electrons were negligibly small over the integration path, the number of atoms on this path remaining much larger than unity. Further, a random increment $\Delta\theta$ of transverse momentum associated with incoherent multiple scattering of the particle from atoms and electrons of the medium was played; it was assumed that the probability density of the small-angle multiple incoherent scattering of ultrarelativistic particles through the angle $\Delta\theta = \{\Delta\theta_x, \Delta\theta_y\}$ on the path of length $\Delta z \approx \Delta t$ has the Gaussian form

$$P(\Delta\theta) = 2\frac{\Delta\theta \exp(-(\Delta\theta)^2/\langle\theta_s^2\rangle)}{\langle\theta_s^2\rangle}, \tag{20}$$

where the mean square of the multiple scattering angle of a channeled particle on the path Δz is defined as

$$\langle\theta_s^2(\mathbf{r})\rangle = 16\pi e^4(\Delta z/E^2) \times [n_a(\mathbf{r})Z^2L_n + n_e(\mathbf{r})L_e].$$

This increment was added to $\mathbf{p}_{\perp 1}$, and the sum was assumed to be the actual value of transverse momentum at time t_1. After this, the above procedure (except the playing of coordinates at the beginning of the interval) was repeated on the next integration interval from t_1 to $t_2 = t_1 + \Delta t_2$.

Since the equations of motion can be solved only numerically in view of the complex form of the averaged potential, and the initial transverse coordinates of particles and their momenta are also random (due to the actual angular spread of particles in the beam), the method of taking into account incoherent scattering developed by us for channeling in fullerites is much simpler and more natural than the method of kinetic equations (see, for example, [2]) at least in the case of axial channeling, when the phase space for transverse motion is four-dimensional. As regards the calculation of trajectories by the method of binary collisions of a particle with crystal atoms [15], this approach proves to be unproductive in the case of high energies since dechanneling lengths are relatively large and an extremely large number of collisions must be taken into consideration. On the other hand, it will be proved by subsequent calculations that the integration intervals Δt for particles with energy of hundreds of gigaelectronvolts, the integration intervals Δt contain more than 10^2 atoms (in this connection, the method used by us is sometimes referred to as the method of aggregative collisions [16]), which reduces the time of computation of dechanneling lengths in the corresponding proportion.

Before analyzing the results of specific numerical calculations, we estimate various aspects of the effect of incoherent scattering on the dynamics of propagation of a particle beam in fullerites. For example, the equilibrium spatial distribution of the flow of channeled particles shown in Figs. 3 and 4 may turn out to be inaccessible since incoherent scattering on the relatively long path of its formation (it was mentioned above that the path length amounts at least to $10L_0$) may lead to a considerable redistribution of particles in the phase space if the path length is comparable with the dechanneling length. The dechanneling length l_{dc} can be estimated qualitatively by equating the mean square angle of multiple scattering over this length to the square of the Lindhard angle. This leads to the relation

$$l_{dc} \approx \frac{2U_0E}{E_s^2}t_0. \tag{21}$$

Here, $E_s = \sqrt{4\pi\hbar/e^2} \approx 21.2$ MeV, and t_0 is the radiative unit of length defined by the equality

$$\frac{1}{t_0} = \frac{4e^6}{\hbar}(Z^2n_aL_n + n_eL_e). \tag{22}$$

In our estimates, we use the values of nuclear and electron number densities n_a and n_e averaged over the volume of the fullerite. If the inequality $l_{dc} \gg 10L_0$ is satisfied, the effect of incoherent scattering on the equilibrium distribution can obviously be neglected, and the previous results of calculation of the spatial distribution for particle beams in channels remain in force. According to numerical estimates, this inequality holds for electrons and positrons only for high energies of these particles ($E \gg 5$ GeV).

The self-consistency of this approach requires that the dechanneling length be considerably larger than the characteristic length L_0 over which radial vibrations of particles in the axial channel take place; otherwise, incoherent scattering cannot be regarded as a relatively small perturbation, and the concept of averaged potential is inapplicable (at least, in the case of classical motion). This condition restricts the region of electron and positron energies to values $E \gtrsim 1$ GeV.

The results of more accurate numerical calculations of dechanneling lengths for particles with different energies E are given below. The method of aggregative collisions was used for calculating random trajectories of $N = 10^3$ particles for each value of total energy E. It was assumed for simplicity that a particle beam is incident on the fullerite parallel to the crystallographic axes and has a negligibly small initial angular divergence. The computation of each energy value from those given below took less than 25 h on a computer having a capacity of 2 GFLOPS. Figure 6 shows the dependence of the relative number N_{ch}/N of ultrarelativistic positively charged particles (protons, π^+ mesons, or positrons) remaining in the [100] axial channel on the depth z of beam penetration in the target. It follows from these calculations that the dechanneling length increases almost linearly with the particle energy, which is in accord with the simple estimates obtained in [21]. Slowing down of dechanneling at relatively large depths is apparently associated with the fact that the channels at such depths predominantly contain particles which channel in the space between the chains, where the effect of incoherent scattering is weaker (see above).

The effectiveness of deflection of positively charged ultrarelativistic particles with an energy of 150 GeV with the help of fullerites whose [100] axial channels are bent in the (001) plane is illustrated by the family of curves in Fig. 7. Following Tsyganov [12], we introduced the critical radius of curvature $R_c = RE/U_0 \approx 3.91$ m, where R is the radius of fullerene and $U_0 \approx 13.5$ eV is the depth of the (deepest) potential well. In the region of relatively small deflection angles and, hence, small penetration depths in fullerite crystal, the number of channeled particles varies nonmontonically with the depth. This is due to the fact that the probability of rechanneling, i.e., recapture of over-the-barrier particles in the potential well, is quite high at such depths. According to the results presented here, the turning of a particle beam is most effective for a radius of curvature close to R_c; in this case, approximately 20% of particles in the beam may be turned through relatively small angles of 0.2 mrad (corresponding to several tens of Lindhard angles). The existence of the optimal radius of curvature is associated with the effect of two competing factors: smaller radii facilitate rotation through a given angle for a smaller crystal length, thus suppressing the dechanneling effect; this is accompanied by an increase in the centrifugal field, decreasing the effective potential well depth that is so important for channeling.

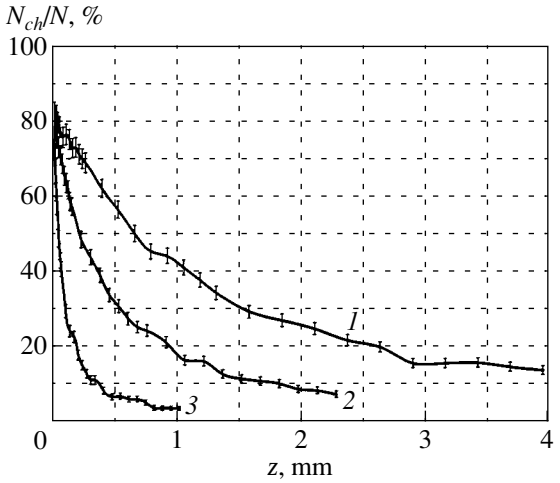

Fig. 6. Relative number N_{ch}/N of ultrarelativistic positive particles channeled along the [100] axis at the beam penetration depth z in the target. Curve *1* corresponds to the particle energy $E = 150$ GeV, curve *2* to 50 GeV, and curve *3* to 10 GeV.

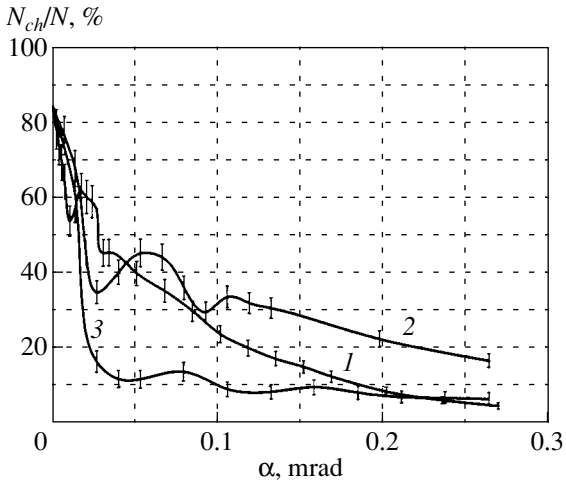

Fig. 7. Relative number N_{ch}/N of positive particles with energy $E = 150$ GeV channeled along the bent [100] axes of fullerite as a function of the beam deflection angle α. Curve *1* corresponds to the radius of curvature $R_b = 2R_c$, curve *2* to $R_b = R_c$, and curve *3* to $R_b = 0.5R_c$.

Figure 8 shows the angular distribution of particles emerging from fullerite having a thickness $T = 1.31$mm and bent with the radius of curvature $R_b = 2R_c$, which corresponds to the rotation of the [100] axis through the angle $\alpha = 1.68 \times 10^{-4}$. The initial angular distribution is presented by point with the coordinates $\theta_{0x} = \theta_{0y} = 0$ in the momentum space. It can be seen that a considerable fraction of particles in the beam follow the channel bends and are turned through angles of the order of α. These particles have an angular spread close to the

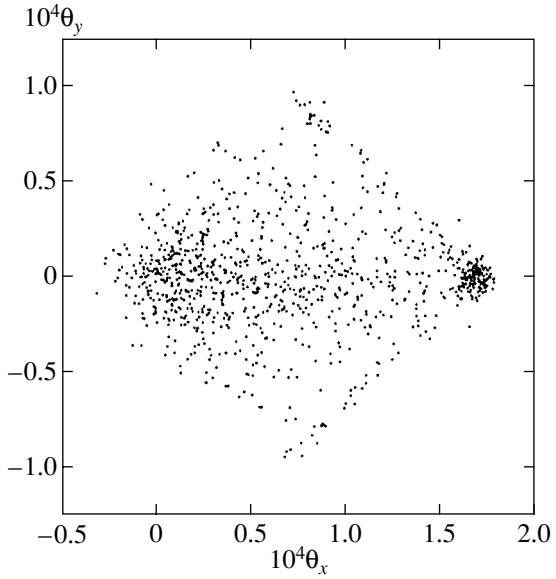

Fig. 8. Angular distribution of 10^3 positive particles with energy $E = 150$ GeV emerging from a fullerite of thickness $T = 1.31$ mm, which is bent with the radius of curvature $R_b = 2R_c$.

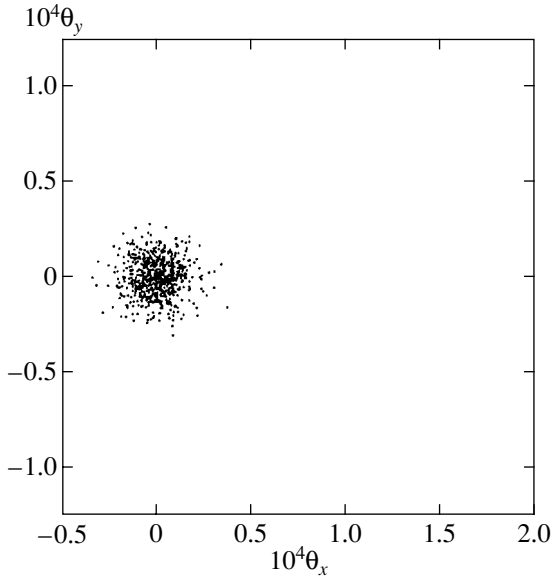

Fig. 9. Angular distribution of 10^3 positive particles with energy $E = 150$ GeV emerging from a straight fullerite of thickness $T = 1.31$ mm.

Lindhard angle. The remaining particles are turned through angles smaller than α and are characterized by a considerably larger angular spread. These are particles which followed the channel bend for some time and dechanneled at various depths $z < T$ as a result of incoherent scattering. Figure 9 shows for comparison a similar angular distribution for a direct crystal ($R_b = \infty$).

According to the results of recent experiments carried out at CERN [17], radiation energy loss for light particles (electrons and positrons) with energies of hundreds of gigaelectronvolts during channeling in diamond crystals is almost two orders of magnitude higher than the corresponding loss in an amorphous medium. Thus, high-energy electrons and positrons may lose a considerable part of their energy E at depths much smaller than the radiation length t_0 in an amorphous target (nonoriented crystal), which amounts to 25.5 cm in the case of fullerite. This is due to the enhancement of electromagnetic radiation of channeled particles in the entire energy range ω of emitted photons, including the region $\omega \sim E$. If the radiation length becomes comparable with the depth of penetration of particles in the crystal, it is necessary to take into account radiation effects in channeling and dechanneling processes. In the case of fullerites, the parameter $\chi = \hbar E|\nabla U(\mathbf{r})|$ determining the effect of quantum recoil in the positron radiation (see, for example, [3]) is found to be small (≤ 0.05) if the positron energy does not exceed ~1 TeV. This allows us to use the classical formula for radiation loss per unit time,

$$\frac{dE}{dt} = \frac{2e^4E^2}{3}|\nabla U(\mathbf{r})|^2, \qquad (23)$$

where $\mathbf{r} = \mathbf{r}(t)$ is the transverse coordinate of the positron, to estimate the influence of radiation effects in fullerites. For energies $\gtrsim 1$ TeV, the emission spectrum is displaced in the region of $\omega \sim E$. In accordance with the quantum theory of radiation, the quadratic dependence of radiation loss of the particle energy in formula (23) is replaced by a weaker dependence (radiation loss becomes proportional to $E^{2/3}$). Expression (23) was averaged further in transverse coordinates with the distribution functions presented in Figs. 3 and 4. As a result, it turned out that positrons with an energy of 150 GeV may lose no more than 0.9% of their energy by emission on the entire path $T = 1.31$ mm. Energy losses for electrons are slightly larger and amount approximately to 4%. Thus, in contrast to diamond, we can obviously disregard the effect of radiation loss for axial channeling of positrons in fullerites up to positron energies of the order of 1 TeV. This is due to the fact that axial channels in fullerite are relatively shallower and wider; for this reason, channeled positrons move on the average in the region of a lower potential gradient than in diamond. On the contrary, channeled electrons move precisely at the periphery of fullerenes, where the potential gradient has the maximum value and, hence, the effect of radiation loss on electrons may be significant at lower energies.

5. CONCLUDING REMARKS

Channeling of fast particles in crystals made of fullerenes is characterized by a number of features distinguishing it from channeling in ordinary crystals due

to specific molecular structure of the fullerite crystal lattice sites. For example, fullerites have deep, wide, and nearly axisymmetric potential wells for positive as well as negative particles, facilitating a more effective trapping of particles in the axial channeling mode.

Axial channeling in bent fullerites makes it possible to turn ultrarelativistic particle beams through relatively large angles in contrast to ordinary crystals in which axial channeling is ineffective for this purpose. The total momentum of particles is rotated in this case in contrast to planar channeling in bent crystals, in which only one of the momenta components is rotated [12].

The dechanneling mechanisms in fullerites also exhibit peculiarities associated with molecular rotation. It is important to note, however, that the dechanneling length for high-energy particles is quite large even if we take into account the fluctuations of the averaged potential associated with this rotation.

In addition to fullerites consisting of C_{60} fullerenes and considered in detail in this article, there exist similar molecular crystals consisting of nonspherical C_{70} molecules [18] as well as crystalline compounds of fullerenes with different atoms (fullerides) [19]. Obviously, the features of channeling described above must be observed in such structures also.

Under the action of high pressure and temperature, fullerites may experience polymerization [20] hampering the rotation of molecules at lattice sites. In this case, as well as in fullerides in which neighboring fullerenes are strongly linked through atoms of other elements, averaging of the potential over molecular rotations is meaningless, and the channeling in such a structure requires a further analysis.

ACKNOWLEDGMENTS

The authors are grateful to Xavier Artru for fruitful discussions of the results.

This work was supported financially by INTAS (project no. 97-30392).

REFERENCES

1. D. S. Gemmell, Rev. Mod. Phys. **129**, 46 (1974).
2. V. A. Bazylev and N. K. Zhevago, Usp. Fiz. Nauk **160** (12), 47 (1990) [Sov. Phys. Usp. **33**, 1021 (1990)].
3. H. W. Kroto, J. R. Heath, S. C. O'Brien, *et al.*, Nature **318**, 162 (1985).
4. P. A. Heiney, J. E. Fischer, A. R. McGhie, *et al.*, Phys. Rev. Lett. **66**, 2911 (1991).
5. S. Amelinckx, C. van Heurck, D. van Dyck, and G. van Tendeloo, Phys. Status Solidi A **131**, 589 (1992).
6. L. G. Gevorgyan, K. A. Ispiryan, and R. K. Ispiryan, Pis'ma Zh. Éksp. Teor. Fiz. **66**, 339 (1997) [JETP Lett. **66**, 322 (1997)].
7. N. K. Zhevago and V. I. Glebov, Phys. Lett. A **250**, 360 (1998); Zh. Éksp. Teor. Fiz. **118**, 579 (2000) [JETP **91**, 504 (2000)].
8. N. K. Zhevago and V. I. Glebov, Phys. Lett. A **282**, 97 (2001).
9. P. A. Doyle and P. S. Turner, Acta Crystallogr. A **24**, 390 (1968).
10. E. N. Malsen, A. G. Fox, and M. A. O'Keefe, *International Tables for Crystallography*, Ed. by A. J. C. Wilson (Kluwer, Dordrecht, 1992), Vol. C.
11. N. A. Aksenova, A. P. Isakina, A. I. Prokhvatilov, and M. A. Strzhemechnyĭ, Fiz. Nizk. Temp. **25**, 964 (1999) [Low Temp. Phys. **25**, 724 (1999)].
12. E. N. Tsyganov, Preprints FNAL-TM-682, FNAL-TM-684 (1976); Pis'ma Zh. Éksp. Teor. Fiz. **26**, 403 (1977) [JETP Lett. **26**, 279 (1977)].
13. A. I. Akhiezer and N. F. Shul'ga, Usp. Fiz. Nauk **137**, 561 (1982) [Sov. Phys. Usp. **25**, 541 (1982)].
14. Y. S. Tsai, Rev. Mod. Phys. **46**, 815 (1974).
15. M. T. Robinson and O. S. Oen, Phys. Rev. **132**, 2385 (1963).
16. R. Berger, *Methods of Computational Physics* (Academic, New York, 1963), pp. 1, 135.
17. K. Kirsenbom, U. Mikkelsen, E. Uggerhöj, *et al.*, Nucl. Instrum. Methods Phys. Res. B **174**, 274 (2001).
18. A. Talyzin and U. Jansson, J. Phys. Chem. **104**, 5064 (2000).
19. O. Zhou, J. E. Fischer, N. Cousel, *et al.*, Nature **351**, 462 (1991).
20. V. D. Blank, S. G. Buga, N. R. Serebryanaya, *et al.*, Phys. Lett. A **220**, 149 (1996).

Translated by N. Wadhwa

Journal of Experimental and Theoretical Physics, Vol. 94, No. 6, 2002, pp. 1134–1139.
Translated from Zhurnal Éksperimental'noĭ i Teoreticheskoĭ Fiziki, Vol. 121, No. 6, 2002, pp. 1321–1327.

SOLIDS
Structure

The Study of the Vibrational Spectra of NH_4Cl and NH_4Br at High Pressures

V. P. Glazkov[a], D. P. Kozlenko[b, *], B. N. Savenko[b], V. A. Somenkov[a], G. F. Syrykh[a], and A. S. Telepnev[b, c]

[a] *Institute of Molecular Physics, Russian Research Centre Kurchatov Institute, pl. Akademika Kurchatova 1, Moscow, 123182 Russia*

[b] *Joint Institute for Nuclear Research, Dubna, Moscow oblast, 141980 Russia*

** e-mail: denk@nf.jinr.ru*

[c] *Institute of High-Pressure Physics, Russian Academy of Sciences, Troitsk, Moscow oblast, 142092 Russia*

Received November 20, 2001

Abstract—The vibrational spectra of NH_4Cl at pressures of up to 2.6 GPa and of NH_4Br at pressures of up to 7 GPa are investigated by the method of inelastic incoherent scattering of neutrons. It is found that a linear baric dependence of a librational mode changes its slope above the pressure of transition from a disordered cubic phase into an ordered cubic phase with a CsCl-type structure. The slope of the baric dependence of the transverse optical translational mode remains invariant. Estimates for the Grüneisen parameters are presented and the shape of the potential function is calculated in the one-dimensional approximation for librational vibrations in disordered and ordered cubic phases with a CsCl-type structure. It is shown that the phenomena observed are attributed to the high anharmonicity in the disordered phase. *© 2002 MAIK "Nauka/Interperiodica".*

1. INTRODUCTION

The investigation of the effect of high pressures on ammonium halides is of interest for finding out a relationship between the changes in the structure and the dynamics of the latter and the phase transitions that occur under a volume decrease [1]. One of the important problems in the investigation of the dynamics of ammonium halides is the study of the effect of high pressure on the librational and translational modes of ammonium ions and a change in their behavior under phase transitions [2]. An answer to these questions can be obtained by investigating the vibrational spectra of crystals at high pressures by the methods of optical and neutron spectroscopy. The methods of optical spectroscopy are weakly sensitive to a librational mode; information on the latter can only be obtained from overtones and combination modes. In contrast, the method of neutron spectroscopy allows one to directly determine the position of a librational peak. However, experiments on inelastic scattering of neutrons under sufficiently high pressures have become possible quite recently, due to the development of the anvil technique.

Under normal conditions, NH_4Cl and NH_4Br have a cubic CsCl-type structure where ammonium ions are orientationally disordered between two equivalent positions (phase II). As pressure increases (at $P \approx 1$ GPa in NH_4Cl and $P \approx 3$ GPa in NH_4Br), a phase transition to a cubic phase IV occurs with a CsCl-type structure in which ammonium ions are arranged parallel to each other [3]. The vibrational spectra of NH_4Cl and NH_4Br at high pressures were investigated by the methods of Raman [4, 5] and neutron [2, 6, 7] spectroscopy. The vibrational spectra of NH_4Cl at pressures of up to 4 GPa were investigated in [2], where the frequencies of librational and transverse optical translational modes in the orientationally ordered cubic phase IV were obtained as functions of pressure. At the same time, the effect of pressure on the behavior of the librational mode in the orientationally disordered phase II in NH_4Cl, which exists at pressures below 1 GPa, has been studied insufficiently. In [7], the splitting of the librational peak was observed near the point of the orientational phase transition II–IV in NH_4Br at high pressures. A similar effect was also observed in NH_4Cl near the same transition point at low temperature and normal pressure [8]. The Raman spectroscopy data [5] suggested that the pressure dependence of the librational mode frequency changes its character due to the orientational phase transition from the disordered phase II to the ordered phase IV. It was assumed that this effect is associated with a strong anharmonicity of the interatomic potential in the disordered phase II [5, 6].

The aim of the present paper is to study the behavior of vibrational modes in related crystals NH_4Cl and NH_4Br in a wide range of pressures above and below the orientational phase transition II–IV by the method of inelastic incoherent neutron scattering.

2. SETTING UP EXPERIMENTS

Experiments were carried out at room temperature on a DN-12 spectrometer [9] on an IBR-2 high-flux pulse reactor in the Frank Laboratory of Neutron Physics, Joint Institute for Nuclear Research (Dubna). An

1063-7761/02/9406-1134$22.00

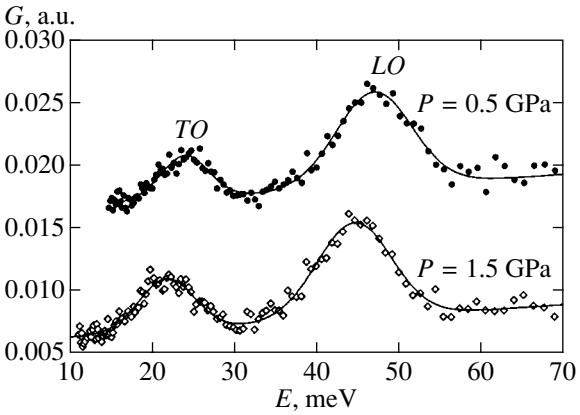

Fig. 1. Generalized density of vibrational states in NH_4Cl under different pressures. The shape of the peak is described by a Gaussian curve, and the background, by a linear polynomial.

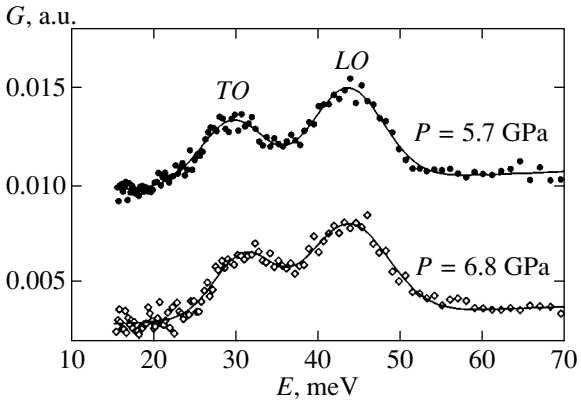

Fig. 2. Generalized density of vibrational states in NH_4Br under different pressures. The shape of the peak is described by a Gaussian curve, and the background, by a linear polynomial.

NH_4Cl crystal was investigated under pressures of up to 2.6 GPa attained in a high-pressure vessel with sapphire anvils [10]. The sample volume was $V \approx 5$ mm^3. The chamber pressure was measured by the shift of a ruby luminescence line with an accuracy of 0.05 GPa. An NH_4Br crystal was measured under a pressure of 7 GPa obtained in a high-pressure vessel designed at the Institute of High-Pressure Physics by Yu.A. Sadkov and S.M. Stishov. This chamber had Toroid-type tungsten carbide anvils that were originally designed by L.G. Khvostantsev and L.F. Vereshchagin for diffraction investigations [11]. The sample volume was $V \approx$ 100 mm^3. The vessel pressure was determined by the known equation of state [12] for NH_4Br by the variation of the lattice parameter, whose value was determined from additional diffraction experiments. The energy transmission was analyzed with the use of a cooled beryllium filter [13] in the case of NH_4Cl and a conventional beryllium filter in the case of NH_4Br, which were situated at a scattering angle of $2\theta = 90°$. The final energy of detected neutrons was $E = 4$ meV. A typical time needed for measuring one spectrum was 12 hours for NH_4Cl and 50 hours for NH_4Br.

3. MAIN RESULTS

The spectra of the generalized density $G(E)$ of vibrational states in NH_4Cl and NH_4Br for various pressures are shown in Figs. 1 and 2. They contain two peaks corresponding to transverse optical translational (*TO*) and librational (*LO*) modes. As pressure increases, the frequencies of these modes increase with different slopes (Fig. 3). The pressure dependence of the *LO* mode frequency in NH_4Cl slightly differs from the results of Raman spectroscopy [5], while those of *LO* and *TO* modes in NH_4Br are in a good agreement with the results of our recent neutron diffraction studies at lower pressures [7].

Near the point of the phase transition from the orientationally disordered cubic phase II to the ordered cubic phase IV in NH_4Cl ($P_{tr} \approx 1$ GPa) and NH_4Br ($P_{tr} \approx 3$ GPa), the slope of the pressure dependence of the *LO* mode varies, the variation being more conspicuous in the ammonium chloride (Fig. 3). In both compounds, the pressure dependence of the *TO* mode in phases II and IV is close to linear and does not have any singularities near the point of phase transition. Within the energy resolution, we could not observe any noticeable variations in the shape of the librational mode peak in NH_4Cl and NH_4Br in the entire range of pressures considered. The analysis of the pressure dependence of the half-width w of the librational peak (Fig. 4) in NH_4Cl showed that w decreases in approaching the point of transition to the ordered phase, while w remains approximately constant within this phase.

The table represents the Grüneisen parameters $\gamma_i = -(d\ln\omega_i/d\ln V)_T$ for *LO* and *TO* modes in NH_4Cl and NH_4Br as well as the derivatives $d\omega_i/dP$. These parameters are calculated for the disordered phase II under normal pressure and for the ordered phase IV for $P =$ 1.5 GPa and $P = 3$ GPa, respectively. We used the following values of the compression modulus B in our calculations:

$$NH_4Cl: B(P = 0) = 17.9 \text{ GPa},$$
$$B(P = 1.5 \text{ GPa}) = 26.0 \text{ GPa};$$
$$NH_4Br: B(P = 0) = 16.4 \text{ GPa},$$
$$B(P = 3.0 \text{ GPa}) = 30.8 \text{ GPa [3]}.$$

The values of the Grüneisen parameter of the librational mode γ_L obtained here slightly differ from those given in [5], which were obtained by the method of Raman spectroscopy (see table). Due to the orientational phase transition that is accompanied by the ordering of NH_4^+ ions, γ_L in NH_4Cl appreciably decreases from 1.55 to 0.50. In NH_4Br, the variation of

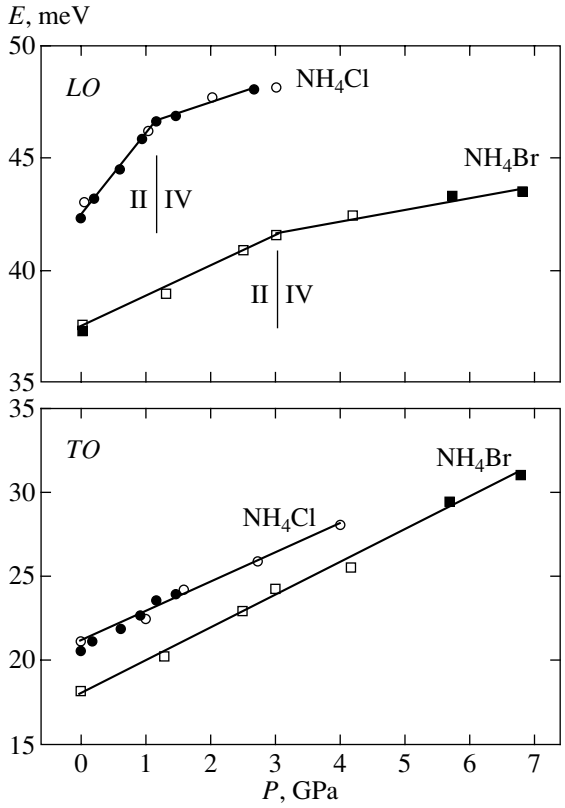

Fig. 3. Frequencies of *LO* (top) and *TO* (bottom) modes versus pressure in phases II and IV in NH_4Cl and NH_4Br interpolated by linear functions: ● and ■ represent the results obtained in the present paper, ○ are the Raman data [5], and □ are the neutron diffraction data [7].

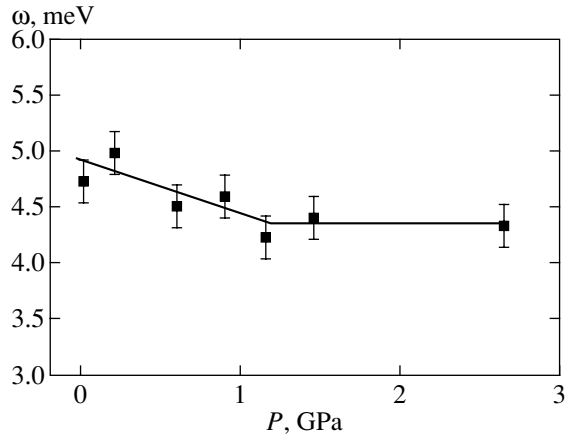

Fig. 4. Half-width of the librational peak in NH_4Cl as a function of pressure.

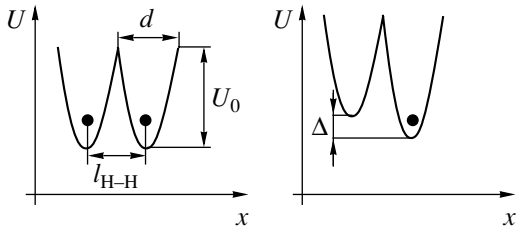

Fig. 5. Shape of the interatomic potential in the disordered phase II and ordered phase IV in NH_4Cl and NH_4Br.

γ_L is not so significant; this parameter decreases from 0.59 to 0.38.

4. DISCUSSION OF THE RESULTS

The results obtained can be explained under the assumption that the interatomic potential in the disordered phases of NH_4Cl and NH_4Br exhibits a clear-cut anharmonic character (the anharmonicity of NH_4Cl being greater) and that, when passing to the ordered phase, the shape of the potential becomes closer to a harmonic one due to the deepening of the potential well (Fig. 5). To verify this assumption, we carried out the following simple estimations.

Grüneisen parameters of *LO* and *TO* modes in NH_4Cl and NH_4Br for phases II and IV

Mode	Phase	P, GPa	$d\omega_i/dP$, meV/GPa	γ_i
		NH_4Cl		
LO	II	0	3.66	1.55(5)
	II, data [5]	0	–	1.30(17)
	IV	1.5	0.92	0.50(4)
	IV, data [5]	–	–	0.29(6)
TO	II, IV	0	2.57	2.30(5)
		NH_4Br		
LO	II	0	1.35	0.59(5)
	II, data [5]	0	–	0.72(9)
	IV	3.0	0.52	0.38(5)
TO	II, IV	0	1.93	1.75(5)

In the case of small oscillations near the minimum of the potential energy, the simplest one-dimensional anharmonic potential can be represented as

$$U(x) = \frac{m\omega^2 x^2}{2} + \alpha x^3 + \beta x^4, \quad (1)$$

where m is the oscillator mass, ω is the oscillator frequency in the harmonic approximation, and α and β are constants that determine the degree to which potential (1) is distorted as compared with the harmonic potential.

The frequency of a harmonic oscillator is determined by the parameters of the potential well, the height U_0 and the width d:

$$\omega = \sqrt{2U_0/md^2}. \quad (2)$$

Then, the expression for the energy levels of the anharmonic oscillator within perturbation theory is given by [14]

$$E_n = \hbar\omega\left(n + \frac{1}{2}\right) - \frac{15}{4}\frac{\alpha^2}{\hbar\omega}\left(\frac{\hbar}{m\omega}\right)^3 \times\left(n^2 + n + \frac{11}{30}\right) + \frac{3}{2}\beta\left(\frac{\hbar}{m\omega}\right)^2\left(n^2 + n + \frac{1}{2}\right). \quad (3)$$

In a CsCl-type cubic structure, ammonium ions are situated at the center of the unit cell, and the hydrogen atoms occupy the positions (*xxx*) along the cube diagonals. There exist two possible equivalent positions for NH_4^+ ions in the disordered phase, and ammonium ions can perform reorientational jumps between these positions [15, 16]. Hence, the frequency of librational oscillations of an ammonium ion corresponds to the oscillation frequency of each hydrogen atom in the potential well. The height of this well is determined by the rotational potential barrier U_0 for the reorientations of ammonium ions, while its width d is of the order of the distance between neighboring equivalent positions for hydrogen atoms, $d \sim l_{\text{H-H}}$ (Fig. 5). The orientational phase transition responsible for the ordering of ammonium ions is associated with the deepening of one of the two adjacent potential wells, so that only one of the two equivalent (in the disordered state) orientations of ammonium ions becomes energetically favorable (Fig. 5).

The frequency of the librational mode in NH_4Cl and NH_4Br corresponds to the transition between the ground and the first excited energy states of the anharmonic oscillator. Considering, for simplicity, one-dimensional oscillations of a hydrogen atom in the potential well described above, we obtain the following expression from (2) and (3):

$$E_L = \hbar\omega_L = \frac{\hbar}{d}\sqrt{\frac{2U_0}{m}} - \frac{30}{16m}\left(\frac{\hbar\alpha d^2}{U_0}\right)^2 + \frac{6}{4}\frac{\beta\hbar d^2}{mU_0}. \quad (4)$$

Quantity d in phases II and IV in NH_4Cl under normal pressure can be evaluated by formula (2) from the known values of the librational mode frequency E_L [6] and the values of the activation energy W for the reorientations of ammonium ions [17], which correspond to the rotational potential barrier in the classical approximation. For phase II at $T = 290$ K, $E_L = 42.3$ meV [6], and $W^{\text{II}} = 18.84$ kJ/mol [17], we have $d_{\text{II}} = 0.952$ Å. For phase IV at $T = 80$ K, $E_L = 46.8$ meV [6], and $W^{\text{IV}} = 23.03$ kJ/mol [17], we have $d_{\text{IV}} = 0.953$ Å, which is roughly equal to d_{II}. Since the cooling from 290 to 80 K corresponds to the variation of the lattice parameter a in NH_4Cl from 3.866 to 3.834 Å (the linear thermal expansion coefficient $\alpha_L = 5 \times 10^{-5}$ K^{-1} [18]), which is equivalent to the application of a pressure of $P = 0.5$ GPa at room temperature, one can assume to a good accuracy that d is invariant in the range of pressures considered, $d_{\text{Cl}} \approx 0.95$ Å. A similar calculation for NH_4Br with the use of the values of E_L, W^{II}, and W^{IV} from [7, 17] yields a close value of $d_{\text{Br}} = 0.94$ Å. Thus, the variation of the librational mode frequency under the variation of pressure (or under a decrease in the interatomic distance) is mainly determined by the variation of the potential well depth U_0.

In the simplest approximation, the dependence of the height U_0 of the potential barrier on the interatomic distance (or on pressure) can be described by the power function [19]

$$U_0(a) = M/a^C, \quad (5)$$

where a is the lattice parameter and M and C are experimental constants.

Assuming that the shape of the interatomic potential in the ordered phase IV is close to a harmonic one, we interpolate by function (5) the dependence of the librational mode frequency on the lattice parameter $E_L(a)$ (Fig. 6) calculated using the experimental function $E_L(P)$ and the known equations of state for NH_4Cl and NH_4Br [12, 20]. Thus, we obtain the following results:

NH_4Cl: $M = 2.59(5) \times 10^6$ kJ/mol, $C = 3.56(1)$,

NH_4Br: $M = 1.79(5) \times 10^6$ kJ/mol, $C = 3.40(1)$.

To calculate the interatomic potential in phase II, one has to determine the parameters α and β. From the interpolation of the experimental function $E_L(a)$ by function (4) (Fig. 6), taking into account expression (5) and the calculated values of M and C, we obtain $\alpha = 6.61 \times 10^{-20}$ J/Å^3 and $\beta = 18.58 \times 10^{-20}$ J/Å^4 for NH_4Cl and $\alpha = 2.60 \times 10^{-20}$ J/Å^3 and $\beta = 4.05 \times 10^{-20}$ J/Å^4 for NH_4Br. In these calculations, we took into account that the transition is accompanied by a stepwise variation in the potential well depth by $\Delta \approx 4$ kJ/mol in NH_4Cl and by $\Delta \approx 2$ kJ/mol in NH_4Br [17].

Formulas (4) and (5) describe the behavior of the librational mode frequency as a function of the lattice

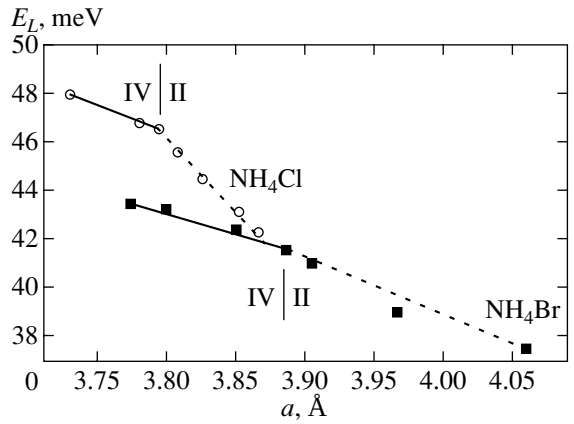

Fig. 6. Frequency of the librational mode as a function of the lattice parameter in phases II and IV in NH_4Cl and NH_4Br. The solid and dashed curves represent the results of computations with the use of the functions (4) for phase II and (5) for phase IV.

parameter. Using these formulas, we can calculate the Grüneisen parameter in phases II and IV, representing the appropriate formula as

$$\gamma_L = -\left(\frac{d\ln\omega_L}{d\ln V}\right)_T = -\frac{V}{\omega_L}\left(\frac{d\omega_L}{da}\right)_T \Big/ \left(\frac{dV}{da}\right)_T = \frac{a}{3\omega_L}\left(\frac{d\omega_L}{da}\right)_T, \quad (6)$$

where a is the lattice parameter. The calculated values of Grüneisen parameters were $\gamma_L = 1.78$ for NH_4Cl and $\gamma_L = 0.89$ for NH_4Br in phase II at $P = 0$ and $\gamma_L = 0.59$ ($P = 1.5$ GPa) for NH_4Cl and $\gamma_L = 0.56$ ($P = 3.0$ GPa) for NH_4Br in phase IV. Although these values are somewhat greater than the experimental values (see table), the agreement between them can be considered as satisfactory for a simple estimation. Anyway, qualitatively, the experimental situation is fully described. A more accurate calculation of γ_L requires a detailed analysis of the contributions of various interatomic interactions to the potential energies of NH_4Cl and NH_4Br in the three-dimensional case. Note that the phenomenon observed occurs only with a librational mode responsible for the transition and does not occur (or is incomparably small) in the case of a translational optical mode because of the smaller amplitude and frequency of oscillations. A variation in the width of the librational peak in the disordered phase of NH_4Cl that falls outside the resolution is likely to be associated with the variation in the lifetime of excitations in approaching the transition pressure to the ordered state. The absence of the splitting of the librational peak in the ordered state in NH_4Cl near the transition point, which was observed in NH_4Br [7, 8] and was associated with excitations in two potential wells in incomplete ordering, is obviously attributed to the insufficient energy resolution of the DN-12 spectrometer.

5. CONCLUSION

The results obtained in this work show that the orientational phase transition II–IV in NH_4Cl and NH_4Br results in an appreciable change in the behavior of the librational mode as a function of pressure; this fact manifests itself in the strong variation in the Grüneisen parameter and the narrowing of the librational peak. Such a behavior is associated with the fact that the ordering of ammonium ions changes the shape of the rotational potential from strongly anharmonic in the disordered phase II to nearly harmonic in the ordered phase IV. Because the phenomenon observed seems to be of a sufficiently general nature, one can expect that it will also manifest itself in other molecular crystals under orientational phase transitions, as well as in the variation of the properties associated with the anharmonicity, in particular, in thermal expansion.

ACKNOWLEDGMENTS

We are grateful to V.A. Sidorov for fabricating washers and assistance in calibrating the high-pressure vessel.

This work was supported by the Russian Foundation for Basic Research (project no. 00-02-17199) by the program for leading scientific schools (project nos. 00-15-96778 and 00-15-96712), and by the State Scientific and Engineering Program "Neutron Investigations of Matter."

REFERENCES

1. N. G. Parsonage and L. A. Stavely, *Disorder in Crystals* (Oxford Univ. Press, Oxford, 1979; Mir, Moscow, 1982), Vol. 1.
2. A. M. Balagurov, D. P. Kozlenko, B. N. Savenko, *et al.*, Fiz. Tverd. Tela (St. Petersburg) **40**, 142 (1998) [Phys. Solid State **40**, 127 (1998)].
3. A. M. Balagurov, B. N. Savenko, A. V. Borman, *et al.*, High Press. Res. **14**, 55 (1995).
4. A. M. Heyns, J. Phys. Chem. Solids **41**, 769 (1980).
5. Y. Ebisuzaki, J. Chem. Phys. **61**, 3170 (1974).
6. A. N. Ivanov, D. F. Litvin, Ya. Maĭer, *et al.*, Preprint No. 80-91, ITÉF (Institute of Theoretical and Experimental Physics, Moscow, 1991).
7. V. P. Glazkov, V. A. Somenkov, G. F. Syrykh, and B. N. Savenko, High Press. Res. **17**, 289 (2000).
8. G. Venkataraman *et al.*, J. Phys. Chem. Solids **27**, 1103 (1966).
9. V. L. Aksenov, A. M. Balagurov, V. P. Glazkov, *et al.*, Physica B (Amsterdam) **265**, 258 (1999).
10. V. P. Glazkov and I. V. Goncharenko, Fiz. Tekh. Vys. Davleniĭ **1**, 56 (1991).

11. L. G. Khvostantsev, L. F. Vereshchagin, and A. P. Novikov, High Temp.-High Press. **9**, 637 (1977).

12. O. Schulte and W. B. Holzapfel, High Press. Res. **4**, 321 (1991).

13. A. M. Balagurov, V. P. Glazkov, D. P. Kozlenko, *et al.*, Preprint No. R13-97-312, OIYaI (Joint Inst. for Nuclear Research, Dubna, 1997).

14. L. D. Landau and E. M. Lifshitz, *Course of Theoretical Physics*, Vol. 3: *Quantum Mechanics: Non-Relativistic Theory* (Nauka, Moscow, 1989, 4th ed.; Pergamon, New York, 1977, 3rd ed.).

15. J. Töpler, D. R. Richter, and T. Springer, J. Chem. Phys. **69**, 3170 (1978).

16. R. E. Lechner, G. Badurek, A. J. Dianoux, *et al.*, J. Chem. Phys. **73**, 934 (1980).

17. P. S. Leung, T. I. Taylor, and W. W. Havens, Jr., J. Chem. Phys. **48**, 4912 (1968).

18. B. B. Weiner and C. W. Garland, J. Chem. Phys. **56**, 155 (1972).

19. V. P. Glazkov, D. P. Kozlenko, B. N. Savenko, and V. A. Somenkov, Zh. Éksp. Teor. Fiz. **117**, 362 (2000) [JETP **90**, 319 (2000)].

20. S. N. Vaidya and G. C. Kennedy, J. Phys. Chem. Solids **32**, 951 (1971).

Translated by I. Nikitin

Journal of Experimental and Theoretical Physics, Vol. 94, No. 6, 2002, pp. 1140–1148.
Translated from Zhurnal Éksperimental'noĭ i Teoreticheskoĭ Fiziki, Vol. 121, No. 6, 2002, pp. 1328–1338.

SOLIDS
Electronic Properties

The Magnetic Susceptibility of Two-Dimensional Ising Model on a Finite-Size Lattice

A. I. Bugrij* and O. O. Lisovyy

Bogolyubov Institute for Theoretical Physics, National Academy of Sciences of Ukraine, Kiev, 03143 Ukraine
**e-mail: abugrij@bitp.kiev.ua*

Received December 13, 2001

Abstract—The form factor representation of the correlation function of the 2D Ising model on a cylinder is generalized to the case of arbitrary arrangement of correlating spins. The magnetic susceptibility on a lattice, one of whose dimensions (N) is finite, is calculated in both the ferromagnetic and the paramagnetic region of the parameters of the model. The structure of singularities of susceptibility in the complex temperature plane at finite values of N and the transition to the thermodynamic limit $N \longrightarrow \infty$ are discussed. © *2002 MAIK "Nauka/Interperiodica".*

1. INTRODUCTION

The Ising model has long been attracting the attention of researchers. The computation of free energy [1], and spontaneous magnetization [2], and the representation of correlation functions in the form of series [3, 4], as well as the derivation and solution of nonlinear differential equations [5, 6] for the correlation functions, are the most important advances of present-day mathematical physics. The problem on the computation of the partition function in the 2D Ising model with interaction between nearest neighbors in the absence of an external field is exactly solved [7] both in the thermodynamic limit and on a finite-size lattice with due regard for different boundary conditions. The elegance and simplicity of the corresponding expressions enable one to thoroughly study the special features of transition to the thermodynamic limit and get an idea of the mechanism of the emergence of critical singularities in thermodynamic quantities from both the physical and the mathematical standpoint.

The analytical expressions for thermodynamic quantities, which include the dependence on the lattice size, are useful from the standpoint of possible applications as well. They may be used for reference in solving problems of computer simulation of thermodynamic and quantum-field systems for quantitative estimation of the number of degrees of freedom at which a discrete numerical model may be taken to be adequate to the initial continuous and infinite system. Such results may further be used as the starting point in theoretical analysis of problems associated with modern experiments and technologies, where one has to deal with an explicitly noninfinite number of particles.

In this paper, exact expressions are given for the pair correlation function and susceptibility in the Ising model on a lattice with one finite, N = const, and the other infinite, $M \longrightarrow \infty$, dimension in the form analogous to form factor expansion [8, 9]. We will investigate the structure of singularities of susceptibility at finite values of N and discuss the transition to the thermodynamic limit $N \longrightarrow \infty$.

2. CORRELATION FUNCTION $\langle\sigma(0, 0)\sigma(x, 0)\rangle$

The Ising model on an $M \times N$ square lattice (see Fig. 1) is defined by the Hamiltonian $H[\sigma]$,

$$H[\sigma] = -J\sum_{\mathbf{r}}\sigma(\mathbf{r})(\nabla_x + \nabla_y)\sigma(\mathbf{r}),$$

where the two-dimensional vector $\mathbf{r} = (x, y)$ labels the lattice sites: $x = 1, 2, \ldots, M$, $y = 1, 2, \ldots, N$; the Ising spin $\sigma(\mathbf{r})$ in each site assumes the values of ± 1; the parameter $J > 0$ defines the coupling energy of a pair of

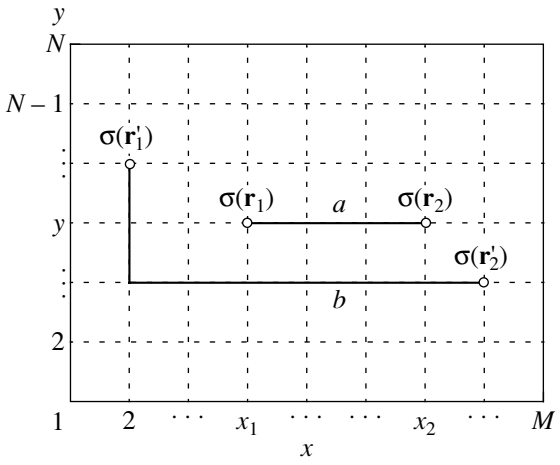

Fig. 1. The numbering of the lattice sites and the variants of arrangement of correlating spins: (a) spins are arranged on a line parallel to the cylinder axis, and (b) arbitrary arrangement of spins on the lattice.

adjacent spins. The shift operators ∇_x and ∇_y act as

$$\nabla_x\sigma(x, y) = \sigma(x + 1, y), \quad \nabla_y\sigma(x, y) = \sigma(x, y + 1).$$

The partition function at the given temperature β^{-1}

$$Z = \sum_{[\sigma]} e^{-\beta H[\sigma]} \tag{2.1}$$

and the pair correlation function

$$\langle\sigma(\mathbf{r}_1)\sigma(\mathbf{r}_2)\rangle = Z^{-1}\sum_{[\sigma]} e^{-\beta H[\sigma]}\sigma(\mathbf{r}_1)\sigma(\mathbf{r}_2) \tag{2.2}$$

are given by sums over all possible spin configurations. We will use the following dimensionless parameters:

$$K = \beta J, \quad t = \tanh K, \quad s = \sinh 2K. \tag{2.3}$$

We will treat an Ising lattice with periodic boundary conditions along both axes. For the shift operators, these conditions lead to the equalities

$$(\nabla_x)^M = 1, \quad (\nabla_y)^N = 1.$$

With these boundary conditions, the partition function given by Eq. (2.1) may be represented as the sum of four terms [7],

$$Z = (2\cosh^2 K)^{MN}\frac{1}{2}(Q^{f,f} + Q^{f,b} + Q^{b,f} - Q^{b,b}), \tag{2.4}$$

each of which is a Pfaffian of the operator $\hat{D}$ (the lattice analog of the Dirac operator),

$$Q = \mathrm{Pf}\hat{D}, \tag{2.5}$$

where

$$\hat{D} = \begin{pmatrix} 0 & 1 & 1 + t\nabla_x & 1 \\ -1 & 0 & 1 & 1 + t\nabla_y \\ -1 - t\nabla_{-x} & -1 & 0 & 1 \\ -1 & -1 - t\nabla_y & -1 & 0 \end{pmatrix}. \tag{2.6}$$

The superscripts (f, b) of the quantities Q in Eq. (2.4) indicate the type of boundary conditions for the operators (∇_x, ∇_y), respectively, which enter the matrix given by Eq. (2.6),

$$(\nabla_x^b)^M = (\nabla_y^b)^N = 1, \quad (\nabla_x^f)^M = (\nabla_y^f)^N = -1. \tag{2.7}$$

If one of the lattice dimensions exceeds considerably the other one, for example, $M \gg N$, i.e., the torus degenerates into a cylinder, then only the "antiperiodic" contribution survives on the right-hand side of Eq. (2.4),[1]

$$Z = (2\cosh^2 K)^{MN} Q^{f,f}. \tag{2.8}$$

[1] This is taken to mean that $Z = (2\cosh^2 K)^{MN} Q^{f,f}(1 + \epsilon(M, N, s))$; here, the function $\epsilon(M, N, s)$ has, at $s > 0$ and $N \geq 1$, a well-defined limit $\lim_{M\to\infty}\epsilon(M, N, s) = 0$. It is obvious that $\epsilon(M, N, 0) = 0$, because all Pfaffians in Eq. (2.4) $Q^{\alpha,\beta} = 1$. By way of illustration, consider the asymptotic expression for $\epsilon(M, N, 1)$ at $M \gg N \gg 1$ $\epsilon(M, N, 1) \approx \exp[-(\pi M)/(4N)]$.

The operator $\hat{D}$ is translationally invariant and diagonalized by Fourier transformation, and the Pfaffian given by Eq. (2.5) is readily calculated. As a result, the following factorized representation is derived for the partition function given by Eq. (2.8):

$$Z = 2^{MN}\prod_{\mathbf{q}}^{f,f}(s^2 + 1 - s\cos q_x - s\cos q_y)^{1/2}. \tag{2.9}$$

The superscript f on the sign of products (or summation, in what follows) indicates that the quasimomentum components q_x and q_y run in the Brillouin zone over half-integer values in the units $2\pi/M$ and $2\pi/N$, respectively; the superscript b indicates integer values. For example,

$$\prod_{q_y}^{f}\mathcal{F}(q_y) = \prod_{l=1}^{N}\mathcal{F}\left(\frac{2\pi}{N}\left(l + \frac{1}{2}\right)\right),$$

$$\prod_{q_y}^{b}\mathcal{F}(q_y) = \prod_{l=1}^{N}\mathcal{F}\left(\frac{2\pi}{N}l\right).$$

The product on the right-hand side of Eq. (2.9) with respect to one of the components of momentum may be taken in an explicit form, and the partition function takes the form

$$Z = (2s)^{MN/2}\prod_{q}^{f} e^{M\gamma(q)/2}(1 + e^{-M\gamma(q)}), \tag{2.10}$$

where the function $\gamma(q)$ is defined by the positive root of the equation

$$\sinh\frac{\gamma(q)}{2} = \sinh^2\frac{\mu}{2} + \sin^2\frac{q}{2}, \tag{2.11}$$

$$\sinh\frac{\mu}{2} = \frac{1}{\sqrt{2}}(\sqrt{s} - 1/\sqrt{s}). \tag{2.12}$$

If $q \neq 0$, $\gamma(q)$ remains positive in the entire permissible range of variation of the parameter $0 < s < \infty$. However, $\gamma(0)$ as a function of s changes its sign after crossing the critical point $s = 1$. Because the product in Eq. (2.10) is taken over the fermion spectrum which does not have a point $q = 0$, no problems are caused by the fact that $\gamma(0)$ is of alternating sign. However, we will run ahead somewhat and note that the ambiguity in the definition of $\gamma(0) = \pm\mu$ results in two different representations for the correlation function.

The sum over spin configurations on the right-hand side of expression (2.2) for the correlation function may also be represented in the form of a combination of Pfaffians of some operators [10]. However, the respective matrices are not translationally invariant, which complicates the calculations drastically compared with the computation of the partition function. Nevertheless, the ratio of the Pfaffians, in terms of which the correlation function is expressed in the final analysis, may be

reduced to the determinant of a matrix of much smaller dimension,

$$\langle \sigma(0)\sigma(\mathbf{r})\rangle = \det A^{(\dim)}, \quad (2.13)$$

where the dimension dim = dim(**r**) is defined by the distance between the correlating spins. Subsequent operations (which are far from simple) consist in calculating the determinant, or, to be more precise, in transforming representation (2.13) to a representation in which the dependence on distance would be in an analytical form. Papers on this subject are still being published, although forty years have passed since the pioneer paper [3], which points to the complexity of the problem.

Most acceptable from the physical standpoint appears to be the so-called form factor representation of the Ising model, which was first obtained by Palmer and Tracy [8] for an infinite lattice in the ferromagnetic region ($K > K_c$, $s > 1$) and later generalized by Yamada [9] to the paramagnetic case ($K < K_c$, $s < 1$). Note that a similar representation for the two-point Green's function was derived somewhat earlier [11] within the *S*-matrix approach [12] for a quantum-field model with a factorable *S* matrix ($S_2 = -1$), which is usually associated with the scaling limit of the Ising model. The discovery of the form factor representation gave rise to the development of a separate trend [13] in exactly integrable models of the quantum field theory.

Naturally, the problem is much more complicated for a finite lattice; however, the result of [14] proves, in a way, to be even simpler. In a particular case, when the spins are arranged along one of the principal axes of the lattice, the matrix in the right-hand part of Eq. (2.13) takes the Toeplitz form, and the problem is simplified. Let the sites at which the correlating spins are located be arranged on a line parallel to the horizontal axis, as is shown in Fig. 1 (line *a*). Then,

$$\langle \sigma(\mathbf{r}_1)\sigma(\mathbf{r}_2)\rangle = \det A^{(|x|)}, \quad \mathbf{r}_2 - \mathbf{r}_1 = (x, 0), \quad (2.14)$$

where the matrix $A^{(|x|)}_{k,k'}$ of size $|x| \times |x|$ has the form [14]

$$A^{(|x|)}_{k,k'} = \frac{1}{MN} \times \sum_{\mathbf{p}}^{f,\,f} \frac{e^{ip_x(k-k')}[2t(1+t^2) - (1-t^2)(e^{ip_x} + t^2 e^{-ip_x})]}{(1+t^2)^2 - 2t(1-t^2)(\cos p_x + \cos p_y)}, \quad k, k' = 0, 1, \ldots, |x| - 1, \quad (2.15)$$

and its elements on diagonals parallel to the principal diagonal ($k - k'$ = const) are identical.

As is demonstrated in [14], the Wiener–Hopf technique of integral equations [7] properly adapted to the case of a finite-size lattice may be used to analytically calculate the Toeplitz determinant given by Eqs. (2.14), and the correlation functions are represented as

$$\langle \sigma(\mathbf{r}_1)\sigma(\mathbf{r}_2)\rangle = (\xi\xi_T)e^{-|x|/\Lambda} \sum_{l=0}^{[N/2]} g_{2l}(x) \quad (2.16)$$

at $\gamma(0) = \mu$,

$$\langle \sigma(\mathbf{r}_1)\sigma(\mathbf{r}_2)\rangle = (\xi\xi_T)e^{-|x|/\Lambda} \sum_{l=0}^{[(N-1)/2]} g_{2l+1}(x) \quad (2.17)$$

at $\gamma(0) = -\mu$,

$$g_n(x) = \frac{e^{-n/\Lambda}}{n!N^n} \sum_{[q]}^{b} \left(\prod_{i=1}^{n} \frac{e^{-|x|\gamma_i - \eta_i}}{\sinh\gamma_i} \right) F_n^2[q], \quad g_0 = 1, \quad (2.18)$$

$$F_n[q] = \prod_{i<j}^{n} \frac{\sin((q_i - q_j)/2)}{\sinh((\gamma_i + \gamma_j)/2)}, \quad F_1 = 1, \quad (2.19)$$

where $\gamma_i = \gamma(q_i)$ and $\eta_i = \eta(q_i)$. Expressions (2.16) and (2.17) are the sums of a finite number of contributions g_n; however, the upper limits of summation may be formally extended to infinity, because one can see in Eqs. (2.19) that the form factors $F_n[q]$ vanish at $n > N$. Note an important detail, namely, that the summation over the phase volume in (2.18) is taken over the boson spectrum of quasimomenta, in contrast with the initial fermion spectrum which defines, in particular, the matrix given by Eq. (2.15) as well. The remaining quantities appearing in Eqs. (2.16)–(2.19) are given by

$$\xi = \left|1 - s^{-4}\right|^{1/4}, \quad (2.20)$$

$$\ln\xi_T = \frac{N^2}{2\pi^2} \int_0^\pi \frac{dp\,dq\,\gamma'(p)\gamma'(q)}{\sinh(N\gamma(p))\sinh(N\gamma(q))} \times \ln\left|\frac{\sin((p+q)/2)}{\sin((p-q)/2)}\right|, \quad (2.21)$$

$$\Lambda^{-1} = \frac{1}{\pi}\int_0^\pi dp \ln\coth\left(\frac{N\gamma(p)}{2}\right), \quad (2.22)$$

$$\eta(q) = \frac{1}{\pi}\int_0^\pi \frac{dp(\cos p - e^{-\gamma(q)})}{\cosh\gamma(q) - \cos p} \ln\coth\left(\frac{N\gamma(p)}{2}\right). \quad (2.23)$$

One can see in Eqs. (2.21)–(2.23) that the quantities ξ_T, Λ^{-1}, and $\eta(q)$, which will be referred to as cylindrical parameters, explicitly depend on the number of sites *N* on the cylinder circumference. Their asymptotic behavior for high values of *N*, or, to be more precise, for $N|\mu| \gg 1$, is as follows:

$$\ln\xi_T \approx \frac{1}{\pi}e^{-2N|\mu|}, \quad (2.24)$$

$$\Lambda^{-1} \approx e^{-N|\mu|}\sqrt{\frac{2\sinh|\mu|}{\pi N}}, \quad (2.25)$$

$$\eta(q) \approx \frac{4e^{-N|\mu|}}{(e^{\gamma(q)}-1)}\sqrt{\frac{\sinh|\mu|}{2\pi N}}. \quad (2.26)$$

Outside of the critical point, as N increases, the cylindrical parameters Λ^{-1}, $\ln\xi_T$, and $\eta(q)$ decrease exponentially and go to zero on an infinite lattice. The finite sums given by Eqs. (2.16) and (2.17) transform into series, the summation over the phase volume in (2.18) is replaced by integration, and, as a result, form factor representations on a cylinder transform into form factor representations on an infinite lattice [8, 9]. For any finite values of N, both expansions (i.e., in terms of even values of n (2.16) and in terms of odd values of n (2.17)) are valid in both the ferromagnetic ($s > 1$) and the paramagnetic ($s < 1$) region. However, for $N \longrightarrow \infty$, the series in terms of even values of n is well-defined and convergent in the ferromagnetic region, and the series in terms of odd values of n, in the paramagnetic region. It will be recalled that the starting quantity was the determinant given by Eq. (2.14) of a matrix of size $|x| \times |x|$; the number of terms in the formal definition of this determinant increases very rapidly with $|x|$. However, form factor representations (2.16)–(2.19) are the finite sum of terms for a fixed value of N, with the number of those terms being independent of $|x|$. This offers a unique possibility of verifying expressions (2.16)–(2.19) by comparing them with the results of, for example, transfer-matrix calculations for N-row Ising chains, and we took the advantage of this possibility. For a given value of N, the transfer matrix for an N-row chain of Ising spins is $2^N \times 2^N$. Therefore, for small values of N, one can analytically solve the respective set of equations and derive all of the eigenvalues and eigenvectors. We managed to perform such verification analytically for $N = 2, 3, 4$ and numerically for $N = 5, 6$. Naturally, the result was positive.

3. CORRELATION FUNCTION $\langle\sigma(0, 0)\sigma(x, y)\rangle$

It will be recalled that a rigorous derivation of form factor representation on a cylinder was given in [14] only for the particular case of the correlating spins arranged along the cylinder axis. We have not yet succeeded in generalizing the method to the case of the correlating spins arranged on the cylinder circumference, much less for their arbitrary configuration (Fig. 1, line *b*). Meanwhile, in order to obtain a momentum representation for the correlation function

$$\tilde{G}(\mathbf{p}) = \sum_{\mathbf{r}} e^{i\mathbf{p}\cdot\mathbf{r}}\langle\sigma(0)\sigma(\mathbf{r})\rangle \quad (3.1)$$

or the magnetic susceptibility related to the value of $\tilde{G}(\mathbf{p} = 0)$, one must have the explicit dependence of the correlation function on both components of the radius vector $\mathbf{r}$. From the physical standpoint, the form factor representation (2.16)–(2.19) being treated has a very transparent structure. This enables one to make reasonable assumptions for respective generalizations; the above-mentioned possibility of independent verification enables one to eliminate false hypotheses and make a correct choice. In principle, with a nonzero value of the y component of the vector $\mathbf{r}$, all quantities appearing in Eqs. (2.16)–(2.19) may be modified. However, the variation that clearly suggests itself, for example, in the case of respective expressions for the correlation function in a system of free bosons or fermions on a lattice, is primarily the substitution

$$e^{-|x|\gamma(q)} \longrightarrow e^{-|x|\gamma(q) - iyq}.$$

Surprisingly enough, this proves to be sufficient. If one uses the expression

$$g_n(\mathbf{r}) = \frac{e^{-n/\Lambda}}{n!N^n}\sum_{[q]}^{b}\prod_{j=1}^{n}\left(\frac{e^{-|x|\gamma_j - iyq_j - \eta_j}}{\sinh\gamma_j}\right)F_n^2[q], \quad (3.2)$$
$$g_0 = 1,$$

instead of $g_n(x)$ in Eq. (2.18), the correlation functions given by Eqs. (2.16) and (2.17) will exactly (in an analytical form) agree with the results of transfer-matrix calculations for $N = 2, 3, 4$ in the entire range of the parameters x, y, and K. The results of numerical calculations confirm this for higher values of $N = 5, 6$. In the case of $N > 6$, the size of the transfer matrix is too large for numerical computer calculations as well. We have no doubt that generalization (3.2) is true. Hopefully, the knowledge of the correct answer will facilitate its rigorous derivation.

For illustration, consider the example with $N = 3$. By their structure, expansions (2.16) and (2.17) in view of (3.2) are very similar to the representation of the correlation function in the form of an expansion in a power series in the eigenvalues of the transfer matrix,

$$\langle\sigma(0)\sigma(\mathbf{r})\rangle = a_1(y)(\lambda_1/\lambda_0)^{|x|} + a_2(y)(\lambda_2/\lambda_0)^{(x)} + \ldots, \quad (3.3)$$

where λ_0 is the highest eigenvalue, and the coefficients $a_j(y)$ are expressed in terms of bilinear combinations of components of eigenvectors. In order to reduce, for example, Eq. (2.17) to the form of (3.3), we will use the following expressions for the cylindrical parameters ξ_T and Λ^{-1}, as well as $\eta(q)$:

$$\Lambda^{-1} = \frac{1}{2}\left(\sum_q^f\gamma(q) - \sum_q^b\gamma(q)\right), \quad (3.4)$$

$$\exp(-\Lambda^{-1} - \eta(q_i)) = \frac{\prod_q^b\sinh\left(\frac{\gamma(q)+\gamma(q_i)}{2}\right)}{\prod_q^f\sinh\left(\frac{\gamma(q)+\gamma(q_i)}{2}\right)}, \quad (3.5)$$

$$\xi_T^4 = \left(\prod_q^b \prod_p^f \sinh^2\left(\frac{\gamma(q)+\gamma(p)}{2}\right)\right) \times \left[\prod_q^b \prod_p^b \sinh\left(\frac{\gamma(q)+\gamma(p)}{2}\right) + \prod_q^f \prod_p^f \sinh\left(\frac{\gamma(q)+\gamma(p)}{2}\right)\right]^{-1}. \quad (3.6)$$

These expressions are derived from Eqs. (2.21)–(2.23) if we change to contour integrals in $z = e^{iq}$. After contracting the integration contours, the respective integrals are expressed in terms of sums of residues at the poles, which produces the representations given by Eqs. (3.4)–(3.6).

For $N = 3$, Eqs. (3.4)–(3.6) and (2.20) give

$$\Lambda^{-1} = \frac{1}{2}\left[\gamma(\pi) + 2\gamma\left(\frac{\pi}{3}\right) - \gamma(0) - 2\gamma\left(\frac{2\pi}{3}\right)\right], \quad (3.7)$$

$$\xi\xi_T = \frac{\sinh\frac{\gamma(0)+\gamma(\pi/3)}{2}\sinh\frac{\gamma(\pi)+\gamma(2\pi/3)}{2}\sinh^2\frac{\gamma(2\pi/3)+\gamma(\pi/3)}{2}}{\sinh\frac{\gamma(0)+\gamma(2\pi/3)}{2}\sinh\frac{\gamma(\pi)+\gamma(\pi/3)}{2}\sinh\gamma(\pi/3)\sinh\gamma(2\pi/3)}, \quad (3.8)$$

$$\exp(-\Lambda^{-1} - \eta(q)) = \frac{\sinh\frac{\gamma(0)+\gamma(q)}{2}\sinh^2\frac{\gamma(2\pi/3)+\gamma(q)}{2}}{\sinh\frac{\gamma(\pi)+\gamma(q)}{2}\sinh^2\frac{\gamma(\pi/3)+\gamma(q)}{2}}. \quad (3.9)$$

As a result, we derive

$$\ln\frac{\lambda_0}{\lambda_1} = \Lambda^{-1} + \gamma(0), \quad (3.10)$$

$$\ln\frac{\lambda_0}{\lambda_2} = \Lambda^{-1} + \gamma\left(\frac{2\pi}{3}\right), \quad (3.11)$$

$$\ln\frac{\lambda_0}{\lambda_3} = \Lambda^{-1} + \gamma(0) + 2\gamma\left(\frac{2\pi}{3}\right), \quad (3.12)$$

$$a_1(y) = \frac{1}{3}\frac{\sinh\frac{\gamma(0)+\gamma(2\pi/3)}{2}\sinh\frac{\gamma(\pi)+\gamma(2\pi/3)}{2}\sinh^2\frac{\gamma(2\pi/3)+\gamma(\pi/3)}{2}}{\sinh\frac{\gamma(0)+\gamma(\pi/3)}{2}\sinh\frac{\gamma(\pi)+\gamma(\pi/3)}{2}\sinh\gamma(\pi/3)\sinh\gamma(2\pi/3)}, \quad (3.13)$$

$$a_2(y) = \frac{2}{3}\frac{\sinh\frac{\gamma(0)+\gamma(\pi/3)}{2}\sinh\frac{\gamma(0)+\gamma(\pi)}{2}}{\sinh\gamma(\pi/3)\sinh\frac{\gamma(\pi/3)+\gamma(\pi)}{2}}\cos\left(\frac{2\pi y}{3}\right), \quad (3.14)$$

$$a_3(y) = \frac{1}{64}\left[\sinh\frac{\gamma(0)+\gamma(\pi/3)}{2}\sinh\frac{\gamma(\pi)+\gamma(\pi/3)}{2} \times \sinh\frac{\gamma(0)+\gamma(2\pi/3)}{2}\sinh\frac{\gamma(\pi)+\gamma(2\pi/3)}{2} \times \sinh\gamma\left(\frac{\pi}{3}\right)\sinh\gamma\left(\frac{2\pi}{3}\right)\sinh^2\frac{\gamma(\pi/3)+\gamma(2\pi/3)}{2}\right]^{-1}. \quad (3.15)$$

The $2^3 \times 2^3$ transfer matrix has eight eigenvalues, but some of them are identical. In addition, some components of the respective eigenvectors go to zero. Therefore, only three (rather than seven) eigenvectors remain in the expression (3.3) for the correlation function. In view of the definition (2.11), (2.12) of the function $\gamma(q)$ for particular values of the momentum $q = 0, \pi/3, 2\pi/3, \pi$, these contributions exactly correspond to Eqs. (3.10)–(3.15).

4. MOMENTUM REPRESENTATION OF THE CORRELATION FUNCTION

Given expression (3.2) for $g_n(\mathbf{r})$, which contains an explicit dependence on the projections of $\mathbf{r}$, we will take the Fourier transform. We will write momentum representation (3.1) in the form of the sum of partial contributions similarly to Eqs. (2.16) and (2.17),

$$\tilde{G}(\mathbf{p}) = \xi\xi_T \sum_n \tilde{g}_n(\mathbf{p}), \tag{4.1}$$

$$\tilde{g}_n(\mathbf{p}) = \sum_{\mathbf{r}} e^{-|x|/\Lambda} g_n(\mathbf{r}) e^{i\mathbf{p}\mathbf{r}}, \tag{4.2}$$

where

$$\sum_{\mathbf{r}} = \sum_{x=-\infty}^{\infty} \sum_{y=1}^{N}. \tag{4.3}$$

We perform summation in Eq. (4.2) to derive

$$\tilde{g}_n(\mathbf{p}) = \frac{e^{-n/\Lambda}}{n! N^{n-1}} \sum_{[q]}^{b} \left(\prod_{j=1}^{n} \frac{e^{-\eta_j}}{\sinh j} \right) \times \frac{\sinh\left(\Lambda^{-1} + \sum_{j=1}^{n} \gamma_j \right) F_n^2[q]}{\cosh\left(\Lambda^{-1} + \sum_{j=1}^{n} \gamma_j \right) - \cos p_x} \delta\left(p_y - \sum_{j=1}^{n} q_j \right). \tag{4.4}$$

The quasimomentum component p_x has a continuous spectrum in the $[-\pi, \pi]$ range, and p_y is discrete,

$$p_y = \frac{2\pi l}{N}, \quad l = 1, 2, \ldots, N.$$

Accordingly, the δ function on the right-hand side of Eq. (4.4) has the meaning of the Kronecker symbol,

$$\delta\left(p_y - \sum_{j=1}^{n} q_j \right) = \delta\left(l - \sum_{j=1}^{n} l_j \right)\Bigg|_{\mathrm{mod}\, N}.$$

The function $\tilde{g}_n(\mathbf{p})$ is periodic in p_x, p_y, with the period 2π. We introduce unity under the summation sign in Eq. (4.4),

$$1 = \int_{\Lambda^{-1} + n\gamma(0)}^{\Lambda^{-1} + n\gamma(\pi)} d\omega \delta\left(\Lambda^{-1} + \sum_{j=1}^{n} \gamma_j - \omega \right)$$

(here, the Dirac δ function is under the integral), and change the order of summation and integration to derive

$$\tilde{g}_n(\mathbf{p}) = \int_{\Lambda^{-1} + n\gamma(0)}^{\Lambda^{-1} + n\gamma(\pi)} d\omega \frac{\sinh\omega}{\cosh\omega - \cos p_x} \rho_n(\omega, p_y), \tag{4.5}$$

$$\rho_n(\omega, p_y) = \frac{e^{-n/\Lambda}}{n! N^{n-1}} \sum_{[q]}^{b} \left(\prod_{j=1}^{n} \frac{e^{-\eta_j}}{\sinh\gamma_j} \right) \times F_n^2[q] \delta\left(\Lambda^{-1} + \sum_{j=1}^{n} \gamma_j - \omega \right) \delta\left(p_y - \sum_{j=1}^{n} q_j \right). \tag{4.6}$$

On an infinite lattice in the scaling limit, the rotation symmetry is restored and, as a result, the set of equations (4.5) and (4.6) changes to the classical Lehmann representation in quantum field theory.

5. MAGNETIC SUSCEPTIBILITY

If a rectangular lattice has a size $M \times N$ and the same interaction energies for the vertical and horizontal couplings, the partition function Z depends on four variables,

$$Z = Z(K, h, N, M) = \sum_{[\sigma]} e^{-\beta H[\sigma] + h\sum_{\mathbf{r}} \sigma(\mathbf{r})}, \tag{5.1}$$

where the dimensionless parameter $h = \beta\mathcal{H}$, and $\mathcal{H}$ is the magnetic field. The specific magnetization $\mathfrak{M}$ and magnetic susceptibility χ are expressed in terms of field derivatives of the partition function,

$$\mathfrak{M}(K, h, N, M) = \frac{1}{MN} \frac{\partial \ln Z}{\partial h} = \langle \sigma \rangle, \tag{5.2}$$

$$\beta^{-1}\chi(K, h, N, M) = \frac{\partial \mathfrak{M}}{\partial h} = \sum_{\mathbf{r}} (\langle \sigma(0)\sigma(\mathbf{r}) \rangle - \langle \sigma \rangle^2). \tag{5.3}$$

Due to Z_2 symmetry of the Ising model, the magnetization goes to zero at $h = 0$ for any finite dimensions M and N, and even if one of these dimensions is held finite. In the latter case, when, for example, $M \longrightarrow \infty$ and $N = \mathrm{const}$, a two-dimensional Ising model degenerates into an N-row chain of Ising spins; from the thermodynamic standpoint, this chain is a one-dimensional system in which a spontaneous violation of symmetry is impossible. We represent the susceptibility in the form of the sum of partial contributions to derive from Eqs. (4.1)–(4.4)

$$\chi = \chi_0 + \sum_{l=1}^{[N/2]} \chi_{2l} \quad \text{at} \quad \gamma(0) = \mu, \tag{5.4}$$

$$\beta^{-1}\chi_0 = \xi\xi_T N \coth(1/2\Lambda), \tag{5.5}$$

$$\chi = \sum_{l=0}^{[(N-1)/2]} \chi_{2l+1} \quad \text{at} \quad \gamma(0) = -\mu, \tag{5.6}$$

$$\beta^{-1}\chi_n = \frac{e^{-n/\Lambda}}{n!N^{n-1}}\sum_{[q]}^{b}\left(\prod_{i=1}^{n}\frac{e^{-\eta_i}}{\sinh\gamma_i}\right) \times F_n^2[q]\coth\left[\frac{1}{2}\left(\Lambda^{-1}+\sum_{i=1}^{n}\gamma_i\right)\right]\delta\left(\sum_{i=1}^{n}q_i\right). \quad (5.7)$$

In the paramagnetic region ($s < 1$), expression (5.6) admits the limit $N \longrightarrow \infty$ and transforms to susceptibility on an infinite lattice owing to the absence of spontaneous magnetization in the paramagnetic phase. In the ferromagnetic region ($s > 1$), the transition to the limit $N \longrightarrow \infty$ is possible only for the quantity χ_F,

$$\chi_F = \chi - \chi_0 = \sum_{l=1}^{\infty}\chi_{2l}, \quad (5.8)$$

which reproduces what is usually regarded as the magnetic susceptibility of the Ising model at $h = 0$ in the thermodynamic limit. For high but finite values of N, the main contribution to susceptibility is made by the term χ_0, as is seen from Eq. (5.5),

$$\beta^{-1}\chi_0 \approx 2\xi N\Lambda \approx \frac{\sqrt{\pi}\xi N^{3/2}}{\sqrt{\sinh|\mu|}}e^{N|\mu|}, \quad (5.9)$$

which exponentially increases with the cylinder circumference. It follows from Eq. (5.9) that, the higher the value of N, the lower the perturbing field $\delta h \sim e^{-N|\mu|}$ required for ordering all spins on the lattice.

Although the two-dimensional Ising model is usually referred to as exactly solvable, no exact solution for the partition function in the presence of an external field has yet been found either in the thermodynamic limit or for a finite-size lattice. However, the very fact of the emergence of spontaneous magnetization for an infinite-size lattice may be ascertained from analysis of high- and low-temperature expansions for free energy in the Ising model without appealing to the exact solution. A rigorous definition of spontaneous magnetization is given by the following order of limiting processes in accordance with Bogolyubov's concept of quasiaverages,

$$\mathfrak{M}_0(K) = \lim_{h\to 0}\left[\lim_{M,N\to\infty}\mathfrak{M}(K, h, N, M)\right]. \quad (5.10)$$

However, assuming the permutability of the respective limits and the weakening of correlations over long distances, one can derive an exact expression for the square of spontaneous magnetization and relate it to the value given by Eq. (2.20) of pair correlation function for the Ising model on an infinite lattice with zero magnetic field,

$$\mathfrak{M}_0^2(K) = \lim_{|\mathbf{r}|\to\infty}\langle\sigma(0)\sigma(\mathbf{r})\rangle = \langle\sigma(0)\rangle\langle\sigma(\infty)\rangle = \langle\sigma\rangle^2 = \xi. \quad (5.11)$$

Meanwhile, in the thermodynamic limit, the sum over the lattice of each one of the terms on the right-hand side of Eq. (5.3) taken separately is divergent. Therefore, the replacement of $\mathfrak{M}^2(K, 0, \infty, \infty)$ in the last stage of the limiting processes $h \longrightarrow 0$ and $M, N \longrightarrow \infty$ by the limiting values of the correlation function (equal to ξ) under the (infinite) summation sign implies both equality (5.11) and the existence of the limit

$$\lim_{h\to\infty}\left\{\lim_{M,N\to\infty}MN[\mathfrak{M}^2(K, h, M, N) - \xi]\right\} = f(K), \quad (5.12)$$

and, in addition,

$$f(K) = 0. \quad (5.13)$$

The explicit form of dependence of the correlation function on the dimension N, namely, the exponentially fast tendency of the cylindrical parameters to their limiting values given by Eqs. (2.24)–(2.26) may serve as indirect proof of the validity of equalities (5.12) and (5.13).

One can see in Eqs. (2.18) and (3.2) that the behavior of the correlation function over long distances in the ferromagnetic region is largely defined by the first term in expansion (2.16); note that this term does not depend on the y projection,

$$G_0(|\mathbf{r}|) = \xi\xi_T e^{-|x|/\Lambda}. \quad (5.14)$$

One can see that the distance of the order of Λ, within which the spins are rigidly correlated, increases very rapidly (see Eq. (2.25)) with N. Physically, this means that, in the ferromagnetic temperature region, the cylinder is divided into highly extended regions (domains) with nonzero magnetization, while the average magnetization of the entire infinitely long cylinder remains zero. It would be reasonable if the (square of) spontaneous magnetization in such a pattern was provided by the value of the correlation function at distances $|\mathbf{r}| = R(N)$, which are fairly long but do not exceed the domain size, rather than in the limit $|\mathbf{r}| \longrightarrow \infty$,

$$N \ll R(N) \ll \Lambda.$$

One can see in Eq. (2.25) that, at fairly high values of N, such inequalities may be valid. In accordance with this, the summation in infinite limits over the coordinate x in the definition of the thermodynamic limit of susceptibility given by Eq. (5.3) must be replaced by the summation within limits that do not exceed the characteristic domain size. In this case, definition (5.8) for susceptibility in the ferromagnetic phase is formally substantiated by the condition of vanishing of the quantity

$$\sum_{x=-R}^{R}\sum_{y=1}^{N}[G_0(|\mathbf{r}|) - G_0(R)] \approx \xi NR^2/\Lambda \xrightarrow[N\to\infty]{} 0$$

at $N \longrightarrow \infty$, which leads to the estimation of the thermodynamic cutoff parameter $R(N)$,

$$R(N) \ll \sqrt{\Lambda/N}\xi \approx e^{N|\mu|/2}[\pi/(2N\sinh|\mu|)]^{1/4}.$$

We believe that these estimations clarify to a certain extent the physical meaning of the formal procedure of thermodynamic limit.

6. STRUCTURE OF SINGULARITIES

The initial expression (2.1) for the partition function in the Ising model is a polynomial in s, and the solution given by Eq. (2.9) is a factorized notation of this polynomial. It provides a good example of the mechanism of Lee–Yang "zeros" [15], which causes the emergence of critical singularities in the thermodynamic limit. The roots of the polynomial given by Eq. (2.9) are arranged on the circle $|s| = 1$ in the complex s plane. For any finite values of M and N, no zero appears on the real axis $s = 1$ because of the absence of the value of quasimomentum $q_x = q_y = 0$ from the fermion spectrum. If at least one of the dimensions increases indefinitely, zeros crowd on the circle $|s| = 1$ to form a dense set. In the $M \longrightarrow \infty$, N = const limit, they transform into a finite number (equal to N) of branch points of the root type on the circle $|s| = 1$, as is demonstrated by representation (2.10) and Eqs. (2.11) and (2.12) defining $\gamma(q)$ as a function of s. In their turn, these branch points crowd, as N increases, to form a dense set; however, in the limit $N \longrightarrow \infty$, they transform into four isolated branch points of the logarithmic type at $s = \pm 1, \pm i$. As a result of such transformations, the specific heat in the thermodynamic limit becomes divergent ($\sim \ln|1 - s|$) at the critical point; however, in so doing, the specific heat is expressed in the form of one and the same function both above and below the phase transition temperature.

One would expect the pattern to be the same in the case of magnetic susceptibility as a function of the complex variable s. Indeed, the initial expression (2.2) for the correlation function with finite values of M and N is a ratio of polynomials in s. The denominator contains the partition function; we have briefly described above the formation of the structure of its singularities. Unfortunately, the polynomial in the numerator cannot be represented in an equally simple factorized form. Nevertheless, the form factor representation with $M \longrightarrow \infty$ and finite value of N obtained by us indicates that the correlation function has a finite number of root branch points on the circle $|s| = 1$. Their number is doubled compared with the case of the partition function, because expressions (2.16)–(2.19) and (3.2) contain functions $\gamma(q)$ (2.11) which correspond to the quasimomentum values from both the fermion and the boson spectrum. The susceptibility on a cylinder is given by the infinite sum of correlation functions, which, in principle, may bring about the emergence of additional singularities. One can make sure, however, that such singularities do not arise on the first sheet of the Riemann surface.

By way of example, we will explicitly write expression (5.4) for χ for $N = 3$, using representations (3.7)–(3.9) for cylindrical parameters, as well as expressions (3.13)–(3.15),

$$\begin{aligned}\beta^{-1}\chi &= \frac{\sinh\frac{\gamma(0)+\gamma(2\pi/3)}{2}\sinh\frac{\gamma(\pi)+\gamma(2\pi/3)}{2}\sinh^2\frac{\gamma(2\pi/3)+\gamma(\pi/3)}{2}}{\sinh\frac{\gamma(0)+\gamma(\pi/3)}{2}\sinh\frac{\gamma(\pi)+\gamma(\pi/3)}{2}\sinh\gamma(\pi/3)\sinh\gamma(2\pi/3)}\coth\left(\frac{\Lambda^{-1}+\gamma(0)}{2}\right)\\ &+\frac{1}{64}\frac{1}{\sinh\frac{\gamma(0)+\gamma(\pi/3)}{2}\sinh\frac{\gamma(\pi)+\gamma(\pi/3)}{2}\sinh\frac{\gamma(0)+\gamma(2\pi/3)}{2}\sinh\frac{\gamma(\pi)+\gamma(2\pi/3)}{2}}\\ &\times\frac{1}{\sinh\gamma(\pi/3)\sinh\gamma(2\pi/3)\sinh^2\frac{\gamma(\pi/3)+\gamma(2\pi/3)}{2}}\coth\left(\frac{\Lambda^{-1}+\gamma(0)+2\gamma(2\pi/3)}{2}\right).\end{aligned} \tag{6.1}$$

Singularities in s could have arisen due to the vanishing of the denominator in expression (6.1). One can readily see, however, that the respective factors

$$\sinh\frac{\gamma(q)+\gamma(q')}{2} = (\cos q' - \cos q)/\sinh\frac{\gamma(q)-\gamma(q')}{2}$$

are always other than zero if $q \neq q'$. One can further demonstrate that, on the first sheet of the Riemann surface (which is defined by the condition of positivity of $\gamma(q)$ as a function of s for real values of $s > 0$), the arguments of cotangents appearing in Eq. (6.1) do not vanish either: these factors result from infinite summation over the coordinate x. Therefore, the complete set of singularities of susceptibility is reduced to the branch points which are contained in the functions

$$\begin{aligned}e^{\gamma(q)} &= \left[\sqrt{\frac{1}{2}(s+s^{-1})+\sin^2\frac{q}{2}}\right.\\ &\left.+\sqrt{\frac{1}{2}(s+s^{-1})-\cos^2\frac{q}{2}}\right]^2.\end{aligned} \tag{6.2}$$

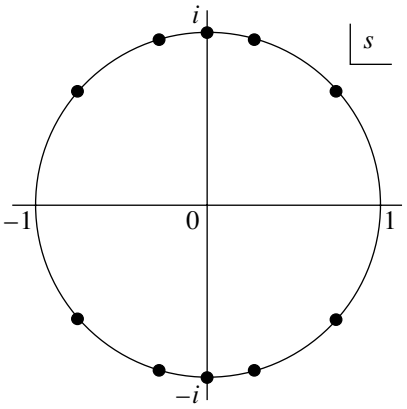

Fig. 2. The position of singularities in the complex plane for the magnetic susceptibility χ as a function of $s = \sinh 2\beta J$ for a particular value of $N = 3$.

For each value of quasimomentum $q \neq 0, \pi$, the function given by Eq. (6.2) has four branch points. If we denote them by $s_c = |s_c|e^{\pm i\varphi_c}$, then

$$|s_c| = 1, \quad \cos\varphi_c = \begin{cases} \cos^2 q/2, \\ -\sin^2 q/2. \end{cases} \tag{6.3}$$

One can see in Eq. (6.2) that only two branch points $s_c = \pm i$ are present at $q = 0, \pi$. It is easy to calculate that, for a given value of N, the complete number of singularities is $4N - 2$ and that all singularities lie on the circle $|s| = 1$. For $N = 3$, the respective pattern is given in Fig. 2. Note that singularities corresponding to the vanishing of the arguments of hyperbolic cotangents in Eq. (6.1) emerge on other sheets of the Riemann surface; these points do not lie on the circle $|s| = 1$. For the moment, we cannot say anything definite about the situation in the limit $N \longrightarrow \infty$ when the singularities on $|s| = 1$ crowd to form a dense set. This problem was subjected to a very thorough analysis by Nickel [16, 17], who is inclined to conclude that the crowding of singular points results in the emergence in the complex s plane of a singularity of the type of natural boundary.

ACKNOWLEDGMENTS

We are grateful to Dr. V.N. Shadura for his assistance in our work and for the discussion of our results; we are also grateful to Prof. B.M. McCoy for valuable remarks regarding the form factor representation of the correlation function on a cylinder and for bringing to our attention the importance of the problem of singularities in magnetic susceptibility.

This study was supported by the INTAS program (grant no. 00-00055) and the State Foundation for Basic Research of Ukraine (project no. 02.07/00152).

REFERENCES

1. L. Onsager, Phys. Rev. **65**, 117 (1944).
2. C. N. Yang, Phys. Rev. **85**, 808 (1952).
3. E. W. Montroll, R. B. Potts, and J. C. Ward, J. Math. Phys. **4**, 308 (1963).
4. T. T. Wu, B. M. McCoy, C. A. Tracy, and E. Barouch, Phys. Rev. B **13**, 316 (1976).
5. B. M. McCoy, E. Barouch, and T. T. Wu, Phys. Rev. Lett. **31**, 1409 (1973).
6. M. Jimbo and T. Miwa, Proc. Jpn. Acad., Ser. A: Math. Sci. **56**, 405 (1980).
7. B. M. McCoy and T. T. Wu, *The Two-Dimensional Ising Model* (Harvard Univ. Press, Cambridge, 1973).
8. J. Palmer and C. A. Tracy, Adv. Appl. Math. **2**, 329 (1981).
9. K. Yamada, Prog. Theor. Phys. **71**, 1416 (1984).
10. A. I. Bugrij and V. N. Shadura, Zh. Éksp. Teor. Fiz. **109**, 1024 (1996) [JETP **82**, 552 (1996)].
11. B. Berg, M. Karowski, and P. Weisz, Phys. Rev. D **19**, 2477 (1979).
12. A. B. Zamolodchikov and Al. B. Zamolodchikov, Ann. Phys. **120**, 253 (1979).
13. F. A. Smirnov, in *Form Factors in Completely Integrable Models of Quantum Field Theory* (World Sci., Singapore, 1992), Adv. Series in Math. Phys., Vol. 14.
14. A. I. Bugrij, Teor. Mat. Fiz. **127**, 143 (2001).
15. T. D. Lee and C. N. Yang, Phys. Rev. **87**, 410 (1952).
16. B. Nickel, J. Phys. A **32**, 3889 (1999).
17. B. Nickel, J. Phys. A **33**, 1693 (2000).

Translated by H. Bronstein

Journal of Experimental and Theoretical Physics, Vol. 94, No. 6, 2002, pp. 1149–1159.
Translated from Zhurnal Éksperimental'noĭ i Teoreticheskoĭ Fiziki, Vol. 121, No. 6, 2002, pp. 1339–1351.

SOLIDS
Electronic Properties

Dispersion of Permittivity of Two-Component Media

Yu. P. Emets*
Institute of Electrodynamics, National Academy of Sciences of Ukraine, Kiev, 03680 Ukraine
**e-mail: emets@irpen.kiev.ua*
Received December 17, 2001

Abstract—The dispersion of permittivity of 2D inhomogeneous matrix materials with various structures is studied. Effective parameters of the systems under investigation permit an exact analytic calculation, which makes it possible to analyze the effect of concentration of inclusions and their shape on the frequency dependences of the complex permittivity of inhomogeneous materials. The conditions under which the permittivity dispersion is not manifested are specified. © *2002 MAIK "Nauka/Interperiodica".*

1. INTRODUCTION

The electric spectroscopy of heterogeneous dielectrics attracts attention in numerous fields of physics [1–9]. It may be used to obtain important information about the structure of composite materials, their composition, and the physical properties of the components. The methods of investigation of the dispersion of dielectric materials find application in studying condensed media whose material characteristics are described by complex permittivity. They are used, for example, in the physics of high-resistance semiconductors, in biophysics, in colloid chemistry, and in the physics of artificial dielectrics and magnets [1–3]. However, the interpretation of experimental data in determining the structure of inhomogeneous systems remains a complicated problem. The ambiguity in interpreting the results of experimental investigations arises even in the case of materials of a relatively simple structure. A certain contribution to the investigation of this problem can be made by analyzing exactly solvable models which were recently subjected to intensive studies.

The most consistent theory of dielectric dispersion has been developed for condensed media with the orientation mechanism of polarization of matter. This theory was constructed by Debye on the basis of concepts of relaxation processes of dipoles with one and the same relaxation time [4]. In reality, it is only in a relatively few cases that the spectral characteristics of real materials strictly fit the Debye spectral dependences and the Cole–Cole classical circle diagram [2, 5]. Therefore, generalized diagrams such as the diagrams and equations of Cole–Davidson, Havriliak–Negami, Fuoss–Kirkwood, Williams–Watts, and other authors [6–9] were proposed to describe experimental results not corresponding to an ideal diagram of complex permittivity. However, all of these modified diagrams and equations, used for systematization of numerous experimental data, contain empirical parameters which lack physical justification from the standpoint of molecular physics and geometric structure of materials.

The Debye theory applies to all orientationally polarized media (liquid and solid), irrespective of the reasons which cause their polarizations. In view of this, the Debye theory was extended to heterogeneous media, in particular, to layered systems [5]. In reality, individual phases of dielectric composite materials may contain mobile charge carriers which enter traps in the bulk or on the surface of different media and remain free. If the displacement of free charges is possible only in bounded regions, these regions by and large behave as macroscopic dipoles. This form of bulk or surface polarization of heterogeneous media is associated with the names of Maxwell and Wagner, who were the first to investigate the scope of problems with such phenomena in samples of composite dielectrics. Materials with a one-dimensional (layered) structure [10, 11] were investigated.

In recent years, several exact results of the calculation of effective parameters of two-dimensional structures were obtained in the theory of heterogeneous systems. Such structures are mostly doubly periodic two-component matrix systems characterized by a high degree of geometric symmetry. In the case of such systems, it proved possible to exactly calculate the local electric field in different phases and to analytically determine the averaged characteristics. Owing to this, one can study the dispersion of permittivity of two-component media as a function of the physical properties of the components, their concentration, and the form of inclusions. Our paper deals with the investigation of these problems. It is demonstrated that a certain correlation indeed exists between the frequency spectrum and the structure of composite dielectrics. For some of the treated periodic systems, it is possible to obtain, in a closed form, expressions which define diagrams of the Cole–Cole type. They play an important part in revealing the mechanisms of relaxation of charges in dielectrics and enable one to extrapolate

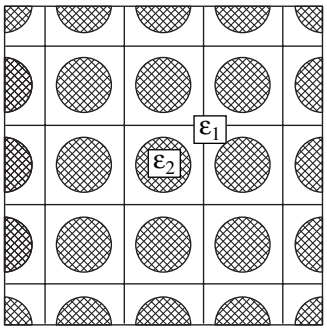

Fig. 1. A fragment of a composite dielectric material with circular cylindrical inclusions.

experimental data to hard-to-measure frequency ranges.

Polarization processes in an inhomogeneous medium are described in a quasi-stationary approximation [12]. This suggests that the wavelength of an external variable electric field is large as compared with the characteristic dimensions of the sample being investigated. Consequently, the spatial dispersion in matter is insignificant, and an equilibrium Maxwell–Wagner polarization is established in the inhomogeneous medium, which manages to follow the variation of the electric field in time. It is further assumed that other forms of polarization in individual phases of a composite material produce no significant contribution to the polarization of matter. Dielectric materials are investigated under conditions in which the magnetic field may be disregarded. With these assumptions, the investigation of dielectric dispersion reduces first to finding the electric field in the composite material and then to calculating its effective parameters with a preassigned frequency of the external field which varies according to a harmonic law. Each phase of the structure is characterized by its own complex permittivity. In the first stage of solution of the problem, one can use the mathematical apparatus for stationary fields and then introduce the complex permittivities of components, which depend on the frequency of the external electric field.

2. DOUBLY PERIODIC MATRIX SYSTEMS

Investigated below is a dielectric medium of permittivity ε_1, in which similar, doubly periodically alternating, cylindrical inclusions of permittivity ε_2 are regularly located. The matrix and the dispersed phase have the conductivities σ_1 and σ_2, respectively. Two systems are analyzed, namely, one with circular cylinders and the other with square cylinders. Such systems allow the analytical calculation of effective parameters, which simplifies the analysis of the solution and enables one to study the effect of structural elements on the dielectric spectrum.

2.1. Dielectric Spectrum as a Function of the Concentration of Inclusions

We will first consider a fibrous material with a regular structure, in which round fibers of radius r form a perfect square lattice of spacing h (Fig. 1). In the transverse direction towards the axes of cylinders, the medium by and large is isotropic. By virtue of the periodic structure of the inhomogeneous system, its effective parameters may be determined from the solution of the field problem for a single cell of the spacing. Such a problem was first investigated by Rayleigh [13] in application to electrically conducting media (the solution was obtained in the general case for a rectangular cell, this corresponding to a system which is, on the average, anisotropic). Later on, the method for the calculation of effective parameters developed by Rayleigh was extended to studying other structures [14, 15]. New techniques were suggested for solving the Rayleigh problem [16–18].

If the concentration of inclusions is not high, $s \le 0.5$, then, as is demonstrated in [17], the effective permittivity of the medium being treated is defined by the following expression:

$$\varepsilon_{\text{eff}} = \varepsilon_1 \frac{1 - s\Delta_{\varepsilon 12}}{1 + s\Delta_{\varepsilon 12}}, \qquad (1)$$

where s is the concentration of inclusions ($s = \pi r^2/h^2$), and $\Delta_{\varepsilon 12}$ is the relative permittivity of the medium,

$$\Delta_{\varepsilon 12} = \frac{\varepsilon_1 - \varepsilon_2}{\varepsilon_1 + \varepsilon_2}, \quad -1 \le \Delta_{\varepsilon 12} \le 1. \qquad (2)$$

In the above range of variation of the concentration of inclusions, formula (1) is valid with a high degree of approximation even in the case of a large difference between the phase permittivities ε_1 and ε_2 or, what is equivalent, at high magnitudes of the parameter $\Delta_{\varepsilon 12}$.

In studying the Maxwell–Wagner polarization in inhomogeneous materials, the displacement and conduction currents are taken into account in the basic equations of electromagnetic field [2]. This means that the generalized complex permittivity $\tilde{\hat{\varepsilon}}(\omega)$ (in relative units) is introduced for the periodically varying electric field $\mathbf{E} = \mathbf{E}_0 \exp(-i\omega t)$,

$$\tilde{\hat{\varepsilon}}(\omega) = \tilde{\varepsilon}'(\omega) - i\tilde{\varepsilon}''(\omega) = \hat{\varepsilon}(\omega) - i\frac{\hat{\sigma}(\omega)}{\varepsilon_0 \omega}, \qquad (3)$$

where ε_0 is the electric constant, ω is the angular frequency, and $\hat{\varepsilon}(\omega) = \varepsilon'(\omega) - i\varepsilon''(\omega)$ and $\hat{\sigma}(\omega) = \sigma'(\omega) - i\sigma''(\omega)$ are the complex values of the permittivity and conductivity of the material.

The main contribution to the polarization of inhomogeneous material is made by the Maxwell–Wagner polarization. Here, other forms of polarization may be regarded as unimportant. In this case, a locally inhomogeneous medium is usually characterized by constant

values of permittivity $\hat{\varepsilon}_{1,2}(\omega) = \varepsilon_{1,2}$ and conductivity $\hat{\sigma}_{1,2}(\omega) = \sigma_{1,2}$; consequently, the generalized permittivity is characterized by the explicit dependence on the frequency, $\tilde{\hat{\varepsilon}}_{1,2} = \varepsilon_{1,2} - i\sigma_{1,2}/\varepsilon_0\omega$. With $\omega \longrightarrow \infty$, the permittivity of the components with finite conductivity increases infinitely. However, the dielectric spectrum of a heterogeneous medium by and large possesses such a property only in the case of a certain combination of the physical properties of the components of the entire system.

In a complex form, the effective permittivity given by Eq. (1) is written as

$$\hat{\varepsilon}_{\text{eff}}(\omega) = \varepsilon'_{\text{eff}}(\omega) - i\varepsilon''_{\text{eff}}(\omega) = \tilde{\hat{\varepsilon}}_1\frac{1 - s\hat{\Delta}_{12}(\omega)}{1 + s\hat{\Delta}_{12}(\omega)}. \quad (4)$$

Here, the complex parameter $\hat{\Delta}_{12}(\omega) = \Delta'_{12}(\omega) - i\Delta''_{12}(\omega)$ is introduced, whose components are defined by the formulas

$$\Delta'_{12}(\omega) = \frac{\Delta_{\varepsilon 12}(1-\Delta_{\sigma 12})^2 + \Gamma_2^2(\omega)\Delta_{\sigma 12}(1-\Delta_{\varepsilon 12})^2}{(1-\Delta_{\sigma 12})^2 + \Gamma_2^2(\omega)(1-\Delta_{\varepsilon 12})^2},$$
$$\Delta''_{12}(\omega) = \frac{\Gamma_2(\omega)(\Delta_{\sigma 12} - \Delta_{\varepsilon 12})(1-\Delta_{\sigma 12})(1-\Delta_{\varepsilon 12})}{(1-\Delta_{\sigma 12})^2 + \Gamma_2^2(\omega)(1-\Delta_{\varepsilon 12})^2}, \quad (5)$$

where $\Delta_{\sigma 12}$ is the relative conductivity of inhomogeneous medium,

$$\Delta_{\sigma 12} = \frac{\sigma_1 - \sigma_2}{\sigma_1 + \sigma_2}, \quad -1 \le \Delta_{\sigma 12} \le 1. \quad (6)$$

In formulas (5), $\Gamma_2(\omega)$ is the frequency parameter which, for convenience of subsequent analysis, is referred to the dispersed phase (it will be recalled that the characteristics of this phase are marked by the subscript 2): $\Gamma_2(\omega) = \omega_{02}/\omega$ ($\omega_{02} = \sigma_2/\varepsilon_0\varepsilon_2$ is the Maxwell frequency). It should be noted that the two-component system under investigation can be characterized by introducing another frequency parameter, $\Gamma_1(\omega)$, corresponding to phase 1 (matrix): $\Gamma_1(\omega) = \omega_{01}/\omega$ ($\omega_{01} = \sigma_1/\varepsilon_0\varepsilon_1$). The parameters $\Gamma_1(\omega)$ and $\Gamma_2(\omega)$ are not independent: they are related by

$$\Gamma_1(\omega) = \frac{\varepsilon_2\sigma_1}{\varepsilon_1\sigma_2}\Gamma_2(\omega), \quad (7)$$

or, what is the same,

$$\Gamma_1(\omega) = \frac{(1-\Delta_{\varepsilon 12})(1+\Delta_{\sigma 12})}{(1+\Delta_{\varepsilon 12})(1-\Delta_{\sigma 12})}\Gamma_2(\omega). \quad (8)$$

It follows from formulas (7) and (8) that, provided the condition

$$\varepsilon_1\sigma_2 = \varepsilon_2\sigma_1 \quad (\Delta_{\varepsilon 12} = \Delta_{\sigma 12}) \quad (9)$$

is valid, the parameters $\Gamma_1(\omega)$ and $\Gamma_2(\omega)$ are equal to each other and, therefore, the system is characterized by a single frequency parameter

$$\Gamma(\omega) = \Gamma_1(\omega) = \Gamma_2(\omega).$$

In this singular case, the real component of the complex parameter $\hat{\Delta}_{12}(\omega)$ is independent of the frequency, and its imaginary component is zero,

$$\Delta'_{12}(\omega) = \Delta_{\varepsilon 12}, \quad \Delta''_{12}(\omega) = 0. \quad (10)$$

In what follows, the parameter $\Gamma_2(\omega)$ may be conveniently represented as

$$\Gamma_2(\omega) = \frac{1 - \Delta_{\omega 2}(\omega)}{\Delta_{\omega 2}(\omega)}, \quad (11)$$

where $\Delta_{\omega 2}$ is the relative frequency,

$$\Delta_{\omega j}(\omega) = \frac{\omega}{\omega_{0j} + \omega},$$
$$0 \le \Delta_{\omega j}(\omega) \le 1 \quad (j = 1, 2). \quad (12)$$

Expressions (4) and (5) are used to determine the real and imaginary part of the effective complex permittivity of the system,

$$\varepsilon'_{\text{eff}}(\omega) = \varepsilon_1\left[m(\omega) + n(\omega)\Gamma_2(\omega)\frac{(1-\Delta_{\varepsilon 12})(1+\Delta_{\sigma 12})}{(1+\Delta_{\varepsilon 12})(1-\Delta_{\sigma 12})}\right],$$
$$\varepsilon''_{\text{eff}}(\omega) = \varepsilon_1\left[m(\omega)\Gamma_2(\omega)\frac{(1-\Delta_{\varepsilon 12})(1+\Delta_{\sigma 12})}{(1+\Delta_{\varepsilon 12})(1-\Delta_{\sigma 12})} - n(\omega)\right]. \quad (13)$$

Here, the following notation is used:

$$m(\omega) = \frac{1 - s^2[\Delta'^2_{12}(\omega) + \Delta''^2_{12}(\omega)]}{[1 + s\Delta'_{12}(\omega)]^2 + [s\Delta''_{12}(\omega)]^2},$$
$$n(\omega) = \frac{2s\Delta''_{12}(\omega)}{[1 + s\Delta'_{12}(\omega)]^2 + [s\Delta''_{12}(\omega)]^2}. \quad (14)$$

If condition (9) is valid, then, in view of formulas (10), we find that

$$m(\omega) = \frac{1 - s\Delta_{\varepsilon 12}}{1 + s\Delta_{\varepsilon 12}}, \quad n(\omega) = 0,$$

and expressions (13) take the form

$$\varepsilon'_{\text{eff}}(\omega) = \varepsilon_1\frac{1 - s\Delta_{\varepsilon 12}}{1 + s\Delta_{\varepsilon 12}},$$
$$\varepsilon''_{\text{eff}}(\omega) = \varepsilon'_{\text{eff}}\Gamma_2(\omega)\frac{(1-\Delta_{\varepsilon 12})(1+\Delta_{\sigma 12})}{(1+\Delta_{\varepsilon 12})(1-\Delta_{\sigma 12})}. \quad (15)$$

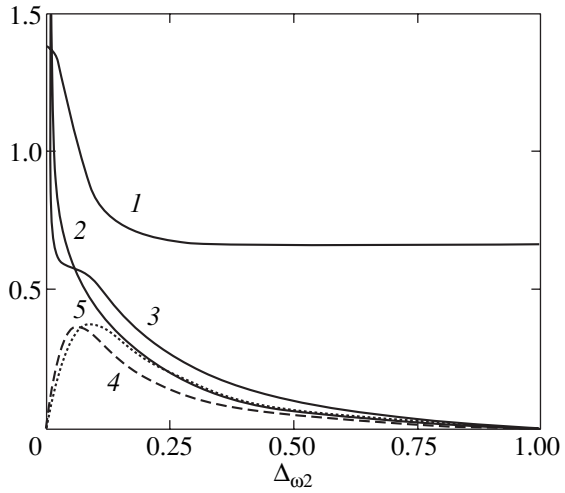

Fig. 2. (*1*) Effective permittivity $\varepsilon'_{\text{eff}}$, (*2*) effective loss factor $\varepsilon''_{\text{eff}}$, (*3*) effective dielectric loss tangent $\tan\delta_{\text{eff}}$, and functions (*4*) χ_{eff} and (*5*) $\tan\lambda_{\text{eff}}$ versus relative frequency $\Delta_{\omega 2}$ with the concentration of inclusions $s = 0.25$ and with the ratios of parameters $\varepsilon_2/\varepsilon_1 = 0.1$ and $\sigma_2/\sigma_1 = 10$.

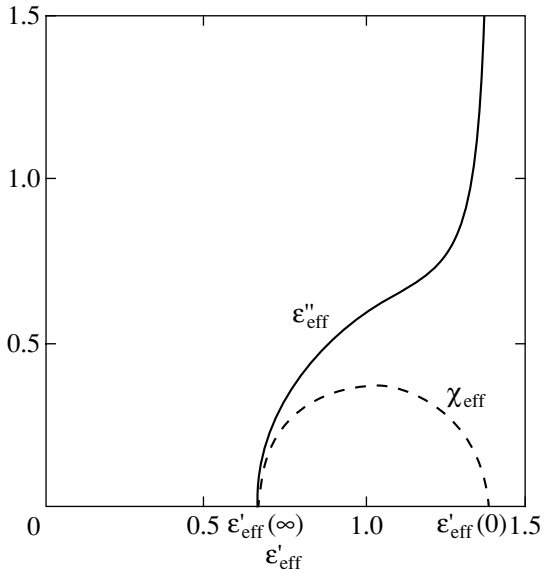

Fig. 3. The diagram of effective complex permittivity of an inhomogeneous dielectric with the same parameters as in Fig. 2.

In this singular case, one can see that the effective permittivity $\varepsilon'_{\text{eff}}(\omega)$ is independent of the frequency, and the effective dielectric loss factor $\varepsilon''_{\text{eff}}(\omega)$ varies inversely with the frequency (because $\Gamma_2(\omega) \propto 1/\omega$).

Therefore, relation (9) defines the condition subject to which the dispersion of permittivity of an inhomogeneous medium does not show up. As is revealed by analysis, this relation is valid for all known two-dimensional two-component matrix systems and, apparently, is general. From the physical standpoint, the relation defines the conditions under which no surface charge is formed at the interface between different media.

In the general case, when $\varepsilon_1\sigma_2 \neq \varepsilon_2\sigma_1$ ($\Delta_{\varepsilon 12} \neq \Delta_{\sigma 12}$), as the frequency varies, the effective permittivity of a composite material in the limit varies from the electrostatic value at $\omega \longrightarrow 0$,

$$\varepsilon'_{\text{eff}}(0) = \varepsilon_1\left[\frac{1 - s\Delta_{\sigma 12}}{1 + s\Delta_{\sigma 12}} + 2s\frac{(\Delta_{\sigma 12} - \Delta_{\varepsilon 12})(1 + \Delta_{\sigma 12})}{(1 + \Delta_{\varepsilon 12})(1 + s\Delta_{\sigma 12})^2}\right], \quad (16)$$

to the optical value at $\omega \longrightarrow \infty$,

$$\varepsilon'_{\text{eff}}(\infty) = \varepsilon_1\frac{1 - s\Delta_{\varepsilon 12}}{1 + s\Delta_{\varepsilon 12}}. \quad (17)$$

The latter formula coincides with (1) and with the respective expression in (15).

For a material with bulk conductivity, the effective loss factor is characterized by singularity at $\omega \longrightarrow 0$ and assumes zero value at $\omega \longrightarrow \infty$,

$$\varepsilon''_{\text{eff}}(0) \longrightarrow \infty, \quad \varepsilon''_{\text{eff}}(\infty) = 0. \quad (18)$$

In accordance with expressions (16)–(18), the effective values of permittivity and loss factor in a composite dielectric essentially depend on the concentration of inclusions and on the correlation between the dielectric and conducting properties of the components of the material.

Given for illustration in Fig. 2 are the effective values of permittivity $\varepsilon'_{\text{eff}}(\omega)$, dielectric loss factor $\varepsilon''_{\text{eff}}(\omega)$, and dielectric loss tangent $\tan\delta_{\text{eff}}(\omega) = \varepsilon''_{\text{eff}}(\omega)/\varepsilon'_{\text{eff}}(\omega)$ as functions of the relative frequency $\Delta_{\omega 2}$ (see formula (12)). The curves are constructed for the relative values of $\varepsilon'_{\text{eff}*} = \varepsilon'_{\text{eff}}/\varepsilon_1$ and $\varepsilon''_{\text{eff}*} = \varepsilon''_{\text{eff}}/\varepsilon_1$ (in what follows, the asterisks are omitted for brevity). The diagram of effective complex permittivity for this case is given in Fig. 3. The dashed curves in these drawings indicate the functions $\chi_{\text{eff}}(\omega)$ and $\tan\lambda_{\text{eff}}(\omega)$ corresponding to the dependences $\varepsilon''_{\text{eff}}(\omega)$ and $\tan\delta_{\text{eff}}(\omega)$, from which the singular term is omitted,

$$\chi_{\text{eff}}(\omega) = \varepsilon''_{\text{eff}}(\omega) - \varepsilon''_{\text{eff}}(0), \quad \tan\lambda_{\text{eff}}(\omega) = \frac{\chi_{\text{eff}}(\omega)}{\varepsilon'_{\text{eff}}(\omega)}. \quad (19)$$

One can see that the latter correspond to the Debye relaxation spectrum and Cole–Cole circle diagram [19]. The graphs are plotted for the concentration of inclusions $s = 0.25$ and for the following values of permittivity and conductivity of components of the mate-

rial: $\varepsilon_1 = 10$, $\varepsilon_2 = 1$ ($\Delta_{\varepsilon 12} = 0.818$), $\sigma_1 = 1$, $\sigma_2 = 10$ ($\Delta_{\sigma 12} = -0.818$).

From the practical standpoint, the greatest interest is attracted by systems in which the ideal dielectric medium, $\tilde{\hat{\varepsilon}}_1 = \varepsilon_1$, $\sigma_1 = 0$ ($\Delta_{\sigma 12} = -1$), contains inclusions whose properties are described by the complex permittivity, $\tilde{\hat{\varepsilon}}_2 = \varepsilon_2 - i\sigma_2/\varepsilon_0\omega$. In this case, the effective complex permittivity of the material is defined by

$$\hat{\varepsilon}_{\text{eff}}(\omega) = \varepsilon_1[m(\omega) + in(\omega)], \tag{20}$$

where the parameters $\Delta'_{12}(\omega)$ and $\Delta''_{12}(\omega)$ now have the following expressions:

$$\Delta'_{12}(\omega) = \frac{4\Delta_{\varepsilon 12} - \Gamma_2^2(\omega)(1-\Delta_{\varepsilon 12})^2}{4 + \Gamma_2^2(\omega)(1-\Delta_{\varepsilon 12})^2},$$
$$\Delta''_{12}(\omega) = \frac{2\Gamma_2(\omega)(\Delta_{\varepsilon 12}^2 - 1)}{4 + \Gamma_2^2(\omega)(1-\Delta_{\varepsilon 12})^2}. \tag{21}$$

With $\omega \longrightarrow 0$, the effective dielectric loss factor in such a material assumes zero value, and the effective electrostatic permittivity is defined only by the permittivity of the matrix and volume of inclusions irrespective of their properties,

$$\varepsilon'_{\text{eff}}(0) = \varepsilon_1\frac{1+s}{1-s}, \quad \varepsilon''_{\text{eff}}(0) = 0. \tag{22}$$

In the limiting case, $\omega \longrightarrow \infty$, we obtain

$$\varepsilon'_{\text{eff}}(\infty) = \varepsilon_1\frac{1-s\Delta_{\varepsilon 12}}{1+s\Delta_{\varepsilon 12}}, \quad \varepsilon''_{\text{eff}}(\infty) = 0. \tag{23}$$

Expressions (22) and (23) may also be derived directly from formulas (16)–(18) assuming that $\sigma_1 = 0$ ($\Delta_{\sigma 12} = -1$).

It is interesting to note that the matrix conductivity does not affect the value of the effective optical permittivity: in the two cases treated above, the expressions for $\varepsilon'_{\text{eff}}(\infty)$ coincide (compare formulas (17) and (23)).

Curves illustrating the behavior of effective permittivity in the entire frequency range with the concentration $s = 0.25$ are given in Fig. 4, where $\varepsilon_1 = 10$, $\varepsilon_2 = 1$ ($\Delta_{\varepsilon 12} = 0.818$) and $\sigma_1 = 0$, $\sigma_2 = 10$ ($\Delta_{\sigma 12} = -1$). In appearance, they are close to curves for dependences following from the Debye theory. Also indicative of this is the fact that the diagram of effective complex permittivity almost coincides with a semicircle (see the respective curve in Fig. 6).

Therefore, in the case being treated, the Debye relaxation equations may be extended to the Maxwell–Wagner polarization processes. The special feature of the latter consists in that they bring about field perturbations in large volumes and are caused by the shift of free charges in the region of inclusions and their accumulation at the interface between different media. Also indicative of this are the results of calculation of the

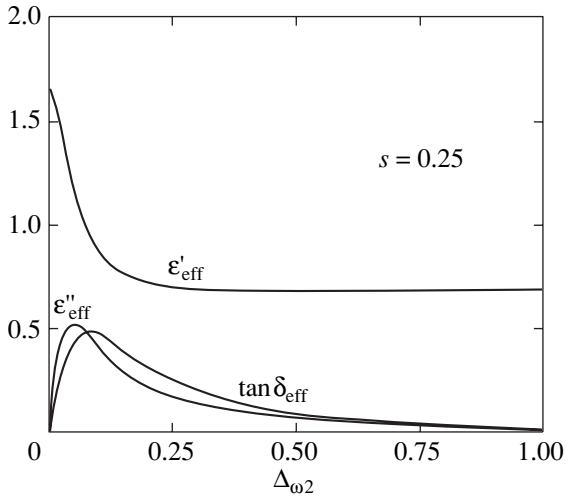

Fig. 4. Curves of dispersion of a two-component dielectric with the parameters $\varepsilon_1 = 10$, $\varepsilon_2 = 1$ and $\sigma_1 = 0$, $\sigma_2 = 10$ for the concentration of inclusions $s = 0.25$.

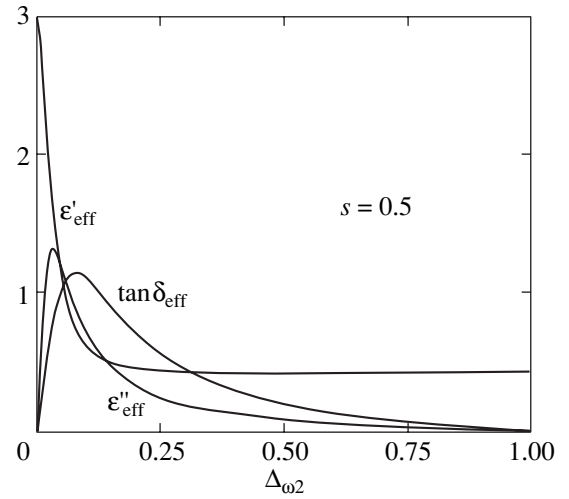

Fig. 5. Curves of dispersion of a two-component dielectric with the parameters $\varepsilon_1 = 10$, $\varepsilon_2 = 1$ and $\sigma_1 = 0$, $\sigma_2 = 10$ for the concentration of inclusions $s = 0.5$.

electric field in the system. The field formed by inclusions has a dipole representation. The inclusions behave as induced macroscopic line dipoles.

If the concentration of inclusions increases, the dielectric spectrum retains its form, and only the qualitative correlations vary as compared with a material of lower concentration. One can see this when comparing the respective dependences in Figs. 4, 5, and 6, which give the results of calculations of one and the same system with the concentrations of inclusions $s = 0.25$ and 0.5, when $\varepsilon_1 = 10$, $\varepsilon_2 = 1$ ($\Delta_{\sigma 12} = 0.818$) and $\sigma_1 = 0$, $\sigma_2 = 10$ ($\Delta_{\sigma 12} = -1$). One can see that the difference between the optical and electrostatic permittivities of the material increases appreciably with the concentra-

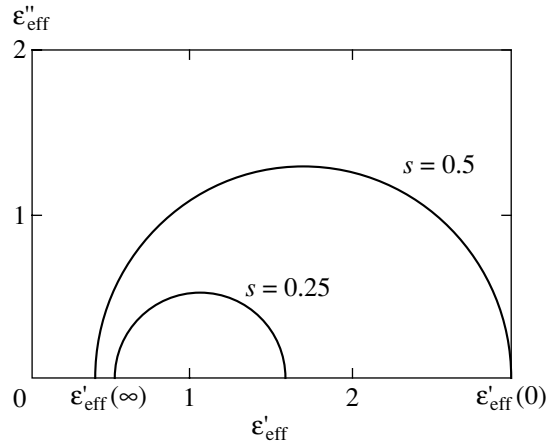

Fig. 6. The diagram of effective complex permittivity of an inhomogeneous dielectric for the concentration of inclusions $s = 0.25$ and 0.5. The characteristics of the material are the same as in Figs. 4 and 5.

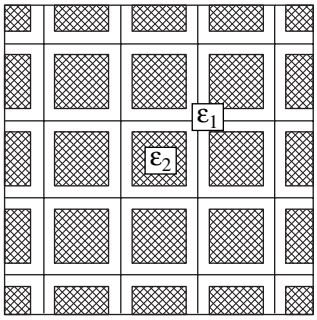

Fig. 7. A fragment of a composite dielectric material with square cylindrical inclusions.

tion of inclusions. In the case of a twofold increase in the concentration of inclusions, the effective dielectric loss factor increases by a factor of more than two.

The pattern of variation of the loss during the Maxwell–Wagner polarization is associated with the loss due to the displacement and conduction currents in the bulk of inclusions. At low frequencies, the conduction currents prevail, and the magnitude of these currents is the greater, the higher the concentration of inclusions. The measure of the loss ratio between the conduction and displacement currents is provided by the frequency dependence of the effective dielectric loss tangent $\tan\delta_{\text{eff}}$.

Because the diagram of effective complex permittivity is close to a semicircle, one can use this diagram and follow the Debye theory to determine the maximum value of the effective dielectric loss factor by the increment of permittivity

$$\varepsilon''_{\text{eff, max}}(\omega_c) = (\varepsilon'_{\text{eff}}(0) - \varepsilon'_{\text{eff}}(\infty))/2$$

with the critical frequency ω_c and critical wavelength λ_c at which the Maxwell–Wagner polarization is halved. For the adopted parameters, we have $\varepsilon''_{\text{eff, max}} = 0.5035$ and 1.2905 at $s = 0.25$ and 0.5, respectively.

2.2. The Effect of the Shape of Inclusions on the Dielectric Spectrum

The polarization processes in a composite material depend obviously on its structure. In view of this, it is interesting to find out how sensitive the dispersion of permittivity is to the variation of the shape of inclusions, all other parameters of the inhomogeneous system remaining invariable. The presence of recently obtained exactly solvable models enables one to perform such analysis.

Let a matrix inhomogeneous medium retain its regular structure but, instead of round filaments, contain square filaments. A cross-sectional view of a fragment of such a system is given in Fig. 7. By and large, the system remains isotropic and differs from the previous system mainly in that the boundary contours of inclusions have sharp edges in the neighborhood of which the electric field intensity is high, this increasing the inhomogeneity of the field in the material.

With the concentration of inclusions $s = 0.25$, the system allows an exact calculation of a stationary electric field and effective parameters [20]. This enables one to calculate the dielectric spectrum of the system and compare it with the frequency spectrum of a medium containing round inclusions with similar concentrations and properties of components.

The effective permittivity of the material shown in Fig. 7 in a stationary electric field is given by the following expression [20]:

$$\varepsilon_{\text{eff}} = \varepsilon_1\sqrt{\frac{2-\Delta_{\varepsilon 12}}{2+\Delta_{\varepsilon 12}}}. \tag{24}$$

In a variable electric field, when the matrix and inclusions are described by the complex permittivity under the same conditions as in the previous case, the effective complex permittivity in view of Eq. (24) is written as

$$\hat{\varepsilon}_{\text{eff}}(\omega) = \frac{\varepsilon_1}{\sqrt{2}}\left\{u(\omega) \pm v(\omega)\Gamma_2(\omega)\frac{(1-\Delta_{\varepsilon 12})(1+\Delta_{\sigma 12})}{(1+\Delta_{\varepsilon 12})(1-\Delta_{\sigma 12})}\right. \tag{25}$$

$$\left. - i\left[u(\omega)\Gamma_2(\omega)\frac{(1-\Delta_{\varepsilon 12})(1+\Delta_{\sigma 12})}{(1+\Delta_{\varepsilon 12})(1-\Delta_{\sigma 12})} \pm v(\omega)\right]\right\},$$

where

$$u(\omega) = \sqrt{\sqrt{\beta^2(\omega)+\gamma^2(\omega)}+\beta(\omega)},$$

$$\nu(\omega) = \sqrt{\sqrt{\beta^2(\omega) + \gamma^2(\omega)} - \beta(\omega)},$$
$$\beta(\omega) = \frac{1 - (\Delta_{12}'^2 + \Delta_{12}''^2)/4}{(1 + \Delta_{12}'^2/2) + \Delta_{12}''^2/4}, \quad (26)$$
$$\gamma(\omega) = \frac{\Delta_{12}''}{(1 + \Delta_{12}'^2/2) + \Delta_{12}''^2/4}.$$

Here, the parameters Δ_{12}' and Δ_{12}'' are defined by formulas (5); the upper sign in expression (25) is taken at $\Delta_{\varepsilon 12} > \Delta_{\sigma 12}$, and the lower sign, at $\Delta_{\varepsilon 12} < \Delta_{\sigma 12}$.

It follows from formulas (25) and (26) that, in the case of validity of condition (9), the dispersion of permittivity does not show up. In this case, the effective permittivity retains the constant value which it has in the stationary field,

$$\varepsilon_{\text{eff}}'(\omega) = \varepsilon_1\sqrt{\frac{2 - \Delta_{\varepsilon 12}}{2 + \Delta_{\varepsilon 12}}}. \quad (27)$$

The effective dielectric loss factor varies with the parameter $\Gamma_2(\omega)$,

$$\varepsilon_{\text{eff}}''(\omega) = \varepsilon_{\text{eff}}'\Gamma_2(\omega). \quad (28)$$

In the general case, when $\varepsilon_1\sigma_2 \neq \varepsilon_2\sigma_1$ ($\Delta_{\varepsilon 12} \neq \Delta_{\sigma 12}$), the dispersion of permittivity is defined by the correlation between the parameters of the inhomogeneous material.

With $\omega \longrightarrow 0$, the effective permittivity of a material tends to a value defined by the conducting properties of the matrix and inclusions, i.e., depends on the parameter $\Delta_{\sigma 12}$,

$$\varepsilon_{\text{eff}}'(0) = \varepsilon_1\sqrt{\frac{2 - \Delta_{\sigma 12}}{2 + \Delta_{\sigma 12}}}. \quad (29)$$

In this case, the effective dielectric loss factor increases indefinitely, $\varepsilon_{\text{eff}}''(0) \longrightarrow \infty$. If $\omega \longrightarrow \infty$, the effective permittivity of a composite material depends only on the dielectric properties of the components, i.e., on the parameter $\Delta_{\varepsilon 12}$,

$$\varepsilon_{\text{eff}}'(\infty) = \varepsilon_1\sqrt{\frac{2 - \Delta_{\varepsilon 12}}{2 + \Delta_{\varepsilon 12}}}, \quad \varepsilon_{\text{eff}}''(\infty) = 0. \quad (30)$$

The first one of formulas (30) coincides with Eq. (24), as it must in the Debye theory.

Expressions (25)–(30) characterize the frequency spectrum of composite materials characterized by the bulk conductivity (σ_1, $\sigma_2 \neq 0$). In such materials at $\omega \longrightarrow 0$, the loss increases indefinitely. Accordingly, on the complex plane of $\hat{\varepsilon}_{\text{eff}} = \varepsilon_{\text{eff}}' - i\varepsilon_{\text{eff}}''$, the dependence $\varepsilon_{\text{eff}}''(\varepsilon_{\text{eff}}')$ tends to infinity at $\varepsilon_{\text{eff}}'(\omega) \longrightarrow \varepsilon_{\text{eff}}'(0)$. We eliminate the singular term $\varepsilon_{\text{eff}}''(0)$ from the frequency dependences $\varepsilon_{\text{eff}}''(\omega)$ and $\tan\delta_{\text{eff}}(\omega)$ to obtain a spectrum typical of the Debye theory.

Although the expressions defining the dependence of the dielectric properties on the frequency for a material with square cylinders outwardly differ from similar expressions for a material with round inclusions, in reality they produce almost identical results. One can readily see this on comparing the dependence curves constructed by the formulas for the first and second models. Computer calculations showed the respective curves to differ from one another by not more than one percent. So, the frequency spectra of isotropic dielectric materials with round and square cylindrical inclusions in a relatively low concentration ($s = 0.25$) actually coincide.

This conclusion is also valid for materials in which only the inclusions possess electrically conducting properties ($\sigma_1 = 0$, $\sigma_2 \neq 0$ ($\Delta_{\sigma 12} = -1$)). In this case, it follows from formulas (25)–(30) that, with $\omega \longrightarrow 0$,

$$\varepsilon_{\text{eff}}'(0) = \sqrt{3}\varepsilon_1, \quad \varepsilon_{\text{eff}}''(0) = 0, \quad (31)$$

and, at $\omega \longrightarrow \infty$, the parameters $\varepsilon_{\text{eff}}'(\infty)$ and $\varepsilon_{\text{eff}}''(\infty)$ are defined by formulas (30). The numerically obtained formulas produce results which are close to the respective values for a system with round inclusions for the same concentration of inclusions $s = 0.25$.

Note the following important fact. For a dielectric composite with square cylindrical inclusions, when the matrix is an ideal dielectric and the inclusions are electrically conductive ($\sigma_1 = 0$, $\sigma_2 \neq 0$ ($\Delta_{\sigma 12} = -1$)), it is possible to reveal the presence of explicit correlation between the functions $\varepsilon_{\text{eff}}'(\omega)$ and $\varepsilon_{\text{eff}}''(\omega)$, an analog of the Cole–Cole diagram. Indeed, after simple transformations of expressions (25) and (26) at $\Delta_{\sigma 12} = -1$, one can derive the relation

$$[\varepsilon_{\text{eff}}'^2(\omega) + \varepsilon_{\text{eff}}''^2(\omega)]^2 - [\varepsilon_{\text{eff}}'^2(0) + \varepsilon_{\text{eff}}'^2(\infty)] \times [\varepsilon_{\text{eff}}'^2(\omega) - \varepsilon_{\text{eff}}''^2(\omega)] = -\varepsilon_{\text{eff}}'^2(0)\varepsilon_{\text{eff}}'^2(\infty), \quad (32)$$

where the effective values of static and optical permittivities, $\varepsilon_{\text{eff}}'(0)$ and $\varepsilon_{\text{eff}}'(\infty)$, correspond to expressions (30) and (31).

In the coordinates $\varepsilon_{\text{eff}}'(\omega)$ and $\varepsilon_{\text{eff}}''(\omega)$, relation (32) defines a fourth-order plane curve which is symmetric relative to the coordinate axes. These are Cassinian ovals (a particular case of Perseus curves) with centers at the points

$$c = \pm\frac{1}{\sqrt{2}}(\varepsilon_{\text{eff}}'^2(0) + \varepsilon_{\text{eff}}'^2(\infty))^{1/2} \quad (33)$$

on the abscissa. Because the effective permittivity and the effective loss factor assume only positive values, $\varepsilon_{\text{eff}}'(\omega)$, $\varepsilon_{\text{eff}}''(\omega) > 0$, it is only a part of the curve,

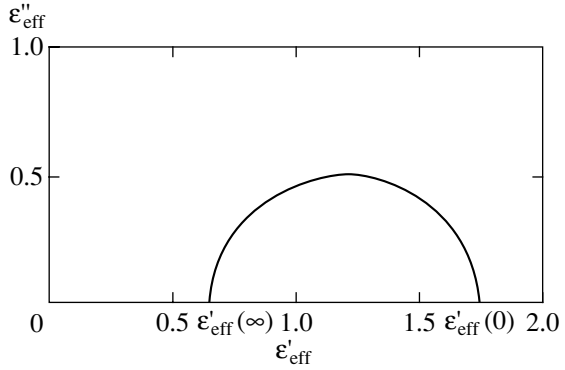

Fig. 8. The diagram of effective complex permittivity of an inhomogeneous dielectric with square cylinders ($\varepsilon_2/\varepsilon_1 = 0.1$ and $\sigma_1 = 0$).

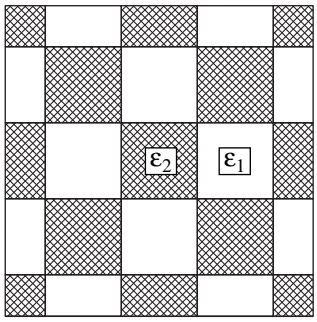

Fig. 9. A fragment of a doubly periodic material with equal concentrations of two components.

namely, a semioval in the first quadrant, that has a physical meaning rather than the entire curve. It will be recalled that, in the classical Debye theory, the dependence $\varepsilon''_{\text{eff}}(\varepsilon'_{\text{eff}})$ is represented by a semicircle. The curve described by expression (32) is given in Fig. 8 for a system with the parameters $\varepsilon_1 = 10$, $\varepsilon_2 = 1$ and $\sigma_1 = 0$, $\sigma_2 = 10$.

Equality (33) is apparently one of a few relations that gives an explicit expression of the diagram of effective permittivity for an exactly solvable model of inhomogeneous dielectric with Maxwell–Wagner polarization. Complex diagrams are usually constructed on the basis of experimental data; for the majority of composite materials, they are approximated by arcs of circles whose centers are located below the abscissa [2, 5, 6].

Note that Cassinian ovals are encountered in describing a number of other physical effects. For example, they give the structure of magnetic lines of force developed by two parallel currents flowing in thin conductors of infinite length. A family of Cassinian ovals may also be observed when examining a saltpeter plate in polarized light.

3. A SYSTEM WITH CRITICAL COMPOSITION OF COMPONENTS

If the volume of inclusions in a composite dielectric is increased continuously, their certain concentration referred to as critical may cause in the material a transition from the dielectric to metallic state. A convenient theoretical model for studying the dielectric dispersion of such composites may be provided by a doubly periodic two-component system with a checkerboard structure (Fig. 9). The effective permittivity of such a system has the exact expression [21–23]

$$\varepsilon_{\text{eff}} = \sqrt{\varepsilon_1\varepsilon_2}. \tag{34}$$

If the components of the material exhibit conducting properties with the electrical conductivities σ_1 and σ_2, in a variable harmonic field the material is by and large characterized by the effective complex permittivity

$$\hat{\varepsilon}_{\text{eff}}(\omega) = \varepsilon'_{\text{eff}}(\omega) - i\varepsilon''_{\text{eff}}(\omega) = \sqrt{\tilde{\hat{\varepsilon}}_1(\omega)\tilde{\hat{\varepsilon}}_2(\omega)}, \tag{35}$$

where $\tilde{\hat{\varepsilon}}_1(\omega) = \varepsilon_1 - i\sigma_1/\varepsilon_0\omega$ and $\tilde{\hat{\varepsilon}}_2(\omega) = \varepsilon_2 - i\sigma_2/\varepsilon_0\omega$ denote the generalized permittivity of the phases.

The real and imaginary parts of $\hat{\varepsilon}_{\text{eff}}(\omega)$ are defined by the following formulas:

$$\varepsilon'_{\text{eff}}(\omega) = \sqrt{\frac{\varepsilon_1\varepsilon_2}{2}}$$
$$\times \left[\sqrt{[1+\Gamma_1^2(\omega)][1+\Gamma_2^2(\omega)]} + 1 - \Gamma_1(\omega)\Gamma_2(\omega)\right]^{1/2},$$
$$\varepsilon''_{\text{eff}}(\omega) = \sqrt{\frac{\varepsilon_1\varepsilon_2}{2}} \tag{36}$$
$$\times \left[\sqrt{[1+\Gamma_1^2(\omega)][1+\Gamma_2^2(\omega)]} - 1 - \Gamma_1(\omega)\Gamma_2(\omega)\right]^{1/2}.$$

It will be recalled that here the dimensionless frequency parameters

$$\Gamma_1(\omega) = \frac{\sigma_1}{\varepsilon_0\varepsilon_1\omega}, \quad \Gamma_2(\omega) = \frac{\sigma_2}{\varepsilon_0\varepsilon_2\omega}$$

are related as in Eq. (7). In formulas (36), the parameters ε_j and the functions $\Gamma_j(\omega)$ ($j = 1, 2$) are of equivalent importance, which is reflective of the full geometric symmetry of the system relative to the phases which are equally represented in the inhomogeneous material.

If the permittivities and conductivities of the components are such that relation (9) is valid, dielectric dispersion does not show up. Under these conditions, we have

$$\varepsilon'_{\text{eff}}(\omega) = \sqrt{\varepsilon_1\varepsilon_2}, \quad \varepsilon''_{\text{eff}}(\omega) = \sqrt{\varepsilon_1\varepsilon_2}\Gamma(\omega), \tag{37}$$

where $\Gamma(\omega) = \Gamma_1(\omega) = \Gamma_2(\omega)$.

In the general case, $\varepsilon_1\sigma_2 \neq \varepsilon_2\sigma_1$ ($\Delta_{\varepsilon 12} \neq \Delta_{\sigma 12}$), the dispersion of permittivity of the system in the limiting

cases leads to the following values of effective permittivity and effective loss factor:

at $\omega \longrightarrow 0$,

$$\varepsilon'_{\text{eff}}(0) = \frac{\varepsilon_1\sigma_2 + \varepsilon_2\sigma_1}{2\sqrt{\sigma_1\sigma_2}}, \quad \varepsilon''_{\text{eff}}(0) \longrightarrow \infty; \tag{38}$$

at $\omega \longrightarrow \infty$,

$$\varepsilon'_{\text{eff}}(\infty) = \sqrt{\varepsilon_1\varepsilon_2}, \quad \varepsilon''_{\text{eff}}(\infty) \longrightarrow 0. \tag{39}$$

The first of expressions (38) gives the following. In the absence of electrical conduction in one of the phases of a composite material, the effective static permittivity assumes an infinite value; i.e., the material acquires metallic properties. This is due to the fact that the cells of each phase are not electrically insulated from one another: they have contacts at corners of squares.

The sum and difference of the effective values of static and optical permittivities are related as follows:

$$\begin{aligned}\varepsilon'_{\text{eff}}(0) + \varepsilon'_{\text{eff}}(\infty) &= \frac{\left(\sqrt{\varepsilon_1\sigma_2} + \sqrt{\varepsilon_2\sigma_1}\right)^2}{2\sqrt{\sigma_1\sigma_2}},\\ \varepsilon'_{\text{eff}}(0) - \varepsilon'_{\text{eff}}(\infty) &= \frac{\left(\sqrt{\varepsilon_1\sigma_2} - \sqrt{\varepsilon_2\sigma_1}\right)^2}{2\sqrt{\sigma_1\sigma_2}}.\end{aligned} \tag{40}$$

The latter relation, which defines the permittivity increment, demonstrates that, in the system being treated, the effective static permittivity always exceeds the effective optical permittivity. The equality $\varepsilon'_{\text{eff}}(0) = \varepsilon'_{\text{eff}}(\infty)$ is possible only in the exceptional case of validity of condition (9).

By way of example, Fig. 10 gives plotted dependences $\varepsilon'_{\text{eff}}(\omega)$, $\varepsilon''_{\text{eff}}(\omega)$, and $\tan\delta_{\text{eff}}(\omega)$ for the case of $\varepsilon_1 = 10$, $\varepsilon_2 = 1$ ($\Delta_{\varepsilon 12} = 0.818$) and $\sigma_1 = 1$, $\sigma_2 = 10$ ($\Delta_{\sigma 12} = -0.818$). As previously, the curves are constructed for relative quantities as functions of the relative frequency $\Delta_{\omega 2}$.

One can readily find that the real and imaginary components of effective complex permittivity are related by the relation

$$\begin{aligned}\varepsilon'^2_{\text{eff}}(0)[\varepsilon'^2_{\text{eff}}(\omega) - \varepsilon''^2_{\text{eff}}(\omega)] + \varepsilon'^2_{\text{eff}}(\omega)\varepsilon''^2_{\text{eff}}(\omega)\\ = \varepsilon'^2_{\text{eff}}(\omega)\varepsilon'^2_{\text{eff}}(\infty),\end{aligned} \tag{41}$$

which defines a second-order curve on the $\varepsilon'_{\text{eff}}(\omega)$, $\varepsilon''_{\text{eff}}(\omega)$ plane. This curve for the parameters identified above is given in Fig. 11.

Therefore, a two-component system with a checkerboard structure serves as yet another exactly solvable model, for which an explicit dependence exists between the real and imaginary components of effective complex permittivity.

If only one of two phases exhibits electrical conduction, for example, the second phase ($\tilde{\tilde{\varepsilon}}_2 = \varepsilon_2 - i\sigma_2/\varepsilon_0\omega$),

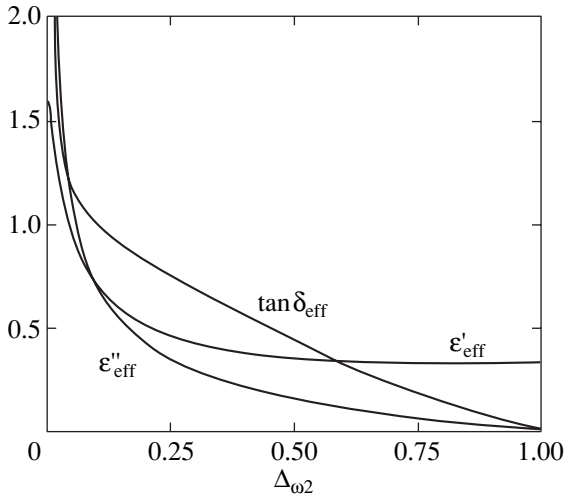

Fig. 10. Curves of dispersion of a two-component doubly periodic material with equal concentrations of the components for the ratios of the parameters $\varepsilon_2/\varepsilon_1 = 0.1$ and $\sigma_2/\sigma_1 = 10$.

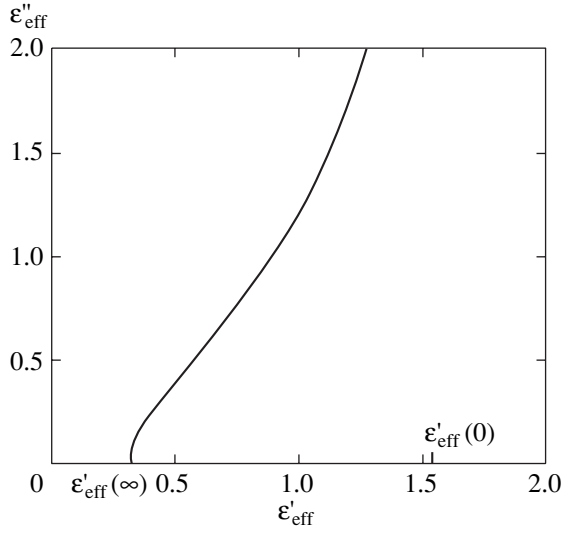

Fig. 11. The diagram of effective complex permittivity of the system represented in Fig. 9, with the ratios of the parameters $\varepsilon_2/\varepsilon_1 = 0.1$ and $\sigma_2/\sigma_1 = 10$.

while the first phase is an ideal dielectric ($\tilde{\tilde{\varepsilon}}_1 = \varepsilon_1$), the system is characterized by one frequency parameter $\Gamma_2(\omega)$ ($\Gamma_1(\omega) = 0$). For this case, expressions (36) yield the effective values of permittivity and loss factor,

$$\begin{aligned}\varepsilon'_{\text{eff}}(\omega) &= \sqrt{\frac{\varepsilon_1\varepsilon_2}{2}}\sqrt{\sqrt{1+\Gamma_2^2(\omega)}+1},\\ \varepsilon''_{\text{eff}}(\omega) &= \sqrt{\frac{\varepsilon_1\varepsilon_2}{2}}\sqrt{\sqrt{1+\Gamma_2^2(\omega)}-1}.\end{aligned} \tag{42}$$

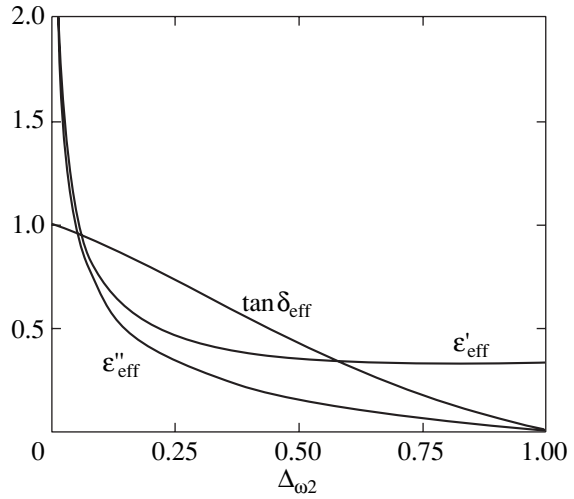

Fig. 12. Curves of dispersion of a two-component doubly periodic material with equal concentrations of the components for $\varepsilon_2/\varepsilon_1 = 0.1$ and $\sigma_1 = 0$.

Hence it follows that, in the low-frequency region, the effective values of permittivity and loss factor increase indefinitely to the same extent, as $1/\omega$ at $\omega \longrightarrow 0$: $\varepsilon'_{eff}(0) = \varepsilon''_{eff}(0) \longrightarrow \infty$. Such a behavior of the effective parameters was observed above when analyzing expression (38).

In the other limiting case of $\omega \longrightarrow \infty$, the effective parameters $\varepsilon'_{eff}(\infty)$ and $\varepsilon''_{eff}(\infty)$ are defined by formulas (39).

Formulas (42) were used to construct in Fig. 12 the dependences $\varepsilon'_{eff}(\omega)$, $\varepsilon''_{eff}(\omega)$, and $\tan\delta_{eff}(\omega)$ for the case of $\varepsilon_1 = 10$, $\varepsilon_2 = 1$ ($\Delta_{\varepsilon 12} = 0.818$) and $\sigma_1 = 0$, $\sigma_2 = 10$ ($\Delta_{\sigma 12} = -1$). The dependences are given for the relative quantities as functions of the relative frequency $\Delta_{\omega 2}$.

Comparison of the frequency dependences in Figs. 10 and 12 reveals that, at high frequencies, the system behaves similarly, although in the former case both phases are conducting, and in the latter case, only one phase. At low frequencies, the system behavior in these cases is essentially different. If only one phase is conducting, the effective dielectric loss tangent at $\omega \longrightarrow 0$ tends to unity (Fig. 12). This means that, in the above-identified limit, the ohmic loss in the material and the loss due to the displacement currents are similar.

The effective parameters $\varepsilon'_{eff}(\omega)$ and $\varepsilon''_{eff}(\omega)$ satisfy the relation

$$\varepsilon'^2_{eff}(\omega) - \varepsilon''^2_{eff}(\omega) = \varepsilon'^2_{eff}(\infty), \qquad (43)$$

which, on the complex plane, defines an equilateral hyperbola.

The results of our analysis demonstrate that the effective static permittivity of an inhomogeneous material with a checkerboard structure assumes finite values only in the case of both components being electrically conducting.

4. CONCLUSION

Experimental methods of investigation are used mainly in studying the dispersion of permittivity. Recently, the numerical simulation of composite systems has found extensive application. In this respect, great importance is attached to exactly solvable models which allow an analytical description of results in a closed form. Such solutions provide for definiteness in interpreting the experimental data and, in addition, may serve as reference samples for estimating the accuracy of numerically calculated systems. Unfortunately, the number of exactly solvable models is not large; most of these models belong to the class of two-component matrix systems with a periodic structure of inhomogeneities. We have analyzed some basic models of this class.

Note the following of the results obtained in studying the dielectric dispersion of investigated systems. The condition is confirmed under which the dielectric dispersion of two-component systems does not show up (relation (9)). It has been found that this relation is valid for all of the treated models. It was previously known for one-dimensional laminated systems [10, 11].

The dispersion of permittivity of inhomogeneous systems essentially depends on the physical properties of the components, on the concentration of inclusions, and on their form. By the pattern of these dependences, matrix systems may be conventionally divided into two forms, namely, inhomogeneous dielectric materials, in which both phases exhibit conducting properties, and dielectric components, in which only inclusions isolated in the material exhibit conducting properties. In the former case, the effective dielectric loss factor increases indefinitely as the frequency tends to zero. For the latter group of materials, this factor, on the contrary, assumes zero value in the above-identified limit. The pattern of dispersion of permittivity of such matrix systems is somewhat similar to the frequency dependences of the complex impedance of *RC* circuits with parallel and series connections of capacitances and ohmic resistances.

The calculations have revealed that the diagram of effective complex permittivity with round cylindrical inclusions actually coincides with the Cole–Cole diagram and, therefore, the classical Debye dispersion theory with a single relaxation time may apply to these diagrams. This statement is true of systems with low and medium concentrations of inclusions. For systems with a high concentration of inclusions, when, rather than using a single-dipole approximation (on which the derivation of formula (1) is based), one must take multidipole interactions into account, special investigations are necessary. As is demonstrated by the example treated above, the shape of inclusions modifies the dia-

gram of effective complex permittivity even in the case of a low concentration of inclusions. For square cylindrical inclusions, the diagram is represented by Cassinian semiovals.

The dispersion of permittivity of an inhomogeneous material with a checkerboard structure is characterized by interesting features. In such a system, the transition from the dielectric to metallic state is realized. Two moments are important in this case. First, as opposed to other treated systems, the dielectric loss factor increases indefinitely with the frequency tending to zero, irrespective of whether the conducting properties are exhibited by two phases or only one phase. Second, the effective static permittivity at zero frequency assumes finite values only in the case when two phases possess electrical conductivity; it increases indefinitely if only one phase exhibits conduction, irrespective of the magnitude of the phase. This fact is not obvious and was revealed as a result of calculations.

The dispersion of permittivity in a composite material is affected by various factors. In this paper, we have analyzed two of those factors, namely, the concentration of inclusions and their shape. In order to maintain similar conditions, the properties of the components are fixed. The problem of the effect of the characteristics of the material on the dispersion of permittivity calls for separate treatment.

Analysis of the dispersion of permittivity of inhomogeneous systems is rendered much simpler by the use of dimensionless parameters and characteristic numbers which naturally appear in analytical calculations.

REFERENCES

1. A. P. Vinogradov, A. N. Logarkov, and V. E. Romanenko, Electromagnetics **17**, 213 (1997).
2. T. L. Chelidze, A. I. Derevyanko, and O. D. Kurilenko, *Electric Spectroscopy of Heterogeneous Systems* (Kiev, Naukova Dumka, 1977), p. 232.
3. Yu. V. Gorokhovatskiĭ and G. A. Bordovskiĭ, *Thermoactivated Current Spectroscopy of High-Resistance Semiconductors and Dielectrics* (Nauka, Moscow, 1991), p. 248.
4. P. Debye, *Polar Molecules* (Chemical Catalog Co., New York, 1929; Gostekhizdat, Moscow, 1931).
5. A. R. Hippel, *Dielectries and Waves* (Wiley, New York, 1954; Inostrannaya Literatura, Moscow, 1960).
6. D. V. Davidson and R. H. Cole, J. Chem. Phys. **19**, 1484 (1951).
7. S. Havriliak and S. Negami, Polymer **8**, 161 (1967).
8. R. M. Fuoss and J. G. Kirkwood, J. Amer. Chem. Soc. **8**, 161 (1967).
9. G. Williams and D. C. Watts, Trans. Faraday Soc. **66**, 80 (1970).
10. J. C. Maxwell, *Treatise on Electricity and Magnetism* (Dover, New York, 1954; Nauka, Moscow, 1989), Vol. 1.
11. K. W. Wagner, *Die Isolierstoffe der Electrotechnik* (Springer-Verlag, Berlin, 1924).
12. L. D. Landau and E. M. Lifshitz, *Course of Theoretical Physics*, Vol. 8: *Electrodynamics of Continuous Media* (Nauka, Moscow, 1982; Pergamon, New York, 1984).
13. Lord Rayleigh, Philos. Mag. **34**, 87 (1892).
14. W. T. Perrins, D. R. McKenzie, and R. C. McPhedran, Proc. Roy. Soc. London, Ser. A **369**, 207 (1979).
15. R. D. Manteufel and N. E. Todreas, Int. J. Heat Mass Transf. **37**, 647 (1994).
16. B. Ya. Balagurov and V. A. Kashin, Zh. Éksp. Teor. Fiz. **117**, 978 (2000) [JETP **90**, 850 (2000)].
17. Yu. P. Emets, Zh. Éksp. Teor. Fiz. **118**, 1207 (2000) [JETP **91**, 1046 (2000)].
18. Yu. P. Emets, Prikl. Mekh. Tekh. Fiz. **42** (4), 165 (2001).
19. K. S. Cole and R. H. Cole, J. Chem. Phys. **9**, 341 (1941).
20. Yu. V. Obnosov, Dokl. Akad. Nauk SSSR **319**, 1125 (1991) [Sov. Phys. Dokl. **36**, 573 (1991)].
21. Yu. P. Emets, *Electrical Properties of Composites with Regular Structure* (Naukova Dumka, Kiev, 1986), p. 191.
22. Yu. P. Emets, Zh. Éksp. Teor. Fiz. **96**, 701 (1989) [Sov. Phys. JETP **69**, 397 (1989)].
23. Yu. P. Emets and Yu. V. Obnosov, Dokl. Akad. Nauk SSSR **309**, 319 (1989) [Sov. Phys. Dokl. **34**, 972 (1989)].

Translated by H. Bronstein

Journal of Experimental and Theoretical Physics, Vol. 94, No. 6, 2002, pp. 1160–1168.
Translated from Zhurnal Éksperimental'noĭ i Teoreticheskoĭ Fiziki, Vol. 121, No. 6, 2002, pp. 1352–1361.

SOLIDS
Electronic Properties

Quantization of Acoustoelectric Current in a Ballistic Channel

V. A. Margulis*, M. P. Trushin, and A. V. Shorokhov
Mordovian State University, ul. Bol'shevistskaya 68, Saransk, 430000 Russia
**e-mail: margulisva@mrsu.ru*
Received December 25, 2001

Abstract—The electric current induced by an ultrasonic phonon flux in a ballistic quasi-two-dimensional quantum channel is investigated theoretically. Two types of confining potential are considered. An analytic expression for the acoustoelectric current is derived, and its dependence on the chemical potential and on the magnitude of the longitudinal magnetic field is investigated. It is shown that the dependence of the acoustoelectric current on the chemical potential may be of the experimentally observed step type. The oscillatory dependence of the acoustoelectric current on the magnetic field is considered for the cases of weak and strong magnetic quantization. © *2002 MAIK "Nauka/Interperiodica".*

1. INTRODUCTION

The advances in experimental techniques have made it possible in recent years to operate with high acoustic frequencies and to measure currents of the order of a picoampere. Among other things, the acoustoelectric (AE) effect in a quantum channel could be investigated. A number of publications are devoted to experimental investigation of the AE effect in 2D layers of electron gas [1–3]. However, the measurements of AE current in quantum channels are rather scarce. The experimental investigation of the AE effect in such a system was reported for the first time in [4], where it was found that the AE current exhibits an oscillatory dependence on the gate voltage, the oscillation peaks corresponding to the conductance quantization thresholds in this structure.

Quantized AE current was studied in subsequent experimental works [5, 6]. In contrast to [4], acoustic waves of higher intensity corresponding to a stronger AE current were used in [6]. It was found that, as the ultrasound intensity increases (together with the AE current), the step dependence of the AE current on the gate voltage becomes more pronounced.

The AE effect in quantum channels can be described by using either of the following two approaches. In the first approach, the motion of electrons is described by the Boltzmann equation [4, 7–10], while second approach is of the quantum-mechanical type, i.e., is based on direct calculation of the coefficients of electron transmission through the structure [11, 12]. It should be noted that, in the analysis of the AE current using the second approach, numerical methods were mainly used and estimates were obtained only for certain limiting cases.

Giant quantum oscillations in the relaxation time approximation were explained in [4]. This approach was developed further in [7]. It was shown that electrons could effectively interact with an acoustic wave only if the Fermi level is near the bottom of a certain energy band (i.e., near the conductance quantization threshold). For other values of chemical potential, electrons at the Fermi level have too high a velocity as compared to the velocity of sound, and the AE current is minimal in this case. Precisely this effect was observed in [4].

The AE effect in the ballistic transport regime was described in [8, 9], where ultrasound is presented as a phonon flux. In these publications, oscillations [4] were explained and it was shown that the AE current in a ballistic quasi-one-dimensional channel attenuates at ultrasound frequencies ω_q lower than the threshold frequency

$$\omega_{\text{th}} = 2m^*s^2/\hbar. \quad (1)$$

Here, m^* and s are the electron effective mass and velocity of sound in the channel, respectively. In addition, the formula for the AE current conventional for subsequent applications was derived; we will use this method here for analyzing the AE effect in a quasi-two-dimensional channel.

In the recent publication by Entin-Wohlman *et al.* [10], the AE current in a ballistic channel was also investigated, but the ultrasonic wave was assumed to be a classical force in the Boltzmann equation. It should be noted that a detailed comparison of the results obtained in [10] with previous data [7, 9] was carried out.

In all theoretical publications mentioned in the review, only the oscillations of the AE current were studied. In the present work, we consider a quantized AE current in a ballistic channel. It will be shown, among other things, that the AE current may display either an oscillatory or a step variation upon a change in the chemical potential. The necessary conditions for the existence of quantization steps will be determined.

It should be noted that a magnetic field creates additional opportunities for studying the AE current in nanostructures. This is due to the fact that the magnetic field may enhance the existing lateral confinement or create an additional one in a nanostructure, thus changing the period of AE current oscillations. However, an arbitrarily directed magnetic field may considerably complicate the description of the AE effect, given in [8]. This is due to the emergence of an additional term in the kinetic equation, which is associated with the Lorentz force. In the present work, we consider only the longitudinal magnetic field. In this case, the magnetic induction is parallel to the direction of the AE current, and the kinetic equation has a form similar to that in [8].

Using the approach proposed in [8] in a realistic case when the temperature satisfies the condition $\hbar\omega_q \ll T$, we can derive a more general expression for the AE current through a quasi-two-dimensional ballistic channel in the form

$$J = \frac{2em^{*2}\Lambda^2 SL}{\rho\hbar^3\omega_{\text{th}}}\frac{\partial}{\partial\mu} \times \sum_{nm} f^F\left(\varepsilon_{nm} + \frac{\hbar\omega_{\text{th}}}{4} + \frac{\hbar\omega_q^2}{4\omega_{\text{th}}} - \mu\right), \quad (2)$$

where S is the intensity of ultrasound, Λ is the deformation potential constant, ε_{nm} is the discrete component of the electron energy spectrum, μ is the chemical potential of the system, L is the channel length, e is the electron charge, ρ is the mass density, and f^F is the Fermi distribution function.

In the case of the piezoelectric interaction, which is more typical of heterostructures of the AlAs/AlGaAs type, the AE current in the isotropic case can be derived from Eq. (2) by using the substitution [8]

$$\Lambda^2 \longrightarrow \Lambda_a^2 + \left[\frac{4\pi e\beta\nu(\mathbf{q}, a)}{q\varepsilon}\right]^2, \quad (3)$$

where Λ_a denotes the deformation potential constant for an acoustic wave belonging to the branch a, β is the piezoelectric modulus, ε is the dielectric constant, $\nu(\mathbf{q}, a)$ is the unit polarization vector, and $\mathbf{q}$ is the wave vector of a phonon.

It will be proved below that the necessary quantization conditions for the AE current weakly depend on the form of the confinement potential. We will consider two models of quantum channel with different confining potentials. The channel width in both cases can be simulated by a parabolic confinement. In order to simulate the layer thickness, a parabolic confinement potential is used the first case and a hard-wall potential is employed in the second case.

2. QUANTUM CHANNEL WITH A SOFT-WALL POTENTIAL

In order to simulate a quantum channel, we will use in this section the potential of a soft wall. The electron energy spectrum in this model is similar to the electron spectrum for a parabolic quantum wire with an elliptic cross section [13]. In the case when the system is in a longitudinal magnetic field of induction B, the electron energy is the sum of the spectra of two harmonic oscillators and the energy of free motion along the longitudinal axis z:

$$\varepsilon_{nmp} = \hbar\omega_1\left(n + \frac{1}{2}\right) + \hbar\omega_2\left(m + \frac{1}{2}\right) + \frac{p^2}{2m^*}, \quad (4)$$

where

$$\omega_{1,2} = \frac{1}{2}\left(\sqrt{\omega_c^2 + (\omega_x + \omega_y)^2} \pm \sqrt{\omega_c^2 + (\omega_x - \omega_y)^2}\right).$$

Here, ω_x and ω_y are the characteristic frequencies of size quantization, ω_c is the cyclotron frequency, and n, $m = 0, 1, 2, \ldots$.

In order to calculate the AE current through such a channel, we use formula (2). We can separate the oscillatory terms from Eq. (2) by transforming it with the help of the formula [14]

$$\frac{1}{1 + e^x} = \frac{1}{2i}\int_{\gamma - i\infty}^{\gamma + i\infty}\frac{dye^{-yx}}{\sin\pi y}, \quad 0 < \gamma < 1. \quad (5)$$

After the summation of series over n and m, the integral with respect to y can be evaluated easily with the help of residue theory (by closing the integration contour in the left half-plane). Considering that $\hbar\omega_{1,2} \gg \hbar\omega_q$, we obtain the following expression for the AE current in the channel:

$$J = \frac{2em^{*2}S\Lambda^2 L}{\rho\hbar^5\omega_1\omega_2\omega_{\text{th}}}\mu + \frac{4\pi^2 em^{*2}TS\Lambda^2 L}{\rho\hbar^5\omega_{\text{th}}} \times \sum_{k=1}^{\infty}(-1)^k k\left[\frac{1}{\omega_1^2}\frac{\sin(2\pi k\mu/\hbar\omega_1)}{\sinh(2\pi^2 kT/\hbar\omega_1)\sin(\pi k\omega_2/\omega_1)} + \frac{1}{\omega_2^2}\frac{\sin(2\pi k\mu/\hbar\omega_2)}{\sinh(2\pi^2 kT/\hbar\omega_2)\sin(\pi k\omega_1/\omega_2)}\right]. \quad (6)$$

It should be noted that an analysis of convergence of series of the type (6) is carried out in [15].

Let us first consider expression (6) in the limit of zero magnetic field (in this case, $\omega_1 = \omega_x$, $\omega_2 = \omega_y$) and the case when the size quantization along the x axis is considerably stronger than along the y axis so that $\omega_x \gg \omega_y$. We take into account the fact that the contribution from harmonics with $k \gg 1$ to current (6) is small since the expression $\sinh^{-1}(2\pi^2 kT/\hbar\omega_{1,2})$ rapidly tends to zero upon an increase in k at high temperatures. For the

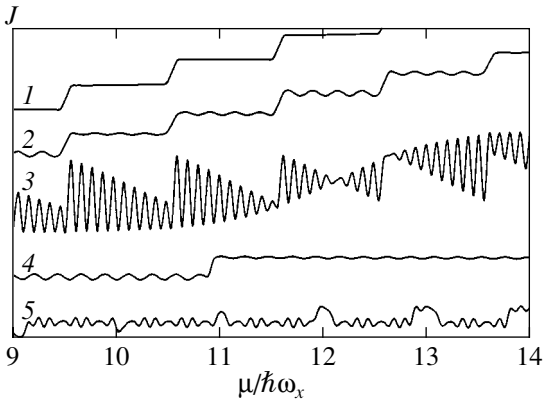

Fig. 1. Effect of the magnetic field, channel width, and temperature on the dependence of the AE current on the chemical potential in a quantum channel with a soft-wall potential: the AE current quantization in a strongly asymmetric channel ($\omega_x = 10^{13}$ s^{-1}, $\omega_y = 0.5136 \times 10^{12}$ s^{-1}, $B = 0$, $T = 1.3$ K) (curve *1*); fine structure of the AE current quantization steps ($\omega_x = 10^{13}$ s^{-1}, $\omega_y = 0.6365 \times 10^{12}$ s^{-1}, $B = 0$, $T = 1.3$ K) (curve *2*); destruction of the plateau of the AE current quantization steps ($\omega_x = 10^{13}$ s^{-1}, $\omega_y = 0.98765 \times 10^{12}$ s^{-1}, $B = 0$, $T = 0.5$ K) (curve *3*); effect of the magnetic field on the length of AE current quantization steps ($\omega_x = 10^{13}$ s^{-1}, $\omega_y = 2 \times 10^{12}$ s^{-1}, $B = 10$ T, $T = 1.3$ K) (curve *4*); and AE current oscillations in the quantum channel for close frequencies of parabolic confinement ($\omega_x = 10^{13}$ s^{-1}, $\omega_y = 9.1234 \times 10^{12}$ s^{-1}, $B = 0$, $T = 1.3$ K) (curve *5*).

first few harmonics, we have $\sin(\pi k\omega_2/\omega_1) \sim \pi k\omega_y/\omega_x$ in view of the smallness of ω_y/ω_x. Taking into account the above arguments, we can write Eq. (6) in the form

$$J = J^{\text{step}} + J^{\text{osc}}.$$

Here,

$$J^{\text{step}} = \frac{2em^{*2}SL\Lambda^2}{\rho\hbar^4\omega_{\text{th}}\omega_y} \times \left[\frac{\mu}{\hbar\omega_x} + \sum_{k=1}^{\infty}(-1)^k C_k(T)\sin\frac{2\pi k\mu}{\hbar\omega_x}\right], \quad (7)$$

where the Fourier coefficients have the form

$$C_k(T) = \frac{2\pi^2 T}{\hbar\omega_x}\frac{1}{\pi}\sinh^{-1}\frac{2\pi^2 kT}{\hbar\omega_x},$$

and

$$J^{\text{osc}} = \frac{4\pi^2 em^{*2}TS\Lambda^2 L}{\rho\hbar^5\omega_{\text{th}}\omega_y^2} \times \sum_{k=1}^{\infty}\frac{(-1)^k k\sin(2\pi k\mu/\hbar\omega_y)}{\sinh(2\pi^2 kT/\hbar\omega_y)\sin(\pi k\omega_x/\omega_y)}. \quad (8)$$

Thus, the expression for the AE current in a strongly asymmetric channel splits into two terms. It can be seen from expression (7) that the term J^{step} is the sum of two functions. One of them has a linear and the other a sawtooth dependence on the chemical potential. Their sum gives a step dependence $J^{\text{step}}(\mu)$. It should be noted that the step height does not depend on temperature. The term J^{osc} exhibits an oscillatory dependence on the chemical potential with a period $\hbar\omega_y$, the amplitude of oscillations strongly depending on temperature.

It should be noted that the $J(\mu)$ dependence in a strongly asymmetric channel is determined to a considerable extent by the relation between the parameters of size quantization and temperature. For $\hbar\omega_y \ll 2\pi^2 T \ll \hbar\omega_x$, the amplitude of oscillations of J^{osc} is much smaller than the height of the quantization steps of J^{step}. For such parameters, the dependence of the AE current on chemical potential has clearly manifested quantization steps, the length of the plateau of the quantization current $J(\mu)$ being equal to $\hbar\omega_x$ (Fig. 1, curve *1*). If $\hbar\omega_y \lesssim 2\pi^2 T \ll \hbar\omega_x$, the oscillatory term J^{osc} leads to a fine structure of steps (Fig. 1, curve *2*). Figure 1 (curves *1* and *2*) and expression (7) show that the step thresholds on the $J(\mu)$ dependence correspond to half-integral values of $\mu/\hbar\omega_x$. As the temperature decreases, the term J^{osc} increases; consequently, oscillations destroy the plateau of the quantization steps of the AE current for $T \ll \hbar\omega_y, \hbar\omega_x$ (curve *3* in Fig. 1).

In the opposite case, when $\hbar\omega_y \ll 2\pi^2 T \lesssim \hbar\omega_x$, the temperature smearing of step thresholds considerably affects the pattern of quantization of the AE current. It can be seen from Eqs. (7) and (8) that, as the temperature increases, all terms in the expression for $J(\mu)$ (excepts the monotonic term) decrease, and the $J(\mu)$ dependence becomes linear for $T \gg \hbar\omega_y, \hbar\omega_x$:

$$J = \frac{2em^{*2}S\Lambda^2 L}{\rho\hbar^5\omega_1\omega_2\omega_{\text{th}}}\mu + o\left(\frac{\hbar\omega_x}{T}, \frac{\hbar\omega_y}{T}\right). \quad (9)$$

If the condition $\omega_x \gg \omega_y$ does not hold, the term J^{step} displays an oscillatory dependence with period $\hbar\omega_x$ on the chemical potential instead of the step dependence. Consequently, for $\omega_x \sim \omega_y$, the AE current is the sum of two oscillatory terms with close periods. Consequently, the oscillations of the AE current in this case have the form of beats (curve *5* in Fig. 1).

In numerical computation of the AE current on the basis of formula (2), we used the values of the effective electron mass $m^* = 0.06m_0$, velocity of sound $s = 5 \times 10^5$ cm/s, and the ultrasonic wave frequency $\omega_q = 5 \times 10^9$ s^{-1} typical of structures GaAs–$Al_xGa_{1-x}As$.

Let us now consider the magnetic-field dependence of the AE current (6). The $J(B)$ dependence is obviously oscillatory by nature (giant quantum oscillations [8, 9, 16]), the period of the function $J(B)$ being determined by the relation between the size-quantization (ω_x, ω_y)

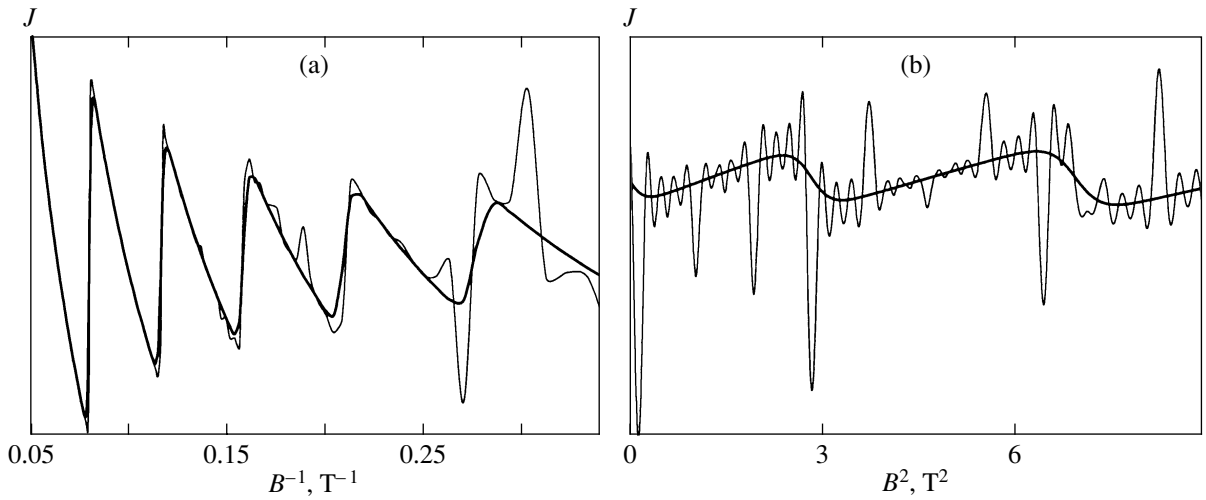

Fig. 2. Effect of temperature on giant quantum oscillations of the AE current in a quasi-two-dimensional quantum channel with parameters $\omega_x = 10^{13}$ s^{-1}, $\omega_y = 0.7778 \times 10^{12}$ s^{-1}, $\mu = 10^{-13}$ erg (thin curves correspond to $T = 1$ K and bold curves to $T = 4$ K): (a) $J(B^{-1})$ in the case of strong magnetic quantization; (b) oscillations of $J(B^2)$ in the case of weak magnetic quantization.

and magnetic quantization (ω_c) parameters. In the case of a strong magnetic quantization ($\omega_c \gg \omega_y, \omega_x$), the frequencies ω_1 and ω_2 can be presented in the form

$$\omega_1 = \omega_c\left[1 + o\left(\frac{\omega_x^2 + \omega_y^2}{\omega_c^2}\right)\right],$$
$$\omega_2 = \frac{\omega_x\omega_y}{\omega_c} + \omega_c o\left(\frac{\omega_x\omega_y}{\omega_c^2}\right)^2. \tag{10}$$

In this case, the first oscillatory term in relation (6) gives oscillations in $1/B$ with a period $\Delta_1(1/B) = e\hbar/m^*c\mu$, which are similar to oscillations of the coefficient of sound absorption by an electron gas in a quantizing magnetic field [16]. It can be seen from relations (10) that, in the case of strong magnetic quantization, the relation $\omega_1 \gg \omega_2$ always holds. Consequently, at a nonzero temperature and in a strong magnetic field, the second oscillatory term in Eq. (6) is considerably smaller than the first term. It can be seen from Fig. 2a that it creates a fine structure of oscillations of the AE current in strong fields. It follows from relations (10) that the second oscillatory term in Eq. (6) is periodic in the magnetic field with period

$$\Delta_2(B) = \frac{m^*c}{e}\omega_y\frac{\hbar\omega_x}{\mu}. \tag{11}$$

In the opposite case, when $\omega_c \ll \omega_y, \omega_x$, the situation becomes more complicated. If we impose additional constraint $\omega_x \gg \omega_y$, the approximate formulas for estimating ω_1 and ω_2 assume the form

$$\omega_1 = \omega_x\left[1 + \frac{\omega_c^2}{\omega_x^2} + o\left(\frac{\omega_c^2 + \omega_y^2}{\omega_x^2}\right)^2\right],$$
$$\omega_2 = \omega_y\left[1 - \frac{\omega_c^2}{2\omega_x^2} + o\left(\frac{\omega_y^2}{\omega_x^2}\right) + o\left(\frac{\omega_c^4}{\omega_x^4}\right)\right]. \tag{12}$$

In this case, the expression for the AE current is the sum of two terms periodic in B^2 with periods

$$\Delta_1(B^2) = \left(\frac{cm^*\omega_x}{e}\right)^2\frac{\hbar\omega_x}{\mu},$$
$$\Delta_2(B^2) = 2\left(\frac{cm^*\omega_x}{e}\right)^2\frac{\hbar\omega_y}{\mu}. \tag{13}$$

It should be noted that, in the region of high temperatures such that $2\pi^2T \gg \hbar\omega_2$, the first oscillating term in Eq. (6) is considerably larger than the second term in this case also (Fig. 2b), and $\Delta_1(B^2) \gg \Delta_2(B^2)$. If the hybrid frequencies ω_1 and ω_2 are close, the magnetic-field-induced oscillations of the AE current have the form of beats.

It is important to note that, in accordance with relations (10) and (12), a longitudinal magnetic field always enhances the asymmetry of a parabolic channel. Thus, the magnetic field improves the quantization pattern for the AE current (Fig. 3). In the case of strong magnetic quantization, the plateau length of the steps on the $J(\mu)$ dependence is proportional to induction B and is equal to $\hbar\omega_1$ (see curve *4* in Fig. 1).

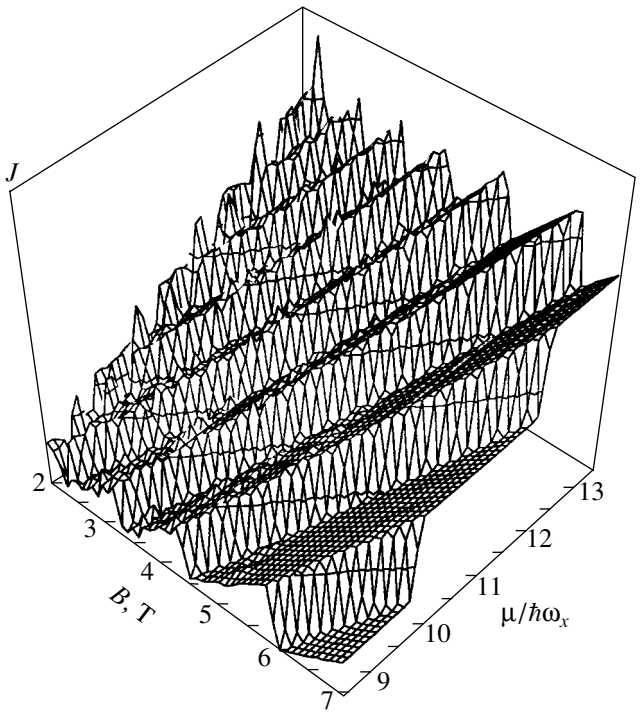

Fig. 3. Effect of magnetic field on the AE current quantization steps for a channel with a soft-wall potential ($\omega_x = 10^{13}$ s^{-1}, $\omega_y = 1.012 \times 10^{12}$ s^{-1}, $T = 1.7$ K).

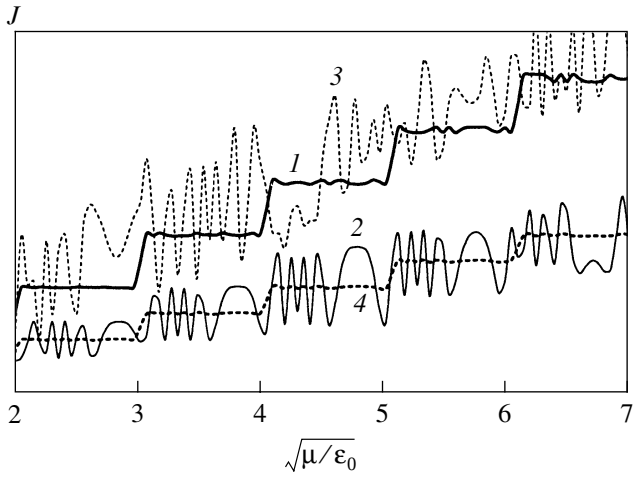

Fig. 4. Effect of magnetic field, channel width, and temperature on the dependence of the AE current on the chemical potential in a channel with a hard-wall confining potential: AE current quantization in a strongly asymmetric channel ($T = 1.3$ K, $d = 3 \times 10^{-6}$ cm, $\omega_0 = 0.5 \times 10^{12}$ s^{-1}, $B = 0$) (curve *1*); destruction of the quantization step plateau of AE current by a low temperature ($T = 1.3$ K, $d = 3 \times 10^{-6}$ cm, $\omega_0 = 1 \times 10^{12}$ s^{-1}, $B = 0$) (curve *2*); destruction of the quantization step plateau of AE current by a magnetic field ($T = 1.3$ K, $d = 3 \times 10^{-6}$ cm, $\omega_0 = 10^{12}$ s^{-1}, $B = 1$ T) (curve *3*); and quantization of AE current at a comparatively high temperature ($T = 3$ K, $d = 3 \times 10^{-6}$ cm, $\omega_0 = 10^{12}$ s^{-1}, $B = 0$) (curve *4*).

3. QUANUM CHANNEL WITH A HARD-WALL POTENTIAL

Let us consider the AE effect in a quasi-two-dimensional quantum channel with a hard-wall potential. In this case, the situation slightly changes as compared to the previous case. In particular, the longitudinal magnetic field may destroy the quantization steps.

Let us consider the case when the motion along the y axis is confined, as before, by the soft-wall potential $U = m^*\omega_0 y^2/2$ and simulate the finite thickness d of the quantum channel by imposing on the wave function the zero boundary conditions along the x axis, such that $\psi(0, y, z) = \psi(d, y, z) = 0$. Choosing the vector potential in the form $\mathbf{A} = (-By, 0, 0)$, we find that the electron energy spectrum of the quasi-two-dimensional channel is the sum of the spectrum of a harmonic oscillator with frequency $\omega = \sqrt{\omega_0^2 + \omega_c^2}$, the spectrum of a 1D potential well with a hard wall and the reduction factor ω_0^2/ω^2, and the energy spectrum of free motion in the direction of the field:

$$\varepsilon_{nmp} = \hbar\omega\left(n + \frac{1}{2}\right) + \varepsilon_0\frac{\omega_0^2}{\omega^2}m^2 + \frac{p^2}{2m^*}. \qquad (14)$$

Here, the size confinement energy is $\varepsilon_0 = \pi^2\hbar^2/2m^*d^2$, $n = 0, 1, \ldots$, $m = 1, 2, \ldots$.

Using the spectrum (14), we can find the AE current in the quasi-two-dimensional channel if the electron concentration is high enough so that $\mu \gg \hbar\omega$. Using the results obtained in [17] as applied to the case of low temperatures ($T \ll \hbar\omega$), we obtain

$$\sum_{nm} f^F(\varepsilon_{nm} - \mu) \approx \sum_{m=1}^{N}\left(\frac{\mu}{\hbar\omega} - \frac{\varepsilon_0\omega_0^2}{\hbar\omega^3}m^2\right)$$
$$+ \frac{2\pi T}{\hbar\omega}\sum_{m=1}^{N}\sum_{k=1}^{\infty}(-1)^k \sin\left[2\pi k\left(\frac{\mu}{\hbar\omega} - \frac{\varepsilon_0\omega_0^2}{\hbar\omega^3}m^2\right)\right] \qquad (15)$$
$$\times \sinh^{-1}\left(\frac{2\pi^2 kT}{\hbar\omega}\right),$$

where N is the integral part of the quantity $(\omega\sqrt{\mu/\varepsilon_0})/\omega_0$.

Let us transform the finite sums in (15) into Fourier series [17]. The expression for the AE current J can be presented as the sum of two terms:

$$J = J_1 + J_2,$$

where

$$J_1 = \frac{2em^{*2}\Lambda^2 SL}{\rho\hbar^4\omega_{th}\omega_0}\left(\sqrt{\frac{\mu}{\varepsilon_0}} - \frac{1}{2}\right) + \frac{2em^{*2}\Lambda^2 SL}{\pi\rho\hbar^4\omega_{th}\omega}\sum_{k=1}^{\infty}\frac{1}{k}\sin\left(2\pi k\frac{\omega}{\omega_0}\sqrt{\frac{\mu}{\varepsilon_0}}\right) + o\left(\frac{\hbar\omega}{\mu}, \frac{T^2}{\hbar^2\omega^2}\right), \quad (16)$$

$$J_2 = \frac{4\pi em^{*2}\Lambda^2 SL}{\rho\hbar^4\omega_{th}\omega}\sqrt{\frac{\hbar\omega}{\varepsilon_0}} \times \sum_{k=1}^{\infty}\left[C_k^+(T)\cos\left(\frac{2\pi k\mu}{\hbar\omega}\right) + C_k^-(T)\sin\left(\frac{2\pi k\mu}{\hbar\omega}\right)\right] + \frac{8\pi^2 em^{*2}\Lambda^2 SL}{\rho\hbar^4\omega_{th}\omega}\sum_{k=1}^{\infty}C_k^0(T)\cos\left(\frac{2\pi k\mu}{\hbar\omega}\right) + o\left(\frac{\hbar\omega}{\mu}, \frac{T^2}{\hbar^2\omega^2}\right). \quad (17)$$

The Fourier coefficients appearing in these expressions have the form

$$C_k^0(T) = \frac{(-1)^{k+1}kT}{\hbar\omega\sinh(2\pi^2 kT/\hbar\omega)},$$

$$C_k^{\pm}(T) = \frac{\pm(-1)^k\sqrt{k}T}{\hbar\omega_0\sinh(2\pi^2 kT/\hbar\omega)} \times \int_0^{\infty}\left[\sin\left(\frac{\hbar\omega^3 x^2}{8\pi k\varepsilon_0\omega_0^2}\right) \pm \cos\left(\frac{\hbar\omega^3 x^2}{8\pi k\varepsilon_0\omega_0^2}\right)\right] \times \left[\frac{\sin(Nx)}{2}\cot\left(\frac{x}{2}\right) + \cos^2(Nx)\right]dx. \quad (18)$$

Let us consider the AE current through a channel in zero magnetic field. In this case, $\omega = \omega_0$, and the sum of the series in expression (16) can be evaluated easily [18]. This gives the following simple expression for J_1:

$$J_1 = \frac{2em^{*2}\Lambda^2 SL}{\rho\hbar^4\omega_{th}\omega_0}N_0 + o\left(\frac{\hbar\omega}{\mu}, \frac{T^2}{\hbar^2\omega^2}\right), \quad (19)$$

where N_0 is the integral part of the quantity $\sqrt{\mu/\varepsilon_0}$.

It is interesting to note that, in contrast to J_2, J_1 in this case is a step function of the chemical potential. It should also be noted that J_1 depends on temperature only slightly, while J_2 decreases rapidly upon heating. Therefore, for comparatively high temperatures (curve *4* in Fig. 4) or for a comparatively weak parabolic confinement $\omega_0 \sim 2\pi^2 T/\hbar$ (curve *1* in Fig. 4), the term J_1 gives the most significant contribution to the total AE current J. In this case, the total AE current $J(\mu)$ exhibits a step dependence on the chemical potential, the term $J_2(\mu)$ being responsible for the fine structure of the steps (curve *1* in Fig. 4). As the temperature decreases, the amplitude of current oscillations $J_2(\mu)$ increases, and the dependence of the AE current on the chemical potential for $\hbar\omega_0 \gg 2\pi^2 T$ has the form of giant quantum oscillations (curve *2* in Fig. 4). It should be emphasized that the physical meaning can be attached only to the sum $J = J_1 + J_2$, and the splitting of the AE current into two terms is convenient only for an analysis.

It should be noted that the height of the quantization steps of the AE current (19) depends on the frequency of the parabolic confinement, while the width of plateaus of the steps is determined by the channel thickness d. It follows from formula (19) that, as the frequency ω_0 decreases (i.e., as the channel width increases) together with decreasing thickness d of the electron gas layer, the height and the lengths of the plateau on the steps increase. Thus, the channel asymmetry is responsible for the existence of clearly manifested quantization steps in the AE current. Note that the step dependence of the AE current on the voltage across the shutter was observed experimentally in [6].

In the case when the system is in a longitudinal magnetic field, the AE current is defined by formulas (16) and (17). The form of the $J(\mu)$ dependence changes strongly in this case. It can be seen from formula (16) and Fig. 4 (curve *3*) that the magnetic field destroys the quantization steps and that the dependence $J_1(\mu)$ (together with $J(\mu)$ is oscillatory by nature.

In strong fields, the term J_2 makes a decisive contribution to the total AE current J. The dependence of J_2 on the chemical potential is determined to a considerable extent by the channel thickness d. If $\varepsilon_0 \ll \hbar\omega$, which corresponds to a large thickness of the quantum layer and a strong magnetic field, the Fourier coefficients (18) do not make a significant contribution to the $J(\mu)$ dependence. In this case, the interval between the peaks of giant oscillations of the AE current upon a change in the chemical potential is $\hbar\omega$. If the magnetic field is strong enough ($\omega_c \gg \omega_0$), the separations between peaks on the $J(\mu)$ curve depend linearly on the magnetic field and are equal to $\hbar\omega_c$ to within terms of the order $o(\omega_0^2/\omega_c^2)$ (curve *1* in Fig. 5), the AE current having the maximum value for half-integral values of $\mu/\hbar\omega_c$. However, as the channel thickness decreases, additional oscillations associated with size quantization along the x axis are imposed on the giant oscillations of the AE current (curves *2* and *3* in Fig. 5).

The magnetic-field dependence of the AE current in a quantum channel is also determined to a considerable extent by the relation between the parameters ω_c, ω_0, and ε_0. If $\omega_c \gg \omega_0$, $\varepsilon_0/\hbar$, we have $J_2 \gg J_1$, and the AE current experiences giant quantum oscillations in reciprocal field with period

$$\Delta\left(\frac{1}{B}\right) = \frac{e\hbar}{m^* c\mu}$$

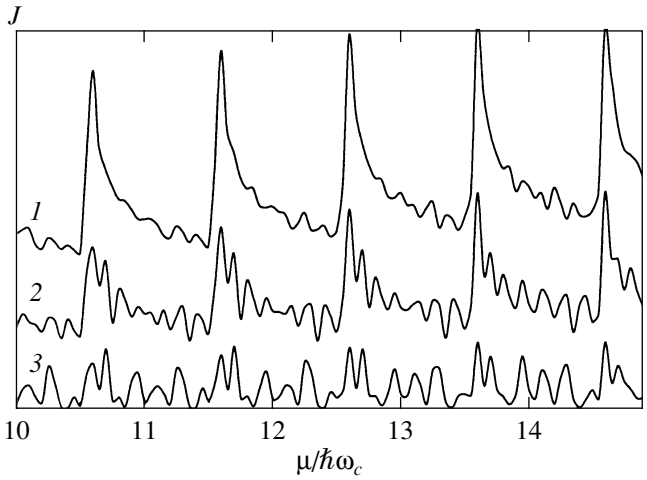

Fig. 5. Giant oscillations of AE current in a magnetic field $B = 3$ T at $T = 1$ K, $\omega_0 = 10^{12}$ s^{-1} as a function of the chemical potential in channels of various thickness determined by the hard-wall potential: $d = 3.1 \times 10^{-5}$ cm (curve *1*), $d = 1.6 \times 10^{-5}$ cm (curve *2*), and $d = 3.14 \times 10^{-6}$ cm (curve *3*).

(Fig. 6a). The origin of such oscillations is similar to the origin of giant quantum oscillations of the sound absorption coefficient in metals [16]. If the condition $\hbar\omega \gg \varepsilon_0$ is violated, the Fourier coefficients (18) make a noticeable oscillatory contribution to the total AE current, and the dependence $J(B)$ has a more complicated form. It should be noted that the form of the AE current oscillations upon a change in the magnetic field in the quantum channel is completely analogous to the form of the magnetic response in a quantum ring of a nonzero width [19]. For example, in the case of weak magnetic quantization, $\omega_c \ll \omega_0, \varepsilon_0/\hbar$, the AE current J is the sum of two terms, J_1 and J_2, oscillating in B^2 and such that $J_1 \gg J_2$ if $\hbar\omega \lesssim 2\pi^2 T$. The periods of these oscillations were determined in [19]. For oscillations of the first type, J_1, we have

$$\Delta_1(B^2) = 2\left(\frac{m^*c}{e}\right)^2 \omega_0^2 \sqrt{\frac{\varepsilon_0}{\mu}}. \quad (20)$$

For the term J_2, the period of oscillations has the form

$$\Delta_2(B^2) = 2\left(\frac{m^*c}{e}\right)^2 \omega_0^2 \frac{\hbar\omega_0}{\mu}. \quad (21)$$

Figure 6b shows the superpositions of the small-amplitude $J_2(B^2)$ oscillations with period (21) on the $J_1(B^2)$ oscillations with period (20).

4. CONCLUSIONS

We have analyzed the AE current in a ballistic quantum channel in a longitudinal magnetic field. Two models of confining potential are considered: the soft-wall and the hard-wall potential models. It is found that, in both cases under investigation, steps on the dependences of the AE current on the chemical potential, as well as giant oscillations on the magnetic-field dependence of the AE current, may appear for certain values of the parameters of the system.

The behavior of the AE current in the cases of the soft-wall potential as well as hard-wall potential strongly depends on the relation between the characteristic frequencies of the parabolic confinement potential and on the temperature (in zero magnetic field). For example, for the soft-wall potential, for $\hbar\omega_y \ll 2\pi^2 T \ll \hbar\omega_x$, the dependence of the AE current on the chemical potential is of the step form. Such a behavior of the $J(\mu)$ curve is associated with the filling of energy levels with the second quantum number m. As the temperature

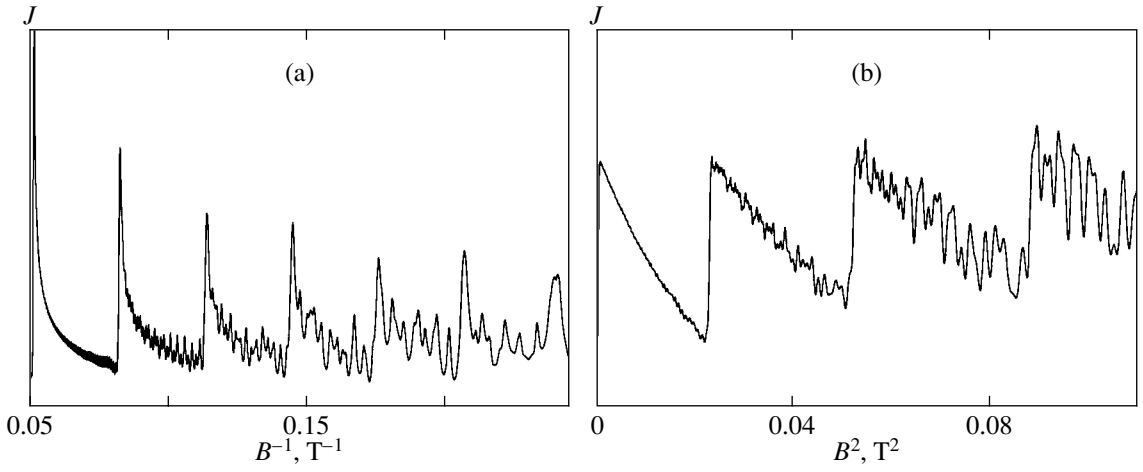

Fig. 6. Giant quantum oscillations of AE current in a quasi-two-dimensional quantum channel of thickness $d = 3 \times 10^{-6}$ cm and chemical potential $\mu = 10^{-13}$ erg at $T = 2$ K as a function of (a) B^{-1} for $\omega_0 = 10^{12}$ s^{-1} and (b) B^2 for $\omega_0 = 0.5 \times 10^{12}$ s^{-1}.

increases so that $\hbar\omega_y \ll 2\pi^2 T \lesssim \hbar\omega_x$, the dependence is gradually transformed into a linear dependence. Upon a decrease in temperature, for $\hbar\omega_y \lesssim 2\pi^2 T \ll \hbar\omega_x$, the quantization steps acquire a fine structure, and quantization is completely violated at a temperature $T \ll \hbar\omega_x$, $\hbar\omega_y$. Such a behavior of quantization of the AE current is due to the competition of two factors. First, the temperature must be high enough for the AE current oscillations, which may destroy the quantization step, to be suppressed by temperature. Second, the temperature should not be high enough for smearing the step thresholds. It should be noted that the existence of the AE current quantization is determined to a considerable extent by the asymmetry of the system. In particular, the condition $\omega_y \ll \omega_x$ may correspond to a quasi-two-dimensional type of the channel. In the case when ω_x is of the same order of magnitude as ω_y, oscillations have the form of beats. It is important to note that, in the case of a soft-wall potential, the magnetic field improves the AE current quantization pattern, while even a relatively weak magnetic field ($\omega_c \sim \omega_0$) suppresses quantization in the case of a hard-wall potential. This circumstance makes it possible to determine the profile of the confinement potential from the experimental data on the behavior of the AE current in a magnetic field.

The magnetic-field dependence of the AE current in the case of a soft-wall potential has the form of giant quantum oscillations, the periodic properties of the function $J(B)$ being determined by the relation between the magnetic and size quantizations. In particular, in the case of a strong magnetic quantization for a strongly asymmetric channel, the magnetic-field dependence of the AE current has the form of Shubnikov–de Haas oscillations with a fine structure determined by the Aharonov–Bohm oscillations. In the opposite case of a strong size quantization, the magnetic-field dependence of the AE current is a superposition of two oscillatory terms periodic in the squared magnetic field.

It was mentioned above that the behavior of the AE current in the case of a hard-wall potential is also determined by the relation between the geometrical parameters of the system and the temperature. For example, the AE current steps appear at a high temperature or for a weak parabolic confinement potential. As the temperature decreases (or the frequency of the confinement potential increases), the dependence of the AE current on the chemical potential has the form of giant quantum oscillations. It is interesting that the height of the quantization steps of the AE current strongly depends on the frequency of the parabolic potential (geometry along the *y* axis), while the width of the quantization plateau of the AE current strongly depends on the channel thickness (geometry along the *x* axis). This is also valid for a channel with a soft-wall potential, which was described in Section 2.

The dependence of the AE current on the chemical potential in a magnetic field strongly depends on the channel asymmetry and the magnitude of the magnetic field. For example, in the case of a large channel thickness and a strong field, the interval between the peaks of giant oscillations is equal to $\hbar\omega_c$. As the channel thickness decreases, additional oscillations associated with size effects along the *x* axis are superimposed on the giant oscillations.

It should be noted that the behavior of the AE current as a function of the magnetic field in the case of a hard-wall potential is similar to the behavior of the magnetic moment of a 2D quantum ring considered by us earlier [19]. In particular, the periods of magnetic response oscillations determined in that work coincide with the periods of the AE current oscillations.

An interesting feature of the AE effect in a quasi-two-dimensional channel with a hard-wall potential is a weak temperature smearing of the AE quantization thresholds in zero magnetic field. This feature is due to the quadratic dependence of the electron energy spectrum on the quantum number *m*.

It follows from the above analysis that the following two conditions must be satisfied for the existence of AE current steps. The first is the strong asymmetry of the system; i.e., the thickness of the quantum layer must be much smaller than the quantum channel width. It is important to note that this condition can be satisfied only for a quasi-two-dimensional channel. We will prove that the step dependence of the AE current in the channel is a consequence of its quasi-two-dimensional nature. For this purpose, we consider the limiting transition from a quasi-two-dimensional to a quasi-one-dimensional channel. We assume that $B = 0$; then, expression (15) for the AE current in a quasi-two-dimensional channel of thickness *d* has the form

$$J = \frac{2em^{*2}\Lambda^2 SL}{\rho\hbar^4\omega_{\text{th}}\omega_0}\left\{N_0 + \frac{4\pi^2 T}{\hbar\omega_0} \times \sum_{m=1}^{N_0}\sum_{k=1}^{\infty}\frac{(-1)^k k\cos[2\pi k(\mu - \varepsilon_0 m^2)/\hbar\omega_0]}{\sinh(2\pi^2 kT/\hbar\omega_0)}\right\}. \quad (22)$$

It should be noted that the oscillatory component in this expression is the sum of N_0 terms corresponding to the AE current in a quasi-one-dimensional channel. Thus, expression (22) for the AE current in a quasi-two-dimensional channel consists of two parts. One of them gives quantization steps of the AE current, which are slightly blurred by temperature, while the second is the sum of oscillatory terms.

We assume that the thickness *d* of the electron gas layer is so small that $1 \le \mu/\varepsilon_0 < 2$. It should be noted that the electron layer can be regarded as two-dimensional

if its thickness $d \sim \pi\hbar/\sqrt{2m^*\mu}$. In this case, $N_0 = 1$ and expression (22) assumes the form

$$J = \frac{2em^{*2}\Lambda^2 SL}{\rho\hbar^4\omega_{th}\omega_0}\left[1 + \frac{4\pi^2 T}{\hbar\omega_0} \times\left(\sum_{k=1}^{\infty}(-1)^k\right)k\cos\left(2\pi k\frac{\mu-\varepsilon_0}{\hbar\omega_0}\right)\sinh^{-1}\left(\frac{2\pi^2 kT}{\hbar\omega_0}\right)\right]. \quad (23)$$

Thus, the AE current in a quasi-one-dimensional channel exhibits an oscillatory dependence on the chemical potential.

The second condition depends on the parameters of the system and must be imposed on temperature so that each step on the $J(\mu)$ curve corresponds to the inclusion of new electron modes in an energy region of width T in the vicinity of the Fermi level.

It is important to note that the step dependence of the AE current and giant quantum oscillations in a quantum channel were observed experimentally (see, for example, [6]). Let us estimate the height of the AE current quantization steps. For this purpose, we use formula (7) or (19) and the parameters from [20]. For the ultrasound intensity $S \sim 0.001$ CGS units, we find that, in the case of deformation-controlled interaction, the height of the current step threshold is of the order of a nanoampere, which is in accord with the experimental data [6]. Using relation (3) and the value of the piezoelectric coefficient from [8], we find that, in the case of a piezoelectric interaction, the current is one or two orders of magnitude stronger (depending on the phonon frequency) than in the case of a pure deformation-controlled interaction.

ACKNOWLEDGMENTS

The work was supported financially by the Russian Foundation for Basic Research and by the Federal Special Program “Integration.”

REFERENCES

1. A. Esslinger, A. Wixforth, R. W. Winkler, *et al.*, Solid State Commun. **84**, 939 (1992).
2. J. M. Shilton, D. R. Mace, V. I. Talyanskii, *et al.*, Phys. Rev. B **51**, 14770 (1995).
3. J. M. Shilton, D. R. Mace, V. I. Talyanskii, *et al.*, J. Phys.: Condens. Matter **7**, 7675 (1995).
4. J. M. Shilton, D. R. Mace, V. I. Talyanskii, *et al.*, J. Phys.: Condens. Matter **8**, L337 (1996).
5. J. M. Shilton, V. I. Talyanskii, M. Pepper, *et al.*, J. Phys.: Condens. Matter **8**, L531 (1996).
6. V. I. Talyanskii, J. M. Shilton, M. Pepper, *et al.*, Phys. Rev. B **56**, 15180 (1997).
7. H. Totland and Yu. M. Galperin, Phys. Rev. B **54**, 8814 (1996).
8. V. L. Gurevich, V. B. Pevzner, and G. J. Iafrate, Phys. Rev. Lett. **77**, 3881 (1996).
9. V. L. Gurevich, V. I. Kozub, and V. B. Pevzner, Phys. Rev. B **58**, 13088 (1998).
10. O. Entin-Wohlman, Y. Levinson, and Yu. M. Galperin, Phys. Rev. B **62**, 7283 (2000).
11. F. A. Maaø and Yu. M. Galperin, Phys. Rev. B **56**, 4028 (1997).
12. Y. Levinson, O. Entin-Wohlman, and P. Wölfle, Phys. Rev. Lett. **85**, 634 (2000).
13. V. A. Geyler and V. A. Margulis, Phys. Rev. B **61**, 1716 (2000).
14. N. G. Galkin, V. A. Geyler, and V. A. Margulis, Zh. Éksp. Teor. Fiz. **117**, 593 (2000) [JETP **90**, 517 (2000)].
15. V. A. Geyler and V. A. Margulis, Phys. Rev. B **55**, 2543 (1997).
16. V. L. Gurevich, V. G. Skobov, and Yu. A. Firsov, Zh. Éksp. Teor. Fiz. **40**, 786 (1961) [Sov. Phys. JETP **13**, 552 (1961)].
17. V. A. Margulis, A. V. Shorokhov, and M. P. Trushin, Phys. Lett. A **276**, 180 (2000).
18. A. P. Prudnikov, Yu. A. Brychkov, and O. I. Marichev, *Integrals and Series* (Nauka, Moscow, 1981; Gordon and Breach, New York, 1986).
19. V. A. Margulis, A. V. Shorokhov, and M. P. Trushin, Physica E (Amsterdam) **10**, 518 (2001).
20. T. Brandes and A. Kawabata, Phys. Rev. B **54**, 4444 (1996).

Translated by N. Wadhwa

Journal of Experimental and Theoretical Physics, Vol. 94, No. 6, 2002, pp. 1169–1175.
Translated from Zhurnal Éksperimental'noĭ i Teoreticheskoĭ Fiziki, Vol. 121, No. 6, 2002, pp. 1362–1369.

SOLIDS
Electronic Properties

Excitons in CdS and CdSe Semiconducting Quantum Wires with Dielectric Barriers

V. S. Dneprovskiĭ[a, *], E. A. Zhukov[a], O. A. Shalygina[a], V. L. Lyaskovskiĭ[a], E. A. Muljarov[b], S. A. Gavrilov[c], and Y. Masumoto[d]

[a]*Moscow State University, Moscow, 119899 Russia*
**e-mail: scon281@phys.msu.su*
[b]*Institute of General Physics, Russian Academy of Sciences, Moscow, 117942 Russia*
[c]*Moscow Institute of Electronic Technology (Technical University), Moscow, 103498 Russia*
[d]*Tsukuba University, 305-8571 Tsukuba, Japan*
Received December 28, 2001

Abstract—Features of the photoluminescence spectra observed for various polarizations and intensities of the pumping radiation and the kinetics of photoluminescence of the CdS and CdSe nanocrystals grown in hollow nanochannels of an Al_2O_3 matrix are explained in terms of exciton transitions in semiconducting quantum wires with dielectric barriers. The observed exciton transition energies coincide with the values calculated with an allowance for the effects of quantum confinement and the "dielectric enhancement" of excitons. The latter effect is manifested by a significant increase in the Coulomb attraction between electrons and holes (the exciton binding energy exceeds 100 meV) due to a difference between the permittivities of semiconductor and insulator. It is shown that the exciton transition energy remains constant when the quantum wire diameter varies within broad limits. This is related to the fact that a growth in the one-dimensional bandgap width of the quantum wire caused by a decrease in the diameter is compensated by an increase in the exciton binding energy. © *2002 MAIK "Nauka/Interperiodica".*

1. INTRODUCTION

Researchers devote considerable effort to the study of excitons in semiconducting quantum wires (QWRs) with dielectric barriers, which represent structures where both charge carriers and excitons can freely move only in one direction. This interest is related to the fact that, besides the quantum confinement effects leading to a growth in the exciton binding energy ($E_{ex}^{1D} \propto \mathrm{Ry}[\ln(R/a_{ex}^{3D})]^2$ for the wire radius $R < a_{ex}^{3D}$, where Ry is the exciton Rydberg and a_{ex}^{3D} is the Bohr radius of the exciton in the bulk semiconductor [1]) and in the oscillator strength of a one-dimensional exciton with decreasing QWR diameter, the system features the so-called "dielectric enhancement" effect producing a significant additional increase in both the binding energy and the oscillator strength.

The phenomenon of dielectric enhancement (manifested by an increase in the Coulomb attraction between electrons and holes) is caused by redistribution of the electric field (generated by these electrons and holes) in the QWR related to the permittivity of a dielectric (insulator) being much smaller as compared to that of a semiconductor. The contribution of the insulator as a barrier to the electron–hole interaction (most of the field lines between electrons and holes pass through the insulator) accounts for a significant increase in the exciton binding energy and the oscillator strength of the exciton transition. The dielectric enhancement of excitons was theoretically predicted in [2–4] and then theoretically studied for quantum wells [5-10], superlattices [11, 12], quantum wires [13–15], and quantum dots [16]. In particular, it was demonstrated [1] that the exciton binding energy in semiconducting QWRs with dielectric barriers may exceed 100 meV. Experiments [17, 18] showed that the exciton binding energy in semiconducting (GaAs, CdSe, InP) QWRs crystallized in transparent dielectric nanotubes of chrysotile asbestos is significantly increased as compared to the values in bulk semiconductors and quasi-two-dimensional semiconducting structures. By selecting semiconductor and insulator materials with various permittivities for the nanostructures, it is possible to modify the exciton binding energy and oscillator strength within broad limits, thus implementing the concept of "Coulomb interaction engineering" [1].

Below, we report the results of investigation of the features of the photoluminescence (PL) spectra and kinetics observed for CdS and CdSe nanocrystals grown in the hollow nanochannels of a transparent dielectric Al_2O_3 matrix. An analysis of variations in the intensity of emission observed in the samples excited by laser radiation with various polarizations and a comparison of the experimental energies of radiative transitions to the results of theoretical calculations allowed

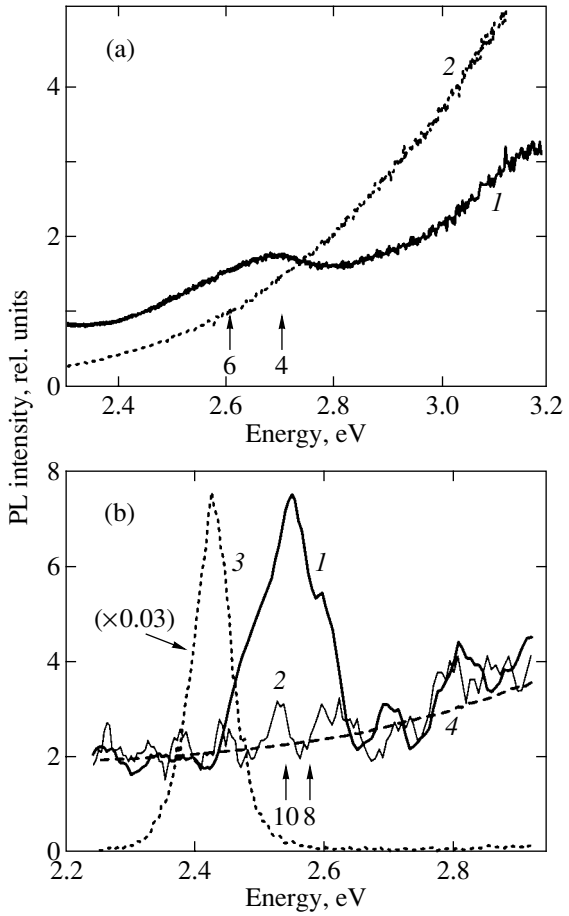

Fig. 1. (a) The low-temperature (2 K) PL spectra of (*1*) CdS nanocrystals grown in hollow channels with a diameter of 4–6 nm in the Al_2O_3 matrix and (*2*) the pure Al_2O_3 matrix; (b) the room-temperature PL spectra of (*1, 2*) CdS nanocrystals grown in hollow channels with a diameter of 8–10 nm in the Al_2O_3 matrix excited with a laser radiation polarized at (*1*) 45° and (*2*) 90° relative to the axis of nanochannels, (*3*) a CdS single crystal grown from the gas phase, and (*4*) the pure Al_2O_3 matrix.

us to evaluate the exciton binding energies and conclude that the PL is related mostly to the excitons in nanostructures crystallized predominantly in the form of QWRs.

The observed time variation (a shift toward lower energies) of the PL spectra of QWRs, which exhibit inhomogeneous broadening due to dispersion of the transverse dimensions of nanocrystals, is explained by a decrease in the exciton recombination time in QWRs of smaller diameter as compared to that in the wires of greater diameter.

We have also observed a nonlinear dependence of the PL intensity on the excitation level and a shift of the emission maximum toward higher energies in the PL spectra of QWRs excited with high-power second harmonic radiation of a Nd:YAG laser, which is probably explained by a nonlinear absorption related to the dominating effect of filling of the exciton phase space.

2. EXPERIMENTAL RESULTS AND DISCUSSION

In recent years, various methods were developed for the fabrication of semiconducting QWRs with dielectric barriers. These techniques are based on the crystallization of a semiconductor incorporated into hollow channels of a nanometer transverse size in a dielectric matrix. The matrices represent either natural materials (e.g., chrysotile asbestos [19] with a structure comprising closely packed transparent dielectric nanotubes) or specially synthesized media (e.g., mica in which nanochannels are created by high-energy ion bombardment in a particle accelerator [20]).

Our samples were prepared by creating hollow nanochannels in a transparent dielectric matrix (an Al_2O_3 film with a thickness of several microns on a 10-μm-thick aluminum foil) by means of electrochemical etching. The etching was performed at room temperature in a 10% aqueous solution of sulfuric acid at an anodic current density of 1 mA/cm^2. The etching time was either 0.5 h, which ensured the formation of pores (nanochannels) with a diameter of 4–6 nm, or 1 h, which provided for thicker pores 8–10 nm in diameter. Diameters of the hollow channels were determined with the aid of an atomic force microscope [21]. The nanocrystals of CdS were prepared by cathode deposition in an aqueous solution of 0.1 M $Na_2S_2O_3$ and 0.1 M $CdSO_4$. The process was conducted at a constant current density of 1 mA/cm^2 for 300 s at room temperature. Then the samples were annealed for 1 h at 300°C. The nanocrystals of CdSe were obtained by room-temperature cathode deposition in an aqueous solution of 0.01 M $CdSO_4$ and 0.02 M H_2SeO_3 at a current density of 1.5 mA/cm^2. These samples were annealed for 10 min in air at 430°C.

The photoluminescence spectra of CdS and CdSe nanostructures crystallized in the pores of various cross sections in Al_2O_3 matrices are presented in Figs. 1 and 2 in comparison with the spectrum of a pure dielectric matrix free of nanocrystals. Figures 1b and 2 also shows the PL spectra measured for various polarizations of the exciting radiation. For the comparison, these figures also present the PL spectra of a CdS single crystal grown from the gas phase and of a crystalline CdSe film. The PL band maxima exhibited a shift toward shorter wavelengths for the samples with semiconductors in nanopores in comparison to the peak position for single crystals: 2.65 eV for CdS crystallized in a matrix with the average pore diameter D = 4–6 nm (Fig. 1a); 2.54 eV for CdS in the pores with D = 8–10 nm (Fig. 1b); 1.86 eV for CdSe in the pores with D = 4–6 nm, and 1.75 eV for CdSe in the pores with $D \approx 30$ nm (Fig. 2). A analysis of these data suggested that the pores contained nanocrystals. The presence of CdS and CdSe nanocrystals in the pores of the Al_2O_3

matrix was confirmed by the phonon spectra of the sample structures measured using IR Fourier transform spectroscopy [22].

The PL bands at 2.65 and 2.54 eV (Fig. 1) and 1.86 eV (Fig. 2) can be attributed either to an electron–hole transition (in some papers, this transition is referred to as an exciton transition) in quantum dots, or to an exciton transition in quantum wires, or to transitions of both types.[1]

Assuming that the nanostructures represent quantum dots (QDs), we may estimate the average QD radius (R) using calculated [23] dependences of the lowest electron–hole transition energy on the R value (the QD dimensions are comparable with the Bohr radius of excitons in a bulk semiconductor). For example, the energy of the PL band maximum for the CdS nanocrystals in the pores with D = 8–10 nm (Fig. 1b) corresponds to the lowest electron–hole transition energy in QDs with $R \approx 6$ nm. With an allowance for the electron–hole attraction being enhanced by the dielectric environment of the QD [16], the transition energy significantly decreases and the estimated radius reduces to 3–4 nm. The estimated dimensions of CdS and CdSe QDs agree with the measured transverse size of nanochannels in the matrix, in which these nanocrystals can occur. However, it should be noted that effective PL bands were observed only in cases (Figs. 1 and 2) when the exciting laser radiation contained a field component oriented along the axis of nanochannels. This fact suggests that the nanostructures studied have predominantly the form of QWRs, rather than QDs.

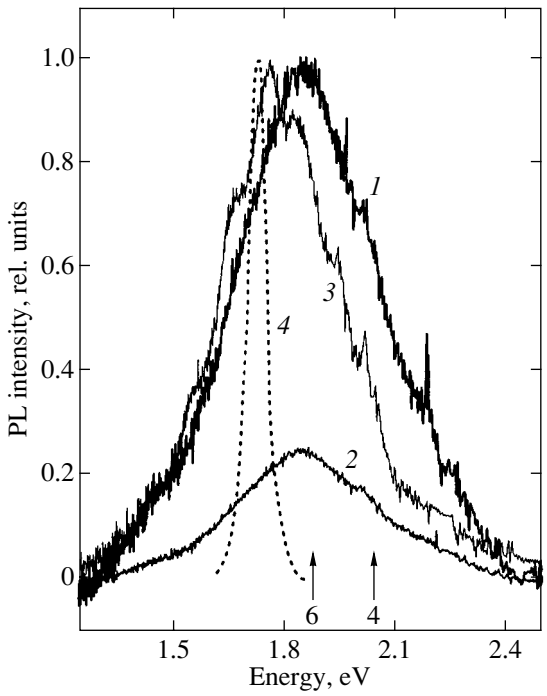

Fig. 2. The room-temperature PL spectra of (*1*, *2*) CdSe nanocrystals grown in hollow channels with a diameter of 4–6 nm in the Al_2O_3 matrix excited with a laser radiation polarized at (*1*) 45° and (*2*) 90° relative to the axis of nanochannels, (*3*) CdSe nanocrystals grown in hollow channels with a diameter of about 30 nm in the Al_2O_3 matrix (excited with a laser radiation polarized at 45° relative to the axis of nanochannels), and (*4*) a crystalline CdSe film.

Inside the thin (QWR radius is significantly smaller than the exciting radiation wavelength) parallel semiconducting QWRs surrounded by a dielectric medium, the field component perpendicular to the wire axis is significantly decreased due to the boundary conditions [24]. The parallel and perpendicular field components inside the wire are as follows:

$$E^{\parallel} = E^{\parallel}_{\infty}, \quad E^{\perp} = \delta E^{\perp}_{\infty},$$

where $\delta = 2\varepsilon_d/(\varepsilon_d + \varepsilon_s)$, E_∞ is the field strength far from the wire, and ε_d and ε_s are the permittivities of dielectric and semiconductor, respectively. In the dipole approximation, the PL intensity is proportional to the square product of the field amplitude and the dipole matrix element of the transition. Assuming that the dipole matrix element d_{cv} of the transition between one-dimensional valence band and conduction band is isotropic, the degree of linear polarization of the emission (related to a difference in the efficiency of absorption of the differently polarized pumping radiation) can be expressed as

$$\sigma = \frac{I^{\parallel} - I^{\perp}}{I^{\parallel} + I^{\perp}} = \frac{1 - \delta^2}{1 + \delta^2},$$

where $I^{\parallel, \perp}$ is the PL intensity for the semiconducting QWRs excited with the radiation polarized along and across the wire, respectively. For CdS QWRs in the pores with D = 8–10 nm (Fig. 2), $\sigma = 0.5 \pm 0.08$, while, for CdSe QWRs in the pores with D = 4–6 nm (Fig. 3), $\sigma = 0.56 \pm 0.05$. These estimates agree with the calculated σ values of 0.47 (0.57) obtained for $\varepsilon_s = 5.24$ (6.4) in CdS (CdSe). Thus, we believe that the PL of nanostructures grown in the hollow channels of the Al_2O_3 matrix is primarily related to the emission from semiconducting QWRs with dielectric barriers, rather than from QDs.

Figure 3 presents the results of calculations of the exciton transition energy, one-dimensional bandgap width, and exciton binding energy as functions of the radius of CdS and CdSe quantum wires with Al_2O_3 dielectric barriers. The width of the one-dimensional bandgap in QWRs is increased as compared to analogous values for the bulk semiconductors, which is related both to the quantum confinement effects and to

[1] Strictly speaking, the electron–hole excitation in a quasi-zero-dimensional system (quantum dot) is not the exciton, by which we imply a mobile quasi-particle. The electron and hole wave functions are fixed due to the quantum confinement effect, while the energy of the Coulomb interaction between electron and hole is small as compared to the separation of quantum confinement energy levels of free electrons and holes.

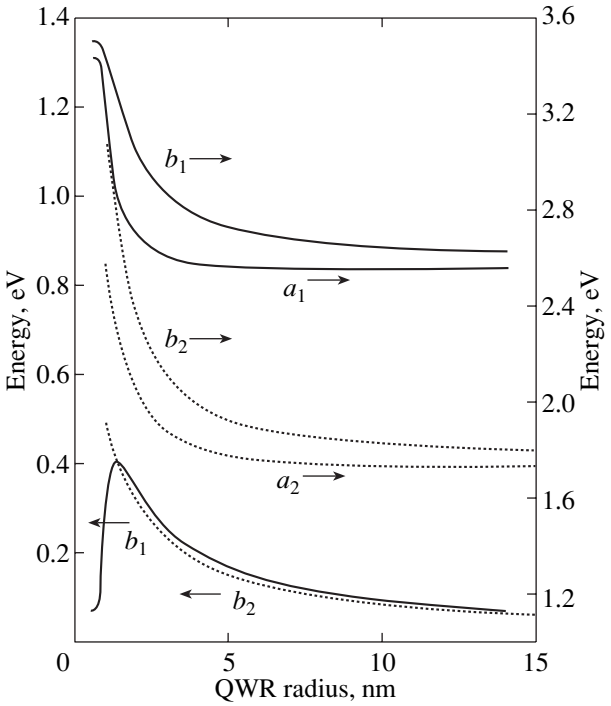

Fig. 3. Theoretically calculated dependences of the (a) exciton transition energy, (b) one-dimensional bandgap width, and (c) exciton binding energies versus quantum wire radius for CdS (solid curves) and CdSe (dashed curves) QWRs with dielectric (Al_2O_3) barriers.

a considerable influence of the self-action potentials [18] leading to an additional repulsion of charge carriers from the semiconductor–insulator interface. Large values of the exciton binding energy and the oscillator strength are due to the Coulomb interaction between electrons and holes being significantly enhanced by the image potentials. Comparing the experimental data on the exciton transition energies to the theoretically calculated values, we can see that the peaks of the PL bands correspond to the exciton transitions in the CdS QWRs with a diameter of 4–6 nm and an exciton binding energy of $E_{ex} \approx 300$ meV (Fig. 1), in the CdS QWRs with a diameter of 8–10 nm and $E_{ex} \approx 130$ meV (Fig. 2), and in the CdSe QWRs with a diameter of 4–6 nm and $E_{ex} \approx 240$ meV (Fig. 3). Unfortunately, a large spectral broadening of the PL bands did not allow us to separate the exciton transitions A and B (i.e., the transitions related to the valence bands A and B, respectively).

The estimates obtained for the QWR diameters do not contradict the measured dimensions of pores (nanochannels) in the Al_2O_3 matrix, where the crystallization of semiconductors took place. As can be seen in Fig. 3, variations in the energy of the free electron–hole transition in the region of QWR diameters exceeding 5 nm are virtually completely compensated by changes in the exciton binding energies. As a result, the exciton transition energy is independent of the QWR radius in a broad range of values, which can partly suppress the inhomogeneous broadening of the exciton absorption and emission bands in the samples with considerable dispersion of the transverse dimensions of QWRs.

The absence of dependence of the exciton transition energy on the QWR radius for the wire radius above 5 nm (Fig. 3) and a smaller influence of the nonradiative recombination (related to a decrease in the role of surface states in the QWRs of a greater diameter) probably account for a smaller broadening of the exciton PL band observed for the QWRs of greater diameter: 120 meV in CdS QWRs with D = 8–10 nm (Fig. 1b) versus 250 meV in the QWRs with D = 4–6 nm (Fig. 1a); 450 meV in CdSe QWRs with D = 4–6 nm versus 340 meV in the QWRs with $D \approx 30$ nm (Fig. 2). We believe that the observed considerable broadening of the PL spectra (Figs. 1 and 2) is related to structural inhomogeneities appearing during the growth of the CdS and CdSe nanocrystals, which influence the semiconductor parameters (bandgap width, effective masses of charge carriers) determining the exciton transition energy.

In order to study the kinetics of PL from semiconducting QWRs with dielectric barriers, we measured a time sequence of the PL spectra. The spectra were excited using a focused second harmonic radiation ($\hbar\omega$ = 3.1 eV) of a Ti–sapphire laser pumped with an argon laser. The second harmonic radiation pulses had a duration of 1.5 ps. a repetition frequency of 82 MHz, and a pulse energy of about 0.2 μJ/cm^2. The spectra were recorded using a high-speed synchroscan streak camera of the Hamamatsu C1587 type with a polychromator. The time resolution of the system was not worse than 50 ps, and the spectral resolution was about 1 meV.

Figures 4 and 5 show the PL spectra of CdS and CdSe QWRs grown in the pores of an Al_2O_3 matrix with D = 4–6 nm. These spectra were recorded with various time delays after an excitation pulse. Note that the maximum intensity shifts toward smaller energies at the expense of a rapid decrease in intensity of the high-frequency spectral components. This is confirmed by the PL kinetics observed in various parts of the spectrum. As can be seen in Figs. 4 and 5, the PL intensity in the low-frequency part of the spectrum decays at a slower rate. The decrease in the PL intensity with time in various parts of the spectrum exhibits slow and fast components, which can be approximately described by a sum of two exponentials:

$$I(t) = C_1 \exp(-t/\tau_1) + C_2 \exp(-t/\tau_2).$$

For example, the fast decay component of curve *4* in Fig. 4b has a characteristic time of $\tau_1 \approx 70$ ps, while the slow component decays with a time constant of $\tau_2 \approx$ 3 ns. For curve *1*, the corresponding times are greater by a factor of 4 and more than 2.5, respectively.

The kinetic properties of semiconducting nanostructures with dielectric barriers significantly differ from the analogous properties of analogous nanostructures

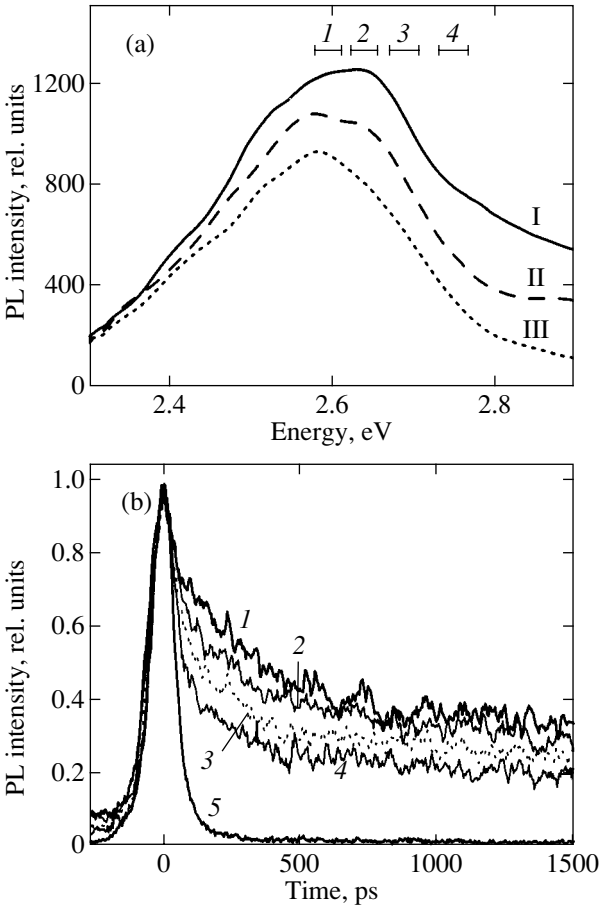

Fig. 4. (a) The low-temperature (2 K) PL spectra of CdS QWRs with dielectric barriers measured sequentially with various time delay relative to a 1.5-ps exciting second harmonic radiation pulse of a Ti–sapphire laser: (I) 0–100 ps, (II) 100–200 ps, and (III) 200–300 ps; (b) time variation of the PL intensity of (*1–4*) the CdS QWRs with dielectric barriers (in the regions *1–4* indicated in the spectra (a)) and (*5*) Al_2O_3 matrix.

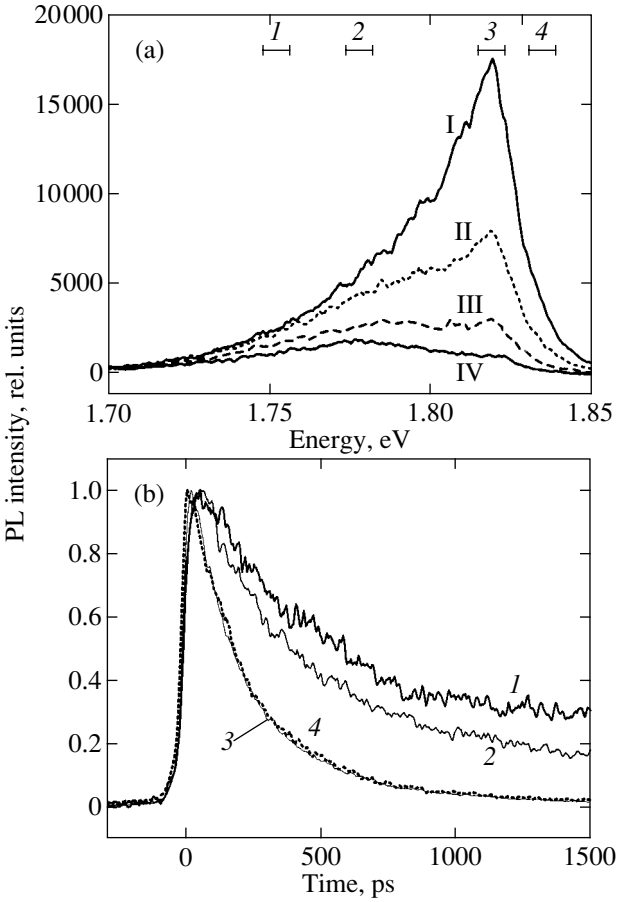

Fig. 5. (a) The low-temperature (2 K) PL spectra of CdSe QWRs with dielectric barriers measured sequentially with various time delay relative to a 1.5-ps exciting second harmonic radiation pulse of a Ti–sapphire laser: (I) 0–80 ps, (II) 150–270 ps, (III) 460–540 ps, and (IV) 720–820 ps; (b) time variation of the PL intensity of (*1–4*) the CdSe QWRs with dielectric barriers in the regions *1–4* indicated in the spectra (a).

with semiconductor barriers because the barrier material and interfaces determine the properties of electron and exciton systems. In the former structures, relaxation of the energy of excited electron–hole pairs and excitons proceeds via both radiative and nonradiative mechanisms [25, 26]. We relate the fast component of the PL decay kinetics with radiative and nonradiative recombination of excitons in quantum wires and the slow component with the trapping of excited charge carriers and excitons by traps at the semiconductor–insulator interface, followed by release.

The shorter time of the PL intensity relaxation in the high-frequency part of the spectrum, as well as the longwave shift of the PL peak position, is probably related to a difference in the times of nonradiative recombination in the QWRs of various transverse dimensions. In the QWRs of smaller diameter, the nonradiative recombination time is shorter because of a more significant role of the surface. A shift of the PL peak can also be explained by a fast trapping of excitons on the local states [26]. The magnitude of the shift indicates that the traps are about 50 meV deep. Unfortunately, this type of traps cannot be identified at present. It should be noted that the observed kinetic features of the PL spectra are not related to nonlinear processes, since the energy density of the laser radiation exciting emission from the samples was insufficient for the observation of nonlinear effects.

A nonlinear dependence of the PL intensity from CdSe QWRs in Al_2O_3 on the excitation level was observed for the absorption of the second harmonic radiation ($\hbar\omega$ = 2.34 eV) of a Nd:YAG laser operating in the Q-switching mode at a pulse duration of 14 ns, the excitation pulse energy of up to 2 mJ, and a laser spot area of $S = 10^{-2}$ cm^2. As can be seen in Fig. 6, the high excitation levels leads to "saturation" of the PL intensity and a short-wave shift of the PL intensity maximum. We relate the nonlinear dependence of the

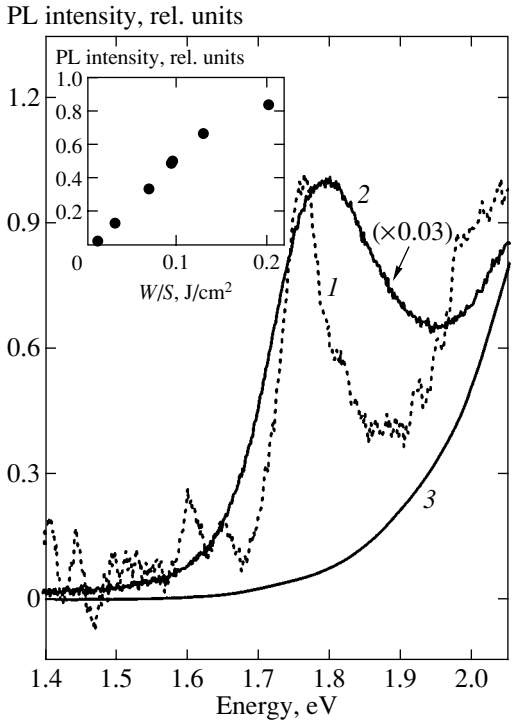

Fig. 6. The room-temperature (300 K) PL spectra: (*1*, *2*) CdSe QWRs with dielectric barriers measured at various levels of excitation with second harmonic radiation of a Nd:YAG laser (*1*) 0.012 and (*2*) 0.2 J/m^2; (*3*) Al_2O_3 matrix. The inset shows a plot of the room-temperature (300 K) PL intensity versus excitation energy density *W*/*S* for a sample containing CdSe QWRs with dielectric barriers (second harmonic radiation of a Nd:YAG laser; pulse duration, 14 ns; pulse energy *W*, up to 2 mJ; laser spot size *S*, 10^{-2} cm^2).

PL intensity on the excitation level to a nonlinear absorption in the samples with QWRs exhibiting a significant dispersion in the transverse size.

At a high excitation level, various nonlinear processes may coexist and compete with each other in the QWRs [17, 27, 28], including the screening of excitons, filling of the phase space of excitons, occupation of the one-dimensional electron and hole energy bands, and renormalization of the width of a one-dimensional forbidden band (the bandgap width decreases with an increase in the excitation level). Apparently, a dominating effect in the QWRs with dielectric barriers (e.g., those with higher exciton binding energies) is the exciton phase space filling which leads to a decrease (saturation) in the absorption and, hence, a decrease in the PL intensity with increasing excitation level. The phase space filling takes place first in the QWRs of a large diameter (i.e., in the QWRs with a greater effective exciton length). This circumstance can explain a shortwave shift of the PL maximum observed for the samples with QWRs.

The results of theoretical calculations of the effective exciton length (5–10 nm) in semiconducting (CdSe) 6- to 10-nm-thick QWRs with dielectric barriers allowed us to evaluate the linear density of excitons (i.e., the number of excitons per unit length) necessary for pronounced manifestations of the phase space filling effect: $n_{ph} \approx 10^6$ cm^{-1}. Estimates show that this exciton density was probably reached in the experiment. Indeed, the linear concentration of excitons (for the measured exciton lifetime $\tau \approx 10^{-10}$ s being much shorter than the exciting laser pulse duration Δt) can be evaluated as

$$n \approx \beta \frac{\tau W}{\Delta t S L \hbar \omega N} \approx 10^6\text{–}10^7 \text{ cm}^{-1}.$$

This estimate was obtained for an energy of $W = 0.2$ mJ (maximum pumping level) absorbed in the sample with a thickness of $L \approx 5$ μm (the second harmonic radiation absorption was measured using the samples with windows etched through the nontransparent substrate). The density of hollow channels (pores determined with the aid of an atomic force microscope) filled with a semiconductor was $N \approx 10^{11}$ cm^{-2} [21], and the quantum yield of the conversion of absorbed photons into excitons was $\beta \approx 0.5$.

3. CONCLUSION

We have analyzed the experimental PL spectra of semiconducting (CdS, CdSe) nanostructures crystallized in the hollow channels of nanometer transverse size formed in a transparent dielectric Al_2O_3 matrix, including data about (i) high-energy shifts of the PL maxima as compared to the case of bulk semiconductors (in agreement with the theoretical predictions), (ii) dependence of the PL intensity on the polarization of exciting radiation, (iii) kinetics of the PL intensity, (iv) nonlinear dependence of the PL intensity on the laser excitation level, and (v) changes in the PL spectra measured at high pumping levels. The whole body of data indicates that the nanostructures represent predominantly crystalline semiconducting quantum wires with an approximately 20% dispersion of the transverse size (diameter), in which the dominating process is related to exciton transitions.

A comparison of the experimentally measured exciton transition energies to the results of theoretical calculations with an allowance for the quantum confinement and dielectric enhancement effects allowed the exciton binding energy in semiconducting QWRs with dielectric barriers to be evaluated as approximately 250 meV for CdS and CdSe QWRs with a diameter of 4–6 nm.

It was demonstrated that the exciton luminescence spectrum in semiconducting QWRs with dielectric barriers exhibits inhomogeneous broadening related to the transverse size dispersion, which can be partly suppressed because an increase in the one-dimensional bandgap width in the QWRs with decreasing diameters is compensated within broad limits by an increase in the

exciton binding energy, so that the resulting exciton transition energy remains virtually unchanged.

ACKNOWLEDGMENTS

This study was supported by the Russian Foundation for Basic Research (project nos. 99-02-18327 and 02-02-16167) and by the Federal Program "Physics of Solid State Nanostructures."

REFERENCES

1. L. V. Keldysh, Phys. Status Solidi A **164**, 3 (1997).
2. N. S. Rytova, Dokl. Akad. Nauk SSSR **163**, 1118 (1965) [Sov. Phys. Dokl. **10**, 754 (1966)].
3. A. V. Chaplik and M. V. Éntin, Zh. Éksp. Teor. Fiz. **61**, 2496 (1971) [Sov. Phys. JETP **34**, 1335 (1972)].
4. L. V. Keldysh, Pis'ma Zh. Éksp. Teor. Fiz. **29**, 716 (1979) [JETP Lett. **29**, 658 (1979)].
5. E. Hanamura, N. Nagaosa, M. Rumagai, and T. Takagahara, Mater. Sci. Eng. B **1**, 255 (1988).
6. M. Kumagai and T. Takagahara, Phys. Rev. B **40**, 12359 (1989).
7. D. B. Tran Thoai, R. Zimmermann, M. Grundmann, and D. Bimberg, Phys. Rev. B **42**, 5906 (1990).
8. L. Wendler and B. Harwig, J. Phys.: Condens. Matter **3**, 9907 (1991).
9. X. Zhang, Y. Li, Z. Kong, and Ch. Wei, Phys. Rev. B **49**, 10432 (1994).
10. J. Cen, R. Chen, and K. K. Bajai, Phys. Rev. B **50**, 10947 (1994).
11. R. R. Guseinov, Phys. Status Solidi B **125**, 237 (1984).
12. E. A. Muljarov, S. G. Tikhodeev, N. A. Gippius, and T. Ishihara, Phys. Rev. B **51**, 14370 (1995).
13. S. Glutsch, F. Bechstedt, W. Wegsheider, and G. Schedelbeck, Phys. Status Solidi A **164**, 405 (1997).
14. V. S. Babichenko, L. V. Keldysh, and A. P. Silin, Fiz. Tverd. Tela (Leningrad) **22**, 1238 (1980) [Sov. Phys. Solid State **22**, 723 (1980)].
15. E. A. Mulyarov and S. G. Tikhodeev, Zh. Éksp. Teor. Fiz. **111**, 274 (1997) [JETP **84**, 151 (1997)].
16. T. Takagahara, Phys. Rev. B **47**, 4569 (1993).
17. V. S. Dneprovskiĭ, E. A. Zhukov, E. A. Mulyarov, and S. G. Tikhodeev, Zh. Éksp. Teor. Fiz. **114**, 700 (1998) [JETP **87**, 382 (1998)].
18. E. A. Muljarov, E. A. Zhukov, V. S. Dneprovskii, and Y. Masumoto, Phys. Rev. B **62**, 7420 (2000).
19. V. N. Bogomolov, Usp. Fiz. Nauk **124**, 171 (1978) [Sov. Phys. Usp. **21**, 77 (1978)].
20. V. Dneprovskii, E. Zhukov, V. Karavanskii, *et al.*, Superlattices Microstruct. **23**, 1217 (1998).
21. S. F. Gavrilov, V. V. Gusev, V. S. Dneprovskiĭ, *et al.*, Pis'ma Zh. Éksp. Teor. Fiz. **70**, 216 (1999) [JETP Lett. **70**, 216 (1999)].
22. A. I. Belogorokhov, private communication.
23. S. V. Nair, S. Sinha, and R. S. Rustagi, Phys. Rev. B **35**, 4098 (1987).
24. P. Ils, Ch. Greus, A. Forchel, *et al.*, Phys. Rev. B **51**, 4272 (1995).
25. S. G. Romanov, C. M. Sotomayor-Torres, H. M. Yates, *et al.*, J. Appl. Phys. **82**, 380 (1997).
26. E. A. Zhukov, Y. Masumoto, E. A. Muljarov, and S. G. Romanov, Solid State Commun. **112**, 575 (1999).
27. S. Benner and H. Haug, Europhys. Lett. **16**, 579 (1991).
28. S. Benner and H. Haug, Phys. Rev. B **47**, 15750 (1993).

Translated by P. Pozdeev

Journal of Experimental and Theoretical Physics, Vol. 94, No. 6, 2002, pp. 1176–1178.
Translated from Zhurnal Éksperimental'noĭ i Teoreticheskoĭ Fiziki, Vol. 121, No. 6, 2002, pp. 1370–1373.

SOLIDS
Electronic Properties

Surface Superconductivity and Supercooling in Lead

I. N. Khlyustikov[a, b, *] and V. A. Berezin[a, b]

[a]*Kapitza Institute of Physical Problems, Russian Academy of Sciences, Moscow, 117334 Russia*

[b]*Institute of Problems of Microelectronic Technology and Ultrapure Materials, Russian Academy of Sciences, Chernogolovka, Moscow oblast, 142432 Russia*

**e-mail: khly@kapitza.ras.ru*

Received January 9, 2002

Abstract—Observations are made of metastable supercooled normal bulk states in lead samples. It is demonstrated that such states are realized when the critical field of surface superconductivity H_{c3} is lower than the critical field H_c and in the opposite case. Therefore, the surface superconductivity is not a nucleus with supercritical parameters for the bulk superconductivity. *© 2002 MAIK "Nauka/Interperiodica".*

1. INTRODUCTION

The investigations of the superconductivity of the twinning plane reported in [1] revealed that the sample volume surrounding the twinning plane may remain in a metastable supercooled normal state even though the twinning plane is already in the superconducting state. The same qualitative result was obtained in [2], where the plane *N*–*S* interface (the interface between the normal and superconducting phases) was formed due to the "neighborhood effect" upon contact between two different superconductors. Therefore, it is demonstrated in these papers for type I superconductors that the nucleus of the superconducting phase in neither case has the parameters leading to the absolute instability of the thermodynamically disadvantageous normal state.

The third system (historically, it appears to be the first one to have been treated) in which the plane *N*–*S* interface appears is the interface produced by surface superconductivity. This problem was treated, for example, in the well-known paper by Saint-James and de Gennes [3]. According to them, in type I superconductors with a relatively low value of the Ginzburg–Landau parameter, $\kappa < 0.42$, the critical magnetic field of surface superconductivity $H_{c3} < H_c$ is observed as the boundary between possible metastable normal states in the bulk of samples. As to type I superconductors with a high value of this parameter, $0.42 < \kappa < 1/\sqrt{2}$, in which $H_{c3} > H_c$, the existence of surface superconductivity results in that metastable supercooled states turn out to be forbidden in general. In other words, it is inferred that the surface superconductivity always represents a nucleus with supercritical parameters. Cardona and Rosenblum [4] fully agreed with the inferences made by Saint-James and de Gennes [3].

Somewhat later, for example, in [5, 6], an attempt was made at performing more thorough investigations of the effect of the surface superconductivity on the bulk one. In these studies, data were obtained which indicated that the results obtained by Saint-James and de Gennes [3] should be revised and refined to a considerable extent. However, the studies reported in [5, 6] were not brought to their logical conclusion, and the viewpoint of Saint-James and de Gennes [3], reproduced by de Gennes in his monograph [7], remained the most popular one.

It was the objective of this study to find out whether the surface superconductivity is indeed a nucleus with supercritical characteristics in the bulk of samples.

2. DETAILS OF EXPERIMENTS AND SAMPLES

The characteristic features indicative of the existence of metastable states during first-order phase transitions include the hysteresis and the abrupt variation of the properties of samples being investigated. The presence of hysteresis is determined by the energy barrier between the possible states of the system, and the jump occurs because, at the time the stability of metastable states is disturbed, the system is already far from the conditions of phase equilibrium, and a new phase arises immediately in quantity or with a high amplitude. It is to these characteristic features of the existence of metastable states, i.e., the hysteresis and the abrupt variation of the properties of samples, that major attention is given in our study.

We selected lead as the sample material. Because lead has a cubic close-packed crystal structure, no twins are produced in the case of plastic strain, which may affect the width of the region of metastable states (see [1]). In addition, $H_{c3} < H_c$ for lead at a relatively high temperature in the vicinity of the superconducting transition temperature, and, at lower temperatures, $H_{c3} > H_c$ (see, for example, [4]). This enables one to use the same sample during the same helium experiment to perform

measurements of critical fields both with $\kappa < 0.42$ and with $\kappa > 0.42$.

The sample previously investigated by Mina and Khaĭkin [8] was used for measurements. This sample was a single-crystal plane-parallel plate $13 \times 6 \times 1$ mm in size.

We recorded the HF loss (high-frequency signal loss) in a sample located inside a helical resonator. The shape of the helical resonator replicated the sample shape. The resonator length was approximately one-third of the sample length, so that the end parts of the sample would not affect the HF response where possible. The resonance frequency was defined by the resonator geometry and, in our experiments, amounted to approximately 450 MHz. The helical resonator axis lay in the horizontal plane in parallel with the vertically arranged plane of the sample. An electromagnet was used to generate a magnetic field. The electromagnet was capable of rotating in the horizontal plane; as a result, the magnetic field could be directed in parallel with the sample plane. A more detailed description of the experimental facility and of the measurement procedure is found in [9].

3. MEASUREMENT RESULTS

Figure 1 gives an example of experimental recording of the dependence of the Q factor of the measuring circuit (in relative units) on the magnetic field at $T = 4.15$ K. The field was scanned in the range from about −1 kOe to approximately +1 kOe. The "horizontal" regions of the recording with a relatively low Q factor of the circuit in the case when the external magnetic field applied to the sample is high correspond to the normal state of the sample. If the sample is in the superconducting state, the Q factor of the measuring circuit increases. The value of the magnetic field H_c determined on the basis of this recording is 535 Oe.

Figure 2 shows a segment of the same recording in the vicinity of H_c. This region exhibits all of the characteristic features which prove the fact of existence of metastable states in the sample. The magnetic fields confining the hysteresis region are marked in the figure by arrows and denoted by H_c and H_{sc}. One can clearly see that, in the field H_{sc}, the sample properties vary abruptly. The direction of the jump in the figure is likewise indicated by an arrow. The lower branch of the hysteresis loop, in which the Q factor of the measuring circuit corresponds to the normal state of the sample, is formed when the external magnetic field decreases from values exceeding H_c. On the contrary, the upper branch is formed when the external magnetic field increases. A jump in the field H_{sc} is observed only when the field decreases. Note that it is just because of the need to exceed the applied external magnetic field of magnitude H_c that this point may be identified as the critical magnetic field of bulk superconductivity.

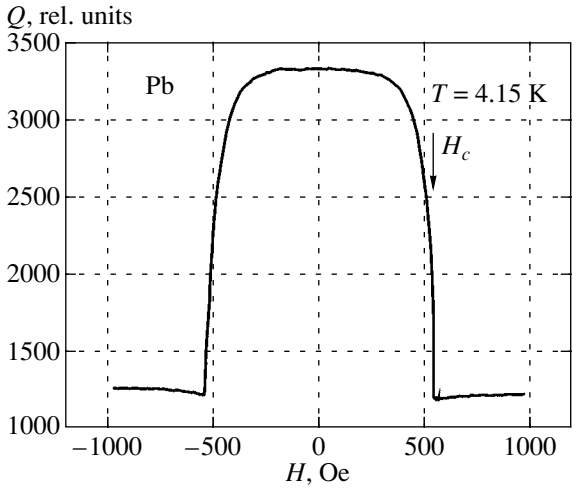

Fig. 1.

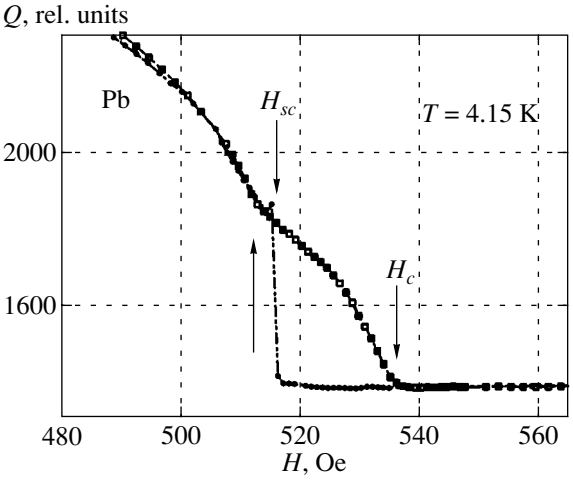

Fig. 2.

No manifestation of the existing metastable states associated with heating exists on the recording shown in Fig. 2, because, due to the finite length of the sample, they are shifted away from H_c towards lower fields and are located (in Fig. 1) in the region of deviation of the Q factor of the measuring circuit from the maximal value. The left-hand side of the curves in Fig. 2 corresponds to the intermediate state of the sample, in which both the normal and the superconducting phases are present simultaneously. Note that, when samples of other-than-ellipsoidal shape are used, investigations of the effect of superheating in superconductors make no sense because of the indeterminacy of the magnitude of the demagnetization factor.

At lower temperatures down to 1.5 K, the presence of metastable supercooled states is recorded against the background of a signal due to the surface superconductivity. An example of such experimental recording is given in Fig. 3. For better illustration, a recording made

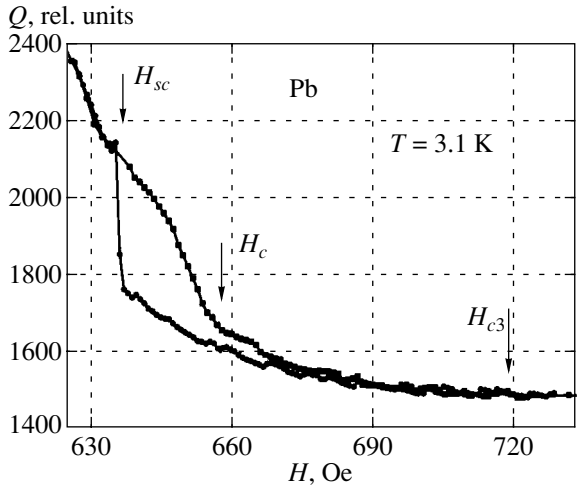

Fig. 3.

at a temperature of 3.1 K is selected, in which the contributions to the variation of the Q factor of the measuring circuit due to surface superconductivity and to metastable states are close to each other; the misalignment between the curves at point H_c is associated with the signal drifts during measurements. Because of surface superconductivity, the Q factor of the measuring circuit exceeds the level corresponding to the normal state of the sample. This level is indicated in Fig. 3 by a horizontal dashed line. The characteristic point determined by the deviation of the $Q(H)$ dependence from the horizontal is indicated by an arrow in Fig. 3 and denoted by H_{c3}. Naturally, this determination of H_{c3} gives only the lower estimate of the critical magnetic field of surface superconductivity; however, at a given moment, only the fact that H_{c3} exceeds both H_c and H_{sc} is of importance to us. These critical fields are also indicated in Fig. 3.

4. CONCLUSIONS

In all three investigated (in [1, 2] and in this study) cases of plane *N–S* interface, it has been found that there is always a possibility of existence of metastable supercooled normal states in the bulk of samples. These results lead one to conclude that neither the superconductivity of the twinning plane, nor the superconductivity induced due to the neighborhood effect, nor the surface superconductivity serves as a nucleus with above-critical parameters for the bulk superconductivity. Proceeding from the reasoning about the balance between the surface and bulk energies during first-order phase transitions, one must conclude that the surface energy of the *N–S* interface increases with the distance from the source of nucleation of superconductivity. This experimentally established fact may in no way be fitted to the principles of the theoretical model [3, 7], which postulate the independence of the surface energy of the coordinate of the location of the plane interface between the normal and superconducting phases.

The region of observation of metastable states turns out to be narrower than that in the absence of "extraneous" (for the sample volume) sources of superconducting phase, with the observed critical field being $H_{sc} > H_{c3}/1.7 = H_{c2}$. Hence, it follows that the extraneous superconductivity indeed affects the stability of metastable supercooled states. Nevertheless, the results of our study demonstrate that even the intrinsic surface superconductivity does not fully prohibit the possibility of observing the effect of supercooling in type I superconductors. Moreover, one must conclude that an entire line of critical magnetic fields H_{sc} must exist on the phase diagram for superconductors, which lies below the line of critical fields H_c on which the stability of normal supercooled states in the bulk of type I superconductors is disturbed in the presence of surface superconductivity.

ACKNOWLEDGMENTS

We are grateful to V.A. Tulin, V.S. Edel'man, V.I. Marchenko, and E.R. Podolyak for repeated discussions. This study received support from the Russian Foundation for Basic Research (project no. 00-02-16250).

REFERENCES

1. I. N. Khlyustikov, Zh. Éksp. Teor. Fiz. **94** (3), 311 (1988) [Sov. Phys. JETP **67**, 607 (1988)].
2. I. N. Khlyustikov, Zh. Éksp. Teor. Fiz. **112**, 1119 (1997) [JETP **85**, 609 (1997)].
3. D. Saint-James and P. G. de Gennes, Phys. Lett. **7**, 306 (1963).
4. M. Cardona and B. Rosenblum, *Proceedings of the 9th International Conference on Low Temperature Physics, LT9* (Plenum, New York, 1965), Part A, p. 560.
5. J. Feder, Solid State Commun. **5**, 299 (1967).
6. J. P. McEvoy, D. P. Jones, and J. G. Park, Solid State Commun. **5**, 641 (1967).
7. P. G. de Gennes, *Superconductivity of Metals and Alloys* (Benjamin, New York, 1966; Mir, Moscow, 1968).
8. R. T. Mina and M. S. Khaĭkin, Zh. Éksp. Teor. Fiz. **45**, 1304 (1963) [Sov. Phys. JETP **18**, 896 (1964)].
9. V. A. Berezin and V. A. Tulin, Zh. Éksp. Teor. Fiz. **110**, 1054 (1996) [JETP **83**, 582 (1996)].

Translated by H. Bronstein

Journal of Experimental and Theoretical Physics, Vol. 94, No. 6, 2002, pp. 1179–1187.
Translated from Zhurnal Éksperimental'noĭ i Teoreticheskoĭ Fiziki, Vol. 121, No. 6, 2002, pp. 1374–1383.

SOLIDS
Electronic Properties

Anomalous Acoustoelectric Effect and the Transport Properties of Thin $La_{0.67}Ca_{0.33}MnO_3$ Films

Yu. V. Ilisavskii[†a], A. V. Goltsev[a], K. V. Dyakonov[a, *], N. F. Kartenko[a], V. V. Popov[a], E. Z. Yakhkind[a], V. P. Dyakonov[b, c], and A. V. Klimov[b, c]

[a]*Ioffe Physicotechnical Institute, Russian Academy of Sciences, ul. Politekhnicheskaya 26, St. Petersburg, 194021 Russia*
[b]*Donetsk Physicotechnical Institute, National Academy of Sciences of Ukraine, Donetsk, 340114 Ukraine*
[c]*Institute of Physics, Academy of Sciences of Poland, 02-668, Warsaw, Poland*
**e-mail: K.Dyakonov@pop.ioffe.rssi.ru*

Received February 6, 2002

Abstract—A complex of studies of the physical properties of thin lanthanum manganite $La_{0.67}Ca_{0.33}MnO_3$ films were performed for a monolithic layered structure consisting of a $LiNbO_3$ substrate and a $La_{0.67}Ca_{0.33}MnO_3$ thin epitaxial film. For the first time, not only ordinary acoustoelectric (AE) current of charge carriers dragged by a surface acoustic wave, but also longitudinal anomalous AE current, which flowed in a distinguished direction independent of the direction of the surface acoustic wave propagation, was observed. The anomalous AE effect predominated close to the metal–insulator transition, whereas the odd AE effect predominated at high and low temperatures. The sign of the ordinary odd AE effect corresponded to hole conduction of the film. A theoretical analysis showed that the anomalous AE effect is due to a strong film conduction modulation caused by deformation created by the surface acoustic wave. The theoretical results were in close agreement with experiment. The temperature dependences of resistivity ρ (both in the absence of a magnetic field and in fields of up to 3 T), high-frequency magnetic susceptibility, and thermoelectric power were studied. © *2002 MAIK "Nauka/Interperiodica".*

1. INTRODUCTION

In recent years, perovskite manganites $R_{1-x}A_xMnO_3$, where R = La, Nd, and Pr and A = Ca, Sr, and Ba, have been extensively studied. These compounds attract attention not only by the diversity of their magnetic, structural, and electronic properties but also because they offer much promise for technical applications.

It has been shown that the properties of manganites are determined not only by the double exchange mechanism [1] but also by strong electron–phonon coupling [2] of the Jahn–Teller type. Strong electron–phonon coupling forms polaronic states. The transport properties in the paramagnetic state are therefore determined by thermally activated jumps of polarons. Double exchange responsible for the ferromagnetic transition with critical temperature T_c changes semiconducting behavior of resistivity $\rho(T)$ above T_c into metallic behavior below T_c. There are direct experimental data substantiating this physical picture, namely, a giant isotope shift of T_c, thermally activated transport in the paramagnetic state, Arrhenius behavior of the drift and Hall mobilities, a comparatively low activation energy of the thermoelectric effect, etc. (e.g., see reviews [3–6]).

It has been discovered recently [7] that pressure has a strong influence on the transport and magnetic properties. This is one more piece of evidence of strong electron–phonon coupling in these materials. Nevertheless, there exist quite a number of open, still unanswered questions concerning the physical properties of manganites. In particular, recent conduction measurements [8] have shown that the polaron effect plays an important role in the low-temperature metallic phase. Not only the mechanism of conduction in various temperature intervals but also the problem of determining the type of charge carriers attracts attention. Hall effect and thermoelectric effect measurements give contradictory information on the sign of charge carriers. For instance, thermoelectric power (TEP) in $La_{0.67}Ca_{0.33}MnO_3$ is negative in the whole temperature range of measurements, which is evidence in favor of electron conduction [9, 10], whereas Hall effect measurements show that the Hall coefficient changes sign [11]. These discrepancies are difficult to explain in terms of the simple one-band model with holes as charge carriers.

In our view, gaining a deeper insight into the physical properties of metal manganites requires further thorough studies with the use of new experimental techniques. Of special interest in this respect are, in our view, measurements of the acoustoelectric (AE) effect, which give independent and important information about the properties of a system of charge carriers.

[†]Deceased.

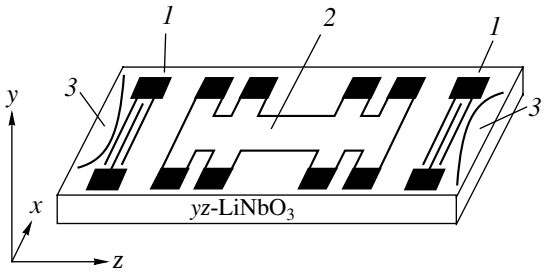

Fig. 1. Scheme of a monolithic layered structure consisting of a $LiNbO_3$ substrate and a $La_{0.67}Ca_{0.33}MnO_3$ thin film: (*1*) interdigital transducers; (*2*) film with contacts; (*3*) surface acoustic wave absorbers. Axes show film orientation.

In this work, we report the first studies of the AE effect in a monolithic layered structure consisting of a $LiNbO_3$ piezodielectric substrate and a $La_{0.67}Ca_{0.33}MnO_3$ thin epitaxial film in a wide temperature range including the region of the metal–insulator transition. In such a structure, both deformation created by a surface acoustic wave (SAW) and a piezoelectric field, which accompanies the propagation of acoustic waves over the piezodielectric substrate, act on charge carriers. The SAW drags free charges in the film and generate either AE voltage if the electric circuit including the film is disconnected or AE current if the circuit is closed. As the energy of a SAW propagating over the substrate is largely concentrated in the surface layer of thickness of the order of its length, SAW-induced deformation can attain very large values of about 10^{-3}, which is, in the system under consideration, equivalent to pressure of about 1 kbar. As mentioned, high pressure can, in turn, substantially change manganite film conductivity. In this respect, our approach essentially differs from the early experiments, in which the film was only subjected to the action of an electric field [12].

We found that longitudinal AE current had a strong temperature dependence with a maximum close to the metal–insulator transition. Our most interesting result was, however, the observation of two contributions to AE current. In addition to the ordinary AE current, which is odd with respect to the wave vector of a SAW (that is, changes sign when the wave vector takes on the opposite value), we observed an anomalous current component, which was even with respect to the wave vector. The sign of the ordinary AE current corresponded to hole conduction in the whole temperature range of measurements, 77–300 K. The anomalous AE current was strongly different from the ordinary AE current in magnitude and in temperature behavior and had a different nature determined by the strong pressure dependence of manganite film conductivity (see below). The even longitudinal AE effect was earlier observed in other objects, for instance, in piezosemiconductors with traps [13] and asymmetric ballistic contacts [14]. In contrast to these objects, our lanthanum manganite films did not contain traps and were spatially homogeneous. Some analogy can only be found with the first theoretical works on the even AE effect in crystals without an inversion center; this effect was for the first time considered in [15]. Our lanthanum manganite films have an inversion center but are in mechanical contact with a piezodielectric substrate, which has no inversion center. The role of the mechanical contact and the properties of layers in the arising of the anomalous AE effect is discussed in Sections 5 and 6. A short communication on the observations of the anomalous AE current was published in [16].

2. EXPERIMENTAL PROCEDURE

Lanthanum manganite films were grown on the *yz*-cut optically polished $LiNbO_3$ substrate by pulsed laser-deposition technique with the use of $La_{0.67}Ca_{0.33}MnO_3$ stoichiometric ceramics as a target. During the deposition, the substrate temperature equaled 730°C, and the oxygen pressure was 300 mTorr. The deposited film was cooled to room temperature at the same oxygen pressure. The film was then used to prepare a four-probe sample for measurements with the use of optical photolithography and chemical etching; the film was 10 mm long, 2 mm wide, and 100–200 nm thick. Sample resistance R was measured by the four-point-probe method under the conditions of a 10 μA stabilized transport current, which did not cause noticeable film heating.

The AE effect was studied by exciting a Rayleigh SAW, which propagated over the surface of the $LiNbO_3$ piezodielectric substrate. The SAW pulses were generated and received by interdigital transducers situated at the opposite ends of the lithium niobate substrate. The aperture of the acoustic beam was 3 mm; that is, it was larger than the film width in all experiments. Measurements were taken at a resonance transducer frequency of 87 MHz (the acoustic wave length was $\lambda = 40$ μm). The sample geometry is shown in Fig. 1.

During measurements, the samples were placed into a cryostat filled with helium or nitrogen vapor. Temperature was controlled by a heater, whose magnetic field could be ignored ($H < 0.1$ Oe), and measured by a thermocouple with accuracy of 0.05 K or higher. SAWs were excited in a pulsed mode with a 50 Hz pulse repetition rate. Acoustic pulse width τ depended on the kind of the experiment and could be varied from 1 to 4 μs. In AE effect measurements, the SAW pulse width equaled the time of sound traversal through the whole film if the whole film participated in measurements or through the film region that was studied in the experiment. The SAW intensity at the entrance to the sample, Φ, was controlled by an attenuator in 1-dB steps and was independent of the acoustic pulse width. In all AE effect measurements, transport current through samples was zero.

A trivial source of the even AE effect might be spatial nonuniformity of the electric properties of the film.

For this reason, film uniformity was thoroughly checked by various techniques. X-ray studies showed that the film was epitaxial and single-phase, had a pseudocubic lattice with constant $a = 0.3853$ nm, and was oriented parallel to the (211) plane. The chemical composition of the film and its uniformity were proved by electron-probe microanalyses in various film regions. According to the chemical analysis data, the chemical composition of the film differed from that of the ceramic target within 2%. Electric uniformity of the film was checked by measuring the resistance of various film regions. In addition, the results obtained in TEP measurements were also not only in qualitative but also in close quantitative agreement with the available data. The aforesaid leads us to conclude that the structural, magnetic, and electric properties of the lanthanum manganite films studied in this work were spatially uniform.

3. TRANSPORT AND MAGNETIC MEASUREMENTS

The $R(T)$ dependences in zero magnetic field and in field $H_\perp = 25.5$ kOe perpendicular to the film surface are shown in Fig. 2. The $R(T)$ curve has a maximum at $T \approx 224$ K. Applying magnetic field H shifted the $R(T)$ curve peak to a higher temperature, $T \approx 231$ K; substantially increased sample conductivity; and, through this, produced the colossal magnetoresistance effect, which amounted to about 80% at 25.5 kOe in our experiments, in complete agreement with the published data [3–5]. A fairly sharp shape of the peak was evidence of a high film quality and the absence of a noticeable contribution of granules to conductivity. The dependence of $\ln(R/T)$ on $1/T$ is plotted in the inset in Fig. 2.

In the theory of adiabatic jumps of small polarons [17], the temperature dependence of resistivity is described by the equation

$$\rho(T) = \rho_0 T^\alpha \exp(E_A/k_B T), \qquad (1)$$

where E_A is the activation energy of jumps and k_B is the Boltzmann constant. On the assumption that $\alpha = 1$, we obtained $E_A = 142$ mV for $H = 0$ and $E_A = 52$ mV in field $H_\perp = 25.5$ kOe from our data on the paramagnetic state region (see inset in Fig. 2, curves *1* and *2*, respectively). It follows that a magnetic field sharply decreases the activation energy. As a consequence, $R(T)$ decreases in a magnetic field in the region of the metal–insulator transition. This result coincides fairly well with the literature data [18].

In high-frequency magnetic susceptibility measurements shown in Fig. 3, an alternating magnetic field with a 5-Oe amplitude and an $f = 625$ Hz frequency was applied parallel to the film plane. Both real (χ') and imaginary (χ'') susceptibility parts were measured. The Curie temperature was determined as the temperature corresponding to the inflection of the $\chi'(T)$ curve and approximately equaled $T = 215$ K. According to our data, the resistance peak was situated close to the ferromagnetic phase transition.

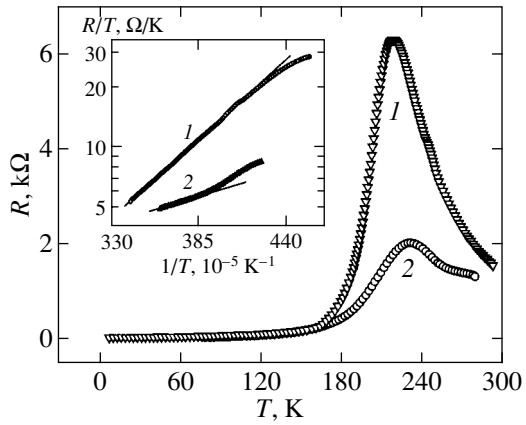

Fig. 2. Temperature dependences of film resistance in various magnetic fields normal to the film surface: (*1*) $H = 0$ and (*2*) $H = 25.5$ kOe. Shown in the inset are the plots of $\ln(R/T)$ versus $1/T$: (*1*) $H = 0$, activation energy $E_a = 142$ meV; (*2*) $H = 25.5$ kOe, $E_a = 53$ meV.

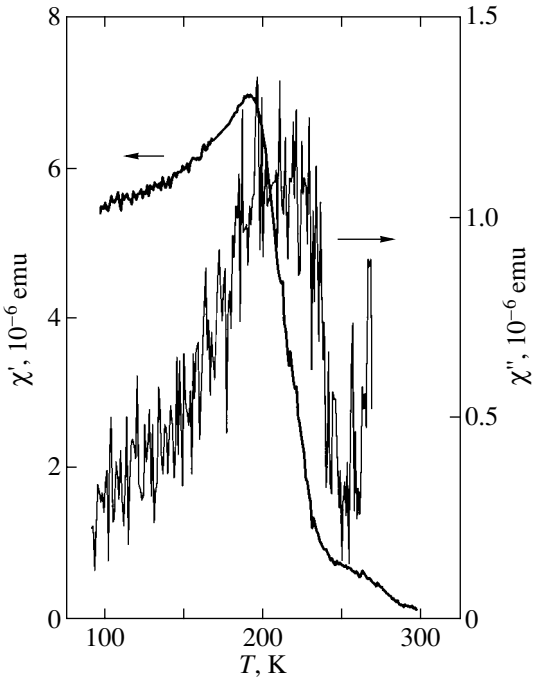

Fig. 3. Temperature dependences of real χ' and imaginary χ'' $La_{0.67}Ca_{0.33}MnO_3$ magnetic susceptibility components.

The temperature dependence of the Seebeck coefficient (S) at $H = 0$ measured by the standard technique is shown in Fig. 4. One end of the lithium niobate substrate with a deposited film was fixed between two massive sapphire blocks for heat removal. A thermal gradient along the film was created by a miniature heater mounted on the opposite substrate end and controlled by two thermocouples. The figure shows that the TEP

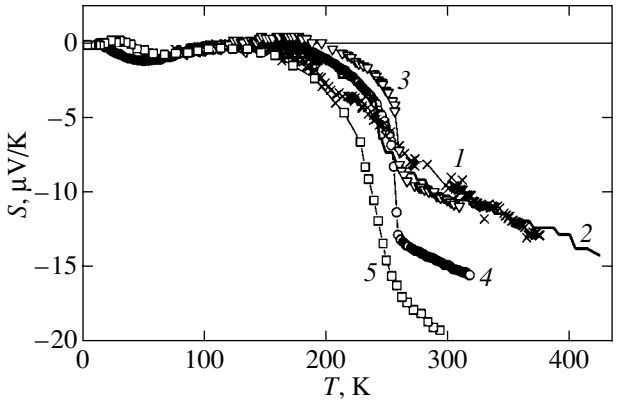

Fig. 4. Temperature dependences of Seebeck coefficient S for $La_{0.67}Ca_{0.33}MnO_3$ compounds: (*1*) our experimental data on manganite films and data from (*2*) [10], (*3*) [19], (*4*) [20], and (*5*) [21].

was largest in magnitude in the region of the activation character of conductivity with the participation of small-radius polarons and decreased almost to zero as the system approached the metallic phase region. Characteristically, in the whole temperature range of measurements including $T = 300$ K, the Seebeck coefficient S was negative, although, according to Hall effect measurements and the existing theoretical concepts, holes should be charge carriers in lanthanum manganite in the high-temperature region. Figure 4 also contains the literature data [10, 19–21] on the temperature dependence of the Seebeck coefficient in lanthanum manganite. These data insignificantly differ from those obtained in this work, and the Seebeck coefficient is negative according to all of them. Note that, in many instances, unambiguous conclusions on the type of conductivity cannot be made based on TEP measurements because the sign of TEP is determined not only by the sign of charge carriers but also by the special features of scattering and the energy spectrum of these quasiparticles.

4. ACOUSTOELECTRIC MEASUREMENTS

The results of longitudinal AE effect measurements for $La_{0.67}Ca_{0.33}MnO_3$ films in zero magnetic field are shown in Fig. 5a. These results were obtained for the acoustic wave vector **q** in both positive (curve *1*) and negative (curve *2*) directions along the z axis of the lithium niobate substrate (this axis is distinguished because the substrate has no inversion center). First, note the large value of the observed AE current in comparison not only with normal metals, in which the AE effect is exceedingly weak, but also with semiconductors. Estimates of the contribution of TEP, which might arise as a result of sound attenuation in the sample, to the observed AE voltage show that this contribution is negligibly small, because the TEP value is fairly small in the samples under consideration. In addition, the substrate with the film was in contact with a massive optically polished copper base through an In–Ga eutectic layer to remove heat and thereby decrease stray TEP. This decreased the stray temperature gradient in the film to 0.05 K or less.

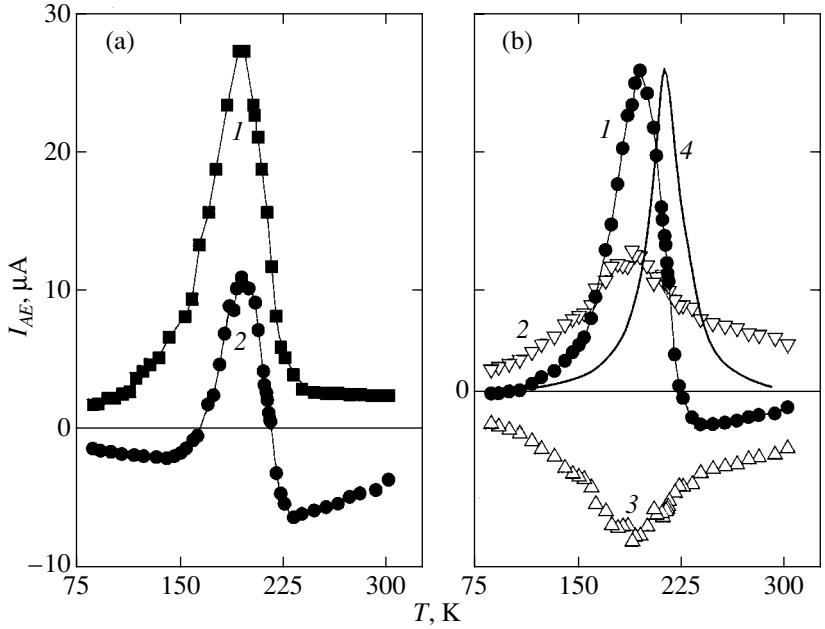

Fig. 5. Temperature dependences of AE current: (a) experimental data for (*1*) **q** || $+z$ and (*2*) **q** || $-z$ and (b) AE current components: (*1*) even (anomalous), (*2*) odd (ordinary) at **q** || $+z$, (*3*) odd at **q** || $-z$, and (*4*) even component theoretically calculated by (6).

When a SAW with **q** in the positive direction along the *z* axis was excited, AE current I_{AE} at $T = 300$ K was positive and equaled approximately 2 μA at a surface acoustic wave intensity of $\Phi \approx 3$ W/cm (Fig. 5a, curve *1*). AE current increased as temperature lowered and reached a maximum (approximately 25 μA) near the metal–insulator transition. A further decrease in temperature decreased the AE current to about 1 μA at $T = 77$ K.

As mentioned in the Introduction, the ordinary longitudinal AE effect is odd with respect to the **q** SAW vector. We therefore expected to observe only sign reversal when the surface acoustic wave with **q** in the negative *z* axis direction was excited. Contrary to this expectation, the behavior of AE current was surprising. It twice changed sign close to the metal–insulator transition. Namely, when temperature decreased from 300 K, AE current was first negative, increased in magnitude, then sharply changed sign, reached a maximum, further decreased in magnitude, and, lastly, changed sign once more. These results are shown in Fig. 5a (curve *2*).

Such an unexpected dependence of AE current on the direction of the wave vector of the SAW can be explained on the assumption that there are two contributions to AE current,

$$I_{AE} = I_{\text{even}} + I_{\text{odd}}.$$

The first contribution (I_{even}) is anomalous and even with respect to the SAW vector **q**. The second contribution (I_{odd}) is the ordinary (odd) AE current. We separated these two contributions based on the experimental data and the following relations:

$$I_{\text{odd}}(-\mathbf{q}) = -I_{\text{odd}}(\mathbf{q}), \quad I_{\text{even}}(-\mathbf{q}) = I_{\text{even}}(\mathbf{q}).$$

The results are shown in Fig. 5b. According to this figure, the anomalous longitudinal AE effect predominates near the metal–insulator phase transition and approximately twofold exceeds the ordinary AE effect (see Fig. 5b, curve *1*). We stress once more that the observed anomalous even AE current (I_{even}) always flows in the positive direction along the *z* axis of the substrate. The ordinary odd AE effect (I_{odd}) (Fig. 5b, curves *2*, *3*) predominates at both high and low temperatures, and its sign corresponds to hole conduction in the whole temperature range of our measurements, as expected for the $La_{0.67}Ca_{0.33}MnO_3$ composition.

Note that we subjected the AE origin of the observed effect to meticulous verification. For this purpose, we thoroughly examined the dependence of AE current on the SAW power *W* and pulse width τ in the whole temperature range. The typical results for $T = 300$ K are shown in Fig. 6. According to these measurements, I_{AE} linearly depended on *W*. The $I_{AE}(\tau)$ dependence was also linear until the SAW pulse width reached $\tau \approx 2.5$ μs, and the spatial acoustic pulse dimensions became approximately equal to the length of the film. Naturally, a further increase in τ should have caused saturation of the $I_{AE}(\tau)$ dependence, as was observed experimentally. Such dependences of I_{AE} on *W* and τ fully correspond to what should be expected for the classical pulsed AE effect [22].

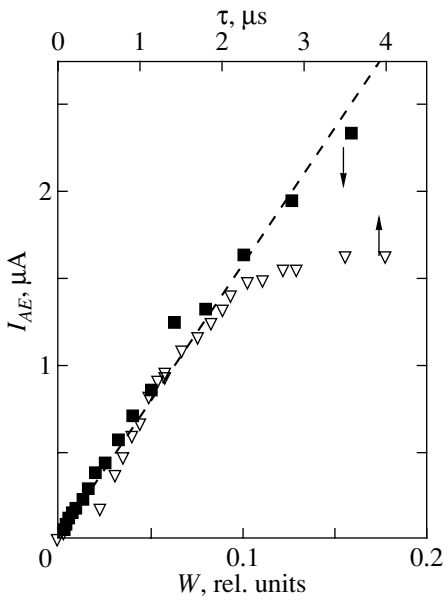

Fig. 6. AE current as a function of surface acoustic wave power *W* and pulse width τ.

5. THEORETICAL ANALYSIS

A theoretical study of the interaction of a SAW with a thin metallic film deposited on a lithium niobate substrate and having a mechanical contact with the latter was performed using the frame of reference whose positive *y* axis direction was normal to the surface of the substrate (see Fig. 1). The substrate–film boundary was the *xz* plane. The film had thickness *a*; the free surface was therefore the $y = a$ plane. A SAW of frequency ω propagated along the *z* axis and was accompanied by both electric field $\mathbf{E}(y, z, t)$ and deformation $S_{ij}(y, z, t)$. In our geometry, only the *y* and *z* components of the electric field and lattice displacement were nonzero. Electric field **E** in turn created the local current density

$$J_i(y, z, t) = \sigma_{ij}(y, z, t)E_j(y, z, t)$$

in the film. Here, σ_{ij} is the film conductivity tensor (the diffusive contribution to the current can be ignored in the long-wave limit). Note that, for the acoustic frequencies used in our experiments ($\omega \sim 10^8$ s^{-1}), the dependence of σ on ω can be ignored because the strong frequency dependence of polaronic conductivity only arises in the frequency region $\omega \sim (4/\hbar)E_a \sim 10^{13}$ s^{-1} for activation energy $E_a \approx 142$ meV (e.g., see [23]).

Electric field **E** and deformation S_{ij} induce local modulation of conductivity tensor σ_{ij} components,

$$\sigma_{zz}(y, z, t) = \sigma_0 + \sigma_1(y, z, t) + \sigma_2(y, z, t),$$

where σ_0 is the unperturbed conductivity; the term

$$\sigma_1(y, z, t) = n_s(y, z, t)\frac{\partial\sigma_0}{\partial n}$$

describes the influence of electric field **E** and is a consequence of modulation of the concentration of charge carriers $n = n_0 + n_s$, where n_0 is the unperturbed density of charge carriers and n_s is a change in this density ($n_s \ll n_0$) caused, by electric field **E** (the influence of field **E** on drift mobility can be ignored); and the last term,

$$\sigma_2(y, z, t) = \sigma_0[\Pi_{3333}S_{zz} + \Pi_{3322}S_{yz} + \Pi_{3323}S_{yz}],$$

describes deformation-induced modulation of the σ_{zz} component. The $\Pi_{ijkl} \equiv \partial\ln\sigma_{ij}/\partial S_{kl}$ tensor calculated at $S_{kl} = 0$ and fixed temperature describes deformation effects on σ_{ij}. Changes in electron drift mobility and concentration also make a contribution and are taken into account in Π_{ijkl}. Pseudocubic symmetry of lanthanum manganite allows us to set $\Pi_{3323} = 0$. We simplify the notation for the other tensor components as $\Pi_{3333} \equiv \Pi_{33}$ and $\Pi_{3322} \equiv \Pi_{32}$.

The longitudinal AE current excited by a SAW in the film per unit length in the x direction is given by

$$\begin{aligned} j_{AE} &= \frac{1}{\theta}\int_0^\theta dt\int_0^a dy J_z(y, z, t) \\ &= \frac{1}{\theta}\int_0^\theta dt\int_0^a dy(\sigma_1 E_z + \sigma_2 E_z) \equiv j_{AE}^{(1)} + j_{AE}^{(2)}, \end{aligned} \tag{2}$$

where $\theta = 2\pi/\omega$. To determine j_{AE}, we must use the equations relating E_z, S_{ij}, and n_s, which follow from the Maxwell and piezoelectric equations and the boundary conditions at the $y = 0$ and $y = a$ surfaces. We do not give either these equations or the method for solving them; they are well known and can be found, e.g., in [24]. In the problem under consideration, film thickness a is small compared with acoustic wave length λ but much larger than the λ_D Debye length; that is, $\lambda_D \ll a \ll \lambda$. In addition, in a wide temperature interval near the resistance peak, the conductivity of the manganite film is low and is close to that of a semiconductor. This allows us to use the Ingebrigtsen approach [24] to study the interaction between SAWs and charge carriers in the film. Within the framework of this approach, we must first describe the penetration of the electric field of a SAW into the film and the formation of surface charges on the $y = 0$ and $y = a$ surfaces as a result of screening. Motion of surface charges in turn creates surface electric currents. The constant component of the total surface electric current per unit length in the x direction is the $j_{AE}^{(1)}$ current,

$$j_{AE}^{(1)} = q\Gamma\Phi\sigma_0/e\omega n_0. \tag{3}$$

Here, e is the charge of charge carriers; Φ is the intensity of the SAW; and Γ is the coefficient of attenuation of SAWs ($\Phi = \Phi_0 e^{-\Gamma z}$):

$$\Gamma = \frac{2\pi K^2}{\lambda}\frac{\sigma_\square/\sigma_m}{1 + \sigma_\square/\sigma_m}, \tag{4}$$

where K^2 is the square of the electromechanical coupling coefficient, $\sigma_\square = a\sigma_0$ is the conductivity "per square," and σ_m is the substrate material constant [24]. The $j_{AE}^{(1)}$ current is the ordinary longitudinal AE current, which is odd with respect to **q** [22, 24, 25]. The substitution of the experimental temperature dependence of film conductivity, $\sigma_\square(T)$, into (4) gives good qualitative and quantitative agreement between the theoretical attenuation coefficient and experimental attenuation of SAWs.

Calculating the $j_{AE}^{(2)}$ anomalous AE current component arising as a result of film deformation requires the determination of the S_{zz}, S_{yy}, and E_z values. As the film is thin ($aq \ll 1$), we assume that S_{zz} and S_{yy} insignificantly vary over film thickness; that is, $S_{zz}(y, z, t) \approx S_{zz}(0, z, t)$ at $0 < y < a$. Deformation S_{yy} can be estimated from the relation $S_{yy}(y, z, t) \approx -\nu S_{zz}(0, z, t)$, which is exact at the $y = a$ free surface, where $\nu = c_{12}/c_{11} \approx 0.4$ according to the measurements performed in [26]; c_{11} and c_{12} are the manganite film elasticity tensor components.

Deformation S_{zz} in lithium niobate is related to electric displacement D_z and electric field E_z as

$$D_z = \varepsilon_{33}E_z + p_{33}S_{zz},$$

where ε_{33} and p_{33} are the dielectric and piezodielectric tensor components, respectively (for simplicity, we set $p_{32} = 0$ because, for lithium niobate, this parameter is small and taking it into account gives corrections not exceeding 1%). Equation (2) therefore yields

$$\begin{aligned} j_{AE}^{(2)} &= \frac{a\sigma_0}{p_{33}}(\Pi_{33} - \nu\Pi_{32})\frac{1}{\theta} \\ &\times\int_0^\theta dt[D_z(+0, z, t) - \varepsilon_{33}E_z(0, z, t)]\bar{E}_z(z, t), \end{aligned} \tag{5}$$

where $\bar{E}_z(z, t)$ is the electric field averaged over film thickness. If $aq \ll 1$, we have $\bar{E}_z(z, t) \approx E_z(0, z, t)$. Estimating the contribution of induction D_z to $j_{AE}^{(2)}$ in (5) shows that D_z can be ignored if $1 \ll \sigma_0/\varepsilon\omega \ll 1/q\lambda_D$, where ε is the static film permittivity. This condition is

well satisfied in our experiments. Using the relation $E_z(0) = iq\varphi(0)$ and expressing surface potential $\varphi(0)$ through Φ and Γ in (5), we obtain

$$j_{AE}^{(2)} = -\Gamma\Phi\varepsilon_{33}(\Pi_{33} - \nu\Pi_{32})/p_{33}. \quad (6)$$

This result shows that the $j_{AE}^{(2)}$ current is even with respect to **q**, and its direction is determined by the signs of p_{33} and Π_{3i}. Note that $j_{AE}^{(2)}$ is the bulk current (in contrast to the $j_{AE}^{(1)}$ surface current), because the deformation and the longitudinal electric field component E_z penetrate through the whole film thickness. The Π_{3i} coefficients determine the pressure dependence of conductivity,

$$2\Pi_{32} + \Pi_{33} = -\frac{3}{k}\frac{\partial \ln\sigma_0}{\partial P},$$

where k is the compressibility coefficient of the film. According to the pressure experiments on manganites [7], the $\partial\ln\sigma_0/\partial P$ value is positive and strongly depends on temperature. Namely, this parameter is small at high and low temperatures and attains a maximum value of about 3.5 GPa^{-1} at a temperature slightly below that corresponding to the resistance maximum. Since $\partial\ln\sigma_0/\partial P$ is positive, the coefficients Π_{3i} are negative. Numerical estimates were obtained on the assumption that $\Pi_{33} \approx \Pi_{32}$. Substituting $k^{-1} = 85$ GPa [27] yields $\max\Pi_{ij} \approx -300$.

It follows from (6) that the anomalous even AE effect can be observed if the following conditions are satisfied: film conductivity depends on pressure ($\Pi_{3i} \neq 0$), the substrate has piezoelectric properties ($p_{33} \neq 0$), and there is a distinguished direction in the substrate. These conditions will be discussed in more detail in the next section.

The theory developed above gives close agreement with experiment. In the selected frame of reference, the p_{33} constant is positive [28]. Therefore, according to (6), the $j_{AE}^{(2)}$ AE current flows in the $+z$ direction. Substituting the well-known lithium niobate parameters and our experimental data on maximum attenuation ($\Gamma \sim 2$ cm^{-1}) into (6) yields $j_{AE}^{(2)} \approx 30$ μA/cm as a maximum if the intensity of SAWs equals $\Phi \approx 3$ W/cm. Our experimental data (Fig. 5b, curve *1*) give a maximum value of $j_{AE}^{(2)} \approx 100$ μA/cm. Considering the approximate character of our Γ, Φ, and Π_{3i} values, we estimate agreement between theory and experiment as satisfactory. In addition, (6) describes the temperature behavior of $j_{AE}^{(2)}$ very well (see Fig. 5b, curve *4*). The theoretical curve normalized with respect to the experimental value at a maximum (Fig. 5b) was calculated by (6) using the experimental $\Gamma(T)$ dependence and the temperature dependence of $\partial\ln\sigma_0/\partial P$ obtained from the experimental pressure data [7]. The experimentally observed $j_{AE}^{(2)}$ current maximum is shifted by approximately 15 K to lower temperatures compared with theoretical predictions. This shift can be caused by a possible difference of the temperatures corresponding to a maximum $\partial\ln\sigma_0/\partial P$ parameter value in our films and in a massive lanthanum manganite sample [7]. Note also that the maximum odd AE current value, $\max j_{AE}^{(1)} \approx 10$ μA/cm, estimated by (3) fairly closely agrees in order of magnitude with the $\max j_{AE}^{(1)} \approx 50$ μA/cm experimental value (Fig. 5b, curves *2* and *3*). Agreement between theory and experiment can be improved on the assumption that thin manganite films have a somewhat higher sensitivity to pressure than massive samples. This assumption, however, requires additional inquiries.

6. DISCUSSION AND CONCLUSION

In this work, we studied the AE effect that arose in the monolithic layered structure consisting of a $LiNbO_3$ piezodielectric substrate and a $La_{0.67}Ca_{0.33}MnO_3$ manganite thin film under the action of a SAW. In experiments on exciting SAWs in the $+z$ direction (the z crystallographic axis is distinguished in $LiNbO_3$ piezodielectric crystals), we expected that exciting the wave in the opposite ($-z$) direction would only change the sign of the AE current in the film, as followed from the generally accepted views on the nature of the ordinary AE effect. Instead, we observed an unordinary effect; namely, AE currents flowing in the $+z$ and $-z$ directions in the layered structure under study were substantially different not only in magnitude but also in their temperature behavior. It was found that the absence of symmetry in the AE effect between the $+z$ and $-z$ directions was caused by the appearance of an anomalous AE current, which only flowed in the $+z$ direction irrespective of the direction of SAW propagation along the z axis. A detailed theory of the an anomalous AE effect was developed in Section 5. Here, we sum up the theoretical results and give a simple physical picture of this phenomenon in comparison with the ordinary AE effect.

First, consider the nature of the AE effect in a monolithic layered structure. Recall that SAWs propagating over the surface of a lithium niobate piezodielectric substrate create high- and low-pressure regions, which correspond to negative (compression) and positive (expansion) deformation regions. Because of the piezoelectric effect, deformations, in turn, create an electric field varying in space (and time). The relation between the sign of the deformation and the sign of the electric field component along the z axis is only determined by the sign of the corresponding piezodielectric tensor component and is therefore independent of whether the

SAW propagates in the +*z* or –*z* direction. For lithium niobate, the *z* electric field component is positive in compression and negative in expansion regions.

Next, consider the interaction of a SAW with a conducting film placed on the surface of a piezodielectric substrate. If the film and the substrate are in mechanical contact with each other, the film experiences both electric field and mechanical deformation actions. The electric field that accompanies SAWs penetrates into the film and creates screening surface charges on the film because of the screening effect. The SAW drag these charges to produce surface currents. The constant total surface current component is the ordinary AE current [see (3)] [24]. This is a quasi-classical picture of the ordinary AE effect. In terms of quantum theory, the SAW can be treated as a flow of phonons. The two mechanisms described above are responsible for interaction between these phonons and charge carriers in the film and make two additive contributions to AE current. Phonons transfer momentum directly to charge carriers and thereby generate the ordinary AE current. This effect exists if there is at least one interaction mechanism (for instance, in the absence of a mechanical contact between a film and a substrate, charge carriers are only dragged by the electric field).

Consider the nature of the anomalous AE effect in a manganite film. The theoretical analysis in Section 5 showed that the anomalous AE effect is caused by the existence of a strict correlation between the deformation sign and the sign of the *z* electric field component when SAWs propagate in the $LiNbO_3$ piezodielectric substrate in either +*z* or –*z* direction; namely, the substrate (and the film on it) becomes compressed in wave regions where the varying electric field of the SAW is directed along +*z* and expanded, where the field is directed along –*z*. In film compression regions, the mobility of charge carriers increases and, therefore, film conductivity grows. In expansion regions, the conductivity and mobility of charge carriers decrease. For this reason, the time and film volume mean current produced by the varying electric field of a SAW is larger in the +*z* direction than the current in the –*z* direction because of a higher mobility of electrons. As a result, a constant (anomalous) component of the total current in the +*z* direction appears in the film. It follows that the appearance of the anomalous AE effect requires simultaneous and in-phase mechanical deformation and electric field actions and metallic film sensitivity to deformations. Such an effect can also be expected for other conducting materials whose conductivity depends on pressure. The observation of the anomalous AE effect in $La_{0.67}Ca_{0.33}MnO_3$ manganite is independent proof of a very high sensitivity of such substances to external pressure.

Based on the mechanism of the anomalous AE effect described above, we may predict such an unusual phenomenon as AE current generation by a standing SAW, when the ordinary AE effect is absent.

ACKNOWLEDGMENTS

The authors are grateful to S.J. Levandowski and H. Szymczak (Institute of Physics, Warsaw, Poland) for fruitful discussions and active assistance in work.

This work was supported by the Government of Poland (KBN, Grants 2 PO3 139 18 and PBZ-KBN-013/TO8/19) and the Russian Foundation for Basic Research (projects nos. 99-02-18333 and 01-02-17479).

REFERENCES

1. C. Zener, Phys. Rev. **82**, 403 (1951).
2. A. J. Millis, P. B. Littlewood, and B. I. Shraiman, Phys. Rev. Lett. **74**, 5144 (1995).
3. J. M. D. Coey, M. Viret, and S. von Molnär, Adv. Phys. **48**, 167 (1999).
4. L. P. Gor'kov, Usp. Fiz. Nauk **168**, 665 (1998) [Phys. Usp. **41**, 589 (1998)].
5. É. L. Nagaev, Usp. Fiz. Nauk **166**, 833 (1996) [Phys. Usp. **39**, 781 (1996)].
6. D. L. Khomski and G. A. Sawatzky, Solid State Commun. **102**, 87 (1997).
7. Y. S. Wang, A. K. Heilman, B. Lorentz, *et al.*, Phys. Rev. B **60**, R14998 (1999); J. J. Neumeier, M. F. Hundlley, Y. D. Thompson, and R. H. Heffer, Phys. Rev. B **52**, R7006 (1995).
8. Guo-meng Zhao, V. Smolyaninova, W. Prelleir, and H. Keller, Phys. Rev. Lett. **84**, 6086 (2000).
9. M. F. Hundley and J. J. Neumeier, Phys. Rev. B **55**, 11511 (1997).
10. T. T. M. Palstra, A. P. Ramizer, S.-W. Cheong, and B. R. Zegarski, Phys. Rev. B **56**, 5104 (1997).
11. G. Jakob, F. Martin, W. Westerburg, and H. Adrian, Phys. Rev. B **57**, 10252 (1998); S. H. Chun, M. B. Salamon, Y. Lyanda-Geller, *et al.*, Phys. Rev. Lett. **84**, 757 (2000).
12. Li Wang, J. Yin, S. Huang, *et al.*, Phys. Rev. B **60**, R6976 (1999).
13. A. I. Morozov, Pis'ma Zh. Éksp. Teor. Fiz. **2**, 362 (1965) [JETP Lett. **2**, 228 (1965)].
14. O. Entin-Wohlman, Y. Levinson, and Yu. M. Galperin, Phys. Rev. B **62**, 7283 (2000).
15. V. L. Gurevich and A. L. Éfros, Zh. Éksp. Teor. Fiz. **44**, 2131 (1963) [Sov. Phys. JETP **17**, 1432 (1963)]; V. L. Gurevich, Fiz. Tekh. Poluprovodn. (Leningrad) **2**, 1557 (1968) [Sov. Phys. Semicond. **2**, 1299 (1969)].
16. Y. Ilisavskii, A. Goltsev, K. Dyakonov, *et al.*, Phys. Rev. Lett. **87**, 146602 (2001).
17. D. Emin and T. Holstein, Ann. Phys. **53**, 439 (1969).
18. G. Jakob, W. Westburg, F. Martin, and H. Adrian, J. Appl. Phys. **85**, 4803 (1999).

19. P. Mandal, Phys. Rev. B **61**, 14675 (2000).
20. A. K. Heilman, Y. Y. Xue, Y. Y. Sun, *et al.*, Phys. Rev. B **61**, 8950 (2000).
21. B. Chen, C. Vher, D. R. Morelli, *et al.*, Phys. Rev. B **53**, 5094 (1996).
22. G. Weinreich, Phys. Rev. **107**, 317 (1957).
23. H. G. Reik, Solid State Commun. **1**, 67 (1963); M. I. Klinger, Phys. Lett. **7**, 102 (1963).
24. K. A. Ingebrigtsen, J. Appl. Phys. **41**, 454 (1970).
25. A. R. Hutson and D. L. White, J. Appl. Phys. **33**, 40 (1962).
26. C. Zhu and R. Zheng, J. Appl. Phys. **87**, 3579 (2000).
27. C. Zhu, R. Zheng, J. Su, and J. He, Appl. Phys. Lett. **74**, 3504 (1999).
28. R. T. Smith and F. S. Welsh, J. Appl. Phys. **42**, 2219 (1971); R. A. Graham, J. Appl. Phys. **48**, 2153 (1977).

Translated by V. Sipachev

Journal of Experimental and Theoretical Physics, Vol. 94, No. 6, 2002, pp. 1188–1192.
Translated from Zhurnal Éksperimental'noĭ i Teoreticheskoĭ Fiziki, Vol. 121, No. 6, 2002, pp. 1384–1389.

SOLIDS
Electronic Properties

The Frequency and Width of a Surface Plasmon in a Small Cluster

Yu. N. Ovchinnikov

Landau Institute for Theoretical Physics, Russian Academy of Sciences, Chernogolovka, Moscow oblast, 142432 Russia
e-mail: ovc@itp.ac.ru; ovchin@mpipks-dresden.mpg.de

Received January 31, 2002

Abstract—The dependence of the frequency and width of a surface plasmon ω_s on the cluster size is analyzed. In the process of the investigation, a large numerical parameter appears that determines the shape of the potential of the electromagnetic field inside the cluster and leads to a wide plateau on the dependence of ω_s on the cluster radius. © *2002 MAIK "Nauka/Interperiodica".*

1. INTRODUCTION

Recently, there has been a surge of activity in the study of small particles (clusters). Clusters consisting of several through several thousand atoms can be created and studied experimentally [1, 2]. The classical theory [3] predicts the existence of a surface plasmon with the frequency depending mainly on the shape of the surface and the type of excitation. For a spherical particle in vacuum, the dependence of the surface plasmon frequency ω_L on the orbital moment L is determined by the simple equation $\omega_L \propto (L/(2L+1))^{1/2}$ [4, 5]. The cluster size is assumed to be much less than the photon wavelength in vacuum. The experimental width of the surface plasmon is always much greater than the radiation width and weakly depends on the cluster size [2]. It follows from the experimental data reported in [2] that there is a rather wide plateau in the range $5 < R < 20$ Å on the dependence of the frequency of the surface plasmon on the cluster radius. In the range $R > 20$ Å, the correction to the "volume" magnitude of the surface plasmon frequency is proportional to $-(\kappa R)^{-1}$, where κ is the dynamic depth of the electric field screening. The proportionality coefficient is a large quantity, which leads to the appearance of a plateau.

Below, we show that the spatial and frequency dispersion of nuclei, which relate the density of current and charge to the electromagnetic field, significantly affect the dependence of the surface plasmon frequency on cluster radius.

2. EQUATIONS FOR THE DENSITY OF CHARGE AND CURRENT

Equations for the density of charge and current are obtained using the temperature Green's function technique with the subsequent analytical continuation with respect to frequency. This technique was designed for superconductors [6]; as applied to a normal metal, it is rather simple:

$$\left(\mathbf{v}\frac{\partial \hat{G}_p^1}{\partial \mathbf{r}}\right) + \omega_0\tau_Z\hat{G}_p^1 + \frac{1}{\tau}\tau_Z\hat{G}_p^1 - \tau_Z n v\int d\Omega_{p_1}\sigma_{pp_1}\hat{G}_{p_1}^1 = 2ie\tau_Z(\varphi - (\mathbf{v}\cdot\mathbf{A}_1)\tau_Z). \quad (1)$$

Here, n is the concentration of impurities; σ_{pp_1} is the scattering cross section; $\tau^{-1} = nv\int d\Omega_{p_1}\sigma_{pp_1}$ is the scattering time of an electron; $\mathbf{A}_1$ and φ are the vector and scalar potentials, respectively; p and v are the momentum and speed on the Fermi surface, respectively. The temperature Green's function $\hat{G}_p^1$ is nonzero only in the region

$$\omega_n(\omega_n + \omega_0) < 0,$$

where

$$\omega_n = 2\pi T(n + 1/2), \quad n = 0, \pm1, \pm2, \ldots,$$

T is the temperature, and $\omega_0 = 2\pi TN$ is the frequency of the external field. The analytical continuation is carried out from the domain $\omega_0 > 0$.

Equation (1) is true only within the domain specified above. The densities of the charge and current, ρ and $\mathbf{j}_1$, are related to Green's function $\hat{G}_p^1$ by the equations

$$\mathbf{j}_1 = -\frac{iep}{\pi}T\sum_{\omega_n}\int\frac{d\Omega_p}{4\pi}(\mathbf{p}\hat{G}_p^1)_{11},$$
$$\rho = -e\nu\left\{2e\varphi + i\pi T\sum_{\omega_n}\int\frac{d\Omega_p}{4\pi}\mathrm{Sp}\hat{G}_p^1\right\}, \quad (2)$$

where $\nu = mp/2\pi^2$ is the density of states on the Fermi surface. The solution to Eq. (1) can be represented in the form

$$\hat{G}_p^1 = B_p\tau_Z + D_p, \quad (3)$$

where B_p and D_p are functions of the momentum $\mathbf{p}$ on the Fermi surface and of the coordinate $\mathbf{r}$. The functions B_p and D_p satisfy the system of equations

$$\begin{aligned}\left(\mathbf{v}\frac{\partial B_p}{\partial \mathbf{r}}\right) + \omega_0 D_p + \frac{1}{\tau}D_p \\ - n v\int d\Omega_{p_1}\sigma_{pp_1}D_{p_1} = 2ie\varphi, \\ \left(\mathbf{v}\frac{\partial D_p}{\partial \mathbf{r}}\right) + \omega_0 B_p + \frac{1}{\tau}B_p - n v\int d\Omega_{p_1}\sigma_{pp_1}B_{p_1} \\ = -2ie(\mathbf{v}\cdot\mathbf{A}_1).\end{aligned} \tag{4}$$

Formally, the solution to the second equation in (4) can be written as

$$\begin{aligned}B_p = -\left[\omega_0 + \frac{1}{\tau} - n v\int d\Omega_{p_1}\sigma_{pp_1}\right]^{-1} \\ \times\left(2ie(\mathbf{v}_1\cdot\mathbf{A}_1) + \left(\mathbf{v}_1\frac{\partial D_{p_1}}{\partial \mathbf{r}}\right)\right).\end{aligned} \tag{5}$$

Substitute (5) into the first equation in (4) to obtain an equation for D_p:

$$\begin{aligned}\hat{L}D_p = 2ie \\ \times\left\{\varphi + \left(\mathbf{v}\frac{\partial}{\partial \mathbf{r}}\right)\left[\omega_0 + \frac{1}{\tau} - n v\int d\Omega_{p_1}\sigma_{pp_1}\right]^{-1}(\mathbf{v}_1\cdot\mathbf{A}_1)\right\},\end{aligned} \tag{6}$$

where the operator $\hat{L}$ has the form

$$\begin{aligned}L = \omega_0 + \frac{1}{\tau} - n v\int d\Omega_{p_1}\sigma_{pp_1} \\ -\left(\mathbf{v}\frac{\partial}{\partial \mathbf{r}}\right)\left[\omega_0 + \frac{1}{\tau} - n v\int d\Omega_{p_1}\sigma_{pp_1}\right]^{-1}\left(\mathbf{v}_1\frac{\partial}{\partial \mathbf{r}}\right).\end{aligned} \tag{7}$$

The sum over the frequency ω_n in Eqs. (2) is easily calculated; as a result, we have

$$\begin{aligned}\mathbf{j}_1 = -\frac{iep\omega_0}{2}\int\frac{d\Omega_p}{4\pi}(\mathbf{p}B_p), \\ \rho = -ev\left\{2e\varphi + i\omega_0\int\frac{d\Omega_p}{4\pi}D_p\right\}.\end{aligned} \tag{8}$$

The analytical continuation in Eqs. (5), (6), and (8) is reduced to the substitution $\omega_0 \longrightarrow -i\omega$.

Equations (8) of the density of the charge and current should be supplemented with Maxwell's equations

$$\begin{aligned}\mathbf{E} = -\frac{\partial\varphi}{\partial \mathbf{r}} - \frac{\partial \mathbf{A}}{\partial t}, \quad \mathbf{H} = \operatorname{curl}\mathbf{A}, \\ \operatorname{curl}\mathbf{H} = 4\pi\mathbf{j} + \frac{\partial \mathbf{E}}{\partial t}, \quad \operatorname{curl}\mathbf{E} = -\frac{\partial \mathbf{H}}{\partial t}.\end{aligned} \tag{9}$$

Now, we can formulate the eigenvalue problem for surface (and volume) plasmons in the general case.

The plasmon frequency ω is a solution to the system of equations (8), (9) with an outgoing electromagnetic wave at infinity. This problem is not self-adjoint, and ω is complex. However, we show below that, for cluster sizes of experimental interest, the radiation width is small and proportional to $(R\omega_p/c)^3$, where ω_p is the plasmon frequency and c is the speed of light. The greater part of the plasmon width is explained by the scattering of electrons from crystal defects or from impurities. In order to derive inverse operators in Eqs. (5) and (7), boundary conditions should be used. These can be mirror or diffusion boundary conditions, or their combination.

3. A SURFACE PLASMON IN A CLUSTER

There are two types of solutions to the eigenvalue problem for a particle of a small size. For the first type, the dominant term is the scalar potential φ, and for the second type, the vector potential $\mathbf{A}_1$.

Consider the first family of solutions. In the principal approximation with respect to the parameter $(R\omega_p/c)^2$, we can neglect the vector potential $\mathbf{A}_1$ within the particle and away from it at a distance much less than c/ω_p. Within the particle, the scalar potential φ is the solution to the equation

$$\begin{aligned}\frac{\partial^2\varphi}{\partial \mathbf{r}^2} = \frac{8\pi\nu e^2}{\omega + i/\tau_{\text{tr}}}\left\langle\left[\omega + \frac{i}{\tau} - in v\int d\Omega_{p_1}\sigma_{pp_1}\right.\right. \\ \left.+\left(\mathbf{v}\frac{\partial}{\partial \mathbf{r}}\right)\left(\omega + \frac{i}{\tau} - in v\int d\Omega_{p_1}\sigma_{pp_1}\right)^{-1}\left(\mathbf{v}_1\frac{\partial}{\partial \mathbf{r}}\right)\right]^{-1} \\ \left.\times\left(\mathbf{v}_1\frac{\partial}{\partial \mathbf{r}}\right)\left(\mathbf{v}_1\frac{\partial}{\partial \mathbf{r}}\right)\varphi\right\rangle,\end{aligned} \tag{10}$$

where τ_{tr} is the transport scattering time; away from the particle, φ is the solution to the equation

$$\frac{\partial^2\varphi}{\partial \mathbf{r}^2} = 0. \tag{11}$$

The second (current) branch of the plasmon can be analyzed in a similar fashion.

Consider a spherically symmetric cluster of radius R. Outside the cluster, the solution to Eq. (11) is

$$\varphi_{\text{ext}} = \frac{C}{r^{l+1}}Y_l^m e^{-i\omega t}, \quad r > R, \quad r = |\mathbf{r}|, \tag{12}$$

where C is a constant and Y_l^m are the spherical functions.

Inside the cluster, φ is a sum of two terms:

$$\varphi(\mathbf{r}, t) = Y_l^m(\tilde{E}r^l + \phi)e^{-i\omega t}. \tag{13}$$

The function ϕ in Eq. (13) is exponentially damping inside the cluster; in the vicinity of its surface, it can be written in the form

$$\phi = \hat{\phi}\left(\frac{R}{r}\right)^{\gamma} e^{-\kappa(R-r)}. \tag{14}$$

The parameter κ in Eq. (14) is the inverse dynamic screening depth. Both parameters κ and γ can be found from Eq. (10) and the corresponding boundary conditions: the scalar potential is a continuous function on the cluster surface, the derivative along the surface normal is continuous, and $\mathbf{n} \cdot \mathbf{j}_1 = 0$ on the cluster surface ($\mathbf{n}$ is a normal vector to the surface).

In what follows, we assume that the cluster is rather large, such that $\kappa R \gg 1$. In the principal approximation, the frequency of a surface plasmon is independent of the cluster size [2, 3]. Our first goal is to find a correction term proportional to $(\kappa R)^{-1}$. To this end, we define the zero-order approximation operator $\hat{L}_0$

$$\begin{aligned}\hat{L}_0 &= \omega + \frac{i}{\tau} - inv\int d\Omega_{p_1}\sigma_{pp_1} \\ &+ \kappa^2(\mathbf{v}\cdot\mathbf{e}_p)\left(\omega + \frac{i}{\tau} - inv\int d\Omega_{p_1}\sigma_{pp_1}\right)^{-1}(\mathbf{v}_1\cdot\mathbf{e}_\rho),\end{aligned} \tag{15}$$

where $\mathbf{e}_p = \mathbf{r}/r$ is the unit vector oriented along $\mathbf{r}$. From Eqs. (10) and (14), we derive an equation for the function ϕ with allowance made for the principal and first correction terms with respect to the parameter $(\kappa R)^{-1}$:

$$\begin{aligned}\left[\kappa^2 - \frac{2\kappa(\gamma-1)}{r}\right]\phi &= \frac{8\pi\nu e^2}{\omega + i/\tau_{\mathrm{tr}}} \\ \times\left\langle \hat{L}_0 - \frac{2\kappa\gamma}{r}(\mathbf{v}\cdot\mathbf{e}_p)\left(\omega + \frac{i}{\tau} - inv\int d\Omega_{p_1}\sigma_{pp_1}\right)^{-1}(\mathbf{v}_1\cdot\mathbf{e}_\rho)\right. \\ + \frac{\kappa(\mathbf{v}\cdot\mathbf{e}_\theta)}{r}\left(\omega + \frac{i}{\tau} - inv\int d\Omega_{p_1}\sigma_{pp_1}\right)^{-1}(\mathbf{v}\cdot\mathbf{e}_\theta) \\ + \frac{\kappa(\mathbf{v}\cdot\mathbf{e}_\varphi)}{r}\left(\omega + \frac{i}{\tau} - inv\int d\Omega_{p_1}\sigma_{pp_1}\right)^{-1}(\mathbf{v}\cdot\mathbf{e}_\varphi)\Bigg]^{-1} \\ \left.\times\left[(\mathbf{v}_1\cdot\mathbf{e}_\rho)^2\left(\kappa^2 - \frac{2\kappa(\gamma+1/2)}{r}\right) + \frac{\kappa v^2}{r}\right]\phi\right\rangle.\end{aligned} \tag{16}$$

Here, the angle brackets denote averaging over the angles of the vector $\mathbf{p}$.

The principal term in Eq. (16) yields the value of κ:

$$1 = \frac{3\omega_p^2}{\omega + i/\tau_{\mathrm{tr}}}\langle \hat{L}_0^{-1}\cos^2\theta_p\rangle, \tag{17}$$

where $\omega_p^0 = 8\pi\nu e^2 v^2/3$ is the frequency of plasma vibrations.

The correction term yields an equation for γ:

$$\begin{aligned}1 &= \frac{\omega_p^2}{\omega + i/\tau_{\mathrm{tr}}}\langle \hat{L}_0^{-1}\rangle \\ &+ \frac{2(\gamma+1/2)\omega_p^2\kappa^2 v^2}{(\omega + i/\tau_{\mathrm{tr}})^2}\langle \hat{L}_0^{-1}\cos^2\theta_p \hat{L}_0^{-1}\cos^2\theta_{p1}\rangle \\ &- \frac{\omega_p^2\kappa^2 v^2}{(\omega + i/\tau_{\mathrm{tr}})^2}\langle \hat{L}_0^{-1}\hat{L}_0^{-1}1\rangle.\end{aligned} \tag{18}$$

Below, we show that γ is a large quantity; this leads to the appearance of a wide plateau on the dependence of the frequency of a surface plasmon on cluster radius. In order to describe this phenomenon, we apply an interpolation procedure. Assume that the function ϕ satisfies the following equation when L is of the order of unity ($L = 1.2$) (see Eq. 13):

$$\phi'' + \frac{2\gamma}{r}\phi' - \kappa^2\phi = 0. \tag{19}$$

Here, the parameters κ and γ are determined from Eqs. (17) and (18), and the prime denotes the differentiation with respect to r. The solution to Eq. (19) can be represented in terms of a Bessel function:

$$\phi = \tilde{C}(\kappa r)^{1/2-\gamma} I_{\gamma-1/2}(\kappa r). \tag{20}$$

From formulas (12), (13), and (20), we find two boundary conditions (the continuity condition for φ and for its normal derivative at $r = R$):

$$\begin{aligned}\frac{C}{R^{l+1}} &= \tilde{C}(\kappa R)^{1/2-\gamma} I_{\gamma-1/2}(\kappa R) + \tilde{E}R^l, \\ -\frac{C(l+1)}{R^{l+1}} &= \tilde{C}\left[\left(\frac{1}{2} - \gamma\right)(\kappa R)^{1/2-\gamma} I_{\gamma-1/2}(\kappa R)\right. \\ &+ (\kappa R)^{1/2-\gamma}((\kappa R) I_{\gamma+1/2}(\kappa R) + (\gamma - 1/2) I_{\gamma-1/2}(\kappa R))\Big] \\ &+ \tilde{E}lR^l.\end{aligned} \tag{21}$$

Now, eliminate the constant C in the system of equations (21) to find an equation for the coefficients $\tilde{C}$ and $\tilde{E}$:

$$\begin{aligned}&\tilde{E}(2l+1)R^l + \tilde{C}(\kappa R)^{1/2-\gamma} \\ &\times\{(l+1)I_{\gamma-1/2}(\kappa R) + (\kappa R) I_{\gamma+1/2}(\kappa R)\} = 0.\end{aligned} \tag{22}$$

Using formulas (5) and (6), we reduce Eq. (8) for the density of the current $\mathbf{j}_1$ to the form

$$\begin{aligned}\mathbf{j}_1 &= -\frac{e^2 p\omega}{\pi^2(\omega + i/\tau_{\mathrm{tr}})} \\ &\times\left\{\frac{pv}{3}\mathbf{A}_1 + \left\langle \mathbf{p}\left(\mathbf{v}\frac{\partial}{\partial\mathbf{r}}\right)\hat{L}_{p_1}^{-1}\left(\varphi + \frac{i\left(\mathbf{v}_1\frac{\partial}{\partial\mathbf{r}}\right)(\mathbf{v}_1\cdot\mathbf{A}_1)}{\omega + i/\tau_{\mathrm{tr}}}\right)\right\rangle\right\}.\end{aligned} \tag{23}$$

In the case under consideration, the vector potential $\mathbf{A}_1$ is small and can be neglected. As a result, the condition that the normal component of the current goes to zero on the cluster surface is written as

$$\left\langle \mathbf{n}\cdot\mathbf{p}\left(\mathbf{v}\frac{\partial}{\partial\mathbf{r}}\right)\hat{L}_{p_1}^{-1}(\tilde{E}r^l+\tilde{C}(\kappa r)^{1/2-\gamma}I_{\gamma-1/2}(\kappa r)) \times Y_l^m(\mathbf{r}/r)\right\rangle_S = 0. \tag{24}$$

In the principal approximation, the action of the operator $\partial/\partial r$ on the function ϕ is reduced to multiplying it by the parameter κ. In this approximation, we derive the well-known formula for the frequency of a surface plasmon from Eqs. (17), (22), and (24):

$$\omega\left(\omega+\frac{i}{\tau_{tr}}\right) = \omega_p^2\frac{l}{2l+1}. \tag{25}$$

Let us return to the analysis of the dependence of the plasmon frequency on cluster size. In the approximation under consideration, Eq. (24) can be written as

$$R^{l-1}\frac{\tilde{E}l}{3\omega}+\tilde{C}\left\langle \cos^2\theta_p\frac{\partial}{\partial r}\left[\omega+\frac{i}{\tau}-in\nu\int d\Omega_{p_1}\sigma_{pp_1} + \frac{\nu^2}{\omega+i/\tau_{tr}}\left(\cos^2\theta_p\left(\frac{\partial^2}{\partial r^2}-\frac{1}{r}\frac{\partial}{\partial r}\right)+\frac{1}{r}\frac{\partial}{\partial r}\right)\right]^{-1} \times(\kappa r)^{1/2-\gamma}I_{\gamma-1/2}(\kappa r)\right\rangle_{r=R} = 0. \tag{26}$$

Solving Eq. (26), we obtain

$$R^l\frac{\tilde{E}l}{3} = \tilde{C}\int_0^1 dZZ^2\sum_{M=1}^{\infty}2MR^{2M}\sum_{m=0}^{M-1}C_m(-1)^{M-m} \times\left(\frac{\omega(\omega+i/\tau_{tr})}{4\nu^2Z^2}\right)^{M-m}\frac{\Gamma(m+1)\Gamma(m+(1/2)Z^2)}{\Gamma(M+1)\Gamma(M+(1/2)Z^2)}. \tag{27}$$

The coefficients C_m in (27) are the coefficients of the expansion of the Bessel function into the Taylor series

$$(\kappa r)^{1/2-\gamma}I_{\gamma-1/2}(\kappa r) = \sum_{m=0}^{\infty}C_m r^{2m},$$
$$C_m = \frac{1}{m!\Gamma(m+\gamma+1/2)}\left(\frac{\kappa}{2}\right)^{2m}\times 2^{-\gamma+1/2}. \tag{28}$$

The solvability condition for the system of Eqs. (22), (27) determines the spectrum of surface plasmons:

$$-\frac{l}{3(2l+1)}(\kappa R)^{1/2-\gamma} \times\{(l+1)I_{\gamma-1/2}(\kappa r)+(\kappa R)I_{\gamma+1/2}(\kappa R)\} = \int_0^1 dZZ^2\sum_{M=1}^{\infty}2MR^{2M}\sum_{m=0}^{M-1}C_m(-1)^{M-m} \times\left(\frac{\omega(\omega+i/\tau_{tr})}{4\nu^2Z^2}\right)^{M-m}\frac{\Gamma(m+1)\Gamma(m+(1/2)Z^2)}{\Gamma(M+1)\Gamma(M+(1/2)Z^2)}. \tag{29}$$

The quantity κ in (29) is found from Eq. (17). As a rule, the width of plasmons is small compared to their frequency, and it can be neglected when calculating κ. Within this accuracy, we find from Eq. (17) that

$$1 = \frac{3\omega_p^2}{\kappa^2\nu^2}\left[1-\frac{\omega}{\kappa\nu}\arctan\left(\frac{\kappa\nu}{\omega}\right)\right]. \tag{30}$$

In order to determine γ at $R\longrightarrow\infty$, we need the mean value of the operators in formula (18):

$$\langle\hat{L}_0^{-1}1\rangle = \int_0^1\frac{dZ\omega}{\omega^2+\kappa^2\nu^2Z^2} = \frac{1}{\kappa\nu}\arctan\left(\frac{\kappa\nu}{\omega}\right),$$
$$\langle\hat{L}_0^{-1}\cos^2\theta_p\rangle = \int_0^1\frac{dZZ^2\omega}{\omega^2+\kappa^2\nu^2Z^2} = \frac{\omega}{\kappa^2\nu^2}\left[1-\frac{\omega}{\kappa\nu}\arctan\left(\frac{\kappa\nu}{\omega}\right)\right], \tag{31}$$
$$\langle\hat{L}_0^{-1}\cos^2\theta_p\hat{L}_0^{-1}\cos^2\theta_{p_1}\rangle = \int_0^1\frac{dZ\omega^2Z^4}{(\omega^2+\kappa^2\nu^2Z^2)^2} = \frac{\omega^2}{(\kappa\nu)^4}\left[1+\frac{\omega^2}{2(\omega^2+\kappa^2\nu^2)}-\frac{3}{2}\frac{\omega}{\kappa\nu}\arctan\left(\frac{\kappa\nu}{\omega}\right)\right].$$

As $R\longrightarrow\infty$, we use Eqs. (18), (25), and (31) to find the following value of γ at $l=1$:

$$\gamma = 9.04. \tag{32}$$

In the framework of perturbation theory, we find the following expression replacing Eq. (25) for the frequency of a surface plasmon when the shift of its frequency is small:

$$\omega\left(\omega+\frac{i}{\tau_{tr}}\right) = \omega_p^2\frac{l}{2l+1} \times\frac{1-\dfrac{\gamma-(l+1)}{\kappa R}}{1+\dfrac{3}{\kappa R}\left[1-\left(\dfrac{\omega_p^2}{\omega^2}-\dfrac{\kappa^2\nu^2}{3\omega^2}\right)\right]}. \tag{33}$$

Owing to the large value of γ, the domain of applicability of Eq. (33) is severely restricted from below. Interpolation formulas (29), (30), and (32) make it pos-

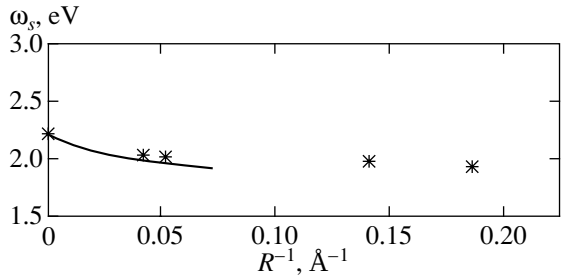

The dependence of the frequency of a surface plasmon Na on the cluster radius R. Crosses mark the experimental results reported in [2]. The solid curve is the plot of the theoretical dependence (29).

sible to extend this domain up to values of R of about 10 Å.

The figure shows the dependence of the frequency of plasmon vibrations for Na on the cluster radius, which follows from formulas (29), (30), and (32), and experimental data reported in [2]. Formulas (29), (30), and (32) do not involve adjustable parameters. For the speed on the Fermi surface and for the density Na, we used the tabular magnitudes

$$\begin{aligned} v &= 1.07 \times 10^8 \text{ cm/s}, \\ \text{density} &= 2.65 \times 10^{22} \text{ particles/cm}^3. \end{aligned} \tag{34}$$

In the domain $R < 12$ Å, the dependence of γ on the cluster size cannot be neglected. In this domain, the problem is reduced to solving Eq. (10) for the potential ϕ with a required accuracy.

4. CONCLUSIONS

A method for analyzing the dependence of the frequency of a surface plasmon on the cluster shape and size is suggested. It is shown that a large numerical parameter γ appears that is involved in the dependence of the potential on coordinates. As a result, a wide plateau appears on the plot of the plasmon frequency dependence on the cluster radius $\omega = \omega(R)$. It seems probable that the profile of the potential barrier outside the cluster becomes significant when the cluster size is on the order of several angströms. Note that the experimental width of a surface plasmon weakly depends on the cluster size [2]. Under our approach, the plasmon width is related to the scattering of electrons from impurities or defects of the crystalline lattice. The dependence of damping on the cluster size is mainly related to the fact that the plasmon frequency appears in all the relations only in the form $\omega(\omega + i/\tau_{tr})$.

ACKNOWLEDGMENTS

I am grateful to V.V. Kresin and V.Z. Kresin for discussions and valuable remarks.

The work was supported by the US Civilian Research & Development Foundation (CRDF Award no. RP1-2251) and by the US National Science Foundation.

REFERENCES

1. V. V. Kresin, Phys. Rep. **220**, 1 (1992).
2. C. Brechignac and J. P. Connerade, J. Phys. B **27**, 3795 (1994).
3. G. Mie, Ann. Phys. (Leipzig) **25**, 377 (1908).
4. A. A. Lushnikov and A. J. Simonov, Z. Phys. **270**, 17 (1974).
5. U. Kreibig and M. Vollmer, *Optical Properties of Metal Clusters* (Springer-Verlag, Berlin, 1995).
6. A. I. Larkin and Yu. N. Ovchinnikov, J. Low Temp. Phys. **10**, 407 (1973).

Translated by A. Klimontovich

Journal of Experimental and Theoretical Physics, Vol. 94, No. 6, 2002, pp. 1193–1200.
Translated from Zhurnal Éksperimental'noĭ i Teoreticheskoĭ Fiziki, Vol. 121, No. 6, 2002, pp. 1390–1398.

NONLINEAR PHYSICS

Dynamic Correlations in a Thermalized System Described by the Burgers Equation

I. V. Kolokolov* and K. S. Turitsyn

Budker Institute of Nuclear Physics, Siberian Division, Russian Academy of Sciences, pr. Akademika Lavrent'eva 11, Novosibirsk, 630090 Russia

Novosibirsk State University, Novosibirsk, 630000 Russia

**e-mail: kolokolov@inp.nsk.su*

Received October 4, 2001

Abstract—For the field $u(x, t)$ governed by the Burgers equation with a thermal noise, short-time asymptotics of multipoint correlators are obtained. Their exponential parts are independent of the correlator number. This means that they are determined by a single rare fluctuation and exhibit an intermittency phenomenon. © *2002 MAIK "Nauka/Interperiodica".*

1. INTRODUCTION

Values of various observables in a field system in a chaotic state undergo fluctuations in space and time. To describe them, correlation functions of various orders are usually used; moreover, nonsimultaneous correlators carry more detailed information about the system than simultaneous ones. The main contribution to the measured average quantities is made by events of superposition of weakly correlated signals arriving from different points in space. Statistical properties of this kind are exhibited by free fields. For such fields, the statistics of fluctuations in a thermodynamic equilibrium is a Gaussian one; i.e., both the simultaneous and nonsimultaneous correlation functions reduce to a sum of products of second-order correlators. However, it is possible that a set of average quantities of interest is determined by a rare but large (in natural units) fluctuation that is coherent with respect to space. Such a situation is referred to as intermittency. Formally, it manifests itself in that the irreducible correlation functions, which are distinct from zero in any nonlinear system, become much greater then the reducible parts of total correlators. A classical example is hydrodynamic turbulence [1, 2]. Here, the magnitude of total correlators as compared to their reducible parts is characterized by the Reynolds number $\mathrm{Re} = l/r_d$, where l is the scale of either initial perturbations or external sources of energy, and r_d is the scale at which the energy dissipates.

Intermittency also occurs in fields of another type—wave functions Ψ of electrons in a random one-dimensional and two-dimensional potential. Indeed, due to localization effects, all moments of the density $|\Psi|^2$ are inversely proportional to the volume V; therefore,

$$\langle |\Psi|^{2n} \rangle \gg \langle |\Psi|^2 \rangle^n \text{ at } V \longrightarrow \infty$$

(see [3, 4]). Here, we face the case when an infinite set of correlation functions is determined by a single rare event.

By itself, a large value of fluctuations does not necessarily lead to intermittency. For example, even at the point of a second-order phase transition, irreducible and total correlators have the same scale dimension and are, therefore, of the same order of magnitude [5]. For this reason, intermittency effects under thermal equilibrium had not been discussed in the literature until [6, 7]. In these studies, the statistics of a vortex field in two-dimensional films was investigated, and it was discovered that nonsimultaneous correlators of various orders are determined by a single fluctuation evolving in time. Hence, the correlators are proportional to the small probability of this fluctuation. However, the reducible parts of higher order correlators include this probability to powers greater than unity; as a result, the values of reducible parts are much less than the values of the total correlation functions.

In [8], it was shown that similar properties are characteristic of nonsimultaneous correlation functions in systems whose evolution obeys the one-dimensional Burgers equation with a thermal noise

$$u_t + uu_x - \nu u_{xx} = \xi. \tag{1}$$

Here, $u(x, t)$ is a function of the spatial coordinate x and time t, the parameter ν plays the role of viscosity, and $\xi(x, t)$ is a random short-correlated (in space and time) force with a zero average satisfying Gaussian statistics.

Equation (1) describes a system of one-dimensional weak shock waves. In this case, the field $u(x, t)$ is proportional to the speed of the medium with respect to a reference frame moving at the speed of sound [1, 9]. This equation also appears in the problem on fluctuations of solution–precipitate type interfaces that grow due to a random inflow of atoms from the solution. In

this case, $u = \partial_x h$, where h is the height of the surface, and the equation of evolution of the field $h(x, t)$, which is derived from Eq. (1), is called the (1 + 1)-dimensional Kardar–Parisi–Zhang equation [10]. A problem of the same type arises in the study of statistics of vortex lines in superconductors with impurities [11]. In what follows, we will use hydrodynamic terms and call $u(x, t)$ the velocity field.

We consider the second-order correlator of the random force $\xi(x, t)$ in the form

$$\langle \xi(x, t)\xi(x_1, t_1)\rangle = -\nu\beta^{-1}\delta''(x - x_1)\delta(t - t_1). \quad (2)$$

Then, there exists a time-independent distribution $\mathcal{P}[u]$ of the field u that has the form of the Gibbs distribution

$$\mathcal{P}[u] = \mathcal{N}\exp\{-\mathcal{F}[u]\}, \quad \mathcal{F}[u] = \beta\int dx u^2(x). \quad (3)$$

Here, $\mathcal{N}$ is a normalization constant. It is seen from (3) that the parameter β plays the role of the inverse temperature, so that the statistics of the velocity field at a given instant of time is also Gaussian with the two-point average

$$\langle u(x, t)u(x', t)\rangle = (2\beta)^{-1}\delta(x - x'), \quad (4)$$

corresponding to the zero correlation length.

In this paper, we study the asymptotic behavior of the correlation functions

$$\mathcal{H}(X, t) = \langle u(0, 0)u(X, t)\rangle,$$
$$T(X, Y, t) = \langle u(0, 0)u(Y, 0)u(X, t)\rangle, \quad (5)$$
$$S(X, Y, \Delta, t) = \langle u(0, 0)u(Y, 0)u(X, t)u(X + \Delta, t)\rangle$$

at a small time t and a large distance X. It is assumed that the viscosity is very small ($\nu \longrightarrow 0$). However, it is crucial for the theory that it be distinct from zero (see below). It is natural to assume that the influence of the noise ξ can be neglected at small time intervals t (below, we consider this assumption in more detail). Then, averaging is performed over distribution (3) of the field values $u_0(x) = u(x, 0)$. In [8], principal exponential asymptotics terms of correlators (5) were found. The derivation used the fact that, for $\nu \longrightarrow 0$, the dynamics of the correlation of velocities at spatially distant points is a Lagrangian transition. Therefore, the correlator $\mathcal{H}(X, t)$ is determined by the probability of an initial fluctuation $u_0(x)$ such that a Lagrangian particle travels from 0 to the point X in time t. It was shown in [8] that the optimal profile is linear:

$$u_0^*(x) = (X - x)/T, \quad 0 < x < X, \quad u_0(x) = 0, \quad x < 0, \quad x > X. \quad (6)$$

The exponential asymptotics part of the function $\mathcal{H}(X, t)$ is written as

$$\mathcal{P}[u_0^*] = \exp(-\beta X^3/3t^2). \quad (7)$$

Notice that the same fluctuation "brings" all particles from the interior of the interval $(0, X)$ to the point $x = X$ in time t. Then, we conclude that, for $\Delta \ll X$ and $0 < Y < X$, we have

$$\mathcal{H}(X, t) \sim T(X, Y, t) \sim S(X, Y, \Delta, t) \sim \exp\left(-\frac{\beta X^3}{3t^2}\right). \quad (8)$$

The condition $\Delta \ll x$ ensures a small difference of the optimal profile from the linear profile (6). The asymptotics under consideration corresponds to the inequality

$$\beta X^3/t^2 \gg 1,$$

and relations (8) are interpreted as intermittency.

In the reasoning above, we assumed that correlation functions of form (5) tend to a finite limit as $\nu \longrightarrow 0$. This assumption was made in [12]. It was also mentioned in that study that there exists only a single dimensionless combination of the parameters $\beta X^3/t^2$ in this limit, which is usually formulated in terms of dispersion as

$$\omega_k \propto k^{3/2}.$$

The smallness of ν implies the inequality

$$x^2(\nu t)^{-1} \gg \beta X^3 t^{-2}.$$

The absence of divergences as $\nu \longrightarrow 0$ can be verified as follows. If there is a divergence, then the main contribution to the averages is made by short-wave fluctuations. For these fluctuations, the term proportional νu_{xx} dominates in the equation of motion (1). Then, perturbation theory could be applied to the nonlinear terms. An analysis confirming the existence of a limit as $\nu \longrightarrow 0$ based on Wild's diagram technique was carried out in [13]. Note that, in the case under consideration, the convergence of the renormalized diagrams of perturbation theory at $\nu \longrightarrow 0$ implies that this theory is inapplicable. However, it must be stressed that ν cannot be immediately set to zero. Indeed, shock waves, which can be correctly described only with regard for the dissipative term in Eq. (1), play a key role in the dynamics of finite fluctuations. The approach used in [8] was based on Lagrangian trajectories. For this reason, an independent confirmation of the basic result of [8] is of interest. Moreover, the approach used in [8] does not yield preexponential coefficients in the expressions for correlators. In the same paper, it was noted that the integral over fluctuations at the background of the optimal profile (6) is not Gaussian; thus, the problem is not reduced to the applications of the standard saddle point method to functional integrals.

In this paper, we calculate complete asymptotic expressions for the correlation functions (5) at $\beta X^3/3t^2 \gg 1$ in the framework of the approximation whereby the effect of noise on the interval t is neglected. We immediately note that the asymptotic expressions obtained are in agreement with estimate (8); they are also in complete agreement with the opti-

mal fluctuation if it is assigned the following measure in the functional space:

$$\Omega = \left(\frac{\beta X^3}{t^2}\right)^{-1/3} (2\mathrm{Ai}'(-a_0))^{-1} \exp\left(-a_0\left(\frac{\beta X^3}{t^2}\right)^{1/3}\right). \quad (9)$$

Here, $-a_0$ is the first zero of the Airy function:

$$\mathrm{Ai}(-a_0) = 0.$$

The measure is defined in the same way as in the calculus of instantons in quantum field theory [14]: the average of the product of the velocity field values is calculated by substituting the optimal profile (6) into it and by multiplying the result by the Gibbs weight (7) and by the measure Ω. It is seen from the expression for Ω that fluctuations are small relative to (6); indeed, Ω decreases with growing X^3/t^2. However, the dependence of Ω on the saddle point parameter $(\beta X^3/t^2)^{1/2}$ is substantially nonanalytic. Such a behavior of the measure implies that it cannot be calculated using the quadratic (in fluctuations) expansion of the effective action.

The turbulence phenomenon for the Burgers equation with the initial distribution (3) for the case of correlator decomposition was studied in [15, 16]. However, only the simultaneous statistics, which does not exhibit intermittency for the velocity field, was considered in [15]. In the paper [16], the case $t \longrightarrow \infty$, which is opposite to the case considered here, was studied. Moreover, nosimultaneous and multipoint averages were not considered in [16]. We note that the intermittency of simultaneous structure functions of the velocity field caused by discontinuous fluctuations was correctly described in [15, 16]. It is also characteristic of the general statement of the problem on the Burgers turbulence [2, 17–19], which assumes that the length L of the external noise correlation or the initial distribution of velocities is considerably greater than the dissipation scale r_d. Moreover, the distances r for which the correlations are analyzed are assumed to belong to the inertia interval; i.e., $r_d \ll r \ll L$.

2. CORRELATORS AT A SMALL DIFFERENCE OF TIMES

We begin with the calculation of asymptotic expressions for the function $\mathcal{H}(X, t)$ at $\beta X^3/t^2 \gg 1$. Since the averaging over the initial condition $u_0(x)$ is carried out with the Gaussian weight (3), the correlator $\mathcal{H}$ can be written as

$$\mathcal{H}(X, t) = \frac{1}{2\beta}\left\langle \frac{\delta u(X, t)}{\delta u_0(0)}\right\rangle. \quad (10)$$

When calculating the variational derivative in (10), we consider $u(X, t)$ as a functional of the field $u_0(x)$. The solution to the Cauchy problem for Eq. (1) is obtained with the help of the well-known Cole–Hopf substitution such that

$$u(X, t) = -2\nu\partial_X \ln\left\{\int_{-l}^{l_1} dz F(z, X)\right\},$$
$$F(z, X) = \exp\left(-\frac{(z-X)^2}{4t\nu} - \frac{1}{2\nu}\int_{-l}^{z} u_0(y)dy\right). \quad (11)$$

Here, $-l$ and l_1 are the coordinates of the remote endpoints of the interval occupied by the medium. Formula (11) is valid for $l, l_1 \longrightarrow \infty$. In this limit, l and l_1 do not appear in the final expressions for the correlators, although it is convenient to retain them in the process of intermediate manipulations. The independence of $\mathcal{H}(X, t)$ of l and l_1 makes it possible to shift the interval endpoints as follows:

$$(-l, l_1) \longrightarrow (-l + X, l_1 + X).$$

Using the translational invariance of the energy $\mathcal{F}$, we replace $u_0(x)$ by $u_0(x - X)$. After these transformations, taking the variational derivative, and differentiation with respect to X in (10) and (11), the correlator takes the simple form

$$\mathcal{H}(X, t) = \frac{1}{2\beta}\left\langle F(-X, 0)\left\{\int_{-l}^{l_1} dz F(z, 0)\right\}^{-1}\right\rangle$$
$$= \frac{1}{2\beta}\int_0^\infty d\lambda \left\langle \exp\left(-\int_{-l}^{l_1} dz \exp\left(-\frac{\Phi(z)}{2\nu}\right)\right)\right\rangle. \quad (12)$$

Here,

$$\Phi(z) = -2\nu\ln\lambda + \frac{z^2 - X^2}{2t} + \int_{-X}^{z} d\tau u_0(\tau). \quad (13)$$

The averaging $\langle\ldots\rangle$ is performed as the functional integration with respect to $\mathcal{D}u_0$. Now, using formula (13), we change the integration variable $u_0(z)$ for $\Phi(z)$. By construction, $\Phi(z)$ satisfies the condition

$$\Phi(-X) = -2\nu\ln\lambda. \quad (14)$$

Expressing $\mathcal{F}$ in terms of Φ as

$$\mathcal{F}[\Phi] = \mathcal{S}[\Phi] - \frac{2\beta}{t}(l_1\Phi(l_1) + l\Phi(-l)) + \frac{\beta}{3t^2}(l_1^3 + l^3), \quad (15)$$
$$\mathcal{S}[\Phi] = \int_{-l}^{l_1} dx\left\{\left(\frac{d\Phi}{dx}\right)^2 + \frac{2}{t}\Phi\right\},$$

and taking into account Eq. (12), we reduce the calculation of $\mathcal{H}(X, t)$ to the Feynman–Kac path integral

[20]. It follows from (14) that the integration with respect to $d\lambda$ removes the boundary condition imposed on $\Phi(x)$ at the point $x = -X$, and the correlator $\mathcal{H}(X, t)$ is expressed in terms of the matrix element of the Euclidean quantum mechanics as

$$\mathcal{H}(X,t) = \frac{\exp\left\{-\frac{\beta}{3t^2}(l_1^3 + l^3)\right\}}{4\nu\beta}\left\langle \exp\left(\frac{2\beta l_1}{t}\Phi\right)\right|$$
$$\times \exp(-(l_1 - X)\hat{H})\exp\left(-\frac{\Phi}{2\nu}\right)\exp(-(l + X)\hat{H}) \quad (16)$$
$$\times\left|\exp\left(\frac{2\beta l}{t}\Phi\right)\right\rangle$$

with the Hamiltonian

$$\hat{H} = -\frac{1}{4\beta}\frac{d^2}{d\Phi^2} + U(\Phi),$$
$$U(\Phi) = \frac{2\beta}{t}\Phi + \exp\left(-\frac{\Phi}{2\nu}\right). \quad (17)$$

Unfortunately, we failed to find the basis diagonalizing the operator $\hat{H}$ in a closed form. However, problem (16), (17) admits an analytical solution for $\nu \longrightarrow 0$ and $\beta X^3/t^2 \gg 1$.

Indeed, for small ν, the axis Φ can be decomposed into two domains such that one of the terms in $U(\Phi)$ is dominant in each domain. In the leading approximation with respect to ν, the eigenfunctions of $\hat{H}$ are easily found:

$$\hat{H}\psi_n(\Phi) = \left(\frac{\beta}{t^2}\right)^{1/3} a_n \psi_n(\Phi), \quad (18)$$

$$\psi_n(\Phi) = \begin{cases} 4\nu\left(\frac{8\beta^2}{t}\right)^{1/2} K_0\left(8\nu\sqrt{\beta}\exp\left(-\frac{\Phi}{4\nu}\right)\right), \\ \Phi < \nu\ln\frac{1}{\nu}, \\ \frac{1}{\mathrm{Ai}'(-a_n)}\left(\frac{8\beta^2}{t}\right)^{1/6}\mathrm{Ai}\left(\left(\frac{8\beta^2}{t}\right)^{1/3}\Phi - a_n\right), \\ \Phi > \nu\ln\frac{1}{\nu}. \end{cases} \quad (19)$$

Here, K_0 is the elliptic Macdonald function. In (19), $-a_n$ such that $a_n > 0$ and $a_{n+1} > a_n$ ($n = 0, 1, \ldots$) form the sequence of zeros of the Airy function: $\mathrm{Ai}(-a_n) = 0$. When calculating the average in Eq. (16), we have to find the result of the action of the "evolution" operator $\exp(-T\hat{H})$ on the initial state $\exp(\alpha\Phi)$. This state cannot be normalized. Hence, an expansion in basis (19) is either possible or not, depending on the relationship between T and α. The values of α corresponding to the boundary wave functions in Eq. (16) are large:

$$\alpha^3 t/\beta^2 \gg 1.$$

Then, the scalar product $\langle\psi_n|\exp(\alpha\Phi)\rangle$ has the following form up to terms that vanish as $\nu \longrightarrow 0$:

$$c_n(\alpha) = \langle\psi_n|\exp(\alpha\Phi)\rangle = \frac{1}{\mathrm{Ai}'(-a_n)}\left(\frac{t}{8\beta^2}\right)^{1/6}$$
$$\times \exp\left(\alpha a_n\left(\frac{t}{8\beta^2}\right)^{1/3} + \alpha^3\frac{t}{8\beta^2}\right). \quad (20)$$

The following series for the function

$$f(\Phi, X) = \exp\left(-\frac{\beta l^3}{3t^2}\right)\exp(-(l + X)\hat{H})$$
$$\times \exp\left(\frac{2\beta l}{t}\Phi\right) \quad (21)$$

is convergent:

$$f(\Phi, X) = \sum_n c_n\left(\frac{2\beta l}{t}\right)$$
$$\times \exp\left(-\frac{\beta l^3}{3t^2} - a_n\left(\frac{\beta}{t^2}\right)^{1/3}(l + X)\right)\psi_n(\Phi) \quad (22)$$
$$= \sum_n \frac{1}{\mathrm{Ai}'(-a_n)}\exp\left(-a_n\left(\frac{\beta}{t^2}\right)^{1/3}X\right)\psi_n(\Phi).$$

At $\beta X^3/t^2 \gg 1$, the sum in (22) is determined by the contribution of the ground state. For the further considerations, only the domain $\Phi < \nu\ln(1/\nu)$, in which

$$f(\Phi, X) \approx \frac{4\nu}{\mathrm{Ai}'(-a_0)}\left(\frac{8\beta^2}{t}\right)^{1/3}$$
$$\times K_0\left(8\nu\sqrt{\beta}\exp\left(-\frac{\Phi}{4\nu}\right)\right)\exp\left(-a_0\left(\frac{\beta}{t^2}\right)^{1/3}X\right), \quad (23)$$

is of importance.

A series for the state

$$g(\Phi, X) = \exp\left(-\frac{\beta l_1^3}{3t^2}\right)\exp(-(l_1 - X)\hat{H})$$
$$\times \exp\left(\frac{2\beta l_1}{t}\Phi\right), \quad (24)$$

which is similar to (22), is divergent. However, for $\beta X^3/t^2 \gg 1$, we can use the fact that the main part of the function $g(\Phi, \tau)$ for $\tau > X$ belongs to the domain where

the linear term in $U(\Phi)$ is dominating. The corresponding evolution problem is easily solved:

$$g_0(\Phi, X) = \exp\left(\frac{2\beta X}{t}\Phi - \frac{\beta X^3}{3t^2}\right). \quad (25)$$

The behavior of $g(\Phi, X)$ for small and negative Φ can be found using the substitution

$$g(\Phi, \tau) = g_0(\Phi, \tau)G(\Phi, \tau),$$
$$G(\Phi \longrightarrow +\infty, \tau) \longrightarrow 1, \quad G(\Phi \longrightarrow -\infty, \tau) \longrightarrow 0. \quad (26)$$

The solution to the equation

$$\partial_\tau G = \left(\frac{1}{4\beta}\partial_\Phi^2 + \frac{\tau}{t}\partial_\Phi - \exp\left(-\frac{\Phi}{2\nu}\right)\right)G \quad (27)$$

for G with the boundary conditions (26) can be found, for large τ, using the adiabatic expansion. In the leading approximation, the right-hand side of equality (27) vanishes, and an explicit expression for G is easily found. Then, the total function $g(\Phi, X)$ has the following form in the principal order with respect to $\beta X^3/t^2$:

$$g(\Phi, X) = 8\beta\nu\frac{X}{t}$$
$$\times K_{8\beta\nu X/t}\left(8\sqrt{\beta}\nu\exp\left(-\frac{\Phi}{4\nu}\right)\right)\exp\left(-\frac{\beta X^3}{3t^2}\right). \quad (28)$$

In the domain $\Phi < \nu\ln(1/\nu)$, we may neglect the fact that the index of the Macdonald function is different from zero. The substitution of (28) and (23) into (16) yields the final expression for the short-time asymptotics of the second-order correlator for the velocity field:

$$\mathcal{H}(X, t) \approx \frac{(X/t)^2}{2\mathrm{Ai}'(-a_0)}\left(\frac{\beta X^3}{t^2}\right)^{-1/3}$$
$$\times \exp\left(-\frac{\beta X^3}{3t^2} - a_0\left(\frac{\beta}{t^2}\right)^{1/3}X\right). \quad (29)$$

We see that the correlator $\mathcal{H}(X, t)$ is indeed finite at $\nu \longrightarrow 0$. Furthermore, it follows from (29) that the integral over fluctuations in the vicinity of the optimal profile (6) depends on the parameter of the theory $\beta X^3/t^2$; more precisely, it is proportional to $((\beta X^3/t^2)^{-1/3}\exp(-a_0(\beta X^3/t^2)^{1/3})$ and cannot be obtained by a Gaussian integration.

In the approximation that takes into account the decomposition of correlators, the third-order correlation function $T(X, Y, t)$ (see (5)) is also expressed in terms of the variational derivatives of the solution (11) with respect to the initial field:

$$T(X, Y, t) = \frac{1}{4\beta^2}\left\langle\frac{\delta^2 u(X, t)}{\delta u_0(0)\delta u_0(Y)}\right\rangle. \quad (30)$$

Manipulations similar to (12)–(15) yield the following operator representation for $T(X, Y, t)$:

$$T(X, Y, t) = -\frac{1}{16\nu^2\beta^2}$$
$$\times \exp\left\{-\frac{\beta}{3t^2}(l_1^3 + l^3)\right\}\partial_X\int_{-l}^{-X}dz_1\int_{Y-X}^{l_1}dz_2$$
$$\times\left\langle\exp\left(\frac{2\beta l_1}{t}\Phi\right)\middle|\exp(-(l_1 + z_1)\hat{H})\right. \quad (31)$$
$$\times\exp\left(-\frac{\Phi}{2\nu}\right)\exp(-(z_2 - z_1)\hat{H})$$
$$\left.\times\exp\left(-\frac{\Phi}{2\nu}\right)\exp(-(l - z_2)\hat{H})\middle|\exp\left(\frac{2\beta l}{t}\Phi\right)\right\rangle.$$

For the functions f and g defined in (21) and (24), representation (31) takes the form

$$T(X, Y, t) = -\frac{\partial_X}{16\nu^2\beta^2}\int_X^l dz_1\int_{-l_1}^{-Y+X}dz_2$$
$$\times\left\langle g(\Phi, z_1)\middle|\exp\left(-\frac{\Phi}{2\nu}\right)\right. \quad (32)$$
$$\left.\times\exp(-(z_1 - z_2)\hat{H})\exp\left(-\frac{\Phi}{2\nu}\right)\middle|f(\Phi, z_2)\right\rangle.$$

It follows from (28) that, for $\beta X^3/t^2 \gg 1$, the main contribution to the integral with respect to dz_1 is made by a small neighborhood near the upper limit $z_1 = -X$. Note that the intermittency effect (8) manifests itself (at this stage of the calculations) in that the function $g(\Phi, X)$ cannot be resolved in the complete set of eigenfunctions (19); for this reason, $g(\Phi, X)$ has the form (28). If $X - Y \sim X \sim Y$, the matrix element in (32) is determined by the contribution of the intermediate ground state ψ_0 (the product of $g(\Phi, X)$ by $\exp(-\Phi/2\nu)$ can be resolved in the basis (19)). In the integral with respect to dz_2, the domain $-X + Y < z_2 < 0$ makes the major contribution. Inside this domain, the dependence of the average in (32) on z_2 can be neglected. As a result, we obtain the expression

$$T(X, Y, t) \approx \frac{(X/t)^2}{2\mathrm{Ai}'(-a_0)}\left(\frac{\beta X^3}{t^2}\right)^{-1/3}\frac{X - Y}{t}$$
$$\times\exp\left(-\frac{\beta X^3}{3t^2} - a_0\left(\frac{\beta}{t^2}\right)^{1/3}X\right) \approx \frac{X - Y}{t}\mathcal{H}(X, t), \quad (33)$$

which is in agreement with the fact that the initial profile (6) is dominating.

The scheme for the calculation of the fourth-order correlation function

$$S(X, Y, \Delta, t) = S^{(1)}(X, X_1) + S^{(2)}(X, X_1) + S^{(1)}(X_1, X) + S^{(2)}(X_1, X), \tag{34}$$

$$S^{(1)}(X, X_1) = \frac{1}{4\beta^2}\left\langle \frac{\delta^2 u(X, t)}{\delta u_0(0)\delta u_0(y)} u(X_1, t)\right\rangle,$$
$$S^{(2)}(X, X_1) = \frac{1}{4\beta^2}\left\langle \frac{\delta u(X, t)}{\delta u_0(0)}\frac{\delta u(X_1 t)}{\delta u_0(y)}\right\rangle, \tag{35}$$

where $X_1 = X + \Delta$, is somewhat different from the cases of the second- and third-order correlators. This is explained by the fact that the expression to be averaged includes both the combinations $F(z, X_1)$ and $F(z, X)$. The averages are reduced to path integrals by the change

$$\Phi(z) = -2\nu \ln\lambda - 2\nu \ln n_F(z - \mu) + \frac{z^2 - X^2}{2t} + \int_{-X}^{z} d\tau u_0(\tau),$$

where $n_F(z)$ is the Fermi distribution

$$n_F(z) = \left[1 + \exp\left(\frac{\Delta}{2\nu t} z\right)\right]^{-1}. \tag{36}$$

Unfortunately, closed expressions can be obtained only for small $\Delta \ll X$. However, Δ remains much greater than the dissipative scale: $\Delta^2(\nu t)^{-1} \gg 1$. Formally, the smallness of Δ allows us to replace the vertex $\exp(2\beta\Delta/t)$ by 1 in the operator representation of $S^{(1)}$ and $S^{(2)}$. As a result, for the average $S^{(1)}(X, X_1)$, we obtain

$$S^{(1)} = \partial_X \frac{\Delta}{32\beta^2\nu^3 t^2}\hat{\mathcal{L}} \times \left\langle f(\Phi, \zeta_1)\left|\exp\left(-\frac{\Phi}{2\nu}\right)\exp(-(\zeta_1 - \zeta_2)\hat{H}) \times \exp\left(-\frac{\Phi}{2\nu}\right)\exp(-(\zeta_2 - \zeta_3)\hat{H}) \times \exp\left(-\frac{\Phi}{2\nu}\right)\right| g(\Phi, \zeta_3)\right\rangle, \tag{37}$$

where

$$\hat{\mathcal{L}} = \int_{Y-X}^{l_1} dz_1 \int_{-l}^{-X} dz_2 \int_{-l}^{l_1} dz_3 (z_3 - \Delta) \times \int_{-l}^{l_1} d\mu\, n_F(\mu - z_1) n_F(\mu - z_2) n_F(z_3 - \mu), \tag{38}$$

and $\{\zeta_n\}$ is a permutation of the integration variables $\{z_n\}$ such that $\zeta_k < \zeta_{k+1}$. (In effect, (37) is the matrix element of the chronologically arranged product of operators.)

Note that the integrand in (37) has a singularity as a function of $\zeta_3 - \zeta_2$ as $\nu \longrightarrow 0$. Indeed, the matrix elements of the operator

$$\exp\left(-\frac{\Phi}{2\nu}\right)\exp(-(\zeta_3 - \zeta_2)\hat{H})\exp\left(-\frac{\Phi}{2\nu}\right)$$

at $\zeta_3 - \zeta_2 \sim \beta\nu^2/t$ are about ν^{-3} times greater than the values at the separation $\zeta_3 - \zeta_2 \sim X$. This singularity can be singled out using the rule

$$\frac{1}{\nu}\exp\left(-\frac{\Phi}{2\nu}\right)\exp(-(\zeta_3 - \zeta_2)\hat{H})\exp\left(-\frac{\Phi}{2\nu}\right) \longrightarrow \frac{2\beta}{t}\delta(\zeta_3 - \zeta_2), \quad \nu \longrightarrow 0. \tag{39}$$

The factor of order $1/\nu$ is compensated in (37) by the result of the integration over the domain $\mu > z_3$, which has the order $\nu t/\Delta$. The contribution of the domain $z_{1,2} < \mu < z_3$, which has no singularities determined by formula (39), is of order Δ and is, therefore, insignificant. Finally, we have, for $\Delta \ll X$,

$$S^{(1)}(X, X_1) = \frac{(X - Y)^2}{2t^2}\mathcal{H}(X, t). \tag{40}$$

The average $S^{(2)}(X, X_1)$ is calculated similarly to the third-order correlator $T(X, Y, t)$; indeed, the identity

$$\partial_X \frac{\int_{-l}^{l_1} F(z, X)dz}{\int_{-l}^{l_1} F(z, X)dz} = -\partial_X \frac{\int_{-l}^{-l} F(z, X)dz}{\int_{-l}^{l_1} F(z, X)dz}$$

allows us to eliminate singularities of type (39):

$$S^{(2)}(X, X_1) = \frac{X^2 - Y^2}{2t^2}\mathcal{H}(X, t). \tag{41}$$

$S^{(1)}(X_1, X)$ and $S^{(2)}(X_1, X)$ are calculated according to the same scheme with the replacement $\Delta \longrightarrow -\Delta$. The result is such that these terms in (34) can be neglected at $\nu \longrightarrow 0$. The total expression for the four-point correlator is

$$S(X, Y, \Delta, t) \approx \frac{X(X - Y)}{t^2}\mathcal{H}(X, t), \tag{42}$$

which confirms, along with (29) and (33), that the initial fluctuation in (6) is a determining factor. It is also in agreement with formula (9) for the measure of the fluctuation.

3. CONCLUSIONS

The main results obtained in this paper are expressions (29), (33), and (42). The exponential smallness of the values of these correlation functions means that the fluctuation that determines these functions occurs rarely. The fact that the exponential parts of those expressions coincide implies the uniqueness of this fluctuation for various averages, i.e., the intermittency phenomenon.

Strictly speaking, formulas (29), (33), and (42) pertain to the initial distribution (3), which corresponds to the case when the correlators decompose. Returning to problem (1), (2), we should estimate the role of the noise ξ. For example, for the second-order correlator, the base expression is

$$\mathcal{H}(X, t) = \langle u(0, 0)\langle u(X, t)\rangle_\xi\rangle, \qquad (43)$$

where the outer averaging is carried out over the initial ensemble (3) and $\langle\ldots\rangle_\xi$ denotes the average over the noise ξ that acted on the time interval $(0, t)$. If the noise is taken into account in the framework of perturbation theory against the background of the evolving profile (6), then the correction in $\langle u(X, t)\rangle_\xi$ appears in the second order and can be easily estimated from dimensional considerations—the correlator $\langle\xi\xi\rangle$ is proportional to the temperature β^{-1}, which is reduced (without ν) to the dimensionless form in a unique fashion. The additional factor $(\beta X^3/t^2)^{-1}$ thus obtained confirms the applicability of expressions (29), (33), and (42) to solving the Burgers equation with the Langevin-type pumping (2). The viscosity that appears as a result of averaging over the noise ξ is compensated by large values of the gradients of the field $u(x, t)$ at the instant of shock formation of the optimal fluctuation.

In conclusion, we make some remarks concerning the conventional turbulent problem statement for the Burgers equation. The main results obtained up to the present time pertain to various asymptotic expressions for simultaneous distribution functions of the gradient of the velocity field u_x and to the difference of velocities $u(r, t) - u(0, t)$ [21–25]. In this case, the problem is reduced to finding an optimal fluctuation that determines the desired far [19, 21–23, 26] or intermediate [18, 24, 25] asymptotics. The decisive role is played by a large value of the argument of the distribution function or, which is the same, the number of the moment to be calculated (see [27–29] for the discussion in a more general context). The asymptotics of correlators (5) studied in this paper are determined by a large (with respect to the parameter $\beta X^3/t^2$) initial fluctuation of the velocity field. For this reason, it would be interesting to analyze this problem in the framework of the direct instanton approach [19, 27–29].

It has already been mentioned that the intermittency phenomenon is, in a certain sense, an inverse limiting case with respect to the problems that are correctly described by perturbation theory; hence, this phenomenon is important for statistical physics as a whole. However, there are only few systems for which a consistent analytical description of this phenomenon can be given. In addition to the studies mentioned above, we also cite the papers [30, 31] in which the problem of transport of a passive scalar by a turbulent flow is solved for certain limiting cases. From this point of view, explicit formulas for the asymptotics of correlation functions (5) and measure (9) seem to be very illustrative.

ACKNOWLEDGMENTS

We are grateful to V.V. Lebedev and M.V. Chertkov for numerous discussions and advice. We also thank M.G. Stepanov, G.E. Fal'kovich, and A. Fukson for useful remarks. The work of I.V.K. was supported in part by the Einstein Center at the Weizmann Institute; by the Russian Foundation for Basic Research, project no. 00-02-17652; and by a personal grant of the Russian Foundation for Support of Science.

REFERENCES

1. L. D. Landau and E. M. Lifshitz, *Course of Theoretical Physics*, Vol. 6: *Fluid Mechanics* (Nauka, Moscow, 1986; Pergamon, New York, 1987).
2. U. Frisch, *Turbulence. The Legacy of A. N. Kolmogorov* (Cambridge Univ. Press, Cambridge, 1995).
3. I. M. Lifshits, S. A. Gredeskul, and L. A. Pastur, *Introduction to the Theory of Disordered Systems* (Nauka, Moscow, 1982; Wiley, New York, 1988).
4. K. Efetov, *Supersymmetry in Disorder and Chaos* (Cambridge Univ. Press, Cambridge, 1997).
5. A. Z. Patashinskiĭ and V. L. Pokrovskiĭ, *Fluctuation Theory of Phase Transitions* (Nauka, Moscow, 1982; Pergamon, Oxford, 1979).
6. V. V. Lebedev, Pis'ma Zh. Éksp. Teor. Fiz. **70**, 675 (1999) [JETP Lett. **70**, 691 (1999)].
7. V. V. Lebedev, Phys. Rev. E **62**, 1002 (2000).
8. I. V. Kolokolov, Pis'ma Zh. Éksp. Teor. Fiz. **71**, 20 (2000) [JETP Lett. **71**, 12 (2000)].
9. J. M. Burgers, *The Nonlinear Diffusion Equation* (Reidel, Dordrecht, 1974).
10. M. Kardar, G. Parisi, and Y. Zhang, Phys. Rev. Lett. **56**, 889 (1986).
11. G. Blatter, M. V. Feigelman, V. B. Geshkenbein, *et al.*, Rev. Mod. Phys. **66**, 1125 (1994).
12. D. Forster, D. R. Nelson, and M. J. Stephen, Phys. Rev. A **16**, 732 (1977).
13. V. V. Lebedev and V. S. L'vov, Pis'ma Zh. Éksp. Teor. Fiz. **58**, 301 (1993) [JETP Lett. **58**, 310 (1993)].
14. A. M. Polyakov, *Gage Fields and Strings* (Udmurtskiĭ Univ., Izhevsk, 1999).
15. L. Frachenbourg and Ph. A. Martin, cond-mat/9905056.
16. R. Tribe and O. Zaboronski, Comm. Math. Phys. **101**, 415 (2000).
17. V. Yakhot and A. Chekhlov, Phys. Rev. Lett. **77**, 3118 (1996).

18. E. Weinan, K. Khanin, A. Mazel, and Y. Sinai, Phys. Rev. Lett. **78**, 1904 (1997).
19. E. Balkovsky, G. Falkovich, I. Kolokolov, and V. Lebedev, Phys. Rev. Lett. **78**, 1452 (1997).
20. R. P. Feynmann and A. R. Hibbs, *Quantum Mechanics and Path Integrals* (McGraw-Hill, New York, 1965).
21. M. V. Feĭgel'man, Zh. Éksp. Teor. Fiz. **79**, 1095 (1980) [Sov. Phys. JETP **52**, 555 (1980)].
22. V. Gurarie and A. Migdal, Phys. Rev. E **54**, 4908 (1996).
23. S. A. Boldyrev, Phys. Rev. E **55**, 6907 (1997).
24. T. Gotoh and R. H. Kraichnan, Phys. Fluids **10**, 2859 (1998).
25. J. Bec and U. Frisch, Phys. Rev. E **61**, 1395 (2000).
26. A. I. Chernykh and M. G. Stepanov, Phys. Rev. E **64**, 026306 (2001).
27. G. Falkovich, I. Kolokolov, V. Lebedev, and A. Migdal, Phys. Rev. E **54**, 4896 (1996).
28. M. Chertkov, Phys. Rev. E **55**, 2722 (1997).
29. E. Balkovsky and V. Lebedev, Phys. Rev. E **58**, 5776 (1998).
30. M. Chertkov, G. Falkovich, I. Kolokolov, and V. Lebedev, Phys. Rev. E **52**, 4924 (1995).
31. K. Gawedzki and A. Kupianen, Phys. Rev. Lett. **75**, 3834 (1995).

Translated by A. Klimontovich

Journal of Experimental and Theoretical Physics, Vol. 94, No. 6, 2002, pp. 1201–1215.
From Zhurnal Éksperimental'noĭ i Teoreticheskoĭ Fiziki, Vol. 121, No. 6, 2002, pp. 1399–1414.

MISCELLANEOUS

Spectra of Regular Quantum Graphs¶

Yu. Dabaghian*, R. V. Jensen, and R. Blümel
Department of Physics, Wesleyan University, Middletown, CT 06459-0155, USA
e-mail: ydabaghian@mail.wesleyan.edu
Received December 18, 2001

Abstract—We consider a class of simple quasi-one-dimensional classically nonintegrable systems that capture the essence of the periodic orbit structure of general hyperbolic nonintegrable dynamical systems. Their behavior is sufficiently simple to allow a detailed investigation of both classical and quantum regimes. Despite their classical chaoticity, these systems exhibit a "nonintegrable analogue" of the Einstein–Brillouin–Keller quantization formula that provides their spectra explicitly, state by state, by means of convergent periodic orbit expansions. © *2002 MAIK "Nauka/Interperiodica".*

1. INTRODUCTION

Very few quantum systems can be solved explicitly. Among them are the standard textbook examples, such as the harmonic oscillator or the hydrogen atom [1]. In all of these cases, the spectrum of the quantum system is obtained as an explicit analytical formula of the form $E_n = \ldots$, where n is the quantum number of the system. This procedure already fails for some of the simplest quantum systems, which are still considered elementary textbook problems. An example is a quantum particle in a box with a step potential inside, as shown in Fig. 1. Even for the simple problem in Fig. 1, explicit analytical solutions of the form "$E_n = \ldots$" are no longer available because the problem leads to a transcendental spectral equation. The recommended method of solution is either numerical or graphical [1–3]. We recently found a way [4–6] of obtaining explicit analytical solutions of a wide class of problems such as the one shown in Fig. 1, thus obtaining an explicit analytical solution of textbook problems that until now were relegated to numerical or graphical solution techniques. Our methods are also a step forward in the mathematical theory of almost periodic functions [7], because we obtain explicit formulas for the zeros of a wide class of almost periodic functions. Furthermore, the classical dynamics of the quantum systems discussed in this paper is chaotic. Because it may well be true in general that the quantized versions of classically chaotic systems do not admit the existence of quantum numbers (see, e.g., [8, 9] for a detailed discussion of this important point), our "$E_n = \ldots$" spectral formulas, containing an explicit quantum number n, may come as a surprise. At this point, we feel that it is important to stress that our results are not conjectures, approximations, or merely formal identities. Our results are exact, explicit, convergent periodic orbit expansions that can be cast into the form of mathematical theorems. We will publish the rigorous mathematical underpinnings of our results elsewhere [10].

It is well known [11] that the periodic orbit theory leads to completely different approaches for quantizing integrable and nonintegrable dynamical systems. For integrable systems, there is a simple procedure [11, 12] that allows quantizing the action variables individually for each degree of freedom. The situation is completely different for the chaotic case, where the periodic orbit theory (11) allows evaluating only certain global characteristics of the spectrum, e.g., the density of states

$$\rho(E) = \sum_{j=1}^{\infty} \delta(E - E_j) \approx \bar{\rho}(E) + \frac{1}{\pi}\mathrm{Im}\sum_{p} T_p(E) \sum_{\nu=1}^{\infty} A_p^{\nu}(E)\exp(i\nu S_p(E)), \quad (1.1)$$

typically with only semiclassical accuracy [13]. Here, $\bar{\rho}(E)$ is the average density of states; $S_p(E)$, $T_p(E)$, and $A_p(E)$ are, respectively, the action, the period, and the weight factor of the prime periodic orbit labeled by p; and ν is the repetition index. In this approach, individ-

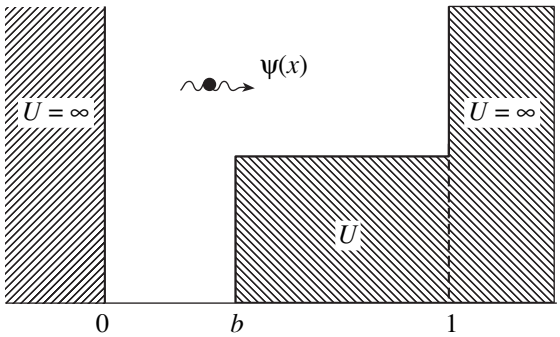

Fig. 1. Sketch of a step potential in a box, a well-known textbook quantum problem.

¶This article was submitted by the authors in English.

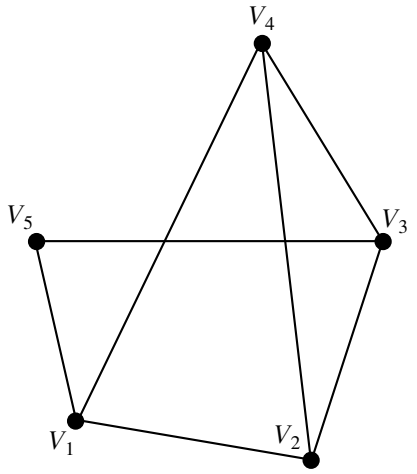

Fig. 2. Sample graph with five vertices and seven bonds.

ual energy levels are obtained indirectly as the singularities of the sum in Eq. (1.1), As for the idea of expressing them directly in terms of the periodic orbits, M.V. Berry wrote in 1991 [14]: "We do not know how, or even whether, the closed orbit sum generates the individual δ_s in the level density for chaotic systems. This is a serious—perhaps shocking—situation, because it means that we are ignorant of the mechanism of quantization."

In the case of quantum graphs, Berry's question can be answered definitely. The periodic orbit sums representing the spectral density of quantum graphs do provide the individual levels in the form of δ spikes in (1.1) and only those [15–18]. In addition, we recently showed [4–6] that the answer to Berry's question can be taken one step forward: not only do periodic orbit expansions for quantum graphs produce δ functions for the quantum states in the level density, but for certain classes of quantum graphs there also exist explicit convergent periodic orbit expansions for individual energy levels. Because they provide explicit formulas for the energy levels of classically chaotic systems, these periodic orbit expansions may be considered as "nonintegrable analogues" of the Einstein–Brillouin–Keller (EBK) quantization formula [11, 12] that applies to integrable systems.

This paper is organized as follows. In Section 2, we briefly review the theory of quantum graphs and extend the theory by defining "dressed graphs," i.e., quantum graphs with arbitrary potentials on their bonds. In Section 3, we define an important class of dressed quantum graphs: regular quantum graphs. Based on a detailed study of their spectral properties in Section 3, we derive explicit analytical spectral formulas for regular quantum graphs in Section 4. In Section 5, we present a variety of regular quantum graphs illustrating the use and convergence of the spectral formulas. In Section 6, we summarize our results and conclude the paper.

2. DYNAMICAL NETWORKS

We consider a particle moving on a quasi-one-dimensional network of bonds and vertices. These networks are known as graphs in the mathematical literature. They were and still are the subject of intensive investigations in all areas of science ranging from mathematics over computer science to chemistry and physics. An example of a simple graph with five vertices and seven bonds is shown in Fig. 2. The particle scatters randomly at every vertex V_i along different bonds B_{ij} that meet at that vertex. We assume that the graph contains a finite number of bonds and vertices (N_B and N_V, respectively). The key assumption about the dynamics of the particle is that the turning points of any particle trajectory on the graph coincide with the vertices of the graph, and the shape of the trajectories is therefore uniquely determined by the geometry of the graph. The trajectories of the particle are simply the joint sequences of graph bonds, which are easily described and enumerated. For instance, every trajectory can be represented by a sequence of N_B symbols, each of which corresponds to a certain bond [19]. Because the trajectories correspond to various bond sequences, every trajectory is described by a code word consisting of N_B symbols.

We "dress" the bonds B_{ij} of the graph with potentials $U_{ij}(x)$, which may affect the way a particle moves along the bonds. However, it is required that these dressings do not violate the geometry of the particle trajectories, i.e., do not add turning points other than the original vertices of the graph. This condition is required to hold at all energies. To comply with this requirement, the bond potentials are allowed to depend on the energy E of the particle, i.e., $U_{ij} = U_{ij}(x, E)$, such that $E > U_{ij}(x, E)$ is fulfilled for all E and all i, j. This in fact leads to many additional simplifications that have a deep physical meaning in the context of the semiclassical periodic orbit theory [4–6, 19–21].

The shapes of the trajectories (and, in particular, of the periodic orbits) become increasingly complicated as their lengths grow. This makes them similar to the generic (dynamical) chaotic systems. In fact, the number of possible periodic orbits increases exponentially with their lengths (or, equivalently, the number of vertex scatterings), with a rate which depends only on the topology of the graph. Every graph Γ can be characterized by its topological entropy (the global average rate of the exponential proliferation of periodic orbits)

$$\Lambda_\Gamma = \lim_{l\to\infty} \frac{\ln[\#(l)]}{l}, \tag{2.1}$$

where l characterizes the lengths of the periodic orbits in terms of the lengths of their code words and $\#(l)$ is the total number of periodic orbits of the length $\le l$ [9]. Because the phase space of the system is bounded, the dynamics of the particle is mixing [16], and hence, the structure of the periodic orbit set on dynamical net-

works closely imitates the behavior of the closed trajectories of generic chaotic systems [22, 23]. On the other hand, dynamical networks can be easily quantized [4–6, 17–19, 24], which makes them very convenient models for studying various aspects of quantum chaology.

The details of the classical dynamics on graphs are discussed in numerous publications [16, 25]. Below, we investigate the quantum-mechanical description of these systems. In particular, we discuss their spectra in the context of the periodic orbit theory. We now briefly outline some details of the graph quantization procedure that are used in the subsequent discussion.

A quantum graph system is a quantum particle that moves on a one-dimensional network Γ dressed with the potentials $U_{ij}(x, E)$. Below, we consider the case of scaling potentials discussed in [6, 26-28],

$$U_{ij}(E) = \lambda_{ij}E, \quad \lambda_{ij} = \lambda_{ji}, \tag{2.2}$$

where λ_{ij} are constants. This choice of the dressing potentials allows us to avoid certain mathematical complications, which are irrelevant for the physical context of our discussion. For more details on scaling potentials and their relevance to the semiclassical periodic orbit analysis, see [4, 6, 19].

The Schrödinger equation for graphs with potentials (2.2) can be written as

$$\hat{\pi}_{ij}^2\psi_{ij}(x) = \beta_{ij}^2 E\psi_{ij}(x), \tag{2.3}$$

where

$$\hat{\pi}_{ij} = -i\frac{d}{dx} - A_{ij} \tag{2.4}$$

is the generalized momentum operator and

$$\beta_{ij}^2 = 1 - \lambda_{ij}.$$

The coordinate $0 \le x \le L_{ij}$ is measured along B_{ij} from i to j, and $L_{ij} = L_{ji}$ is the length of the bond. The magnetic field vector potential $A_{ij} = -A_{ji}$ is assumed to be a constant real matrix; it can be used as a tool for breaking the time-reversal symmetry.

Classically, the particle can travel along the bond B_{ij} if its energy is above the scaled potential height, $E > U_{ij}(E)$ ($\lambda_{ij} < 1$). In this case, the solution to Eq. (2.3) on the bond B_{ij} is a combination of free waves,

$$\psi_{ij}(x) = a_{ij}\frac{\exp(i(-\beta_{ij}k + A_{ij})x)}{\sqrt{\beta_{ij}k}} + b_{ij}\frac{\exp(i(\beta_{ij}k + A_{ij})x)}{\sqrt{\beta_{ij}k}}, \tag{2.5}$$

where $k = \sqrt{E}$ and the factors $(\beta_{ij}k)^{-1/2}$ are introduced to separate the physically meaningful flux amplitudes from the coefficients a_{ij} and b_{ij}. In the opposite case where $\lambda_{ij} > 1$, the bond B_{ij} carries a linear combination of tunneling solutions. Due to the scaling assumption, there is no transition between these two cases as a function of E. From now on, we assume that the energy E is kept above the maximum scaled potential height,

$$\lambda_{ij} < 1, \quad i, j = 1, \ldots, N_V. \tag{2.6}$$

At every vertex V_i, the bond wave functions satisfy the boundary conditions

$$\psi_{ij}(x = 0) = \varphi_i C_{ij}, \qquad \sum_{j=1}^{N_V} C_{ij}\hat{\pi}_{ij}\psi_{ij}(x)\big|_{x=0} = -i\lambda_i\varphi_i \tag{2.7}$$

for all $i, j = 1, \ldots, N_V$. Here, C_{ij} is the connectivity matrix of the graph; φ_i is the value of the wave function at the vertex V_i; and λ_i are free parameters of the problem, scaled as $\lambda_i = \lambda_i^0 k$ (see the Appendix). We note that the double-indexed scaling constants λ_{ij} refer to the bonds, whereas the single-indexed constants λ_i refer to the scattering strengths at the vertices. We believe that this notation is natural and does not lead to confusion.

Conditions (2.7) are consistent only for a discrete set of energy levels $E_n = k_n^2$ that define the spectrum of the dressed quantum graph problem (2.3) and (2.7). As shown in [6, 16–18, 24] (see the Appendix), using the scattering quantization approach [29] allows one to obtain the spectral equation for any quantum graph problem in the form

$$\Delta(k) = \det[1 - S(k)] = 0, \tag{2.8}$$

where $S(k)$ is the finite unitary graph scattering matrix [16]. The indices that define the matrix elements S_{IJ} of the matrix S correspond to the graph bonds. It is important that the bond $B_I \equiv B_{ij}$ is considered to be different from the (geometrically identical) reversed bond $B_{I'} \equiv B_{ji}$; the bonds of the graph are therefore directed [4–6, 16, 18]. Hence, the dimensionality of the scattering matrix is $2N_B \times 2N_B$. It is shown in the Appendix that $S = TD(k)$, where T is a constant $2N_B \times 2N_B$ unitary matrix and D is the diagonal unitary matrix with the matrix elements

$$D_{IJ} = \delta_{IJ}\exp(i(\beta_I k + A_I)L_I), \quad I = 1, \ldots, 2N_B. \tag{2.9}$$

Because $\Delta(k)$ is a complex function, it is convenient to define the spectrum via the zeros of its absolute value,

$$|\Delta(k)| = \exp(-i\Theta_0(k))\Delta(k), \tag{2.10}$$

where $\Theta_0(k)$ is the complex phase of $\Delta(k)$. The logarithmic derivative of $|\Delta(k)|$ produces a delta peak for each of its roots,

$$-\frac{1}{\pi}\mathrm{Im}\lim_{\epsilon\to 0}\frac{d}{dk}\ln|\det[1-S(k+i\epsilon)]| = \sum_{n=1}^{\infty}\delta(k-k_n), \tag{2.11}$$

which, by definition, is the density of the momentum states $\rho(k)$ [6]. On the other hand, using (2.10) and expanding the logarithm of determinant (2.8), the density of states can be written as

$$\rho(k) = \frac{1}{\pi}\frac{d\Theta_0(k)}{dk} + \frac{1}{\pi}\mathrm{Im}\frac{d}{dk}\sum_{n=1}^{\infty}\frac{1}{n}\mathrm{Tr}[S(k)]^n. \tag{2.12}$$

It can then be easily seen from the structure of the scattering matrix S [16, 24] that the matrix elements of its nth power are defined on connected sequences of n bonds and the trace of S^n generates terms defined on closed connected sequences of n bonds [6, 17, 24, 25].

These periodic connected sequences of n bonds B_{ij} can be viewed as the periodic orbits traced by a classical point particle moving on the graph. We note that the phase of the exponential in (2.9) is exactly the action of a classical point particle trajectory traversing the bond B_I,

$$\mathcal{S}_I = \int_{B_I}(\beta_I k + A_I)dx = (\beta_I k + A_I)L_I. \tag{2.13}$$

Therefore, the semiclassical transition amplitudes $\exp(i\mathcal{S}_I)$ between the vertices connected by the bond B_I determine the scattering matrix $S(k)$. As a consequence [4–6, 16, 19], the "closed bond sequence expansion" (2.12) can be explicitly written as a periodic orbit expansion in terms of phases (2.13),

$$\rho(k) = \bar{\rho}(k) + \frac{1}{\pi}\mathrm{Re}\sum_p S_p^0\sum_{\nu=1}^{\infty}A_p^{\nu}\exp(i\nu S_p^0 k), \tag{2.14}$$

where S_p^0 is the k-independent "action length" of the orbit p,

$$S_p = \sum_p \beta_{ij}L_{ij}k \equiv S_p^0 k, \tag{2.15}$$

and A_p is its weight containing the constant factor $\exp(i\sum_p A_{ij}L_{ij})$. Because of the scaling assumption (see the Appendix), the weight factor A_p is k-independent. The first term in this expression corresponds to the average density of states of the momentum $\bar{\rho}(k)$,

$$\bar{\rho}(k) = \frac{1}{\pi}\frac{d\Theta_0(k)}{dk}, \tag{2.16}$$

while the periodic orbit sum in (2.14) describes the fluctuations around the average.

The periodic orbit expansion for the staircase function

$$N(k) = \sum_{n=1}^{\infty}\Theta(k-k_n) \tag{2.17}$$

can be obtained by direct integration of (2.11) and (2.14). We obtain

$$N(k) = \bar{N}(k) + \tilde{N}(k), \tag{2.18}$$

where the first term

$$\bar{N}(k) = \int_0^k \bar{\rho}(k')dk' + \bar{N}(0) \tag{2.19}$$

represents the average behavior of the staircase function and

$$\tilde{N}(k) = \mathrm{Im}\frac{1}{\pi}\sum_p\sum_{\nu=1}^{\infty}\frac{A_p^{\nu}}{\nu}\exp(i\nu S_p^0 k) \tag{2.20}$$

describes zero-mean oscillations around the average.

As discussed in the Introduction (see also [4–6, 16, 25]), quantum graphs are chaotic in the classical limit. The classical scattering probabilities are obtained in the limit as $\hbar \longrightarrow 0$ from the quantum mechanical transition amplitudes [4–6] (see the Appendix). In the scaling case, they are k-independent, and therefore, the quantum scattering amplitudes do not depend on $\hbar$ at all. They determine the quantum and the classical scattering probabilities simultaneously.

3. REGULAR GRAPHS AND THEIR SPECTRA

The spectral determinant is a polynomial of degree $2N_B$ of the matrix elements of S. It was shown in [6] that the total phase of this polynomial is

$$\Theta_0(k) = \frac{1}{2}\mathrm{Im}\ln\det S(k) = kS_0 - \pi\gamma_0, \tag{3.1}$$

where

$$S_0 = \sum_{(ij)}L_{ij}\beta_{ij}$$

is the total action length of the graph Γ and

$$\gamma_0 = \frac{N_B + N_V}{2} + \frac{1}{\pi}\sum_{i=1}^{N_V}\arctan\left(\frac{\lambda_i^0}{\nu_i}\right), \tag{3.2}$$

where

$$\nu_i = \sum_j C_{ij}\beta_{ij}. \tag{3.3}$$

The average density of states is therefore a constant,

$$\bar{\rho} = \frac{1}{\pi}\frac{d}{dk}\Theta_0(k) = \frac{S_0}{\pi}, \tag{3.4}$$

and the average staircase function in Eq. (2.19) is

$$\bar{N}(k) = \frac{S_0}{\pi}k + \bar{N}(0). \tag{3.5}$$

The spectral equation $|\Delta(k)| = 0$ can be written as

$$\cos(S_0 k - \pi\gamma_0) = \sum_{i=1}^{N_\Gamma} a_i \cos(S_i k - \pi\gamma_i), \tag{3.6}$$

where the frequencies $S_i < S_0$ are combinations of the reduced classical actions $S_{ij}^0 = \beta_{ij}L_{ij}$, and γ_0, γ_i are constants. The number N_Γ of terms in (3.6) is bounded by $N_\Gamma \le 3^{N_B}$ [6].

The frequency S_0 in $\Theta_0(k)$ is the largest frequency in expansion (3.6). While it is the only characteristic of the graph contained on the left-hand side of (3.6), the right-hand side,

$$\Phi(k) \equiv \sum_{i=1}^{N_\Gamma} a_i \cos(S_i k - \pi\gamma_i), \tag{3.7}$$

contains the complete information about the graph system. We call $\Phi(k)$ the characteristic function of the graph.

A graph Γ is called regular [4–6] if its characteristic function $\Phi(k)$ satisfies

$$\sum_{i=1}^{N_\Gamma} |a_i| \equiv \alpha < 1. \tag{3.8}$$

For regular graphs, spectral equation (3.6) can be solved formally [4–6] to yield the implicit equation of its eigenvalues,

$$k_n = \frac{\pi}{S_0}[n + \mu + \gamma_0] + \frac{1}{S_0} \times \begin{cases} \arccos[\Phi(k_n)] & \text{for } n+\mu \text{ even}, \\ \pi - \arccos[\Phi(k_n)] & \text{for } n+\mu \text{ odd}, \end{cases} \tag{3.9}$$

where μ is a fixed integer chosen such that k_1 is the first positive solution of (3.6). The index $n \in \mathbb{N}$ labels the roots of (3.6) in their natural order.

The implicit form of Eq. (3.9) immediately implies that, because the second term in (3.9) is bounded by π/S_0, the deviations of solutions to this equation from the points

$$\hat{k}_n = \frac{\pi}{S_0}(n + \mu + \gamma_0 + 1) \tag{3.10}$$

never exceed π/S_0 in absolute value for any n. The quantities $\hat{k}_n$ are very important in what follows because they determine the root structure of (3.6).

The roots k_n can be decomposed into an average part $\bar{k}_n$ and a fluctuating part $\tilde{k}_n$. From (3.9), we obtain

$$k_n = \bar{k}_n + \tilde{k}_n, \tag{3.11}$$

where

$$\bar{k}_n = \frac{\pi}{S_0}\left[n + \mu + \gamma_0 + \frac{1}{2}\right], \tag{3.12}$$

and

$$\tilde{k}_n = \frac{(-1)^{n+\mu}}{S_0}\left\{\arccos[\Phi(k_n)] - \frac{\pi}{2}\right\}. \tag{3.13}$$

We note that the constant $\mu + \gamma_0$ can be related to the initial value $\bar{N}(0)$ of the average staircase function (3.5). We now consider the integral

$$\lim_{n\to\infty} \frac{1}{\hat{k}_n}\int_0^{\hat{k}_n} N(k')dk'. \tag{3.14}$$

The integration in (3.14) can be easily performed because the function $N(k)$ has simple form (2.17),

$$\frac{1}{\hat{k}_n}\int_0^{\hat{k}_n} N(k')dk' = n - \frac{1}{\hat{k}_n}\sum_{i=1}^{n} k_i, \tag{3.15}$$

since there are n roots to the left of $\hat{k}_n$. The fluctuations of both $N(k)$ and k_n around their average values have zero mean, and in the limit of $n \gg 1$ we can therefore use $\bar{N}(k)$ and $\bar{k}_n$ instead of $N(k)$ and k_n in (3.15) and write

$$\frac{1}{\hat{k}_n}\int_0^{\hat{k}_n} \bar{N}(k')dk' = n - \frac{1}{\hat{k}_n}\sum_{i=1}^{n} \bar{k}_i, \quad n \gg 1. \tag{3.16}$$

Using the explicit forms of $\hat{k}_n$, $\bar{k}_n$, and $\bar{N}(k)$, we obtain

$$\bar{N}(0) + \frac{1}{2}(n + \mu + \gamma_0 + 1) = \frac{n}{n + \mu + \gamma_0 + 1}\left(\frac{n}{2} + \mu + \gamma_0 + 1\right). \tag{3.17}$$

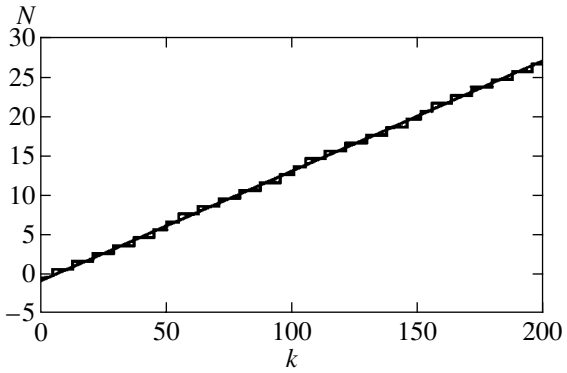

Fig. 3. The exact spectral staircase function $N(k)$ and its average $\bar{N}(k)$ for the scaling step potential shown in Fig. 1 with $b = 0.3$ and $\lambda = 1/2$. The average $\bar{N}(k)$ crosses every "stair" of $N(k)$ (piercing average) at the equally spaced separating points $\hat{k}_n$.

Expanding the right-hand side and keeping terms up to the order $1/n$ yields

$$\bar{N}(0) + \frac{1}{2}(n + \mu + \gamma_0 + 1) = n - \left(1 - \frac{\mu + \gamma_0 + 1}{n}\right)\left(\frac{n}{2} + \mu + \gamma_0 + 1\right). \quad (3.18)$$

The terms proportional to n cancel. Comparing the constants in (3.18) yields

$$\bar{N}(0) = -(\mu + \gamma_0 + 1). \quad (3.19)$$

It can be verified by direct substitution that

$$\bar{N}(\hat{k}_n) = n, \quad (3.20)$$

which implies that function (3.10) is the inverse of average staircase function (3.5). The points $\hat{k}_n$ can also be viewed as the intersection points of staircase function (2.17) and its average (3.5),

$$\bar{N}(\hat{k}_n) = N(\hat{k}_n) = n, \quad (3.21)$$

and hence, the fluctuations $\tilde{N}(k)$ of the spectral staircase vanish at the points $\hat{k}_n$,

$$\tilde{N}(\hat{k}_n) = \mathrm{Im}\frac{1}{\pi}\sum_p \sum_{\nu=1}^{\infty} \frac{A_p^\nu}{\nu}\exp(i\nu S_p^0 \hat{k}_n) = 0. \quad (3.22)$$

Geometrically, Eq. (3.22) means that the average staircase function $\bar{N}(k)$ intersects every step of the staircase function $N(k)$. We therefore call $\bar{N}(k)$ the piercing average. This is illustrated in Fig. 3, which shows the spectral staircase function $N(k)$ for the scaling step potential shown in Fig. 1 and discussed in more detail in Section 5, example 1, below. We used the parameters $\lambda = 1/2$ and $b = 0.3$. Also shown is the average staircase $\bar{N}(k)$ for this case. It clearly pierces all the steps of $N(k)$, providing an example of a system with a piercing average.

Because $\Phi(k)$ contains only frequencies smaller than S_0, every open interval $I_n = (\hat{k}_{n-1}, \hat{k}_n)$ contains only one root of (3.6), namely k_n, and therefore, $\hat{k}_n$ play the role of separating points between adjacent roots [4–6, 10]. Moreover, because of (3.8), the "allowed zones" $R_n \subset I_n$ where the roots k_n can be found narrow to

$$k_n \in R_n \equiv \left(\frac{\pi}{S_0}(n + \mu + \gamma_0 + u), \frac{\pi}{S_0}(n + \mu + \gamma_0 + 1 - u)\right), \quad (3.23)$$

where $u = \arccos\alpha/S_0$. Correspondingly, there are forbidden regions F_n,

$$F_n \equiv \left(\frac{\pi}{S_0}(n + \mu + \gamma_0 - u), \frac{\pi}{S_0}(n + \mu + \gamma_0 + 1 + u)\right), \quad (3.24)$$

where roots of (3.6) never appear. In the limit as $\alpha \longrightarrow 1$ ($u \longrightarrow 0$), the allowed zones R_n tend to occupy the entire root interval, $R_n \longrightarrow I_n$.

4. SPECTRAL FORMULAS

Once the existence of separating points $\hat{k}_n$ has been established, it is possible to obtain an exact periodic orbit expansion separately for every root of (2.8). The derivation is based on the identity

$$k_n = \int_{\hat{k}_{n-1}}^{\hat{k}_n} k\rho(k)dk. \quad (4.1)$$

Substituting exact periodic orbit expansion (2.14) for $\rho(k)$ in (4.1) yields

$$k_n = \int_{\hat{k}_{n-1}}^{\hat{k}_n} k\frac{S_0}{\pi}dk + \frac{1}{\pi}\int_{\hat{k}_{n-1}}^{\hat{k}_n} k\,\mathrm{Re}\sum_p S_p^0 \sum_{\nu=1}^{\infty} A_p^\nu \exp(i\nu S_p^0 k)dk = \frac{\pi}{S_0}\left(n + \mu + \gamma_0 + \frac{1}{2}\right) + \hat{k}_n \mathrm{Im}\frac{1}{\pi}\sum_p \sum_{\nu=1}^{\infty}\frac{A_p^\nu}{\nu}\exp(i\nu S_p^0 \hat{k}_n) - \hat{k}_{n-1}\mathrm{Im}\frac{1}{\pi}\sum_p \sum_{\nu=1}^{\infty}\frac{A_p^\nu}{\nu}\exp(i\nu S_p^0 \hat{k}_{n-1}) + \mathrm{Re}\frac{1}{\pi}\sum_p \frac{1}{S_p^0} \quad (4.2)$$

$$\times \sum_{\nu=1}^{\infty} \frac{A_p^\nu}{\nu^2} (\exp(i\nu S_p^0 \hat{k}_n) - \exp(i\nu S_p^0 \hat{k}_{n-1})).$$

Using (3.22), we simplify (4.2) to

$$k_n = \frac{\pi}{S_0}\left(n + \mu + \gamma_0 + \frac{1}{2}\right) - \frac{1}{\pi}\mathrm{Im}\sum_p \frac{2}{S_p^0}\sum_{\nu=1}^{\infty}\frac{A_p^\nu}{\nu^2}\sin\left[\frac{\nu\omega_p}{2}\right] \times \exp\left[i\nu\omega_p\left(n + \mu + \gamma_0 + \frac{1}{2}\right)\right], \quad (4.3)$$

where $\omega_p = \pi S_p^0/S_0$. The series expansion for k_n in Eq. (4.3) is more than a formal identity. It is rigorously convergent; however, it converges only conditionally, which means that the result of the summation depends on how the summation is performed. Indeed, according to the well-known Riemann reordering theorem, one can obtain any result by rearranging the terms of a conditionally convergent series [30]. For the proper convergence of (4.3) to the exact roots of spectral equation (3.6), we must therefore specify how the terms in (4.3) are to be summed.

The mathematical details of the convergence properties of (4.3) are presented in [10]. We mention here the main result, which states that the terms in (4.3) must be summed according to the length of the symbolic codes [6, 19] of the periodic orbits, and not according to their action lengths. If (4.3) is summed in this way, it not only converges, but also converges to the exact roots k_n of spectral equation (3.6).

Equation (4.3) therefore provides an explicit representation of the roots of spectral equation (2.8) in terms of the geometric characteristics of the graph. In accordance with (3.12), the first term in (4.3) is the average value $\bar{k}_n$ and the following periodic orbit sum is an explicit expression for the fluctuation of the root $\tilde{k}_n$. This method is not limited to obtaining explicit analytical periodic orbit expansions for k_n. In fact, using the identity

$$f(k_n) = \int_{\hat{k}_{n-1}}^{\hat{k}_n} f(k)\rho(k)dk, \quad (4.4)$$

we can obtain periodic orbit expansions for any function of the eigenvalues $f(k_n)$, for instance, for the energy $E = k^2$.

In the simplest case where $\lambda_i^0 = 0$, $A_{ij} = 0$, and $\mathrm{Im}A_p = 0$, we have

$$k_n = \frac{\pi}{S_0}n - \frac{2}{\pi}\sum_p \frac{1}{S_p^0}\sum_{\nu=1}^{\infty}\frac{A_p^\nu}{\nu^2}\sin\left(\frac{1}{2}\nu\omega_p\right)\sin(\nu\omega_p n). \quad (4.5)$$

We note that $k_{-n} = -k_n$ in this case.

Both the EBK theory and formula (4.3) allow us to compute energy eigenvalues explicitly. In this sense, formula (4.3) may be regarded as an analogue of the EBK quantization formula [11, 12] for a chaotic system. The complexity of this expansion, structurally similar to (1.1), reflects the geometrical complexity of the periodic orbit set for graph systems.

Finally, for explicit calculations (see Section 5), it remains to determine the explicit form of the expansion coefficients A_p. For some simple graphs, this was done in [16, 19]. In the Appendix, we solve the problem for general dressed graphs. We show that every passage of an orbit p from a bond B_{ij} to $B_{ij'}$ through a vertex V_i contributes a factor $\sigma_{ji,ij'}$ (a matrix element of the matrix T—see the Appendix) to the weight A_p of the orbit,

$$A_p = \prod \sigma_{jj'}^{(i)}, \quad (4.6)$$

where the product is taken over the sequence of the bonds traced by the orbit p.

5. EXAMPLES

In (3.8), we provided the definition of regular quantum graphs; in (3.9)–(3.24), we then discussed analytical properties of their spectra. The discussion of regular quantum graphs culminated in Section 4 with the derivation of explicit spectral formulas for individual quantum states of regular quantum graphs. However, the above definition of regular quantum graphs does not imply that regular quantum graphs actually exist. Examples 1–3, discussed below, provide specific instances of quantum graphs that are regular for all choices of their parameters. Examples 4 and 5 present quantum graphs that exhibit both regular and irregular regimes. Finally, Examples 6 and 7 provide illustrations of a new class of quantum graphs, marginal quantum graphs, for which

$$\sum_{i=1}^{N_\Gamma} |a_i| = 1.$$

Except for special choices of their dressing potentials, these graphs can still be accommodated within the mathematical framework set up in Sections 3 and 4 and also admit an explicit representation of their spectra in accordance with the spectral formulas derived in Section 4.

Example 1: Scaling step potential in a box. We consider a particle confined to a box $0 < x < 1$ containing the scaling step potential (see Figs. 1 and 4a)

$$U(x) = \begin{cases} 0 & \text{for} \quad 0 < x \le b, \\ \lambda_{23}E & \text{for} \quad b < x < 1. \end{cases} \quad (5.1)$$

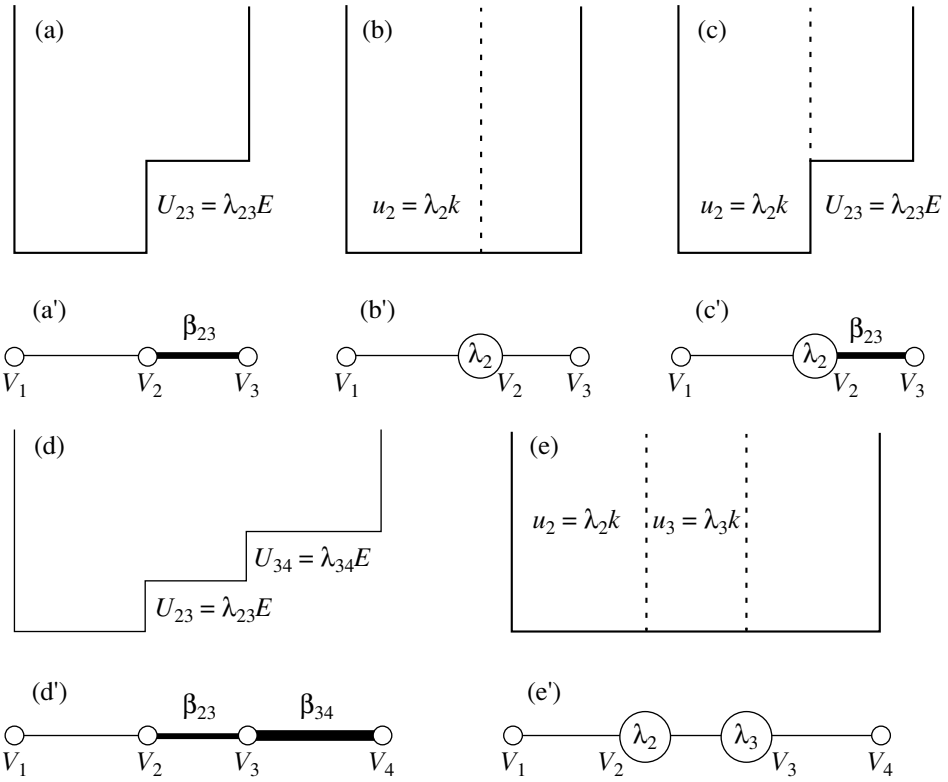

Fig. 4. Collection of potentials and their associated linear quantum graphs that serve as examples to illustrate the concept of regular quantum graphs. (a) Scaling step potential in a box and its associated three-vertex linear graph (a'). (b) Scaling δ function in a box and its corresponding three-vertex linear graph (b'). Combined scaling δ function and step potential in a box (c) with its linear three-vertex quantum graph (c'). Two scaling steps (d) and two scaling δ functions (e) in a box together with their associated four-vertex dressed linear quantum graphs (d') and (e'), respectively.

This is equivalent to a three-vertex linear chain graph (Fig. 4a') with $\lambda_2 = 0$, $A_{ij} = 0$, and the Dirichlet boundary conditions at V_1 and V_3. This example is also discussed in [4, 5, 6, 19, 31]. In this case, spectral equation (3.6) can be written as [4, 5]

$$\sin[k(S_{21}^0 + S_{23}^0)] = r\sin[k(S_{21}^0 - S_{23}^0)], \qquad (5.2)$$

where

$$r = \frac{1-\beta_{23}}{1+\beta_{23}} < 1 \qquad (5.3)$$

is the reflection coefficient at the vertex V_2. Regularity condition (3.8) is therefore automatically satisfied and this graph is always regular. In Section 4, we already discussed the convergence properties of (4.3), including the fact that a rigorous mathematical proof for the convergence of (4.3) exists [10]. Here, we present solid numerical evidence for the convergence of (4.3) in the context of scaling step potential (5.1). As discussed in [4, 5, 6, 19], every periodic orbit in potential (5.1) can be described by a binary code word. Figure 5 shows the relative error

$$\epsilon_n^{(l)} = \frac{\left|k_n^{(l)} - k_n\right|}{k_n}, \quad n = 1, 10, 100,$$

of the result $k_n^{(l)}$ predicted by (4.3) compared to the numerically obtained exact result k_n as a function of the

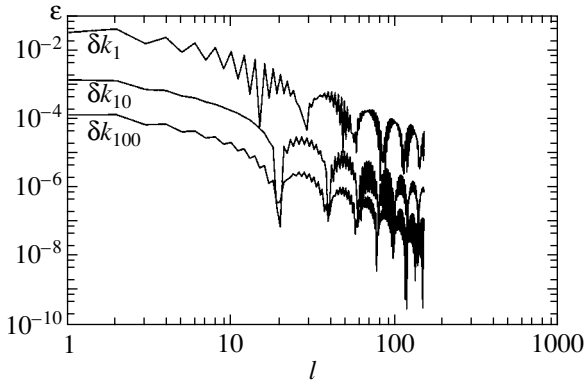

Fig. 5. Comparison between the exact eigenvalues k_n and the k_n values computed via (4.3) for the scaling step potential in Fig. 1. Shown is the relative error $\epsilon_n^{(l)} = \left|k_n^{(l)} - k_n\right|/k_n$, $n = 1, 10, 100$, of the result $k_n^{(l)}$ predicted by (4.3) compared to the numerically obtained exact result k_n as a function of the binary code length l of the orbits used in expansion (4.3). We used $b = 0.3$ and $\lambda = 1/2$.

binary code length l of the orbits used in expansion (4.3). We used $b = 0.3$ and $\lambda = 1/2$. Figure 5 also demonstrates that, using all periodic orbits up to the binary code length $l \sim 150$, we obtain an accuracy on the order 10^{-4}–10^{-7} for the roots k_n of (5.2). Although the convergence of the series is slow (according to Fig. 5, it is approximately of the order $1/l^2$ on average), one can obtain a sufficiently good estimate for the roots using all orbits of the code length 20 and smaller.

Example 2: Scaling δ function in a box. This potential, shown in Fig. 4b, is again equivalent to a three-vertex quantum graph. This time, however, the potentials on the bonds are identically zero, whereas the vertex V_2 is dressed with a scaling δ function of strength

$$\lambda_2 = \lambda_2^0 k > 0.$$

We apply the Dirichlet boundary conditions at the open ends. In this case, spectral equation (3.6) becomes

$$\cos[k(S_{21}^0 + S_{23}^0) - \pi\gamma_0] = -|r|\cos[k(S_{21}^0 - S_{23}^0)], \quad (5.4)$$

where

$$\gamma_0 = 1 - \frac{1}{\pi}\arcsin\left(\frac{2}{\sqrt{4 + (\lambda_2^0)^2}}\right) \quad (5.5)$$

and the reflection coefficient r is given by

$$r = \frac{\lambda_2^0}{2i - \lambda_2^0}. \quad (5.6)$$

Because $|r| < 1$, the characteristic function of (5.4) also satisfies regularity condition (3.8). Therefore, the scaling δ function in a box is another example of a regular quantum graph.

Example 3: Combined scaling step and scaling δ-potential in a box (Fig. 4c). This is equivalent to a three-vertex dressed linear graph (Fig. 4c') with $\lambda_2 = \lambda_2^0 k > 0$. Spectral equation (3.6) then becomes

$$\begin{aligned}&\cos[k(S_{21}^0 + S_{23}^0) - \pi\gamma_0] \\ &= a_1\cos[k(S_{21}^0 - S_{23}^0) - \pi\gamma_1],\end{aligned} \quad (5.7)$$

where

$$\begin{aligned}\gamma_0 &= 1 - \frac{1}{\pi}\arcsin\left(\frac{\beta_{12} + \beta_{23}}{\sqrt{(\beta_{12} + \beta_{23})^2 + (\lambda_2^0)^2}}\right), \\ \gamma_1 &= 1 - \frac{1}{\pi}\arcsin\left(\frac{\beta_{12} - \beta_{23}}{\sqrt{(\beta_{12} - \beta_{23})^2 + (\lambda_2^0)^2}}\right),\end{aligned} \quad (5.8)$$

and the coefficient a_1 is

$$a_1 = \sqrt{\frac{(\beta_{21} - \beta_{23})^2 + (\lambda_2^0)^2}{(\beta_{21} + \beta_{23})^2 + (\lambda_2^0)^2}} < 1. \quad (5.9)$$

Therefore, the characteristic function of (5.7) once again satisfies the regularity condition for any linear three-vertex graph with nontrivial bond potentials $\beta_{21}^2 + \beta_{23}^2 \neq 0$ [6].

Quantum graphs that are regular for all of their parameter values are quite exceptional. In general, quantum graphs may have a regular regime for a certain range of the parameter values or the regular regime may not exist at all. The following example illustrates this point.

Example 4: Two scaling steps in a box (Fig. 4d). As an example of a graph that has both a regular and an irregular regime, we consider a quantum particle in a box with two scaling steps (Fig. 4), which is equivalent to the four-vertex linear graph shown in Fig. 4d'. Because there are no δ functions present, we have $\lambda_2 = \lambda_3 = 0$. We assume the Dirichlet boundary conditions at the dead ends of this graph. In this case, spectral equation (3.6) is given by

$$\begin{aligned}\sin(S_0 k) &= -r_2\sin(kS_1) \\ &- r_2 r_3\sin(kS_2) + r_3\sin(kS_3),\end{aligned} \quad (5.10)$$

where

$$\begin{aligned}S_0 &= S_{21}^0 + S_{23}^0 + S_{34}^0, \quad S_1 = S_{23}^0 + S_{34}^0 - S_{21}^0, \\ S_2 &= S_{21}^0 + S_{34}^0 - S_{23}^0, \quad S_3 = S_{21}^0 + S_{23}^0 - S_{34}^0,\end{aligned} \quad (5.11)$$

and

$$r_2 = \frac{\beta_{12} - \beta_{23}}{\beta_{12} + \beta_{23}}, \quad r_3 = \frac{\beta_{23} - \beta_{34}}{\beta_{23} + \beta_{34}} \quad (5.12)$$

are the reflection coefficients at the corresponding vertices V_i. For

$$|r_3| + |r_2 r_3| + |r_2| < 1, \quad (5.13)$$

the four-vertex linear graph (Figs. 4d' and 6a) is regular. Regularity condition (5.13) is fulfilled in a diamond-shaped region of the (r_2, r_3) parameter space shown as the shaded area in Fig. 6b. The difference between the regular and the irregular regimes is clearly reflected in the staircase functions. Figure 7a shows the staircase function $N(k)$ together with the average staircase $\bar{N}(k)$ in the regular regime for the parameter combination $r_2 = 0.2$ and $r_3 = 0.3$. The piercing-average condition is clearly satisfied. Figure 7b shows the staircase function $N(k)$ together with the average staircase $\bar{N}(k)$ in the irregular regime for the parameter combination $r_2 = 0.98$ and $r_3 = 0.99$. In this case, the piercing-average condition is clearly violated, consistently with the irregular nature of this regime.

Example 5: Two scaling δ functions in a box (Fig. 4e). This potential is equivalent to the four-vertex graph shown in Fig. 4e' with

$$\lambda_2 = \lambda_2^0 k > 0, \quad \lambda_3 = \lambda_3^0 k > 0,$$

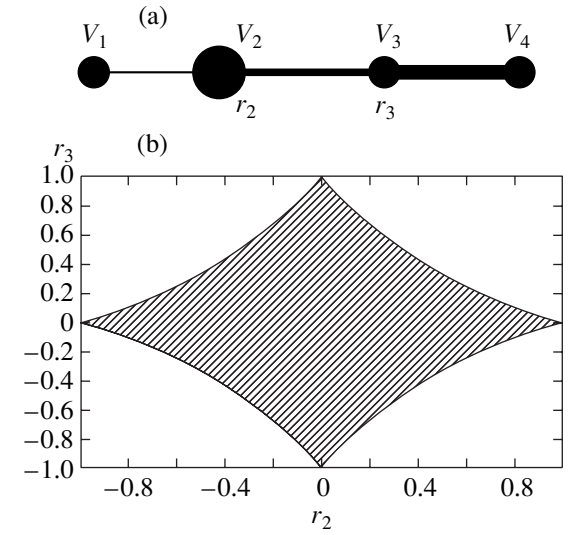

Fig. 6. Four-vertex linear chain graph (a) and the corresponding space (r_2, r_3) of reflection coefficients (b). The shaded region in the (r_2, r_3) space corresponds to the regular regime of the quantum graph shown in (a). This demonstrates that the subset of regular quantum graphs within the set of all four-vertex linear quantum graphs is nonempty and has a finite measure.

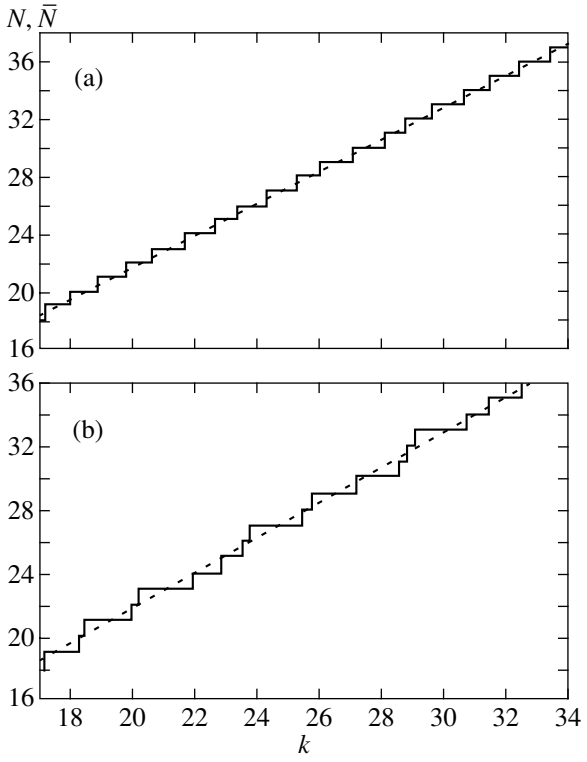

Fig. 7. The exact spectral staircase function $N(k)$ and its average $\bar{N}(k)$ for the regular $r_2 = 0.2$, $r_3 = 0.3$ (a) and the irregular $r_2 = 0.98$, $r_3 = 0.99$ (b) regimes of the four-vertex linear graph shown in Fig. 6a. In the regular regime (a), the average staircase function $\bar{N}(k)$ pierces every step of $N(k)$. This is not the case in (b), characteristic of the irregular regime.

and the Dirichlet boundary conditions at the dead ends V_1 and V_4. In this case, spectral equation (3.6) is given by

$$\cos(kS_0 - \pi\gamma_0) = a_1\cos(kS_1 - \pi\gamma_1) + a_2\cos(kS_2 - \pi\gamma_2) + a_3\cos(kS_3 - \pi\gamma_3), \tag{5.14}$$

where

$$a_1 = \frac{\lambda_2^0}{\sqrt{4 + (\lambda_2^0)^2}}, \quad a_2 = \frac{\lambda_3^0}{\sqrt{4 + (\lambda_3^0)^2}}, \quad a_3 = \frac{\lambda_2^0\lambda_3}{\sqrt{[4 + (\lambda_2^0)^2][4 + (\lambda_3^0)^2]}}, \tag{5.15}$$

and

$$\gamma_0 = \frac{1}{\pi}\arcsin\left(\frac{\lambda_2^0\lambda_3^0 - 4}{\sqrt{[4 + (\lambda_2^0)^2][4 + (\lambda_3^0)^2]}}\right), \quad \gamma_1 = \frac{1}{\pi}\arcsin a_2, \quad \gamma_2 = \frac{1}{\pi}\arcsin a_1, \quad \gamma_3 = \frac{1}{2}. \tag{5.16}$$

The sum of the amplitudes in (5.15) ranges between 0 and 3, and therefore, this system has regular and irregular regimes. The regular regime corresponds to a finite area in the $(\lambda_2^0, \lambda_3^0)$ parameter space. All linear chain graphs with a finite number of vertices and the Dirichlet boundary conditions at the two dead-end vertices at the beginning and at the end of the graph have a finite-measure regular regime and an irregular regime. This fact is proved in [10].

Graphs of a new type are marginal quantum graphs. A marginal quantum graph is defined by

$$\sum_{i=1}^{N_\Gamma} |a_i| = 1. \tag{5.17}$$

For marginal quantum graphs, apart from a small set of "special" graphs, explicit spectral formulas still exist. Explicit examples are provided by circular graphs (see Example 6) and star graphs (see Example 7).

Example 6: Scaling step potential in a box with periodic boundary conditions. This system is identical with the two-vertex circular graph shown in Fig. 8. In the case of a circular graph, a minor notational problem arises because starting from a vertex V_1; e.g., the vertex V_2 can be directly reached via two different bonds. For the purposes of this example, we solve the problem as follows. We first introduce a positive sense of rotation, i.e., mathematically positive, or counterclockwise, for

the circular graph in Fig. 8. We then introduce the scaling coefficient β_{12} referring to the bond that connects the vertex V_1 with the vertex V_2 traversing the graph in the mathematically positive sense. We introduce the scaling coefficient β_{21} that refers to the bond connecting V_2 with V_1, again in the mathematically positive sense. We use the same notation for the two reduced actions S_{12}^0 and S_{21}^0 referring to the two different bonds (in the mathematically positive sense), respectively. This notation is not confusing here, because no magnetic field is switched on ($A_{ij} = 0$). With this notation, the spectral equation is given by

$$\cos(kS_0) = a_1 + a_2\cos(kS_2), \tag{5.18}$$

where

$$S_0 = S_{12}^0 + S_{21}^0, \quad S_1 = S_{12}^0 + S_{21}^0, \qquad a_1 = \frac{4\beta_{12}\beta_{21}}{(\beta_{12}+\beta_{21})^2}, \tag{5.19}$$

and

$$a_2 = \left(\frac{\beta_{12}-\beta_{21}}{\beta_{12}+\beta_{21}}\right)^2. \tag{5.20}$$

We note that $a_1 + a_2 = 1$. Condition (5.17) is satisfied and the circular quantum graph with a scaling step potential is marginal.

Although the strict inequality in Eq. (3.8) is violated, it is important to note that, even in the marginal case, the separating points $\hat{k}_n$ are still not solutions to (5.18) in general. This occurs only for special parameter combinations and, therefore, for special quantum graphs for which the equation

$$(-1)^{n+\mu+1} = a_1 + a_2\cos(\hat{k}_n S_2) \tag{5.21}$$

is exactly satisfied for some n. Because the sequence $\hat{k}_n$ is countable and Eq. (5.21) involves irrational frequency ratios and irrational coefficients in general, this equation is only accidentally satisfied for some n for a measure zero set of graph parameters. Hence, in general, even for marginal quantum graphs, the points $\hat{k}_n$ still serve as separating points and the roots of the spectral equation can still be obtained via expansion (4.3).

Example 7: Star graph. Another example of a marginal quantum graph is provided by the star graph shown in Fig. 9. We consider the case with three different scaling potentials on its three bonds and the Dirichlet boundary conditions at the three dead ends. The spectral equation is given by

$$\cos(S_0 k) = a_1\cos(S_1 k) + a_2\cos(S_2 k) + a_3\cos(S_3 k), \tag{5.22}$$

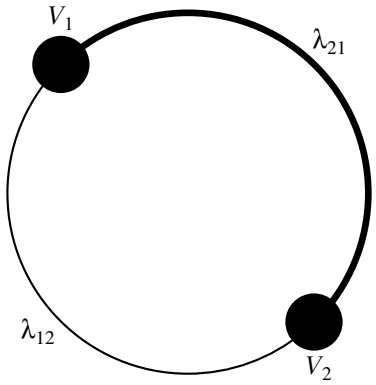

Fig. 8. Two-vertex circular graph. In the mathematically positive sense, β_{12} is the scaling coefficient of the bond connecting the vertex V_1 with the vertex V_2, β_{21} is the scaling coefficient of the bond connecting V_2 with V_1. This labeling is possible only in the absence of a magnetic field ($A_{ij} = 0$), where the sense of traversal of a bond is irrelevant.

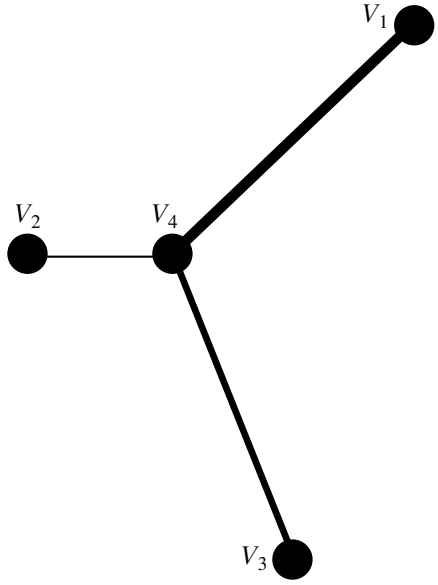

Fig. 9. Scaling star graph with three bonds and four vertices.

where

$$S_0 = S_{14}^0 + S_{24}^0 + S_{34}^0, \quad S_1 = S_{14}^0 - S_{24}^0 + S_{34}^0, \quad S_2 = S_{14}^0 - S_{24}^0 - S_{34}^0, \quad S_3 = S_{14}^0 + S_{24}^0 - S_{34}^0, \tag{5.23}$$

and

$$a_1 = \frac{\beta_{14}-\beta_{24}+\beta_{34}}{\beta_{14}+\beta_{24}+\beta_{34}}, \quad a_2 = \frac{-\beta_{14}+\beta_{24}+\beta_{34}}{\beta_{14}+\beta_{24}+\beta_{34}}, \quad a_3 = \frac{\beta_{14}+\beta_{24}-\beta_{34}}{\beta_{14}+\beta_{24}+\beta_{34}}. \tag{5.24}$$

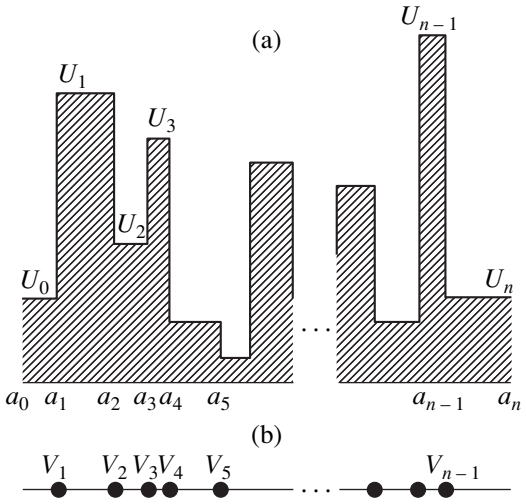

Fig. 10. Sketch of a piecewise constant potential ("Manhattan potential") (a) and its associated linear graph (b).

It is straightforward to verify that

$$\sum_{i=1}^{3} |a_i| = 1$$

independently of the sign of each a_i in (5.24). Condition (5.17) is therefore satisfied, and the star graph shown in Fig. 9 is another example of a marginal quantum graph. As discussed in the context of Example 6, with the exception of a set of measure zero of the star-graph parameter space, spectral expansion (4.3) is still valid and can be used to obtain each of the star-graph eigenvalues individually and independently of all the other eigenvalues.

6. SUMMARY, DISCUSSION, AND CONCLUSIONS

Exact periodic orbit expansions for the global density of states are known for many chaotic systems [15, 32, 33], However, Eq. (4.3) is the first example of an explicit expression for the individual quantum-mechanical levels obtained as a function of the level index n for a classically chaotic system. Additional explicit quantization formulas may be found for other quantum graph systems or even for quantum systems unrelated to quantum graphs as long as two essential requirements are fulfilled. First, an exact periodic orbit expansion for the density of states must exist. Second, it must be determined that one of the system levels, k_*, is the only one in an interval $\hat{k}'_* < k_* < \hat{k}''_*$. Then one can always obtain the corresponding periodic orbit expansion for k_*,

$$k_* = \int_{\hat{k}'_*}^{\hat{k}''_*} k\rho(k)dk, \qquad (6.1)$$

based on the periodic orbit expansion for $\rho(k)$.

It is reasonable to expect that generically there exist separating points $\hat{k}'_*$ and $\hat{k}''_*$ that separate every k_* from its neighbors, such that k_* is the only root of the spectral equation in the interval $[\hat{k}'_*, \hat{k}''_*]$. Hence, expansions similar to (4.3) do exist in general. However, knowing the positions of the separators k'_* and k''_* around a particular level k_* does not help finding the separators for the other levels. The most important task in obtaining a general expression for all the levels of a quantum chaotic system is therefore to find a global function for the separating points similar to (3.10), which naturally enumerates the separators. Therefore, even though it might be possible to find the separators for a particular quantum level k_* for some systems and then to obtain a periodic orbit expansion for this level in accordance with (6.1), the expansion would work only for the level k_* and would not represent a formula that can be used to obtain other levels.

The problem of finding a global expression for the separating points as a function of their ordering index n is directly related to another well-known problem of spectral theory of differential operators, namely, the problem of approximating staircase function (2.17) by a smooth average $\bar{N}(k)$. Indeed, suppose that there exists a separating point $\hat{k}'_n$, i.e., a solution of the equation

$$\bar{N}(\hat{k}') = N(k), \qquad (6.2)$$

between every two roots of the spectral equation (similar to (3.20) and (3.21)). Because $\bar{N}(k)$ is a monotonic function, the separating points can then be found by inverting Eq. (6.2),

$$\hat{k}_N = k(N), \qquad (6.3)$$

where the value of the staircase function plays the role of the separator index $\hat{k}_N$. Equation (6.3) generalizes Eq. (3.10), which can be used in (6.1) to obtain the periodic orbit expansions for all the roots.

The smooth curve defined by (6.3) with N considered a continuous variable intersects every stair of spectral staircase function (2.17). Unfortunately, finding a smooth function that approximates the spectral staircase function for a general differential operator with generic boundary conditions is a rather complicated task. It was proven by Weyl in 1912 that one can

approximate $\bar{N}(k)$ by the phase-space volume of the system in question,

$$\bar{N}(E) \approx \int \Theta(E - H(x, p)) \frac{d^D x d^D p}{(2\pi\hbar)^D}, \tag{6.4}$$

where D is the dimensionality of the phase space; however, this average is certainly not guaranteed to satisfy the "piercing average" condition (6.2). Since Weyl, this problem has been addressed by numerous researchers (see, e.g., [34]), who succeeded in giving many improved estimates for $\bar{N}(k)$ but none of them a priori satisfy (6.2).

The important feature of the regular quantum graph systems is that there exists a global piercing average (3.10), which uniformly enumerates all the points separating one root from another, and it is therefore possible to obtain formula (4.3) as a function of the index n. In other words, the index n in (4.3) is a quantum number, and expression (4.3) for the energy levels of a chaotic system in terms of classical periodic orbits can therefore be considered as a nonintegrable analogue of the EBK quantization scheme [11, 12].

It should be mentioned that, despite the existence of a quantum number n in (4.3), the actual dependence of the energy levels on the value of its quantum number is quite different from the simple EBK scheme for integrable systems. The expansion of the fluctuating part of roots (3.11) involves an intricate, conditionally convergent series and is rather "chaotic." The difference in complexity of formulas (4.3) and the EBK formula apparently reflects the complexity of the geometry of the periodic orbits of the classically chaotic quantum graphs.

ACKNOWLEDGMENTS

Yu. D. and R. B. gratefully acknowledge financial support by NSF grants PHY-9900730 and PHY-9984075; Yu. D. and R. V. J., by NSF grant PHY-9900746.

APPENDIX

For completeness, we here present a simple derivation of the spectral determinant in Eq. (2.8), starting from the boundary conditions at the vertex V_i,

$$\varphi_{ij}(x)\big|_{x=0} = \varphi_i C_{ij} \tag{A.1}$$

and

$$\sum_{j=1}^{N_V} C_{ij}\left(i\frac{d}{dx_{ij}} + A_{ij}\right)\psi_{ij}(x_{ij})\bigg|_{x=0} = \lambda_i \varphi_i. \tag{A.2}$$

We represent the wave function

$$\psi_{ij}(x) = \frac{1}{\sqrt{\beta_{ij}k}}(a_{ij}\exp(-i\beta_{ij}kx) + b_{ij}\exp(i\beta_{ij}kx)) \tag{A.3}$$

that satisfies these boundary conditions as a superposition of the partial waves

$$\varphi_{jj'}^{(i)}(x_j) = \delta_{jj'}\frac{\exp(i(-\beta_{ij}k + A_{ij})x_j)}{\sqrt{\beta_{ij}k}} + \sigma_{ji,ij'}\frac{\exp(i(\beta_{ij}k + A_{ij})x_j)}{\sqrt{\beta_{ij}k}} \tag{A.4}$$

scattering on the vertices of the graph. We thus have

$$\begin{aligned}\psi_{ij}(x_j) &= \sum_{j'=1}^{N_V} a_{ij'}\psi_{j,j'}^{(i)}(x_j) \\ &= \frac{a_{ij}}{\sqrt{\beta_{ij}k}}\exp(-i(\beta_{ij}k - A_{i,j})x_j) \\ &+ \frac{\exp(i(\beta_{ij}k + A_{i,j})x_j)}{\sqrt{\beta_{ij}k}}\sum_{j'=1}^{N_V} a_{ij'}\sigma_{ji,ij'},\end{aligned} \tag{A.5}$$

with the appropriate weights $a_{ij'}$ corresponding to the incoming flux on the bond $B_{j'i}$ towards the vertex V_i. Comparing this expression with (A.3) yields

$$b_{ij} = \sum_{j'=1}^{N_V} \sigma_{ji,ij'} a_{ij'}. \tag{A.6}$$

Substituting (A.5) into boundary conditions (A.1) and (A.2) at the vertex V_i, we obtain the respective relations

$$\sum_{j'=1}^{N_V} \frac{a_{ij'}}{\sqrt{\beta_{ij}k}}(\delta_{jj'} + \sigma_{ji,ij'}) = \varphi_i C_{ij} \tag{A.7}$$

and

$$\sum_{j,j'=1}^{N_V} C_{ij} a_{ij'}\sqrt{\beta_{ij}k}(\delta_{jj'} - \sigma_{ji,ij'}) = i\lambda_i \varphi_i. \tag{A.8}$$

Inserting (A.7) in (A.8), we obtain

$$\begin{aligned}C_{ij}\sum_{lj'=1}^{N_V} C_{il} a_{ij'}\sqrt{\beta_{il}k}(\delta_{lj'} - \sigma_{l,j'}^{(i)}) \\ = i\lambda_i \sum_{j'=1}^{N_V}\frac{a_{ij'}}{\sqrt{\beta_{ij}k}}(\delta_{jj'} + \sigma_{ji,ij'}).\end{aligned} \tag{A.9}$$

In the case of the linear scaling $\lambda_i = k\lambda_i^0$, this yields

$$\sum_{j'=1}^{N_V} a_{ij'} C_{ij} \sum_{l=1}^{N_V} C_{il}\sqrt{\beta_{il}}(\delta_{lj'} - \sigma_{li,\,ij'}) = i\lambda_i^0 \sum_{j'=1}^{N_V} \frac{a_{ij'}}{\sqrt{\beta_{ij}}}(\delta_{jj'} + \sigma_{ji,\,ij'}). \tag{A.10}$$

Comparing the coefficients in front of $a_{ij'}$, we obtain

$$C_{ij}\sum_{l=1}^{N_V} C_{il}\delta_{lj'}\sqrt{\beta_{il}} - C_{ij}\sum_{l=1}^{N_V} C_{il}\sqrt{\beta_{il}}\sigma^{(i)}_{l,\,j'} - i\lambda_i^0 \frac{\delta_{jj'}}{\sqrt{\beta_{ij}}} = \frac{i\lambda_i^0}{\sqrt{\beta_{ij}}}\sigma_{ji,\,ij'}, \tag{A.11}$$

or, after performing the summation over l,

$$C_{ij}C_{ij'}\sqrt{\beta_{ij'}} - C_{ij}\Gamma^i_{i,\,j'} - i\lambda_i^0 \frac{\delta_{jj'}}{\sqrt{\beta_{ij}}} = \frac{i\lambda_i^0}{\sqrt{\beta_{ij}}}\sigma_{ji,\,ij'}, \tag{A.12}$$

where

$$\Gamma^i_{i,\,j'} = \sum_{l=1}^{N_V} C_{il}\sqrt{\beta_{il}}\sigma_{li,\,ij'}.$$

Multiplying both sides by $C_{ij}\beta_{ij}$ and summing over j yields

$$\nu_i C_{ij'}\sqrt{\beta_{ij'}} - \nu_i\Gamma^i_{i,\,j'} - i\lambda_i^0 C_{ij'}\sqrt{\beta_{ij'}} = i\lambda_i^0\Gamma^i_{i,\,j'}, \tag{A.13}$$

where

$$\nu_i = \sum_j C_{ij}\beta_{ij}.$$

Hence,

$$\frac{\nu_i - i\lambda_i^0}{\nu_i + i\lambda_i^0} C_{ij'}\sqrt{\beta_{ij'}} = \Gamma^i_{i,\,j'}, \tag{A.14}$$

which can be used in (A.12) to obtain

$$C_{ij}C_{ij'}\sqrt{\beta_{ij'}} - C_{ij}\frac{\nu_i - i\lambda_i^0}{\nu_i + i\lambda_i^0} C_{ij'}\sqrt{\beta_{ij'}} - i\lambda_i^0 \frac{\delta_{jj'}}{\sqrt{\beta_{ij}}} = \frac{i\lambda_i^0}{\sqrt{\beta_{ij}}}\sigma_{ji,\,ij'} \tag{A.15}$$

or

$$\sigma_{ji,\,ij'} = \left(-\delta_{jj'} + \frac{2\sqrt{\beta_{ij}\beta_{ij'}}}{\nu_i + i\lambda_i^0}\right) C_{ji}C_{ij'}. \tag{A.16}$$

We see that, in the scaling case, the matrix elements $\sigma_{ji,\,ij'}$ of the vertex scattering matrix σ are k-independent constants.

The matrix element $\sigma_{ji,\,ij}$ has the meaning of the reflection coefficient from the vertex V_i along the bond B_{ij} and the elements $\sigma_{ji,\,ij'}$, $j \neq j'$ are the transmission coefficients for transitions between different bonds. Equation (A.6) can be written as

$$\mathbf{b} = \tilde{T}\mathbf{a}, \tag{A.17}$$

where

$$\tilde{T} \equiv \tilde{T}_{ij,\,nm} = \delta_{in}C_{ji}C_{nm}\sigma_{ji,\,im}. \tag{A.18}$$

In the symmetric basis $\psi_{ji}(L_{ij} - x) = \psi_{ij}(x)$, we have

$$\psi_{ji}(L_{ij} - x) = a_{ji}\frac{\exp[i(-\beta_{ij}k + A_{ji})(L_{ij} - x)]}{\sqrt{\beta_{ij}k}} + b_{ji}\frac{\exp[i(\beta_{ij}k + A_{ji})(L_{ij} - x)]}{\sqrt{\beta_{ij}k}} = \psi_{ij}(x), \tag{A.19}$$

and the coefficient a_{ij} and b_{ij} are therefore related as

$$a_{ji} = b_{ij}\exp[i(\beta_{ij}k + A_{ij})L_{ij}], \qquad b_{ji} = a_{ij}\exp[i(-\beta_{ij}k + A_{ij})L_{ij}]. \tag{A.20}$$

The coefficients a_{ij} and a_{ji} (b_{ij} and b_{ji}) are considered to be different, and the bonds of the graph are therefore "directed."

Equations (A.20) can be written in the matrix form

$$\mathbf{a} = P\tilde{D}(k)\mathbf{b}, \tag{A.21}$$

where $\mathbf{a}$ and $\mathbf{b}$ are $2N_B$-dimensional vectors of coefficients and $\tilde{D}$ is a diagonal matrix in the $2N_B \times 2N_B$ space of directed bonds,

$$\tilde{D}_{ij,\,pq}(k) = \delta_{ip}\delta_{jq}\exp[i(\beta_{ij}k + A_{ij})L_{ij}], \tag{A.22}$$

and

$$P = \begin{pmatrix} 0 & 1_{N_B} \\ 1_{N_B} & 0 \end{pmatrix}, \tag{A.23}$$

where 1_{N_B} is the N_B-dimensional unit matrix. The pairs of indices (ij), (pq) identifying the bonds of the graph Γ play the role of the indices of the matrix $\tilde{D}(k)$.

Equations (A.21) and (A.17) together result in

$$\mathbf{a} = S(k)\mathbf{a}, \tag{A.24}$$

with the matrix $S(k)$ (the total graph scattering matrix) given by

$$S(k) = D(k)T, \tag{A.25}$$

where $D = P\tilde{D}P$ and $T = P\tilde{T}$.

REFERENCES

1. L. D. Landau and E. M. Lifshitz, *Course of Theoretical Physics*, Vol. 3: *Quantum Mechanics: Non-Relativistic Theory* (Nauka, Moscow, 1989, 4th ed.; Pergamon, New York, 1977, 3rd ed.).
2. A. Messiah, *Quantum Mechanics* (North-Holland, Amsterdam, 1961; Nauka, Moscow, 1978).
3. S. Flügge, *Practical Quantum Mechanics* (Springer-Verlag, Berlin, 1999).
4. R. Blümel, Yu. Dabaghian, and R. V. Jensen, submitted to Phys. Rev. Lett.
5. Yu. Dabaghian, R. V. Jensen, and R. Blümel, Pis'ma Zh. Éksp. Teor. Fiz. **74**, 258 (2001) [JETP Lett. **74**, 235 (2001)].
6. R. Blümel, Yu. Dabaghian, and R. V. Jensen, submitted to Phys. Rev. E.
7. H. Bohr, *Almost Periodic Functions* (Chelsea, New York, 1951).
8. H. Friedrich, *Theoretical Atomic Physics* (Springer-Verlag, Berlin, 1990).
9. H.-J. Stöckmann, *Quantum Chaos* (Cambridge Univ. Press, Cambridge, 1999).
10. R. Blümel, Yu. Dabaghian, and R. V. Jensen, *Mathematical Foundations of Regular Quantum Graphs*, in preparation.
11. M. Gutzwiller, *Chaos in Classical and Quantum Mechanics* (Springer-Verlag, New York, 1990).
12. J. B. Keller, Ann. Phys. (N.Y.) **4**, 180 (1958).
13. R. I. Szabo, hep-th/9608068.
14. M. V. Berry, in *New Trends in Nuclear Collective Dynamics*, Ed. by Y. Abe, H. Huriuchi, and K. Matsuyanagi (Springer-Verlag, Berlin, 1991), Springer Proc. Phys., Vol. 58, p. 177.
15. J.-P. Roth, in *Théorie du Potentiel*, Ed. by A. Dold and B. Eckmann (Springer-Verlag, Berlin, 1984), Lect. Notes Math., Vol. 1096, p. 521.
16. T. Kottos and U. Smilansky, Phys. Rev. Lett. **79**, 4794 (1997); Ann. Phys. (N.Y.) **274**, 76 (1999).
17. M. Pascaud and G. Montambaux, Phys. Rev. Lett. **82**, 4512 (1999).
18. H. Schanz and U. Smilansky, Phys. Rev. Lett. **84**, 1427 (2000).
19. Y. Dabaghian, R. V. Jensen, and R. Blümel, Phys. Rev. E **63**, 066201 (2001).
20. Y. C. Lai, C. Grebogi, R. Blümel, and M. Ding, Phys. Rev. A **45**, 8284 (1992).
21. M. Keeler and T. J. Morgan, Phys. Rev. Lett. **80**, 5726 (1998).
22. V. I. Arnold and A. Avez, *Ergodic Problems of Classical Mechanics* (Addison-Wesley, Redwood City, 1989).
23. V. I. Arnold, *Mathematical Methods of Classical Mechanics* (Springer-Verlag, New York, 1997).
24. E. Akkermans, A. Comtet, J. Desbois, *et al.*, cond-mat/9911183.
25. F. Barra and P. Gaspard, Phys. Rev. E **63**, 066215 (2001).
26. R. E. Prange, E. Ott, T. M. Antonsen, *et al.*, Phys. Rev. E **53**, 207 (1996).
27. R. Blümel, T. M. Antonsen, Jr., B. Georgeot, *et al.*, Phys. Rev. Lett. **76**, 2476 (1996); Phys. Rev. E **53**, 3284 (1996).
28. L. Sirko, P. M. Koch, and R. Blümel, Phys. Rev. Lett. **78**, 2940 (1997).
29. U. Smilansky, in *Chaos et Physique Quantique–Chaos and Quantum Physics: Les Houches Session LII, 1989*, Ed. by M.-J. Giannoni, A. Voros, and J. Zinn-Justin (Elsevier, Amsterdam, 1991), p. 371.
30. R. Courant and D. Hilbert, *Methods of Mathematical Physics* (Interscience, New York, 1953).
31. R. Blümel and Yu. Dabaghian, submitted to J. Math. Phys.
32. A. Selberg, J. Indian Math. Soc. B **20**, 47 (1956); in *Atle Selberg: Collected Works* (Springer-Verlag, Berlin, 1989), Vol. 1, p. 423.
33. K. G. Anderson and R. B. Melrose, Invent. Math. **41**, 197 (1977).
34. H. P. Baltes and E. R. Hilf, *Spectra of Finite Systems* (Bibliographisches Institut AG, Zürich, 1976).